Mark J. Jackson · Waqar Ahmed *Editors*

Micro and Nanomanufacturing Volume II

Springer

Micro and Nanomanufacturing Volume II

Mark J. Jackson • Waqar Ahmed
Editors

Micro and Nanomanufacturing Volume II

Springer

Editors
Mark J. Jackson
School of Interdisciplinary Studies
Kansas State University
Manhattan, KS, USA

Waqar Ahmed
School of Mathematics and Physics
University of Lincoln
Lincoln, UK

ISBN 978-3-319-67130-7 ISBN 978-3-319-67132-1 (eBook)
DOI 10.1007/978-3-319-67132-1

Library of Congress Control Number: 2006932032

Printed on acid-free paper

This Springer imprint is published by Springer Nature
The registered company is Springer International Publishing AG
The registered company address is: Gewerbestrasse 11, 6330 Cham, Switzerland

Contents

Chapter 1
Aligned Nanowire Growth

V. Cientanni, W.I. Milne, and M.T. Cole

With many thousands of different varieties to date, the nanowire (NW) library continues to grow at pace. With the continued and hastened maturity of nanotechnology, significant advances in materials science have allowed for the rational synthesis of a myriad of NW types of unique electronic and optical properties, allowing for the realisation of a wealth of novel devices, whose use is touted to become increasingly central in a number of emerging technologies. Nanowires, structures defined as having diameters between 1 and 100 nm, provide length scales at which a variety of inherent and unique physical effects come to the fore [1], phenomena which are often size suppressed in their bulk counterparts [2–4]. It is these size-dependent effects that have underpinned the growing interest in the growth and fabrication, at ever more commercial scales, of nanoscale structures. Nevertheless, many of the intrinsic properties of such NWs become largely smeared and often entirely lost, when they adopt disordered ensembles. Conversely, ordered and aligned NWs have been shown to retain many such properties, alongside proffering various new properties that manifest on the micro- and even macroscale that would hitherto not occur in their disordered counterparts.

V. Cientanni and M.T. Cole contributed equally to this work.

V. Cientanni
Electrical Engineering Division, Department of Engineering, Cambridge University, Cambridge, UK

W.I. Milne
Electrical Engineering Division, Department of Engineering, Cambridge University, Cambridge, UK

Quantum Nanoelectronics Research Center, Tokyo Institute of Technology, Okayama, Tokyo, Japan

M.T. Cole (✉)
Department of Electronic & Electrical Engineering, University of Bath, Bath, UK
e-mail: M.T.Cole@bath.ac.uk

M.J. Jackson, W. Ahmed (eds.), *Micro and Nanomanufacturing Volume II*,
DOI 10.1007/978-3-319-67132-1_1

Nanotechnology is already beginning to present itself as a catalyst for change in many industries and commercial sectors, from nanoparticles in sunscreen [5] to nanotube-infused composites in bicycles [6]. Industries are increasingly commercialising nanomaterials, principally because of the opportunities that occur by downsizing existing microstructures and also because of the many advantages that nanostructures afford. The electronics industry is perhaps one of the best examples of how nanostructures have revolutionised computing. Moore's Law [7] captured the near-annual exponential performance gains from computer processing power, but this stimulus has also demanded increased storage capacity and high-resolution displays, alongside reduced power consumption. All of these aspects of computing have benefited from nanotechnology and the continued miniaturisation to the current 14-nm node due to progressive improvements in top-down conventional Si processing procedures. Almost exclusively, across all technologies, the continued quest for performance improvements rests on engagement with increasingly miniaturised engineering.

NW alignment remains a critical component in the development chain. Alignment underpins much of the success of NW integration into many devices, particularly in the electronics and optics industries. More complicated structures, with potential 3D integration thereafter, such as vertical field-effect transistors [8], room temperature UV nanowire lasers [9], integrated circuits [10], solar cells [11], displays [12] and biosensors [13], have all been shown to benefit greatly from alignment of their consistent nanocomponents. Although the amorphous, disorder ensemble growth of 1D nanostructures has been well documented [14], the focus of this chapter is on the aligned growth of NWs.

Aligned 1D nanostructures, wires, belts, rods and tubes [15], are herein termed NWs. NWs have been extensively studied these past two decades, with particular attention given to carbon nanotubes (CNTs) [16] and semiconducting NWs [17]. Though free-standing-aligned NWs have been reported [18], most practical applications of aligned nanostructures typically require a substrate on to which to adhere and are therefore either grown aligned directly on the substrate (in situ) or are aligned post-growth (ex situ) [19]. Broadly, alignment is either perpendicular (vertical) or parallel (horizontal) to the substrate plane. The reproducible production of horizontally aligned NWs has proven particularly challenging, principally due to the nature of the growth processes involved [20]. The vast wealth of literature on CNTs however, both vertically and horizontally aligned (VA-CNTs and HA-CNTs), warrants dedicated discussion which we will consider latterly in the chapter. Nanostructure alignment methods tend to vary between material types, with similar methods (such as chemical vapour deposition, CVD) differing, often dramatically so, between materials. This chapter does not aim to provide a concise overview of the varied nanomaterial production processes; such a review would be prohibitive in scope. Rather, here we discuss the vertical alignment of the three key NW classes that are central to the fabrication of field-effect transistors, namely, NWs that are either metallic, semiconducting or insulating. We also consider the newly emerging class of inorganic NWs, alongside the more established organic NW family (viz. the carbon nanotubes and nanofibres). In each class we consider

only the most common NW types. For the outlined NW types, we explore the production methods, as well as examining the principle growth mechanisms, the degree of alignment and linear packing densities associated with each.

Following the seminal NW synthesis studies in the late 1990s, various growth kinetics have since been reported. Though a great many varied growth models have been proposed, the most popular growth methods typically adopt vapour–liquid–solid (VLS) growth-based approaches. Traditionally, this mechanism involves three components, a substrate (upon which the NWs are grown), a catalyst (which mediates NW nucleation) and a precursor media (which serves as the NW feedstock). To best outline a general NW growth, here we overview the growth of Si NWs, a prototypical system whose general process flow is, at least in part, applicable to most currently available NW types. In most cases, standard crystalline Si substrates are employed as the growth support, with, in the case of Si NW growth, a gold catalyst deposited by physical vapour deposition (often by sputtering, thermal or electron beam deposition techniques) onto its surface. By increasing the temperature to the substrates eutectic point, a surface alloying between the Au-Si occurs, and the resulting phase becomes liquid. In the case of Si NWs, the precursor gas is typically silicon tetrachloride ($SiCl_4$) or silane (SiH_4). These gaseous molecules disassociate into their constituent components on contact with the liquid catalyst. The liquid catalyst, following some process-specific critical time, becomes supersaturated with dissociated Si. Precursor disassociation continues despite the supersaturated liquid catalyst, resulting in the extrusion or 'freezing' out formation of crystalline Si NWs [21].

CVD and functionally similar reactors are some of the most popular methods for implementing Si NW growth [22–24]. Unconventional VLS has also been demonstrated via oxide-assisted growth, where oxides play an important role in the nucleation and growth instead of more conventional metallic catalysts [25]. The field continues to grow. With ever finer in situ metrology being reported, a greater understanding of the growth kinetics is coming increasingly into focus. Other growth mechanisms for Si NWs have been reported, analogous to the VLS mechanism is the solid-liquid-solid (SLS) and vapour–solid–solid (VSS) growth mechanisms [26, 27]. Figure 1.1 illustrates the key features of the VLS and VSS growth mechanisms.

1.1 Metallic NWs

A wide range of metallic NWs have been produced to date. Of the more than 90 metallic elements, only around 20% have been synthesised into pure metallic NWs, including Ni [28], Co [29], Cu [30], Fe [31], Ni [32], Mo [33], Al [34], Au [35], Ag [36], Zn [37], Sn [38], Na [39] and Mg [40]. A similarly wide variety of alloyed NWs have also been reported, with Ni variants dominating this space, including NiCo [41], NiTi [42], NiAu [43], NiCu [44], PtCu [45], $In_xGa_{1-x}P$ [46] and YFe [47]. Though varied, of these alloyed and pure metallic NWs, it is gold and

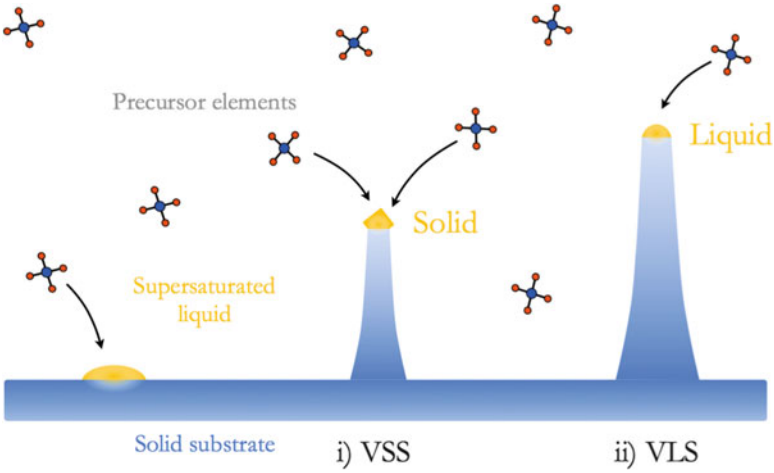

Fig. 1.1 *NW Growth*. Scheme depicting vapour–solid–solid (VSS) and vapour–liquid–solid (VLS) growth regimes. (i) VSS growth occurs at typically lower temperature with a solid catalyst forming on the nanowire tip, whilst (ii) VLS occurs at higher temperature, with the catalyst in the liquid phase

silver NWs that have gleaned perhaps the most attention, in part due to their particularly high electrical and thermal conductivities, facile self-assembly and biocompatibility, all of which have resulted in a breadth of applications, from microelectronics to biosensing [48, 49].

Gold NWs [35, 48–59] are typically prepared from either the self-assembly of gold nanoparticles (bottom-up approach) or from the downscaling or etching of larger systems (top-down approach). The former is typically more popular due to its practicality and scalability and can involve either templated or template-less methods to produce aligned NWs. Here such templates control the NWs direction of growth, often using a porous membrane which serves as a rigid aligning scaffold. There are many soft and hard template methods [52, 56]; however, for aligned gold NWs, hard templates are almost invariably used. A porous anodic aluminium oxide (AAO) or polycarbonate (PC) template is submerged in a solution containing gold nanoparticles which are electrochemically deposited to form NWs [35, 53, 55, 57]. The template is subsequently removed, via etching techniques, leaving vertically aligned NWs. Figure 1.2a shows a typical scanning electron micrograph of vertically aligned Au NWs. Some of the most aligned and densely packed NW forests have been generated by patterning the substrate with either catalysts or pores in some way to introduce isometry to what is an otherwise inherently anisotropic substrate on an atomic level.

Another popular method for synthesising gold NWs is by dielectrophoresis. By applying a potential difference across two electrodes submerged within a gold-containing solution (such as $HAuCl_4$ in n-hexane), NWs grow between the contact electrodes [58, 59]. This powerful method allows accurate control over the macro-scale shape of the NWs with the NW placement dictated by the plating solution.

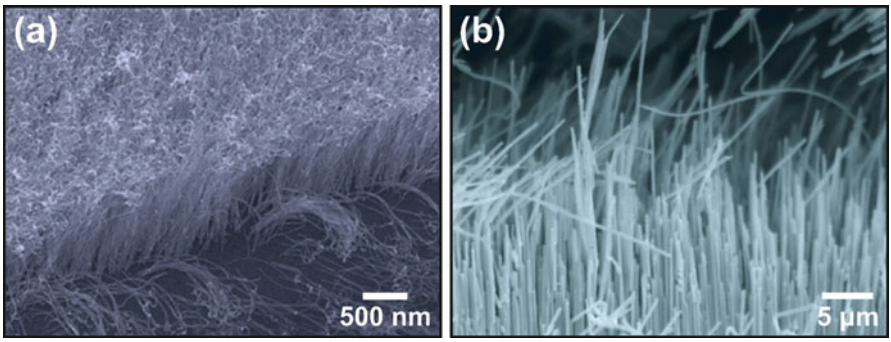

Fig. 1.2 *Metallic NWs*. Example scanning electron micrographs of (**a**) Au NW growth in a polar solution of 4-mercaptobenzoic acid and Au seeds anchored on oxide substrates to catalyse growth of vertically aligned ultrathin Au NWs with 6 nm diameter [51]. (Scale bar, 500 nm) (Copyright American Chemical Society, 2013). (**b**) Ag NW arrays demonstrating concurrent high aspect ratio and high packing density, produced using potentiostatic electrodeposition within confined nanochannels of a commercial porous anodic aluminium oxide (AAO) template [64] (Scale bar, 5 μm) (Copyright Elsevier, 2009)

Nevertheless, the growth of individual NWs is often sporadic, with little to directionality in their growth. The spacing between electrodes has been shown to affect the areal packing density and the degree of alignment. Closely spaced electrodes tend to produce higher degrees of alignment. Higher voltages tend to decrease the time required to align the NWs but also stimulate the formation of larger Au nanoparticles and polycrystalline NWs.

Silver NWs [36, 60–70] have also been widely researched with fervour. Of all the transition metals, silver offers one of the highest electrical conductivities, whilst concurrently exhibiting excellent thermal transport. Figure 1.2b shows a typical scanning electron micrograph of vertically aligned Ag NWs. Nanostructured silver surfaces have also been shown to mediate enhanced Raman scattering for the identification and study of surface-bound molecules, and they have subsequently become particularly attractive as mediators for surface-enhanced Raman spectroscopy. Many methods exist to produce silver NWs. As with gold, silver NW synthesis can be broadly subdivided into template-assisted or template-less methods. The templates are often hard, porous structures, such as polymers, silicon wafers and anodic aluminium oxide (AAO), whereas template-less approaches follow a ‘soft solution’ method, involving the surfactant-assisted reduction of silver oxide with platinum seeds (termed the polyol method) [36, 60].

1.2 Semiconducting NWs

Since some of the first studies on the synthesis of nanowhiskers by Hitachi in the early 1990s [71], the field of semiconducting NW growth has developed at an unusually fast pace. Including direct and indirect, as well as pure and compound,

there are more than 130-bulk semiconducting systems known. Of these, but a few semiconducting NWs—including single component, compound, functional oxides, nitrides and carbides—have been synthesised, including IV–IV Group, Si [72], Ge [73] and $Si_{(1-x)}Ge_x$; III–V Group (binary), InP [74], lnAs [71], GaAs [75] and GaP [76]; III–V Group (ternary), $Ga(As_{(1-x)}P_x)$ [77], $ln(As_{(1-x)}P_x)$ [78], $(Ga_{(1-x)}ln_x)P$ [79], $(Ga_{(1-x)}ln_x)As$ [80] and $(Ga_{(1-x)}ln_x)(As_{(1-x)}P_x)$ [81]; II–VI Group (binary), ZnS [82], ZnSe [83], CdS [84] and CdSe [85]; IV–VI Group (binary), PbSe [86], Bi_2Te_3 [87] and PbTe [87]; as well as the nitrides and carbides, GaN [88], Si_xN_y [89] and SiC [90] and the functional oxides, ZnO [37], TiO_2 [91], SnO_2 [92], CuO [93] and In_2O_3 [94]. Of these, Si has been at the centre of study for many decades and represents a prototypical growth system on which many of the latterly demonstrated alloyed NWs have been based.

Si NWs [17, 21–27, 72, 95–105] have been researched for nearly 60 years; although in truth, the wires produced in 1957 by Treuting et al. were not what we would now strictly classify as NWs due to their overly large diameter [98]. Following a hiatus in research, a reinvigorated research community gave rise to a sprawl of publications since the turn of the millennium, principally in light of advances in ever more miniaturised microelectronics. Morales et al., in 1998, published one of the first reports on truly nanoscale Si NW [100], introducing controlled laser ablation to the wider materials community. Today Si NWs are still extensively researched due to their potential use in computing and microelectronic applications. Aside from CVD, other reported experimental growth systems for the synthesis of aligned Si NWs include reactive atmospheric annealing [105], evaporation of SiO [99], solution-based [72] and laser ablation [95]. Figure 1.3a shows a typical scanning electron micrograph of vertically aligned Si NWs.

Due to its high compatibility with Si-based technologies, Ge has also been researched at length. Figure 1.3b shows a typical scanning electron micrograph of vertically aligned Ge NWs. Ge has some important advantages over Si, in particular it's higher charge carrier mobility and larger Bohr exciton radius. Ge NWs have been successfully integrated in lithium-ion batteries [106], field-effect transistors [107], computing memory [108] and many optoelectronic applications [109]. Based on established VLS kinetics, Ge is typically synthesised using systems similar to those used for Si, with CVD and MO-CVD dominating this space, along with molecular beam epitaxy (MBE), and template methods being some of the most popular techniques.

Together with the arguably more conventional Si and Ge, ZnO is one of the most widely studied semiconducting NWs due to its wide band gap, high electron mobility, high room temperature luminescence and high optical transparency [37]. ZnO has been favoured for photodetectors and sensors to, more recently, UV lasers. Figure 1.3c shows a typical scanning electron micrograph of vertically aligned ZnO NWs. Typical production methods include thermal evaporation, MO-CVD (metal-oxide assisted), high-pressure laser ablation and aqueous synthesis (including hydrothermal). Sol–gel processes have also been demonstrated. Typically used for the fabrication of metal oxides of Si and Ti, sol–gel approaches have proven to be extremely popular. Here monomers are converted into a colloidal

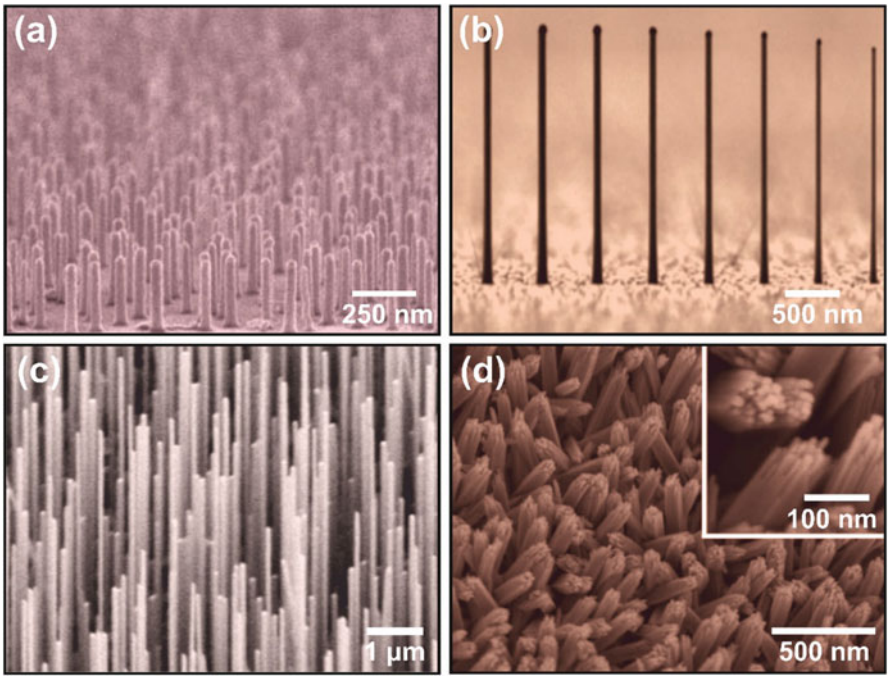

Fig. 1.3 *Semiconducting NWs*. Example scanning electron micrographs depicting the (**a**) effect of growth temperature on the tapering of Si NWs by epitaxial vapour–solid–solid growth via Al-catalysis [27]. (Scale bar, 250 nm) (Copyright Nature Publishing Group, 2006). (**b**) A linear array of Ge NWs grown from lithographically patterned Au catalyst dots. Note the systematic reduction in NW length with decreasing diameter (*left* to *right*) [191] (Scale bar, 3 µm) (Copyright ACS Publications, 2010). (**c**) VLS growth of highly aligned vertical ZnO NWs, grown using a 5 nm Au catalyst [192] (Scale bar, 500 nm) (Copyright Hindawi Publishing Corporation, 2012). (**d**) A scanning electron micrograph of TiO_2 NWs grown in an atmospheric glass vessel, using 0.3 mL $TiCl_3$ and 15 g lauric acid [114] (Scale bar, 1 µm) (Copyright Nature Publishing Group, 2015)

diphase solution which is a precursor for a generated particulate/polymer network, termed the 'gel'. In order to form aligned NWs, in situ, this method is often combined with AAO or similar hard templating techniques [110]. The comparatively low-cost and simple experimental setups associated with hydrothermal and sol–gel techniques have made them especially prevalent in growing research communities.

Wide band gap TiO_2 NWs have shown varied unique solid state chemical and physical properties. Their applications range from electrodes in lithium-ion batteries and fuel cells to hydrogen production and containment, photovoltaics and supercapacitors [111, 112].

Titanium dioxide is generally compatible with CVD, electrochemical tempting and solvo−/hydrothermal techniques. Hydrothermal/solvothermal synthesis methods are normally performed in high-pressure stainless steel vessels

(or Teflon reactors) termed autoclaves. Using substrates such as indium tin oxide (ITO), Si/SiO_2 or glass, an aqueous solution is prepared, and the substrates submerged. The solution often contains a titanium precursor and a strong solvent such as hydrogen chloride. The experimental procedure requires a temperature higher than the boiling temperature of the solvent, which limits their safety and makes large-scale production challenging. Typical hydrothermal synthesis of TiO_2 nanowires requires high concentrations of either strongly base or strongly acidic environments, which results in equipment corrosion, produces volatile waste products and significant issues surrounding process safety, viability and scalability [91, 113].

Surface-limited reaction CVD is popular for TiO_2 synthesis; however, large-scale production has proven problematic due to the high melting point and very low vapour pressure of Ti. The resulting deposition window is small and selective, confining the crystalline nature of the formed NWs [111]. A novel method capable of achieving alignment with high packing densities has been reported, involving low temperature and atmospheric pressure mixing of titanium oxide with fatty acids. Self-hydrolysis, nucleation and crystallisation result in a sealed vial, at room temperature. The NWs can be easily fabricated by careful manipulation of the saturated fatty acids [114].

1.3 Dielectric NWs

Various dielectric nanowires have been reported, including MgO [115], Si_3N_4 [116], SiO_2 [117], Al_2O_3 [118], NiO [119–126], BN [127–136] and WO [137]. Figure 1.4 shows typical scanning electron micrographs of vertically aligned SiO_2 and Si_3N_4 NWs. Ambient pressure, high-temperature thermal annealing has been widely used to synthesise stoichiometric dielectric NWs. Of these Si_3N_4 and *a*-SiO_2 NWs have been demonstrated, with yields and morphologies which show a clear dependence on the flow rates of the gaseous reactants [116]. In the case of SiO_2 NWs, one-pot electrospinning is gaining significant traction due to its low cost and potentially high throughput [138]. Aerosol-mediated spontaneous SiO_2 NW growth via flame spray pyrolysis of organometallic solutions (hexamethyldisiloxane or tetraethyl orthosilicate) has shown potential, though low yields and scale-up issues make the approach otherwise commercially challenging; nevertheless, compatibility with a range of substrates has been suggested increasing the appeal of the approach [139]. Though various metal-catalysed growths are possible [140, 141], such systems pose clear limitations for the realisation of high dielectric constant NWs. Catalyst attrition during growth and sub-nm metallic remnants along the NWs length fundamentally limit the usefulness of these techniques in realising high purity dielectric NWs. Pure-metallic-catalyst-free carbothermal reduction of CuO powders under Ar/O_2 flow has been shown to be one possible approach, though extraneous SiC formation must be quenched if commercially viable purities and yield are to be achieved [142]. As with other

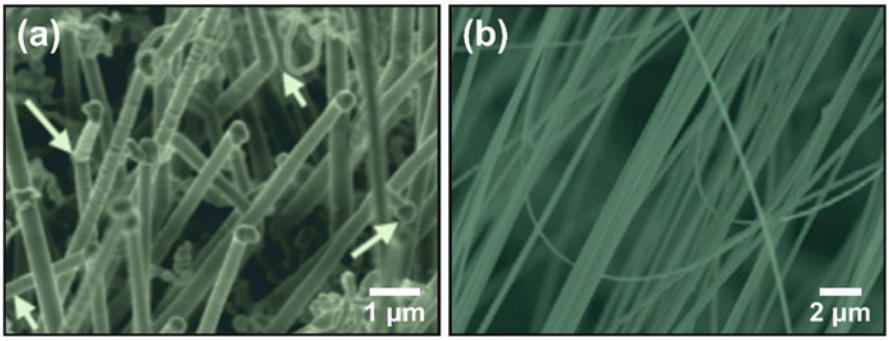

Fig. 1.4 *Dielectric NWs*. Example scanning electron micrographs of (**a**) CVD-synthesised aligned SiO_2 NWs [117] (Scale bar, 1 μm) (Copyright American Chemical Society, 2006). (**b**) Centimetre-long α-Si_3N_4 NWs by template-free pyrolysis of polymeric precursors [193]. (Scale bar, 2 μm) (Copyright Institute of Physics, 2008)

CVD process, though many varied catalysts have demonstrated catalytic potential, the yields of each are extremely varied, with, in most cases, metal catalysts producing some of the highest yields, clearly at the expense of the NWs dielectric properties. This issue similarly plagues SiO_2 NW growth; annealing of SiO catalysts on Si and subsequent growth via SLS proffer an attractive and entirely metal-free system, though extremely low areal yields and very poor alignment limit the approach.

1.4 Inorganic NWs

Inorganic molecular NWs have emerged as a new material with radically new functional properties, particularly molybdenum halide and the chalcogenide polymers, along with various other molybdenum chain-based variants. These 1D polymers behave distinctly from CNTs and other NWs, demonstrating anionic bridges with high strength, non-Newtonian mechanical properties and remarkably high Young's moduli [143]. Molecular NWs of the form $Mo_6 S_{9-x} I_x$ (herein MoSI) have been identified as some of the most promising within the wider NW family, with the ability to form bundles with air-stable single wire dispersions, high scalability and reproducibility [144–146].

Typically, MoSI molecular NWs are formed in a sealed and evacuated quartz ampoule, containing metallic Mo platelets, placed in a single zone furnace at approximately 1000 K, with some annealing the samples for up to 72 h. This creates fur-like NWs, with high mechanical strength and toughness [144, 147]. Bundles can have lengths of over 5 mm; however, shear and mechanical exfoliation of the bundles is simple due to the relatively low inter-wire Van der Waals forces. Alongside this furnace method, hydrothermal/solvothermal methods are also becoming increasingly routine for producing MoSI NWs, with reasonably high

alignment and high linear packing density. Another production route is via soft lithography using PDMS micromolds. Here, networks are created in which the NWs grow, between a substrate such as silicon or glass and the micromold. Dissolving single crystals of $LiMo_3Se_3$ in polar solvents, such as dimethyl sulfoxide or *N*-methylformamide, are then used to form individual MoSe NWs [148, 149]. The attainable packing density associated with these methods is limited by the resolution obtainable on the stamp between individual trenches. Nevertheless, such stamping techniques tend to produce NWs with excellent alignment as the NWs tend to form in the predetermined channels. Low packing densities are common, though high NW linearity and degree of alignment are often evidenced, with reasonable reproducibility compared to other methods, such as optical lithography which is otherwise well established and widely accepted.

1.5 Organic NWs

Carbon nanotubes (CNTs) are an important member of the NW family. CNTs are seamlessly bonded, rolled sheets of hexagonally latticed carbon atoms consisting of one or more cylindrically nested layers of graphene. Those CNTs consisting of one wall are termed single-walled carbon nanotubes (SWNTs), whilst those with more than one wall are termed multi-walled carbon nanotubes (MWNTs). Since the popularising paper of Iijima in 1991, CNTs have drawn much attention due to their incredible electrical and mechanical properties and wide-ranging potential commercial applications, including the use as electrical conductors, high strength composites, nanosized interconnects and electromagnet shielding (but to name a few) [16, 150]. For many of the mentioned applications, it is highly desirable to produce aligned CNTs (either vertically, VA-CNTs or horizontally, HA-CNTs). The production methods for aligned CNTs are diverse, yielding many different packing densities and degrees of alignment for each method. One of the most popular and scalable methods for producing VA-CNTs is via CVD, with many variants reported, such as water-assisted CVD (WA-CVD) [151], plasma-enhanced CVD (PE-CVD) [152] and photo thermal CVD [153].

Compared to the wider family of NWs, VA-CNTs typically present higher areal packing densities for comparable length scales, along with higher degrees of alignment. CNT forests also tend to be more uniform in nature compared to many other CVD-synthesised NW types. However, at a scale of 2–10 nm (the typical diameter of a SWNT), CNTs tend to afford much less local alignment. SWNTs tend to intertwine and wrap around one another, whereas the wider family of crystalline NWs discussed prior is much more aligned and maintains this alignment across all length scales. Unlike the CNTs, whose morphology can be sinuous and softly varying, any change in growth direction for the majority of NWs tends to be sharp, straight and angular. The issue with isolating individual CNTs and also the loss in the performance of bulk CNTs compared to single tubes currently limits their commercial viability and device performance. VA-CNTs also tend to have less

variance in the alignment and packing density compared to other NW types. This is likely attributed to the fact that CVD methods dominate the research landscape for the production of VA-CNTs, whilst nanowires can be produced with a plethora of methods all yielding different degrees of alignment and nanowire densities. It should also be mentioned that MWNT compared to SWNT tends to present a generally larger degree of vertical alignment and often does not present local spindling.

Horizontally aligned CNTs can be produced in bulk, post synthesis (often from VA-CNT forests), via ex situ alignment. In situ alignment corresponds to manifest directional control during growth. Focussing on in situ, as the literature presented in this chapter thus far has been exclusively directed towards growth methods and hence in situ techniques, there are a number of ways of horizontally aligning CNTs during growth. The three most popular methods used for in situ growth of HA-CNTs are graphoepitaxy (lattice guided), gas flow directed and electric or magnetic field alignment. The first of these methods exploits asymmetries in the atomic lattice of the substrate or through physical contouring of the substrate [154–171]. This method typically presents high alignment, because of the substrates highly orientated lattice. However, the packing density is often reasonably low (10 μm^{-1}). Combined gas flow and lattice orientation have been used to achieve high alignment with high packing densities. CNTs aligned with either magnetic or electric fields require growth to be conducted between magnetic poles or electrodes with an applied external electric field (which can be either DC or AC). Electric field-aligned CNTs often show a degree of variance in both the packing density and alignment, likely attributed to spatial and temporal variations in the aligning field. The alignment is strongly dependent on the strength and direction of the electric field as well as the underpinning growth which augments the local fields during the growth. DC and AC fields have been used, with little correlation to alignment en mass [172–181]. Gas flow alignment involves the flow of gases during growth, typically of the growth precursors, which align the CNTs along the velocity vector of the flowing gas. To increase their alignment, gas flow-aligned CNTs are often dependent upon the kinetics of the predetermined catalyst loaded into the reactor. This explains, at least in part, the variation in the resulting distribution in both packing density and degree of alignment [182–190].

1.6 Degree of Alignment and Linear Packing Density

From the majority of the NW types presented above, we have conducted an outline meta-analysis to evaluate both their linear packing density (NW per μm) and their degree of alignment. Packing density was determined using a quantitative method, by plotting contrast histograms from extracted SEM imagery or from packing densities explicitly quoted. Out of necessity, the degree of alignment (DoA) was assessed qualitatively. As the assessed DoA is scale dependent and as each source image had invariably differing scales, only broad banding of the DoA was possible.

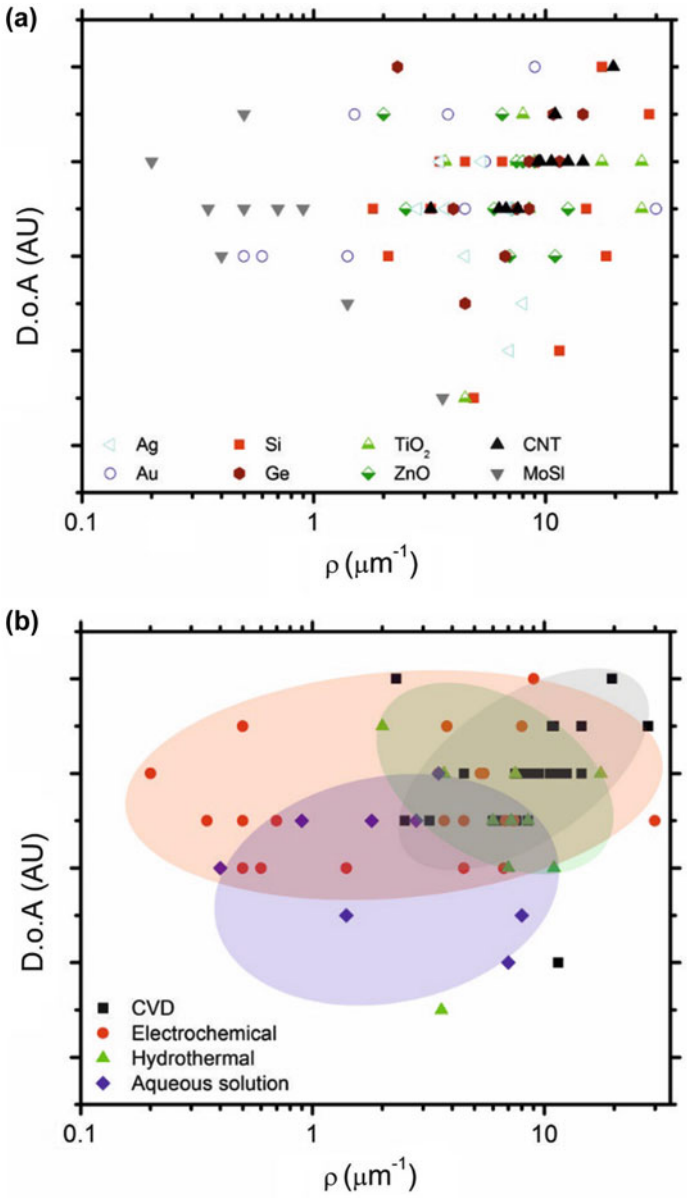

Fig. 1.5 Variation in the degree of alignment (DOA) as a function of linear packing density (ρ), for a select cross-section of the wide class of vertically aligned NWs as a function: (**a**) material (including the metallic NWs, Au [35, 48–59] and Ag [36, 60–70], the semiconducting NWs, Si [17, 21–27, 72, 95–105] and Ge [73, 191, 194–202] and dielectric NWs, TiO_2 [203] and ZnO [60, 110, 192, 203–211]. Also shown are typical organic (CNTs [150–153, 212–219]) and inorganic (MoSI [33, 143–149, 220, 221] NWs) and (**b**) synthesis method. Note the distinct grouping of CVD methods (densely packed and highly aligned) as well as electrochemical templating (high alignment). Hydrothermal methods produce relatively modest packing densities, whilst aqueous solution methods appear to produce relatively low packing density and low alignment

To enhance the rigour of the analysis, a randomly selected partial set of images, all of a comparable length scale, was taken, and the DoA was independently quantified using the image analysis methodology as outlined in [18]. A ranking was thereby generated and compared to our original ranking. The two showed a high correlation, herewith independently confirming our initial ranking.

As shown in Fig. 1.5a, b, the growth technique rather than the NW material tends to dominate the DoA. Etching templating produces NWs with generally high density and with good alignment, with none of the characteristic kinking, or sudden change in direction of growth typical of VLS. Figure 1.5b shows the DoA as a function of linear packing density and growth method. Note the formation of zones coarsely associated with each growth method. Of these, CVD appears to produce growth which tended to have high alignment and high packing density. This is likely due to the nature of the growth, which supports high nucleation and concurrent alignment due to Van der Waals interactions associated with the surrounding NWs. Zoning of the MoSI and broader class of PDMS-printed molecular NWs is evident, with high DoA and low packing density. Other electrochemical methods have produced a range of linear packing densities but almost always give high DoA due to the templating process. Solvo- and hydrothermal methods generally allow for high linear packing densities with a broad range of possible alignments.

1.7 Conclusion

In the present chapter, we have attempted to capture a broad overview of the current status in the field of aligned nanowire growth. Summarising the core nanowire types, we have outlined the leading as well as some of the more exotic growth techniques as they pertain to in situ nanowire alignment. The field is diverse and inevitably governed by the eventual application of the nanoengineered structures. Nonetheless, an inclusive meta-analysis of the present literature suggests that, with the continued miniaturisation of engineering components, CVD techniques allow for controlled alignment and linear packing density and as such represent a clear route to market and an eventual means of gaining commercial traction in the next decade.

References

1. Hornyak GL (2009) Fundamentals of nanotechnology. Taylor & Francis Group, Boca Raton, FL
2. Nalwa HS (2000) Handbook of nanostructured materials and nanotechnology. Academic Press, New York, NY
3. Alivisatos P, Barbara PF, Castleman AW, Chang J, Dixon DA, Klein ML, McLendon GL, Miller JS, Ratner MA, Rossky PJ, Stupp SI, Thompson ME (1998) From molecules to materials: current trends and future directions. Adv Mater 10(16):39

4. Shalaev VM, Moskovits M (1999) Nanostructured materials: clusters, composites, and thin films. American Chemical Society, Washington, DC
5. Smijs TG, Pavel S (2011) Titanium dioxide and zinc oxide nanoparticles in sunscreens: focus on their safety and effectiveness. Nanotechnol Sci Appl 2011(4):17. Dovepress
6. Suhr J et al (2005) Viscoelasticity in carbon nanotube composites. Nat Mater 4(2):134–137
7. Moore GE (1998) Cramming more components onto integrated circuits. Proc IEEE 86(1):4
8. Ng HT et al (2004) Single crystal nanowire vertical surround-gate field-effect transistor. Nano Lett 4(7):1247–1252
9. Huang MH et al (2001) Room-temperature ultraviolet nanowire nanolasers. Science 292 (5523):1897–1899
10. Thelander C et al (2006) Nanowire-based one-dimensional electronics. Mater Today 9 (10):28–35
11. Law M et al (2005) Nanowire dye-sensitized solar cells. Nat Mater 4(6):455–459
12. Sun XW, Wang JX (2008) Fast switching electrochromic display using a viologen-modified Zno nanowire array electrode. Nano Lett 8(7):1884–1889
13. Patolsky F et al (2004) Electrical detection of single viruses. Proc Natl Acad Sci U S A 101 (39):14017–14022
14. Xia Y et al (2003) One-dimensional nanostructures: synthesis, characterization, and applications. Adv Mater 15(5):353–389
15. Wang ZL (2000) Characterizing the structure and properties of individual wire-like nanoentities. Adv Mater 12(17):1295–1298
16. De Volder MFL et al (2013) Carbon nanotubes: present and future commercial applications. Science 339(6119):535–539
17. Schmidt V et al (2009) Silicon nanowires: a review on aspects of their growth and their electrical properties. Adv Mater 21(25–26):2681–2702
18. Cole MT et al (2014) Ultra-broadband polarisers based on metastable free-standing aligned carbon nanotube membranes. Adv Opt Mater 2(10):929–937
19. Zhang Q et al (2016) In situ fabrication and investigation of nanostructures and nanodevices with a microscope. Chem Soc Rev 45(9):2694–2713
20. Ghoshal T et al (2014) Fabrication of ordered, large scale, horizontally-aligned Si nanowire arrays based on an in situ hard mask block copolymer approach. Adv Mater 26(8):1207–1216
21. Wagner RS, Ellis WC (1964) Vapor-liquid-solid mechanism of single crystal growth. Appl Phys Lett 4(5):89–90
22. Ho T-W, Hong FC-N (2012) A reliable method to grow vertically-aligned silicon nanowires by a novel ramp-cooling process. Appl Surf Sci 258(20):7989–7996
23. Hochbaum AI et al (2005) Controlled growth of Si nanowire arrays for device integration. Nano Lett 5(3):457–460
24. Wacaser BA et al (2009) Growth system, structure, and doping of aluminum-seeded epitaxial silicon nanowires. Nano Lett 9(9):3296–3301
25. Zhang R-Q, Lifshitz Y, Lee S-T (2003) Oxide-assisted growth of semiconducting nanowires. Adv Mater 15(7–8):635–640
26. Yan HF et al (2000) Growth of amorphous silicon nanowires via a solid–liquid–solid mechanism. Chem Phys Lett 323(3–4):224–228
27. Wang Y et al (2006) Epitaxial growth of silicon nanowires using an aluminium catalyst. Nat Nanotechnol 1(3):186–189
28. Thongmee S et al (2009) Fabrication and magnetic properties of metallic nanowires via aao templates. J Magnetism Magn Mater 321(18):2712–2716
29. Cantu-Valle J et al (2015) Mapping the magnetic and crystal structure in cobalt nanowires. J Appl Phys 118(2):024302
30. Cui F et al (2015) Synthesis of ultrathin copper nanowires using tris(trimethylsilyl)silane for high-performance and low-haze transparent conductors. Nano Lett 15(11):7610–7615
31. Haehnel V et al (2010) Towards smooth and pure iron nanowires grown by electrodeposition in self-organized alumina membranes. Acta Mater 58(7):2330–2337

32. Kim J et al (2016) Organic devices based on nickel nanowires transparent electrode. Sci Rep 6:19813
33. Zach MP, Ng KH, Penner RM (2000) Molybdenum nanowires by electrodeposition. Science 290(5499):2120–2123
34. Lee JW et al (2010) Single crystalline aluminum nanowires with ideal resistivity. Scr Mater 63(10):1009–1012
35. Dou R, Derby B (2008) The growth and mechanical properties of gold nanowires. MRS Online Proceedings Library Archive. 1086: pp 1086–U08-01 (6 pages)
36. Cao Y et al (2006) A technique for controlling the alignment of silver nanowires with an electric field. Nanotechnology 17(9):2378
37. Chen YJ et al (2007) Controlled growth of zinc nanowires. Mater Lett 61(1):144–147
38. Djenizian T et al (2008) Electrochemical fabrication of tin nanowires: a short review. C R Chim 11(9):995–1003
39. Yanson AI, Yanson IK, van Ruitenbeek JM (1999) Observation of shell structure in sodium nanowires. Nature 400(6740):144–146
40. Li W et al (2007) Magnesium nanowires: enhanced kinetics for hydrogen absorption and desorption. J Am Chem Soc 129(21):6710–6711
41. Thongmee S et al (2009) Unique nanostructures in nico alloy nanowires. Acta Mater 57 (8):2482–2487
42. Hou H, Hamilton RF (2015) Free-standing niti alloy nanowires fabricated by nanoskiving. Nanoscale 7(32):13373–13378
43. Kumar S, Saini D (2013) Large-scale synthesis of Au–Ni alloy nanowires using electrochemical deposition. Appl Nanosci 3(2):101–107
44. Wang CZ et al (2002) Structure and magnetic property of Ni-Cu alloy nanowires electrodeposited into the pores of anodic alumina membranes. J Phys D Appl Phys 35(8):738
45. Liao Y et al (2016) Composition-tunable ptcu alloy nanowires and electrocatalytic synergy for methanol oxidation reaction. J Phys Chem C 120(19):10476–10484
46. Kornienko N et al (2015) Solution phase synthesis of indium gallium phosphide alloy nanowires. ACS Nano 9(4):3951–3960
47. Wang X et al (2016) Preparation and characterization of Y-Fe alloy nanowires by template-assisted electrodeposition from aqueous solution. J Nanopart Res 18(3):1–12
48. Dawson K, Riordan AO (2011) Towards nanowire (bio) sensors. J Phys Conf Series 307 (1):012004
49. Zhang Y et al (2014) New gold nanostructures for sensor applications: a review. Materials 7 (7):5169
50. Chi S, Farias SL, Cammarata RC (2012) Synthesis of vertically aligned gold nanowire-ferromagnetic metal matrix composites. ECS Trans 41(35):119–122
51. He J et al (2013) Forest of gold nanowires: a new type of nanocrystal growth. ACS Nano 7 (3):2733–2740
52. Kline TR et al (2006) Template-grown metal nanowires. Inorg Chem 45(19):7555–7565
53. Liu J et al (2006) Electrochemical fabrication of single-crystalline and polycrystalline au nanowires: the influence of deposition parameters. Nanotechnology 17(8):1922
54. Reinhardt HM, Bücker K, Hampp NA (2015) Directed assembly of gold nanowires on silicon via reorganization and simultaneous fusion of randomly distributed gold nanoparticles. Opt Express 23(9):11965–11974
55. Reynes O, Demoustier-Champagne S (2005) Template electrochemical growth of polypyrrole and gold-polypyrrole-gold nanowire arrays. J Electrochem Soc 152(9):D130–D135
56. Shi S et al (2011) Fabrication of periodic metal nanowires with microscale mold by nanoimprint lithography. ACS Appl Mater Interfaces 3(11):4174–4179
57. Zheng L, Li S, Burke PJ (2004) Self-assembled gold nanowires from nanoparticles: an electronic route towards DNA nanosensors. Proc. SPIE 5515:117–124

58. Venkatesh R et al (2015) Directed assembly of ultrathin gold nanowires over large area by dielectrophoresis. Langmuir 31(33):9246–9252
59. Zhang M et al (2013) Controllable growth of gold nanowires and nanoactuators via high-frequency Ac electrodeposition. Electrochem Commun 27:133–136
60. Lu L et al (2012) Direct synthesis of vertically aligned ZnO nanowires on FTO substrates using a CVD method and the improvement of photovoltaic performance. Nanoscale Res Lett 7(1):1–8
61. Yang R et al (2007) Silver nanowires prepared by modified AAO template method. Mater Lett 61(3):900–903
62. Sun Y et al (2002) Uniform silver nanowires synthesis by reducing AgNO3 with ethylene glycol in the presence of seeds and poly(vinyl pyrrolidone). Chem Mater 14(11):4736–4745
63. Sun Y et al (2002) Crystalline silver nanowires by soft solution processing. Nano Lett 2 (2):165–168
64. Sun B et al (2009) Single-crystal silver nanowires: preparation and surface-enhanced raman scattering (sers) property. Mater Lett 63(29):2570–2573
65. Mohammad A et al (2014) Optical characteristics of vertically aligned arrays of branched silver nanowires. 14th IEEE international conference on nanotechnology, pp 563–566
66. Malandrino G, Finocchiaro ST, Fragala IL (2004) Silver nanowires by a sonoself-reduction template process. J Mater Chem 14(18):2726–2728
67. Kazeminezhad I et al (2007) Templated electrodeposition of silver nanowires in a nanoporous polycarbonate membrane from a nonaqueous ionic liquid electrolyte. Appl Phys A 86 (3):373–375
68. Han Y-H (2008) High density silver nanowire arrays using self-ordered anodic aluminum oxide (AAO) membrane. J Korean Ceramic Soc 45(4):191–195
69. Chun-Nuan Y et al (2004) Growth mechanism of vertically aligned Ag(TCNQ) nanowires. Chin Phys Lett 21(9):1787
70. Cao Y, He J, Sun J (2009) Fabrication of oriented arrays of porous gold microsheaths using aligned silver nanowires as sacrificial template. Mater Lett 63(1):148–150
71. Yazawa M et al (1992) Effect of one monolayer of surface gold atoms on the epitaxial growth of inas nanowhiskers. Appl Phys Lett 61(17):2051–2053
72. Holmes JD et al (2000) Control of thickness and orientation of solution-grown silicon nanowires. Science 287(5457):1471–1473
73. Nakata M et al (2015) Transfer-free synthesis of highly ordered ge nanowire arrays on glass substrates. Appl Phys Lett 107(13):133102
74. Duan X et al (2001) Indium phosphide nanowires as building blocks for nanoscale electronic and optoelectronic devices. Nature 409(6816):66–69
75. Lindberg C et al (2016) Silver as seed-particle material for gaas nanowires—dictating crystal phase and growth direction by substrate orientation. Nano Lett 16(4):2181–2188
76. Zhang G et al (2008) Growth and characterization of gap nanowires on Si substrate. J Appl Phys 103(1):014301
77. Zhang Y et al (2014) Self-catalyzed ternary core–shell gaasp nanowire arrays grown on patterned Si substrates by molecular beam epitaxy. Nano Lett 14(8):4542–4547
78. Tateno K et al (2012) VLS growth of alternating InAsP/InP heterostructure nanowires for multiple-quantum-dot structures. Nano Lett 12(6):2888–2893
79. Kriegner D et al (2013) Structural investigation of gainp nanowires using X-ray diffraction. Thin Solid Films 543:100–105
80. Tateno K, Zhang G, Nakano H (2008) Growth of GaInAs/AlInAs heterostructure nanowires for long-wavelength photon emission. Nano Lett 8(11):3645–3650
81. Shindo T et al (2011) GaInAsP/InP lateral-current-injection distributed feedback laser with a-Si surface grating. Opt Express 19(3):1884–1891
82. Zhang Y, Xu H, Wang Q (2010) Ultrathin single crystal zns nanowires. Chem Commun 46 (47):8941–8943

83. Zhang XT et al (2003) Growth and luminescence of zinc-blende-structured ZnSe nanowires by metal-organic chemical vapor deposition. Appl Phys Lett 83(26):5533–5535
84. Yan S et al (2011) Novel regrowth mechanism of CdS nanowire in hydrothermal synthesis. New J Chem 35(2):299–302
85. Wu H et al (2012) Dislocation-driven CdS and CdSe nanowire growth. ACS Nano 6 (5):4461–4468
86. Cho K-S et al (2005) Designing PbSe nanowires and nanorings through oriented attachment of nanoparticles. J Am Chem Soc 127(19):7140–7147
87. Finefrock SW et al (2014) Large-scale solution-phase production of Bi2te3 and PbTe nanowires using Te nanowire templates. Nanoscale 6(14):7872–7876
88. Zettler JK et al (2015) High-temperature growth of GaN nanowires by molecular beam epitaxy: toward the material quality of bulk GaN. Cryst Growth Des 15(8):4104–4109
89. Young Kim H, Park J, Yang H (2003) Synthesis of silicon nitride nanowires directly from the silicon substrates. Chem Phys Lett 372(1–2):269–274
90. Kim HY, Park J, Yang H (2003) Direct synthesis of aligned silicon carbide nanowires from the silicon substrates. Chem Commun (2):256–257
91. Kumar A, Madaria AR, Zhou C (2010) Growth of aligned single-crystalline rutile TiO2 nanowires on arbitrary substrates and their application in dye-sensitized solar cells. J Phys Chem C 114(17):7787–7792
92. Wang X et al (2014) Aligned epitaxial SnO2 nanowires on sapphire: growth and device applications. Nano Lett 14(6):3014–3022
93. Jiang X, Herricks T, Xia Y (2002) CuO nanowires can be synthesized by heating copper substrates in air. Nano Lett 2(12):1333–1338
94. Fanhao Z et al (2004) Large-scale growth of In 2 O 3 nanowires and their optical properties. Nanotechnology 15(5):596
95. Zhang YF et al (1998) Silicon nanowires prepared by laser ablation at high temperature. Appl Phys Lett 72(15):1835–1837
96. Wong YY et al (2005) Controlled growth of silicon nanowires synthesized via solid–liquid–solid mechanism. Sci Technol Adv Mater 6(3–4):330–334
97. Wang C et al (2011) Growth of straight silicon nanowires on amorphous substrates with uniform diameter, length, orientation, and location using nanopatterned host-mediated catalyst. Nano Lett 11(12):5247–5251
98. Treuting RG, Arnold SM (1957) Orientation habits of metal whiskers. Acta Metall 5(10):598
99. Pan ZW et al (2001) Temperature-controlled growth of silicon-based nanostructures by thermal evaporation of SiO powders. J Phys Chem B 105(13):2507–2514
100. Morales AM, Lieber CM (1998) A laser ablation method for the synthesis of crystalline semiconductor nanowires. Science 279(5348):208–211
101. Krause A et al (2015) Comparison of silicon nanowire growth on SiO2 and on carbon substrates. ECS Trans 70(1):69–78
102. Kim J, Ji C, Anderson WA (2004) Silicon nanowire growth at relatively low processing temperature. MRS Online Proceedings Library Archive. 818: p. M11.11.1 (6 pages).
103. Cheng SL, Chung CH, Lee HC (2007) Fabrication of vertically aligned silicon nanowire arrays and investigation on the formation of the nickel silicide nanowires. Electron Devices and Solid-State Circuits, 2007. EDSSC 2007. IEEE Conference. pp 121–124.
104. Banerjee D et al (2016) Phonon processes in vertically aligned silicon nanowire arrays produced by low-cost all-solution galvanic displacement method. Appl Phys Lett 108 (11):113109
105. Sandulova AV, Bogoyavlenskii PS, Dronyum MI (1964) Preparation and some properties of whisker and needle-shaped single crystals of germanium, silicon and their solid solutions. Sov Phys Solid State 5:1883
106. Kennedy T et al (2014) High-performance germanium nanowire-based lithium-ion battery anodes extending over 1000 cycles through in situ formation of a continuous porous network. Nano Lett 14(2):716–723

107. Wang D et al (2003) Germanium nanowire field-effect transistors with SiO2 and High-κ Hfo2 gate dielectrics. Appl Phys Lett 83(12):2432–2434
108. Zhang Y et al (2007) An integrated phase change memory cell with Ge nanowire diode for cross-point memory. In 2007 I.E. Symposium on VLSI Technology, 12 Jun, pp 98–99
109. O'Regan C et al (2014) Recent advances in the growth of germanium nanowires: synthesis, growth dynamics and morphology control. J Mater Chem C 2(1):14–33
110. He Y et al (2005) Vertically well-aligned ZnO nanowires generated with self-assembling polymers. Mater Chem Phys 94(1):29–33
111. Yuan Z-Y, Su B-L (2004) Titanium oxide nanotubes, nanofibers and nanowires. Colloids Surf A Physicochem Eng Asp 241(1–3):173–183
112. Shi J, Wang X (2011) Growth of rutile titanium dioxide nanowires by pulsed chemical vapor deposition. Cryst Growth Des 11(4):949–954
113. Faruque MK et al (2012) Fabrication, characterization, and mechanism of vertically aligned titanium nitride nanowires. Appl Surf Sci 260:36–41
114. Wang X et al (2015) Confined-space synthesis of single crystal TiO(2) nanowires in atmospheric vessel at low temperature: a generalized approach. Sci Rep 5:8129
115. Yin Y, Zhang G, Xia Y (2002) Synthesis and characterization of MgO nanowires through a vapor-phase precursor method. Adv Funct Mater 12(4):293–298
116. Zhang Y et al (2001) A simple method to synthesize Si3N4 and SiO2 nanowires from Si or Si/SiO2 mixture. J Cryst Growth 233(4):803–808
117. Xiao Z et al (2006) High-density, aligned SiO2 nanowire arrays: microscopic imaging of the unique growth style and their ultraviolet light emission properties. J Phys Chem B 110 (32):15724–15728
118. Chang C-C et al (2012) Synthesis and growth twinning of Al2O3 nanowires by simple evaporation of Al-Si alloy powder. CrstEngComm 14(3):1117–1121
119. Dang TTL, Tonezzer M, Nguyen VH (2015) Hydrothermal growth and hydrogen selective sensing of nickel oxide nanowires. J Nanomater 2015:8
120. Das S et al (2010) Formation of NiO nanowires on the surface of nickel strips. J Alloys Compd 505(1):L19–L21
121. Lin Y et al (2003) Ordered nickel oxide nanowire arrays and their optical absorption properties. Chem Phys Lett 380(5–6):521–525
122. Pang H et al (2010) Selective synthesis of nickel oxide nanowires and length effect on their electrochemical properties. Nanoscale 2(6):920–922
123. Patil RA et al (2013) An efficient methodology for measurement of the average electrical properties of single one-dimensional NiO nanorods. Sci Rep **3**:3070
124. Sekiya K et al (2012) Morphology control of nickel oxide nanowires. Microelectron Eng 98:532–535
125. Wei ZP et al (2010) A template and catalyst-free metal-etching-oxidation method to synthesize aligned oxide nanowire arrays: NiO as an example. ACS Nano 4(8):4785–4791
126. Zeng W et al (2012) Facile synthesis of NiO nanowires and their gas sensing performance. Trans Nonferrous Met Soc Chin 22:s100–s104
127. Bechelany M et al (2007) Synthesis of boron nitride nanotubes by a template-assisted polymer thermolysis process. J Phys Chem C 111(36):13378–13384
128. Cao L et al (2002) Synthesis of well-aligned boron nanowires and their structural stability under high pressure. J Phys Condens Matter 14(44):11017
129. Cao LM et al (2001) Well-aligned boron nanowire arrays. Adv Mater 13(22):1701–1704
130. Deepak FL et al (2002) Boron nitride nanotubes and nanowires. Chem Phys Lett 353 (5–6):345–352
131. Huo KF et al (2002) Synthesis of boron nitride nanowires. Appl Phys Lett 80(19):3611–3613
132. Kalay S et al (2015) Synthesis of boron nitride nanotubes and their applications. Beilstein J Nanotechnol 6:84–102
133. Patel RB, Chou T, Iqbal Z (2015) Synthesis of boron nanowires, nanotubes, and nanosheets. J Nanomater 2015:7

134. Su C-H et al (2015) Self-templating noncatalyzed synthesis of monolithic boron nitride nanowires. RSC Adv 5(92):75810–75816
135. Zhou J et al (2014) Vertically-aligned BCN nanotube arrays with superior performance in electrochemical capacitors. Sci Rep 4:6083
136. Zhu Y-C et al (2004) New boron nitride whiskers: showing strong ultraviolet and visible light luminescence. J Phys Chem B 108(20):6193–6196
137. Polleux J et al (2006) Template-free synthesis and assembly of single-crystalline tungsten oxide nanowires and their gas-sensing properties. Angew Chem 118(2):267–271
138. An G-H et al (2011) One-pot fabrication of hollow SiO2 nanowires via an electrospinning technique. Mater Lett 65(15–16):2377–2380
139. Antonio T et al (2010) Scalable flame synthesis of SiO 2 nanowires: dynamics of growth. Nanotechnology 21(46):465604
140. Zamchiy A, Baranov E, Khmel S (2014) New approach to the growth of SiO2 nanowires using Sn catalyst on Si substrate. physica status solidi (c) 11(9–10):1397–1400
141. Li Y et al (2011) Growth of SiO 2 nanowires on different substrates using Au as a catalyst. J Semiconduct 32(2):023002
142. Yu-Chiao L, Wen-Tai L (2005) Growth of SiO 2 nanowires without a catalyst via carbothermal reduction of CuO powders. Nanotechnology 16(9):1648
143. Mihailovic D (2009) Inorganic molecular wires: physical and functional properties of transition metal chalco-halide polymers. Prog Mater Sci 54(3):309–350
144. Daniel V et al (2004) Air-stable monodispersed Mo 6 S 3 I 6 nanowires. Nanotechnology 15 (5):635
145. Potel M et al (1980) New pseudo-one-dimensional metals: M2Mo6Se6 (M = Na, in, K, Ti), M2Mo6S6 (M = K, Rb, Cs), M2Mo6Te6 (M = in, Ti). J Solid State Chem 35(2):286–290
146. Remskar M et al (2010) The Mos2 nanotubes with defect-controlled electric properties. Nanoscale Res Lett 6(1):1–6
147. Dvorsek D et al (2007) Growth and field emission properties of vertically aligned molybdenum–sulfur–iodine nanowires on molybdenum and quartz substrates. J Appl Phys 102(11):114308
148. Messer B, Song JH, Yang P (2000) Microchannel networks for nanowire patterning. J Am Chem Soc 122(41):10232–10233
149. Wu Y et al (2002) Inorganic semiconductor nanowires: rational growth, assembly, and novel properties. Chemistry A 8(6):1260–1268
150. Chen H et al (2010) Controlled growth and modification of vertically-aligned carbon nanotubes for multifunctional applications. Mater Sci Eng R Rep 70(3–6):63–91
151. Patole SP et al (2008) Alignment and wall control of ultra long carbon nanotubes in water assisted chemical vapour deposition. J Phys D Appl Phys 41(15):155311
152. Chhowalla M et al (2001) Field emission from short and stubby vertically aligned carbon nanotubes. Appl Phys Lett 79(13):2079–2081
153. Shang NG et al (2010) High-rate low-temperature growth of vertically aligned carbon nanotubes. Nanotechnology 21(50):505604
154. Ago H et al (2011) Ultrahigh-vacuum-assisted control of metal nanoparticles for horizontally aligned single-walled carbon nanotubes with extraordinary uniform diameters. J Phys Chem C 115(27):13247–13253
155. Almaqwashi AA et al (2011) Variable-force microscopy for advanced characterization of horizontally aligned carbon nanotubes. Nanotechnology 22(27):275717
156. Cui R et al (2010) Comparison between copper and iron as catalyst for chemical vapor deposition of horizontally aligned ultralong single-walled carbon nanotubes on silicon substrates. J Phys Chem C 114(37):15547–15552
157. Ding L et al (2009) Selective growth of well-aligned semiconducting single-walled carbon nanotubes. Nano Lett 9(2):800–805
158. Ding L, Yuan D, Liu J (2008) Growth of high-density parallel arrays of long single-walled carbon nanotubes on quartz substrates. J Am Chem Soc 130(16):5428–5429

159. Hong SW, Banks T, Rogers JA (2010) Improved density in aligned arrays of single-walled carbon nanotubes by sequential chemical vapor deposition on quartz. Adv Mater 22 (16):1826–1830
160. Huang L et al (2006) Cobalt ultrathin film catalyzed ethanol chemical vapor deposition of single-walled carbon nanotubes. J Phys Chem B 110(23):11103–11109
161. Huang S et al (2004) Growth mechanism of oriented long single walled carbon nanotubes using "fast-heating"chemical vapor deposition process. Nano Lett 4(6):1025–1028
162. Inoue T et al. High density growth of horizontally aligned single-walled carbon nanotubes on quartz by variation of incubation time. http://www.photon.t.u-tokyo.ac.jp/~maruyama/papers/12/DenseHA.pdf
163. Ismach A, Kantorovich D, Joselevich E (2005) Carbon nanotube graphoepitaxy: highly oriented growth by faceted nanosteps. J Am Chem Soc 127(33):11554–11555
164. Kang SJ et al (2007) High-performance electronics using dense, perfectly aligned arrays of single-walled carbon nanotubes. Nat Nanotechnol 2(4):230–236
165. Kocabas C et al (2005) Guided growth of large-scale, horizontally aligned arrays of single-walled carbon nanotubes and their use in thin-film transistors. Small 1(11):1110–1116
166. Ozel T et al (2009) Nonuniform compressive strain in horizontally aligned single-walled carbon nanotubes grown on single crystal quartz. ACS Nano 3(8):2217–2224
167. Reina A et al (2007) Growth mechanism of long and horizontally aligned carbon nanotubes by chemical vapor deposition. J Phys Chem C 111(20):7292–7297
168. Shadmi N et al (2015) Guided growth of horizontal single-wall carbon nanotubes on M-plane sapphire. J Phys Chem C 119(15):8382–8387
169. Yu Q et al (2006) Mechanism of horizontally aligned growth of single-wall carbon nanotubes on R-plane sapphire. J Phys Chem B 110(45):22676–22680
170. Yuan D et al (2008) Horizontally aligned single-walled carbon nanotube on quartz from a large variety of metal catalysts. Nano Lett 8(8):2576–2579
171. Zhou W et al (2006) Copper catalyzing growth of single-walled carbon nanotubes on substrates. Nano Lett 6(12):2987–2990
172. AuBuchon JF et al (2006) Electric-field-guided growth of carbon nanotubes during DC plasma-enhanced CVD. Chem Vap Deposition 12(6):370–374
173. Chai Y, Xiao Z, Chan PCH (2009) Fabrication and characterization of horizontally aligned carbon nanotubes for interconnect application. 2009 59th electronic components and technology conference, San Diego, CA, May 2009. pp 1465–1469
174. Chai Y, Xiao Z, Chan PCH (2010) Horizontally aligned carbon nanotube bundles for interconnect application: diameter-dependent contact resistance and mean free path. Nanotechnology 21(23):235705
175. Hayashi Y et al (2010) Direct growth of horizontally aligned carbon nanotubes between electrodes and its application to field-effect transistors. 2010 3rd international nanoelectronics conference (INEC). pp 215–216
176. Joselevich E, Lieber CM (2002) Vectorial growth of metallic and semiconducting single-wall carbon nanotubes. Nano Lett 2(10):1137–1141
177. Jung SM, Jung HY, Suh JS (2007) Horizontally aligned carbon nanotube field emitters having a long term stability. Carbon 45(15):2917–2921
178. Jung SM, Jung HY, Suh JS (2008) Horizontally aligned carbon nanotube field emitters fabricated on ITO glass substrates. Carbon 46(14):1973–1977
179. Law JBK, Koo CK, Thong JTL (2007) Horizontally directed growth of carbon nanotubes utilizing self-generated electric field from plasma induced surface charging. Appl Phys Lett 91(24):243108
180. Ural A, Li Y, Dai H (2002) Electric-field-aligned growth of single-walled carbon nanotubes on surfaces. Appl Phys Lett 81(18):3464–3466
181. Zhang Y et al (2001) Electric-field-directed growth of aligned single-walled carbon nanotubes. Appl Phys Lett 79(19):3155–3157

182. Ago H et al (2006) Synthesis of horizontally-aligned single-walled carbon nanotubes with controllable density on sapphire surface and polarized raman spectroscopy. Chem Phys Lett 421(4–6):399–403
183. Hong BH et al (2005) Quasi-continuous growth of ultralong carbon nanotube arrays. J Am Chem Soc 127(44):15336–15337
184. Hsu CM et al (2002) Growth of the large area horizontally-aligned carbon nanotubes by ECR-CVD. Thin Solid Films 420–421:225–229
185. Huang S, Cai X, Liu J (2003) Growth of millimeter-long and horizontally aligned single-walled carbon nanotubes on flat substrates. J Am Chem Soc 125(19):5636–5637
186. Jin Z et al (2007) Ultralow feeding gas flow guiding growth of large-scale horizontally aligned single-walled carbon nanotube arrays. Nano Lett 7(7):2073–2079
187. Li L et al (2012) Electrochemical growth of gold nanoparticles on horizontally aligned carbon nanotubes: a new platform for ultrasensitive DNA sensing. Biosens Bioelectron 33(1):279–283
188. Liu H et al (2009) The controlled growth of horizontally aligned single-walled carbon nanotube arrays by a gas flow process. Nanotechnology 20(34):345604
189. Liu Y et al (2009) Flexible orientation control of ultralong single-walled carbon nanotubes by gas flow. Nanotechnology 20(18):185601
190. Xie H et al (2016) Preloading catalysts in the reactor for repeated growth of horizontally aligned carbon nanotube arrays. Carbon 98:157–161
191. Dayeh SA, Picraux ST (2010) Direct observation of nanoscale size effects in ge semiconductor nanowire growth. Nano Lett 10(10):4032–4039
192. Qi H et al (2012) Growth of vertically aligned ZnO nanowire arrays using bilayered metal catalysts. J Nanomater 2012:7
193. Fengmei G et al (2008) Aligned ultra-long single-crystalline A—Si 3 N 4 nanowires. Nanotechnology 19(10):105602
194. Woodruff JH et al (2007) Vertically oriented germanium nanowires grown from gold colloids on silicon substrates and subsequent gold removal. Nano Lett 7(6):1637–1642
195. Toko K et al (2015) Vertically aligned Ge nanowires on flexible plastic films synthesized by (111)-oriented Ge seeded vapor–liquid–solid growth. ACS Appl Mater Interfaces 7 (32):18120–18124
196. Sierra-Sastre Y et al (2008) Vertical growth of Ge nanowires from biotemplated Au nanoparticle catalysts. J Am Chem Soc 130(32):10488–10489
197. O'Regan C et al (2013) Engineering the growth of germanium nanowires by tuning the supersaturation of Au/Ge binary alloy catalysts. Chem Mater 25(15):3096–3104
198. Li CB et al (2008) Controlled Ge nanowires growth on patterned Au catalyst substrate. 2008 I.E. silicon nanoelectronics workshop, pp 1–2
199. Leu PW et al (2008) Oxide-encapsulated vertical germanium nanowire structures and their DC transport properties. Nanotechnology 19(48):485705
200. Kawamura Y et al (2012) Direct-gap photoluminescence from germanium nanowires. Physical Review B **86**(3):035306
201. Liangbing H, Hecht DS, Grüner G (2009) Infrared transparent carbon nanotube thin films. Appl Phys Lett 94(8):081103. (3 pp)
202. Adhikari H et al (2006) Germanium nanowire epitaxy: shape and orientation control. Nano Lett 6(2):318–323
203. Geng C et al (2004) Well-aligned ZnO nanowire arrays fabricated on silicon substrates. Adv Funct Mater 14(6):589–594
204. Jamali Sheini F et al (2010) Low temperature growth of aligned ZnO nanowires and their application as field emission cathodes. Mater Chem Phys 120(2–3):691–696
205. Ji L-W et al (2009) Effect of seed layer on the growth of well-aligned ZnO nanowires. J Phys Chem Solid 70(10):1359–1362
206. Liu F et al (2005) Well-aligned zinc oxide nanorods and nanowires prepared without catalyst. J Cryst Growth 274(1–2):126–131

207. Tak Y, Yong K (2005) Controlled growth of well-aligned ZnO nanorod array using a novel solution method. J Phys Chem B 109(41):19263–19269
208. Unalan HE et al (2008) Rapid synthesis of aligned zinc oxide nanowires. Nanotechnology 19 (25):255608
209. Xu S et al (2008) Patterned growth of vertically aligned ZnO nanowire arrays on inorganic substrates at low temperature without catalyst. J Am Chem Soc 130(45):14958–14959
210. Zeng Y-J et al (2005) Well-aligned ZnO nanowires grown on Si substrate via metal–organic chemical vapor deposition. Appl Surf Sci 250(1–4):280–283
211. Zhitao H et al (2013) Controlled growth of well-aligned ZnO nanowire arrays using the improved hydrothermal method. J Semiconduct 34(6):063002
212. Lin W et al (2009) Vertically aligned carbon nanotubes on copper substrates for applications as thermal interface materials: from synthesis to assembly. 2009 59th electronic components and technology conference, pp 441–447
213. Qi HJ et al (2003) Determination of mechanical properties of carbon nanotubes and vertically aligned carbon nanotube forests using nanoindentation. J Mech Phys Solids 51 (11–12):2213–2237
214. Qu L, Du F, Dai L (2008) Preferential syntheses of semiconducting vertically aligned single-walled carbon nanotubes for direct use in FETs. Nano Lett 8(9):2682–2687
215. Ren ZF et al (1998) Synthesis of large arrays of well-aligned carbon nanotubes on glass. Science 282(5391):1105–1107
216. Shahzad MI et al (2013) Growth of vertically aligned multiwall carbon nanotubes columns. J Phys Conf Ser 439(1):012008
217. Van Hooijdonk E et al (2013) Functionalization of vertically aligned carbon nanotubes. Beilstein J Nanotechnol 4:129–152
218. Yu M et al (2009) High density, vertically-aligned carbon nanotube membranes. Nano Lett 9 (1):225–229
219. Zhu H et al (2001) Hydrogen adsorption in bundles of well-aligned carbon nanotubes at room temperature. Appl Surf Sci 178(1–4):50–55
220. Remškar DVM et al (2004) Air-stable monodispersed Mo 6 S 3 I 6 nanowires. Nanotechnology 15(5):635
221. Zhang Z et al (2015) Ultrathin inorganic molecular nanowire based on polyoxometalates. Nat Commun 6

Chapter 2
Taxane Formulations: From Plant to Clinic

A. Elhissi, R. Mahmood, I. Parveen, A. Vali, W. Ahmed, and M.J. Jackson

2.1 Plant Origin and Pharmacology of Taxanes

Taxane compounds are anticancer agents derived from a plant source and include paclitaxel and docetaxel (Fig. 2.1). Paclitaxel is isolated from the Pacific yew tree (*Taxus brevifolia*) [1], whilst the semisynthetic taxane docetaxel is derived from the needles of the European yew (*Taxus baccata*) [2, 3]. Taxane formulations can treat various types of cancer including ovarian, breast and bladder carcinomas [4] as well as lung cancer and acute leukaemia [2].

Taxanes are classified as anti-microtubule chemotherapeutic compounds that work by interrupting the microtubule function which is important in cell division. They do so by inhibiting mitosis, causing an incomplete formation of the metaphase plate of chromosomes and hence altering the arrangement of the spindle microtubules [5, 6]. Both paclitaxel and docetaxel bind to ß subunit of tubulin (a protein found in microtubules) [7, 8], producing highly stable dysfunctional microtubules [9]. Microtubules are central to cell division forming spindle fibres permitting separation and alignment of chromosomes during mitosis [10]. Paclitaxel inhibits mitosis in the G-phase of the mitotic cycle, whilst docetaxel causes arrest at the

A. Elhissi (✉)
College of Pharmacy, Qatar University, Doha, Qatar
e-mail: aelhissi@qu.edu.qa

R. Mahmood • I. Parveen • A. Vali
School of Pharmacy and Biomedical Sciences, University of Central Lancashire, Preston PR1 2HE, UK

W. Ahmed
School of Mathematics and Physics, University of Lincoln, Lincoln LN6 7TS, UK

M.J. Jackson
School of Interdisciplinary Studies, Kansas State University, Manhattan, KS 66506, USA

M.J. Jackson, W. Ahmed (eds.), *Micro and Nanomanufacturing Volume II*,
DOI 10.1007/978-3-319-67132-1_2

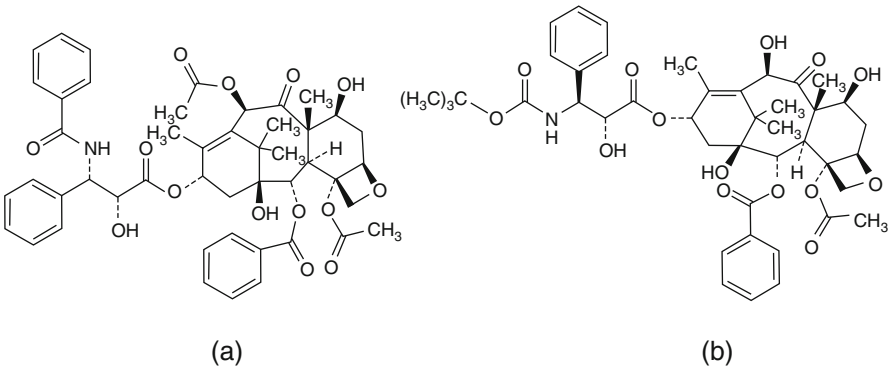

Fig. 2.1 Chemical structure of (**a**) paclitaxel and (**b**) docetaxel

S-phase to prevent cell division and produce apoptosis [11]. Docetaxel has been reported to be twice as potent as paclitaxel at inhibiting microtubules [12].

2.2 Conventional Taxane Formulations in Clinical Use

Paclitaxel and docetaxel are highly lipophilic; hence, they are both regarded to be water-insoluble compounds (Table 2.1), making formulation and administration considerably challenging. Paclitaxel is solubilised using a mixture of Cremophor EL (polyethoxylated castor oil) and dehydrated ethanol (50:50 v/v) to provide a drug concentration of 6 mg/mL [13, 14]. Cremophor EL is a non-ionic surfactant that has the ability to form micelles in biological fluids (e.g. plasma) and increase the solubility of paclitaxel. By contrast, docetaxel is slightly more soluble than paclitaxel; therefore polysorbate 80 (Tween 80) and ethanol are used to solubilise it [15, 16]. These paclitaxel and docetaxel formulations are available for clinical use as Taxol® and Taxotere®, respectively, and are administered by intravenous infusion. Before administration of Taxol®, the formulation is diluted with 5–20-fold using NaCl (0.9%) or dextrose (5%) solutions [9].

2.3 Stability of Taxane Formulations

Stability of taxane is extremely important particularly in situations where chemotherapy is prepared for later administration [17]. In these cases, storage conditions may affect the drug dose received. Docetaxel stability can be influenced by the degree of agitation during preparation and by slight temperature fluctuations during storage [18]. By contrast, for paclitaxel, the optimum storage temperature was

Table 2.1 Paclitaxel and docetaxel have extremely high Log *P* values thus are water-insoluble compounds; hence, to enhance their solubility, they are incorporated into organic vehicles

	Paclitaxel	Docetaxel
Aqueous solubility	Water insoluble	0.025 mg/L water insoluble
LogP	3.20	2.59
Organic vehicle used in formulation	Cremophor EL	Tween 80

found to be 2–8 °C [19], suggesting paclitaxel is less affected by changes in storage temperature compared to docetaxel.

The type of vehicle used and the inclusion of other chemotherapeutic drugs may affect the stability of taxanes on storage. Studies have found that when paclitaxel was diluted to 0.3 or 1.2 mg/mL using 5% dextrose or 0.9% NaCl, the drug remained chemically stable for 72 h under conditions of clinical use [20]. However, when doxorubicin 0.2 mg/mL was added to the formulation, samples were stable for only 24 h, whilst by 72 h some samples showed signs of paclitaxel precipitation. However, by day 5, all samples showed precipitation of the drug; this was independent of storage temperature [21]. This might be attributed to the incorporation of doxorubicin which was relatively easier to solubilise, resulting in salting out of paclitaxel. It has also been found that paclitaxel has an optimum stability when the vehicle had a pH range of 3–5 [22]. Drug concentration may also affect storage stability, with higher drug concentrations producing formulations with longer stability [17].

Administration of taxanes via the intravenous route poses many problems in terms of physical stability of the drug. Waugh et al. (1991) studied the stability of various concentrations of paclitaxel using 5% dextrose or 0.9% NaCl as diluent solutions [23]. The solutions were contained within glass bottles, polyolefin containers or PVC infusion bags and stored for 12–24 h. The chemical stability of the drug was unaffected in all cases; however, the solutions in the polyvinyl chloride (PVC) bags showed signs of leaching of the plasticiser di(2-ethylhexyl) phthalate (DEHP) into the formulation. DEHP is a polymer used in PVC to make it more flexible, since without this constituent, PVC would be very brittle at room temperature [24]. Leaching has also occurred during infusion using PVC administration sets. When a similar study was conducted on docetaxel, DEHP also leached during storage in PVC bags. Moreover, after 5 days the drug began to precipitate in the PVC infusion bags, whereas the solution contained within the polyolefin container was physically and chemically stable for 4 weeks [3]. It is worth to note that DEHP has been reported to be carcinogenic and teratogenic. This indicates that using polyethylene-lined infusion bags and administration kits is more appropriate in terms of safety for the patient when administering taxanes.

2.4 Undesirable Toxicities of Taxane Formulations

Taxane anticancer compounds may produce adverse effects such as myelosuppression, neuropathy, fatigue, alopecia, nausea and vomiting, with docetaxel also causing nail damage [6]. Moreover, an important limitation of taxane formulations is the toxicity of the excipients used to solubilise the drugs, particularly Cremophor EL and polysorbate 80 [25]. An initial fatal hypersensitivity reactions, nephrotoxicity and hypotension may happen because of using these excipients [16, 26]. Cremophor EL commonly causes serious adverse effects such as severe anaphylactoid hypersensitivity reactions, hyperlipidaemia, abnormal lipoprotein patterns, aggregation of erythrocytes and peripheral neuropathy [27]. Patients are premedicated with corticosteroids and histamine antagonists to reduce the incidence and severity of these hypersensitivity reactions [28]. However, even after premedication, 5–30% of the relevant patients are still affected by mild hypersensitivity reactions [29]. Thus, research has been conducted to provide alternative formulations that may enhance taxane solubility and reduce formulation instability and toxicity. Approaches that have been investigated included the use of nanotechnology, i.e. by involving nanocarrier-based formulations such as liposomes, polymeric micelles, nanoparticles, dendrimers, microemulsions (also called nanoemulsions) and cyclodextrins.

2.5 Formulations Developed to Reduce Instability

A number of strategies have been used to develop taxane formulations that are Cremophor EL-free, aiming to solubilise the drug, minimise adverse effects and improve stability. These strategies include formulating taxanes in the form of albumin nanoparticles, micelles, cyclodextrins and liposomes. A main cause of instability of paclitaxel is the lipophilicity of the drug, which makes it extremely difficult to solubilise in an aqueous solution; therefore new formulations should demonstrate improved drug solubility and show equal or better drug action compared to Cremophor EL-based formulations (e.g. Taxol®).

2.5.1 Liposomes

Liposomes are spherical amphiphilic vesicles comprising lipid bilayers that provide a hydrophobic region permitting interaction with hydrophobic drugs, in order to allow for drug incorporation into the lipid bilayer and enhance its solubility. Liposomal formulations of paclitaxel are well researched in terms of taxane delivery and have shown enhanced drug solubilisation, stability and reduced side effects. Sharma and co-workers researched the effect of liposome-incorporated paclitaxel

on toxicity and therapeutic effect in comparison to Taxol® [30]. In comparison to Taxol®, toxicity was markedly reduced using liposomal paclitaxel formulations. Whilst a Taxol® dose of >50 mg/kg in mice (with a human ovarian tumour xenograft) proved fatal, the same dose was well tolerated when administered in liposome formulations. Moreover, liposomal formulations provide a targeted delivery, increasing drug localisation into the tumour tissue due to the enhanced permeability and retention (EPR) effect which may also reduce the toxic effects of the drug on normal cells. Thus, reduced toxicity using liposomes is attributed to the absence of Cremophor EL and promoted targeted delivery to the cancerous cells. Yang and co-workers found that liposomes increased entrapment efficiency and drug solubility to 3.39 mg/mL and exhibited similar antitumour efficacy as compared to paclitaxel in Taxol® [29].

In another study, it has been found that although there was no significant difference in the distribution of the drug, the Cremophor EL-based formulation of paclitaxel is fivefold more toxic to normal tissues when compared to liposomal formulations [31]. Another study showed that when paclitaxel was incorporated into cationic liposomes, it prevented the growth of tumours and decreased the density of blood vessels at the tumour site by limiting the endothelial mitosis, whereas the Cremophor EL formulation elicited an insignificant effect on the growth of tumour and no effect on the blood vessels [32]. Lipusu® (Luye Pharma Group, China) is a recently commercialised liposomal formulation of paclitaxel that has been recommended for the treatment of breast, ovarian and non-small cell lung cancer [33–35]. Recently, we have designed liposomes based on a range of lipid compositions, generated using an ethanol-based proliposome technology. Compared to a Taxol-like formulation, the liposomal formulations of paclitaxel showed higher selectivity towards glioma cells when compared to healthy glial cells of the brain [36].

2.5.2 *Nanoparticles*

Nanoparticles may comprise a novel approach to delivering taxanes, and studies have been carried out using both paclitaxel [37] and docetaxel [38]. Fonseca et al. [39] found that PLGA nanoparticles (biodegradable, biocompatible, stable polymer) prepared using nano-precipitation method entrapped 100% of paclitaxel. Moreover, paclitaxel release from PLGA nanoparticles was initially rapid for the first 24 h after which release was slow and continuous. Furthermore, nanoparticles had a greater cytotoxic effect in comparison to Taxol® [39].

Xu and co-workers [40] used actively targetable nanoparticles (PEG-coated biodegradable polycyanoacrylate nanoparticles conjugated to transferrin) for paclitaxel delivery. Encapsulation efficiency reached as high as 94%, with drug initially released rapidly after which sustained release was achieved (81% of paclitaxel was released over 30 days). The release pattern was similar to that described by Fonseca and co-workers [39], which probably depends on polymer

erosion patterns. Moreover, drug clearance from plasma was low in comparison to Taxol®, which can be due to failure by phagocytic system to recognise the nanoparticles, as previously discussed. Additionally, antitumour activity was enhanced and increased the life span of mice to 60 days [40]. Nanoparticles are also capable of providing targeted drug delivery and concentrate in tumour cells greatly compared to Taxol®. This might be due to transferrin conjugated to the nanoparticle as tumour cells have amplified transferrin receptors hence the greater antitumour activity.

Controlled release formulations have also been studied using docetaxel, where a prodrug of the taxane was incorporated into lipid nanoparticles (LNP). Testing of the prodrug on cancer cell lines revealed the drug easily converted to the active form and showed similar activity in vivo to the parent drug. Once loaded into LNPs, it was found that drug half-life was increased, the drug was well tolerated allowing administration of three times higher than the current max dose, and accumulation in the tumour tissue was 50–100 times more than Taxotere [41]. In that study, the development of a weak-base docetaxel derivative that can be loaded into lipid nanoparticles (LNP) was investigated. The LNP functions as a solubilising agent that is similar to polysorbate 80 and Cremophor EL; however, the lipids are less toxic. LNPs in that study were used to avoid the toxicities associated with polysorbate 80. A weak-base docetaxel derivative was efficiently loaded and retained by LNP. The study found that the prodrug that was formulated using polysorbate 80 had acute toxicity (i.e. changes in body weight at a docetaxel equivalent dose of 20 mg/kg). By contrast, the LNP derivative showed no signs of toxicity (no changes in body weight) at a docetaxel dose of 88 mg/kg. The LNP formulation seemed to have advantages over the traditional docetaxel formulation, as the hypersensitivity reactions were not observed.

A widely studied alternative to Taxol® is ABI-007 that is a novel human albumin-stabilised, lyophilised nanoparticle formulation incorporating paclitaxel. It has an average size of 130 nm and is free of Cremophor EL and ethanol [42]. Ibrahim and co-workers [43] conducted a phase I study of ABI-007 on patients who were diagnosed with an advanced solid tumour or had failed the standard therapy. Nineteen patients received doses of ABI-007 which ranged from 135 to 375 mg/m^2. Three patients received infusions of ABI-007 over 2–3 h, and hypersensitivity reactions were not observed. Therefore, all the other infusions were administered over 30 min, and even at a faster infusion rate, no hypersensitivity reactions were observed [43]. Though this formulation was reported to be safer in terms of avoiding hypersensitivity reactions, other side effects that were dose dependent were reported, for example, haematological toxicity had occurred as one patient was taken to hospital for febrile neutropenia. Non-haematological toxicities were also reported such as nausea and vomiting, and muscle and joint pain were common. Ocular side effects were also reported such as ‘smoky’ vision and dry eyes. Two patients developed keratopathy where lubricating eye drops and ointments were needed to alleviate this [43]. A phase II trial carried out by Ibrahim and co-workers [44] to investigate the ABI-007 formulation in patients with metastatic breast cancer. Seven patients (11%) in that study discontinued treatment

due to adverse effects such as neuropathy. Sixteen patients (25%) required dose reductions for toxicities; toxicities resulting in a dose reduction for two or more patients were uncomplicated neutropenia, sensory neuropathy, febrile neutropenia, myalgia and fatigue. No severe ocular events were reported, and other common taxane-associated toxicities were less severe and less frequent [44]. O'Shaughnessy and co-workers [45] compared the ABI-007 formulation against the standard paclitaxel formulation in patients with metastatic breast cancer. The study involved 454 patients who either received ABI-007260 mg/m^2 infused over 30 min once every 3 weeks without premedication or Taxol® 175 mg/m^2 administered over 3 h once every 3 weeks with premedication, including dexamethasone and antihistamines. This study confirmed no hypersensitivity reactions in patients received ABI-007, despite the absence of premedication. However, 10% of the patients who received ABI-007 experienced sensory neuropathy compared to 2% who received Taxol®. In order to alleviate sensory neuropathy, ABI-007 was withheld for a number of days. Other toxicities such as neutropenia and flushing were less frequent in patients treated with ABI-007 compared to Taxol® [45]. These clinical trials have led to the development of Abraxane® (ABI-007) which is a relatively recent paclitaxel derivative available in the United States. Abraxane® is used as a second-line treatment in patients with breast cancer if combination therapy fails [46]. Abraxane® has been found to be relatively safe so that the need for the corticosteroid therapy prior to paclitaxel administration was eliminated [47]. Infusion requires only 30 min for Abraxane® compared to 3 h for Taxol® [48]. Abraxane is nowadays referred to as 'Nab-paclitaxel'. In combination with carboplatin, Nab-paclitaxel is indicated as first-line treatment of non-small cell lung cancer in patients who may not be cured by surgery or radiation therapy [49].

2.5.3 Polymeric Micelles

Genexol-PM is a novel biodegradable Cremophor EL-free polymeric micelle formulation of paclitaxel. A phase I study of Genexol-PM formulation was carried out in patients with advanced malignancies to determine the toxicities of Genexol-PM [50, 51]. Genexol-PM (1 mL) formulation contains 6 mg paclitaxel and 30 mg methoxy polyethylene glycol-poly (D,L-lactide). Nine patients had previously received taxane therapy, six of which showed tumour progression [50]. It was found that acute hypersensitivity was not observed in these patients; however, other toxicities such as neuropathy and myalgia were observed. These toxicities were dose related and the maximum tolerated dose was 390 mg/m^2. Phase II trials of Genexol-PM were conducted to evaluate the efficacy and safety of the formulation in combination with cisplatin (antineoplastic drug) in patients with advanced non-small-cell lung cancer [52]. Accordingly, 5.8% of the patients experienced hypersensitivity reactions. Recently, it has been reported that Genexol-PM plus carboplatin as first-line treatment in patients with epithelial ovarian cancer showed high efficacy and low toxicity [51].

2.5.4 *Other Formulation Strategies*

Many nanocarrier systems can be used for delivery of poorly soluble drugs (e.g. paclitaxel). For example, dendrimers are monodisperse three-dimensional, hyper-branched polymers [53]. The oligomeric-branched structures of dendrimers can be designed to increase their hydrophobicity, aiming to enhance solubility of hydrophobic drugs. It has been found that when ethylene glycol was included within dendrimer formulation, the solubility of paclitaxel markedly enhanced (1.8–2.3 mg/mL) [54]. Moreover, the solubility of hydrophobic compounds was higher, and release rate was faster when G5 dendrimers were used as compared to low-generation dendrimers (e.g. G4 or G3 dendrimers). Lack of biodegradability of many dendrimer formulations (e.g. PAMAM dendrimers) remains an obstacle for the development of clinically applicable paclitaxel formulations.

Cyclodextrins are carrier systems that have shown the ability to enhance the solubility of paclitaxel and decrease its degradation by complexing with the drug in an aqueous solution [22]. Stability of the drug is increased by increasing its solubility as the drug becomes less likely to precipitate on storage. Other methods of enhancing solubility of paclitaxel include emulsion delivery systems [55, 56]. Recently, we have loaded paclitaxel into clinically established parenteral nutrition nanoemulsions and showed that such delivery systems have cytotoxic effect against glioma cell lines [56].

2.6 Conclusions

Paclitaxel, as the most prominent and common taxane, has been traditionally administered in Cremophor EL-based formulations (e.g. Taxol®); this vehicle is reliable for solubilising paclitaxel, but it causes many adverse effects. Several nanocarrier formulations of paclitaxel have shown to be appropriate alternatives to Cremophor EL formulations, owing to their biodegradability and the fewer adverse effects caused by the drug incorporated into these carriers. Many paclitaxel formulations based on nanotechnology are under investigations, and some are in the pipeline of commercialization.

References

1. Zhang A, Anyarambhatla L, Ma G, Ugwu L, Xuan S, Sardone T, Ahmed T, I. (2004) Development and characterization of a novel Cremophor EL free liposome-based paclitaxel (LEP-ETU) formulation. Eur J Pharm Biopharm 59:177–187
2. Vaishampayan U, Parchment ER, Bhaskara JR, Maha H (1999) Taxanes: an overview of the pharmacokinetics and pharmacodynamics. Urology 54(6):122–129

3. Thiesen J, Krämer I (1999) Physico-chemical stability of docetaxel premix solution and docetaxel infusion solutions in PVC bags and polyolefine containers. Pharm World Sci 21 (3):137–141
4. Verweij J, Clavel M, Chevalier B (1994) Paclitaxel and docetaxel: not simply two of a kind. Ann Oncol 5:495–505
5. Jordan AM, Toso JR, Thrower D, Wilson L (1993) Mechanism of mitotic block and inhibition of cell proliferation by taxol at low concentrations. Proc Natl Acad Sci USA 90:9552–9556
6. DeVita VT, Lawrence TS, Rosenberg SA, Weinberg RA, DePinho RA (2008) DeVita, Hellman, and Rosenberg's cancer: principles & practice of oncology, vol 1. Lippincott Williams and Wilkins, Philadelphia, pp 447–450
7. Schiff PB, Fant J, Horwitz SB (1979) Promotion of microtubule assembly *in vitro* by taxol. Nature 277:665–667
8. Rowinsky EK, Cazenave LA, Donehover RC (1990) Taxol: a novel investigational microtubule agent. J. Natl. Cancer Inst. 82:1247–1259
9. Singla AK, Garg A, Aggarwal D (2002) Paclitaxel and its formulations. Int J Pharm 235:179–192
10. O'Connell CB, Khodjakov AL (2007) Cooperative mechanisms of mitotic spindle formation. J Cell Sci 120:1717–1722
11. Crown J, O'Leary M (2000) Taxanes an update. Lancet 355:1176–1178
12. Kaye S, Piccart JM, Gore M, Huinink BTW, Oosterom VA, Verweij J, Wanders J, Franklin H, Bayssas M (1995) Docetaxel: an active new drug for treatment of advanced epithelial ovarian cancer. J Natl Cancer Inst 87(9):676–681
13. Engblom P, Pulkkinen OJ, Rantanen V, Hirvonen H, Kulmala J, Grènman R, Grènman S (1999) Effects of paclitaxel with or without cremophor EL on cellular clonogenic survival and apoptosis. Eur J Cancer 35(2):284–288
14. Nuijen B, Bouma M, Schellens JHM, Beijnen JH (2001) Progress in the development of alternative pharmaceutical formulations of taxanes. Invest New Drugs 19(2):143–153
15. Immordino ML, Brusa P, Arpicco S, Stella B, Dosio F, Cattel L (2003) Preparation, characterization, cytotoxicity and pharmacokinetics of liposomes containing docetaxel. J Control Release 91:417–429
16. Engels FK, Mathot RAA, Verweij J (2007) Alternative drug formulations of docetaxel: a review. Anticancer Drugs 18:95–103
17. Kattige A (2006) Long-term physical and chemical stability of a generic paclitaxel infusion under simulated storage and clinical-use conditions. Eur J Hosp Pharm Sci 12(6):129–134
18. Eroles AA, Bafalluy IM, Arnaiz JAS (2009) Stability of docetaxel diluted to 0.3 or 0.9 mg/mL with 0.9% sodium chloride injection and stored in polyolefin or glass containers. Am J Health Syst Pharm 66(17):1565–1568
19. Donyai P, Sewell GJ (2006) Physical and chemical stability of paclitaxel infusions in different container types. J Oncol Pharm Pract 12(4):211–222
20. Pourro B, Botta C, Solas C, Lacarelle B, Braguer D (2005) Seventy-two-hour stability of Taxol® in 5% dextrose or 0·9% sodium chloride in Viaflo®, Freeflex®, Ecoflac® and Macoflex N® non-PVC bags. J Clin Pharm Ther 30(5):455–458
21. Trissel LA, Xu QA, Gilbert DL (1998) Compatibility and stability of paclitaxel combined with doxorubicin hydrochloride in infusion solutions. Ann Parmacother 32(10):1013–1016
22. Dordunoo SK, Burt HM (1996) Solubility and stability of taxol: effects of buffers and cyclodextrins. Int J Pharm 133(1–2):191–201
23. Waugh WN, Trissel LA, Stella VJ (1991) Stability, compatibility, and plasticizer extraction of taxol (NSC-125973) injection diluted in infusion solutions and stored in various containers. Am J Hosp Pharm 48(7):1520–1524
24. Murphy SR, Wadey BL (1988) DEHP and toxicity. J Vinyl Technol 10(3):121–124
25. Dorr RT (1994) Pharmacology and toxicology of Cremophor EL diluent. Ann Pharmacother 28:511–514
26. Lilley LL, Scott HB (1993) What you need to know about taxol? Am. J. Nurs. 93:46–50

27. Gelderblom H, Verweij J, Nooter K, Sparreboom A (2001) Cremophor EL: the drawbacks and advantages of vehicle selection for drug formulation. Eur J Cancer 37:1590–1598
28. Lam YW, Chan CY, Kuhn JG (1997) Pharmacokinetics and pharmacodynamics of the taxanes. J. Oncol. Pharm. Pract 3:76–93
29. Yang T, Choi MK, Chung SJ, Shim CK, Kim CC (2007) Liposome formulation of paclitaxel with enhanced solubility and stability. Drug Deliv 5:3
30. Sharma A, Mayhew E, Bolcsak L, Cavanaugh C, Harmon P, Janoff A, Bernacki RJ (1997) Activity of paclitaxel liposome formulations against human ovarian tumor xenografts. Int. J. Cancer 71:103–107
31. Fetterly GJ, Straubinger RM (2003) Pharmacokinetics of paclitaxel-containing liposomes in rats. Am Assoc Pharm Sci 5(4):90–100
32. Kunstfeld R, Wickenhauser G, Michaelis U, Teifel M, Umek W, Naujoks K, Wolff K, Petzelbauer P (2003) Paclitaxel encapsulated in cationic liposomes diminishes tumor angiogenesis and melanoma growth in a "humanized" SCID mouse model. J Invest Dermat 120:476–482
33. Koudelka S, Turánek J (2012) Liposomal paclitaxel formulations. J Control Release 163:322–334
34. Wang H, Cheng G, Du Y, Ye L, Chen W, Zhang L, Wang T, Tian J, Fu F (2013) Hypersensitivity reaction studies of a polyethoxylated castor oil-free, liposome-based alternative paclitaxel formulation. Mol Med Rep 7:947–952
35. Bernabeu E, Cagel M, Lagomarsino E, Moretton M, Chiappetta DA (2017) Paclitaxel: what has been done and the challenges remain ahead. Int J Pharm 526:474–495
36. Najlah M, Jain M, Wan KW, Ahmed W, Albed Alhnan M, Phoenix DA, Taylor KM, Elhissi A (2016) Ethanol-based proliposome delivery systems of paclitaxel for in vitro application against brain cancer cells. J Liposome Res:1–12. https://doi.org/10.1080/08982104.2016.1259628
37. Musumeci T, Vicari L, Ventura CA, Gulisano M, Pignatello R, Puglisi G (2006) Lyoprotected nanosphere formulations for paclitaxel controlled delivery. J Nanosci Nanotechnol 6:1–8
38. Ahmad N, Alam MA, Ahmad R, Naqvi AA, Ahmad FJ (2017) Preparation and characterization of surface-modified PLGA-polymeric nanoparticles used to target treatment of intestinal cancer. Artif Cells Nanomed Biotechnol 1-14. doi:https://doi.org/10.1080/21691401.2017.1324466
39. Fonseca C, Simo'es S, Gaspar R (2002) Paclitaxel-loaded PLGA nanoparticles: preparation, physicochemical characterization and in vitro anti-tumoral activity. J Control Release 83:273–286
40. Xu Z, Gu W, Huang J, Sui H, Zhou Z, Yang Y, Yan Z, Li Y (2005) In vitro and in vivo evaluation of actively targetable nanoparticles for paclitaxel delivery. Int J Pharm 288:361–368
41. Zhigaltsev IV, Winters G, Srinivasulu M, Crawford J, Wong M, Amankwa L, Waterhouse D, Masin D, Webb M, Harasym N, Heller L, Bally MB, Ciufolini MA, Cullis PR, Maurer N (2010) Developement of a weak-base docetaxel derivative that can be loaded into lipid nanoparticles. J Control Release 144:332–340
42. Desai N, Yao Z, Soon-Shiong P, Dykes D (2002) Evidence of enhanced in vivo efficacy at maximum tolerated dose (MTD) of nanoparticle paclitaxel (ABI-007) and taxol in 5 human tumor xenografts of varying sensitivity to paclitaxel. Am Soc Clin Oncol 21:462
43. Ibrahim NK, Desai N, Legha S, Soon-Shiong P, Richard L, Rivera ET, Esmaeli B, Ring ES, Bedikian A, Hortobagyi NG, Ellerhorst AJ (2002) Phase I and pharmacokinetic study of ABI-007, a cremophor-free protein-stabilized, nanoparticle formulation of paclitaxel. Clin Cancer Res 8:1038–1044
44. Ibrahim NK, Samuels B, Page R, Doval D, Patel MK, Rao CS, Nair KM, Bhar P, Desai N, Hortobagyi GN (2005) Multicenter phase II trial of ABI-007, an albumin-bound paclitaxel, in women with metastatic breast cancer. J Clin Oncol 23(25):6019–6026

45. O'Shaughnessy J, Tjulandin S, Davidson N, Shaw H, Desai N, Hawkins MJ (2003) ABI-007 (ABRAXANE™), a nanoparticle albumin-bound (nab) paclitaxel demonstrates superior efficacy vs taxol in MBC: a phase III trial. Proceedings from the 26th annual San Antonio Breast Cancer Symposium, San Antonio, Texas, USA
46. Green MR, Manikhas GM, Orlov S, Afanasyev B, Makhson AM, Bhar P, Hawkins MJ (2006) Abraxane, a novel cremophor-free, albumin-bound particle form of paclitaxel for the treatment of advanced non-small-cell lung cancer. Ann Oncol 17:1263–1268
47. Gradishar WJ, Tjulandin S, Davidson N, Shaw H, Desai N, Bhar P, Hawkins M, O'Shaughnessy J (2005) Phase III trial of nanoparticle albumin-bound paclitaxel compared with polyethylated castor oil-based paclitaxel in women with breast cancer. J Clin Oncol 23 (31):7794–7803
48. Garber K (2004) Improved paclitaxel formulation—hints at new chemotherapy approach. J Natl Cancer Inst 96:90–91
49. Blair HA, Deeks ED (2015) Albumin-bound paclitaxel: a review in non-small cell lung cancer. Drugs 75:2017–2024
50. Kim T-Y, Kim D-W, Chung J-Y, Shin SG, Kim S-C, Heo SD, Kim KN, Bang Y-J (2004) Phase I and pharmacokinetic study of genexol-pm, a cremophor-free, polymeric micelle-formulated paclitaxel, in patients with advanced malignancies. Clin Cancer Res 10:3708–3716
51. Lee SW, Kim YM, Cho CH, Kim YT, Kim SM, Hur SY, Kim JH, Kim BG, Kim SC, Ryu HS, Kang SB (2017) An open-label, randomized, parallel, phase II trial to evaluate the efficacy and safety of a cremophor-free polymeric micelle formulation of paclitaxel as first-line treatment for ovarian cancer: a Korean Gynecologic Oncology Group study (KGOG-3021). Cancer Res Treat. In Press Cancer Res Treat. doi: 10.4143/crt.2016.376
52. Kim D-W, Kim S-Y, Kim H-K, Kim S-W, Shin S-W, Kim SJ, Park K, Lee YM, Heo SD (2007) Multicenter phase II trial of Genexol-PM, a novel Cremophor-free, polymeric micelle formulation of paclitaxel, with cisplatin in patients with advanced non-small-cell lung cancer. European Society for Medical Oncology 18:2009–2014
53. Najlah M, D'Emanuele A (2006) Crossing cellular barriers using dendrimer nanotechnologies. Curr Opin Pharmacol 6:522–527
54. Ooya T, Lee J, Park K (2003) Effects of ethylene glycol-based graft, star-shaped, and dendritic polymers on solubilization and controlled release of paclitaxel. J Control Release 93:121–127
55. Kan P, Chen ZB, Lee CJ, Chu IM (1999) Development of nonionic surfactant/phospholipid o/w emulsion as a paclitaxel delivery system. J Control Release 58:271–278
56. Najlah M, Kadam A, Wan KW, Ahmed W, Taylor KM, Elhissi AM (2016) Novel paclitaxel formulations solubilized by parenteral nutrition nanoemulsions for application against glioma cell lines. Int J Pharm 506:102–109

Chapter 3
Nanotechnology and Its Applications in Knee Surgery

Tariq A. Kwaees, Adrian Pearce, Jo Ring, Paul Sutton, and Charalambos P. Charalambous

3.1 Introduction

Nanotechnology is the application and manipulation of structures, typically particles or molecules within the 'nano' range. Subatomic particles (protons, electrons and neutrons) are the smallest building blocks of atoms, which bond together to form molecules. Elements are many molecules of the same atom, whilst compounds are many molecules of a mixture of atoms. Technically, a single atom is the smallest unit of matter, but matter is regarded as being molecular. The prefix nano in the metric system represents a distance of one billionth of a metre (nm) and is represented numerically as one times ten to the power minus nine (10^{-9} or 0.000000001 m). Nanoparticles have one dimension that measures 100 nm or less and contain 4–400 atoms [1]. The properties of many conventional materials change when formed from or are exposed to nanoparticles as they have a greater surface area to weight ratio making them potentially more reactive to other materials [2]. Nanostructures are 1–100 nm and comprised of molecular nanomaterials which may be natural or artificial. Natural nanostructures include light amplifying pigment particles such as those that occur in the corneas of moths [3], adhesive compounds forming pads on the feet of geckos which aid climbing [4] and nanotubules in some plants which have diverse functions, from a defence against UV radiation in mountain flowers to a self-cleaning mechanism in the lotus flower [5]. The most common artificial nanostructures in current nanotechnologies include graphene nanotubes of single,

T.A. Kwaees • A. Pearce • J. Ring
Department of Trauma and Orthopaedics, Blackpool Victoria Hospital, Blackpool, UK

P. Sutton
Northern General Hospital, Sheffield, South Yorkshire, UK

C.P. Charalambous (✉)
School of Medicine, University of Central Lancashire, Preston, Lancashire PR1 2HE, UK
e-mail: Mr.charalambous@bfwhospitals.nhs.uk

M.J. Jackson, W. Ahmed (eds.), *Micro and Nanomanufacturing Volume II*,
DOI 10.1007/978-3-319-67132-1_3

double or multiple layers which can be oriented into one complete tube inside another (Russian doll configuration) [6] or constructed into a continuous graphene sheet rolled upon itself (parchment configuration) [7]. The various configurations offer a variety of electrical, chemical and mechanical properties.

3.2 Current Concepts in Nanomedicine

Potential nanotechnology applications are currently being explored in medicine generally; however, this chapter is particularly concerned with applications in orthopaedics [1, 8, 9]. Some examples which give an idea of the scope of applications in medicine include nanoconstituent and nanoarchitecture modifications to implant coatings [10–15], diagnostics [16] and patient monitoring [17]. Advances in pharmacokinetics include improving drug targeting [18], efficacy optimisation, potency and side effect reduction [19]. Examples of how these techniques work include polymeric micelle nanoparticles with surface receptors that can specifically identify particular tumours and deliver drugs directly to tumour cells avoiding generalised cell destruction [20]. Another example of a targeting modality involves the attachment of a chemotherapy drug to a nanodiamond which has been used to treat brain tumours [21] and leukaemia [22]. Nanoparticles may be combined with specific antibodies known as 'quantum dots' (Invitrogen) to target neoplastic or infected cells [23]. Docetaxel (Cristal Therapeutics) for the treatment of solid tumours is a good example of the possibilities of nanotechnology and has recently commenced phase I clinical trials in 2015 [24].

In the field of infection control and prevention, nanotechnology has been used to improve the antimicrobial properties of healthcare clothing and equipment. Integrating nanosilicon particles into materials such as scrubs or surgical gowns has been shown to greatly enhance their antimicrobial capacity [25, 26]. Furthermore, polymer-coated iron oxide nanoparticles disrupt clusters of bacteria, with the potential to facilitate more effective treatment of chronic bacterial infections [27]. - Protein-filled nanoparticles have been used in the form of an inhalational vaccine to promote an enhanced immune response [28].

Regenerative and preventative medicine has also been influenced by nanotechnology. Cerium oxide nanoparticles act as an antioxidant to remove oxygen-free radicals following trauma [29], and protein-linked nanodiamonds increase bone growth around dental or joint implants [30]. Nickel nanoparticles combined with a polymer form a self-healing, synthetic skin, which could potentially be used in the development of prosthetics [31]. Of particular interest is the phenomenon the material exhibits when cut, where it spontaneously heals itself within 30 min if held together. It also exhibits electrical resistance properties which change with pressure, giving it the ability to function as a form of synthetic touch. The development of advanced imaging systems may allow disease to be detected and potentially treated even in its early stages [32]. Combining nanoparticles with

dyes or marker substances to allow the intraoperative visualisation of diseased tissue may greatly improve resection accuracy [33]. Implantable nanowires give real-time monitoring of physiological parameters which may aid chronic disease management and access to emergency treatment [34].

Nanoarrays have superseded microarray analysis, which was once regarded as the future of biomolecular analysis [35]. Limitations of microarrays include large sample volumes, longer incubation times, limited detection, bulky instrumentation, laborious sample amplification and labelling ultimately resulting in high running costs and delays. Nanotechnology may improve the speed and quality of diagnostic tests by moving complex tests from specialised centres to the bedside or office. Current operational protocols exist for nanoarray technology in label-free analysis of nucleic acids, protein detection (using conventional optical fluorescence microscopy or novel label-free atomic force microscopy) [35]. Furthermore, multiple tests can be combined onto a single 'lab-on-a-chip' and processed rapidly using hand-held devices [36].

The examples above are not exhaustive but demonstrate the wide and variable uses of nanotechnology and the great potential for further development and use.

3.3 Current Concepts in Nano-Orthopaedic Research

Nanotechnology may provide the means of manipulating the organic and inorganic nanostructures of the bone and its surrounding soft tissues, representing a new avenue for the treatment of musculoskeletal disorders. Ongoing research into the application of nanotechnology within the field of orthopaedics is diverse; however, much of this remains at the laboratory stage with few clinical studies testing technologies in vivo [1, 8]. The current literature suggests three main and overlapping areas of exploration in orthopaedic nanotechnology: nanoscaffolds, implant and tissue integration and drug delivery.

3.3.1 Nanoscaffolds

Nanoscaffolds may be used for local drug or gene therapy delivery or act to regulate cellular processes and can be used as a growth material for tissue engineering purposes. Nanoscaffolds are typically comprised of electrospun nanofibre matrices [37]. These scaffolds are designed to be biomimetic particularly representing extracellular matrix structure and function [38]. This technology has the potential to be incorporated into implants to improve their integration with the bone [39, 40] and to combat biofilm-related infections of implants [14] and can be applied in tissue engineering to create artificial versions of natural substances [41].

3.3.2 Implant Integration

Biological integration of implants into the human body is highly sought after in orthopaedics. Aseptic loosening remains a major cause of revision in arthroplasty surgery [42–45]. Modification of existing materials such as titanium, tantalum, ceramics and hydroxyapatite at the nano level may facilitate biological activity [46, 47]. Evidence from previous research has indicated that if this can be safely harnessed it may decrease the incidence of revision in major joint arthroplasty [9, 14, 48, 49]. Infection is also a leading cause of implant failure and lack of integration. Nanoscale surface modification of orthopaedic implants has been found to be effective in reducing bacterial adherence, biofilm creation and disrupting bacterial cell homeostasis [14]. The fight against primary and secondary bone malignancy, which frequently requires the use of implants, may also be improved with the aid of nanotechnology. Tran et al. conducted an experimental in vitro study which examined the effects of three novel, hybrid implant surfaces of selenium and titanium on cancerous bone tissue. They found that the selenium adherent surfaces chemotherapeutic and osteointegrative when compared to untreated titanium implants [50].

3.4 Drug Delivery

3.4.1 Chemotherapeutics

The avoidance of healthy cells via the targeted delivery of therapeutic substances to diseased tissue is another possible role of nanotechnology which could revolutionise the management of some diseases. There is a potential to improve pharmacokinetics, efficacy, lower doses and lower drug-related toxicity [19]. Drugs contained within nanocapsules consisting of a nanoengineered coat with coded surface protein that unlock at the target cell are one method of applying this technology [18] (Fig. 3.1). The potential applications of such nanocoats could greatly improve orthopaedic care including the targeting of neoplastic bone disease and common orthopaedic conditions such as osteoarthritis and osteoporosis [51]. Bisphosphonates are currently the vessel of choice for improving the targeting of bone using nanotechnology due to their high affinity to the organ [51]. Their use with nanoparticles has been shown to limit metastasis, reduce tumour seeding and angiogenesis [51]. Bisphosphonates have been used in the treatment of bone metastasis to deliver chemotherapeutics directly to the organ, maintaining higher levels of the drug at target tissues and slowing its metabolic breakdown [52]. The treatment of primary bone tumours could also be influenced by nanotechnology. The delivery of chemotherapeutic substances to osteosarcoma has been improved with the use of nanoparticles and was able to tackle multidrug-resistant forms of the disease [53]. The combination of nanomedicine with gene therapy may have an

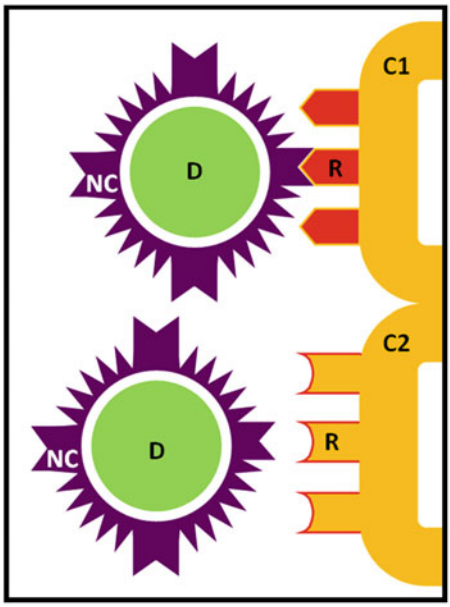

Fig. 3.1 Nanocoating drug system. The drug (D) is contained within a nanocoat (NC) which meets receptors (R) on target cells (C1) whilst avoiding receptors on nontarget tissue (C2)

even greater effect on treating such tumours [54]. Nanoparticles have been used to improve the efficacy of bisphosphonates in treating osteoporosis and have been shown to improve the retention time of interleukin receptor inhibitors in the treatment of osteoarthritis [51]. By similar means nanotechnology could be applied to improve drug delivery in the treatment of osteoarthritis, osteomyelitis and benign neoplastic conditions. The cells responsible for pigmented villonodular synovitis (PVNS) can be made more sensitive to radiotherapy resulting in a reduction of overall radiation dose and its associated risks [55].

3.4.2 Antimicrobial Applications

The use of nanocrystals of silver versus larger molecules in the surface coatings of arthroplasty implants to control and extend the release of antibiotics has been shown to reduce bacterial adhesion [56]. The use of synergistic nanomolecules such as nanophase gold which enhances the transcutaneous uptake of non-steroidal anti-inflammatories as also shown similar results. Currently, nanotechnology is utilised in wound dressings impregnated with silver nanocrystals which have a lower finite amount of silver but have been shown to have increased potency compared with larger molecules [57].

3.5 Nanotechnology Applications in Knee Surgery

3.5.1 Knee Arthroplasty

Total knee arthroplasty is well established with excellent success rates [58]. The standard expected of any new implant entering the market is a ten-year survival rate in greater than 90% of cases; however, aseptic loosening and infection remain leading causes of failure [58]. Aseptic loosening in total knee arthroplasty is a significant challenge and is more common in uncemented rather than cemented and hybrid implants [58]. It is the indication for over 40% of single stage revision knee replacements in the United Kingdom [58]. Target rates of infection in joint arthroplasty are quoted as <0.5%, but actual rates are under 2% [58]. Despite major advances, infection remains a major cause for implant failure and burden in revision surgery [58].

Better osteointegration is brought about by altering the mechanical nature of the implant, i.e. creating a more porous architecture for bone ingrowth or by altering chemical characteristics leading to selective bonding to bone and inhibition of fibrous healing [59]. Nanoengineered coatings may provide chemical, mechanical and ultimately biological enhancement to implant integration, improving long-term performance [60]. The nature of an implant surface dictates implant–host interaction [11, 48, 61–63] and nanotechnology has been employed in the effort to improve osteointegration [64–67] and counter bacterial adhesion and growth [68–74]. Osteoblast adherence to implants occurs on the nanoscale; therefore, altering the surface roughness of an orthopaedic implant from the macro to the nanoscale could improve osteointegration whilst inhibiting suboptimal fibrous tissue from forming [62, 75, 76] (Fig. 3.2). This has been demonstrated in animal studies with good results. Salou et al. assessed the pull-out resistance and histological characteristics between macro-surface implants created through standard manufacturing techniques and nanosurface implants of titanium nanotubules. Pull-out strength and histological evidence of osteointegration were improved with the nanoscale surfaces [77]. Addition of nanoparticles of hydroxyapatite or titanium may further enhance this process [60, 78].

Surface topography can influence bacterial behaviour, and nanotechnology has been shown to reduce adherence [48, 79] (Fig. 3.3). Lab-based research has demonstrated marked reductions in the adherence of multiple bacterial species [80], and silver nanosurfaces have been found to be bactericidal by interfering in bacterial cell homeostasis [74, 81]. Improving the quality of orthopaedic cement, a substance which has remained relatively unchanged for decades, as well as the cement bone interface may also be achieved with nanotechnology leading to lower risk of failure and cement fracture. Khandaker et al. added nanoform magnesium oxide to bone cement and found marked improvement in fracture toughness of the cement which could have implications for implant longevity [82]. Ricker et al. investigated the effects of added barium sulphate and magnesium oxide nanoparticles on methyl methacrylate bone cement. They noted reductions in the

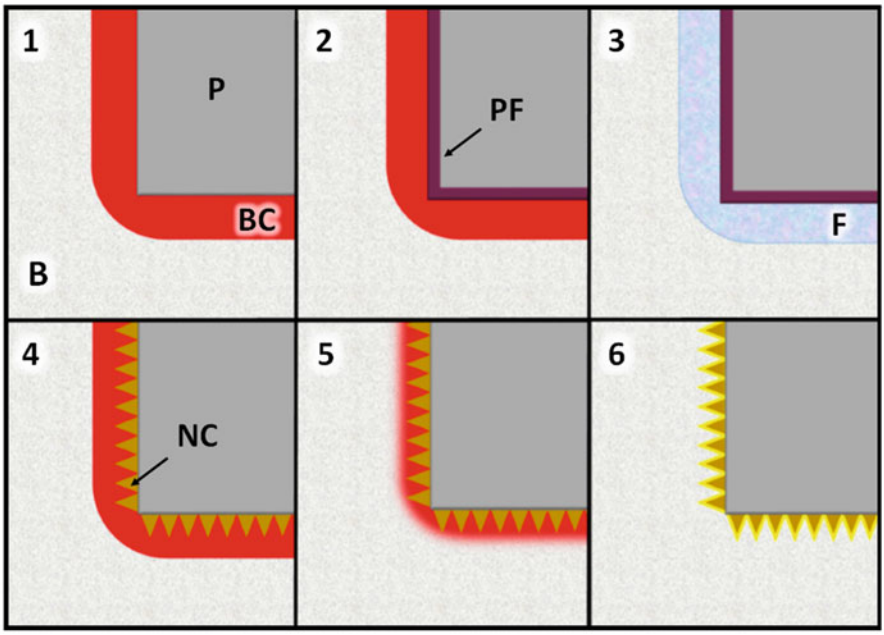

Fig. 3.2 Implant integration with the bone; immediately after bone (B) preparation blood components (BC) surround the prosthesis (P) within the bone (1); platelet-derived factors (PF) coat the prosthesis and prevent integration with healing tissue (2); suboptimal fibrous tissue develops with poor pull-out strength (3); enhanced implant integration with nanosurface modification (NC) prevents PF from binding and allows for better implant bone interface bonding (4–6)

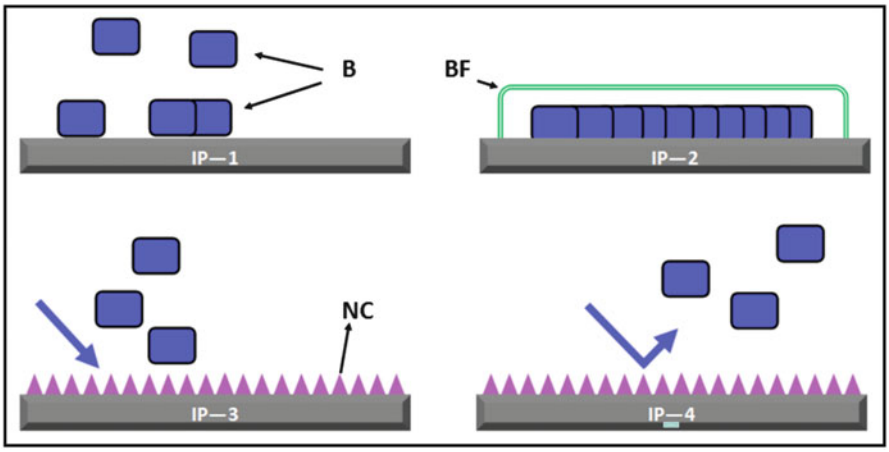

Fig. 3.3 Prevention of bacterial colonisation on implant surfaces. Bacteria (B) seed onto the implant (IP-1) and soon form colonies (P-2) surrounded by biofilm (BF). Nanocoating (NC) can be used to alter the surface of an implant to reduce bacterial adhesion (IP-3 and IP-4)

harm caused during the curing process and an increase in osteointegration with the nanoparticles [83]. Valuable evidence for improved osteointegration using nanotechnology has come from the field of dentistry. Modifications to the surface of implants with bioactive ceramics to improve interaction at the bone implant interface and coating material such as various phosphates, hydroxyapatite and bioactive glasses have been shown to hold promise [59].

3.5.2 Repair and Restoration of Cartilage

One of the more complex aspects of knee surgery is the management of cartilage defects. Restoring, replacing and rejuvenating articular cartilage are all aspirations of the knee surgeon but are currently impossible. Techniques including microfracture, drilling and transplants give rise to suboptimal fibrous scar tissue which does not provide the same biomechanical properties as true cartilage [84]. Innovative techniques such as patch graft repairs with autologous stem cells are laborious, expensive and inconsistent in their results. Nanoscaffolds may provide opportunities to improve this aspect of knee surgery. Creating a three-dimensional structure formed of biodegradable polymers that function as a scaffold for stem cell adherence programmed differentiation according to tissue requirements and eventual integration into the surrounding native tissue [85]. This could be achieved through programmed obsolescence (e.g. hydrolysis) and has been realised in other areas of the body [86]. Kon et al. used a nanostructured scaffold to surgically pack a chronic degenerative chondral lesion in a high demand knee. The response to treatment was monitored clinically with pain-free function at a year following surgery and by MRI which demonstrated healing [87]. Alternatively, a more robust or self-healing synthetic mimic, which retains the biomechanical properties of cartilage, could be created. This is exemplified by newer nanoplastics developed for use in prosthetics, with the ability to self-repair following micro or even macro level damage [41]. These can be created as multilayered structures which may better represent interfaces between tissues such as cartilage and bone [88]. Nanocomposites have been developed using Type I collagen and hydroxyapatite with promising results [88].

3.5.3 Anterior Cruciate Ligament Injury

ACL ruptures are common, with an estimated incidence rate of 37 per 100,000 person-years or approximately 118,000 ruptures in the USA alone [89]. Up to two thirds of these patients (79,000) experience instability that limits their daily activity or sport and recreation [90] with up to 76.6% of such patients requiring surgery [90]. A review of approximately 13,000 ACL reconstructions on the Swedish knee

ligament register reported a 1.6% incidence of revision surgery at 2-year follow-up [91].

Success of an ACL reconstruction relies upon two key ideologies: the constituents of the graft and the integration of the graft with the host [92, 93]. The former primarily addresses the strength of the mobile segment of the repair, its kinematics through ranges of movement and its longevity. The latter is concerned with the degree and speed with which biological integration occurs in the static segments (proximal and distal) of the graft embedded within bone tunnels and the minimisation of factors that would weaken the integration over time. ACL reconstruction represents a unique area in which to test the possible applications of current nanotechnological concepts and to consider new avenues for their development which could aid in addressing these two points. The current focus of investigation includes the creation of artificial ligament replacements which is less common than autograft repair but is still used and the enhancement of bone graft integration [85, 94–97]. The manufacturing of artificial grafts which incorporate into host tissue and function as a native ACL is still at the exploratory stage.

The incorporation of a graft into bone tunnels provides long-term fixation; however, this remains the weak link in ACL reconstruction, accounting for early failures and limiting the speed of rehabilitation [98]. Multiple tissue engineering strategies using nanotechnology are being developed for improved bone graft interface healing and include local delivery of bioactive compounds such as collagen using scaffolds, coating of implants and grafts and augmentation of the canal [99]. Chou et al. undertook an in vivo study looking at the pull-out strength and histological features of collagen and biodegradable poly lactic-co-glycolic acid coated nanofibre membrane graft in the form of a scaffold. Histologically the researchers noted a reduction in tunnel size and greater graft-bone integration in the form of fibre-bone anchors using the scaffold. Pull-out strength was much greater in those treated with the scaffold [100]. Han et al. examined the tissue integration of tendon graft wrapped in polycaprolactone/nanohydroxyapatite/collagen nanofibre and non-wrapped tendon in vitro and in vivo. Wrapped semimembranosus ACL graft was found to have better integration, mineralisation and mechanical stretch [101]. Grant et al. undertook a study in which human tendon impregnated with various combinations of gold and hydroxyapatite nanoparticles was grafted into animal models in place of an ACL. These were compared with nonimpregnated grafts after approximately 3 months, and it was found that grafts with gold nanoparticles had greater new growth of fibrous connective tissue and higher vascularity [102]. These results support the findings by Smith et al. who undertook a similar study of gold and hydroxyapatite nanoparticles and found improved cell viability [103].

Some ACL tears are amenable to repair, but ligament healing forms a fibrous scare resulting in inferior biomechanical properties [100, 104]. It may be possible to enhance this or to create ligament substitutes from nanoengineered materials which may improve integration and physical properties and decrease donor site morbidity. In addition, nanoscaffolds could be used to augment existing grafts to enhance

integration properties with bone [93], which could enhance the pace of healing and the ability to return to activities compared to existing techniques [99, 100].

3.6 Trauma Applications

Given the nanocomposite nature of bone, osseous trauma can be difficult to treat with traditional surgical methods of fixation which lack nanoscale properties. This is especially the case in areas of poor healing such as the femoral head and talus which are at risk of avascular necrosis, stripped soft tissue covering, bone loss and superimposed infection. The key principles of this technology for healing include attractive mechanical characteristics, surface modification of implants to aid fixation and scaffolds for tissue integration or defect filling.

3.6.1 Surface Modification

Modification of existing fracture fixation techniques using nanotechnology to enhance incorporation into the host tissue, to reduce the need for foreign material implantation or to reduce the need for repeated procedures to remove implants once healing is complete is key research areas. The biocompatibility of an implant is determined by its surface characteristics, and nanoscale coating applied to their surface may offer a solution in terms of accelerated bony healing and minimal tissue reaction to foreign material. Surface characteristics include the surface area or roughness, hydrophobicity and immunogenicity which determine the implant's ability to integrate into the body and influence healing [105]. Surface modification at the nanoscale can be achieved by several methods, including altering the structure of endogenous substances such as collagen, creation of artificial nanomaterials applied to the surface of implants or anodization of existing materials, primarily metals [105].

Alteration of metallic and ceramic implant surfaces at the nanoscale has been shown to improve osteoblasts adhesion and proliferation, calcium deposition and alkaline phosphatase activity [105]. A recent study used bioactive and degradable nanocomposite coating on k-wire fixation of animal tibia in vivo and evaluated these at 1 and 2 months postoperatively [106]. The results indicated minimal soft tissue reaction and an increase in healing rate in those treated with the nanocoat. Hydroxyapatite-coated screws have been trialled in hip fracture surgery and have been shown to provide superior fixation in osteoporotic bone [107] as an effective coating for half pins in external fixation constructs. These applications are particularly relevant around the knee where removal or metalwork may be required before subsequent surgery, for example, knee replacement following high tibial osteotomy or tibial plateau fixation. In addition, fixation of osteochondral fractures and meniscal tears within the knee are perfectly suitable for nanoengineered

fixation devices due to the intra-articular environment which better mimic the tissue and incorporate over time as the tissue heals.

3.6.2 Scaffolds

Orthopaedic fixation devices could be engineered to have properties that encourage healing and regeneration which current implants do not offer. Key to fracture healing is the extracellular matrix which not only serves as a scaffold for growth and healing but also acts as a source of growth factors and other key constituents of repair [108]. Implantation of impregnated, degradable scaphoids could enhance bone healing by providing an immediate source of bone-forming cells and materials with minimal tissue reaction. Peptides which undergo self-assembly into nanostructures (termed self-assembling peptides) have been shown to enhance cell replication and proliferation and promote bone regeneration and healing whilst inhibiting demineralization. Another option for surface modification to improve bone healing is with carbon nanotubes, multiple forms of which have been shown to improve bone repair and provide exceptional mechanical stability; however, peptides are more versatile in terms of architecture and are less hydrophobic. Coating of titanium or hydroxyapatite implants with components of the ECM such as collagen and chondroitin sulphate may greatly improve the quality of fracture fixation and speed of bony healing [108]. Recent advances in biologically engineered hydrogels at the nano level have been shown to dramatically improve the osseous forming components following fracture. Hydrogel biomaterials are highly porous structures which can mimic the extracellular matrix and enhancing these at the nanoscale may greatly improve bone healing. Xavier et al. undertook a study in which collagen-based hydrogels impregnated with nanosilicates of orthosilicic acid (bioavailable silicon utilised by living organisms), magnesium and lithium were created and used in the healing of non-united fractures. They found a marked increase in the activity of alkaline phosphatase and the formation of mineralised matrix. They concluded that adequate osteogenesis could occur even in the absence of osteoinductive and growth factors [109]. These substances could be injected into osseous defects both in the immediate postfracture period and in chronic non-unions, optimising healing whilst gradually being replaced by native tissue. Nanocomposite hydrogels may also be used to induce stem cells into a desired cell type by mimicking bone-inducing growth factors [110].

Gao et al. examined the potential applications of nanotechnology in treating avascular necrosis of the femoral head by applying nanoscale decompression cores containing mesenchymal stem cells in 12 patients with early stages of the disease and found that the treatment was effective in alleviating symptomology and improving radiographic appearance [111]. Yang et al. also looked at the applications of nanotechnology on avascular necrosis of the femoral head. Patients were treated with core decompression in combination with a nanohydroxyapatite and polyamide rod and a porous bioglass bone graft, and an equal number were treated

with core decompression with an autologous cancellous bone graft. The clinical failure rate was lower in the non-particle-enhanced approach, and overall, symptomology and functionality were better in this group [112].

3.7 Bone Grafting

There has been much interest in the world of nanotechnology around bone graft substitutes using nanoengineered scaffolds and other techniques. These products would be particularly useful around the knee both in trauma surgery and in revision knee arthroplasty as bone loss can be an issue in some cases following implant removal. Currently bone graft is used for small defects, and larger defects are managed with augments or wedges that are usually metal or polyethylene. The current augmentation techniques are effective but do not reconstitute the patient's bone stock. The use of nanoengineered structural scaffolds with biological properties could be very effective in this area to fill these defects and provide structural stability, whilst natural bone stock is restored during the integration process. Nanoparticles of various bone graft substances are in development, and these have shown promising results in addition to nanoscaffolds in combination with bone morphogenic proteins, the latter having been shown in vivo to be a highly effective osteogenic and osteoconductive graft substance [37]. Other in vivo studies have looked at the potential of filling bone defects with nanotechnology and have shown exciting results. Recent studies have examined the effects of a nanoscale filling material in the form of porous hydroxyapatite as a substitute for bone graft and found that normal bony healing resulted, including a mature haversian system [113].

3.8 Safety Considerations

The question of safety relating to the use of nanotechnology is not without justification. Nanoparticles can be toxic and have been associated with a host of human disease and may result in massive environmental damage with widespread use. Asbestos was once hailed as a miracle material due to its versatility and was used extensively in construction and other industry in the early half of the last century, resulting in disease in the form of asbestosis and mesothelioma [114]. The open questions relating to the safety of nanotechnology have led to developments of the field of nanotoxicology which aims to study this in detail. Although many of the technologies used are based on biological systems or compounds already in use, differences in forms or sizes of materials are responsible for the increased risk. Nanoparticles are more likely to pass undetected by the respiratory immune system [115] and have been known to pass across vascular barriers and potentially alter clotting [116]. Nanoparticles can pass the blood–brain barrier and may be

implicated in degenerative brain disease [117]. In orthopaedics, questions arise relating to the toxicity of wear particles which are a proven risk even when none nanomaterial is utilised in joint replacement surgery [118]. Questions also remain over the long-term toxic effects of nanomaterials in vivo [27]. Despite the exciting and imminent therapeutic advancements offered by nanotechnology, urgent and exhaustive research into the medical and environmental risks associated with its wider use is required [27].

3.9 Conclusions

Currently the published data supports the applicability of a wide variety of nanotechniques which have the potential to revolutionise the management of a plethora of medical and surgical pathologies, once considered refractory to treatment or even incurable. In knee surgery, this potential is diverse in terms of disease type, surgical or nonsurgical options, method of drug or device delivery and overall strategy of applying new technologies. Synergistic strategies encourage organic and inorganic cooperation to improve healing following trauma, better graft integration following ligament repair or reconstruction and creating a nourishing microenvironment for stem cell differentiation and tissue integration. Furthermore, targeting strategies that improve pharmacokinetics in musculoskeletal could aid in the treatment of neoplasia and in symptomatic care of patients with chronic or degenerative disease. Implants used for trauma or arthroplasty may be enhanced by nanotechnology with a concomitant reduction in revision procedures. Infection-resistant materials or coatings, highly integrative implants and revolutionary materials with the ability to repair or regenerate may represent the advent of a new era in arthroplasty. These potential advances are exciting, but enthusiasm for their use must be tempered until the risks of nanotechnology are fully investigated.

References

1. Pleshko N, Grande DA, Myers KR (2012) Nanotechnology in orthopaedics. J Am Acad Orthop Surg 20(1):60–62
2. Favier I, Teuma E, Gómez M (2009) Palladium and ruthenium nanoparticles: reactivity and coordination at the metallic surface. C R Chim 12(5):533–545
3. Park S-C, Kim N, Ji S, Lim H (2016) Fabrication and characterization of moth-eye mimicking nanostructured convex lens. Microelectron Eng 158:35–40
4. Ma S, Wang D, Liang Y, Sun B, Gorb SN, Zhou F (2015) Gecko-inspired but chemically switched friction and adhesion on nanofibrillar surfaces. Small 11(9–10):1131–1137
5. Karthick B, Maheshwari R (2008) Lotus-inspired nanotechnology applications. Resonance 13(12):1141–1145
6. Kawase T, Tanaka K, Shiono N, Seirai Y, Oda M (2004) Onion-type complexation based on carbon nanorings and a buckminsterfullerene. Angew Chem Int Ed 43(13):1722–1724

7. Culpepper ML, DiBiasio CM, Panas RM, Magleby S, Howell LL (2006) Simulation of a carbon nanotube-based compliant parallel-guiding mechanism: a nanomechanical building block. Appl Phys Lett 89:203111. https://doi.org/10.1063/1.2388143
8. Brown CP (2013) Advancing musculoskeletal research with nanoscience. Nat Rev Rheumatol 9(10):614–623
9. Korkusuz F (2013) Editorial comment: nanoscience in musculoskeletal medicine. Clin Orthop Relat Res 471(8):2530–2531
10. Bernthal NM, Stavrakis AI, Billi F et al (2010) A mouse model of post-arthroplasty staphylococcus aureus joint infection to evaluate in vivo the efficacy of antimicrobial implant coatings. PLoS One 5(9):e12580
11. Katainen J, Paajanen M, Ahtola E, Pore V, Lahtinen J (2006) Adhesion as an interplay between particle size and surface roughness. J Colloid Interface Sci 304(2):524–529
12. Zhu H, Guo Z, Liu W (2014) Adhesion behaviors on superhydrophobic surfaces. Chem Commun (Camb) 50(30):3900–3913
13. Goldman M, Juodzbalys G, Vilkinis V (2014) Titanium surfaces with nanostructures influence on osteoblasts proliferation: a systematic review. J Oral Maxillofac Res 5(3):e1
14. Gallo J, Holinka M, Moucha CS (2014) Antibacterial surface treatment for orthopaedic implants. Int J Mol Sci 15(8):13849–13880
15. Holinka J, Pilz M, Kubista B, Presterl E, Windhager R (2013) Effects of selenium coating of orthopaedic implant surfaces on bacterial adherence and osteoblastic cell growth. Bone Joint J 95-B(5):678–682
16. Jain KK (2005) Nanotechnology in clinical laboratory diagnostics. Clin Chim Acta 358 (1–2):37–54
17. Savaliya R, Shah D, Singh R et al (2015) Nanotechnology in disease diagnostic techniques. Curr Drug Metab
18. Ruggiero C, Pastorino L, Herrera OL (2010) Nanotechnology based targeted drug delivery. Conf Proc IEEE Eng Med Biol Soc 2010:3731–3732
19. Hamidi M, Azadi A, Rafiei P, Ashrafi H (2013) A pharmacokinetic overview of nanotechnology-based drug delivery systems: an ADME-oriented approach. Crit Rev Ther Drug Carrier Syst 30(5):435–467
20. Zhang Y, Huang Y, Li S (2014) Polymeric micelles: nanocarriers for cancer-targeted drug delivery. AAPS PharmSciTech 15(4):862–871
21. Kateb B, Chiu K, Black KL et al (2011) Nanoplatforms for constructing new approaches to cancer treatment, imaging, and drug delivery: what should be the policy? Neuroimage 54 (Suppl 1):S106–S124
22. Man HB, Kim H, Kim HJ et al (2014) Synthesis of nanodiamond-daunorubicin conjugates to overcome multidrug chemoresistance in leukemia. Nanomedicine 10(2):359–369
23. Rosenthal SJ, Chang JC, Kovtun O, McBride JR, Tomlinson ID (2011) Biocompatible quantum dots for biological applications. Chem Biol 18(1):10–24
24. Von Hoff DD, Mita MM, Ramanathan RK et al (2016) Phase I study of PSMA-targeted docetaxel-containing nanoparticle BIND-014 in patients with advanced solid tumors. Clin Cancer Res 22(13):3157–3163
25. Freeman AI, Halladay LJ, Cripps P (2012) The effect of silver impregnation of surgical scrub suits on surface bacterial contamination. Vet J 192(3):489–493
26. Parthasarathi V, Thilagavathi G (2013) Developing antiviral surgical gown using nonwoven fabrics for health care sector. Afr Health Sci 13(2):327–332
27. Health Quality Ontario (2006) Nanotechnology: an evidence-based analysis. Ont Health Technol Assess Ser 6(19):1–43
28. Makidon PE, Nigavekar SS, Bielinska AU et al (2010) Characterization of stability and nasal delivery systems for immunization with nanoemulsion-based vaccines. J Aerosol Med Pulm Drug Deliv 23(2):77–89

29. Bailey ZS, Nilson E, Bates JA et al (2016) Cerium oxide nanoparticles improve outcome after in vitro and in vivo mild traumatic brain injury. J Neurotrauma. https://doi.org/10.1089/neu.2016.4644
30. Grausova L, Bacakova L, Kromka A et al (2009) Nanodiamond as promising material for bone tissue engineering. J Nanosci Nanotechnol 9(6):3524–3534
31. Tee BC, Wang C, Allen R, Bao Z (2012) An electrically and mechanically self-healing composite with pressure- and flexion-sensitive properties for electronic skin applications. Nat Nanotechnol 7(12):825–832
32. Cormode DP, Skajaa T, Fayad ZA, Mulder WJ (2009) Nanotechnology in medical imaging: probe design and applications. Arterioscler Thromb Vasc Biol 29(7):992–1000
33. Orringer DA, Koo YE, Chen T, Kopelman R, Sagher O, Philbert MA (2009) Small solutions for big problems: the application of nanoparticles to brain tumor diagnosis and therapy. Clin Pharmacol Ther 85(5):531–534
34. Ali SM, Aijazi T, Axelsson K, Nur O, Willander M (2011) Wireless remote monitoring of glucose using a functionalized ZnO nanowire arrays based sensor. Sensors (Basel) 11 (9):8485–8496
35. Chen H, Li J (2007) Nanotechnology: moving from microarrays toward nanoarrays. Methods Mol Biol 381:411–436
36. Miled MA, Massicotte G, Sawan M (2012) Dielectrophoresis-based integrated lab-on-chip for nano and micro-particles manipulation and capacitive detection. IEEE Trans Biomed Circuits Syst 6(2):120–132
37. Schofer MD, Roessler PP, Schaefer J et al (2011) Electrospun PLLA nanofiber scaffolds and their use in combination with BMP-2 for reconstruction of bone defects. PLoS One 6(9): e25462
38. Deng M, James R, Laurencin CT, Kumbar SG (2012) Nanostructured polymeric scaffolds for orthopaedic regenerative engineering. IEEE Trans Nanobioscience 11(1):3–14
39. Sartori M, Giavaresi G, Parrilli A et al (2015) Collagen type I coating stimulates bone regeneration and osteointegration of titanium implants in the osteopenic rat. Int Orthop 39 (10):2041–2052
40. Li Y, Jiao Y, Li X, Guo Z (2015) Improving the osteointegration of Ti6Al4V by zeolite MFI coating. Biochem Biophys Res Commun 460(2):151–156
41. Amendola V, Meneghetti M (2009) Self-healing at the nanoscale. Nanoscale 1(1):74–88
42. Kelly EW, Coghlan J, Bell S (2004) Five- to thirteen-year follow-up of the GSB III total elbow arthroplasty. J Shoulder Elbow Surg 13(4):434–440
43. Kinov P, Bukarev D, Dimov V, Kazakov K, Tivchev P (2007) Revision total hip arthroplasty with cementing technique—five-year results. Chir Narzadow Ruchu Ortop Pol 72 (4):293–296
44. Poss R, Brick GW, Wright RJ, Roberts DW, Sledge CB (1988) The effects of modern cementing techniques on the longevity of total hip arthroplasty. Orthop Clin North Am 19 (3):591–598
45. Evans BG, Salvati EA, Huo MH, Huk OL (1993) The rationale for cemented total hip arthroplasty. Orthop Clin North Am 24(4):599–610
46. Gittens RA, Olivares-Navarrete R, Schwartz Z, Boyan BD (2014) Implant osseointegration and the role of microroughness and nanostructures: lessons for spine implants. Acta Biomater 10(8):3363–3371
47. Mavrogenis AF, Dimitriou R, Parvizi J, Babis GC (2009) Biology of implant osseointegration. J Musculoskelet Neuronal Interact 9(2):61–71
48. Rieger E, Dupret-Bories A, Salou L et al (2015) Controlled implant/soft tissue interaction by nanoscale surface modifications of 3D porous titanium implants. Nanoscale 7(21):9908–9918
49. Zan X, Kozlov M, McCarthy TJ, Su Z (2010) Covalently attached, silver-doped poly(vinyl alcohol) hydrogel films on poly(l-lactic acid). Biomacromolecules 11(4):1082–1088

50. Tran PA, Sarin L, Hurt RH, Webster TJ (2010) Titanium surfaces with adherent selenium nanoclusters as a novel anticancer orthopedic material. J Biomed Mater Res A 93 (4):1417–1428
51. Gu W, Wu C, Chen J, Xiao Y (2013) Nanotechnology in the targeted drug delivery for bone diseases and bone regeneration. Int J Nanomedicine 8:2305–2317
52. Ramanlal Chaudhari K, Kumar A, Megraj Khandelwal VK et al (2012) Bone metastasis targeting: a novel approach to reach bone using zoledronate anchored PLGA nanoparticle as carrier system loaded with docetaxel. J Control Release 158(3):470–478
53. Susa M, Iyer AK, Ryu K et al (2009) Doxorubicin loaded polymeric nanoparticulate delivery system to overcome drug resistance in osteosarcoma. BMC Cancer 9:399
54. Sun K, Wang J, Zhang J, Hua M, Liu C, Chen T (2011) Dextran-g-PEI nanoparticles as a carrier for co-delivery of adriamycin and plasmid into osteosarcoma cells. Int J Biol Macromol 49(2):173–180
55. Yang L, Webster TJ (2009) Nanotechnology controlled drug delivery for treating bone diseases. Expert Opin Drug Deliv 6(8):851–864
56. Rai M, Yadav A, Gade A (2009) Silver nanoparticles as a new generation of antimicrobials. Biotechnol Adv 27(1):76–83
57. Zhao L, Wang H, Huo K et al (2011) Antibacterial nano-structured titania coating incorporated with silver nanoparticles. Biomaterials 32(24):5706–5716
58. United Kingdom Department of Health (2016) National joint registry for England, wales, Northern Ireland and The Isle of Man, 13th Annual Report. www.njrcentre.org.uk. Accessed May 2017.
59. Tomisa AP, Launey ME, Lee JS, Mankani MH, Wegst UG, Saiz E (2011) Nanotechnology approaches to improve dental implants. Int J Oral Maxillofac Implants 26(Suppl):25–44. discussion 45-9
60. Raimondo T, Puckett S, Webster TJ (2010) Greater osteoblast and endothelial cell adhesion on nanostructured polyethylene and titanium. Int J Nanomedicine 5:647–652
61. Bahl S, Shreyas P, Trishul MA, Suwas S, Chatterjee K (2015) Enhancing the mechanical and biological performance of a metallic biomaterial for orthopedic applications through changes in the surface oxide layer by nanocrystalline surface modification. Nanoscale 7 (17):7704–7716
62. Webster TJ, Ejiofor JU (2004) Increased osteoblast adhesion on nanophase metals: Ti, Ti6Al4V, and CoCrMo. Biomaterials 25(19):4731–4739
63. Price RL, Ellison K, Haberstroh KM, Webster TJ (2004) Nanometer surface roughness increases select osteoblast adhesion on carbon nanofiber compacts. J Biomed Mater Res A 70(1):129–138
64. Singh AV, Vyas V, Patil R et al (2011) Quantitative characterization of the influence of the nanoscale morphology of nanostructured surfaces on bacterial adhesion and biofilm formation. PLoS One 6(9):e25029
65. Shida T, Koseki H, Yoda I, Horiuchi H, Sakoda H, Osaki M (2013) Adherence ability of staphylococcus epidermidis on prosthetic biomaterials: An in vitro study. Int J Nanomedicine 8:3955–3961
66. Ivanova EP, Truong VK, Wang JY et al (2010) Impact of nanoscale roughness of titanium thin film surfaces on bacterial retention. Langmuir 26(3):1973–1982
67. Truong VK, Lapovok R, Estrin YS et al (2010) The influence of nano-scale surface roughness on bacterial adhesion to ultrafine-grained titanium. Biomaterials 31(13):3674–3683
68. Cheng H, Li Y, Huo K, Gao B, Xiong W (2014) Long-lasting in vivo and in vitro antibacterial ability of nanostructured titania coating incorporated with silver nanoparticles. J Biomed Mater Res A 102(10):3488–3499
69. Gao A, Hang R, Huang X et al (2014) The effects of titania nanotubes with embedded silver oxide nanoparticles on bacteria and osteoblasts. Biomaterials 35(13):4223–4235

70. Mei S, Wang H, Wang W et al (2014) Antibacterial effects and biocompatibility of titanium surfaces with graded silver incorporation in titania nanotubes. Biomaterials 35 (14):4255–4265
71. Dong W, Zhu Y, Zhang J et al (2013) Investigation on the antibacterial micro-porous titanium with silver nano-particles. J Nanosci Nanotechnol 13(10):6782–6786
72. Panacek A, Balzerova A, Prucek R et al (2013) Preparation, characterization and antimicrobial efficiency of ag/PDDA-diatomite nanocomposite. Colloids Surf B Biointerfaces 110:191–198
73. Knetsch MLW, Koole LH (2011) New strategies in the development of antimicrobial coatings: The example of increasing usage of silver and silver nanoparticles. Polymer 3:340–366
74. Kvitek L, Panacek A, Soukupova J et al (2008) Effect of surfactants and polymers on stability and antibacterial activity of silver nanoparticles (NPs). J Phys Chem C 112:5825–5834
75. Biggs MJ, Richards RG, Gadegaard N, Wilkinson CD, Dalby MJ (2007) The effects of nanoscale pits on primary human osteoblast adhesion formation and cellular spreading. J Mater Sci Mater Med 18(2):399–404
76. Miyauchi T, Yamada M, Yamamoto A et al (2010) The enhanced characteristics of osteoblast adhesion to photofunctionalized nanoscale TiO_2 layers on biomaterials surfaces. Biomaterials 31(14):3827–3839
77. Salou L, Hoornaert A, Louarn G, Layrolle P (2015) Enhanced osseointegration of titanium implants with nanostructured surfaces: an experimental study in rabbits. Acta Biomater 11:494–502
78. Durmus NG, Webster TJ (2012) Nanostructured titanium: the ideal material for improving orthopedic implant efficacy? Nanomedicine (Lond) 7(6):791–793
79. Antoci V Jr, Adams CS, Parvizi J, Ducheyne P, Shapiro IM, Hickok NJ (2007) Covalently attached vancomycin provides a nanoscale antibacterial surface. Clin Orthop Relat Res 461:81–87
80. Puckett SD, Taylor E, Raimondo T, Webster TJ (2010) The relationship between the nanostructure of titanium surfaces and bacterial attachment. Biomaterials 31(4):706–713
81. Fu J, Ji J, Fan D, Shen J (2006) Construction of antibacterial multilayer films containing nanosilver via layer-by-layer assembly of heparin and chitosan-silver ions complex. J Biomed Mater Res A 79(3):665–674
82. Khandaker M, Li Y, Morris T (2013) Micro and nano MgO particles for the improvement of fracture toughness of bone-cement interfaces. J Biomech 46(5):1035–1039. https://doi.org/10.1016/j.jbiomech.2012.12.006. Epub 2013 Jan 16
83. Ricker A, Liu-Snyder P, Webster TJ (2008) The influence of nano MgO and BaSO4 particle size additives on properties of PMMA bone cement. Int J Nanomedicine 3(1):125–132
84. Argatov I, Mishuris G (2016) Articular contact mechanics from an asymptotic modeling perspective: a review. Front Bioeng Biotechnol 4:83
85. Li H, Jiang J, Wu Y, Chen S (2012) Potential mechanisms of a periosteum patch as an effective and favourable approach to enhance tendon-bone healing in the human body. Int Orthop 36(3):665–669
86. Ch'ng S, Wong GL, Clark JR (2014) Reconstruction of the trachea. J Reconstr Microsurg 30 (3):153–162
87. Kon E, Delcogliano M, Filardo G, Altadonna G, Marcacci M (2009) Novel nano-composite multi-layered biomaterial for the treatment of multifocal degenerative cartilage lesions. Knee Surg Sports Traumatol Arthrosc 17(11):1312–1315. https://doi.org/10.1007/s00167-009-0819-8. Epub 2009 May 26
88. Takakuda K, Koyama Y, Matsumoto HN et al (2007) Material design of bioabsorbable inorganic/organic composites for bone regeneration. J Nanosci Nanotechnol 7(3):738–741
89. Gianotti SM, Marshall SW, Hume PA, Bunt L (2009) Incidence of anterior cruciate ligament injury and other knee ligament injuries: a national population-based study. J Sci Med Sport 12 (6):622–627

90. Joseph AM, Collins CL, Henke NM, Yard EE, Fields SK, Comstock RD (2013) A multisport epidemiologic comparison of anterior cruciate ligament injuries in high school athletics. J Athl Train 48(6):810–817
91. Andernord D, Bjornsson H, Petzold M et al (2014) Surgical predictors of early revision surgery after anterior cruciate ligament reconstruction: results from the Swedish national knee ligament register on 13,102 patients. Am J Sports Med 42(7):1574–1582
92. Kiapour AM, Murray MM (2014) Basic science of anterior cruciate ligament injury and repair. Bone Joint Res 3(2):20–31
93. Vavken P, Fleming BC, Mastrangelo AN, Machan JT, Murray MM (2012) Biomechanical outcomes after bioenhanced anterior cruciate ligament repair and anterior cruciate ligament reconstruction are equal in a porcine model. Arthroscopy 28(5):672–680
94. Liwen L, Hui W, Ming N et al (2014) Enhanced osteointegration of medical titanium implant with surface modifications in micro/nanoscale structures. J Orthop Transl 2:35–42
95. Kadonishi Y, Deie M, Takata T, Ochi M (2012) Acceleration of tendon-bone healing in anterior cruciate ligament reconstruction using an enamel matrix derivative in a rat model. J Bone Joint Surg Br 94(2):205–209
96. Haenle M, Fritsche A, Zietz C et al (2011) An extended spectrum bactericidal titanium dioxide (TiO_2) coating for metallic implants: in vitro effectiveness against MRSA and mechanical properties. J Mater Sci Mater Med 22(2):381–387
97. Hu H, Zhang W, Qiao Y, Jiang X, Liu X, Ding C (2012) Antibacterial activity and increased bone marrow stem cell functions of zn-incorporated TiO_2 coatings on titanium. Acta Biomater 8(2):904–915
98. Stevenson S, Emery SE, Goldberg VM (1996) Factors affecting bone graft incorporation. Clin Orthop Relat Res 324:66–74
99. Liu Y, Ramanath HS, Wang DA (2008) Tendon tissue engineering using scaffold enhancing strategies. Trends Biotechnol 26(4):201–209
100. Chou YC, Yeh WL, Chao CL, Hsu YH et al (2016) Enhancement of tendon-bone healing via the combination of biodegradable collagen-loaded nanofibrous membranes and a three-dimensional printed bone-anchoring bolt. Int J Nanomedicine 11:4173–4186. https://doi.org/10.2147/IJN.S108939
101. Han F, Zhang P, Sun Y, Lin C, Zhao P, Chen J (2015) Hydroxyapatite-doped polycaprolactone nanofiber membrane improves tendon-bone interface healing for anterior cruciate ligament reconstruction. Int J Nanomedicine 10:7333–7343
102. Grant SA, Smith SE, Schmidt H, Pfeiffer F, Kuroki K, Sherman S, White R, Grant DA (2017) In vivo bone tunnel evaluation of nanoparticle-grafts using an ACL reconstruction rabbit model. J Biomed Mater Res A. https://doi.org/10.1002/jbm.a.36000
103. Smith SE, White RA, Grant DA, Grant SA (2016) Gold and hydroxyapatite nano-composite scaffolds for anterior cruciate ligament reconstruction: in vitro characterization. J Nanosci Nanotechnol 16(1):1160–1169
104. Evans S, Shaginaw J, Bartolozzi A (2014) Acl reconstruction—it's all about timing. Int J Sports Phys Ther 9(2):268–273
105. Zhang ZG, Li ZH, Mao XZ, Wang WC (2011) Advances in bone repair with nanobiomaterials: mini-review. Cytotechnology 63(5):437–443. https://doi.org/10.1007/s10616-011-9367-4. Epub 2011 Jul 12
106. Mehdikhani-Nahrkhalaji M, Fathi MH, Mortazavi V, Mousavi SB et al (2012) Novel nanocomposite coating for dental implant applications in vitro and in vivo evaluation. J Mater Sci Mater Med 23(2):485–495. https://doi.org/10.1007/s10856-011-4507-0. Epub 2011 Nov 30
107. Moroni A, Faldini C, Pegreffi F, Giannini S (2004) HA-coated screws decrease the incidence of fixation failure in osteoporotic trochanteric fractures. Clin Orthop Relat Res 425:87–92
108. Forster Y, Rentsch C, Schneiders W et al (2012) Surface modification of implants in long bone. Biomatter 2(3):149–157

109. Xavier JR, Thakur T, Desai P, Jaiswal MK, Sears N, Cosgriff-Hernandez E, Kaunas R, Gaharwar AK (2015) Bioactive nanoengineered hydrogels for bone tissue engineering: a growth-factor-free approach. ACS Nano 9(3):3109–3118. https://doi.org/10.1021/nn507488s. Epub 2015 Feb 25
110. Paul A, Manoharan V, Krafft D, Assmann A et al (2016) Nanoengineered biomimetic hydrogels for guiding human stem cell osteogenesis in three dimensional microenvironments. J Mater Chem B Mater Biol Med 4(20):3544–3554. Epub 2016 Feb 4
111. Gao H, Zhang G, Wang J, Zhao F et al (2015) Clinical effects of novel nanoscaled core decompression rods combined with umbilical cord mesenchymal stem cells on the treatment of early osteonecrosis of the femoral head. J Nanomat:902836. https://doi.org/10.1155/2015/902836
112. Yang P, Bian C, Huang X, Shi A, Wang C, Wang K (2014) Core decompression in combination with nano-hydroxyapatite/polyamide 66 rod for the treatment of osteonecrosis of the femoral head. Arch Orthop Trauma Surg 134(1):103–112. https://doi.org/10.1007/s00402-013-1885-4. Epub 2013 Nov
113. Nandi SK, Kundu B, Ghosh SK, De DK, Basu D (2008) Efficacy of nano-hydroxyapatite prepared by an aqueous solution combustion technique in healing bone defects of goat. J Vet Sci 9(2):183–191
114. Bartrip PW (2004) History of asbestos related disease. Postgrad Med J 80(940):72–76
115. Viswanath B, Kim S (2016) Influence of nanotoxicity on human health and environment: the alternative strategies. Rev Environ Contam Toxicol
116. Kim D, Finkenstaedt-Quinn S, Hurley KR, Buchman JT, Haynes CL (2014) On-chip evaluation of platelet adhesion and aggregation upon exposure to mesoporous silica nanoparticles. Analyst 139(5):906–913
117. Rollerova E, Tulinska J, Liskova A et al (2015) Titanium dioxide nanoparticles: some aspects of toxicity/focus on the development. Endocr Regul 49(2):97–112
118. Korovessis P, Petsinis G, Repanti M, Repantis T (2006) Metallosis after contemporary metal-on-metal total hip arthroplasty. Five to nine-year follow-up. J Bone Joint Surg Am 88 (6):1183–1191

Chapter 4
Advanced Characterisation Techniques for Nanostructures

Brian Freeland, Inam Ul Ahad, Greg Foley, and Dermot Brabazon

4.1 Measurement of the Topology of Nanostructures

4.1.1 Scanning Electron Microscope (SEM)

Scanning electron microscopes (SEM) have been used by researchers since 1935 to examine micrometre-scale structures and are currently the most widely used non-optical microscopy technique. In the past 15 years, more focus has been brought on its application towards nanostructures. This technique allows for a comparably large sample window and for dimensional measurements to be performed. The principle of operation of the SEM involves a focused electron beam which is fired over the surface of the sample, resulting in electrons being emitted from the surface and are then collected by a positively charged detector grid. These are termed secondary electrons. These secondary electrons are recorded for the scanned surface and provide a surface topology. The factors that affect SEM resolution are the primary electron beam spot size and the volume of material with which the electrons interact. In order to ensure best possible resolutions, a high accelerating voltage should be employed (20–30 kV), along with a smaller current and small spot size. Care is needed however in some cases to avoid high electron energies where these can modify or destroy the material structure to be observed. Tungsten and carbon are the traditional emission element filaments used for SEM with LaB_6 emission sources being commonly adopted now due to their offering of longer gun lives and to not necessitating nitrogen cooling. Another type of emitted

B. Freeland • I.U. Ahad • G. Foley • D. Brabazon (✉)
School of Mechanical & Manufacturing Engineering, Dublin City University, Dublin 9, Ireland

I-Form, Advanced Processing Technology Research Centre, Dublin City University, Dublin 9, Ireland
e-mail: dermot.brabazon@dcu.ie

M.J. Jackson, W. Ahmed (eds.), *Micro and Nanomanufacturing Volume II*,
DOI 10.1007/978-3-319-67132-1_4

electrons 'backscattered electrons' are collected by a backscatter collector; they are high-energy electrons resultant of the incident electron beam. The response of these electrons is directly proportional to the density of atoms in the material, allowing surface composition, via relative density difference, to be visualised.

4.1.1.1 SEM Case Studies

Recently the SEM technique has been applied towards a range of applications such as determining the effects of gelling agents on the morphology of $ZnSnO_3$ nanostructures [1], examining the surface morphology and nano-surface features of flat objects [2] and measuring the diameters of silicon, latex and gold spherical nanoparticles with mean diameter of 15 nm [3].

It has been observed that SEM performance can be increased by utilising the secondary electron detector at low magnifications to image TaS_2 nanotube bundles as seen in Fig. 4.1. This configuration allowed for larger scan areas and faster processing times. A 10 kV beam voltage was used with a magnification of 12.4 k× [4].

The SEM typically has at best a spatial resolution of 1–10 nm, and therefore it is generally used to characterise structures greater than 10 nm. Over the years efforts have been made to break this 10 nm barrier. Recently Villarrubia et al. [5] have proposed a technique to improve the resolution of SEM inspection of lithographically patterned SiO_2 used by Intel.

The authors fitted the measured intensity vs. position to a physics-based model which included the lithography lines' dimensions as parameters. A 3D model for patterned SiO_2 was developed as shown in Fig. 4.2. They concluded that with the aid of the model, sub-nanometre resolution could be achieved, an improvement of almost tenfold.

4.1.2 Field Emission Scanning Electron Microscope (FESEM)

A field emission cathode in the electron gun of a SEM provides narrower probing beams resulting in both improved spatial resolution and less sample charging. Such systems are designated as field emission scanning electron microscopes (FESEM). To achieve this increased electron focusing a different gun design is required [6]. In this design, electrons are expelled by applying a high electric field very close to the filament tip. The size and proximity of the electric field to the electron reservoir in the filament controls the degree to which electrons tunnel out of the reservoir. One type of field emission gun commonly used is known as the Schottky in-lens thermal FESEM electron gun. Cold gun alternatives are available for even finer FESEM resolution; however, these suffer rapid degradation and can therefore lead to expensive operation due to relatively frequent placement. The field emission guns

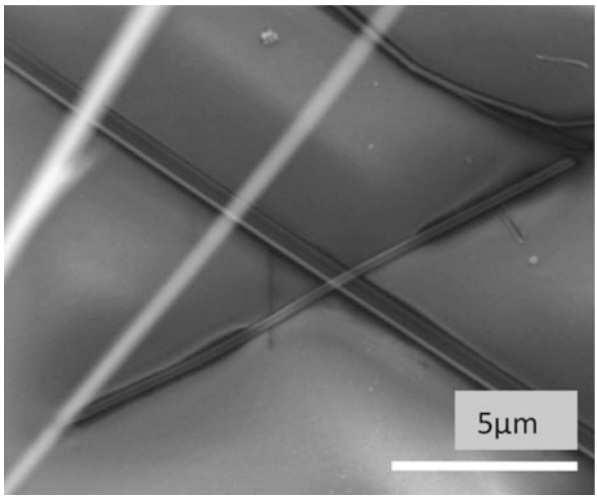

Fig. 4.1 SEM image of a silica fragment within a TaS_2 nanotube bundle [4]

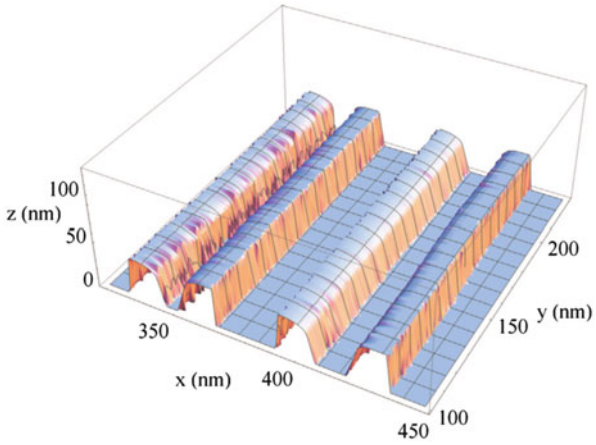

Fig. 4.2 SEM generated 3D reconstruction data of lithography produced SiO_2 channels [5]

have higher stability, can allow higher current and hence provide a smaller spot size. Under good operating conditions, a typical FESEM resolution of 1 nm is achievable. Elements that add to improved operation and FESEM resolution include designs with a beam booster to maintain high beam energy, an electromagnetic multihole beam aperture changer, a magnetic field lens and a beam path which has been designed to prevent electron beam crossover. Nanostructures have been characterised by FESEM in different morphological formations including nanoflowers [7], nanosheets [8], nanoparticles [9] and thin films [10–13]. Molybdenum disulphide (MoS_2) nanosheets exhibit interesting conductive/semiconductive, magnetic, photoluminescence, photocatalytic and field-effect transistor properties. The properties of MoS_2 nanosheets depend upon the method used to generate them, and depending upon the structural properties, these nanosheets can be used for applications in optoelectronics, energy harvesting, spinelectronics

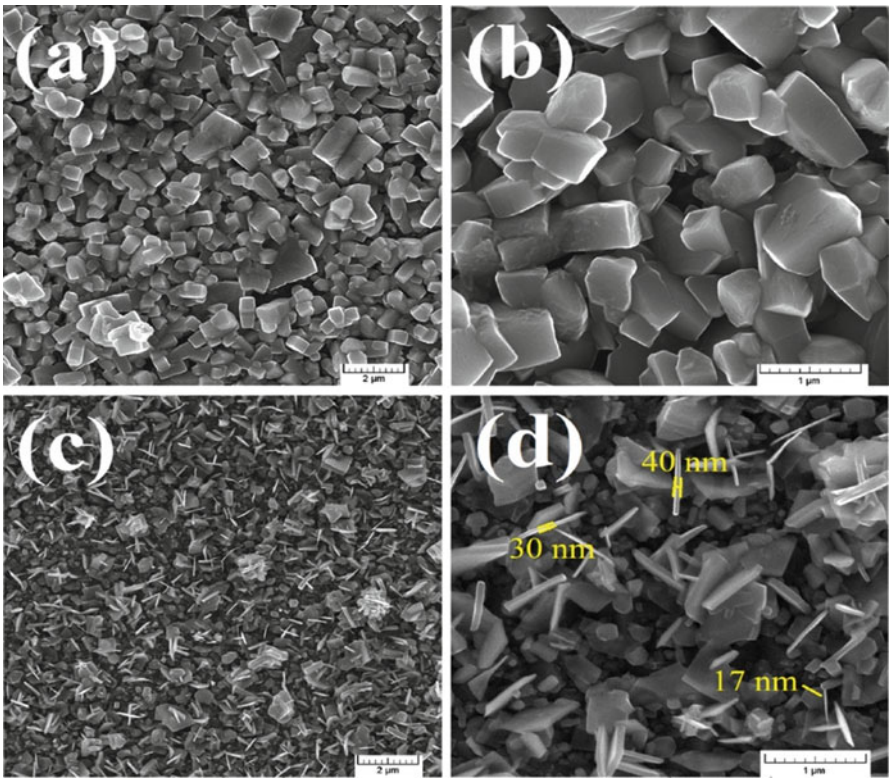

Fig. 4.3 FESEM micrographs of the (**a**, **b**) the ED-SnS and (**c**, **d**) the UAED-SnS produced nanostructures [19]

(fluxtronics), etc. The characterisation of MoS_2 nanosheets morphology has been performed by FESEM in various studies [14–18].

4.1.2.1 FESEM Case Studies

In one study, nanostructured Tin(II) sulphide (SnS) thin film was deposited on FTO glass substrate by electrodeposition (ED) with and with ultrasound assistance electrodeposition (UAED) [19]. Figure 4.3 shows the FESEM micrographs of the ED-SnS and the UAED-SnS produced nanostructures [19]. The effect of using ultrasound waves during electrodeposition on the morphology of the nanostructured SnS films can be clearly seen. The FESEM images showed that without using ultrasound waves, the deposited SnS film had grain-like morphology. Using ultrasound assistance during electrodeposition, the FESEM showed the formation of two distinct nanostructures. The first type was in a formation of 20–60 nm thin plane nanostructures. The second type was in cubical rods type structures with less than one micron height [19].

Other workers have applied FESEM characterisation for the implementation of cryo-SEM natural state colloidal solution capturing and studied the process of simultaneous deposition by immersion plating of palladium and silver seeds from 1 to 100 nm in size on porous silicon [5, 6].

4.1.3 Scanning Probe Microscopy (SPM)

Scanning probe microscopy is the general term associated with several techniques notably scanning tunnelling microscopy (STM) and atomic force microscope (AFM) discussed in this chapter. Both techniques feature a sharp probe with a point diameter as low as one atom is passed over the sample's surface via piezoelectric actuators in order to visualise the surface features.

4.1.3.1 Scanning Tunnelling Microscope (STM)

Binnig and Rohrer developed the scanning tunnelling microscopy technique back in 1981 and their work lead to a Nobel prize in 1986. The most essential component of an STM is the probe which is sharpened to one atom width. Typically, the tip material selection is limited to tungsten, platinum-iridium, gold or carbon nanotube. Recently there have been developments towards graphene-coated probe tips, reducing costs compared with standard Pt-Ir probes [20].

The tip is scanned over the surface to be characterised via three piezoelectric actuators orientated in three dimensions to control the probe's position with respect to the surface. The sample surfaces must be conductive or semiconductive for the technique to operate as a voltage is applied between the tip and the sample, a current is generated via electron tunnelling, and this current is monitored, as the distance between the probe tip and the surface changes the resulting current changes in proportion. Therefore the dimensional precision of the probe tip is essential to the precision of the technique. STM can achieve atomic-scale visualisation, and this accuracy is due to the stages that can provide 0.1 nm lateral and 0.01 nm depth resolution. To achieve these resolutions, vibration must be minimised and consequently the systems are mounted on weighted or specialised anti-vibration plates, while springs are used as part of the tip mechanism for vibration isolation. For the SEM, there are two modes of operation: constant height and the constant current mode. In constant current mode, the tip is scanned over the surface, and its position in the vertical axis is altered to keep the current constant. This change in tip height is recorded and used to map the surface. With constant height mode, the height of the tip and the voltage is maintained at a constant. The change in current required to keep the voltage constant is related to local charge density to provide a record of the surface profile. Constant height mode provides faster scan times compared with constant current and is the preferred mode for larger sample windows.

4.1.3.2 STM Case Studies

Krupski utilised STM to determine the growth of ultra-thin Au films deposited on a Mo (110) substrate at high temperatures (300 K) [21]. They found that by using differing Au depositions, they were able to determine the morphology of the Au layers. This allowed for terracing with a width of 25–180 nm to be characterised on the surface [21]. More recently Huerta et al. (2016) investigated the multilayer growth of 4-aminothiophenol (4-ATP) on an iodine-modified Au (100) substrate. The interaction of ATP molecules and the iodine monolayer was determined over time, the STM providing images of the structure formation from single molecules into chains, which could lead to uses in the production of solid phase micro extraction coatings [22].

Figure 4.4 shows the STM images of APT on an iodine-doped Au layer. Figure 4.4a taken at a potential of +0.1 V with an image size of 130 × 130 nm^2 shows the multilayer growth that occurred, including the formation of holes, pits and trenches between the deposited molecules [23]. The higher-resolution image of Fig. 4.4b with an area of 8.1 × 8.1 nm^2 shows the formation of surface features such as terracing and trenches with a width of 0.4 nm between deposited molecules. Further developments have employed in situ analysis. With this technique thin films were produced utilising pulsed laser deposition within the STM chamber. The film growth was then characterised at an atomic sale without the inhabitation of contaminents [24–27].

Rafati et al. (2017) utilised a NAMA-STM SS-3L1 to characterise gel extracted DNA nanotubes. The measurements were taken using a platinum-iridium tip, with the STM in constant current mode using a current set point 0.1 nA, sample bias voltage 0.2 V and low scan rate. Unlike previous work the images were captured under ambient conditions, without the requirement of high vacuum.

The data was post-processed sequentially by line using averaging filters within the NAMA-STM analysis software. High-resolution three-dimensional and two-dimensional images of elongated nanotubes were attained, as seen in Fig. 4.5. The images suggested the tubes had a height of 46 nm from the topographical surface. The authors proposed STM as a viable technique for ultrastructural characterisation of DNA nanotubes, and they suggested that the helical structure of the tubes can be determined within the images.

4.1.4 Atomic Force Microscope (AFM)

The atomic force microscope (AFM), also called the scanning force microscopy (SFM), was developed in 1986, subsequent to the STM. Similar in operation to the STM, the AFM involves scanning a sharp tip across a sample surface while monitoring the tip–sample interaction to allow the reconstruction of the three-dimensional surface topography. A typical AFM has nanometre lateral and

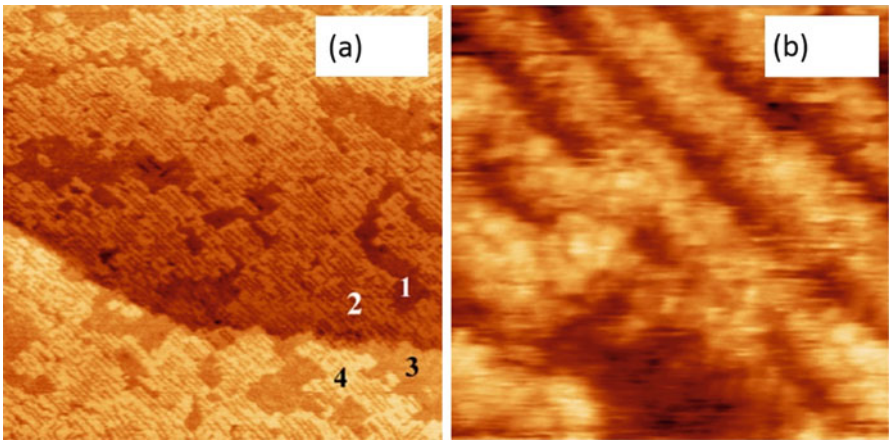

Fig. 4.4 STM images of multilayer growth of APT on an iodine-doped Au layer showing the (**a**) multilayer growth across 130 × 130 nm^2 and (**b**) at high magnification, showing 8.1 × 8.1 nm^2 area, the formation of terracing and trenches [3]

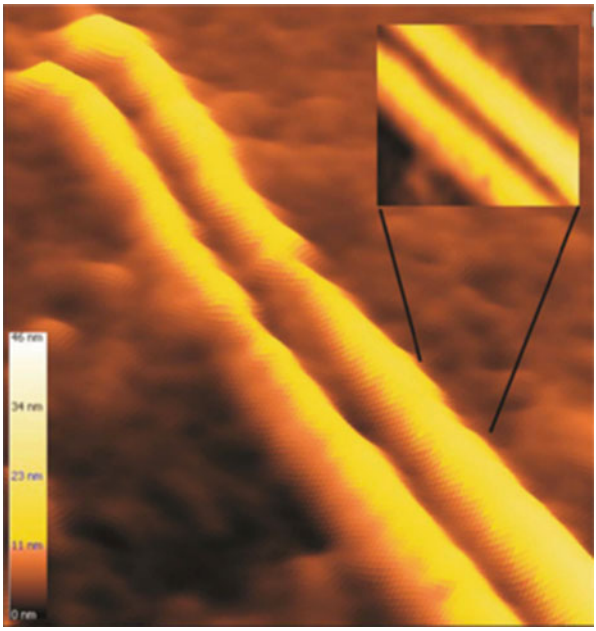

Fig. 4.5 High-resolution STM 3D micrograph image of DNA nanotube with 2D insert showing higher magnification of the structure details [28]

sub-angstrom vertical resolution and can image insulators as well as conductors. UHV AFM resolution is comparable to that available from STM and the transmission electron microscopy (TEM). An AFM consists of a sharp tip on the end of a flexible cantilever which is moved across a sample surface by piezoelectric actuators. The cantilever is typically made from Si or Si_3N_4 with a tip curvature radius

of a few nanometres. Displacement of the tip is recorded by a non-contact laser displacement measurement. A laser light directed onto the cantilever above the laser tip is recorded on a photodetector area which allows calculation of displacement via signal strength measurement or triangulation. A feedback loop maintains a constant tip-surface interaction force by vertically moving the scanner to maintain a constant photodetector difference signal. The distance the scanner moves vertically is recorded at and with each x, y position which allows the surface information to be presented and analysed. A complicated set of forces can be present at the tip-sample interaction. When the tip touches a surface under ambient conditions, a repulsive force is present. When the tip is at a small distance from the surface, attractive forces can be present as well as van der Waals forces and capillary forces arising from condensation of water vapour in the contact area. Operating modes can be roughly classified as contact, non-contact or dynamic.

In contact mode, the scanning tip is dragged across the sample surface and the tip deflection monitored. Using Hook's law, the force between the tip and the surface is automatically kept constant during scanning (typically between 0.1 and 100 nN). Lower stiffness cantilevers (spring constant, $k < 0.1$ N/m) are used in this mode to amplify the deflection signal. Contact mode may not be suitable for soft materials which can be easily deformed or damaged, such as for polymer or molecular imaging. When scanning is performed in the region where the tip is attracted to the surface, the scanning is termed non-contact mode. In this region, the cantilever bends towards the sample. If an oscillatory tip displacement is sufficiently large to pass through both regions, the probe experiences both attractive and repulsive forces. This mode is known as dynamic, intermittent or tapping mode. Tapping mode was developed for investigation of soft materials [29]. In this mode, the cantilever oscillates near its resonant frequency and lightly taps the surface during scanning. The tip rapidly moves in and out of the sample surface with an amplitude that is sufficiently high to overcome adhesion forces so that it stays in contact only for a short fraction of the oscillation period. Depending on the cantilever type, the frequency typically varies from 50 to 500 kHz and amplitudes up to 100 nm are used. The laser spot deflection is used to measure the amplitude of cantilever oscillation, and a feedback loop maintains a constant oscillation amplitude by adjustments to the servo which adjusts the cantilever height.

4.1.4.1 AFM Case Studies

Ahad et al. introduced nanostructures on the surfaces of polymeric biomaterials by extreme ultraviolet (EUV) technology for biomedical engineering applications [30–35]. EUV photons are high-energy radiations (from 10 up to 124 eV) with nanometre wavelengths (124–10 nm); therefore nano-surface structuring is possible. The surfaces of polytetrafluoroethylene (PTFE) polymer samples were irradiated with 50, 200 and 300 EUV pulses. The EUV exposed PTFE samples were investigated by AFM, and images were acquired at two different resolutions (50×50 μm and 25×25 μm) to visualise the effect of EUV irradiation on the

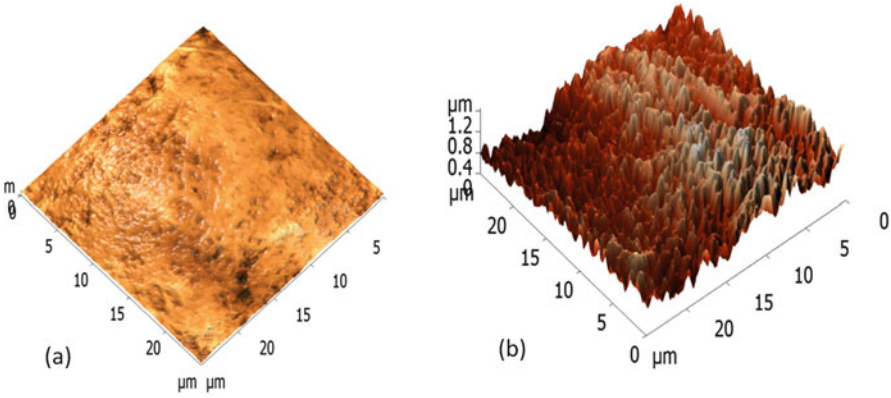

Fig. 4.6 (**a**) AFM image of pristine PTFE sample and (**b**) AFM image of PTFE sample irradiated with 300 EUV shots [31]

surface morphology. In order to establish the relationship between the number of EUV pulses irradiated on the sample and the resulting surface structure, the cross-sectional analysis and histograms of the AFM images were obtained. The AFM images of pristine and EUV irradiated (300 pulses) of PTFE samples are present in Fig. 4.6a, b, respectively [31]. The EUV surface modification resulted in formation of ripple-type regular structures on the PTFE samples. It was observed that with increasing number of EUV pulses, the surface roughness of the PTFE samples were increased and more high-rippled structures were formed on the sample surface.

The surface structuring and wettability control of PET films are often associated with biocompatibility control for biomedical engineering applications [30, 34]. In another study, Ahad et al. used the same EUV source to perform surface modification of polyethylene terephthalate (PET) polymer films in order to investigate the effect of surface structuring on wettability control [33]. The polymer films were irradiated in helium and nitrogen environments with 20 and 30 EUV pulses. AFM was used to measure the surface roughness, and water contact angle measurements were taken to examine the changes in wettability behaviour. The EUV surface modification resulted in the formation of nano- and microstructuring on the polymer surfaces. The results demonstrated that the average surface roughness of PET polymer films was increased from 6.6 to 234 nm and 271 nm when EUV processed in nitrogen and helium gases, respectively. The surface structuring consequently increased the water contact angle making the PET surfaces more hydrophobic. It was observed in this study that for EUV-treated PET polymer surfaces, a direct relationship exists between surface roughness and hydrophobicity for EUV-modified PET samples (see Fig. 4.7).

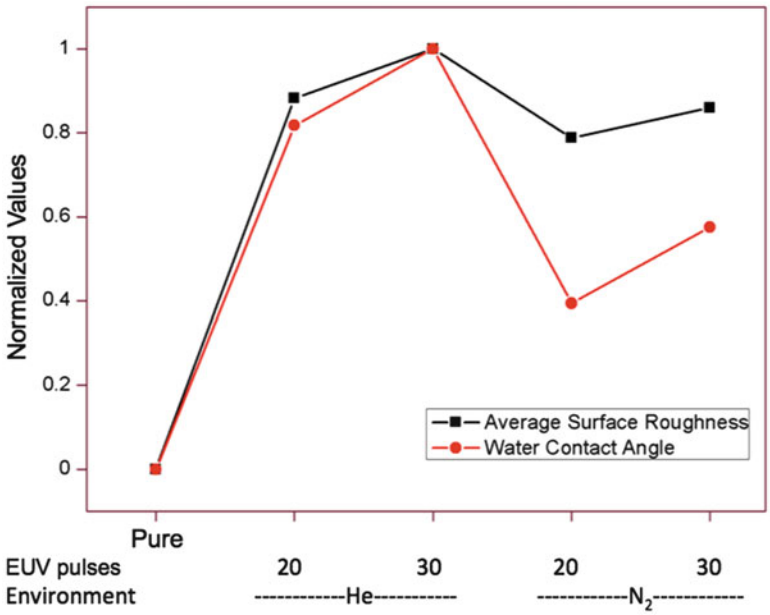

Fig. 4.7 Normalised average surface roughness and water contact angle of pristine and EUV-modified surfaces [33]

4.1.5 Optical Microscopes

4.1.5.1 Confocal Microscopy

In confocal microscopy two focusing arrangements are used to focus on the point in a sample to be imaged. One focuses laser light through an objective lens to the point of interest, and the other focuses the reflected light to the imaging sensor. Light from the point to be imaged is passed through a pinhole such that all extraneous out of focus light is removed. This allows lateral resolutions approximately 1.4 times greater than in conventional microscopes to be achieved with confocal microscopy. The depth of the focal plane depends on the specimen optical properties and importantly on the squared value of the objective lens numerical aperture. Three dimensional reconstructions of cells and surfaces can be achieved with this technique. To achieve this, the sample is scanned such that one 2D slice is recorded, the focal plane of the sample is then moved a prescribed amount where the next 2D slice is recorded and this sequence is repeated until the required volume is scanned. Image processing software is then used to process the collected data to reconstruct the 3D object. Confocal microscopes are most often used to image biological systems and semiconductor surfaces [18–20].

Three variations of scanning are available in confocal microscope systems. In the conventional confocal laser scanning microscope, the sample is raster scanned

which results in a scanning rate of about three frames per second. Such systems provide the highest spatial resolution; however for higher temporal resolution, the spinning disc (Nipkow) and the programmable array microscope (PAM) systems can provide rates of 30 frames per second [36]. In a Nipkow disc system, a thin disc with hundreds of spirally patterned pinholes is spun in the light path to the objective lens. The pinholes only allow perpendicularly oriented rays of light to penetrate which allows high scanning speeds independent of the laser scanning speed. PAM is a variation on this whereby an acousto- or electro-optical filter can be patterned to automatically produce the pinhole pattern required. Such a system can allow for up to 1000 beams to simultaneously scan the entire field at millisecond scan speeds. High-frequency scanning has the added advantage of reducing exposure of sensitive samples to photons which may cause damage due to photobleaching or phototoxicity.

Fluorescent dyes are often added to a surface or flurophores to cellular systems to enable enhanced imaging with confocal fluorescent microscopy. Various excitation laser wavelengths are available for these systems ranging from 442 to 647 nm depending on the flurophore excitation and emission wavelengths used. Reflected and fluoresced light waves are emitted from the sample. A beam splitter can be selected to reflect only the fluoresced light to the detector which provides enhanced signal-to-noise ratio. As described above, the pinhole is also used in this set-up to eliminate the out of focus signal and record only the light from the region of interest.

Confocal Microscopy Case Studies

In a recent study by Ilčíková et al. [37], untreated and polystyrene-modified single and multiwall carbon nanotubes (CNT) were added into a polymer matrix to produce a nanocomposite polymer. These nano-polymers have been shown to possess increased functionality via improved mechanical and electrical properties. However, a significant challenge to the adoption of polymer nanocomposites is ensuring an even distribution of CNTs within the matrix. In this work the authors address the issue by utilising confocal laser scanning microscopy (CLSM) to characterise CNTs dispersed in the matrix. CNTs with a maximum thickness of 25–60 nm were visualised both under reflection and fluorescent mode with the addition of benzothioxanthene fluorescent labelling dye to the polymer for the latter. Figure 4.8 shows the confocal images captures of the CNT nanocomposite matrix under both fluorescence mode and reflectance mode.

From the imagery, it was observed that smaller thickness (8–18 nm) multiwall CNTs were visualised only under fluorescent mode as can be seen in Fig. 4.9a–e. Thus, the fluorescent mode can be a useful and potentially a preferred approach to characterise nanocomposite structures. The CLSM in reflectance mode is as a non-invasive method to determine the dispersions of the CNT through the depth of the polymer by imagining at various z-axis positions and combining slice images into a 3D dispersion profile. This was completed for one micrometre slice depths as

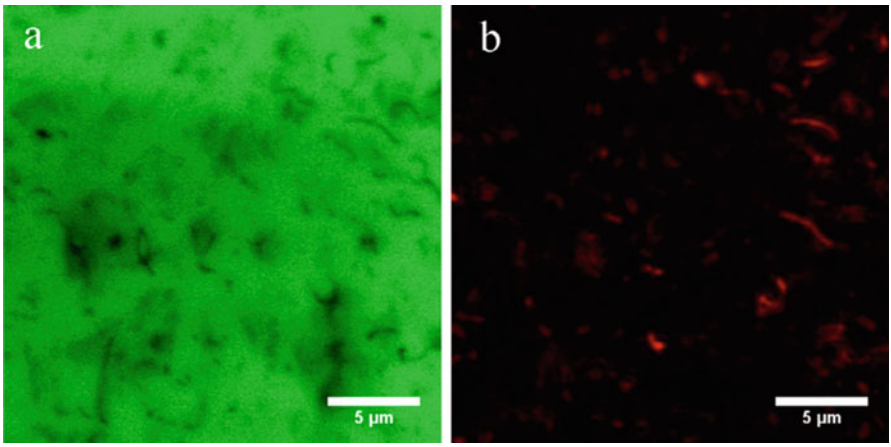

Fig. 4.8 CLSM visualisation of CNT nanocomposite matrix under (**a**) fluorescence mode and (**b**) reflectance mode [37]

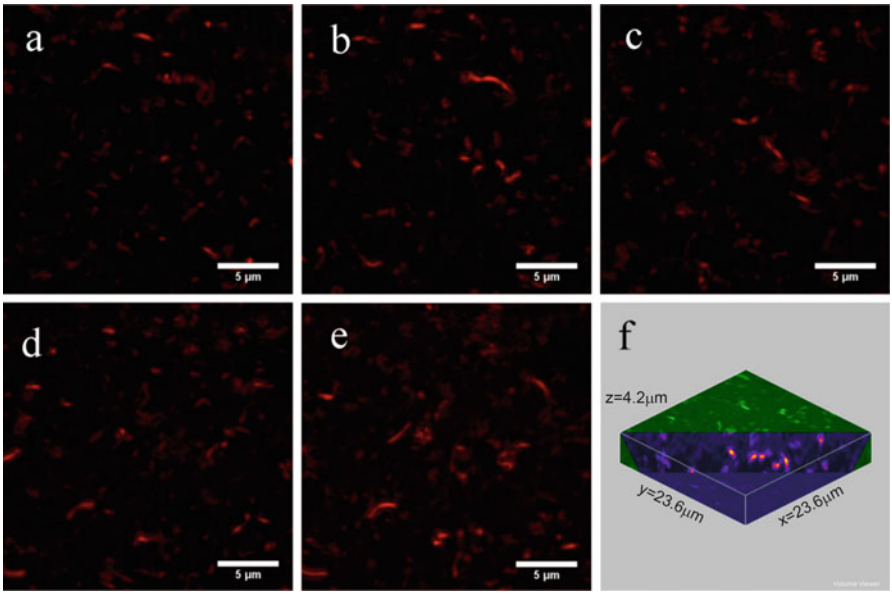

Fig. 4.9 Optical slice images of polymer matrix (**a**–**e**) at various depths and (**f**) as a combined 3D image [37]

shown in Fig. 4.9f. CLSM was therefore demonstrated as a non-invasive technique to monitor the distribution of CNT both on the surface and embedded in the bulk material and offers a solution to bring quality monitoring into nanocomposite fabrication.

In other work, Oyarzún et al. [38] employed 3D confocal microscopy to measure the thickness of TiO_2 nonporous films by examining various height profile points on the sample surface. The authors suggest 3D confocal microscopy as their preferred technique compared with FESEM for thickness measurement of TiO_2 layers as larger measurement areas can be achieved compared with more local results attained from FESEM [38].

4.1.5.2 Near-Field Scanning Optical Microscopy (NSOM)

NSOM can be classified as a SPM technique as the scanning methodology places it in this category. However due to the wave-based principles behind its operation, it is placed under the optical microscopy section within this chapter. When electromagnetic radiation is emitted, the near field is that part of wave front that is within a couple of wavelengths from the surface of the emitter. An evanescent wave is a near-field standing wave exhibiting exponential decay with distance. Evanescent waves are strongest within one-third wavelength (λ) from an electromagnetic emitter. Near-field scanning optical microscopy (NSOM or SNOM) is a surface imaging technique with nanometre resolution.

The main components of a NSOM are the scanning tip, the feedback mechanism and the piezoelectric actuation and the light source. The light source is critical and is composed of a laser beam focused into an optical fibre via a polarizer, a beam splitter and a coupler. The polarizer and beam splitter removes additionally reflected light from the returning reflected light. The scanning probe is generally a sharpened optical fibre. The tip displacement is measured and the reaction normal force is recorded, to ensure the probe is at the correct height at all times. Alternatively, a tuning fork attached to the fibre tip is oscillated at resonant frequency which moves the tip laterally. Changes in amplitude are monitored to provide shear-force feedback.

NSOM Case Studies

Beleites et al. (2012) found that they could use NSOM to analyse the shape of a single Ag nanoparticle that had been post-processed by femtosecond laser irradiation. Commercially available spherical silver nanoparticles suspended in an aqueous solution with mean particle diameter of 40 nm was drop-cast onto a substrate and dried under ambient conditions. Following that, the samples were covered with a 40 nm aluminium layer via atomic layer deposition. The samples were irradiated using a frequency-doubled Yb:KGW laser system with 300 f. pulse length and then annealed for 60 min. Measurement was performed using an aperture-type cantilever-probe-based system in transmission mode.

The topography of the Ag nanoparticle, distinct to the aluminium oxide layer, was observed using a laser source with wavelength of 458 nm (see Fig. 4.10). Along with topography the relative transmission was also able to be calculated by

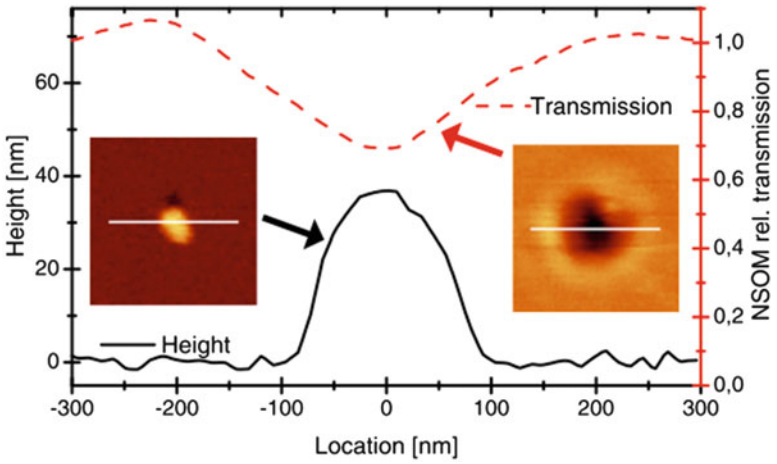

Fig. 4.10 Characterisation of single Ag nanoparticle topography and relative transmission intensity excited at 485 nm [39]

normalising the measured intensity compared with the background intensity. This technique offers promising abilities to characterise nanoparticle profiles while deposited on substrates.

4.1.6 Dynamic Light Scattering (DLS)

Dynamic light scattering (DLS) techniques have been adopted as the primary on-the-bench method for measurement of nanoparticle size distribution in liquid suspensions. DLS is widely used in research and industry; it provides rapid size analysis of nanoparticle colloids. It has attained such market coverage that many nano-colloid researchers rely on it as their sole size characterisation technique. The technique is used for particle analysis in inks, paints and more recently biological diagnostics and disease treatment systems [40, 41], indeed many fields where nanoparticle size is critical. The technique offers possibilities of in situ measurement, which can be important for time-sensitive process and industrial manufacturing.

Unlike microscopy techniques, the size measured is not just a function of the material core size in air, but the hydrodynamic diameter, including effects from fluid stabilisers, surfactants and the electrical double layer thickness [42] while also providing an overall size distribution of the bulk colloid. Thus, the DLS offers a more representative measurement of NPs size while in the liquid phase. This may provide more useful data if the nanoparticle applications are in liquid suspension. Generally, the size distribution measured by DLS is larger than for microscopy techniques such as TEM and SEM where nano-colloids must be transferred to a

substrate and dried. During this process the hydrodynamic properties are lost and drying aggregation may occur. It should be noted that the sample size of drop-cast particles for TEM and SEM is smaller compared with the 'bulk' measurement of DLS. However there are factors which effect the techniques precision, due mainly to its base technology, how light interacts with differing size particles [43], leading to measurement masking effects. DLS operates on the principle that the diffusion coefficient (D) of a particle is size dependent where the Stokes-Einstein equation [43] describes the diffusion coefficient as:

$$D = \frac{K_B T}{6 \pi \eta R_S} \tag{4.1}$$

with K_B being the Boltzmann constant, T the colloid temperature, η the solvent viscosity and R_S the sphere radius. This basically describes that light scatters at different rates with differing particle sizes [44].

During its operation samples are irradiated with a coherent monochromatic polarised laser beam light source, as seen in Fig. 4.11. A scattering detector, positioned typically at an angle of 173° backscatter [45] to the beam collects the dispersed pattern containing intensity fluctuations of light. This dispersed light intensity pattern is due to constructive and destructive inference on different areas of the detector [46]. The scattering of light is related to the position of particles in the sample, and the scattered light from each particle will be in its unique phase while striking the detector surface. This scattering intensity is a function of particle size, solute particle concentration and refractive index difference of solvent and solute particles [47]. Therefore, if measurements are repeated at known time intervals, the intensity change of the scattered patterns over time is accounted for by Brownian motion of particles, and the intensity change can be related to the diffusion coefficient and particle size.

4.1.6.1 Case Studies

Tomaszewska et al. (2013) investigated the detection limits of DLS for the characterisation of polydisperse nanoparticle colloids. To make a controlled, artificial polydisperse colloid, the authors mixed known concentrations of standardly produced and characterised 10, 55 and 80 nm Ag nanoparticles, confirming their measurements with AFM and TEM. They found that the polydispersity of the colloids was problematic to measurement of the true colloid size, as the light scattering intensity from the larger NPs masked out the smaller particles. The authors concluded that as low as a 5% presence of larger NPs in the sample population was enough to mask the detection of the smaller nanoparticle colloid, making up 95% of the sample population [42]. This raise questions over the absolute validity of DLS results for highly polydisperse populations, considering the masking effect of aggregates in the colloid.

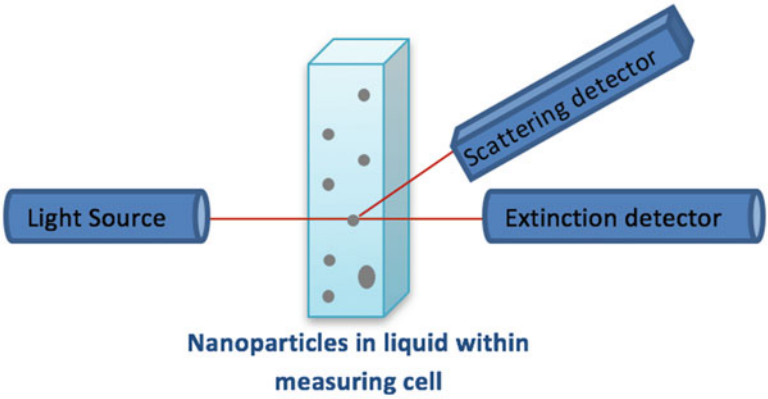

Fig. 4.11 Schematic showing DLS operation, including coherent monochromatic polarised light source, extinction detector and scattering detector placed at a defined incident angle

Horechyy et al. [48] utilised in situ DLS to monitor the growth of silica core shells on copolymers. The authors used disposable DLS cuvettes to hold the copolymer mixture. Silica sol was added to PS-b-P4VP micelles, mixing the reaction mixture for 2 min before placing the cuvette into the Malvern Zetasizer Nano S and starting Z measurements at 2 min intervals. The refractive index and fluid viscosity were set for standard methanol. Each measurement was performed utilising ten autocorrelations each with a 10 s scan period. The data was averaged using dispersion technology software (DTS). Using this technique, the authors observed five distinct stages in silica shell formation [48]. Time-dependent particle diameter for the initial stage after the addition of SiO_2 is illustrated in Fig. 4.12. The authors found that TEM and DLS measurements of the growth stages showed contradictory trends, where within the first hour a dramatic decrease in particle size was observed on the DLS and not so much with the TEM. Also after several days there was an observed increase in the DLS particle size measurement, not evident from TEM analysis. After further inspection the cause of these discrepancies was determined as follows:

1. The increasing density of the silica shell lead to a reduction in the hydrodynamic particle size observed by the DLS.
2. After several days, the hydrodynamic particle size increased due to changes in the fluid viscosity, but the shell growth was substantially smaller.

In this work the authors utilised in situ DLS measurement, concluding that in situ monitoring was a useful tool in understanding the full growth profile of silica shell nanoparticles.

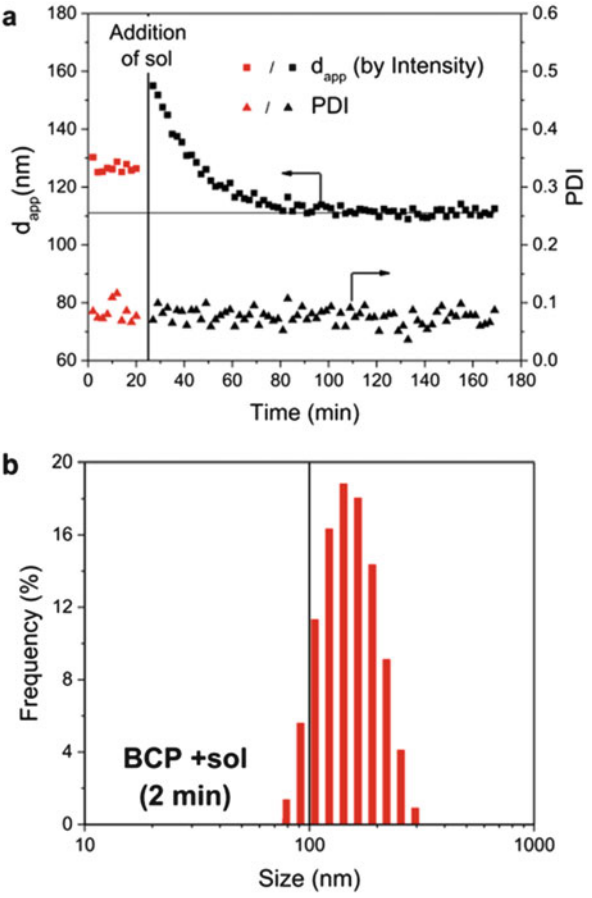

Fig. 4.12 (**a**) Apparent particle size (*squares*) and PDI (*triangles*) of PS-b-P4VP copolymer before (*red*) and after the addition of SiO_2 (*black*) over time showing silica shell evolution and (**b**) intensity of particle size distribution, 2 min after the addition of SiO_2 [48]

4.2 Measurement of Nanostructures Internal Geometries

4.2.1 Transmission Electron Microscope (TEM)

TEM is an established characterisation technique, which can provide both image mode and diffraction mode information from a single sample [49]. It is regarded as one of the main techniques for nanomaterial characterisation, largely due to its high lateral spatial resolution in the region of 0.08 nm [50]. A feature of nanomaterials is that specific properties, for example, colour, can be related to a particle size. Agglomeration of nanoparticles or failure to isolate individual nanostructures is likely to result in anomalous property characterisation. Characterising the elastic or mechanical properties of individual nanoparticle/nanotube/nanofibres is a challenge to many existing testing and measurement techniques. It is difficult to pick

up samples and difficult to clamp samples, in order to test for tensile strength or creep, for example [51].

The modern TEM are capable of formatting nanometre size electron probes having diameters ranging from 2 to 5 nm. This formation is possible by employing a multistage condenser lens system. This lens system makes scanning transmission mode possible, and the resulting electron probe diameter defines the resolution of the system. Therefore, in addition to thin samples, specimens with higher degree of crystallinity and thickness can be imaged by TEM. Multistage condenser lens systems enable recording of secondary and backscattered electrons. This has advantages for imaging thick or crystalline specimens and for recording secondary electrons and backscattered electrons. The inhomogeneity in cathodoluminescence can also be recorded using complex multistage condenser lens system for correlation with structural defects [52]. Cathodoluminescence microscopy is a useful characterisation technique in various fields related to optoelectronics, energy, geology, cellular biology and healthcare [53]. Traditionally scanning electron microscopy (SEM) has been used to study the cathodoluminescence of bulk samples as well as nanoparticles. The limited resolution of SEM (up to 20 nm in the most advanced systems) restricts the use of SEM for microstructure correlation with the cathodoluminescence. Therefore high-resolution cathodoluminescence microscopy is possible using TEM [54–57].

4.2.1.1 TEM Case Studies

TEM has shown itself to be capable of meeting such challenges. It is commonly used specifically for its ability to isolate and examine individual nanoparticles. This approach reduces the potential for agglomeration which can be a problem with wet-based laser scattering techniques. Nanoparticles of various materials produced by different techniques have also been imaged, with remarkable clarity [58–60]. TEM's electron imaging and diffraction options allow property-structure relationships of nanostructures to be understood. It has the resolution to differentiate between nanotubes with subtle nanoscale structural patterns. Interlayer distances of about 0.34 nm have been measured and imaged with impressive clarity, consistent with the (002) plane lattice parameter of graphited carbon [61].

The phase transformation and degradation in the nanostructure of the Si during the lithiation process in the lithium ion batteries results in Si amorphisation to Li_xSi phase. The detailed mechanism of this process is not yet fully understood, and in situ nano-characterisation techniques are required to investigate the charging and discharging processes. TEM provides a unique characterisation platform to investigate the fine details of complex mechanisms, impossible to study otherwise. Wang et al. reported the characteristics of the phase transformation and the variations in the microstructure properties of amorphous Si-coated hollow carbon nanofibre (CNF) composites [35]. The silicon/carbon nanofibre composite was used to coat the interior and exterior of a nanobattery anode. The in situ TEM charging and discharging of the carbon nanofibre composites was performed. The spontaneous

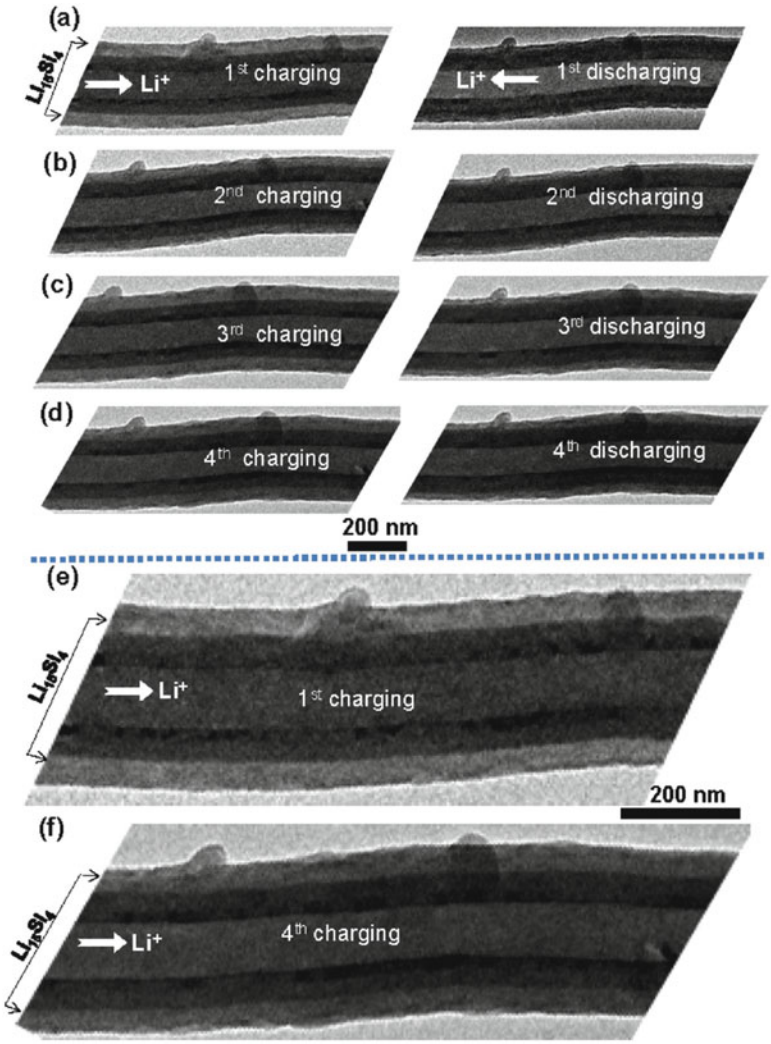

Fig. 4.13 TEM images showing the structural evolution of Si-CNF during the cyclic charging and discharging, showing (**a–d**), the *left* column is charged and the *right* column is discharged, and (**e**) a high magnification image of (**a**) and (**f**) a high magnification image of (**d**)

crystallisation of $Li_{15}Si_4$ from the amorphous Li_xSi was observed. Contrary to classic nucleation and growth progress, the corresponding phase transition process was observed without phase separation or large-scale atomic motion. The coating of amorphous Si layer on the CNF was strong in the starting charge/discharge cycles without any structural defects. However, with increasing charge/discharge cycles, the bond between amorphous Si and CNF weakens as the surface roughness is increased (see Fig. 4.13). This degradation of the nanostructure observed by in situ

TEM eventually reduces the capacity of the composite anode over extended period of charge/discharge cycles.

Note that with cyclic charging and discharging, the surface of the coating layer is gradually crumpling. The two particles shown in this CNF are pre-existing particles. With a very limited number of in situ cycling in the TEM column, the change of the coating layer is not significant. However, as a general trend, it is noted that even with a limited number of cyclic charging/discharging, the surface begins to become rougher. To illustrate this point, the images in Fig. 4.13a 1st charged and Fig. 4.13d 4th charged are shown magnified in Fig. 4.13e, f, respectively. Note the slightly increased surface roughness in (f) as compared with (e) [62].

The in situ observations of other nanostructures and nanoparticles have been extensively studied using TEM to highlight the fine details of many complex nanoscale mechanisms and processes [63–68].

4.2.2 Focused Ion Beam (FIB)

Focused ion beams have become a popular tool for surface modification of materials and functional structure prototyping at the micro- and nanoscale. Modern focused ion beams have spot sizes of <5 nm and are produced by using electrostatic lenses to focus the image of a point source, often gallium liquid metal ion source, onto the substrate and to deflect it in a precise fashion. For a comprehensive review of recent developments in FIB implantation and sputtering, FIB gas-assisted etching and FIB-induced deposition, the reader is referred to Stanishevsky [69].

4.2.2.1 FIB Case Studies

Hitachi pioneered the use of FIBs for integrated circuit cross-sectioning for failure analysis in 1985. FIB technology can quickly and selectively remove specific layers (dielectric or metal) for conducting material analysis of underlying surfaces [69]. FIB can locate, expose and analyse the fault area without destroying the surrounding areas or losing the information at the site of the fault. A growing application area is FIB 'microsurgery' for circuit modification, device modification and defect repair. FIB make-and-break microsurgery combines imaging, restructuring and verification in the same machine.

The provision of transport carriers, large surface area and facile strain relaxation make nanowires a unique solution for various biomedical engineering applications related to biochemical sensing, electrophysiology and intercellular activities recording. The cell viability on any substrate depends upon the interface activities between the substrates and cells. Despite extensive research on cellular interaction with nanostructured surfaces, the biological interactions between nanowires and biological cells are poorly understood. In a study by Wierzbicki et al., low- and high-density nanowire (nanograss) silicon substrates were used to study the in vitro

3T3 fibroblast cell behaviour using SEM-FIB [70]. Four different types of interactions were observed between the nanograss and the cells: (i) the cells lying on the top of the nanowires, (ii) penetration of nanowires into the cells, (iii) the nanowires breaking from the substrate and becoming engulfed by the cells, (iv) weak nanowires being flattened by the cells, (v) cell motility through plasma membrane blebs and (vi) increased vacuolisation (see Fig. 4.14) [70].

4.2.3 X-Ray Diffraction (XRD)

X-ray diffraction (XRD) is a powerful technique used to uniquely identify the crystalline phases present in materials and to measure the structural properties (strain state, grain size, epitaxy, phase composition, preferred orientation and defect structure) of these phases. XRD is non-contact and non-destructive. XRD is most sensitive to high-Z elements; as a consequence, the sensitivity of XRD depends on the material of interest [49]. The regular array of atoms in a crystalline material forms a three-dimensional diffraction grating for waves with a wavelength close to that of the distance between the atoms. When waves enter a crystal, they are scattered in all directions by the atoms. In certain directions, these waves can interfere destructively. In other directions, constructive interference will occur resulting in peaks in X-ray intensity. The diffraction pattern that results is a map of the reciprocal lattice of the crystal and can be used to determine the structure of the crystal [71]. Bragg's law (3.2) is the basis for crystal diffraction:

$$n\lambda = 2d \sin\theta \tag{4.2}$$

where n is an integer known as the order of diffraction, λ the X-ray wavelength, d the spacing between two consecutive scattering planes and θ the angle between the atomic planes and the incident (and diffracted) X-ray beam [47].

4.2.3.1 XRD Case Studies

In a study by Liu et al., graphene-reinforced aluminium metal matrix composites (AMCs) were prepared, and the characterisation of the AMCs was performed by SEM and XRD [72]. The reduced graphene oxide (rGO) was coated on the aluminium powder by mixing and dispersion using three different solvents (acetone, ethanol, and ethanol—water). The clearest dispersion of rGO and Al was observed in acetone solvent mixture. The GO-Al powders were prepared with 0.07%, 0.15%, 0.3%, 0.7% and 2% graphene on a weight basis. Disc-shaped pallets of graphene-reinforced AMCs were compacted and sintered having 20 mm diameter and 0.8–1 mm diameter. The XRD scans for pure aluminium and graphene-reinforced AMC demonstrated major aluminium peaks at 38.8° (111), 45.0° (200), 65.4° (220), 78.5° (311) and 82.7° (222) (see Fig. 4.15). The presence of aluminium

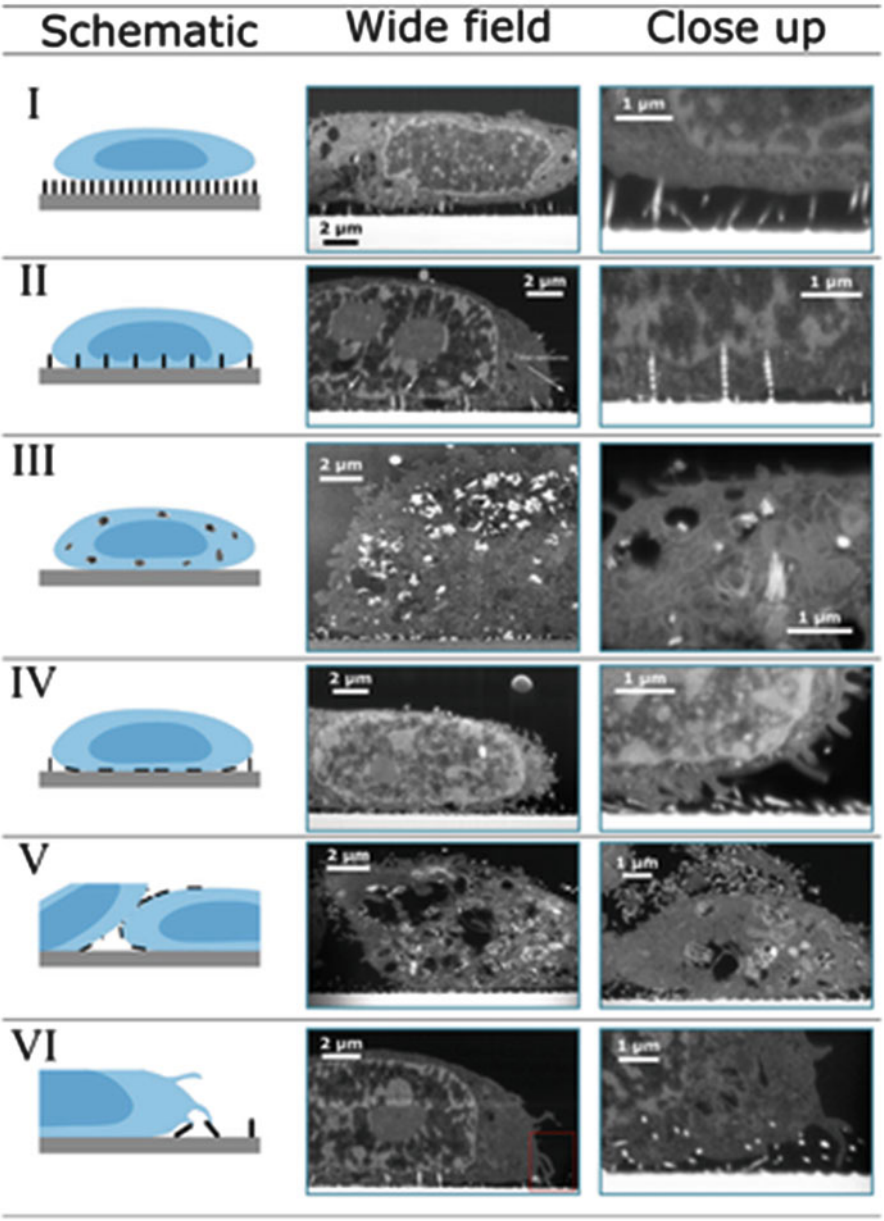

Fig. 4.14 FIB-SEM images of several cases observed by cell–nanograss interaction with associated schematic description [70]

oxide was also observed at 27.1° in all samples. The input variables such as graphene weight percentage, dispersion time, compaction pressure and sintering temperature were optimised. The hardness test measurements demonstrated

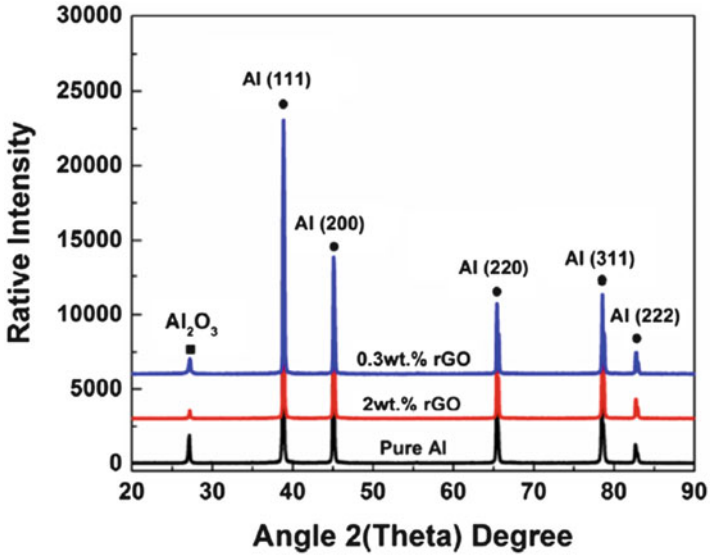

Fig. 4.15 XRD scans of pure aluminium, 0.3 and 2 wt.% rGO-AMCs samples

significant increase in hardness due to graphene nanosheet reinforcements. Graphene nanosheet characterisation has been performed using the XRD technique in various studies related to energy, mechanical properties improvement, and sensor development [73–77].

4.2.4 Mercury Porosimetry

The mercury porosimeter is a device which can generate suitably high pressures while measuring simultaneously both the pressure and volume of mercury taken up by a porous material [78]. Mercury does not wet most substances and will only penetrate pores when forced to do so under high pressure. Entry of mercury into pores requires applying pressure in inverse proportion to pore size. In other words, large pores will fill first, with smaller pores filling at increasingly higher pressures. Equation 2, known as the Washburn equation, is the basis of the mercury porosimeter method for measuring pore size distribution:

$$D = \frac{-4\gamma \cos\theta}{P} \tag{4.3}$$

where D is the pore diameter, γ the surface tension, θ the contact angle and P the applied pressure. Mercury exhibits a high contact angle against most solids. Reported contact angles vary, with 130° being the most widely used value. Liquid mercury has a high surface tension; usually its value is taken to be 485 dyne/cm

[79]. High-pressure mercury porosimeters can normally attain maximum pressures of 30,000 or 60,000 psia. The measurable pore size ranges from a maximum of 360 μm to a minimum of 6 nm (for the 30,000 psia system) or 3 nm (for the 60,000 psia system) [79]. In principle, it would be possible to explore in the pore range below 3 nm if a porosimeter with sufficiently high pressures could be made [78]. In practice, BET surface area is normally employed for micropore (< 2 nm) analysis. In porosimetry, a mercury filling apparatus is used to evacuate the sample and then to surround the sample with mercury. Evacuation is achieved by exposing the sample to a vacuum. The sample to be analysed is contained inside a penetrometer, which is a long glass capillary tube, the sample end being a bulb shape. Using the vacuum control on the filling apparatus, gases and vapours are removed from the sample. The vacuum valve is closed and the penetrometer tilted so that the stem end is immersed in mercury. The vent control valve is then slowly opened so that air fills the mercury chamber. Mercury is forced up the capillary stem and into the bulb. The filled penetrometer is then removed and inserted in the high-pressure porosimeter for pore analysis.

The construction of the glass penetrometer is key to pore measurement. A metal sheath fits over the capillary section. A metal seal attaches to the sample end of the penetrometer as a base electrode. The construction is thus mercury-glass-metal, or conductor-insulator-conductor. In this way a coaxial capacitor is created [79]. The capacitance changes as a result of the change in mercury level within the penetrometer. The mercury level will change as porous samples are filled with mercury under increasingly high pressure. In a similar way, a normal mercury thermometer will change mercury level, indicating a temperature change. Some porosimetry systems operate on the basis of a wire dipped remotely into the mercury, the change in electrical resistance of the wire being used as a means of measuring the volume of mercury taken up by the pores [78].

4.2.4.1 Mercury Porosimetry Case Studies

Terock et al. [80] used mercury porosimetry to measure the pore size distribution of synthesised platinum-nickel nanostructures on porous zirconia, a material widely used in sensor and fuel cell applications including catalytic converters, where maintaining open pores is critical in their operation [80]. An investigation into the mechanical properties and microstructures of fabricated nanocomposite aerogels using mercury porosimetry was conducted by Seraji et al. [81]. These nanocomposites were produced for applications in high-temperature thermal insulation. Silicon carbide (SiC) and carbon/silicon carbide (C/SiC) nanocomposite aerogels were fabricated via a thermal reduction process of high char yield precursors. The initial network structure of the precursor material is maintained during the reduction process; however the pore volume and size distribution along with mechanical surface properties are affected by the high-temperature treatment process. These pore properties are directly related to the insulating properties of the material, and therefore it is necessary to quantify them at the final processing step.

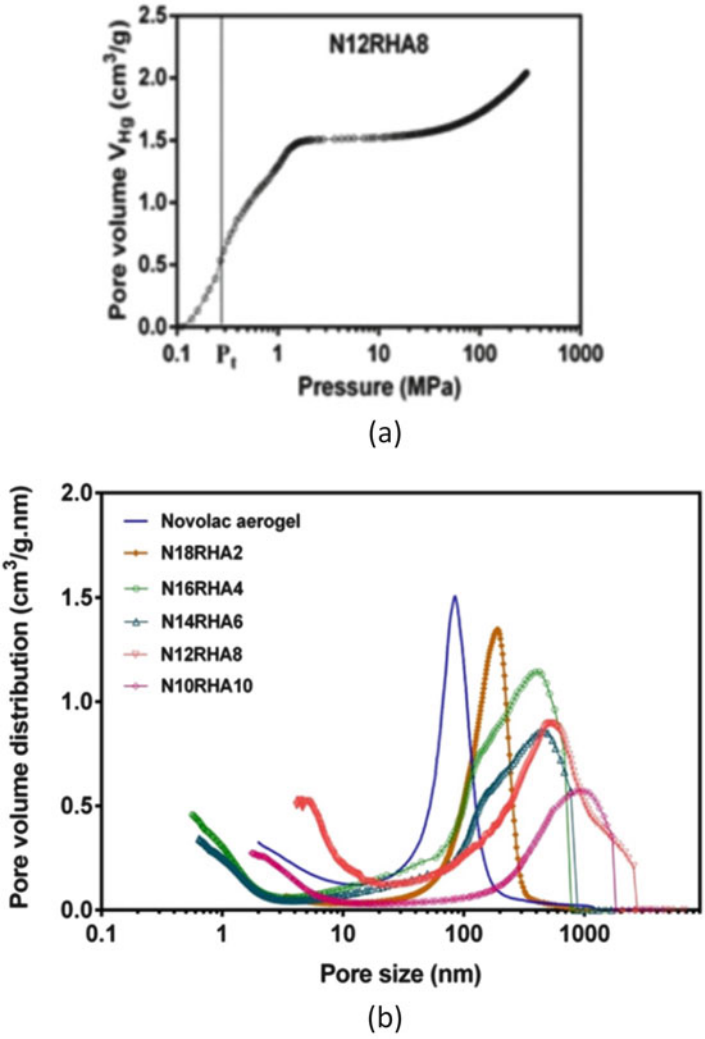

Fig. 4.16 (**a**) Mercury intrusion curves of polymeric novolac/silica nanocomposite aerogels and (**b**) pore size distribution of novolac aerogels [81]

The pore and mechanical properties of novolac-silica hybrid polymer gels fabricated utilising the new solvent-saturated vapour atmosphere (SSVA) method was investigated in this work along with the polymer microstructure and variations of crystalline phase observed by porosity analysis over the course of the heat treatment process. Pore volume and size distribution were measured over a pressure range of 0.01–440 mPa as can be seen by the intrusion curve in Fig. 4.16. The sudden change in the slope of the volume *versus* pressure indicates a pressure transition point (P_t). It was seen from the results for all materials tested that the

initial pressure reduced with increasing amounts of silica. The authors found that with the addition of silica aerogel particles the pore size increased and the microstructure was directly proportional to the silica content.

4.3 Measurement of Composition of Nanostructures

4.3.1 Energy Dispersive X-Ray Spectroscopy (EDS)

Energy dispersive X-ray spectroscopy is one of the most common spectroscopy techniques used as SEMs from the 1960s have been commonly equipped with this chemical analytical device [82]. In this technique, electromagnetic radiation is bombarded into a material surface which causes electrons from inner atomic shells to be ejected and subsequently filled with electrons from higher energy levels. Electromagnetic radiation used to excite the sample is usually a focused high-energy stream of electrons, protons or X-rays. In a typical SEM, a stream of electrons is used. Electron transitions from the higher-energy shells to lower-energy shells cause X-rays to be emitted. A detector of SiLi or more commonly known as silicon drift detector is used to collect and count the number of X-rays emitted at each energy level. The energy level characterises the element from which the X-ray was emitted, while the count of the number of X-rays with this energy level is used to characterise the amount of the element that is present. A typical spectrum presents the count of the X-rays versus the energy level of the X-rays. New EDS systems come pre-calibrated to allow automatic detection and quantification of the elements present within the sample.

Care must be taken when interpreting EDS results. Wrong elements, for example, can often be detected where energy levels emitted from different elements overlap. X-rays can be generated from K, L or M energy-level shells in a typical element. Therefore overlapping of energy levels detected can occur, for example, when Ti and Ba (Ti-K_α and Ba-L), or Mn and Fe (Mn-K_β and Fe-K_α), or Mn and Cr (Mn-K_α and Cr-K_β) are present. Some knowledge of the sample elemental chemistry or knowledge gained from other analytical techniques is often useful for element identification. Wavelength dispersive X-ray spectroscopy (WDS) is similar to EDS but analyses the diffraction patterns from the material–radiation interaction in order to identify one element at a time. WDS provide greater spectral resolution. Often the use of EDS followed by WDS can provide further definition of sample elemental content. The interaction volume from which X-rays are emitted due to the primary electron bombardment is in the shape of a tear drop beneath the surface. The accelerating voltage used and the density of the material define the volume size. The depth from which X-rays are emitted to the detector is usually from 1 to 5 μm and can be calculated from the empirical expression $(0.1 \times E^{1.5})/\rho$ [83]. The width of the volume can be approximated from $(0.077 \times E^{1.5})/\rho$.

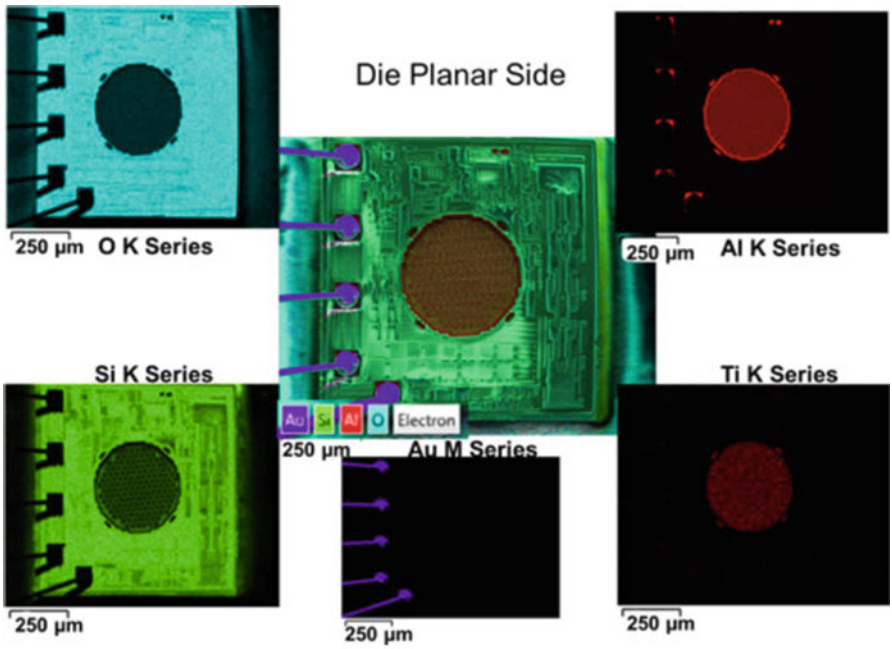

Fig. 4.17 SEM-EDS on planar (*top*) side of the CMOS-MEMS die. O (*sky blue*), Al (*dark red*), Si (*light green*), Au (*indigo*) and Ti (*light red*) [84]

4.3.1.1 EDS Case Studies

The surface characterisation and texture analysis of nanostructured CMOS-based MEMS devices are required to optimise the fabrication process and establishing the relationship between the mechanical and structural design of MEMS diaphragm and the selection of materials. In a study by Khan et al., the surface chemistry of fourth-generation CMOS-MEMS-based digital microphone chip was investigated by Carl Zeiss Ultra Plus SEM with an EDS detector [84]. The microphone chip was fabricated by integration of a diaphragm (MEMS) with a CMOS circuitry for signal processing. The EDS results demonstrated that the diaphragm was mainly composed of aluminium (approx 51 wt%) covered by titanium layer (about 10 wt%). A protective light coat of silicon oxide was observed (see Fig. 4.17). Traces of fluorine were also identified (2 wt%). These trace amounts could be introduced to the chip as by-product during the plasma etching process. The presence of fluorine-based silicon and aluminium radicals induce residual stress and strain on the diaphragm. The stress and strain produced on the diaphragm membrane influence the signal-to-noise ratio and sensitivity and thus reduce the overall efficiency of the chip. The elemental distribution of nanostructures [85–89], nanosheets [90–94] and nanoparticles [95–98] has been investigated extensively by EDS.

4.3.2 X-Ray Photoelectron Spectroscopy (XPS)

When excess electromagnetic energy is transferred to an electron that is in an outer shell, it is called an Auger electron. An analysis of these electrons for chemical identification is known as Auger electron spectroscopy (AES). X-ray photoelectron spectroscopy (XPS) analyses electron emission of similarly high energy [99]. XPS can be used to measure the chemical or electronic state of surface elements, detect chemical contamination or map chemical uniformity of biomedical implant surfaces.

For XPS the material to be examined is irradiated with aluminium or magnesium X-rays. Monochromatic aluminium K_α X-rays are normally produced by diffracting and focusing a beam of non-monochromatic X-rays off of a thin disc of crystalline quartz. Such X-rays have a wavelength of 8.3386 Å, corresponding photon energy of 1486.7 eV, and provide a typical energy resolution of 0.25 eV. Non-monochromatic magnesium X-rays have a wavelength of 9.89 Å, corresponding photon energy of 1253 eV and a typical energy resolution of 0.90 eV. The kinetic energy of the emitted electrons is recorded. This kinetic energy of the ejected electrons is directly related to the element-specific atomic binding energy of the liberated. A plot of these energies against the corresponding number of electron counts provides the spectrum which indicates the qualitative and quantitative elemental composition. At these higher energies, XPS only analyses to a depth of 10 nm into the surface. Electrons emitted at greater depths are recaptured or trapped in various excited states within the material. Spectral profiles up to 1 μm deep can however be obtained by continuous spectral recording during ion etching or from consecutive ion etching and XPS measurement steps.

XPS is usually performed in UHV and typically provides resolutions down to 1000 ppm. With optimum settings and long recording times, resolutions down to 100 ppm can be achieved. Non-monochromatic X-ray sources can produce a significant amount of heat (up to 200 °C) on the surface of the sample as the anode producing the X-rays is typically only a few centimeters from the sample. This level of heat when combined with high-energy Bremsstrahlung X-rays can degrade the surface. Organic chemicals are therefore not routinely analysed by non-monochromatic X-ray sources.

4.3.2.1 XPS Case Studies

During laser surface processing of a sample, two phenomena occurred simultaneously. The material is ablated and chemical modifications are introduced into the surface and bulk of the material. The ablation of the irradiated material depends upon input control variables such as laser wavelength, focal spot size, repetition rate, laser intensity (fluence) and the properties of the sample materials being ablated such as sensitivity and heat capacity, etc. The chemical modification will be the dominating process if the laser intensity is close to the ablation threshold of

Table 4.1 Summarised XPS results for pristine and EUV-irradiated PTFE polymer samples [31]

Atoms	Data	Pristine	50 EUV shots	200 EUV shots	300 EUV shots
F1s	At%	76	71	72	68
	FWHM	1.98	2.46	2.38	2.81
	Position	689	688	688	689
O1s	At%	–	0.51	0.42	0.64
	FWHM	–	1.95	0.66	2.63
	Position	–	535	534	533
N1s	At %	–	–	–	1.10
	FWHM	–	–	–	0.70
	Position	–	–	–	401
C1s	At%	23	27	27	30
	FWHM	1.88	2.46	2.47	2.73
	Position	292	292	292	292

the target material. If the laser intensity crosses the ablation threshold level, laser material ablation will be the dominating process resulting in change of material morphology, and small chemical modifications will be observed. Ahad et al. studied the surface ablation and chemical modifications of polytetrafluoroethylene (PTFE) samples by increasing the extreme ultraviolet (EUV) intensity [31]. The EUV source used in this study produced photons with maximum intensity around 10 nm wavelength, corresponding to 112 eV photon energy. The PTFE samples were irradiated with 50, 200 and 300 EUV pulses. The changes in the surface morphology by EUV ablation were observed by SEM and AFM, and the chemical modifications introduced by the EUV irradiation were examined by XPS. The SEM and AFM results demonstrated the introduction of nano- and microstructures on the EUV-irradiated PTFE samples. The XPS scans were performed for binding energies extending from 0 eV up to 700 eV so that electrons from fluorocarbon-based polymer (PTFE) can be detected. The XPS scans revealed that with increasing the intensity of the EUV beam on the PTFE samples, increase in defluorination was observed (see Table 4.1). This defluorination occurred due to breaking of carbon and fluorine bonding, consequently provide carbon–carbon bonding. The F1s emission reduced from 76 to 68 At% and C1s emission increased from 23 to 30 At%. It was further observed that oxygen present in the irradiation chamber was able to incorporate into the polymer surfaces. By introducing nitrogen during EUV irradiation on PTFE samples, incorporation of nitrogen (1.1 At%) on the polymer samples was also observed.

Nitrogen doping by EUV surface structuring was also observed in polyvinyl fluoride (PVF) polymer by XPS surface characterisation [34].

4.3.3 Secondary Ion Mass Spectroscopy (SIMS)

Secondary ion mass spectroscopy (SIMS) is a destructive analytical technique in which material is removed from a surface by ion beam sputtering and the resultant positive and negative ions are mass analysed in a mass spectrometer [100]. The technique is element-specific and is capable of detecting all elements as well as isotopes and molecular species. Of all the beam techniques, it is the most sensitive with detection limits for some elements in the 10^{14} to 10^{15} cm^{-3} range if there is very little background interference signal. Lateral resolution is typically 100 μm but can be as small as 0.5 μm with depth resolution of 5–10 nm [50].

SIMS works by removing material from a sample by sputtering using an ion beam. The mass/charge ratio of the removed ions is analysed, detected as a mass spectrum, as a count, or displayed on a fluorescent screen [79]. *Static* SIMS employs very low primary ion density of around 1 nA cm^{-2} and low primary ion energy (0.5–2 keV) so that a nearly undisturbed monolayer of the surface can be analysed. *Dynamic* SIMS involves primary ion currents greater than 1 μA cm^{-2}, and usually more than one monolayer is removed during the analysis [71]. Dynamic SIMS can produce depth profiles, and quantitative depth profiling is unquestionably the major strength of SIMS. SIMS lends itself to investigations of grain boundary diffusion or diffusion across interfaces. It is a powerful tool for studying the transport processes in ceramics in the temperature range where diffusion distances are too small to be analysed by serial mechanical sectioning. Fielitz et al. used SIMS depth profiling to investigate oxygen grain boundary diffusion in mullite ceramics and its effect on sintering, grain growth and creep [101]. Kowalski investigated the diffusion of calcium in yttria-stabilised zirconia ceramics [102]. Haneda investigated bizmuth solubility and the grain boundary diffusion of oxygen ions in ZnO ceramics, which is important in terms of understanding electrical transport and the effects on varistor characteristics [103].

4.3.3.1 SIMS Case Studies

Lee et al. (2014) investigated the potential toxicity of zinc oxide nanoparticles (NPs) to human skin cells. ZnO nanoparticles are finding increased applications in many areas from antimicrobial coatings in food packaging, antibacterial coatings for surfaces, additions to waste treatment filters, additions to waste water sludge and as a sun block agent in paints and sun creams. The latter was the subject of the Lee et al. [104] study.

Time-of-flight secondary ion mass spectrometry (TOF-SIMS) was utilised as a visualisation technique to determine the cytotoxicity of the nanoparticles to the cells of choice. ZnO nanoparticles were synthesised from powder using a chemical reduction technique, their morphology examined using TEM. The HaCaT cells were grown to a density of 1.0×10^5 cell per well before addition of nanoparticles at varying concentrations of 0, 5, 10, 50 and 100 μg/mL in an aqueous solution and

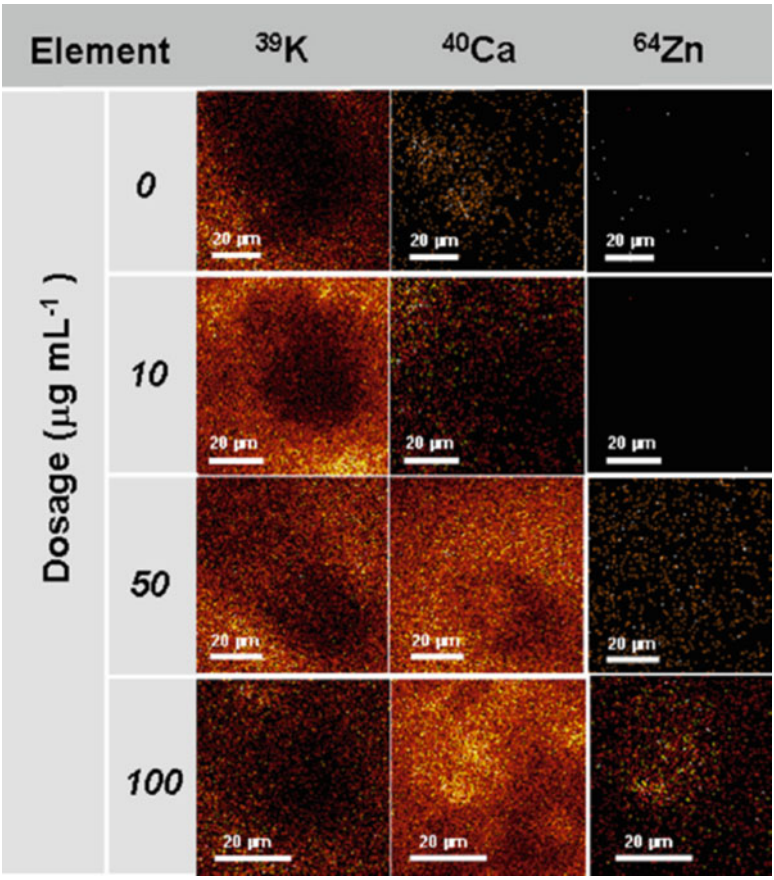

Fig. 4.18 TOF-SIMS ion images of HaCaT cells treated with varying concentrations of ZnO NPs [104]

cultured for a further 24 h within a 1×1 cm^2 silicon wafer. After culturing, the cells were then washed with PBS buffer to remove medium and additional cell residue. They were then freeze dried and subjected to modified molecular-imprint treatment, with the wafer pressed against a silicon wafer coated with a gold layer. A TOF-SIMS instrument was operated with a Ga^+ primary ion gun of 25 keV, 1pA pulse current. This procedure was carried out to ensure that only the internal of the cells was imaged. An example image produced of the ZnO NPs acting as a tracer with HaCaT cells can be seen in Fig. 4.18.

These images lead to conclusions that the modes of action of the NPs on the cells were membrane disruption, cytotoxic response and apoptosis. The authors concluded that TOF-SIMS was a suitable technique to offer rapid determination of cell response to NPs.

4.3.4 Auger Electron Spectroscopy (AES)

When an electron or ion is incident on a semiconductor, it may transfer enough energy to an inner shell electron to eject it from its parent atom. The atom is in an excited state, and, to lower its energy, an electron from a less tightly bound shell may fill the hole while simultaneously emitting a third electron from the atom. This ejected atom is known as an Auger electron [71]. Its energy is related specifically to the electron energy levels involved in the process and, therefore, is characteristic of the atom concerned. Since the Auger process is a three-electron process, neither hydrogen nor helium can be detected since both have less than three electrons. AES has two distinct advantages over EDX analysis. It is a far more surface-sensitive technique. Escape depths range from less than a nanometre to a few nanometres. In EDX it can be difficult to analyse small particles on a substrate, because the electron beam passes through the particles and spreads out in the substrate below it [100]. There is the potential for chemical-state information in Auger spectroscopy, for example, the oxidation state of silicon at a Si–SiO_2 interface may be ascertained [71]. EDX does not provide chemical state information.

AES has found applications in measuring semiconductor composition, oxide film composition, silicides, metallization, particle analysis and the effects of surface cleaning. AES measurements are made in a high vacuum environment (10^{-12}–10^{-10} torr) to retard the formation of hydrocarbon contamination layers on the sample surface [50]. Scanning Auger microscopy (SAM) allows surfaces to be mapped for one selected element at a time. In this mode the electron beam is scanned over a selected area. The Auger intensity is measured at each point of the area [67]. SAM requires higher beam currents and is much slower than SEM/EDX [50].

4.3.4.1 AES Case Studies

Rades et al. [105] used AES to investigate the chemical structure of silica nanoparticles, identified as a high-priority nanomaterial for the industrial market. Given that Auger electron spectroscopy (AES) possesses an analysis depth of only a few nanometres, it is suited to examination of the chemical composition of nanoparticle surfaces. In this study particles were imaged and preselected on a TEM grid before being put forward for AES analysis (see Fig. 4.19). In terms of spectra the signals from Si and O_2 are well distinguishable implying that silica has oxidised. The authors note that there must be a contamination layer on the bulk silica particles containing traces of iron fluorine and nitrogen.

More recently Sharma et al. [106] explored the synthesis of palladium (Pd) nanoparticle supported magnetic catalyst (Pd@Fe_3O_4-NH_2/Starch). Inductively coupled plasma atomic emission spectroscopy (ICP-AES) was used to examine the Pd content that was contained in the catalyst. ICP-AES determined that 2.52 wt% Pd was present on the catalyst [106]. Also, Zhang et al. (2017) used

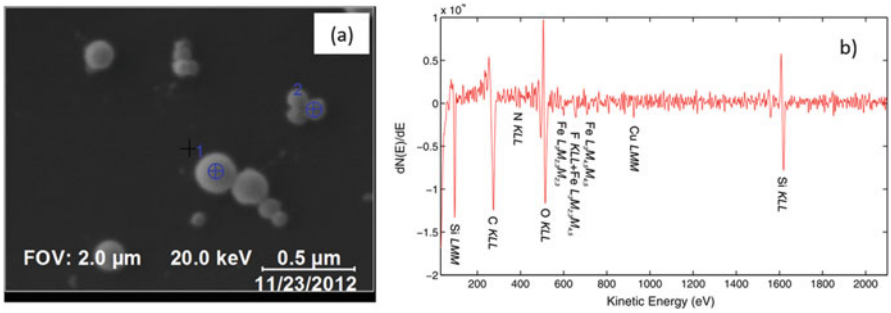

Fig. 4.19 (**a**) Secondary electron image of the TEM grid showing the particles selected for AES analysis and (**b**) the AES spectra for the selected silica particle [105]

ICP-AES to measure the concentration of heavy metal ions in the solution during the synthesis of SnS2 nanostructures.

4.4 Conclusion

Over the past 10 years, nanoparticles and nanostructures have been adopted at an ever-increasing rate throughout research and industry in many diverse fields. They have applied for improving the mechanical and electrical properties of materials as nanocomposites and in electronics where they are being employed as printable conductive inks. They have been used in food packaging to improve the antimicrobial qualities of the packaging and reducing food waste. In water treatment, they have been used to coat filters and as flocculation agents. They have also been employed as paint additives to changing their optical properties. Nanoparticles and structures are being used for separation science applications, separating and detecting chemical and biological species, as well as in drug delivery via bio-tagging.

This wide adaption of nanomaterials places increasing requirements on technology to adapt and enable characterisation of the nanomaterials both in their raw and final product forms. Technology must respond to meet these demands. In this chapter, various approaches to meeting these requirements have been discussed, and with each technique it is seen that higher resolutions, larger viewing sizes and quicker scanning times are being achieved.

References

1. Beshkar F, Amiri O, Salehi Z (2017) Synthesis of $ZnSnO_3$ nanostructures by using novel gelling agents and their application in degradation of textile dye. Sep Purif Technol 184:66–71

2. Mohammadkhani A, Malboubi M, Anthony C, Jiang K (2011) Characterization of surface properties of ordered nanostructures using SEM stereoscopic technique. Microelectron Eng 88(8):2687–2690
3. Buhr E, Senftleben N, Klein T, Bergmann D, Gnieser D, Frase CG, Bosse H (2009) Characterization of nanoparticles by scanning electron microscopy in transmission mode. Meas Sci Technol 20(8):84025
4. O'Shea A, Wallace J, Hummel M, Strauss LH, Kidd TE (2013) Enhanced detection of nanostructures by scanning electron microscopy using insulating materials. Micron 52–53:57–61
5. Villarrubia JS, Vladár AE, Ming B, Kline RJ, Sunday DF, Chawla JS, List S (2015) Scanning electron microscope measurement of width and shape of 10 nm patterned lines using a JMONSEL-modeled library. Ultramicroscopy 154:15–28
6. Jusman Y, Ng SC, Abu Osman NA (2014) Investigation of CPD and HMDS sample preparation techniques for cervical cells in developing computer-aided screening system based on FE-SEM/EDX. Sci World J 2014:1–11
7. Vaughn DD, Hentz OD, Chen S, Wang D, Schaak RE (2012) Formation of SnS nanoflowers for lithium ion batteries. Chem Commun 48(45):5608
8. Kang J-G, Park J-G, Kim D-W (2010) Superior rate capabilities of SnS nanosheet electrodes for Li ion batteries. Electrochem Commun 12(2):307–310
9. Wang Y, Yang X, Wang Z, Lv X, Jia H, Kong J, Yu M (2016) CdS and SnS_2 nanoparticles co-sensitized TiO2 nanotube arrays and the enhanced photocatalytic property. J Photochem Photobiol A Chem 325:55–61
10. Kafashan H, Ebrahimi-Kahrizsangi R, Jamali-Sheini F, Yousefi R (2016) Effect of Al doping on the structural and optical properties of electrodeposited SnS thin films. Phys Status Solidi 213(5):1302–1308
11. Kafashan H, Jamali-Sheini F, Ebrahimi-Kahrizsangi R, Yousefi R (2016) Influence of growth conditions on the electrochemical synthesis of SnS thin films and their optical properties. Int J Miner Metall Mater 23(3):348–357
12. Chalapathi U, Poornaprakash B, Park S-H (2016) Chemically deposited cubic SnS thin films for solar cell applications. Sol Energy 139:238–248
13. Sall T, Mollar M, Marí B (2016) Substrate influences on the properties of SnS thin films deposited by chemical spray pyrolysis technique for photovoltaic applications. J Mater Sci 51 (16):7607–7613
14. Li S, Gu X, Zhao Y, Qiang Y, Zhang S, Sui M (2016) Enhanced visible-light photocatalytic activity and stability by incorporating a small amount of MoS2 into Ag3PO4 microcrystals. J Mater Sci Mater Electron 27(1):386–392
15. Kashid RV, Joag PD, Thripuranthaka M, Rout CS, Late DJ, More MA (2015) Stable field emission from layered MoS2 nanosheets in high vacuum and observation of 1/f noise. Nanomater Nanotechnol 5:1
16. Chen YM, Yu XY, Li Z, Paik U, Lou XWD (2016) Hierarchical MoS2 tubular structures internally wired by carbon nanotubes as a highly stable anode material for lithium-ion batteries. Sci Adv 2(7):e1600021
17. Wang S, Li X, Chen Y, Cai X, Yao H, Gao W, Zheng Y, An X, Shi J, Chen H (2015) A facile one-pot synthesis of a two-dimensional MoS_2/Bi_2S_3 composite theranostic nanosystem for multi-modality tumor imaging and therapy. Adv Mater 27(17):2775–2782
18. Wang Y, Yu L, Lou XWD (2016) Synthesis of highly uniform molybdenum-glycerate spheres and their conversion into hierarchical MoS_2 hollow nanospheres for lithium-ion batteries. Angew Chem Int Ed 55(26):7423–7426
19. Kafashan H, Azizieh M, Nasiri Vatan H (2016) Ultrasound-assisted electrodeposition of SnS: effect of ultrasound waves on the physical properties of nanostructured SnS thin films. J Alloys Compd 686:962–968
20. Chu KKW, Chen JS, Der Chang L, Tsai JTH (2017) Graphene-edge probes for scanning tunneling microscopy. Optik (Stuttg) 130:976–980

21. Krupski A (2011) Scanning tunnelling microscopy study of Au growth on Mo(110). Surf Sci 605(3–4):424–428
22. Mehdinia A, Mohammadi AA, Davarani SSH, Banitaba MH (2011) Application of self-assembled monolayers in the preparation of solid-phase microextraction coatings. Chromatographia 74(5–6):421–427
23. Huerta TF, Valenzuela J (2017) Growth of 4-aminothiophenol on iodine modified Au(100) studied by scanning tunneling microscopy. Surf Sci 655:17–24
24. Koguchi K, Matsumoto T, Kawai T (1995) Atomic-scale images of the growth surface of Ca1-xSrxCuO$_2$ thin films. Science 267(5194):71–73
25. Jung HS, Kim HJ (2002) Initial stage of CdTe on Si(1 0 0) grown by MBE. Curr Appl Phys 2 (5):389–391
26. Seo J, Kim T-H, Kuk Y (2015) Visualization of the inverse layer-plus-island growth in Fe islands on W(110) substrate. Curr Appl Phys 15(9):1042–1046
27. Chang YJ, Phark S (2017) Atomic-scale visualization of initial growth of perovskites on SrTiO 3 (001) using scanning tunneling microscope. Curr Appl Phys 17(5):640–656
28. Rafati A, Gill P (2016) Ultrastructural characterizations of DNA nanotubes using scanning tunneling and atomic force microscopes. J Microsc Ultrastruct 4(1):1–5
29. Chen X, Davies MC, Roberts CJ, Tendler SJB, Williams PM, Davies J, Dawkes AC, Edwards JC (1998) Interpretation of tapping mode atomic force microscopy data using amplitude-phase-distance measurements. Ultramicroscopy 75(3):171–181
30. Ul Ahad I, Bartnik A, Fiedorowicz H, Kostecki J, Korczyc B, Ciach T, Brabazon D (2014) Surface modification of polymers for biocompatibility via exposure to extreme ultraviolet radiation. J Biomed Mater Res A 102(9):3298–3310
31. Ahad IU, Butruk B, Ayele M, Budner B, Bartnik A, Fiedorowicz H, Ciach T, Brabazon D (2014) Extreme ultraviolet (EUV) surface modification of polytetrafluoroethylene (PTFE) for control of biocompatibility. Nucl Instrum Methods Phys Res Sect B 364:98–107
32. Ahad IU, Budner B, Korczyc B, Fiedorowicz H, Bartnik A, Kostecki J, Burdyńska S, Brabazon D (2014) Polycarbonate polymer surface modification by extreme ultraviolet (EUV) radiation. Acta Phys Pol A 125(4):924–928
33. Ahad I, Fiedorowicz H, Budner B, Kaldonski TJ, Vazquez M, Bartnik A, Brabazon D (2016) Extreme ultraviolet surface modification of polyethylene terephthalate (PET) for surface structuring and wettability control. Phys Pol A 129(2):241–243
34. Ahad IU, Budner B, Fiedorowicz H, Bartnik A, Brabazon D (2013) Nitrogen doping in biomaterials by extreme ultraviolet (EUV) surface modification for biocompatibility control. Eur Cell Mater 26(Suppl. 626):145
35. Liberatore C, Bartnik A, Ahad IU, Toufarová M, Matulková I, Hájková V, Vyšín L, Burian T, Juha L, Pina L, Endo A, Mocek T (2015) EUV ablation: a study of the process. SPIE Optics + Optoelectron:951011
36. Fulwyler M, Hanley QS, Schnetter C, Young IT, Jares-Erijman EA, Arndt-Jovin DJ, Jovin TM (2005) Selective photoreactions in a programmable array microscope (PAM): Photoinitiated polymerization, photodecaging, and photochromic conversion. Cytometry A 67A(2):68–75
37. Ilčíková M, Danko M, Doroshenko M, Best A, Mrlík M, Csomorová K, Šlouf M, Chorvát D, Koynov K, Mosnáček J (2016) Visualization of carbon nanotubes dispersion in composite by using confocal laser scanning microscopy. Eur Polym J 79:187–197
38. Oyarzún DP, Pérez OEL, Teijelo ML, Zúñiga C, Jeraldo E, Geraldo DA, Arratia-Perez R (2016) Atomic force microscopy (AFM) and 3D confocal microscopy as alternative techniques for the morphological characterization of anodic TiO$_2$ nanoporous layers. Mater Lett 165:67–70
39. Beleites M, Matyssek C, Blaschek HH, Seifert G (2012) Near-field optical microscopy of femtosecond-laser-reshaped silver nanoparticles in dielectric matrix. Nanoscale Res Lett 7:2–5

40. Bagga K, McCann R, Wang M, Stalcup a, Vázquez M, Brabazon D (2015) Laser assisted synthesis of carbon nanoparticles with controlled viscosities for printing applications. J Colloid Interface Sci 447:263–268
41. Bagga K, McCann R, O'Sullivan F, Ghosh P, Krishnamurthy S, Stalcup A, Vázquez M, Brabazon D (2017) Nanoparticle functionalized laser patterned substrate: an innovative route towards low cost biomimetic platforms. RSC Adv 7(13):8060–8069
42. Tomaszewska E, Soliwoda K, Kadziola K, Tkacz-Szczesna B, Celichowski G, Cichomski M, Szmaja W, Grobelny J (2013) Detection limits of DLS and UV-Vis spectroscopy in characterization of polydisperse nanoparticles colloids. J Nanomater 2013:60
43. Takahashi K, Kato H, Saito T, Matsuyama S, Kinugasa S (2008) Precise measurement of the size of nanoparticles by dynamic light scattering with uncertainty analysis. Part Part Syst Charact 25(1):31–38
44. Bhattacharjee S (2016) DLS and zeta potential—what they are and what they are not? J Control Release 235:337–351
45. Nobbmann U, Morfesis A (2009) Light scattering and nanoparticles. Mater Today 12(5):52–54
46. Freud PJ (2007) Nanoparticle sizing, dynamic light scatteringanalysis in the frequency spectrum mode. Application Note: Microtrach Inc.
47. Brar SK, Verma M (2011) Measurement of nanoparticles by light-scattering techniques. Trends Anal Chem 30(1):4–17
48. Horechyy A, Nandan B, Shajkumar A, Formanek P, Paturej J, Stamm M, Fery A (2016) In-situ monitoring of silica shell growth on PS-b-P4VP micelles as templates using DLS. Polymer (United Kingdom) 107:485–491
49. Brundle CR, Evans CA, Wilson S (1992) Encyclopedia of materials characterization : surfaces, interfaces, thin films. Gulf Professional Publishing, Texas
50. Schroder DK (2005) Semiconductor material and device characterization, 3rd edn. John Wiley & Sons, New Jersey
51. Wang ZL, Poncharal P, De Heer WA (2000) Measuring physical and mechanical properties of individual carbon nanotubes by in situ TEM. J Phys Chem Solid 61(7):1025–1030
52. Lim SK, Brewster M, Qian F, Li Y, Lieber CM, Gradečak S (2009) Direct correlation between structural and optical properties of III−V nitride nanowire heterostructures with nanoscale resolution. Nano Lett 9(11):3940–3944
53. Barbin V (2013) Application of cathodoluminescence microscopy to recent and past biological materials: a decade of progress. Mineral Petrol 107(3):353–362
54. Bertram F, Müller M, Schmidt G, Veit P, Petzold S, Albert S, Bengoechea-Encabo AM, Sánchez-Garcia MÁ, Calleja E, Christen J (2016) Nanoscale imaging of structural and optical properties using helium temperature scanning transmission electron microscopy cathodoluminescence of nitride based nanostructures. Microsc Microanal 22(S3):600–601
55. White E, Howkins A, Williams C (2015) Investigating the origin of luminescence in zinc oxide nanostructures with STEM-cathodoluminescence. Microsc Microanal 21 (S3):1257–1258
56. Hanna G, Glatzel T, Sadewasser S, Ott N, Strunk HP, Rau U, Werner JH (2006) Texture and electronic activity of grain boundaries in Cu(In,Ga)Se 2 thin films. Appl Phys A Mater Sci Process 82(Special Issue 1):1–7
57. den Engelsen D, Fern GR, Ireland TG, Harris PG, Hobson PR, Lipman A, Dhillon R, Marsh PJ, Silver J (2016) Ultraviolet and blue cathodoluminescence from cubic Y_2O_3 and Y_2O_3:Eu^{3+} generated in a transmission electron microscope. J Mater Chem C 4(29):7026–7034
58. Wu J, Helveg S, Ullmann S, Peng Z, Bell AT (2016) Growth of encapsulating carbon on supported Pt nanoparticles studied by in situ TEM. J Catal 338:295–304
59. Buttry D (2016), High resolution TEM study on phase transformations in redox active silver nanoparticles. PRiME 2016/230th ECS Meet, 2–7 October 2016
60. Chee SW, Loh D, Baraissov Z, Matsudaira P, Mirsaidov U (2016) Hopping diffusion of gold nanoparticles observed with liquid cell TEM. Microsc Microanal 22(S3):750–751

61. He C, Zhao N, Shi C, Li J, Li H (2008) Magnetic properties and transmission electron microscopy studies of Ni nanoparticles encapsulated in carbon nanocages and carbon nanotubes. Mater Res Bull 43(8):2260–2265
62. Wang CM, Li X, Wang Z, Xu W, Liu J, Gao F, Kovarik L, Zhang JG, Howe J, Burton DJ, Liu Z, Xiao X, Thevuthasan S, Baer DR (2012) In situ TEM investigation of congruent phase transition and structural evolution of nanostructured silicon/carbon anode for lithium ion batteries. Nano Lett 12(3):1624–1632
63. Huiqun C, Meifang Z, Yaogang L (2006) Decoration of carbon nanotubes with iron oxide. J Solid State Chem 179(4):1208–1213
64. Salvetat J-P, Bonard J-M, Thomson NH, Kulik AJ, Forró L, Benoit W, Zuppiroli L (1999) Mechanical properties of carbon nanotubes. Appl Phys A 69(3):255–260
65. Jose MV, Steinert BW, Thomas V, Dean DR, Abdalla MA, Price G, Janowski GM (2007) Morphology and mechanical properties of Nylon 6/MWNT nanofibers. Polymer (Guildf) 48 (4):1096–1104
66. Musil CR, Bartelt JL, Melngailis J (1986) Focused ion beam microsurgery for electronics. IEEE Electron Device Lett 7(5):285–287
67. Boit C (2005) New physical techniques for IC functional analysis of on-chip devices and interconnects. Appl Surf Sci 252(1):18–23
68. Schlangen R, Kerst U, Boit C, Malik T, Jain R, Lundquist T (1964) Microelectronics and reliability, vol 47. Pergamon Press, Oxford
69. Stanishevsky A (2014) Focused ion beam nanofabircation. In: Nalwa HS (ed) Encyclopedia of nanoscience and nanotechnology, vol 3. American Scientific Publishers, Stevenson Ranch, CA, pp 469–483
70. Wierzbicki R, Købler C, Jensen MRB, Łopacińska J, Schmidt MS, Skolimowski M, Abeille F, Qvortrup K, Mølhave K (2013) Mapping the complex morphology of cell interactions with nanowire substrates using FE-SEM. Plus One 8(1):e53307. Editor: Elena A. Rozhkova
71. Jenkins TE (1998) Semiconductor science; growth and characterisation techniques. Harlow, Essex, Prentice Hall
72. Liu J, Khan U, Coleman J, Fernandez B, Rodriguez P, Naher S, Brabazon D (2016) Graphene oxide and graphene nanosheet reinforced aluminium matrix composites: powder synthesis and prepared composite characteristics. Mater Des 94:87–94
73. Wang Z, Shu J, Zhu Q, Cao B, Chen H (2016) Graphene-nanosheet-wrapped LiV_3O_8 nanocomposites as high performance cathode materials for rechargeable lithium-ion batteries. J Power Sources 307:426–434
74. Lu X, Dou H (2016) Simple and mass-produced mechanochemical preparation of graphene nanosheet/polyaniline composite assisted with bifunctional ionic liquid. Funct Mater Lett 9 (3):1650041
75. Feng X, Xing W, Song L, Hu Y, Liew K (2015) TiO_2 loaded on graphene nanosheet as reinforcer and its effect on the thermal behaviors of poly (vinyl chloride) composites. Chem Eng J 260:524–531
76. Qiu B, Zhou Y, Ma Y, Yang X, Sheng W, Xing M (2015) Facile synthesis of the Ti^{3+} self-doped TiO_2-graphene nanosheet composites with enhanced photocatalysis. Sci Rep 5:8591
77. Fu S, Li N, Wang K, Zhang Q, Fu Q (2015) Reduction of graphene oxide with the presence of polypropylene micro-latex for facile preparation of polypropylene/graphene nanosheet composites. Colloid Polym Sci 293:1495–1503
78. Haul R (1982) S. J. Gregg, K. S. W. Sing: Adsorption, surface area and porosity. 2. Auflage, Academic Press, London 1982. 303 Seiten, Preis: $ 49.50. Ber Bunsen Phys Chem 86 (10):957–957
79. Webb PA, Orr C, Micromeritics Instrument Corporation (1997) Analytical methods in fine particle technology. Micromeritics Instrument Corp, Norcross, GA
80. Terock M, Konrad CH, Popp R, Völkl R, Yang F, McComb DW, Mills MJ, Glatzel U (2016) Tailored platinum-nickel nanostructures on zirconia developed by metal casting, internal oxidation and dealloying. Corros Sci 112:246–254

81. Seraji MM, Ghafoorian NS, Bahramian AR (2016) Investigation of microstructure and mechanical properties of novolac/silica and C/SiO_2/SiC aerogels using mercury porosimetry method. J Non Cryst Solids 435:1–7
82. Goldstein J (2003) Scanning electron microscopy and X-ray microanalysis. Kluwer Academic/Plenum Publishers, New York
83. Lifshin E, Wiley InterScience (Online service) (1999) X-ray characterization of materials. Wiley-VCH, New York
84. Khan MA, Member S, Zheng R (2016) Nanostructural analysis of CMOS-MEMS-based digital microphone for performance optimization. IEEE Trans Nanotechnol 15(6):849–855
85. Dastkhoon M, Ghaedi M, Asfaram A, Goudarzi A, Mohammadi SM, Wang S (2017) Improved adsorption performance of nanostructured composite by ultrasonic wave: optimization through response surface methodology, isotherm and kinetic studies. Ultrason Sonochem 37:94–105
86. Balow R, Tomlinson E, Abu-Omar M (2016) Solution-based synthesis and characterization of earth abundant Cu 3 (As, Sb) Se 4 nanocrystal alloys: towards scalable room-temperature thermoelectric devices. J Mater Chem A 4(6):2198–2204
87. Di Girolamo G, Brentari A, Serra E (2016) Some recent findings on the use of SEM-EDS in microstructural characterisation of as-sprayed and thermally aged porous coatings: a short review. AIMS Mater Sci 3(2):404–424
88. Edalati K, Emami H, Ikeda Y, Iwaoka H, Tanaka I (2016) New nanostructured phases with reversible hydrogen storage capability in immiscible magnesium–zirconium system produced by high-pressure torsion. Acta Mater 108:293–303
89. Dong A, Ye X, Li H, Zhang Y, Wang G (2016) Micro/nanostructured hydroxyapatite structurally enhances the immobilization for Cu and Cd in contaminated soil. J Soil Sediment 16(8):2030–2040
90. Liu Y, Zhu G, Gao J, Hojamberdiev M, Zhu R (2017) Enhanced photocatalytic activity of Bi 4 Ti 3 O 12 nanosheets by Fe 3+-doping and the addition of Au nanoparticles: Photodegradation of Phenol and bisphenol A. Appl Catal B 200:72–82
91. Fan X, Cui Y, Liu P, Gou L, Xu L, Li D (2016) Electrochemical construction of three-dimensional porous Mn 3 O 4 nanosheet arrays as an anode for the lithium ion battery. Phys Chem Chem 18(32):22224–22234
92. Sasaki K, Matsubara K, Kawamura S, Saito K (2016) Synthesis of copper nanoparticles within the interlayer space of titania nanosheet transparent films. J Mater Chem C 4 (7):1476–1481
93. Kim S, Yook S, Kannan A, Kim S, Park C (2016) Enhancement of the electrochemical performance of silicon anodes through alloying with inert metals and encapsulation by graphene nanosheets. Electrochimica 209:278–284
94. Mehraj O, Pirzada B, Mir N, Khan M, Sabir S (2016) A highly efficient visible-light-driven novel pn junction Fe_2O_3/BiOI photocatalyst: surface decoration of BiOI nanosheets with Fe_2O_3 nanoparticles. Appl Surf Sci 387:642–651
95. Pardo T, Martínez-Fernández D, de la Fuente C (2016) Maghemite nanoparticles and ferrous sulfate for the stimulation of iron plaque formation and arsenic immobilization in Phragmites australis. Environ Pollut 219:296–304
96. Landers J, Colon-Ortiz J, Zong K (2016) In situ growth and characterization of metal oxide nanoparticles within polyelectrolyte membranes. Angew Chem Int Ed 55(38):11522–11527
97. Souza V, Scholten J, Weibel D (2016) Hybrid tantalum oxide nanoparticles from the hydrolysis of imidazolium tantalate ionic liquids: efficient catalysts for hydrogen generation from ethanol/water solutions. J Mater Chem A 4(19):7469–7475
98. Li X, Niu Z, Jiang J, Ai L (2016) Cobalt nanoparticles embedded in porous N-rich carbon as an efficient bifunctional electrocatalyst for water splitting. J Mater Chem A 4(9):3204–3209
99. Matthew J (2004) Surface analysis by Auger and x-ray photoelectron spectroscopy. D. Briggs and J. T. Grant (eds). IMPublications, Chichester, UK and Surface Spectra, Manchester, UK, 2003. 900 pp., ISBN 1-901019-04-7, 900 pp. Surf Interface Anal 36(13):1647–1647

100. Gao X-L, Pan J-S, Hsu C-Y (2006) Laser-fluoride effect on root demineralization. J Dent Res 85(10):919–923
101. Balter V, Reynard B (2008) Secondary ionization mass spectrometry imaging of dilute stable strontium labeling in dentin and enamel. Bone 42(1):229–234
102. Qian W, Murakami M, Ichikawa Y, Che Y (2011) Highly efficient and controllable PEGylation of gold nanoparticles prepared by femtosecond laser ablation in water. J Phys Chem C 115(47):23293–23298
103. Watts JF, Wolstenholme J (2003) An introduction to surface analysis by XPS and AES. J. Wiley, New York
104. Lee PL, Chen BC, Gollavelli G, Shen SY, Yin YS, Lei SL, Jhang CL, Lee WR, Ling YC (2014) Development and validation of TOF-SIMS and CLSM imaging method for cytotoxicity study of ZnO nanoparticles in HaCaT cells. J Hazard Mater 277:3–12
105. Rades S, Wirth T, Unger W (2014) Investigation of silica nanoparticles by Auger electron spectroscopy (AES). Surf Interface Anal 46(10–11):952–956
106. Sharma H, Bhardwaj M, Kour M, Paul S (2017) Highly efficient magnetic Pd (0) nanoparticles stabilized by amine functionalized starch for organic transformations under mild conditions. Mol Catal 435:58–68

Chapter 5
TiO_2-Graphene-Based Composites: Synthesis, Characterization, and Application in Photocatalysis of Organic Pollutants

N.R. Khalid, M. Bilal Tahir, A. Majid, E. Ahmed, M. Ahmad, Sadia Khalid, and W. Ahmed

5.1 Introduction

Semiconductor photocatalysis is an emerging field in materials science due to its applications in solar energy conversion and environment remediation. Currently, most efficiently and conventionally studied semiconductor materials for photocatalysis are TiO_2, ZnO, ZnS, CdS, WO_3, Fe_2O_3, and Bi_2WO_4 [1, 2]. Among all these, titanium dioxide (TiO_2) is the most widely used photocatalyst due to its excellent properties, such as high stability in the aqueous media, low cost, relatively low toxicity, and excellent photocatalytic performance for the degradation of organic pollutants. In photocatalysis process, when a semiconductor is irradiated with photons of energy ($h\nu$) that is equal to or higher than the semiconductor band gap energy ($h\nu \geq E_g$), these photons are absorbed by the semiconductor and create high energy electron–hole pairs. The photogenerated electrons and holes that migrate to the surface of the semiconductor without recombination can reduce and oxidize the reactants adsorbed on the semiconductor surface, respectively [3]. Therefore, suppressing the recombination of photogenerated electron–hole pairs and the efficient utilization of visible light are some of the main challenges before making these processes economically feasible [4, 5]. In order to overcome these drawbacks, previously, a lot of approaches have been explored to improve the photocatalytic performance of TiO_2 under visible

N.R. Khalid (✉) • M. Bilal Tahir • A. Majid
Department of Physics, University of Gujrat, Gujrat 50700, Pakistan
e-mail: Khalid.nadeem@uog.edu.pk

E. Ahmed • M. Ahmad •
S. Khalid
Department of Physics, Bahauddin Zakariya University, Multan 60800, Pakistan

W. Ahmed
School of Mathematics and Physics, University of Lincoln, Lincon, UK

M.J. Jackson, W. Ahmed (eds.), *Micro and Nanomanufacturing Volume II*,
DOI 10.1007/978-3-319-67132-1_5

light irradiation. These approaches include doping with metal and nonmetal ions, dye sensitizing, compositing of TiO_2 with narrow band gap semiconductor, etc. [6–17].

These modification strategies have enhanced the photocatalytic activity of TiO_2 by increasing its optical absorption and reducing the recombination of charge carriers. However, TiO_2 modified with these techniques have low quantum yield due to decrease of thermal stability of crystals and recombination of photogenerated charge carriers on the catalyst surface or in the bulk of catalysts [18]. Therefore, exploring a feasible approach to synthesize visible light photoactive TiO_2 with stable and highly active performance under solar irradiation is still urgently demanding. A highly attractive approach toward the development of visible light-responsive nanocomposite photocatalysts relies on the combination of TiO_2 with carbonaceous materials, including mesoporous carbon, fullerene, activated carbon, and carbon nanotubes [19–21], and more recently graphene and graphene-based composites [22–32].

Graphene is an atomic sheet of sp^2-bonded carbon atoms in a dense honeycomb crystal structure, which have unique structural and electronic properties. In particular, this material offers excellent mobility of charge carriers (200,000 $cm^2\ V^{-1}\ s^{-1}$), high thermal conductivity (~5000 $Wm^{-1}\ K^{-1}$), large specific surface area (~2630 $m^2\ g^{-1}$), and good mechanical stability [33, 34]. Therefore, due to abovementioned properties, graphene offers an exciting opportunity for synthesizing photocatalytic nanocomposite with desirable performance for applications in organic pollutant remediation. The nanocomposite based on graphene and TiO_2 make the successful connection between nanometer modules with excellent properties, greatly improving the charge carrier's transmission efficiency during photocatalysis. Recently, the design and preparation of a series of new type of efficient TiO_2-graphene-based nanocomposite photocatalysts with an excellent performance under visible light irradiation is a new focus in photocatalysis for the degradation of organic pollutants.

This chapter is focused on recent research progress of TiO_2-graphene-based nanocomposite photocatalysts. Moreover, synthesis methods, characterization, and application of this functional nanocomposite for degradation of organic pollutants are the major focus of the review. In addition, the prospects and further expected developments of graphene-TiO_2-based nanocomposite in this field are reviewed.

5.2 Photocatalysis Mechanism of TiO_2-Graphene Composites

The basic mechanism of photocatalysis in TiO_2-graphene nanocomposite system under light irradiation is shown in Fig. 5.1. Firstly, graphene-TiO_2 photocatalyst absorbs light of appropriate wavelength to generate electron and hole pairs. Then photogenerated electrons will be transferred to graphene, since the potential of

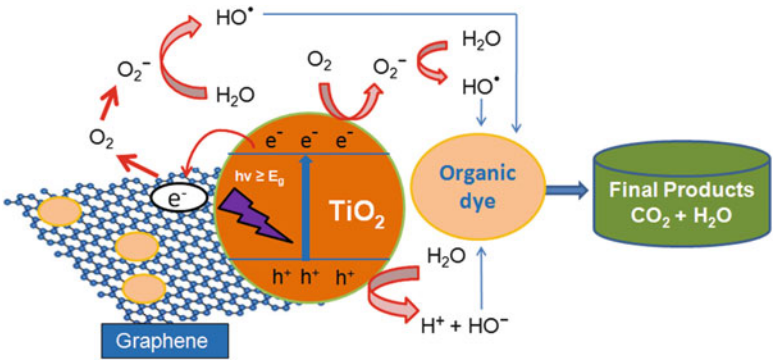

Fig. 5.1 Schematic illustration of photocatalysis mechanism of TiO_2-graphene composite catalyst for organic dye degradation under solar light irradiation

graphene lies below the conduction band of TiO_2. The trapped electrons on graphene surface can react with the dissolved oxygen to form reactive oxygen species (O_2^{-}), which convert water into ($HO^{\bullet}$). In this way, graphene promotes the effective charge separation for photogenerated electrons and holes. The photogenerated electrons on the TiO_2 surface could also be trapped directly by the dissolved oxygen to form reactive oxygen species (O_2^{-}) and finally ($HO^{\bullet}$). On the other hand, holes in the valence band of TiO_2 react with absorbed water or hydroxyl groups to form surface hydroxyl radicals (OH^{-}). These generated free radicals $OH^{\bullet}$ and HO^{-} react with organic pollutant to degrade it into carbon dioxide and H_2O molecules [35]. The stepwise remediation of pollutant is given in Eqs. (5.1), (5.2), (5.3), (5.4), (5.5), (5.6) and (5.7):

$$\text{Graphene} - \text{TiO}_2 + h\nu \rightarrow \text{Graphene} - \text{TiO}\ (\text{e}^- + \text{h}^+) \tag{5.1}$$

$$\text{H}_2\text{O} \rightarrow \text{H}^+ + \text{HO}^- \tag{5.2}$$

$$\text{Graphene}\ (\text{e}^-)/\text{TiO}_2(\text{h}^+) + \text{O}_2 \rightarrow \text{Graphene} - \text{TiO}_2(\text{h}^+) + \text{O}_2^- \tag{5.3}$$

$$\text{Graphene}\ (\text{e}^-) - \text{TiO}_2(\text{h}^+) + \text{HO}^- \rightarrow \text{Graphene}\ (\text{e}^-) - \text{TiO}_2 + \text{HO}^{\bullet} \tag{5.4}$$

$$\begin{aligned}&\text{Graphene}\ (\text{e}^-) - \text{TiO}_2(\text{h}^+) + \text{HO}^- + \text{R}\ (\text{Pollutants})\\ &\rightarrow \text{Graphene}\ (\text{e}^-) - \text{TiO}_2(\text{h}^+) + \text{HO}^- + \text{R}^*(\text{oxidized})\end{aligned} \tag{5.5}$$

$$\begin{aligned}&\text{Graphene}\ (\text{e}^-) - \text{TiO}_2(\text{h}^+) + \text{O}_2^- + \text{R}\ (\text{Pollutants})\\ &\rightarrow \text{Graphene}\ (\text{e}^-) - \text{TiO}_2(\text{h}^+) + \text{O}_2 + \text{R}^{**}(\text{reduced})\end{aligned} \tag{5.6}$$

$$\text{R}^*(\text{oxidized})\ \text{or}\ \text{R}^{**}(\text{reduced}) \rightarrow \text{final products} \rightarrow \text{CO}_2 + \text{H}_2\text{O} \tag{5.7}$$

5.3 Synthesis of TiO_2-Graphene Composites

Chemical technology is an important technique for the preparation of nanostructure TiO_2-graphene composites, which involve some chemical reactions in the process of preparation. According to the literature, TiO_2-graphene composites with varied morphologies could be synthesized by different methods, such as mechanical mixing, sol–gel, hydrothermal, UV light irradiation, microwave assisted, vacuum activation, pyrolysis, CVD, etc. In this section, some of abovementioned methods extensively used for the preparation of TiO_2-graphene composites are reviewed.

5.3.1 Mechanical Mixing Method

Among all synthesis methods, mechanical mixing is the simplest method which involves two steps including mixing and sonication steps, owing to that GO would be exfoliated when added to an aqueous or organic solution. Although the mixing method is very simple, but in most cases the interaction between the two phases is very weak, since chemical bonding is not expected [22]. Zhang et al. [36] prepared P25/GO/Pt hybrid photocatalysts by using mechanical mixing method in different steps. They utilized P25 (Degussa TiO_2), GO, and chloroplatinic acid as precursors during synthesis process. The results of prepared ternary hybrid photocatalyst showed an enhanced performance during photocatalysis for the production of hydrogen from water splitting even there was weak interaction between the hybrids due to mechanical mixing method. The enhanced photocatalytic activity was attributed to the transfer of electrons from TiO_2 to graphene oxide. In another report, the authors employed the same mechanical mixing method in order to prepare P25-loaded boron-doped graphene nanosheets [37]. In first step, boron-doped graphene nanoribbons were prepared by the vacuum activation method, and then TiO_2 nanoparticles were successfully loaded onto boron-doped graphene nanosheets by mechanical stirring and ultrasonic treatment.

Liu et al. [38] also used a mixing-like method at low temperature to prepare self-assembled GO–TiO_2 nanorod composites. TiO_2 nanorods were stabilized by the oleic acid during hydrolysis at room temperature under the stirring for 24 h to develop coordination between graphene oxide and surface of TiO_2 nanorod. They claimed that two-phase approach to synthesize graphene-TiO_2 nanocomposites was first time utilized by their group. This mechanical mixing method is facile and reproducible, which can be utilized for the preparation of other nonpolar organic soluble nanocrystals on graphene oxide sheets. Kamegawa et al. [39] used a mixing procedure at a high temperature for the crystallization of TiO_2 nanoparticles supported on a mesoporous silica surface (TiO_2/MCM-41) along with graphene coating. The TiO_2/MCM-41 surface was made through the formation of surface complex between 2,3-dihydroxynaphthalene and TiO_2 nanoparticles. Then the complex was carbonized under N_2 flow at a high temperature of 1073 K.

5.3.2 Sol–Gel Method

The sol–gel is an advanced method based on inorganic polymerization reactions. Hydrolysis, polycondensation, drying, and thermal decomposition are main steps in the sol–gel process [40]. The raw materials are mixed together in liquid phase and then through hydrolysis and condensation reactions, a stable system of transparent sol is formed. The colloidal particles in the sol aggregate and form three-dimensional network structure of the gel after aging for some hours. Finally the nanomaterials will be prepared after drying and sintering the gel. By controlling solution composition, pH, and temperature, the size of particles can be tuned in this method [41].

GO–TiO_2 composites were prepared by using $TiCl_3$ and GO as reactants through the sol–gel method by Chen et al. [42]. In their study, they found that the graphene oxide ratio in starting solution played an important role in enhancing photocatalytic activity of the composites. Wang et al. [28] used sol–gel method for the synthesis of in situ grown nanocrystalline TiO_2 on the graphene. Firstly, the sol was obtained by mixing sulfate surfactant (i.e., sodium dodecyl sulfate), graphene sheets, titanium sources, and solvents. Then the nucleation and condensation processes resulted into the in situ crystallization of TiO_2 precursors with desired phase and morphology. In another study, TiO_2–GO composites were prepared via the hydrolysis of TiF_4 at 60 °C for 24 h in the presence of an aqueous dispersion of GO by Lambert et al. [43]. Firstly, the reactions were performed on smaller scale by oven heating the TiF_4-GO solutions in a beaker without stirring and later in standard glassware with stirring to form a sol. During reaction, the initial black/brown sol proceeded to form gray gel/precipitate that was collected after centrifugation and washing with water, ethanol, and drying. Zhang et al. [44] prepared the TiO_2–GO intercalated composite by using graphite oxide and titanium sulfate (Ti $(SO_4)_2$) as the precursor and initial reactants at a low temperature (80 °C). Firstly GO was exfoliated by the NaOH and formed single and multilayered graphite oxide mixture, and then hydrolysis of Ti $(SO_4)_2$ was occurred to form TiO_2–GO composite through the sol–gel process.

5.3.3 Hydrothermal/Solvothermal Method

The hydrothermal/solvothermal method is an attractive technique for the preparation of highly homogeneous nanoparticles and nanohybrid and nanocomposite materials [45]. Hydrothermal/solvothermal process is usually performed in stainless steel autoclave under controlled temperature and pressure condition. In this method, by varying temperature, pressure, experimental duration, pH, and solvent, materials with different morphology and structure can be obtained [46]. Several authors have utilized these methods for the preparation of GO–TiO_2 composites [23, 32, 47–52]. They observed partial reduction of GO to RGO/GR or in some cases graphene sheets during the hydrothermal process.

A simple one-step hydrothermal method was used to prepare P25/graphene composites with excellent visible light activity by Zhang et al. [32]. During one-step hydrothermal process, loading of TiO_2 nanoparticles on the surface of graphene as well as reduction of graphene oxide was achieved at the same time. Liang et al. [47] prepared TiO_2–GO hybrid composite using GO as the substrate for the TiO_2 nanoparticle growth by hydrothermal process. In hydrothermal reaction, the functional groups of hydroxyl and carboxyl attached with GO provided reactive and anchoring sites for nucleation and growth of TiO_2 nanoparticles. The authors described the reaction process as two steps. Firstly, the amorphous TiO_2 nanoparticles were coated onto GO sheet surface by hydrolysis of titanium butoxide with sulfuric acid in ethanol and water mixed solvent at 80 °C. This reaction leads to selective growth of TiO_2 on GO surface in order to eliminate free growth of TiO_2 nanoparticles in the solution. It was observed that in the absence of sulfuric acid when only water was used as solvent, a rapid hydrolysis occurred in which most of the TiO_2 particles were grown in the solution rather than associated with GO. In the second step, when hydrothermal treatment of the amorphous TiO_2–GO at 200 °C in a mixture of DMF/water solvent was performed, this process induced anatase crystallization of TiO_2 nanoparticles on GO surface. Fan et al. [48] synthesized TiO_2-graphene composites by different techniques such as UV-assisted photocatalytic reduction, hydrazine reduction, and hydrothermal process. They found that the preparation method has particular influence on incorporation of RGO into P25, which significantly increased the photocatalytic activity of P25-RGO composite. They observed that the composite synthesized by hydrothermal process exhibited the excellent photocatalytic performance.

Lee et al. [49] prepared nanocrystalline graphene-wrapped anatase TiO_2 composite from GO-wrapped amorphous TiO_2 nanoparticles via one-step hydrothermal process. Moreover, the authors also prepared the graphene-TiO_2 nanoparticles by two-step hydrothermal method. In typical process, firstly, GO nanosheets were wrapped on crystallized anatase TiO_2 (not amorphous), and then in the next step, reduction of GO was made applying the same hydrothermal process and calcination. Several researchers have paid attention on the synthesis of graphene-TiO_2 single crystal exposed with high energy facets. Designed and morphological controlled crystal facets of anatase TiO_2 are considered as an effective technique to optimize its photocatalytic activity. Wang et al. [50] used one-pot hydrothermal method for the synthesis of graphene-TiO_2 nanocomposites with controlled crystal facets. They found that by controlling concentration of $(NH_4)_2$ TiF_6 in the precursor solutions and the reaction times, controlled crystal facets can easily be obtained. Long et al. [51] synthesized reduced graphene oxide-TiO_2 (G-TiO_2) composites by hydrothermal process. The results described a strong chemical interaction at the interface of underdeveloped loosely packed polymeric Ti–O–Ti skeletons and GO sheets due to hydrothermal process. Furthermore, it also facilitated to retain more alkoxyl groups, induce crystal disorders, and create oxygen vacancies.

Jiang et al. [52] prepared TiO_2-graphene composites using ethanol-assisted solvothermal process in his report. Typically, in the synthesis process of

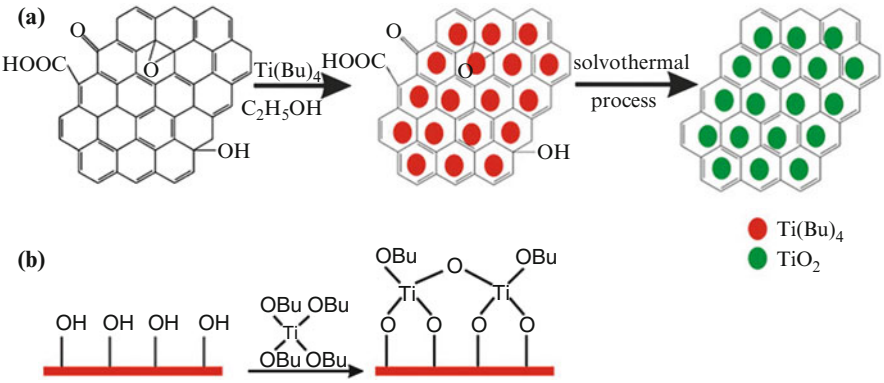

Fig. 5.2 Growth mechanism of TiO_2 nanocrystals on graphene nanosheets by solvothermal process. Reprinted with permission from Ref. [53]. Copyright (2013) Springer

composites, a vacuum-assisted technique combined with the use of a surfactant (cetyltrimethylammonium bromide) was used. Firstly, the vacuum environment played a key role for full infusion of the initial solution of Ti $(OBu)_4$ and the surfactant into the interlayers of expanded graphene. Then, numerous TiO_2 nanoparticles were grown uniformly on the whole exfoliated graphene sheets under solvothermal conditions in ethanol to form TiO_2-graphene composites. In another report, a one-step solvothermal reaction of titanium (IV) butoxide and graphene oxide in an ethanol solvent was used to prepare TiO_2-graphene composites by Zhou et al. [53]. In the reaction process, reduction of graphene oxide and deposition of TiO_2 nanoparticles were achieved at the same time, and synthesis process is schematically shown in Fig. 5.2.

5.3.4 UV Light Irradiation

The reduction of graphene oxide is very important process for the preparation of TiO_2-graphene composites. It determines the properties of graphene such as conductivity of graphene and electron transfer efficiency of photogenerated electrons between graphene and TiO_2. Several authors have used hydrothermal method for the reduction of graphene oxide at a high temperature in the absence of air or in inert gas atmosphere. Compared with hydrothermal method, the UV light irradiation method used for the reduction of graphene oxide is much more attractive owing to its manageable property and low energy consumption. Kim et al. [54] used a two-step oxidation process for the synthesis of size-controlled nanographene oxides (NGOs) having size less than 50 nm. Then prepared NGOs were self-assembled with TiO_2 nanoparticles to form the core-shell-like structures. In the preparation process, required amount of P25 was added in the NGO solution, and then the

mixture was aged under the stirring for overnight. The further reduction of NGOs was made by irradiation with light for 30 min using 200 W mercury lamp.

Mohamed et al. [55] synthesized TiO_2-RGO composite by UV-assisted photocatalytic reduction of graphene oxide mixed with TiO_2 nanoparticles in the ethanol solvent. The mix solution was irradiated with 250 W high-pressure Hg lamp for 24 h under ambient conditions and magnetic stirring. After this process of UV irradiation, it was seen that the color of solution changed into grayish black, which was the clear indication of reduction of graphene oxide into graphene sheets. Akhavan et al. [56] prepared single-layer graphene oxide-TiO_2 composites by a UV light-assisted photoreduction process. The UV-assisted reduction of the graphene oxides along with TiO_2 nanoparticles was nearly completed after 2 h UV illumination. However, it was observed that the longer-time UV light irradiation would decrease the carbon content of reduced graphene and the increased carbon defects on the graphene surface. It showed that reduced graphene sheets were degraded by TiO_2 nanoparticles in the UV-driven photocatalytic process. Therefore, a proper time management of UV light irradiation and conditions are required for high-performance photocatalysts.

5.3.5 Microwave-Assisted Method

Microwave-assisted method is a very simple and suitable approach applied in organic synthesis of materials. It speeds up the reaction up to thousands of time faster than other conventional methods. Difficult complexes can also be synthesized by this technique which is not easily possible with regular preparation methods. The microwave-assisted method is very useful in the synthesis of nanomaterials, pharmaceutical products, and other research-based materials. Liu et al. [57] synthesized RGO-TiO_2 composites via microwave-assisted reduction of graphite oxide in a TiO_2 suspension. Pu et al. [58] prepared the GO–TiO_2 hybrid composites by microwave-assisted combustion process. In the process, gel-like precursor was obtained after heating the solution at 100 °C on a hot plate. Then gel-like precursor was put into a domestic microwave oven (700 W), and combustion was taken place after irradiating the precursor for different time duration to obtain foam-like GO–TiO_2 hybrids.

Some authors introduced modifications to the microwave-assisted method such as use of impurities or semiconductors with the aim to enhance the transfer efficiency of the photogenerated carriers during photocatalysis. Wang et al. [59] prepared graphene-based Au-TiO_2 composites by a facile one-step microwave-assisted hydrothermal process. They have used graphene oxide, P25 (Degussa), and $HAuCl_4$ aqueous solution as raw materials for the preparation of graphene-based Au-TiO_2 composite photocatalysts. Chemically reduced graphene oxide-CdS-TiO_2 composites were prepared using a microwave-assisted method by Lv et al. [60]. The positively charged Cd^{2+} ions form complexes with TiO_2 nanoparticles, and Na_2S provided S^{2-} which moved quickly to react with Cd^{2+}

producing uniform CdS nanoparticles compounded with TiO_2 during the microwave reaction process. Microwave-assisted method was a simple and facile process for the synthesis of CdS-TiO_2-RGO composite photocatalysts.

5.3.6 *Vacuum Activation Method*

Vacuum activation method is simple, low-cost, and low-temperature method to produce oxygen vacancies in TiO_2 lattice and reduction of TiO_2 itself according to some research reports [61–64]. Recently, Xing et al. [63] successfully prepared boron-doped graphene nanoribbons via vacuum activation method in their study. Initially, graphene oxide and H_3BO_3 were mixed and the resulting mixture was dried at low temperature. Then obtained powders were heated at 300 °C for 3 h in vacuum tube furnace. In contrast to other methods, vacuum activation method could provide an anoxic environment, which is useful for the departing of oxygen atoms and creation of lattice defects in graphene. These lattice defects in the graphene sheets readily captured boron atoms. Although authors just assumed the formation mechanism of the nanoribbons because actual mechanism of formation of nanoribbons was unclear according to their report. By employing the same one-step vacuum activation method, Qiu et al. [65] successfully prepared Ti^{3+} self-doped TiO_2-graphene composite photocatalysts. In this study, vacuum activation method has given reduction of GO, self-doping of Ti^{3+} in TiO_2, and the loading of TiO_2 nanoparticles on graphene surface at the same time. In conclusion, authors suggested that simple vacuum activation method will be a useful approach in the future for the synthesis of new nanocomposite photocatalysts with high photocatalytic performance.

5.4 Characterization of TiO_2-Graphene Composites

5.4.1 *X-Ray Diffraction*

Graphene has good conducting properties, which determine the transport of photogenerated electrons from TiO_2 to the graphene surface. However, the graphene oxide obtained from chemical reduction process is very difficult to completely reduce into a single layer of graphene. Even then, the chemical reduction method is still a popular technology in the large-scaled production of graphene due to its low cost and easy operation. Moreover, the reduction of graphene oxide is an important factor for the photocatalytic activity of TiO_2-graphene composites. Therefore, X-ray diffraction is a useful technique to characterize the reduction of graphene oxide in the composite of TiO_2-graphene. In Fig. 5.3a, the graphene oxide has a characteristic peak at 9.7° which is assigned to the (001) interlayer spacing of

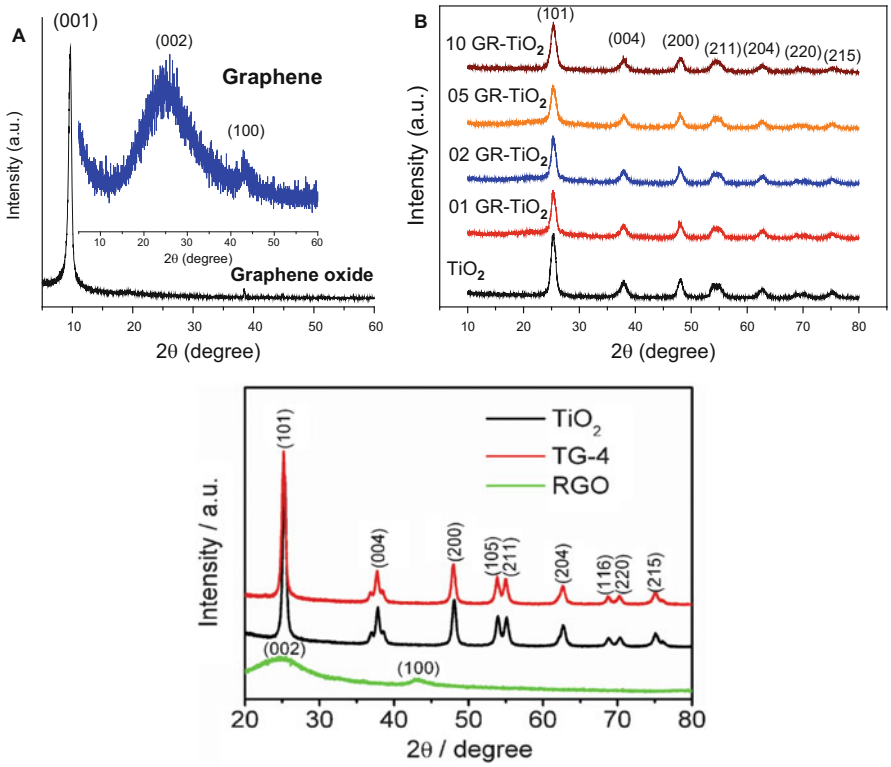

Fig. 5.3 XRD patterns of (**a**) graphene oxide and graphene (Reprinted with permission from Ref. [66]. Copyright (2012) Elsevier), (**b**) Graphene-TiO_2 composite (Reprinted with permission from Ref. [67]. Copyright (2013) Elsevier), and (**c**) TiO_2, RGO, and TG-4 composite (Reprinted with permission from Ref. [57]. Copyright (2011) Royal Society of Chemistry)

0.90 nm [66]. It can be seen that the diffraction peak at 9.7° disappeared and two broad bands at 25.9° and 42.9° were observed, which could be assigned to graphene (002) and (100) planes. In another study, Fan et al. [48] observed the peak for graphene at 2θ of ~25° (corresponding to a d-spacing of 3.6 Å) after hydrothermal process, which was initially at 2θ of ~10.6° for graphene oxide sample. Therefore, the results demonstrate the successful reduction of graphene oxide into graphene by the hydrothermal process. Moreover, in XRD patterns of TiO_2-graphene composites (Fig. 5.3b), graphene peaks were not seen; only slight change in FWHM of (101) peak of TiO_2 was observed. It was attributed to the fact that the characteristic peak (002) at 25.9° of graphene is weak and overlaps with the (101) peak of anatase TiO_2 (25.4°) [67].

XRD patterns of TiO_2-RGO composites synthesized by microwave-assisted method by Liu et al. [57] are shown in Fig. 5.3c. The results show that the main diffraction peaks of pure TiO_2 and TiO_2-RGO composites are similar, which shows that the incorporation of reduced graphene oxide does not result in the growth of

new crystal orientations or changes in preferential orientations of TiO_2. Moreover, no typical diffraction peaks of reduced graphene oxide were observed in the composite photocatalyst, which may be due to the low amount and relatively low diffraction intensity of RGO. Several other researchers found the similar results of XRD for their prepared TiO_2-graphene composites, where graphene peaks were not present in TiO_2-graphene composites [38, 48, 49].

5.4.2 *Transmission Electron Microscopy*

The TEM are high-resolution imaging techniques to characterize the atomic feature of graphene and reduced graphene oxide. It is also considered as the most intuitive characterizations for the surface morphology of TiO_2-graphene composites. In most of reports on TiO_2-graphene composites, the graphene displayed a large-scale layer structure and considered as a support material for successful deposition of TiO_2 nanoparticles. It was also found that the photocatalytic activity of composite photocatalyst depends on the degree of dispersion of TiO_2 nanoparticles on the graphene sheets. Figure 5.4a clearly demonstrates that Au nanoparticles with size of 12–15 nm are homogeneously dispersed on the surface of TiO_2 nanoparticles, in which two-dimensional graphene sheet served as a thin support [59]. The HRTEM image in Fig. 5.4b also confirms the deposition of Au nanoparticles on TiO_2 surface. The results obviously show a good connection among the Au, TiO_2, and graphene components, achieved by the microwave-assisted hydrothermal method. Moreover, such a nanocomposite will be beneficial for the suppression of charge carrier recombination to enhance photocatalytic performance due to excellent surface morphology.

In TEM image of RGO-Ag/TiO_2 synthesized by Leong et al. [68], it was noted that Ag wrapped TiO_2 nanoparticles were successfully deposited on the graphene sheets by hydrothermal process as shown in Fig. 5.4c. The hydrothermal process was found useful for the strong interaction between Ag/TiO_2 nanoparticles and graphene sheets. In our previous work, we also synthesized La-doped TiO_2 nanoparticles decorated on graphene sheets, and TEM image of composite is shown in Fig. 5.4d [24]. The results show that TiO_2 nanoparticles are well separated and have size in the range of 8–12 nm. Furthermore, the obtained composite retained the two-dimensional sheet structure after the hydrothermal process. Because of the distribution of functional groups of graphene oxide, the TiO_2 nanoparticles were dispersed on the whole graphene sheet and eager to accumulate along the wrinkles and edges.

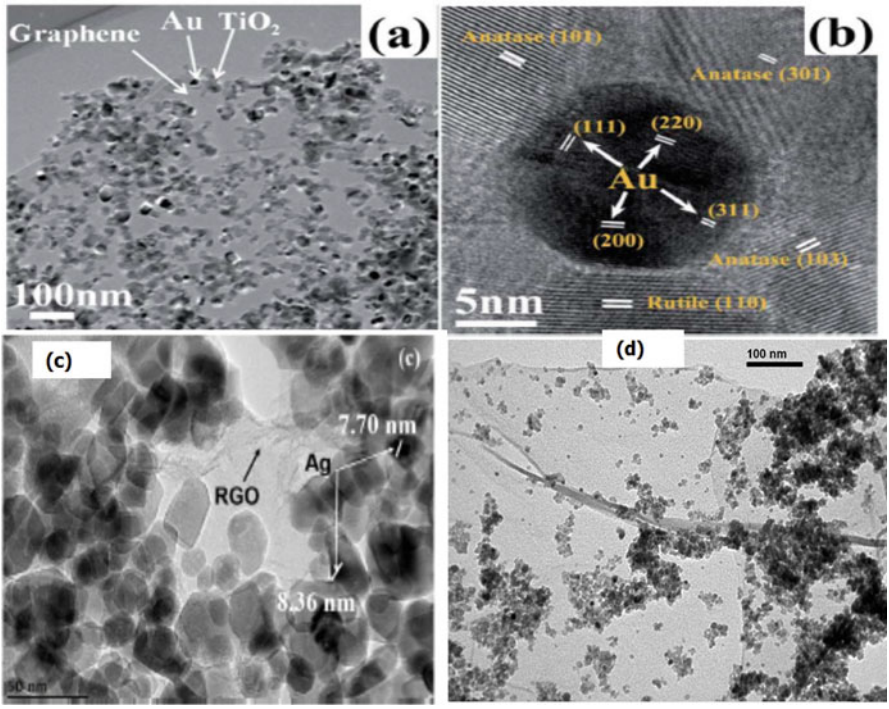

Fig. 5.4 (**a** and **b**) TEM and HRTEM image of Au-TiO_2-graphene composite (Reprinted with permission from Ref. [59]. Copyright (2014) Royal Society of Chemistry); (**c**) TEM image of RGO-Ag/TiO_2 composite (Reprinted with permission from Ref. [68]. Copyright (2015) AIP Publishing LLC); (**d**) TEM image of La/TiO_2-graphene composite (Reprinted with permission from Ref. [24]. Copyright (2013) Elsevier)

5.4.3 Atomic Force Microscopy

AFM is a measurement method of imaging which can effectively represent the surface profile at the nanometer scale. It is a high-resolution scanning probe microscopy and is very useful to probe the thickness of graphene sheets in TiO_2-graphene composites. Kim et al. [54] synthesized size-controlled nanographene oxides (NGOs, < 50 nm) by a two-step oxidation process, where NGOs were successfully coated on TiO_2 nanoparticles to form the core-shell structure of composite. The results of AFM images and analysis showed that the thickness of NGOs were in the range of 0.8–2.0 nm (Fig. 5.5), which means that some of the NGO sheets are stacked as double layers. Figure 5.5 (*bottom* part) corresponds to the size distribution histograms of LGO and NGOs obtained from the AFM images, which have size distribution in the range of 480–520 nm. It can be seen from the results that the average sizes of NGO-100, NGO-200, and NGO-300 were

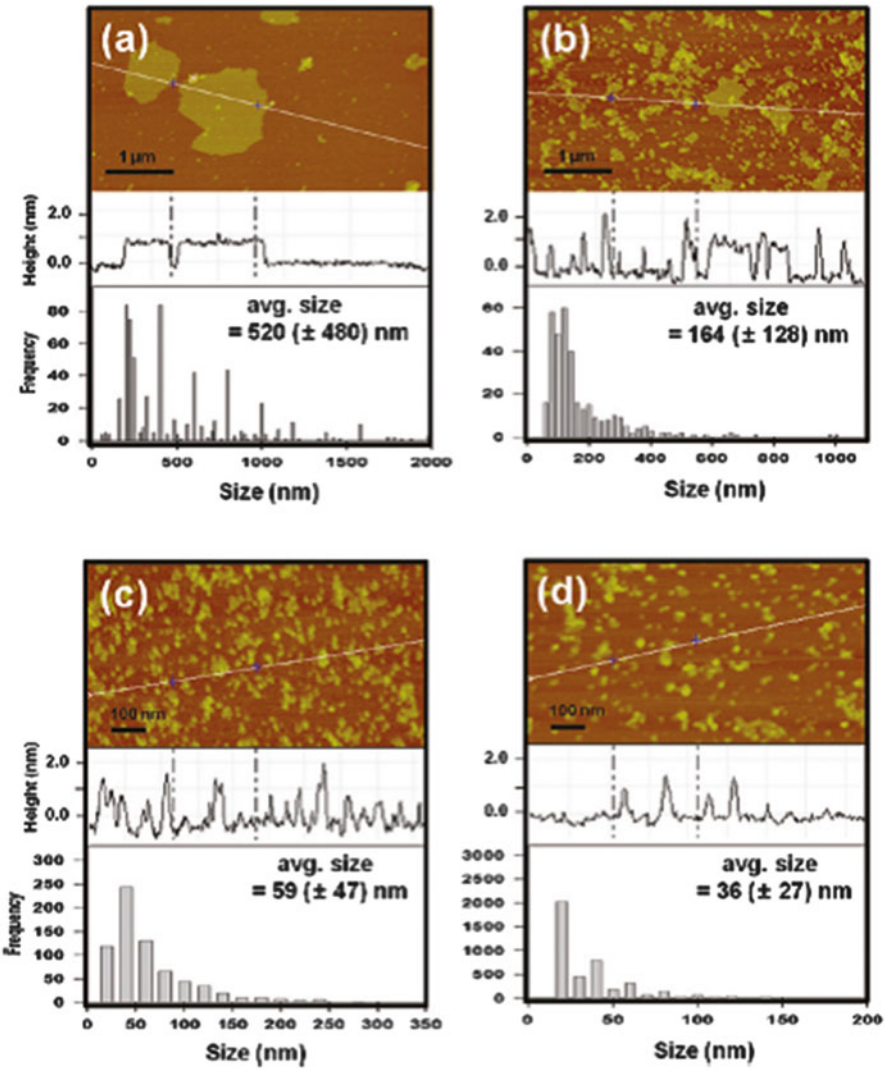

Fig. 5.5 As synthesized LGO and NGOs. Tapping-mode AFM images (*top*) and the height cross-sectional profiles (*middle*) of (**a**) LGO, (**b**) NGO-100, (**c**) NGO-200, and (**d**) NGO-300. The size distribution histograms (*bottom*) were obtained by counting (frequency) from the AFM images. The average sizes of LGO, NGO-100, NGO-200, and NGO-300 are 520 (480) nm, 164 (128) nm, 59 (47) nm, and 36 (27) nm, respectively. Reprinted with permission from Ref. [54]. Copyright (2012) American Chemical Society

successively reduced to 164 nm, 59 nm, and 36 nm, respectively. All prepared NGOs showed narrower size distributions and smaller average sizes as compared to those for parent GO (LGO).

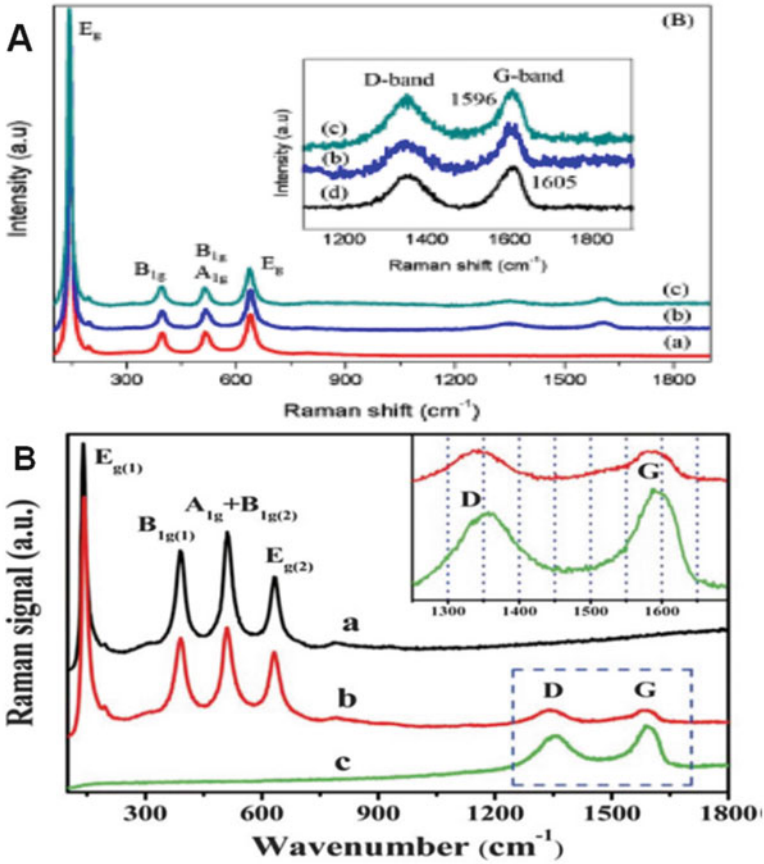

Fig. 5.6 (**A**) Raman spectra of (a) TiO_2, (b) RGO-TiO_2, (c) RGO-Ag/TiO_2, and inset is the (d) GO. (Reprinted with permission from Ref. [68]. Copyright (2015) AIP Publishing LLC) **(B)** Raman spectra of the G0 (a), G1.0 (b), and GO (c) samples. Reproduced from Ref. [69] with permission of Royal Society of Chemistry Copyright (2011)

5.4.4 Raman Spectroscopy

Raman spectroscopy is a powerful and nondestructive tool to characterize the crystalline quality and reduction of graphene oxide in TiO_2-graphene composites. Figure 5.6A shows the Raman spectra of TiO_2, RGO-TiO_2, RGO-Ag/TiO_2, and GO sample synthesized by Leong et al. [68]. The portrait distinct peaks, namely, Eg, B_{1g}, and A_{1g}, were ascribed to anatase phase structure of TiO_2. The Raman spectrum of GO (d inset of Fig. 5.6A) has two intense peaks at 1351 cm^{-1} (D-band) and 1605 cm^{-1} (G-band), where D-band corresponds to the disorder with structural disorders created due to the reduction of GO. Secondly, the G-band can be attributed to the first-order scattering of E_{2g} photon of SP^2 carbon

atoms of graphene. The intensity ratio ID/IG of RGO-TiO_2 (0.95) and RGO-Ag/TiO_2 (0.97) increased from 0.78 for GO; however, the position of D- and G-band is the same for all samples. This increment was due to the removal of oxygenated groups leading to reestablishment of conjugated graphene network after hydrothermal process. The further analysis shows a marginal G-band shift (~9 cm^{-1}) to a lower frequency at 1596 cm^{-1} (RGO-Ag/TiO_2) from 1605 cm^{-1}, which confirms the charge transfer between TiO_2 and graphene.

Xiang et al. [69] synthesized graphene-TiO_2 composites and employed the Raman to investigate the properties of composite after incorporation of graphene. The characteristic peaks observed at 146, 397, 516, and 637 cm^{-1} (Fig. 5.6B) could be attributed to the $E_{g(1)}$, $B_{1g(1)}$, $A_{1g} + B_{1g(2)}$, and $E_{g(2)}$ modes of anatase, respectively, and the peaks at 1354 and 1594 cm^{-1} were due to the D- and G-bonds in graphene oxide, respectively. After the hydrothermal process, the G-bond and D-bond moved to 1342 cm^{-1} and 1585 cm^{-1}, respectively, showing the successful reduction of graphene oxide. Simultaneously, a further observation demonstrating that the graphene-TiO_2 composite showed an increased D/G intensity ratio in comparison to that of pure graphene oxide, which confirms the reduction of graphene oxide.

5.4.5 *Fourier Transform Infrared Spectroscopy*

The interaction between TiO_2 and graphene describes the physical and chemical properties of TiO_2-graphene composite. Figure 5.7a shows FTIR spectra of graphene oxide, P25, and P25/graphene composite synthesized by Zhang et al. [70]. FTIR spectrum of graphene oxide has peaks at 1045 cm^{-1} (C–O), 1045 cm^{-1} (C–O–C), 1250 cm^{-1} (C–OH), 1365 cm^{-1} (C–OH), and 1720 cm^{-1} (C=O) and a broad peak located at the range of 3000–3500 cm^{-1}, which could be attributed to the O-H stretching vibrations of the C–OH groups and water. However, after thermal reaction, all containing functional groups were completely removed as shown in P25/graphene composite sample. The results show the possibility of strong interaction between P25 and graphene. Moreover, for the P25/graphene composite sample, the broad absorption band below 1000 cm^{-1} is due to the vibration of Ti–O–Ti bonds in TiO_2, and the absorption peak around 1600 cm^{-1} is contributed by the skeletal vibration of the graphene sheets.

FTIR spectra of GO, RGO, TiO_2, and TiO_2-RGO composite reported by Liu et al. [57] is shown in Fig. 5.7b. The broad absorption band at 3425 cm^{-1} can be attributed to the hydroxyl groups of absorbed H_2O molecules on TiO_2 surface. The absorption band at 650 cm^{-1} of TiO_2-RGO composite is similar to that of pure TiO_2, which is owing to the stretching modes of Ti-O. Moreover, there is a clear decrease in the intensities of C=O (1627 cm^{-1}), C-OH (1183 cm^{-1}), and C–O (1068 cm^{-1}) stretching vibration peaks in RGO compared to those in GO, which suggests that microwave-assisted reduction is an efficient method to eliminate the oxygen-containing groups of GO.

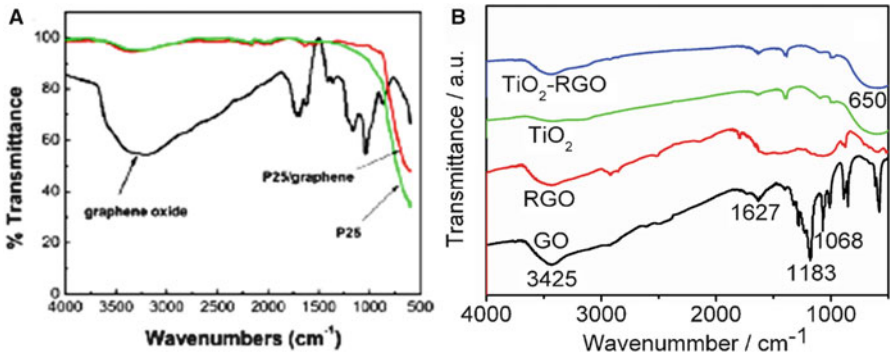

Fig. 5.7 (**a**) FTIR spectra of GO, P25, and P25/graphene composite (Reprinted with permission from Ref. [70]. Copyright (2010) Springer); (**b**) FTIR spectra of GO, RGO, TiO_2, and TG-4. Reprinted with permission from Ref. [57]. Copyright (2011) Royal Society of Chemistry

5.4.6 X-Ray Photoelectron Spectroscopy

XPS characterization is also an important technique to investigate the chemical state and bonding between TiO_2 and graphene in TiO_2-graphene composites. It also describes the reduction of graphene oxide in TiO_2-graphene composites. In Fig. 5.8a, the core-level XPS spectrum of Ti2p reveals two peaks, namely, Ti2p3/2 and Ti2p1/2, located at binding energies of 459.3 eV and 465.1 eV, respectively, which is consistent with the value of Ti^{+4} in the TiO_2 lattice [24]. O1s core-level spectrum (Fig. 5.8b) shows main peak at 530.1 eV due to the metallic oxides Ti–O bond, which is consistent with binding energy of O^{2-} in the TiO_2 lattice, and the peak appearing at 530.9 eV is for oxygen atoms in the surface hydroxyl groups (H–O bonds) and/or in the carboxyl groups (C–O bonds). The third peak appearing at 532.5 eV was attributed to adsorbed OH^- on the surface of TiO_2. In high-resolution XPS spectrum of C1s (Fig. 5.8c), the main peak was observed at 284.6 eV, which corresponds to the adventitious carbon adsorbed on the surface of sample (C–C bond), the second peak at 285.6 is ascribed to elemental carbon (C=C), and the peak at 288.9 eV corresponds to C=O bonds implying coordination bonding between Ti and carboxylic acids on the surface of graphene sheets. The results show clearly the reduction of GO and composite formation at the same time.

XPS spectroscopy was also used by Zhang et al. [70] to study the influence of graphene addition on TiO_2-graphene composite. High-resolution C1s core-level spectrum of TiO_2-graphene (Fig. 5.8d) shows two peaks of carbon bonds, namely, C–C (284.7 eV) and Ti–O–C (288.1 eV). The presence of the Ti–O–C bond verified that the C atoms have substituted some of the Ti atoms in the TiO_2 lattice during the composite formation and there is strong interaction between TiO_2 and graphene.

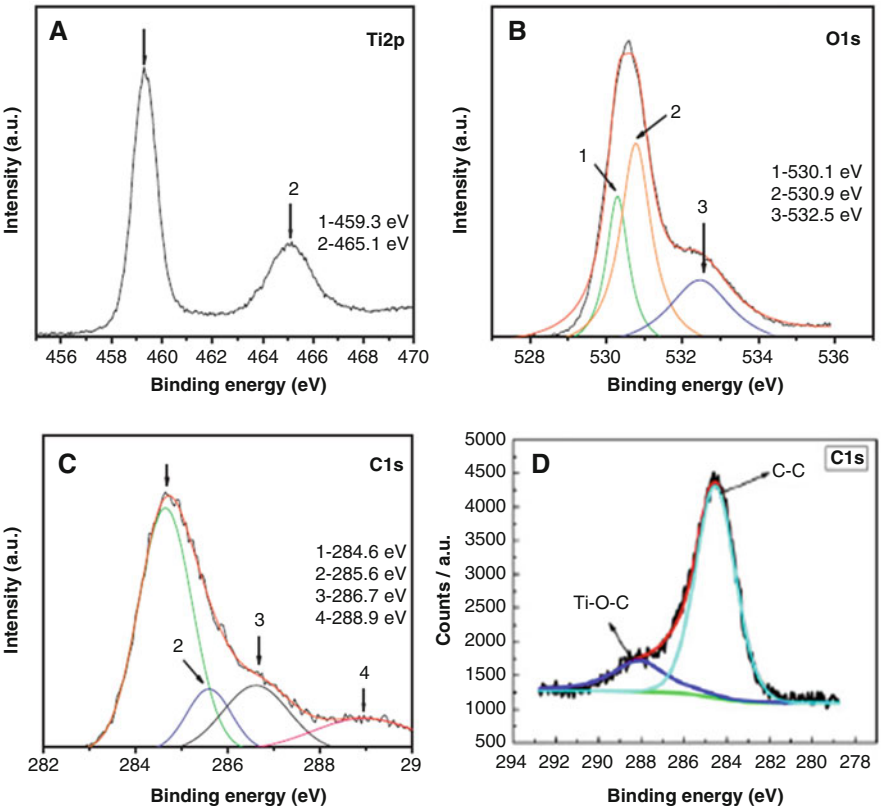

Fig. 5.8 XPS core-level spectra of (**a**) Ti2p, (**b**) O1s, and (**c**) C1s (Reprinted with permission from Ref. [24]. Copyright (2012) Elsevier). (**d**) Core-level spectrum of C1s. Reprinted with permission from Ref. [70]. Copyright (2010) Springer

5.4.7 UV-Visible Absorption Spectroscopy

UV-visible spectroscopy is a technique to study the light absorption properties of TiO_2-graphene composites. Light absorption properties play a vital role in the process of photocatalysis for the degradation of organic compounds. For example, if more light will be absorbed by the photocatalyst, then more charge carriers will be created to participate in the activity of photocatalysis. On the other hand, band gap energy of the material decides the wavelength of absorbing light. For instance, Fig. 5.9A demonstrates the results of UV-visible spectra of graphene-TiO_2 nanoparticles prepared by Lee et al. [49]. As compared to pure TiO_2 nanoparticles, both composite photocatalysts showed a red shift in the absorption edge and a strong absorption in the whole visible light range. From inset of Fig. 5.9A, it can be seen that the band gap of pure anatase TiO_2 nanoparticles is 3.27 eV, while the band gap of graphene-TiO_2 nanoparticles (two-step hydrothermal) was 3.19 eV.

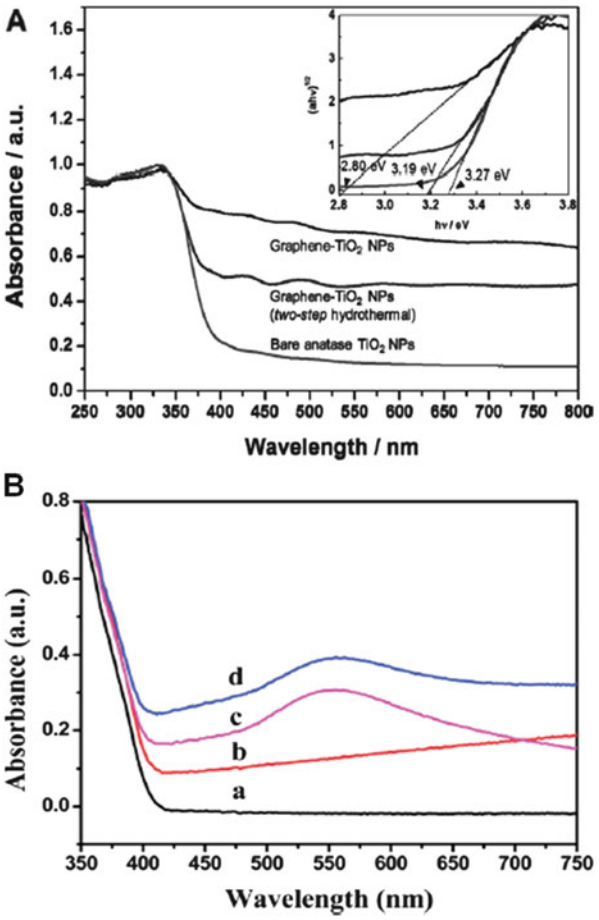

Fig. 5.9 (**A**) UV-visible spectra of bare anatase TiO_2 NPs, graphene-TiO_2 NPs, and graphene-TiO2 NPs (two-step hydrothermal) (Reprinted with permission from Ref. [49]. Copyright (2012) John Wiley and Sons). (**B**) UV-vis diffuse reflectance spectra of the P (a), PG (b), PA25 (c), and PGA25 (d) samples. Reprinted with permission from Ref. [59]. Copyright (2014) Royal Society of Chemistry

Interestingly, the band gap of graphene-TiO_2 nanoparticles was notably reduced to 2.80 eV. Firstly, the authors attributed the decrease in band gap to the phenomenon occurring due to the direct interaction between carbon and Ti atoms on the nanoparticle surface during hydrothermal process. Secondly, during hydrothermal process, Ti atoms in amorphous phase interacted more actively with GO than in crystallized phase. Thirdly, functional groups on the surface of GO (e.g., −OH, −COOH) disappeared during GO reduction into graphene, and the π electrons of C atom cannot bond with others to form a delocalized large π bond. Therefore, the remaining unpaired π electrons should easily bond with more free Ti atoms on the surface of TiO_2 during the phase transformation from the amorphous TiO_2 in the graphene-TiO_2 nanoparticles.

The UV-vis diffuse reflectance spectra of different samples synthesized by Wang et al. [59] are shown in Fig. 5.9B. A typical absorption with an intense transition at ~410 nm was observed in the results of all samples. It showed a band

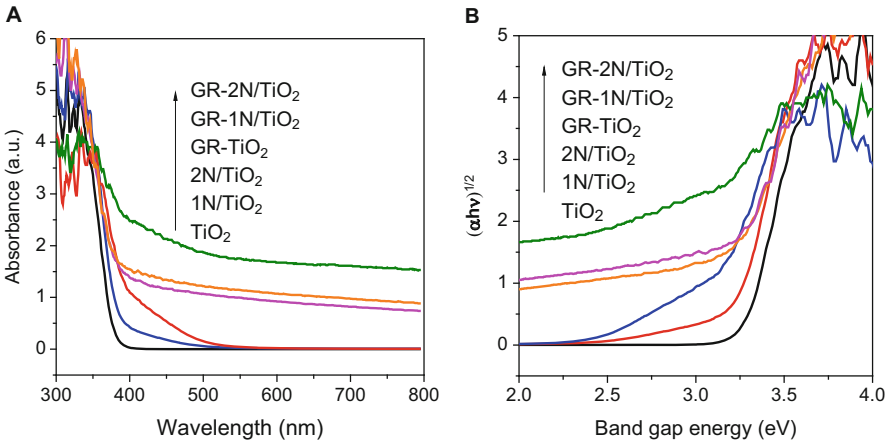

Fig. 5.10 (**a**) UV-visible DRS spectra and (**b**) plots of $(\alpha h\nu)^{1/2}$ versus photon energy ($h\nu$) of N/TiO_2 and GR-N/TiO_2 composite photocatalysts. Reprinted with permission from Ref. [66]. Copyright (2012) Elsevier

gap of 3.0 eV, which corresponds to the intrinsic band gap absorption of rutile TiO_2. Introduction of graphene into graphene-TiO_2 composites (sample PG) exhibits the same absorption edge as pure TiO_2 (sample P), showing that the carbon species were not incorporated into the lattice of TiO_2. However, the graphene-TiO_2 composites extend their broad background absorption into the visible light region, due to the incorporation of graphene into the graphene-TiO_2 composites. Furthermore, synergetic effect of Au nanoparticles and graphene (samples PA25 and PGA25) on TiO_2 nanoparticles has significantly enhanced light absorption in the visible region, with broad band peak located at around 550 nm, which appeared due to SPR effect of gold nanoparticles.

Figure 5.10a presents the results of UV-vis diffuse reflectance spectra of N/TiO_2 and GR-N/TiO_2 composite catalysts prepared by our group [66]. The pure TiO_2 shows absorption edge at about 390 nm, while N doping extended the absorption edge into the visible light region. Further results demonstrate that the absorbance in visible light region increases to higher wavelength with joint effect of nitrogen and graphene. It can be attributed to the fact that inclusion of graphene enhanced the absorption in visible light region due to strong interaction between graphene and TiO_2 nanoparticles after hydrothermal process. Figure 5.10b shows plots of the Kubelka-Munk remission function (i.e., relationship of $[\alpha h\nu]^{1/2}$ versus photon energy) corresponding to each absorption spectrum, which indicates that the band gap energy were 3.18 eV for TiO_2, 3.10 eV for $1N/TiO_2$, 2.90 eV for $2N/TiO_2$, 3.02 eV for GR-TiO_2, 3.0 for GR-$1N/TiO_2$, and 2.64 eV for GR-$2N/TiO_2$ composites, respectively. The origin of this extended visible light absorption may be due to the presence of localized states created near the valence band edge of TiO_2 due to N doping through the mixing of N2p states with O2p states and graphene.

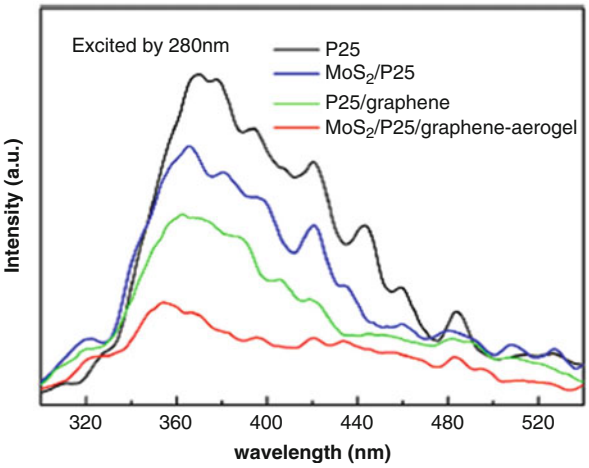

Fig. 5.11 PL spectra of MoS_2/P25/graphene aerogel, P25/graphene, MoS_2/P25, and P25 nanoparticles. Reprinted with permission from Ref. [71]. Copyright (2014) Elsevier

5.4.8 Photoluminescence Spectroscopy

PL emission spectroscopy has been widely used to investigate the efficiency of charge carrier trapping, migration, and transfer and to understand the fate of electron-hole pairs in semiconductor photocatalysis. Moreover, charge carrier recombination is a key factor in photocatalytic activity of composite catalyst. Figure 5.11 displays the PL emission spectra of P25, MoS_2/P25, P25/graphene, and MoS_2/P25/graphene aerogel, respectively, prepared by Han et al. [71]. In pure P25 catalyst, the main peaks at 370 and 379 nm correspond to band gaps of the anatase phase, and the peak appearing at 394 nm is the band gap of rutile phase of TiO_2. The three peaks at 407, 420, and 441 nm can be ascribed to self-trapped excitons localized on TiO_6 octahedral. Moreover, the peaks around 465 nm (459 nm and 483 nm) and around 525 nm can be attributed to the emissions from the charge transfer transition of oxygen vacancy-trapped electrons, respectively. The peaks of the other photocatalysts in the PL emission spectra become feeble as compared to pure P25 sample.

It is well known that PL emission results from the recombination of excited electrons and holes; the lower the PL emission intensity, the lower the recombination rate of the photogenerated charge carriers. It can be seen from the results that the intensity of MoS_2/P25/graphene aerogel is lower than the MoS_2/P25 and P25/graphene samples. The reduction of charge carriers can be ascribed to introduction of MoS_2 nanosheets into composite and the unique 3D graphene-interconnected network structure with porous structure. Therefore, graphene provided maximum accessible sites to enhance the efficient charge separation, prolong the life time of the carriers, and hamper the recombination of photogenerated electron-hole pairs, thereby improving the photocatalytic activity.

5.5 Applications in Photocatalysis of Organic Pollutants

In recent years, many efforts have been utilized for the remediation of environmental pollution, which certainly causes serious harm to the environment and serious threat to the human survival. Moreover, water and air are considered as the most valuable human resources than before and have attracted great deal of attention. The revolution in the industrial process has produced a large amount of wastewater and gas, which directly discharged into rivers and atmosphere. The wastewater coming from different industries contains different types of toxic organic pollutants; some waste compounds are very difficult to degrade by ordinary processing methods. Therefore, the photocatalytic technology has attracted a great interest because of its widespread environmental applications such as air cleanup [72], water disinfection [73], hazardous waste remediation [74], and water purification [75]. The graphene-TiO_2-based composites are extensively applied for the abovementioned environmental applications recently. These composites demonstrated high adsorption capability, enhanced light absorption range, and improved charge separation and transportation properties. In the literature, most of the target pollutants are dyes including methylene blue (MB), methyl orange (MO), acid orange 7, rhodamine B (RB), AO7, etc. [23, 32, 38, 42, 76].

Liu et al. [38] reported GO–TiO_2 nanorod composites with enhanced photocatalytic activity for the degradation of both MB and AO7 under UV light irradiation. The enhanced photocatalytic performance was attributed to effective charge transfer between GO and TiO_2 nanorods and enhanced adsorption of MB on the surface of GO. Moreover, the charge transfer and improved photocatalytic activity by GO–TiO_2 nanorod composite is schematically presented in Fig. 5.12. The transfer of charge through graphene oxide reduced the recombination of electron-hole pairs and increased the photocatalytic performance of TiO_2 nanorods for MB degradation.

The photodegradation of 2,4-D using rGO–TiO_2 thin film photocatalysts was reported by Ng et al. [76]. The results of photocatalytic activity exhibited a fourfold increase in the rate of degradation compared to the pure TiO_2 thin film photocatalyst. The enhancement in photodegradation was ascribed to the presence of graphene in the composite, which could ensure the fast transfer of the carriers and suppress recombination. Moreover, the interaction between graphene and the pollutants also facilitated the organic compound to concentrate near the surface of the catalysts and accelerate the photodegradation process.

Chen et al. [42] also reported the visible light-responsive GO–TiO_2 composite photocatalytic with p/n heterojunction in the degradation of MO. In this study, the p-type semiconductor was formed by GO in the GO–TiO_2 composite; thus, a p/n heterojunction was observed in this composite photocatalyst. During photocatalysis process, the p-type semiconductor was excited by visible light ($\lambda \geq 510$ nm), and it acted as a sensitizer and as an electron transporter in the composite, leading to the visible light-driven photocatalytic performance. Another approach to design visible light-responsive photocatalysts is the attachment of a visible light-reactive species.

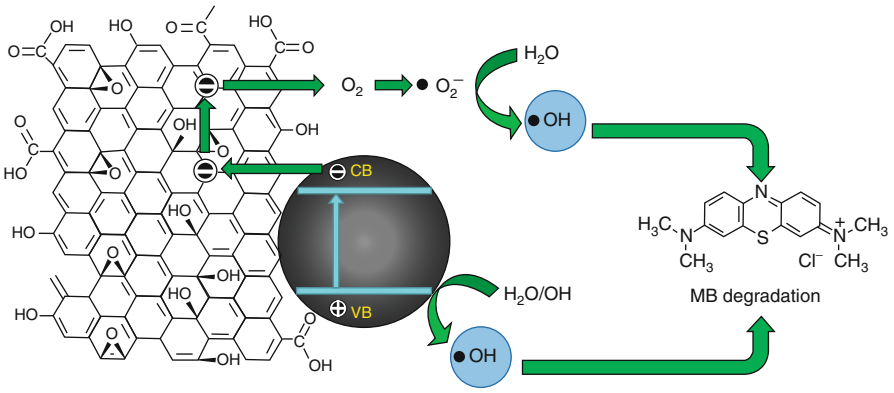

Fig. 5.12 Schematic illustration of high photocatalytic activity for GO–TiO_2 NRCs. Reproduced with permission from Ref. [38]. Copyright (2010) John Wiley and Sons

For instance, Ag-incorporated TiO_2-graphene composite was synthesized by Wen et al. [27]. The enhanced visible light absorption was originated from the strong interaction between graphene and TiO_2 nanoparticles, and it generated surface plasmon effect of silver nanoparticles (Fig. 5.13). Highest photocatalytic performance was due to strong adsorption ability of graphene for dye molecule and suppressed recombination of electron-hole pairs, due to the formation of schlocky junction between Ag nanoparticles and TiO_2. Furthermore, high electron mobility of graphene and enhanced light absorption in visible light region also played key role for the increase of photoactivity. Therefore, photocatalytic activity of Ag−/TiO_2-graphene catalyst in the degradation of MB dye was higher compared to pure TiO_2 and TiO_2-graphene composite.

High-performance GO/P25 composite photocatalyst was reported by Zhang et al. [32]. The composite photocatalyst demonstrated a significant enhancement in the degradation of MB under both UV and visible light irradiations compared to pure P25. The authors attributed the high performance of photocatalyst to adsorption of MB molecules on composite surface, extended light absorption, and charged transportation and separation properties of the composite.

Regarding the role of graphene in extending the photocatalytic performance of TiO_2 under visible light irradiation, important advances have been made in recent years. Our group reported metal−/nonmetal-doped TiO_2-graphene composites [23, 24, 66, 67, 77] for the photodegradation of MO under visible light irradiation ($\lambda \geq 420$ nm). All prepared composites exhibited enhanced photocatalytic activity under visible light irradiation due to the synergetic effects of graphene and metal/nonmetal impurities. A comparison was made among the best visible light-responsive photocatalysts of different prepared series, and results are presented in Fig. 5.14. The results demonstrate that nitrogen-doped and graphene-incorporated composite photocatalyst (GR-2N/TiO_2) has excellent photocatalytic performance under visible light irradiation among all the best photocatalysts. Moreover, results suggest that nonmetal doping is more successful to increase the photocatalytic

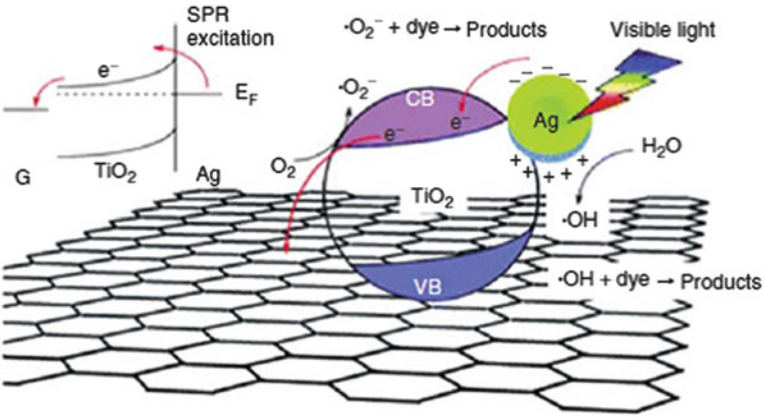

Fig. 5.13 Proposed mechanisms for the photocatalytic degradation of organic dyes over Ag/TiO_2/G nanocomposite under visible light irradiation. Reprinted with permission from Ref. [27]. Copyright (2011) Royal Society of Chemistry

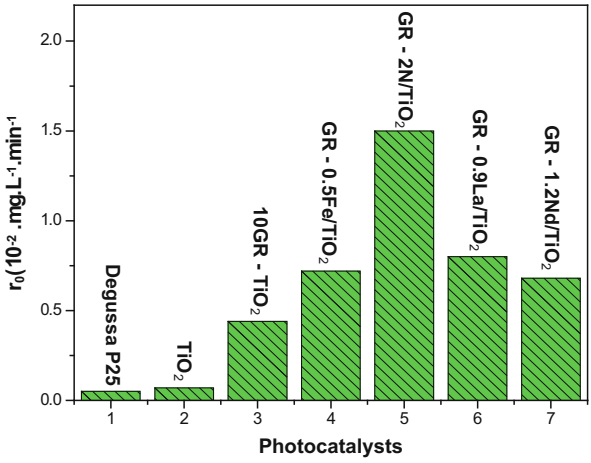

Fig. 5.14 Comparison graph for degradation of methyl orange dye under visible light irradiation ($\lambda \geq 420$ nm) using different best photocatalysts of our previous reports [23, 24, 66, 67, 77]

efficiency of TiO_2-graphene in comparison to metal doping. It can be attributed to the fact that nitrogen doping decreased the band gap of TiO_2 and enhanced the visible light absorption more efficiently compared to other metal-based composites. Furthermore, cooperative effects of MO adsorption on the surface of composite catalyst, extended visible light absorption due to impurity doping and graphene incorporation, and efficient charge separation had played a major role for degradation of MO under visible light illumination.

In another study, Lee et al. [49] synthesized highly photoactive graphene-wrapped anatase TiO_2 nanoparticles via one-step hydrothermal method. Graphene-TiO_2 nanoparticles showed an excellent photocatalytic performance under visible light for the degradation of MB with a rate constant of 3.41×10^{-2}

min^{-1}, which was much higher than that of pure anatase TiO_2 nanoparticles, graphene-TiO_2 nanoparticles (two-step hydrothermal), and commercial P25 powder.

On the other hand, TiO_2-graphene composites with 3D structure also attracted great attention in recent years. The graphene with 3D structure such as hydrogel or aerogel has some distinctive properties [78]. For instance, Zhang et al. [79] reported a TiO_2-graphene nanocomposite hydrogel (TGH) and used for the photodegradation of methylene blue under UV light illumination. The photocatalytic performance of TiO_2-graphene nanocomposite hydrogel was observed higher compared to pure TiO_2 nanoparticles. The increase in photocatalytic activity was attributed to high surface area of the nanohybrid, extended light range, and fast charge transportation due to its high conductivity. Qiu et al. [80] have studied the TiO_2/GAs, which showed a good adsorption capacity and photocatalytic activity for methyl orange degradation. The results exhibited enhanced photocatalytic performance of TiO_2/GAs compared to other TiO_2-graphene composites.

5.6 Conclusions and Future Prospective

TiO_2-graphene-based composites hold great potential for being used as photocatalyst materials to address environmental issues. In this chapter, the current status of the synthesis techniques for TiO_2-graphene composite preparation, characterization to study the influence of graphene on the properties of TiO_2, and applications of TiO_2-graphene composites in photocatalysis of organic pollutants was summarized. The incorporation of graphene into TiO_2 photocatalyst can efficiently improve the photocatalytic activity, owing to the extended light absorption range, enhanced adsorption capacity for pollutant molecules, and excellent electron conductivity of graphene. Despite the demonstrated advances, the research in this field is still at an early stage of development. For example, the inhomogeneous dispersion of TiO_2 nanoparticles on graphene surface, the low connection between graphene sheets and TiO_2, and the uncontrollable morphology of composite make it difficult to attain its industrial applications dealing with environmental issues. Therefore, future works should be focused to develop more well-organized synthesis methods for preparing TiO_2-graphene composites with well-controlled morphology, efficient interfacial connection, and good stability to achieve continuous mode operation of photoreactors.

In addition to above, most of the reports on TiO_2-graphene photocatalysts are focused on binary components. The growth of ternary or multicomponent TiO_2-graphene-based hybrid nanostructures may provide new insight for the development of 3D nanostructures with excellent photocatalytic performance. In this regard, more efforts should be done to construct multicomponent TiO_2-graphene-based hybrid photocatalysts with advanced synthesis techniques. Finally, the

energy applications of graphene-based photocatalysts are still at infancy. Further progress in this field would need multidisciplinary efforts from chemistry, physics, and materials science.

References

1. Gupta S, Tripathi M (2012) An overview of commonly used semiconductor nanoparticles in photocatalysis. High Energy Chem 46:1–9
2. Xiang Q, Yu J, Jaroniec M (2012) Graphene-based semiconductor photocatalysts. Chem Soc Rev 41:782–796
3. Herrmann JM (2005) Heterogeneous photocatalysis: state of the art and present applications. Top Catal 34:49–65
4. Fujishima A, Zhang X, Tryk DA (2008) TiO_2 photocatalysis and related surface phenomena. Surf Sci Rep 63:515–582
5. Kubacka A, Fernandez-Garcia M, Colon G (2011) Advanced nanoarchitectures for solar photocatalytic applications. Chem Rev 112:1555–1614
6. Hamal DB, Klabunde KJ (2007) Synthesis, characterization, and visible light activity of new nanoparticle photocatalysts based on silver, carbon, and sulfur-doped TiO_2. J Colloid Interface Sci 311:514–522
7. Li M, Zhou S, Zhang Y, Chen G, Hong Z (2008) One-step solvothermal preparation of TiO_2/C composites and their visible-light photocatalytic activities. Appl Surf Sci 254:3762–3766
8. Wang J, Tafen DN, Lewis JP, Hong Z, Manivannan A, Zhi M, Li M, NQ W (2009) Origin of photocatalytic activity of nitrogen-doped TiO2 nanobelts. J Am Chem Soc 131:12290–12227
9. Tafen D, Wang J, NQ W, Lewis JP (2009) Visible light photocatalytic activity in nitrogen-doped TiO2 nanobel. Appl Phys Lett 94:093101
10. Carp O, Huisman CL, Reller A (2004) Photoinduced reactivity of titanium dioxide. Prog Solid State Chem 32:133–177
11. Wang J, Uma S, Klabunde KJ (2004) Visible light photocatalysis in transition metal incorporated titania-silica aerogel. Appl Catal Environ 48:151–154
12. Ahmad B, Kusumoto Y, Islam MS (2010) One-step and large scale synthesis of non-metal doped TiO_2 submicrospheres and their photocatalytic activity. Adv Powder Tech 21:292–297
13. Park JY, Choi K, Lee J, Hwang C, Coi D, Lee J (2013) Fabrication and characterization of metal-doped TiO_2 nanofibers for photocatalytic reactions. Mater Lett 97:64–66
14. Ambrus Z, Balazs N, Alapi T, Wittmann G, Sipos P, Dombi A, Mogyorosi K (2008) Synthesis, structure and photocatalytic properties of Fe(III)-doped TiO_2 from $TiCl_3$. Appl Catal Environ 81:27–37
15. Weber AS, Grady AM, Koodali RT (2012) Lanthanide modified semiconductor photocatalysts. Cat Sci Technol 2:683–693
16. Kim W, Tachikawa T, Majima T, Choi W (2009) Photocatalysis of dye sensitized TiO_2 nanoparticles with thin overcoat of Al_2O_3: enhanced activity for H_2 production and dechlorination of CCl_4. J Phys Chem C 113:10603–10609
17. Zhou W, Yin Z, Du Y, Huang X, Zeng Z, Fan Z, Liu H, Wang J, Zhang H (2013) Synthesis of few layer MoS_2 nanosheet-coated TiO_2 nanobelt heterostructures for enhanced photocatalytic activities. Small 9:140–147
18. Xing MY, Fang WZ, Nasir M, Ma YF, Zhang JL, Anpo M (2013) Self-doped Ti^{3+} enhanced TiO_2 nanoparticles with a high-performance photocatalysis. J Catal 297:236–243
19. Zhang LW, HB F, Zhu YF (2008) Efficient TiO_2 photocatalysts from surface hybridization of TiO_2 particles with graphite-like carbon. Adv Funct Mater 18:2180–2189

20. Chen C, Long M, Zeng H, Cai W, Zhou B, Zhang J, Wu Y, Ding D, Wu D (2009) Preparation, characterization and visible-light activity of carbon modified TiO_2 with two kinds of carbonaceous species. J Mol Catal A: Chem 314:35–41
21. Silva CG, Faria JL (2010) Photocatalytic oxidation of benzene derivatives in aqueous suspensions: synergic effect induced by the introduction of carbon nanotubes in a TiO_2 matrix. Appl Catal Environ 101:81–89
22. Morales-Torres S, Pastrana-Martinez LM, Figueiredo JL, Faria JL, Silva AMT (2012) Design of graphene-based TiO_2 photocatalysts—a review. Environ Sci Pollut Res 19:3676–3687
23. Khalid NR, Hong Z, Ahmed E, Zhang Y, Chan H, Ahmad M (2012) Synergistic effects of Fe and graphene on photocatalytic activity enhancement of TiO_2 under visible light. Appl Surf Sci 258:5827–5834
24. Khalid NR, Ahmed E, Hong Z, Ahmad M (2012) Synthesis and photocatalytic properties of visible light responsive La/TiO_2-graphene composites. Appl Surf Sci 263:254–259
25. Rao CNR, Sood AK, Subrahmanyam KS, Govindaraj A (2009) Graphene: the new two-dimensional nanomaterial. Angew Chem Int Ed 48:7752–7777
26. Huang Q, Tian S, Zeng D et al (2013) Enhanced photocatalytic activity of chemically bonded TiO_2/graphene composites based on the effective interfacial charge transfer through the C–Ti bond. ACS Catal 3:1477–1485
27. Wen Y, Ding H, Shan Y (2011) Preparation and visible light photocatalytic activity of Ag/TiO_2/graphene nanocomposite. Nanoscale 3:4411–4417
28. Wang D, Choi D, Li J et al (2009) Self-assembled TiO_2/graphene hybrid nanostructures for enhanced Li-ion insertion. ACS Nano 3:907–914
29. Williams G, Seger B, Kamat PV (2008) TiO_2-graphene nanocomposites UV-assisted photocatalytic reduction of graphene oxide. ACS Nano 2:1487–1491
30. Xin X, Zhou X, Wu J et al (2012) Scalable synthesis of TiO_2/graphene nanostructured composite with high-rate performance for lithium ion batteries. ACS Nano 6:11035–11043
31. Zhang Y, Tang ZR, Fu X, YJ X (2010) TiO_2-graphene nanocomposites for gas-phase photocatalytic degradation of volatile aromatic pollutant: is TiO_2-graphene truly different from other TiO_2-carbon composite materials. ACS Nano 4:7303–7314
32. Zhang H, Lv X, Li Y, Wang Y, Li J (2009) P25-graphene composite as a high performance photocatalyst. ACS Nano 4:380–386
33. Geim AK, Novoselov KS (2007) The rise of graphene. Nat Mater 6:183–191
34. Geim AK (2009) Graphene: status and prospects. Science 324:1530–1534
35. Gunti S, Kumar A, Ram MK (2015) Comparative organics remediation properties of nanostructured graphene doped titanium oxide and graphene doped zinc oxide, photocatalysts. Am J Anal Chem 6:708–717
36. Zhang L, Xi Z, Xing M, Zhang J (2013) Effects of the preparation order of the ternary P25/GO/Pt hybrid photocatalysts on hydrogen production. Int J Hydrogen Energy 38:9169–9177
37. Xing M, Shen F, Qiu B, Zhang J (2014) Highly-dispersed boron-doped graphene nanosheets loaded with TiO_2 nanoparticles for enhancing CO_2 photoreduction. Sci Rep 4:6341–6346
38. Liu J, Bai H, Wang Y, Liu Z, Zhang X, Sun DD (2010) Self-assembling TiO 2 nanorods on large graphene oxide sheets at a two-phase interface and their anti-recombination in photocatalytic applications. Adv Funct Mater 20:4175–4181
39. Kamegawa T, Yamahana D, Yamashita H (2010) Graphene coating of TiO_2 nanoparticles loaded on mesoporous silica for enhancement of photocatalytic activity. J Phys Chem C 114:15049–15053
40. Behnajady MA, Eskandarloo H, Modirshahla N, Shokri M (2011) Investigation of the effect of sol–gel synthesis variables on structural and photocatalytic properties of TiO_2 nanoparticles. Desalination 278:10
41. Burda C, Chen X, Narayanan R, El-Sayed MA (2005) Chemistry and properties of nanocrystals of different shapes. Chem Rev 105:1025–1102
42. Chen C, Cai W, Long M, Zhou B, Wu Y, Wu D, Feng Y (2010) Synthesis of visible-light responsive graphene oxide/TiO_2 composites with p/n heterojunction. ACS Nano 4:6425–6432

43. Lambert TN, Chavez CA, Lu P et al (2009) Synthesis and characterization of titania/graphene nanocomposites. J Phys Chem C 113:19812–19823
44. Zhang Q, He Y, Chen X et al (2011) Structure and photocatalytic properties of TiO_2–graphene oxide intercalated composite. Chin Sci Bull 56:331–339
45. Newman MD, Stotland M, Ellis JI (2009) The safety of nanosized particles in titanium dioxide- and zinc oxide-based sunscreens. J Am Acad Derm 61:685–692
46. Zallen R, Moret MP (2006) The optical absorption edge of brookite TiO_2. Solid State Commun 137:154–157
47. Liang Y, Wang H, Chen Z, Dai H (2010) TiO_2 nanocrystals grown on graphene as advanced photocatalytic hybrid Materials. Nano Res 3:701–705
48. Fan W, Lai Q, Zhang Q, Wang Y (2011) Nanocomposites of TiO_2 and reduced graphene oxide as efficient photocatalysts for hydrogen evolution. J Phys Chem C 115:10694–10701
49. Lee JS, You KH, Park CB (2012) Highly photoactive, low band gap TiO_2 nanoparticles wrapped by graphene. Adv Mater 24:1084–1088
50. Wang Z, Huang B, Dai Y et al (2012) Crystal facets controlled synthesis of graphene@TiO_2 nanocomposites by a one-pot hydrothermal process. Cryst Eng Comm 14:1687–1692
51. Long M, Qin Y, Chen C, Guo X, Tan B, Cai W (2013) Origin of visible light photoactivity of reduced graphene oxide/TiO_2 by in situ hydrothermal growth of undergrown TiO_2 with graphene oxide. J Phys Chem C 117:16734–16741
52. Jian B, Tian C, Zhou W, Wang J, Xie Y, Pan Q, Ren Z, Dong Y, Fu D, Han J, Fu H (2011) In situ growth of TiO_2 in interlayers of expanded graphite for the fabrication of TiO_2–graphene with enhanced photocatalytic activity. Chem A Eur J 17:8379–8387
53. Zhou Q, Zhong Y, Chen X, Liu J, Huang X, Wu Y (2014) Adsorption and photocatalysis removal of fulvic acid by TiO_2–graphene composites. J Mater Sci 46:1066–1075
54. Kim H, Moon G, Park Y, Choi W (2012) Solar photoconversion using graphene/TiO_2 composites: nanographene shell on TiO_2 core versus TiO_2 nanoparticles on graphene sheet. J Phys Chem C 116:1535–1543
55. Mohamed RM (2012) UV-assisted photocatalytic synthesis of TiO_2-reduced graphene oxide with enhanced photocatalytic activity in decomposition of sarin in gas phase. Desalina Water Treat 50:147–156
56. Akhavan O, Abdolahad M, Esfandiar A, Mohatashamifar M (2010) Photodegradation of graphene oxide sheets by TiO_2 nanoparticles after a photocatalytic reduction. J Phys Chem C 114:12955–12959
57. Liu X, Pan L, Lv T, Zhu G, Lu T, Suna Z, Sun C (2011) Microwave-assisted synthesis of TiO_2-reduced graphene oxide composites for the photocatalytic reduction of Cr(VI). RSC Adv 1:1245–1249
58. Pu X, Zhang D, Gao Y, Shao X, Ding G, Li S, Zhao S (2013) One-pot microwave-assisted combustion synthesis of graphene oxide–TiO_2 hybrids for photodegradation of methyl orange. J Alloys Compd 551:382–388
59. Wang Y, Yu J, Xiao W, Li Q (2014) Microwave-assisted hydrothermal synthesis of graphene based Au-TiO_2 photocatalysts for efficient visible-light hydrogen production. J Mater Chem A 2:3847–3855
60. Lv T, Pan L, Liu X, Lu T et al (2012) One-step synthesis of CdS-TiO_2-chemically reduced graphene oxide composites via microwave-assisted reaction for visible-light photocatalytic degradation of methyl orange. Cat Sci Technol 2:754–758
61. Xing M, Zhang J, Chen F, Tian B (2011) An economic method to prepare vacuum activated photocatalysts with high photo-activities and photo-sensitivities. Chem Commun 47:4947–4949
62. Xing M, Zhang J, Qiu B, Tian B, Anpo M, Che M (2014) A brown mesoporous TiO_2-x/MCF composite with an extremely high quantum yield of solar energy photocatalysis for H_2 evolution. Small 11:1920–1929
63. Qiu B, Zhong C, Xing M, Zhang J (2015) Facile preparation of C-modified TiO_2 supported on MCF for high visible-light-driven photocatalysis. RSC Adv 5:17802–17808

64. Xing M, Fang W, Yang X, Tian B, Zhang J (2014) Highly-dispersed boron-doped graphene nanoribbons with enhancing conductibilities and photocatalysis. Chem Commun 136:5852–5855
65. Qiu B, Zhou Y, Ma Y, Yang X, Sheng W, Xing M, Zhang J (2015) Facile synthesis of the Ti^{3+} self-doped TiO_2-graphene nanosheet composites with enhanced photocatalysis. Sci Rep 5:8589–8591
66. Khalid NR, Ahmed E, Hong Z, Zhang Y, Ahmad M (2012) Nitrogen doped TiO_2 nanoparticles decorated on graphene sheets for photocatalysis applications. Current. Appl Phys 12:1485–1492
67. Khalid NR, Ahmed E, Hong Z, Sana L, Ahmad M (2013) Enhanced photocatalytic activity of graphene-TiO_2 composite under visible light irradiation. Curr Appl Phys 13:659–663
68. Leong KH, Sim LC, Bahnemann D, Jang M, Ibrahim S, Saravanan P (2015) Reduced graphene oxide and Ag wrapped TiO_2 photocatalyst for enhanced visible light photocatalysis. APL Mater 3:104503
69. Xiang Q, Yu J, Jaroniec M (2011) Enhanced photocatalytic H_2-production activity of graphene modified titania nanosheets. Nanoscale 3:3670–3678
70. Zhang Y, Pan C (2011) TiO_2/graphene composites from thermal reaction of graphene oxide and its photocatalytic activity in visible light. J Mater Sci 46:2622–2626
71. Han W, Zang C, Huang Z, Zhang H, Ren L, Qi X, Zhong J (2014) Enhanced photocatalytic activities of three-dimensional graphene-based aerogel embedding TiO_2 nanoparticles and loading MoS_2 nanosheets as co-catalyst. Int J Hydrogen Energy 39(34):19502–19512
72. JG Y, Wang WG, Cheng B, BL S (2009) Enhancement of photocatalytic activity of mesoporous TiO_2 powders by hydrothermal surface fluorination treatment. J Phys Chem C 113:6743
73. JC Y, Ho W, Yu J, Yip H, Wong PK, Zhao J (2005) Efficient visible-light-induced photocatalytic disinfection on sulfur-doped nanocrystalline titaniaEnviron. Sci Technol 39:1175
74. JG Y, YR S, Cheng B (2007) Template-free fabrication and enhanced photocatalytic activity of hierarchical macro−/mesoporous titania. Adv Funct Mater 17:1984
75. Cheng B, Le Y, JG Y (2010) Preparation and enhanced photocatalytic activity of Ag@TiO_2 core–shell nanocomposite nanowires. J Hazard Mater 177:971
76. Ng YH, Lightcap IV, Goodwin K, Matsumura M, Kamat PV (2010) To what extent do graphene scaffolds improve the photovoltaic and photocatalytic response of TiO_2 nanostructured films. J Phys Chem Lett 1:2222–2227
77. Khalid NR, Ahmed E, Ahmad M, Zhang Y, Ullah M, Hong Z (2013) Graphene modified Nd/TiO_2 photocatalyst for methyl orange degradation under visible light irradiation. Ceram Int 39:3569–3575
78. Sun H, Xu Z, Gao C (2013) Multifunctional, ultra-fly weight, synergistically assembled carbon aerogels. Adv Mater 25:2554–2560
79. Zhang Z, XiaoF GY, Wang S, Liu Y (2013) One-pot self-assembled three-dimensional TiO_2-graphene hydrogel with improved adsorption capacities and photocatalytic and electrochemical activities. ACS Appl Mater Interfaces 5:2227–2233
80. Qiu B, Xing M, Zhang J (2014) Mesoporous TiO_2 nanocrystals grown in situ on graphene aerogels for high photocatalysis and lithium-ion batteries. J Am Chem Soc 136:5852–5855

Chapter 6
A Short Introduction to the Molecular Dynamics Simulation of Nanomaterials

Danilo Roccatano

All things are made of atoms—little particles that move around in perpetual motion, attracting each other when they are a little distance apart, but repelling upon being squeezed into one another.

—Richard P. Feynman. Six Easy Pieces (1995)

6.1 Introduction

The lecture delivered to the American Physical Society meeting at Caltech in 1959 by the famous scientist R. Feynman is considered the manifesto of nanotechnology revolution [1]. Feynman's brilliant visions of the future development of technology anticipated the possibility to build nanomachines and use them for still unexplored applications. The ideas of Feynman took several years before they could be endorsed in practical realizations, but it contributed to pursue the study of nanodevices using molecular modeling and simulations. In the 60 years after the Feynman's talk, computational chemistry has raised to a very important research methodology in all areas of nanoscience. The recognition of the important role of the computational approach to study molecular systems comes from the recent (2013) Nobel Prize in Chemistry awarded to Martin Karplus, Michael Levitt, and Ariel Warshel, for the development of multi-scale models for complex chemical systems. The exciting prospective of using computer as a "microscope" to reveal details of molecular processes on length of space and time unreachable to experimental observations has been recently highlighted [2, 3]. Nowadays, molecular modeling of molecular systems can be used to accurately calculate structural, dynamics, and functional properties at atomic scale. Along clarifying the

D. Roccatano (✉)
School of Mathematics and Physics, University of Lincoln, Isaac Newton Building, Brayford Pool, Lincoln LN6 7TS, UK
e-mail: droccatano@lincoln.ac.uk

M.J. Jackson, W. Ahmed (eds.), *Micro and Nanomanufacturing Volume II*,
DOI 10.1007/978-3-319-67132-1_6

physicochemical properties of single molecules or systems, this information provides insights for designing and manufacturing of new nanomaterials.

Among the different computational methods, molecular dynamics (MD) simulation is a powerful approach to analyze both structural and dynamic properties of these materials at different at different length and time scales. This chapter aims to provide a general and concise introduction to the MD simulations of different molecular systems. The chapter is partially based on previous publications of the same author oriented to the introduction of MD simulation method of biological molecules [4, 5]. Besides this chapter, the reader interested to a deeper dive into the topic can consult several comprehensive reviews [6–8] and textbooks [9–12, 14] on the topic available in the literature.

6.1.1 Modeling the Molecular World

In the first decade of the last century, the dawn of the quantum mechanics (QM) marked the beginning of the mathematical modeling of the atomic world. The formulation of quantum mechanics by E. Schrödinger with the equation that bears his name (the Schrödinger equation, SE) opened the way to a mathematically elegant and concise description of the molecular world. Unfortunately, analytic solutions of the SE for complex systems do not exist. However, the advent of electronic computers made possible to overcome this impasse by numerically solving it for any number of electrons in the system. Despite the constant improvement of computer performance, the use of QM methods to describe the dynamics properties of large molecules is still far from being a feasible approach. The hurdle resides in the fact that the number of calculations required to solve the SE is proportional at the least to third power of the total number of electrons in the system. Therefore, even the solution of a small molecular system consisting of a mere hundred of atoms becomes computationally expensive for a simulation of just few hundreds of picoseconds [13]. Fortunately, the atomic structure of materials is organized at different levels of lenght and time scale. This hierarchical organization turns to be very useful to simplify the modeling the molecular world [14]. In fact it is possible to blur into the details of the atomic structure (electrons and nucleons) by considering atom classical particles of a given mass and electric charges. The foundation of this approach is the Born-Oppenheimer approximation for which the dynamical behavior of a molecular system in its ground state can be separated in the motion of the nuclei and that of the electrons [9]. The last ones can then be neglected by considering their effect on the molecular structure and dynamics (e.g., bonds between atoms) in a simplified manner (e.g., in the case of bonds, as a harmonic spring). In other words, any molecule can be described in its ground state as composed of simple particles (*viz.* without an internal structure) interacting by means of an effective conservative potential determined by the missing electronic degree of freedom (such us electrons and nucleons). This approach has also the disadvange to the possibility to study chemical reactions,

excited states, and low temperature effects. Neverthenless, it has the great advantage that can be mathematically reduced to simple analytic functions as, for example, the harmonic function. In addition, it is also reasonable to assume that the motion of these particles can be described by the laws of the classical mechanics. With these approximations, the computational demand required to calculate the mechanical and dynamics properties of molecular systems of large sizes (*viz*. more than thousand of particles) on time scales of nanoseconds (or more) is considerably reduced with respect the QM treatment. The first simulation using this approach was performed more than half century ago. Berni J. Alder and Thomas K. Wrainwright developed and used the method to study simple fluid models with atoms represented as rigid spheres [15]. This first pioneering study signs up the birth of the classical MD simulation method. Other important landmarks have been the simulation of polar molecule (such as water) [16, 19, 20], a small polymer chain [17], and a macromolecule (the bovine pancreatic trypsin inhibitor protein) [18], nucleic acids [21], and biological membrane [22]. These initial studies of complex systems have been followed by other important achievements establishing MD simulations as a tool to investigate and predict physicochemical properties of complex molecular systems in conditions not accessible by experimental methods. For more details on the historical development of the computer simulations of molecular systems, the reader should consult, for example, [10, 12].

Nowadays, MD simulation method is used in different fields of chemistry, physics, and biology for studying the dynamical and structural property of bio- and nanomaterial. The progress toward the development of novel computer architectures (*e.g*. quantum computers) is opening unforeseeable perspectives for computer simulations [2, 3]. Just 11 years ago, the group of the late Klaus Schulten, one of the most prolific and cutting-age scientist in MD simulations of biological systems, performed a few tens of nanoseconds long MD simulation of an entire virus [23]. Therefore, it is likely that, in few years, multi-scale simulations of a whole cellular organelles or entire bacterial cells will routinely appear in scientific publications [24].

This chapter is organized as follows. In the first part, the MD simulation method will be introduced by briefly describing the modeling of molecular interactions, the fundamentals of numerical algorithms for the simulations, and the setup of a MD simulation of a molecular system. In the second part, some examples of applications to molecular systems are given to acquaint the readers with the type of results that can be obtained from MD simulations. Finally, in the Perspectives section, an outlook to the future development of the method will be discussed.

6.2 The Physical Model

The atomic interactions in the classical MD simulation are treated using analytic functions, usually referred as *effective potential or force field*. These functions depend on the atomic coordinates and on a number of parameters (i.e., force

constants, partial charges, reference bond distances, and bond angles) derived by experimental data and/or QM calculations. A typical example of *force field* is the following:

$$
\begin{aligned}
&V(r_1, r_2, r_3, \ldots, r_N) = \\
&\left.\begin{aligned}
&\sum_{\text{Bonds}} \frac{1}{2} K_b (b - b_0)^2 + \sum_{\text{angles}} \frac{1}{2} K_\theta (\theta - \theta_0)^2 \\
&+ \sum_{\substack{\text{improper} \\ \text{dihedral}}} \frac{1}{2} K_\xi (\xi - \zeta_0)^2 + \sum_{\substack{\text{Proper} \\ \text{dihedral}}} K_\phi [1 + \cos(n\phi - \delta)]
\end{aligned}\right\} \textbf{\textit{Bonded interactions}} \\
&\left.\begin{aligned}
&\sum_i \sum_{j>i} 4\varepsilon_{ij} \left[\left(\frac{\sigma_{ij}}{r_{ij}} \right)^{12} - \left(\frac{\sigma_{ij}}{r_{ij}} \right)^{6} \right] \\
&+ \\
&+ \sum_i \sum_{j>i} \left(\frac{q_i q_j}{4\pi\varepsilon_o \varepsilon_r r_{ij}} \right)
\end{aligned}\right\} \textbf{\textit{Non-bonded interactions}}
\end{aligned}
\tag{6.1}
$$

This function contains the mathematical representation of bonded and non-bonded molecular interaction energies. The first ones are described using two- to four-body potential functions (i.e., mathematical expressions that depend on the coordinates of 2–4 atoms), and their parameters are usually obtained from experimental crystallographic and spectroscopic data [9, 10, 25]. The first summation term in Eq. (6.1) represents energy contribution from bond vibrations. The bond vibration is approximated with a harmonic function where b_0 represents the equilibrium bond length and k_b the force constant. The values of these two parameters change accordingly to the bond type. Since bond vibrations (in particular bonds containing hydrogen atoms) [10] slightly affect the larger-scale motions of large macromolecules, this term is often not taken in account by keeping the bond rigid using holonomic constraints. This approximation is used to speed up the simulation since it removes the faster vibration modes of the system allowing the use of a longer integration time step. These time-independent constraints are applied at each simulation step using numerical algorithms as SHAKE [9, 10, 14], LINCS [26], and (for water molecules) SETTLE [27]. The second summation term in Eq. (6.1) describes the interaction energy for the bond angle vibrations. This is a three-body interaction function as the bond angle (θ) depends on positions of three atoms involved. Also in this case, the function describes a harmonic motion where θ_o represents the reference value of the bond angle and k_θ the vibration force constant. The next two summation terms in Eq. (6.1) are used to describe four-atom interaction potentials. The first one describes the vibration of the so-called *improper dihedral angle (ζ)*. This term restrains to a reference angle (ζ_0) the geometry of particular functional group in the molecule preventing, for example, the inversion of chiral carbon atoms and out-of-plane deformation of aromatic ring.

The second term, named proper dihedral angles (ϕ) torsion function, calculates the conformational energy generated by in the rotation around a bond and it is modeled using trigonometric functions with k_ϕ the force constant, n the multiplicity, and δ the phase shift.

Finally, the last two summation terms in Eq. (6.1) are used to describe the so-called non-bonded atomic interactions. These functions are used to model, using pair interaction functions, van der Waals and electrostatic interactions. The non-bonded interactions between atoms separated by two bonds are not calculated but accounted as proper dihedral interactions.

Van der Waals interactions are usually modeled using the Lennard-Jones (LJ) function. The function contains two parameters σ_{ij} and ε_{ij} that represent the distance at which it is equal to zero and to its minimum value (located at $r_m = \sigma_{ij} / \sqrt[6]{2}$), respectively. The twelve-power term is used to describe the repulsive interaction. The second term describes the attractive interaction resulting from the interaction of mutually induced electronic dipoles. The LJ parameters (σ_{ij} and ε_{ij}) describing the interaction between different atomic species (i and j) are usually derived using the Lorentz-Berthelot mixing rules based on geometric or arithmetic average of parameters (σ_{ii}, σ_{jj}, ε_{ii}, ε_{jj}) of the atom involved [9, 10] as

$$\sigma_{ij} = \frac{\sigma_{ii} + \sigma_{jj}}{2}; \quad \varepsilon_{ij} = \sqrt{\varepsilon_{ii}\varepsilon_{jj}} \tag{6.2}$$

The electrostatic interactions are modeled using the Coulomb term (last term in Eq. (6.1)). The partial atomic charges, q_i, are calculated from QM calculations. The relative dielectric constant, ε_r, is generally set equal to one (vacuum). This approximation can give a poor description of the phenomena where the polarizability of the atoms plays a significant role. In some case, the model can be improved by increasing the value of partial charges till thermodynamics and/or kinetics experimental data of bulk fluid state are reproduced (an example is the water model SPC/E [28]). However, the correct solution is the explicit treatment of the atomic polarizability in the force field to accurately calculate the electric field effects in simulated system [10, 28, 29]. Several force fields including the tratment of atomic polarizability are already available [29, 30]. However, the explicit treatment of polarizability effects in force fields is still of limited use for large systems since it is computationally expensive.

Even without accounting of explicit polarizzability effects, the calculation of the long-range electrostatic interaction is the most demanding computational part of a MD simulation. In fact, being pairwise interactions, their number is proportional to the square of the number of atoms and, therefore, much more than the bonded ones that just go linearly with the number of atoms. Hence, the computational performance of a MD program is strongly dependent on the use of efficient algorithms that speed up the evaluation of non-bonded interactions. Several methods are used to improve this efficiency [10, 14, 31] and among those, the most commonly used ones (vide infra) are based on force truncation using distance cutoff criteria and on the use of the *so-called* Ewald summation.

6.2.1 Force Field Parameters

The parameters present in the force field potential are usually estimated from both experimental data or from QM calculations. Force constants for the harmonic potential of bonds and bond angles are optimized to reproduce the properties of reference compounds obtained from crystallographic structures, IR/Raman spectroscopy, or QM calculations [32]. The atomic partial charges are usually obtained from Hartree-Fock or density functional theory calculations (usually with basis set 6-31G* or 6-31+G* for anions). The parameters for the LJ function can be derived from experimental data or from QM calculations but usually adapted from a similar atom type present in the library of force field parameters. For small molecules, this initial set of parameters is verified against experimental physicochemical properties of bulk or vapor phases. Properties as the liquid density, the vaporization enthalpy, and the thermal compressibility at constant pressure, dielectric constant, self-diffusion coefficient, and viscosity can be easily calculated from the simulation and directly compared with the experimental values [64]. If a discrepancy beyond the targeted level of accuracy for the model is observed, partial charges and LJ parameters are both manually or automatically adjusted until they reproduce the targeted set of experimental values.

Different libraries of force field parameters have been developed by different research groups. The most impartant ones are reported in Table 6.1 with links to the developer website. For each force field, it is indicated if force field supports the polarizability and the type of molecules that can be studied.

6.2.2 Coarse-Grained Force Fields

The study of large molecular systems with length of scale larger than 50 nm and on time scale >1 μs is still out of the reach using full atomistic force fields. However, it is possible to simplify the description of these systems by reducing the atomic degree of freedoms used in its model. This approach, generically named "coarse-graining" for the increased "granularity" of the physical model of the simulated system, was applied for the first time to biomolecules by a forerunner work of the 2012 Nobel prize winners M. Levitt and A. Warschel [42]. Several coarse-grained (CG) models (especially for the study of biomolecules) have been proposed (see for a general review [43, 44]). MARTINI [45] is an example of versatile and popular CG force field. The coarse-graining of a molecular system consists in grouping functional groups or part of the molecule in a single particle (bead) characterized by a LJ potential and partial charge. The bead can be centered on one or on the center of mass of the removed atoms. In Fig. 6.1, an example of coarse-graining approach (based on the MARTINI force field) to model two types of polymers is shown. In this type of CG model, water molecules are represented by one bead, and it is equivalent to four water molecules [45].The atom of each unit of both polymers are

Table 6.1 Some example of common force fields for macromolecular simulation

Name	Type	Main type of molecules	Website	Ref.
GROMOS (GROningen MOlecular Simulations)	Classic	Protein, nucleic acids, organic solvents, carbohydrates	www.gromos.net	[33, 34]
AMBER (Assisted Model Building and Energy Refinement)	Classic/ polarizable	Protein, nucleic acids	ambermd.org	[35–37]
OPLS (Optimized Potential for Liquid Simulations)	Classic	Protein, nucleic acids, organic solvents, carbohydrates	zarbi.chem.yale.edu/oplsaam.html	[38, 39]
CHARMM (Chemistry at HARvard Macromolecular Mechanics)	Classic/ polarizable	Protein, nucleic acids, organic solvents, carbohydrates	www.charmm.org	[40, 41]

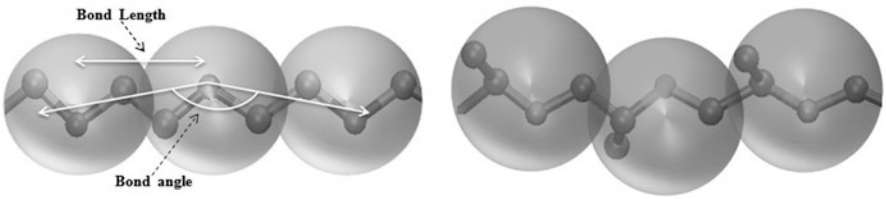

Fig. 6.1 Schematic presentation of MARTINI model in mapping between a chemical structure and the coarse-grained model for different molecules. Reproduced with permission from [46]

rappresented by a baed of equivalent mass (spheres in the figure), in addition, the solvent molecules (water, not shown) are represented by one bead that it is equivalent to four water molecules [45, 46]. The use of beads with large masses permits a larger integration time step (usually 10–20 types larger than the atomistic one) that contributes to extend the simulation time up to microseconds.

Beads are connected by pseudo-bonds (the long white arrows in the Fig. 6.1) forming bond angles and dihedral angles whose interaction parameters are optimized to reproduce the equilibrium geometry of the molecule. Usually the optimization is based on structural and dynamics information from atomistic MD simulations [46].

QM, atomistic and coarse-grained simulations are three levels of the so-called multi-scale approach to the modeling of a physical system. By continuing to introduce approximations, it is possible to coarse-graining further the simulated system to length and time scale that bridge with the macroscopic continuum description of the material. The reader can find a detailed description of this hierarchical approach to the modeling of the matter in the authoritative book by H.J.C Berendsen [14].

6.3 The Simulation

6.3.1 Treatment of Long-Range Interactions

The simplest procedure for calculating the non-bonded interactions is the use of the so-called *cutoff* criterion. It consists of calculating the electrostatic and LJ interactions for each atom of the system with other atoms located within a distance R_c (the *cutoff* distance). This method is based on the approximation that the contribution to the non-bonded energy for atoms located beyond R_c is negligible as it depends at the most by the inverse of the distance. The pair interactions within R_c are stored in a list (the Verlet's list [10]) which is then used to calculate them in the next m steps. To compensate for the errors due to the diffusion of atoms inside and outside R_c during the m steps, a larger *cutoff* radius is used to calculate the interactions at the mth step. The last approach is usually referred as *twin-range* cutoff method [9–11].

In the cutoff method, the number of non-bonded interactions calculated at each step is proportional to the number of atoms within R_c, and so it speeds up considerably the simulation of large systems. The *cutoff* criterion provides a good approximation for the calculation of short-range interactions (as the LJ ones), but it can produce artifacts when it is used for long-range electrostatic interactions. In fact, the discontinuity of the energy functions at the cutoff distance introduces an artificial increase of kinetic energy (aka temperature) of the system. However, this excess of energy can be easily dissipated by using a thermostat (*see* infra). Another method to reduce cutoff artifacts is the use of charge groups in the distribution of partial atomic charges on the molecule [9]. This is achieved by grouping the atoms in the molecule in groups having the sum of partial charges equal to zero or to an integer value. In this way, the electrostatic interaction between charge groups becomes dipolar. Therefore, it decreases faster than charge-charge interactions since it is proportional to the cube of the inverse of the distance (r^{-3}). In this way, the rapid decrease of the electrostatic energy considerably reduces the perturbation due to the cutoff energy truncation. The last approach is used in the GROMOS force fields.

In the last years, the use of the *cutoff* method is progressively vanishing due to the development of faster and more accurate methods for the treatment of the electrostatic interactions. These methods are based on the so-called Ewald summation (named after German crystallographer and physicist P. P. Ewald) [47]. Ewald used his mathematical trick to calculate the properties of ionic crystals. The advantages of the Ewald summation include a substantial reduction of the number of calculations to ~$N \log N$, where N is the number of atoms in the system, and, at the same time, keeping a good accuracy. The popularity of this method spread when it was found that this method could produce better approximation of the electrostatic energy not only for crystals but also for polar solutions. A computational efficient variation of this method suitable for parallel computers is called particle mesh Ewald (PME) [47].

Table 6.2 List of the most common repositories of molecular structures

Crystal structure of small organic and inorganic molecules	
CSD, Cambridge Structural Database	www.ccdc.cam.ac.uk
OCD, Open Crystallographic Database	sdpd.univ.-lemans.fr/cod/index.html
Crystal structure of protein and nucleic acids	
PDB, Protein Data Bank	www.rcsb.org
NDB, Nucleic Acid Bank database	ndbserver.rutgers.edu

6.3.2 Initial Atomic Position

The initial atomic coordinates of simulated systems are normally obtained from X-ray crystallographic or nuclear magnetic resonance structural data. Some of the repositories of molecular structures are reported in the Table 6.2.

When these experimental structures are not available, it is still possible to use molecular modeling software to geometrically generate them. In Fig. 6.2, some examples of starting structures of different types of molecular systems are shown. The models can be generated using plenty of open sources molecular graphics software (vide infra).

6.3.3 The Boundary Condition

The solvent plays an important role in the structural and dynamical properties of macromolecules in solutions. For this reason, it is important to perform simulations of these solutes using reliable solvent model. Water is the most common solvent used for MD simulations. Several water models have been proposed in the last three decades for MD simulations [52]. Only a few of them are commonly used to study biopolymers in solution [28]. The most common models are the SPC [19] (or SPC/E [53]) and TIP4P [20] water models. Most of the force field parameters of biomolecules have been optimized in combination with these models. In a MD simulation the use of any sort of confinement walls for the simulation box (even with a large one) would introduce an artificial environment with properties much different from bulk conditions. The solution to this problem is the use of the so-called *periodic boundary conditions (PBC)* [10]. In a two-dimensional system, these conditions are analogous to those adopted in video games such us the famous Asteroids in which either the spaceship or the asteroid that leaves from one side of the screen reenters from the opposite side. In this case, the space topology corresponds to moving the objects on a torus surface (see Fig. 6.3a). In the case of a three-dimensional simulation box, it corresponds to the surface of a hyper-torus surface. In PBC conditions, a solute molecule is uniformly surrounded by solvent molecules as in a real bulk conditions.

Simulation boxes can have any shapes as long as they are space-filling ones. The cube, the truncated octahedral, and the truncated dodecahedrons are shape

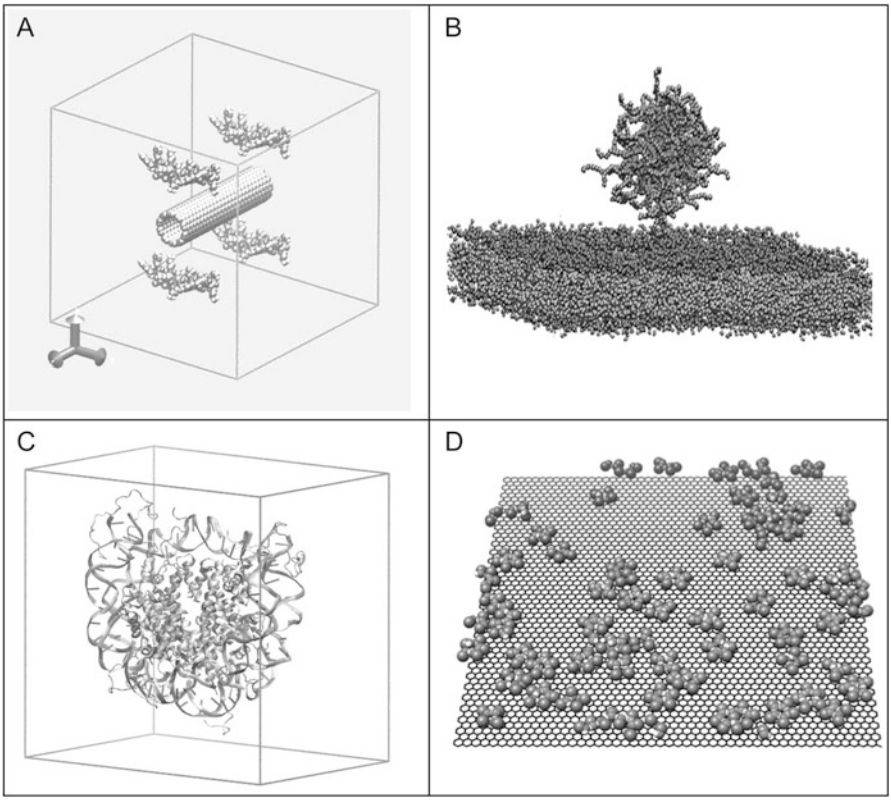

Fig. 6.2 Some examples of starting conformations for different molecular systems. (**a**) An antimicrobial peptide interacting with single-walled carbon nanotubes [48], (**b**) a polymeric micelle on a lipid bilayer [49], (**c**) nucleosome core particle in water [50], and (**d**) methanol molecules on graphene [51]. For clarity, solvent molecules are not shown

geometries normally adopted for simulation boxes listed in descending order of relative volume occupancy (see Fig. 6.3b, c, d).

Once the shape of the box has been chosen, the atomic coordinates of the solute are centered in the box, and the remaining empty volume is filled uniformly with solvent molecules. The initial coordinates of solvent molecules are generated geometrically by superposition of an equilibrated solvent box and removing those molecules overlapping the solute.

The resulting system is energy minimized, usually using the steepest descent and the conjugate gradient algorithm [7]. This procedure is used to remove close contacts between atoms of geometrically generated solvent molecules and those of the solute. A close contact would produce a high energy configuration might cause a numerical integration failure at the starting of the MD simulation. Therefore, it needs to be relaxed to a lower energy state by moving the coordinates of atoms to new lower energy positions by the energy minimization procedure.

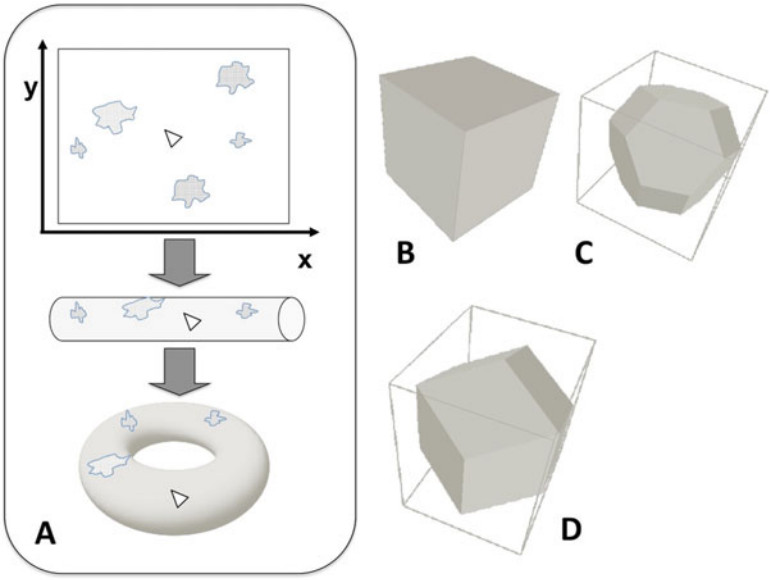

Fig. 6.3 (**a**) The correspondence of two-dimensional PBC conditions of the video game asteroids with the surface of a torus. Different space-filling shapes used in MD simulations: (**b**) cubic (volume = V), (**c**) rhombic dodecahedra (volume = 0.707 V), and (**d**) truncated octahedral (volume = 0.770 V)

6.3.4 The Integration of the Equations of Motion

Once the system is energy minimized, it is possible to run the MD simulation. More than three centuries ago, Isaac Newton published the famous three laws of mechanics in his masterpiece *Philosophiae Naturalis Principia Mathematica*. The same laws, formulated to explain the motion of planets and stars, turn out to be also useful to describe the dynamics of the molecular world. The second Newton's law states that the force ($\mathbf{F}_i$), acting on the ith atom of the system located at position (r_i) and velocity ($\mathbf{v}_i$), is equal to the mass (m_i) of the atom multiplied for its acceleration ($\mathbf{a}_i$). The force is also equal to the gradient of the potential energy by the equation:

$$\mathbf{F}_i = m\mathbf{a}_i = m\frac{d^2\mathbf{r_i}}{dt^2} = -\frac{\partial V}{\partial \mathbf{r}_i} \tag{6.3}$$

This is a second-order differential equation, that, being known the initial conditions of the system (position and velocities of the atoms), can be integrated to obtain new positions and velocities at time $t + dt$. The algorithms that perform such integration are well documented in different textbooks [9–12, 14] and reviews [7]. In most of the programs for MD simulation, a variation of the Verlet's method,

known as *leapfrog*, is normally used for its simplicity, stability, and efficiency [7, 10–12]. In this method, the final equations of motion are given by the formulas:

$$\begin{aligned} \mathbf{r}_i\left(t+\frac{1}{2}\Delta t\right) &= \mathbf{r}_i(i)+\mathbf{v}_i\left(t+\frac{1}{2}\Delta t\right)\Delta t \\ \mathbf{v}_i\left(t+\frac{1}{2}\Delta t\right) &= \mathbf{v}_i\left(t-\frac{1}{2}\Delta t\right)\Delta t+\mathbf{a}_i(t)\Delta t \end{aligned} \tag{6.4}$$

It is important to note that the velocities and the positions of the atoms are calculated at half integration time step ($\Delta t/2$) using the acceleration $a_i\ (t)$. The initial velocities of every atom are randomly assigned by sampling a Maxwell's velocity distribution at the temperature of the simulation. The temperature of the system is calculated from its average kinetic energy (K) with the relation

$$T=\frac{\langle K\rangle}{3k_{\mathrm{B}}}=\frac{\sum_{i=1}^{N} m_i v_i^2}{3Nk_{\mathrm{B}}} \tag{6.5}$$

where N is the number of atoms and k_{B} is the Boltzmann constant and m_{i} is the mass of the ith atom.

6.3.5 Control of Temperature and Pressure

Experimental data are collected in conditions of controlled temperature and pressure. Therefore, a MD simulation needs also to correctly reproduce these conditions in order to produce a realistic model of the system [10]. These conditions can be obtained by coupling the simulated system with an external thermostat and barostat that keep constant temperature and pressure, respectively. Among the methods for coupling the simulated system to an external thermostat, the Berendsen [54] and the Nose-Hoover thermostats [55] are generally used. For the pressure, again the Berendsen [54] and the Parrinello-Rahman [10] barostats are usually applied. Accordingly to the capability to reproduce a correct statistical canonical ensemble, these methods are either approximate or exact. For example, the Berendsen's thermostat is an approximate method since it does not rigorously produce a statistical thermodynamics ensemble but just a good approximation. However, it is very easy to implement in a program for MD simulations [11, 31]. A recent variant of this thermostat, proved to rigorously produce a correct statistical ensemble [56], is replacing the Berendsen's method.

6.4 Running a Simulation

We have now all the ingredients to start a MD simulation. In order to adjust the system density to a correct value, a preliminary equilibration of the system is necessary. The length of the equilibration depends on the size of the system. Normally, a few hundred picoseconds are sufficient for most cases. To avoid possible artificial structural variation of the solute during the equilibration procedure, its atomic coordinates are restrained to a reference position (e.g., the starting structure) by positional restraints, *viz*. harmonic potentials that keep atomic positions vibrating around the reference positions. In this way, solvent molecules can redistribute all around the solute and equilibrate the density of the total system to the expected value. The second step of the equilibration procedure is the structural relaxation of the solute in the solvent. This task is achieved either by progressively heating the system from a low temperature up to the target temperature at which the simulation will be carried out, or by progressively weakening the force constants of the positional restraint potentials. Once the system has been equilibrated, it is ready for the production simulation run(s). The length and number of these simulations depends on the size of the system and property of the investigated phenomenon.

The video game industry is providing a huge benefit to computer simulations by incessantly producing low-cost graphic cards based on parallel graphical processing units (GPU) with increasingly astounding parallel capabilities [57, 58]. Nowadays small molecular systems (up to 20–40 k atoms) can be studied on time scale of hundreds of nanoseconds or even microseconds in relatively short computational time and with inexpensive PC equipped with GPU cards.

Several programs for MD simulations have been developed from different academic groups, and most of them are freely accessible as open-source software. In Table 6.3, the most used MD programs are listed. They have similar basic features but they can differ in their structure and usage. Separate programs for preparing and analyzing simulations compose packages like GROMACS. In others, as for example CHARMM, a single monolithic program performs both the simulation and the analysis of the trajectory. All the packages offer the possibility to run simulations on parallel computers. The programming languages used for the different packages can also be relevant when you want to implement in them new methods. The oldest MD programs as AMBER, CHARMM, and GROMOS have been written in FORTRAN language. More recent ones use the C (GROMACS) and C++ languages (NAMD and GROMOS05).

Table 6.3 List of the most common packages for molecular dynamics simulations and their repository websites

Name	Website
AMBER	http://amber.scripps.edu/
CHARMM	http://www.charmm.org/
GROMACS	www.gromacs.org
GROMOS	http://www.igc.ethz.ch/gromos/
NAMD	http://www.ks.uiuc.edu/Research/namd/
LAMMPS	http://lammps.sandia.gov

6.5 Enhanced Sampling Methods

6.5.1 Steered Molecular Dynamics

The steered molecular dynamics (SMD) method is used to study processes occurring in nonequilibrium conditions like, for example, ligand binding/unbinding to proteins, domain motion, protein folding, and percolation into lipid bilayers [59, 60]. SMD provides a mean to accelerate processes by applying external forces that lower the energy barrier. This methodology simulates experimental single-molecule manipulation techniques such as atomic force microscopy (AFM) [61]. The method consists in applying an external time-dependent force to the system to steer it along a particular degree of freedom. However, due to computational limitation a quantitative comparison with the experimental data is limited by the fact that the applied pulling force generates a displacement velocity that is too fast compared to the one used in the AFM experiment. Nevertheless, the SMD can produce results that can be used to support and help understanding experimental data. Moreover, recent theoretical progress in nonequilibrium thermodynamics are providing new to extract quantitative thermodynamics data from nonequilibrium SMD simulations [62, 63].

6.5.2 Umbrella Sampling

Accurate determinations of energy barriers are usually performed using the umbrella sampling (US) method [9, 14]. The US consists of a set of N separate MD simulations in which a harmonic potential is applied, for example, between the center of mass of the target molecule and a reference group of atoms. The applied umbrella potential

$$U_{bias}(\xi) = \frac{1}{2} K_i (\xi - \xi_i)^2 \tag{6.6}$$

restrains the molecule along the reaction coordinate (ξ) at a distance ξ_i (sampling point) with a force constant of K_i. In each simulation, the value of the distance ξ_i is changed from a maximum value corresponding to the molecule in a given state or environment (e.g., in the bulk solvent phase) to a minimum one at which the molecule is in another state (e.g., in the solvation shell of the solute). From each simulation at sampled position i along ξ, a histogram is calculated representing the probability distribution, $P(\xi_i)$, of conformations along ξ biased by the umbrella potential. The energy profile along the reaction coordinate, called the Potential of Mean Force (PMF), is then calculated from umbrella sampling histograms using the weighted histogram analysis method (WHAM) [65]. This method is based on all the

probability distributions obtained at all the sampling points along ξ. The PMF is given by weighting the these distributions as

$$\mathrm{PMF}(\xi_i) = -k_\mathrm{B}T\ln[\sum_i P(\xi_i)e^{-U_{bias}(\xi_i)/k_BT}] \tag{6.7}$$

where k_B is the Boltzmann constant and T is the temperature of the simulation. PMFs are usually calculated along distances, but other type of reaction coordinates (*viz*. angles) can be used. The quantitative agreement with the experimental data depends by the number and length of the sampling simulations [66]. Therefore, it is important to check if the reaction coordinate is well sampled and the PMF converge at the simulation length.

The US method requires an initial estimate of the reaction pathway to obtain the starting coordinates for the calculations that in some can be generated using the SMD method. Finally, other methods have been proposed trying to overcome this limitation as the *metadynamics*, adaptively biased MD, adaptive reaction coordinate forces and local elevation umbrella sampling [8].

6.6 Analysis of the Trajectories

The analysis of an MD simulation trajectory consists of extracting different structural, thermodynamic, and dynamical properties. Part of these data is usually compared with available experimental data to assess the quality of the model. Once the model is compellingly validated, it is further used to explain and predict properties or processes difficult to measure with experimental methods. The properties to compare are extracted from MD trajectories, in the approximation of equilibrium statistical mechanics condition, using averages and fluctuations of positions, velocities, and energies of the molecules. According to the so-called *ergodic hypothesis* [10], these quantities are representative of a statistical mechanics ensemble if calculated from trajectories long enough to extensively explore the conformational space of the molecular system. An extensive sampling of the entire conformational space of large molecular systems, as, for example a random polymers is currently impossible since the number of possible configurations grows very quickly with the number of units. However, for molecules (for example biopolymers) having conformations constrained in their tridimensional functional structures, a good exploration of their folded state can be feasible though it can be still computational demanding. Therefore, it is important to bear in mind that these simulations usually give an approximate estimation of the properties of the molecular system under investigation.

MD simulations are used to estimate structural, dynamical, and thermodynamics properties of molecular systems. The first ones are evaluated using atomic coordinates of single conformations or their average along the trajectory. The second ones are derived from atomic velocities and coordinates. Finally, the last ones are obtained from averages and fluctuations of different mechanical quantities

Table 6.4 Some examples of experimental data that can be compared with MD simulations

Physical properties	Experimental methods	Gas	Solution	Solid	Surface
Structural					
Positions, size	X-ray diffraction, neutrons, electrons, atomic force microscopy	✓		✓	✓
Distance	Nuclear magnetic resonance (NMR), fluorescence (FRET), and X-ray (EXAFS) spectroscopies		✓	✓	✓
Dynamics					
Debye-Waller factors	X-ray diffraction, neutrons, electrons	✓		✓	✓
Relaxation, contact	NMR, FRET, EXAFS		✓	✓	✓
Vibration frequencies	Infrared/Raman spectroscopies	✓	✓	✓	✓
Spin relaxation, diffusion	NMR		✓	✓	✓
Contacts	Time-resolved laser spectroscopies		✓	✓	✓
Thermodynamics					
Density	Densitometry		✓	✓	✓
Enthalpy of evaporation, heat capacity	Calorimetry		✓		
Viscosity	Viscosimetry		✓		✓

(as energy, coordinates, and forces). These properties can be directly compared to experimental data (see Table 6.4 for some examples). The following paragraphs will give an idea on how some of these properties are calculated using simulations. For this purpose, three MD simulation studies will be used as examples:

1. Structure and dynamics of the protein TEM-1 β-lactamase in water. This is a bacterial enzyme responsible for the hydrolysis of β-lactam and cephalosporin antibiotics. The PDB structure 1BTL was used in the simulations [67].
2. Adsorption of polyether-based block copolymers polymers on carbon nanotubes in water [68].
3. Percolation of polyether-based block copolymers through a lipid bilayer [69, 70].

The simulations of these systems have been performed using the program *Gromacs*, and more details of these studies can be found in the original publications.

6.6.1 Structural Properties

6.6.1.1 Molecular Graphics

The visualization of molecular structure is a powerful tool to analyze the complex dynamics of molecular systems. The quality of the available graphical programs adds a touch of artistic beauty to the scientific content of the molecular structure representation. This artistic impression can, however, be misleading. In fact, wrong molecular models can look gorgeous as correct ones. Hence, caution should be taken in using only a graphical representation as criteria of analysis of a molecular structure. Still, the visualization of molecular dynamics trajectories is the quickest way to perform a first inspection of the structural behavior of the system. There are plenty of programs for molecular visualization (for a list see *wikipedia.org/wiki/List_of_molecular_graphics_systems*). A popular program for molecular visualization is the VMD (www.ks.uiuc.edu/Research/vmd) [71]. This program offers both an interactive user-friendly interface and a script-oriented use for more complex analyses. Most of the molecular representations in this chapter have been created using this program.

6.6.1.2 The Root Mean Square Deviations

The root mean square deviation (RMSD) measures the variation of the macromolecular structure with respect to a reference one [7, 9, 12]. Figure 6.4a showed the superimposition of one frame of an MD simulation (in gray) and the reference structure (in black). The arrows indicate the distances between pairs of corresponding Cα atoms used to calculate the RMSD. The average value of these deviations is calculated at each time frame of the MD trajectory as

$$\mathrm{RMSD}(t) = \sqrt{\frac{1}{N}\sum_i \left(\mathbf{r}_i(t) - \mathbf{r}_i^{\mathrm{ref}}\right)^2} \tag{6.8}$$

where N is the number of selected atoms (e.g., the Cα atoms), $\boldsymbol{r}_i(t)$ are their coordinates, and $\boldsymbol{r}_i^{\mathrm{ref}}$ are the corresponding atoms from a reference structure (e.g., the crystallographic one). In Fig. 6.1b, as an example, the RMSD curves obtained from the simulation of the TEM-1 protein at two different temperatures are shown. The simulation at 300 K (black curve) shows a deviation from the crystal structure of 0.1 nm due to the different environment (solution instead of crystal) and to the approximation of force field model. Depending on the size of the protein, Cα RMSD within 0.2 nm are usually considered acceptable. The figure shown also as the increase of the temperature destabilizes the structure by increasing the RMSD value. The unrealistic value of the temperature (450 K) is purposely used to induce an unfolding of the protein within the simulation time.

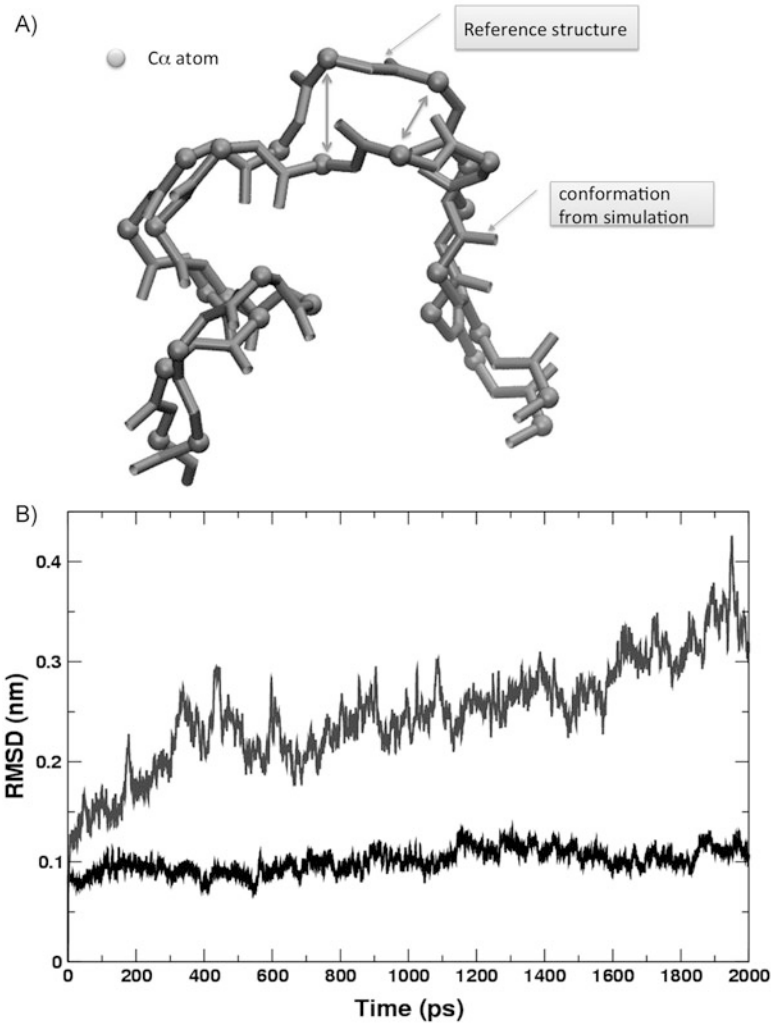

Fig. 6.4 (**a**) Example of superimposition of an MD frame structure (in *gray*) on the reference one (in *black*) using a translation and rotation fit procedure. Some distances between corresponding Cα atoms are indicated. (**b**) Example of backbone RMSD from the simulation of the same protein at two different temperatures (300 K, *black*; 450 K *gray*). The backbone of the protein structures in each analyzed simulation frame has been overlapped to the corresponding atoms of the crystallographic starting structure by a translation and rotation fit procedure. Adapted with permission from [4]

A more detailed analysis of the variation within the protein structure is performed by calculating the average along the trajectory of the RMSD of each atom (or group of atoms) as

$$r\mathrm{RMSD}(i) = \sqrt{\frac{1}{N_\mathrm{c}} \sum_t \left(\mathbf{r}_i(t) - \mathbf{r}_i^{\mathrm{ref}}\right)^2} \tag{6.9}$$

where N_c is the number of analyzed conformations of the simulations that depends on the sampling rate of the MD trajectory. Using a time step of 2 fs, a trajectory of 2 ns produces 10^6 of conformations, but usually only 10^4 or less are used for the analysis. The rRMSD is used to identify amino acids (residues) of the protein having the largest average deformations from a reference structure. In Fig. 6.5, the rRMSD of the TEM-1 protein calculated in the last 1 ns of the simulation is shown. The gray bars on the bottom of the figure indicate the location of α-helices and β-strands secondary structure in the protein. Secondary structure elements can be identified using programs such as DSSP [72] or STRIDE [73]. These programs use hydrogen-bond pattern and/or Ramachandran plot propensity of the ϕ/ψ angles to classify each residue. Using the secondary structure bars as eye guide, it is evident that the higher peaks in the rRMSD curve are mainly located in correspondence of regions of the protein that connect secondary elements (namely, loops or turn regions). At higher temperature, the structural variations of the protein increase by shifting up the rRMSD curve and producing other peaks in correspondence of partially unfolded secondary structure elements.

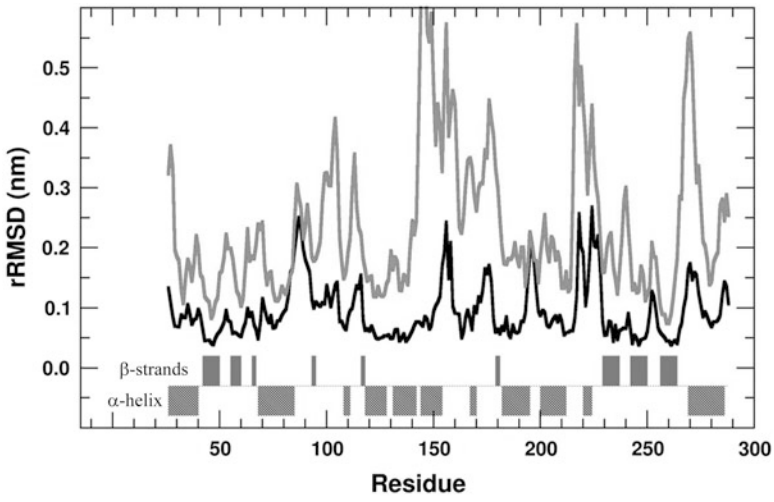

Fig. 6.5 Example of backbone RMSD per residue output for the protein TEM-1 at two different temperatures (300 K, *dark line*, and 450 K, *gray line*). The bars on the bottom indicate the position of the secondary structure elements of the protein. Reproduced with permission from [4]

6.6.1.3 The Root Mean Square Fluctuation

The root mean square fluctuation is a measure of the dynamics of each atom or residue in the protein structure [7, 9, 12]. It is calculated for single or groups of atoms from the fluctuations of atomic positions along the MD trajectory using the equation:

$$\mathrm{RMSF}(i) = \sqrt{\frac{1}{N_c}\sum_t \left(\mathbf{r}_i(t) - \langle \mathbf{r}_i \rangle\right)^2} \tag{6.10}$$

In Fig. 6.6, an example of backbone RMSF from the TEM-1 simulation is reported. The correspondence between the region with higher mobility (higher peaks) and the loop regions of the structure is evident. α-helix and β-strand regions are characterized by a significantly lower mobility due to a stronger stabilization by the network of hydrogen bonds.

6.6.1.4 Solvent Accessible Surface Area

The definition of molecular surface is based on the approximation of the atomic shape as spheres of van der Waals radius. Using this approximation, it is possible to calculate the solvent accessible surface (SAS) of a molecule by rolling over the van der Waals surface a sphere of radius equal to that of a solvent molecule (see

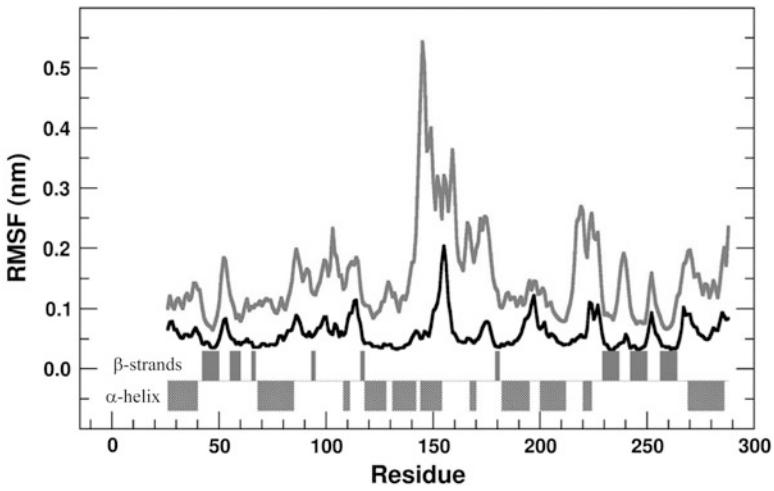

Fig. 6.6 Example of RMSF output for the protein TEM-1 at two different temperatures (300 K, *dark line*, and 450 K, *gray line*). The bars on the bottom indicate the position of the secondary structure elements of the protein. Reproduced with permission from [4]

Fig. 6.7a for a cartoon of the method). The bottom picture shows the 3D printed SAS of the TEM-1 beta lactamase. The STL file for the printer (a WANHAO Duplicator i3 Plus, using a PLA 1.75 mm filament) was generated using the NIH 3D Print Exchange service (3dprint.nih.gov). The SAS surface can be colored according to the polarity of the amino acid that allows to easily differentiate hydrophobic and hydrophilic patches on the surface of the protein associated with functional properties of the protein.

The principal driving force for biopolymer folding is the burying of hydrophobic residues in the core of the three-dimensional structure. The residues exposed on the protein surface are mainly hydrophilic in nature. The compact structure of a folded protein also reduces the surface exposed to the solvent. Therefore, the SAS area graph can be used to evaluate the stability of the protein during the course of the simulation (see Fig. 6.7b). An increase of the hydrophobic area usually indicates that the protein is unfolding and thus it is exposing the hydrophobic residues that are in the interior of the protein.

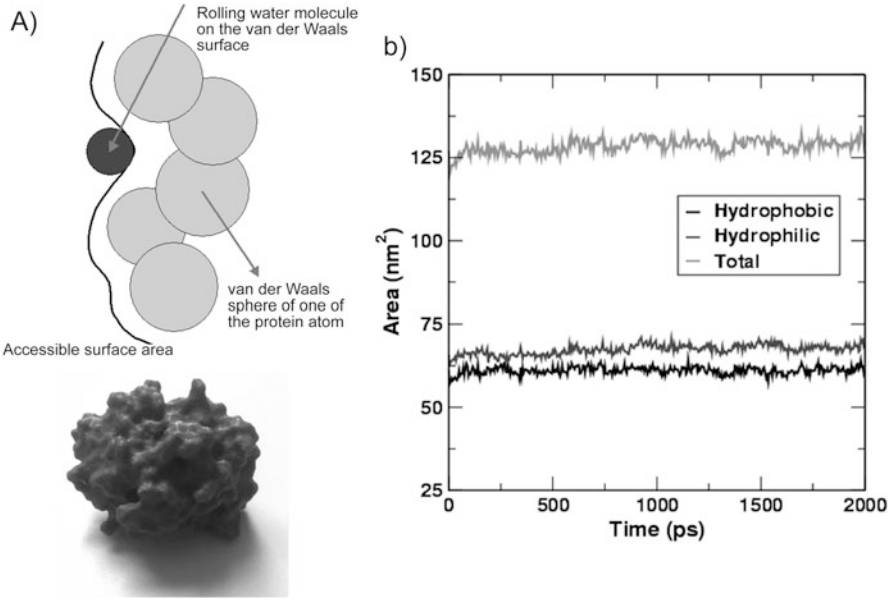

Fig. 6.7 (**a**) *Top*: Cartoon showing the calculation of SAS area. The probe sphere is rolled over the van der Waals surface of the atoms in the molecule. The trajectory of the center of the probe is used to define the surface. *Bottom*: the 3D printed SAS of the TEM-1 β-lactamase. (**b**) Time-series of the different SASA components from the 300 K simulation of the TEM-1 β-lactamase. Adapted with permission from [4]

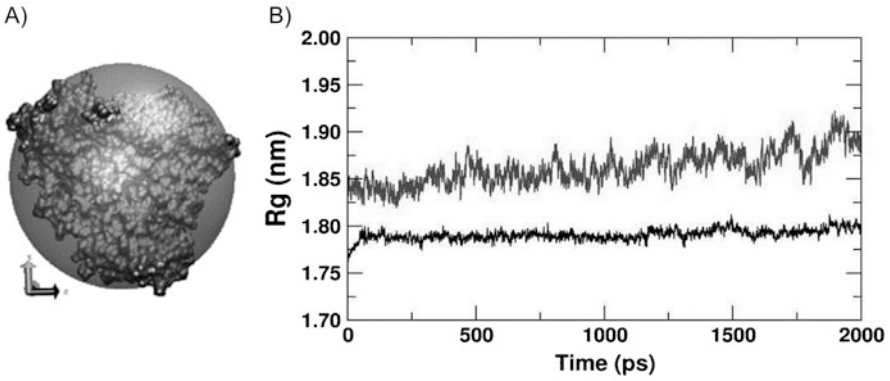

Fig. 6.8 (**a**) The radius of gyration is defined as the average sphere having a uniform mass distribution equal to the total protein mass. (**b**) Example of time course of radius of gyration from the simulation of TEM-1 at two different temperatures (300 K *black*, 450 K *gray*). Reproduced with permission from [4]

6.6.1.5 The Radius of Gyration

The mass distribution of a large molecular system can be evaluated using its radius of gyration (R_g) that corresponds to the radius of a compact sphere having the mass of the protein (see Fig. 6.8a). The R_g is calculated using the following equation:

$$R_g(t) = \sqrt{\frac{\sum_i m_i(\mathbf{r}_i(t) - \mathbf{r}_{com})^2}{\sum_i m_i}} \tag{6.11}$$

where m_i and $\mathbf{r}_i$ are the atomic mass and the position of the ith atom and $\mathbf{r}_{com}$ the position of the center of mass of the molecule, respectively. The R_g provides information on the change in the mass distribution of the molecule during the simulation. In Fig. 6.8b, an example of R_g curve along the TEM-1 simulation is shown. The progressive increase of the curve for the simulation at 450 K indicates an expansion of the protein volume due to the denaturation process.

6.6.1.6 Distribution of Molecules on Surfaces of Nanomaterials

The solvent organization in the bulk phase or around a solute is characterized by structural correlations that can be observed or measured using different experimental techniques. The distribution of water and cosolvent molecules around proteins and peptides has important implication for industrial and medical applications. For example, the stability and catalytic activity of enzymes in nonnatural environments are of fundamental importance for their application in biocatalysis. From MD

simulations, it is possible to obtain detailed information about the structure of the solvent by means of correlation functions [10]. Here, we will see some example of these functions. A more detailed overview on MD simulation methods to study biological molecules in organic solvents can be found in a recent review [74] and book chapter [5] by the author.

The distribution of solvents or other solutes on surfaces and around molecules of complex shapes can be analyzed using spatial distribution function (SDF). This is a three-dimensional probability distributions, and it is given by the expression [75]

$$g_{\mathrm{AB}}(i,j,k) = \left\langle \frac{\frac{1}{N_{\mathrm{A}}} \sum_{n_a=1}^{N_{\mathrm{A}}} \sum_{n_b=1}^{N_{\mathrm{B}}} I_{ijk}\left[\mathrm{R}_{n_a}^{\mathrm{A}}\left(r_{n_b}^{\mathrm{B}} - r_{n_a}^{\mathrm{A}}\right)\right]}{\rho_{\mathrm{B}} l^3} \right\rangle \tag{6.12}$$

where i, j, and k index the various boxes in the mesh, N_{A} denotes the number of molecules of type A, and n_{A} is the molecule index running from 1 to N_{A}. ${r_{nA}}^{A}$ and ${r_{nB}}^{B}$ are the position vector of the molecule numbered n_{A} of type A and n_B of type B, respectively, in the laboratory frame, and ${R_{\mathrm{na}}}^{\mathrm{A}}$ is the rotational transformation from the laboratory frame to the local frame of molecule n_A. The angular brackets denote time average. I_{jkl} is the indicator function, defined as

$$I_{ijk} = \begin{cases} 1 & \mathbf{r} \in \left[l\left(i-\frac{1}{2}\right), l\left(i+\frac{1}{2}\right)\right] \times \left[l\left(j-\frac{1}{2}\right), l\left(j+\frac{1}{2}\right)\right] \times \left[l\left(k-\frac{1}{2}\right), l\left(k+\frac{1}{2}\right)\right] \\ 0 & \text{elsewhere} \end{cases}$$

with l is the edge of the boxes.

In the case of a solute molecule in a solvent, the SDF is calculated by dividing the space surrounding a molecule (or a single atom in a molecule) into a mesh of cubic boxes. At each time step, the mesh is centered on the selected molecule, and the principal axes of the mesh are chosen to coincide with those of the molecule. Hence, the number of solvents in the boxes surrounding the reference molecule is counted. Finally, the content of the box is averaged over the time (i.e., the number of frames used) and divided by the box volume and the number density of the system. In the case of a solute with a planar structure, as, for example, the surface of the graphene, the mesh is created on the top of its surface, and it is extended into the bulk solvent. In Fig. 6.9b,c, an example of the SDF representing the distribution of the atom of four antimicrobial CA-MA peptides (see Fig. 6.9a) adsorbed on the surfaces of a graphene nanosheet (GNS) is shown.

In the case of cylindrical nanomaterials as carbon nanotube (CNT), the distribution of the solvent and/or surfactant molecules can be analyzed using the cylindrical radial distribution function (cRDF), the cylindrical cumulative coordination number, and the density profile along the nanotube axial direction.

The cRDF is calculated using a cylindrical coordinate system of coordinates (r, φ, z) with r the radial distance from the axis of the nanotube, φ the azimuthal angle, and z the position along the axis of the nanotube (see right panel in Fig. 6.10).

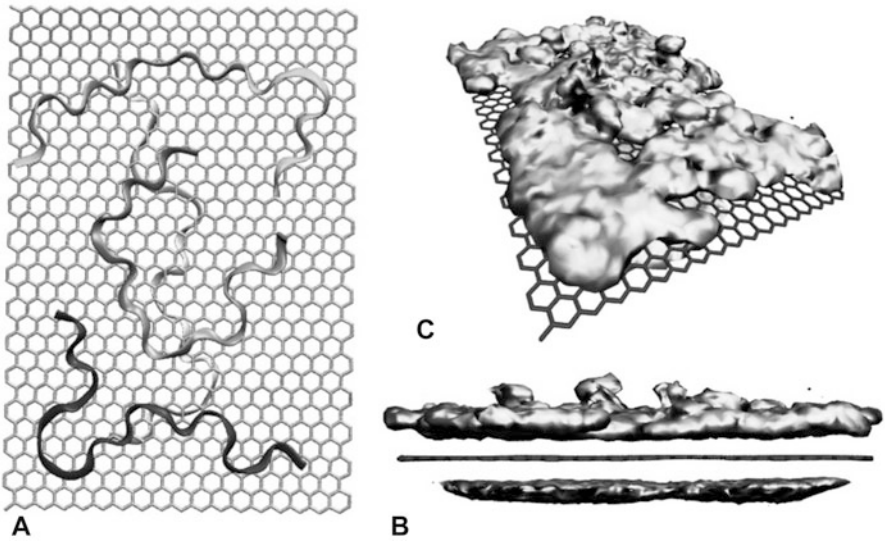

Fig. 6.9 The four CA-MA peptides on the GNS surface. (**a**) *Top view* of the configuration at 350 ns, the peptide is shown in ribbon representation. (**b**, **c**) *lateral view* and *top (perspective) view* of the spatial density distribution of the peptides on the GNS surface. The average GNS conformation is reported as well. Reproduced with permission from [48]

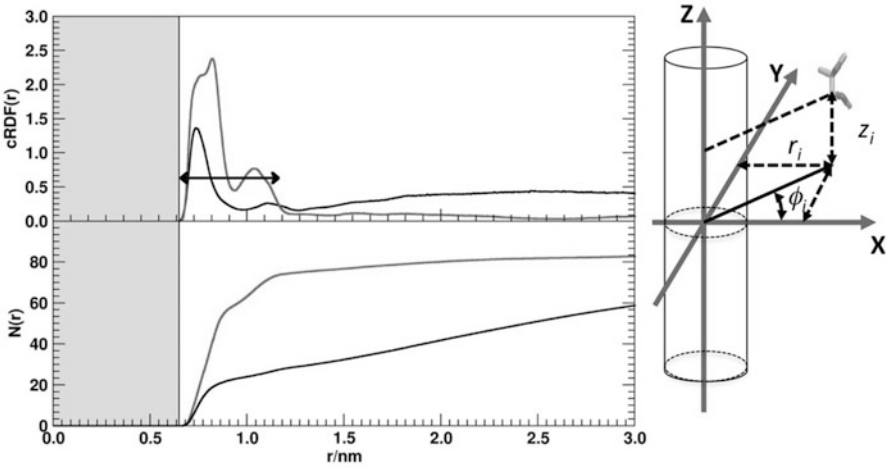

Fig. 6.10 *Left*. Plots of the cRDF (*top*) and $N(r)$ of EO (*black curve*) and PO (*gray lines*) monomers (*bottom*) of the poloxamer L64 versus the SWCNT (5,5) (*gray bands*) axis. The *double arrow* in the cRDF plot indicates the extension of the shell (PO monomers) region around the SWCNT. *Right*. Cylindrical coordinate system (r, φ, z) used for the calculation of the cRDF (adapted with permission from [68])

The origin of the reference frame is at the center of mass of the SWCNT. The interior region of the SWCNT is defined as the volume V_0 of a cylinder of height h given by the nanotube length and with a base of diameter d_0 equal to $V_0 = \frac{\pi}{4} d_0^2 h$. The volume of the nanotube shell is defined by the volume of the hollow cylinder of diameter d around the SWCNT external surface equal to $V_{hc} = \frac{\pi}{4} d^2 h - V_0$. Solvent/surfactant molecules are considered to be inside the SWCNT or in the shell region on its surface if its center of mass is located inside the one of the above-defined volumes. The cylindrical cumulative coordination number $N(r)$ gives the number of molecules within a distance r from the nanotube axis, and it is calculated using the integral [76]

$$N(r) = \int_0^r \int_0^{2\pi} \int_{-z_1}^{z_2} r' dr' d\varphi' dz \rho(r', \varphi', z) \tag{6.13}$$

with r the radial distance from the nanotube axis; $-z_1$ and z_2 the positions, with respect to the axis center, of the two SWCNT extremes; and $\rho(r', \varphi', z)$ the local number density of solute molecules. Note that only the molecules having the position of the CoM in the range $z_1 \leq z \leq z_2$ are used in the calculation of the $N(r)$ (as of the cRDF). The cRDF is defined as

$$cRDF(r) = \frac{N(r + \Delta r, h/2) - N(r, h/2)}{2\pi r h \Delta r} = \frac{1}{\rho_0} \rho(r, \varphi, z)_{\varphi, z'} \tag{6.14}$$

where Δr is a small increment of the radial distance, $\langle \ldots \rangle_{\varphi, z}$ is an average over $(0 \leq \varphi < 2\pi)$ and $(-1.5 \leq z \leq 1.5)$ at given r, and ρ_0 is the density of the solvent in the bulk. The $cRDF(r)$ is normalized in such a way that $cRDF(r) \rightarrow 1$ as $r \rightarrow \infty$. It gives the number of molecules of polymer units in the cylindrical volume within the distance r from the SWCNT axis.

In Fig. 6.10, examples of cRDF and $N(r)$ for ethylene oxide (EO) and propylene oxide (PO) units of the L64 polymer ($EO_{13}PO_{30}EO_{13}$) as a function of the distance from central axes of SWCNT (5.5) are reported. From the peak size of the cRDFs (top graph), it is evident that there is a higher tendency of PO than EO units to bind the SWCNT surface. The cRDF for both EO and PO units is multimodal with a large peak at ~0.75 nm and a smaller one at ~1.0 nm. The $N(r)$ curve of PO monomers shows a rapid increase within 0.65 nm from the SWCNT surface, followed by a plateau. On the contrary, the curve for EO monomers, after an initial fast growth, increases almost linearly indicating the dispersion of the unit in the bulk solvent (see [68] for details).

It is also possible to calculate the density profile $\boldsymbol{\zeta(z)}$ along the nanotube axial direction [76] that it is defined as

$$\zeta(z) = \frac{1}{\pi \rho_0 r^2} \int_0^r \int_0^{2\pi} r' dr' d\varphi' dz \rho(r', \varphi', z) \tag{6.15}$$

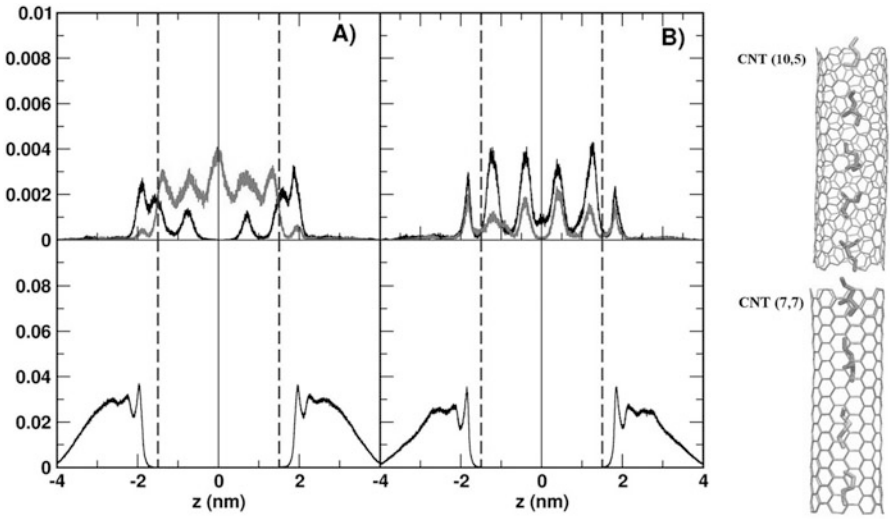

Fig. 6.11 The density profile along the SWCNT axial direction, $\zeta(z)$, of DME, DMP (*top graphs*, black and gray lines, respectively), and water (*bottom graph*) molecules distributed inside the SWCNT with chiral indices (**a**) (10, 5) and (**b**) (7,7), respectively. The dashed lines indicate the SWCNT boundaries. At the right side are shown DME and DMP molecules inside the SWCNT (10, 5) and SWCNT (7, 7) (reproduced with permission from [68])

and which calculate the density averaged along the cylindrical shell region between the nanotube axis ($r' = 0$) and the nanotube radius ($r' = r$).

In Fig. 6.11, an example of application of the density profile $\zeta(z)$ is shown. In this case, $\zeta(z)$ is used to study the distribution of dimethoxyethane (DME) and dimethoxypropane (DMP) inside SWCNT (10,5) and (7,7). The regular spaced peaks of $\zeta(z)$ graphs on the left evidenced a stable file alignment for both DME and DMP molecules. In the right panel of the same figure, two examples of aligned DME and DMP molecules into the SWCNTs are shown. More details on this study can be found in [68].

6.6.2 Interaction of Polymers with Lipid Bilayers

In this paragraph, an example of application of enhanced MD method to study process involving time scale beyond the current capability of MD simulation is reported. The study of the interaction of block copolymer with biological membrane has important application in nanomedicine, and, in particular, in the area of drug delivery systems. Examples from MD simulation studies of the interaction of polymers based on EO and PO monomers with a lipid bilayer will be used to illustrate the analysis of these types of molecular systems [70]. The systems have been studied at both atomistic and coarse-grained levels.

The morphometric properties of the lipid bilayer are important to understand the interaction of polymers on the membrane structure. One important property is the thickness of the lipid bilayer. This can be experimental measured and compared with the model by calculating the average density profile across the membrane from the MD trajectory. If the membrane is oriented parallel to the *x*–*y* plane, then the density profile is calculated using the equation:

$$\rho_M(i) = \left\langle \frac{\sum_{n=1}^{N} I_i p_n}{L_x L_Y \Delta z} \right\rangle \tag{6.16}$$

where i identifies the different slabs, N denotes the number of atoms in the lipid bilayer, Δz is the thickness of the slab used to section the simulation box along z, and p_n is the property of the atoms (number density, mass or number of the electrons) to be averaged. I_i is the indicator function, defined as

$$I_i = \begin{cases} 1 & \mathbf{r} \in \left[\Delta z\left(i - \frac{1}{2}\right), \Delta z\left(i + \frac{1}{2}\right) \right] \\ 0 & \text{elsewhere} \end{cases} \tag{6.17}$$

The electron density profile can be directly compared with small angle X-ray scattering data. In Fig. 6.12a, a snapshot after 500 ns of CG simulation of the block copolymers P85 ($EO_{25}PO_{40}EO_{25}$) and L64 (in dark gray chains) interacting with a

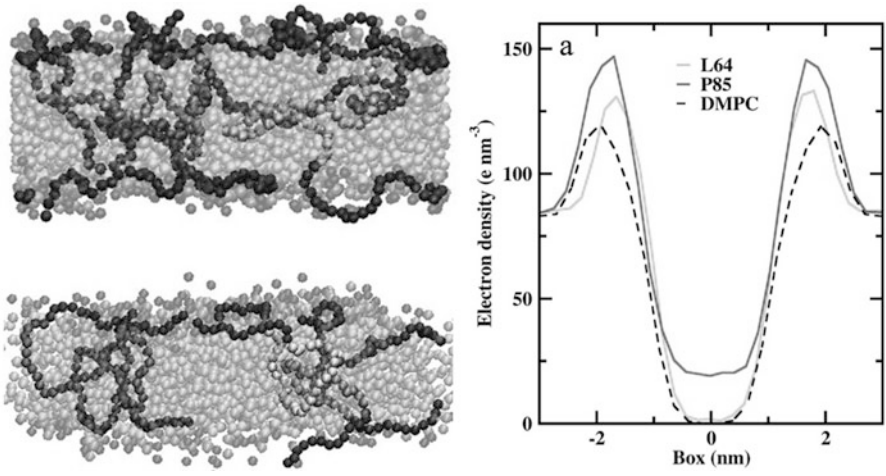

Fig. 6.12 *Left panel*. Snapshots from the simulations of five chains of P85 (*top*) and L64 (*bottom*) with DMPC bilayer. *Right panel*. Electronic density profile obtained from the simulations of DMPC bilayer in the presence of five chains of Pluronics. Detail of the membrane region (*top*) and of the water region (*bottom*). The DMPC curve contains also the water density. Adapted with permission from [46]

lipid bilayer (light gray spheres) is shown. The figure shows a different aggregative tendency for the two types of polymers that is related to the length and contents of the hydrophobic units. In Fig. 6.12b, the calculated electron densities for phosphate head groups, polymer chains, and water from the simulations are shown. The average bilayer thickness (the distance between phosphate head group peaks) were found 6–9% smaller than those for single-chain simulations, evidencing a concentration dependence of the bilayer thinning effect due to the presence of the polymers (see [46] for details).

The energy barrier for the diffusion of the polymer inside the lipid bilayer can be calculated using enhanced MD sampling methods. In particular, combining steered MD with umbrella sampling simulations is possible to calculate the PMF for the permeation of small molecules through a lipid bilayer. As example, some of the results of recent studies [69, 70] using this approach at atomistic level to evaluate the barriers involved in the permeation of a dimyristoylphosphatidylcholine (DMPC) lipid bilayer by polyether-based polymers are reported. The starting conformations for umbrella sampling simulations were generated from SMD simulations. We have studied the DME and DMP, EO and PO dimers (PEO2, PPO2) and trimers (PPO3, PP3), and the poloxamer molecule EO-PO-EO (denoted as Plu1). The different PMF profiles obtained from the US simulations of the molecules are reported in Fig. 6.13.

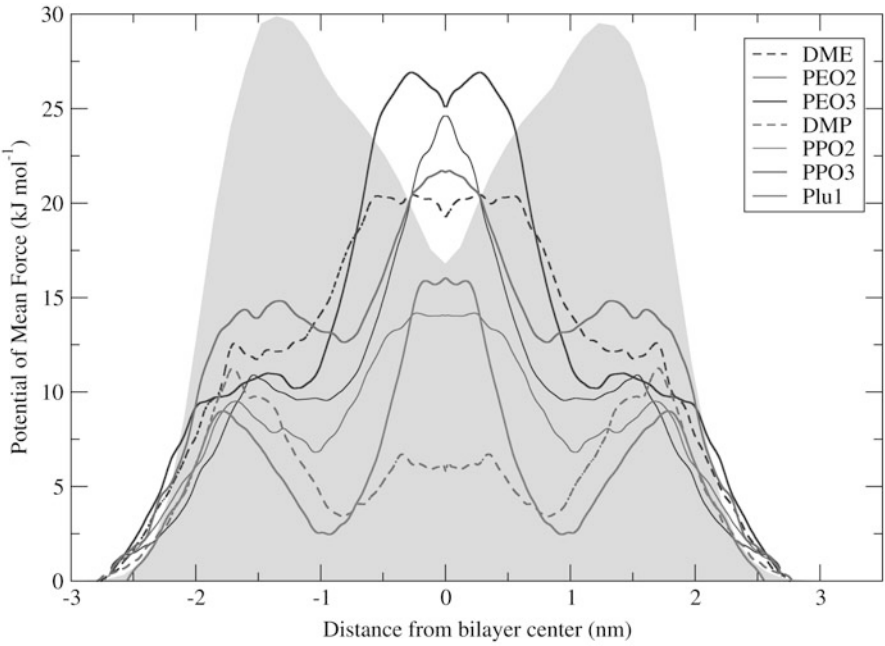

Fig. 6.13 Comparison of PMF profiles of permeation of small polymers using US method. The position of the DMPC bilayer is shown as the gray background. Reproduced with permission from [70]

The graph shows in gray the density profile of the lipid bilayer. The PMF is calculated only for one side of the lipid bilayer, the curve on the other side is obtained by symmetry, and it is reported only for clarity. The PMFs of the different polymers show a gradual increase of the height of the energy barrier for permeation (first peak at the entrance of the lipid bilayer) with the increase of the chain length of the polymers of the same type. It is interesting to note that the bulkier PO chains have lower energy barriers than their corresponding PEO counterparts. We concluded that the relative difference between PEO and PPO could be attributed to the non-bonded and electrostatic energy contributions [69, 70]. Also, the loss of hydrogen bonds with solvent is responsible of the higher PMF barrier for DME/PEO than PPO. Interestingly, the poloxamer Plu1 has lower PMF barrier than both EO_3 (PEO3) and PO_3 (PPO3), though being of comparatively similar length. This suggests that in block copolymer, the hydrophilic-lipophilic balance of the PEO and PPO blocks can facilitate the permeability in lipid bilayer than a PEO or PPO chain of similar length [69].

6.7 Perspectives

The MD simulation method is in constant development to improve its accuracy and extend the range of applications. These improvements will ultimately improve the quality of the MD simulations results to a level comparable to experimental data. One example of development is the improvement of the modeling of electrostatic interactions by accounting for the polarizability effect. Polarizable force fields can, for example, improve the treatment of protonation state of biomolecules in solution by properly reproducing the dielectric conditions in their interior [29].

The other expected development is multiscale methods that will allow exploring systems and phenomena in the scale length up to micrometers and time of micro or milliseconds [49, 77–79]. In this direction, it is beneficial the constant technological development of powerful GPU thanks to the video game industry [57, 58]. It is currently possible to simulate molecular systems containing up to 10^6 atoms for time scales from tens to hundreds of nanoseconds. However, it is likely that in few years this number is going to change of some order of magnitude, making possible to routinely study systems of this size for time length of microseconds [23, 80]. In this way, it will be soon possible to use simulations to design and test complex nanodevices for nanomanufacturing as it is done for macroscopic mechanical and electronic equipment.

References

1. Feynman RP (1960) There's plenty of room at the bottom. Eng Sci 23(5):22–36
2. Lee EH et al (2009) Discovery through the computational microscope. Structure 17 (10):1295–1306

3. Dror RO et al (2012) Biomolecular simulation: a computational microscope for molecular biology. Annu Rev Biophys 41:429–452
4. Roccatano D (2007) Theoretical study of nanostructured biopolymers using molecular dynamics simulations: a practical introduction. In: Nanostructured soft matter. Springer, pp 555–585
5. Roccatano D (2013) Computer simulations of biomolecules in non-aqueous and semi- aqueous solvent conditions. In: Dunn BM (ed) Advances in protein and peptide sciences, vol 318. Science Publishers, Bentham
6. Norberg J, Nilsson L (2003) Advances in biomolecular simulations: methodology and recent applications. Q Rev Biophys 36(3):257–306
7. van Gunsteren WF, Berendsen HJC (1990) Computer simulation of molecular dynamics: methodology, applications, and perspectives. Angew Chem Int Eng Ed 29:992–1023
8. Adcock SA, McCammon JA (2006) Molecular dynamics: survey of methods for simulating the activity of proteins. Chem Rev 106:1589–1615
9. Leach AR (2001) Molecular modelling. Principles and applications, 2nd edn. Prentice Hall, Upper Saddle River
10. Allen MP, Tildesley DJ (1989) Computer simulation of liquids. Oxford University Press, Oxford
11. Frenkel D, Berend JS (2001) Understanding molecular simulation. Academic Press, Cambridge, MA
12. Schlick T (2010) Molecular modeling and simulation: an interdisciplinary guide: an interdisciplinary guide, vol 21. Springer Science & Business Media, New York
13. Marx D, Hutter J (2012) Ab initio molecular dynamics: basic theory and advanced methods. Cambridge University Press, Cambridge
14. Berendsen HJC (2007) Simulating the physical world : hierarchical modeling from quantum mechanics to fluid dynamics. Cambridge University Press, Cambridge, NY, xxvii, 596 p
15. Alder BJ, Wainwright TE (1959) Studies in molecular dynamics 0.1. General method. J Chem Phys 31(2):459–466
16. Rahman A, Stillinger FH (1971) Molecular dynamics study of liquid water. J Chem Phys 55 (7):3336–3359
17. Ryckaert J-P, Bellemans A (1978) Molecular dynamics of liquid alkanes. Faraday Discuss Chem Soc 66:95–106
18. Karplus M (2003) Molecular dynamics of biological macromolecules: A brief history and perspective. Biopolymers 68(3):350–358
19. Berendsen HJC et al (1981) Interaction models for water in relation to protein hydration. In: Pullman B (ed) Intermolecular forces. Reidel, Dordrecht, pp 331–342
20. Jorgensen WL et al (1983) Comparison of simple potential functions for simulating liquid water. J Chem Phys 79(2):926–935
21. Levitt M (1983) Computer simulation of DNA double-helix dynamics. In: Cold Spring Harbor symposia on quantitative biology. Cold Spring Harbor Laboratory Press, Cold Spring Harbor
22. Van der Ploeg P, Berendsen H (1982) Molecular dynamics simulation of a bilayer membrane. J Chem Phys 76(6):3271–3276
23. Freddolino PL et al (2006) Molecular dynamics simulations of the complete satellite tobacco mosaic virus. Structure 14:437–449
24. Duan Y, Harvey SC, Kollman PA (2001) Protein folding and beyond. Wiley-VCH, Weinheim
25. Wang W et al (2001) Biomolecular simulations: Recent developments in force fields, simulations of enzyme catalysis, protein-ligand, protein-protein, and protein-nucleic acid noncovalent interactions. Annu Rev Biophys Biomol Struct 30:211–243
26. Hess B et al (1997) LINCS: a liner constraint solver for molecular simulations. J Comput Chem 18:1463–1472
27. Miyamoto S, Kollman PA (1992) SETTLE: an analytical version of the SHAKE and RATTLE algorithms for rigid water models. J Comput Chem 13:952–962
28. Ponder JW, Case DA (2003) Force fields for protein simulations. In: Protein simulations, pp 27–86

29. Halgren TA, Damm W (2001) Polarizable force fields. Curr Opin Struct Biol 11(2):236–242
30. Yu HB, van Gunsteren WF (2005) Accounting for polarization in molecular simulation. Comput Phys Commun 172(2):69–85
31. Schlick T (2002) Molecular modeling and simulation. An interdisciplinary guide. Springer, New York
32. Dinur U, Hagler AT (1991) New approaches to empirical force fields. VCH Publishers, New York, pp 99–164
33. Oostenbrink C et al (2004) A biomolecular force field based on the free enthalpy of hydration and solvation: the GROMOS force-field parameter sets 53A5 and 53A6. J Comput Chem 25 (13):1656–1676
34. Soares TA et al (2004) Validation of the GROMOS force-field parameter set 45A3 against nuclear magnetic resonance data of hen egg lysozyme. J Biomol NMR 30(4):407–422
35. Case DA et al (2005) The Amber biomolecular simulation programs. J Comput Chem 26 (16):1668–1688
36. Wang JM et al (2005) Development and testing of a general amber force field (vol 25, p 1157, 2004). J Comput Chem 26(1):114–114
37. Wang JM et al (2004) Development and testing of a general amber force field. J Comput Chem 25(9):1157–1174
38. Jorgensen WL (1998) OPLS force fields. In: PVR S (ed) The encyclopedia of computational chemistry. Wiley, Athens, pp 1986–1989
39. Kaminski GA et al (2001) Evaluation and reparametrization of the OPLS-AA force field for proteins via comparison with accurate quantum chemical calculations on peptides. J Phys Chem B 105(28):6474–6487
40. MacKerell AD et al (1998) All-atom empirical potential for molecular modeling and dynamics studies of proteins. J Phys Chem B 102(18):3586–3616
41. Mackerell AD, Wiorkiewiczkuczera J, Karplus M (1995) An all-atom empirical energy function for the simulation of nucleic-acids. J Am Chem Soc 117(48):11946–11975
42. Levitt M, Warshel A (1975) Computer-simulation of protein folding. Nature 253 (5494):694–698
43. Tozzini V (2005) Coarse-grained models for proteins. Curr Opin Struct Biol 15(2):144–150
44. Saunders MG, Voth GA (2012) Coarse-graining of multiprotein assemblies. Curr Opin Struct Biol 22(2):144–150
45. Marrink SJ et al (2007) The MARTINI force field: coarse grained model for biomolecular simulations. J Phys Chem B 111(27):7812–7824
46. Hezaveh S et al (2012) Understanding the interaction of block copolymers with DMPC lipid bilayer using coarse-grained molecular dynamics simulations. J Phys Chem B 116 (49):14333–14345
47. Sagui C, Darden TA (1999) Molecular dynamics simulations of biomolecules: long-range electrostatic effects. Annu Rev Biophys Biomol Struct 28:155–179
48. Roccatano D, Sarukhanyan E, Zangi R (2017) Adsorption mechanism of an antimicrobial peptide on carbonaceous surfaces: a molecular dynamics study. J Chem Phys 146(7):074703
49. De Nicola A et al (2014) Micellar drug nanocarriers and biomembranes: how do they interact? Phys Chem Chem Phys 16(11):5093–5105
50. Roccatano D, Barthel A, Zacharias M (2007) Structural flexibility of the nucleosome core particle at atomic resolution studied by molecular dynamics simulation. Biopolymers 85 (5–6):407–421
51. Zangi R, Roccatano D (2016) Strings-to-rings transition and antiparallel dipole alignment in two-dimensional methanols. Nano Lett 16(5):3142–3147
52. Guillot B (2002) A reappraisal of what we have learnt during three decades of computer simulations on water. J Mol Liq 101(1–3):219–260
53. Berendsen HJC, Grigera JR, Straatsma TP (1987) The missing term in effective pair potentials. J Phys Chem 91:6269–6271

54. Berendsen HJC et al (1984) Molecular dynamics with coupling to an external bath. J Chem Phys 81:3684–3690
55. Hoover WG (1985) Canonical dynamics: equilibrium phase-space distributions. Phys Rev A 31:1695
56. Bussi G, Donadio D, Parrinello M (2007) Canonical sampling through velocity rescaling. J Chem Phys 126(1):014101
57. Loukatou S et al (2014) Molecular dynamics simulations through GPU video games technologies. J Mol Biochem 3:64–71
58. Stone JE et al (2010) GPU-accelerated molecular modeling coming of age. J Mol Graph Model 29(2):116–125
59. Grubmueller H (2004) Protein as molecular machines: force probe simulations. In: KBN A, Grubmueller H, Kremer K (eds) Computational soft matter: from synthetic polymers to proteins. John von Neumann Institute for Computing, Juelich, pp 401–422
60. Istralewitz B, Gao M, Schulten K (2001) Steered molecular dynamics and mechanical functions of proteins. Curr Opin Struct Biol 11:224–230
61. Janshoff A et al (2000) Force spectroscopy of molecular systems-single molecule spectroscopy of polymers and biomolecules. Angew Chem Int Ed Engl 39:3212–3237
62. Jarzynski C (1997) Equilibrium free-energy differences from nonequilibrium measurements: a master equation approach. Phys Rev E 56:5018–5035
63. Jarzynski C (1997) Nonequilibrium equality for free energy differences. Phys Rev Lett 78:2690–2693
64. Caleman C et al (2012) Force field benchmark of organic liquids: density, enthalpy of vaporization, heat capacities, surface tension, isothermal compressibility, volumetric expansion coefficient, and dielectric constant. J Chem Theory Comput 8(1):61–74
65. Kumar S et al (1992) The weighted histogram analysis method for free-energy calculations on biomolecules 0.1. The method. J Comput Chem 13(8):1011–1021
66. Hub JS, De Groot BL, Van Der Spoel D (2010) g_wham: a free weighted histogram analysis implementation including robust error and autocorrelation estimates. J Chem Theory Comput 6(12):3713–3720
67. Roccatano D et al (2005) Dynamical aspects of TEM-1 β-lactamase probed by molecular dynamics. J Comput Aided Mol Des 19(5):329–340
68. Sarukhanyan E, Milano G, Roccatano D (2014) Coating mechanisms of single-walled carbon nanotube by linear polyether surfactants: insights from computer simulations. J Phys Chem C 118(31):18069–18078
69. Samanta S, Hezaveh S, Roccatano D (2013) Theoretical study of binding and permeation of ether-based polymers through interfaces. J Phys Chem B 117(47):14723–14731
70. Samanta S et al (2012) Diffusion of 1,2-dimethoxyethane and 1,2-dimethoxypropane through phosphatidycholine bilayers: a molecular dynamics study. J Phys Chem B 116(17):5141–5151
71. Humphrey W, Dalke A, Schulten K (1996) VMD: visual molecular dynamics. J Mol Graph 14 (1):33–38
72. Kabsch W, Sander C (1983) Dictionary of protein secondary structure: pattern recognition of hydrogen-bonded and geometrical features. Biopolymers 22:2576–2637
73. Frishman D, Argos P (1995) Knowledge-based protein secondary structure assignment. Proteins Struct Funct Genet 23(4):566–579
74. Roccatano D (2008) Computer simulations study of biomolecules in non-aqueous or cosolvent/water mixture solutions. Curr Prot Pept Sci 9(4):407–426
75. Bergman DL, Laaksonen L, Laaksonen A (1997) Visualization of solvation structures in liquid mixtures. J Mol Graph Model 15(5):301–306
76. Shim Y, Kim HJ (2009) Solvation of carbon nanotubes in a room-temperature ionic liquid. ACS Nano 3(7):1693–1702
77. Zhu YL et al (2016) Hybrid particle-field molecular dynamics simulation for polyelectrolyte systems. Phys Chem Chem Phys 18(14):9799–9808

78. Zhao Y et al (2012) Hybrid particle-field molecular dynamics simulations: parallelization and benchmarks. J Comput Chem 33(8):868–880
79. Milano G, Kawakatsu T, De Nicola A (2013) A hybrid particle-field molecular dynamics approach: a route toward efficient coarse-grained models for biomembranes. Phys Biol 10 (4):045007
80. Kitao A et al (2006) Switch interactions control energy frustration and multiple flagellar filament structures. Proc Natl Acad Sci U S A 103(13):4894–4899

Chapter 7
Development of a Nanopaint for Polymeric Auto Components

Simone Schincariol, Maria Fonseca, and Victor Neto

7.1 Introduction

The goal of the research presented in this chapter is to study and develop an alternative methodology to produce painted chrome-plated polymer parts required by the automotive industry. Nowadays the automotive industry is substituting metal parts for plastic ones. However, these new plastic parts must detain the aesthetic and the main properties of the metal components, i.e. the metallic appearance is of utmost importance, as well as the "cold sensation" of metal.

Those features may be obtained by the well-known chrome-plated painting [1, 2], which is no more allowed in the automotive sector due to environmental and health toxicity regulations [3–6]. Physical vapour deposition (PVD) process can produce good quality parts with metallic appearance but with an increased price and very dependent on the quantities produced [7, 8]. Another methodology that can be used to produce parts with metallic-like appearance is the thermal spraying [9]. An alternative is through polymer painting. Such technique is less costly, easier for industrial implementation and can be environmentally friendly.

Coatings have two primary purposes: decoration and protection. Those functions are complementary in most of the paint usages, and about 45% of the worldwide production is intended to save and/or decorate new or existing structures, like buildings, houses and factories. The protection and/or decoration of industrial products use 40% of the coatings. The remaining percentage covers the demand of high-performance coatings for industrial plants and equipment, vehicle refinishing, traffic paints and protection of marine structures and vessels.

S. Schincariol • M. Fonseca • V. Neto (✉)
Department of Mechanical Engineering, Centre for Mechanical Technology and Automation, University of Aveiro, Aveiro, Portugal
e-mail: vneto@ua.pt

M.J. Jackson, W. Ahmed (eds.), *Micro and Nanomanufacturing Volume II*,
DOI 10.1007/978-3-319-67132-1_7

The use of coating is of utmost importance in the way that its usage can extend products life and prevent degradation by environmental conditions (acid, water, sea water, oxidation) or from scratches and hits [10].

The main aim of this chapter is to present the research developed to attain a new polymeric paint with metal aspect and with enhanced thermal properties, to improve the "cold feeling on touch" on plastic part. A way of enhancing the thermal properties of the polymeric paint is through the addition of nanoparticles with high thermal conductivity properties, such as carbon-like nanoparticles (carbon nanotubes) and iron nanoparticles.

7.2 Painted Polymers for Automobile Components

For decades, plastics have proved to be indispensable for the automotive industry, used at first only in the cockpits or for aesthetic external components, such as mirrors, spoilers and bumpers. However, today, plastics are also used for those components that were exclusively in metal sheet, such as doors, hoods, radiators and fenders. The almost unlimited possibilities for shaping plastics involve new experiments in design and promote fuel economy thanks to low weight compared to metals (polymer density is about one-seventh of that of steel). The most widely used plastics in the automotive field are:

PP/EPDM (copolymer of polypropylene/ethylene-propylene-diene), to produce bumper and rear spoilers.

ABS (acrylonitrile butadiene styrene), for mirror supports, wheel covers, car roof box accessories and front and rear spoilers.

PA (polyamide), a robust and elastic material, is suitable for the production of hatches for fuel tanks but especially for wheel covers.

PC (polycarbonate), which detains a high mechanical strength (even at $-100\ ^{\circ}$ C) and good resistance to atmospheric agents, enables PC for the bumper and the radiator grille.

PU (polyurethane) is part of the foams, and its hardness and flexibility can vary considerably, as its density increases from the centre towards the surface, and be used to produce parts of the bumper and rear spoiler.

PBT (polybutylene terephthalate) possesses high rigidity and mechanical strength and good high temperatures, UV and wear resistances, so it is suitable for the manufacture of body parts such as fenders, door handle, hood and trunk.

UP (unsaturated polyester) which is often reinforced with glass fibres to increase its strength and its mechanical hardness in order to compose the most extended parts of the bodywork and used to produce hoods, trunks, sports car fenders and components.

EP (epoxy resin) that is the most used thermosetting polymers to produce advanced composites, and it is the one which reaches the highest performance in mechanical properties; and PVC (polyvinylchloride) is very versatile since it can be

produced in different variants (hard or gummy) and is used to produce covers for trucks and shockproof bars [11].

Although polymers detain a set of considerable functional requirements to be used in automobile components, in the majority of the cases, it is necessary to paint these parts with different colours, being one of the most appealing of the metallic chrome aspect.

The painting or coating has the purpose to match the colour of the part to that of the bodywork, to obtain brightness and brilliance and, if possible, to eliminate minor production defects. An issue that cannot be ignored is the affinity of the paint with the substrate, as the polymeric one, in order to avoid peeling phenomena, cracking of the coatings, physical properties alteration, oxidation, depolymerization, absorption of solvents and softening and swelling of the plastic [12]. The chemical compatibility of different materials has been extensively studied, and the degree of compatibility between different substances and materials can be found elsewhere [12].

The painting process involves essentially two different steps: washing/cleaning and paint application [13, 14]. A common washing/cleaning process is the immersion of the workpiece in a water-based detergent solution (or with a specific solvent) to remove the contaminants by the chemical effect of the fluid. There are different methodologies of paint application at industrial level, each has different characteristics and is suitable for different applications. It is also sometimes necessary that the application of a primer, the first layer of paint that can be transparent or coloured, has the purpose of standardizing the surface and on which is laid the paint. The painting process may be performed by immersion: (a) the continuous immersion and (b) the discontinuous immersion. In the first, the workpieces are immersed in the tanks containing the coating solution with the aid of continuous transport systems (non-stop). With this process the productivity is high, but it is costly to fill the tank because it needed an extra amount of paint by 30–50% compared to that used to coat the product. In a discontinuous immersion, the workpieces are picked up by a robot from the transport chain and immersed in the bath vertically. Then, they are repositioned by the robot on the conveyor chain and taken towards the oven to dry the paint. This system has lower productivity than the previous, due to its intermittence, and has a higher initial investment costs for the robotic mechanisms; however, the used amount of paint is less. In both processes a careful choice of the paint and the amount of diluent to prevent dripping or accumulations of paint are required [14].

Another technique of painting is by airless. Through this way the paint is sucked from a pressure pump towards a gun nozzle, where it is atomized by exploiting the nozzle divergence that does the jet expansion. With this technique, air is not used to spray the paint, preventing almost completely the overspray, and the high speed of application allows a reduction of time and costs of painting. It is generally used for anticorrosion applications [14].

Finally, the painting process can be performed by a pneumatic system. This technique uses a spray gun with the aid of compressed air. The air and the paint

enter the gun by separate channels and then join to form a uniform fan pattern. The air can be joined to the paint before or after the exit from the nozzle; it depends on the type of instrument being used, but in both cases, the paint is sprayed and dispersed from the air at high pressure. This process normally takes more than one pass to paint with the spray gun on the same spot [14].

The paint, as defined on standards ISO 4618; 2:53, is a material in liquid, paste or powder form, which, when applied, will form a protective and decorative cover of the surfaces. It is made of complex chemical materials, which include lacquers, varnishes and other similar products. In most instances, paint is composed by the binders, pigments and extenders used to generate or change physical properties, solvents and additives, which do not have a specific composition but are different from each other. Usually they are added to a coating in small percentages of weight and can modify a wide range of properties such as viscosity, surface tension, gloss, structure, UV resistance and resistance to the environment. The incorporation of nanoscale additives to the paint and the consequences, in their resulting properties, will be the focus of the present chapter, in order to obtain a nanopaint close to the chrome plating.

7.3 Incorporation of Nanoparticles in Paint: The Nanopaint

The addition of nanoparticles to the base materials may be translated into an enhancement of the overall properties of the based material, such as the mechanical, thermal and electrical properties. Keeping this in mind, it can be produced as nanopaint, which can be used as a protective/decorative coating, with enhanced and interesting properties to be applied to the parts of the automotive industry, for example.

What is exactly a nanopaint? Is it a nanofluid or a nanocomposite material? Observing the preparation methodology of a nanopaint, there are similarities with a nanofluid, in a way that before its application, the mixture is in liquid state; on the other hand, after being deposited on the substrate, the nanopaint solidifies, becoming a nanocomposite. So, what is exactly a paint loaded with nanoparticles? Taking into account its final application, the nanopaint is a nanocomposite, since, once applied, it solidifies and the particles do not have freedom of movement as in a fluidic medium, and the only system available to them is the diffusion through the solid medium. Furthermore, the production process of the nanopaint can be described by a production process that is used to prepare the nanocomposites. The process can be described as (1) the paint (polymer) is mixed with a solvent (diluent) in which the nanoparticles are added; (2) the solvent is removed (evaporated). In the case of the nanopaint, the solvent removal occurs through evaporation when the mixture is deposited, resulting into the solidification of the painted layer. The dosage of the diluent must be as accurate as possible, since the solidification is closely linked to evaporation: little thinner involves rapid solidification with problems related to cracking since the polymer chains do not have time to relax; too

Table 7.1 Components of the graphene oxide nanopaint and their purpose [16]

Additive	Material	Purpose	Weight percentage (%)
Pigment	GO sheets	Providing the colour of the paint	16.0
Binder	Linseed alkyd resin	Film-forming component of the paint	64.0
Stabilizer	Nanosized ZnO	Reducing the colour-fading effect of the paint	0.6
Anti-settling agent	Aluminium stearate	Preventing pigment and binder settling	0.5
Thickener	Thickener A	Improving the viscosity and preventing coagulation	0.1
Wetting agent	Soya lecithin	Wetting the pigment in the binder for uniform dispersion	0.6
Inner coat drier	Nanosized zirconia	Chemical cross-linking agent of unsaturated fatty acids	0.6
Outer coat drier	Cobalt naphthenate	Active catalyst for the lipid autoxidation process	0.6
Thinner (solvent)	Mineral turpentine oil	Dispersing agent	17.0

much diluent results in the delays into the solidification, with risks of drip and distension of uneven layer.

In our days, water-based paints are becoming increasingly widespread, as they require less organic solvents with a considerable saving of money and with a reduced environmental pollution [15]. Using water-based coating, the amount of the organic solvents is about 10/15% and that of water is about 40/50%, while, with traditional paints, the quantities of solvent are around 50/70% on the total. Table 7.1 presents an example of the composition of a graphene oxide (GO) nanopaint [16].

Nanopaints can be prepared with a considerable number of different nanoparticles, depending on the final application of the paint. Table 7.2 presented various functions of coatings with nanoparticles, bringing some examples and the pros and cons for each use or application area [17].

In what concerns the production of the nanopaint, the dispersion of the nanoparticles in the paint is a critical stage, whether the nanoparticles are spherical, fibrous or lamellar. The goal is to disperse the additive uniformly in the matrix, so that every single nano-element is separated from the others. In order not to form agglomerates, the filler must be as compatible as possible with the matrix, and it is necessary to use systems that enable the separation between the nano-elements [18]. The nano-dispersion methods can be categorized into high-energy or low-energy approaches. The high-energy methods usually require high-pressure homogenization and ultrasound systems. Instead, the low-energy methods such as spontaneous emulsification, solvent displacement and phase inversion require mechanical or magnetic mixing systems [19]. Although in the past the most used methods for the nano-dispersion were those with high energy for the approach linearity and for ease of implementation in industrial production; in more recent

Table 7.2 Components of the graphene oxide nanopaint and their purpose [16]

Function	Nanomaterial (examples)	Advantage/effect	Industrial branch
Colour brilliance, shade, colour effects (flip-flop effect), reproducible paints, easily dispersible paints	Carbon black; oxides (TiO_2, Fe_2O_3, Fe_3O_4, SiO_2, Cr_2O_3) (on mica flakes or SiO_2 spheres, with metal pigments), ZnO	Intensify effects of metal pigments; stabilize pigments and fillers; positive effects in dispersion paints; prevent crack formation (phyllosilicates/ sheet silicates); improve resistance to fading	Automotive, consumer goods (furniture), construction
Self-cleaning ("easy-to-clean")	Organic-inorganic hybrid polymers (organically modified ceramics), nanosilica/colloidal silica embedded in resin particles following polymerization; silanes (silicon-based mixtures with other chemicals, e.g. fluorine compounds); TiO_2	Dirt and water repellant, protection against algae and fungi; anti-graffiti protection: easy removal of unwanted paint	Automotive, construction (facades), glass
Switchable (electrochromic, photochromic, thermochromic)	Tungsten oxide (WO_3) (electrochromic)	Colour effects	Automotive
"Self-assembly"	Polymer gel, specific organic-inorganic hybrid polymers	Self-healing surfaces	Automotive, cosmetics
Monolayer adhesive films	Polymers	Ultra-thin layers	Automotive, consumer goods
Scratch resistance	Oxide (synthetic amorphous silica), SiO_2, Al_2O_3	Improved scratch resistance	Automotive, parquet flooring, consumer goods (furniture), optics (lenses)
Optimized flow characteristics	Oxide (synthetic amorphous silica)	Generate new rheological properties (elasticity, flow characteristics, thixotropy)	Various
Conductive coatings for electrostatic paint spraying	Carbon: fullerenes, carbon nanotubes (CNT)	Enhanced spraying processes	Automotive
Photocatalytic effect, antimicrobial effect	TiO_2, ZnO_6, Ag	Removal of grease, dirt, algae, bacteria, fungi, odorants and pollutants; transformation of NOx and	Construction (facades, noise barriers, tiles), road surface, vehicles,

(continued)

Table 7.2 (continued)

Function	Nanomaterial (examples)	Advantage/effect	Industrial branch
		ozone from the atmosphere into harmless compounds	wood preservation, glass
Fire retardant	SiO_2	When a certain temperature is exceeded, a heat-insulating carbon foam layer is created on the wood surface followed by a flame-resistant ceramic layer	Construction, protection of wood against fire
Corrosion protection, wood preservation	Zinc or aluminium coated with nano-TiO_2, nano-clay (like hydrotalcite $Mg_4Al_2(OH)_{12}CO_3 \times H_2O$)	Nano-clay coatings delay the fading of wood (which is a result of the bleeding of complex chemicals like tannins)	Construction, automotive, wood preservation
UV protection, IR reflective or IR absorbing	(TiO_2; ZnO, CeO_2, iron oxide pigments (transparent iron oxide); needle-shaped particles with a length of 50–100 nm and width of 2 nm)	Enhanced UV resistance, blocking of IR and visible light, indoor climate control	Construction (facades), wood preservation, glass, plastics

times, the research is focused on low-energy methods. In fact, the latter process requires a lower energy consumption and less expensive equipment. However, to allow the nano-dispersion, the low-energy methods require higher concentrations of surfactants which have the property of lowering the surface tension, facilitating the wettability of the surfaces or the miscibility [19]. In the high-pressure homogenization systems the fluid is subjected to intense fluid-mechanical stress, due to the sudden pressure drop and strong turbulence, which cause the break of the suspended particles into smaller fragments, up to nanometre size (nano-emulsions, nanoparticles and nano-suspensions) [20]. Ultrasonic processes are used as homogenizers of the nanoparticles in the solvent. The dispersion and the breaking of the agglomerates of solids in liquids are important applications of ultrasonic devices. Ultrasonic cavitation generates high shear forces that penetrate in agglomerations and disperse the individual particles. The mixing of powders in liquids is a common step in the formulation of various products, such as paint, ink, shampoo or beverages. The individual particles are held together by attraction forces of various physical and chemical natures, including van der Waals forces and liquid surface tension, which must be countered and overcome to break down agglomerates and disperse the particles in liquids [21]. Instead, the systems of production of nanocomposites or nanofluids at low energy require much less complex mixers of the previous two. They used mechanical and magnetic mixers (if there are no

magnetic nanoparticles) useful for the homogenization of the product, while the nano-dispersion is achieved thanks to the surfactant [19].

7.4 Materials and Processes

In this section the experimental procedure to evaluate the potential use of carbon nanotubes (CNTs) and iron nanoparticles (Fe_3O_4) to attain a coating that enhances the metallic sensation of a polymer component will be presented and discussed. It will be started with the materials that were used, the production of the nanopaint and its experimental characterization.

7.4.1 Materials

The substrate on which the paint was applied for evaluation purposes is made of acrylonitrile butadiene styrene (ABS), with dimensions of about $210 \times 200 \times 25$ mm^3 and a thickness of about 2 mm. Although the substrate material influences the addition of the paint to it, different surface treatments may be needed to be performed in order to promote a good adhesion, for the present study, it is not relevant, since the paint will be peeled from the substrate to be subjected to the different analysis. However, it is worth to mention that the roughness of the substrate is not too high.

The paint and diluent were kindly provided by CIE STRATIS – Tratamentos, Lda. (Varzea, Barcelos, Portugal). The commercial name of the paint and its specifications is "CELEROL®, Basecoat 990-22, Highchrome effect". For the diluent, the commercial name is "CELEROL-Verdünner 902-82", and its composition is listed in Table 7.3.

The used carbon nanotubes (CNTs) were purchased from "Cheap Tubes". It was used multiwalled carbon nanotubes with an external diameter of >50 nm and a length of 10–20 μm; a purity >95% and a density of $\rho = 2.1$ g/cm^3. The used iron nanoparticles (Fe_3O_4) were purchased to "NanoBond", in the form of red power. These nanoparticles have a spherical shape with a size <30 nm and a purity of 99%. The surface area is about >55 m^2/g, and its density is 2.1 g/cm^3.

7.4.2 CNT-Based Nanopaint Production

The paint was firstly shaken to homogenize the blend. Following this stage, it was diluted in diluent. The diluent has been added in a proportion of 200% compared to the paint, as suggested by paint suppliers. It was decided to produce a total of 150 mL of paint. A magnetic stirrer was used to mix the solution for 15 min. Two

Table 7.3 Components of the graphene oxide nanopaint and their purpose [16]

Chemical name	Classification (67/548/CEE)	Classification ((CE) N.o 1272/2008)	Concentration (x)
Ethyl acetate 141-78-6 205-500-4 01-2119475103-46	F; R11 Xi; R36 R66 R67	Flam. Liq. 2; H225 Eye Irrit. 2; H319 STOT SE 3; H336	$40 \leq x \leq 100$
Propanone 67-64-1 200-662-2	F; R11 Xi; R36 R66 R67	Flam. Liq. 2; H225 Eye Irrit. 2; H319 STOT SE 3; H336	$25 \leq x < 40$
n-Butyl acetate 123-86-4 204-658-1 01-2119485493-29	R10 R66 R67	Flam. Liq. 3; H226 STOT SE 3; H336	$20 \leq x < 25$

other mixtures were prepared with different dosages of diluent, obtaining the following three mixtures:

- Paint200%: paint 33.3% (50 mL), diluent 66.7% (100 mL)
- Paint250%: paint 28.6% (50 mL), diluent 71.4% (125 mL)
- Paint300%: paint 25.0% (50 mL), diluent 75.0% (150 mL)

The first nanoparticles to be used to obtain a nanocoating were non functionalized carbon nanotubes (CNTs). It were prepared nanopaints with different weight percentages of CNTs: 0.1; 0.2; 0.3; 0.4; 0.5; 0.7; and 1.0 wt% CNTs. In order to obtain a homogeneous distribution of the CNTs into the base paint, the time of mixture procedure was optimized to be 30 min.

At an initial stage of the work, the available equipment was an ultrasonic tip; however, it heats the mixture due to its ultrasound energy and would evaporate the diluent from the mixture. In order to prevent that, the mixing was stopped every 5 min for 10 min to check the condition of the paint and to unsure that there was any evaporation. The procedures were the following:

1. Five minutes, ultrasonic tip: After 5 min, the paint was heated, but there were no noticeable decreases of the quantities of paint. Sediments of CNTs were visible, arranged radially in the bottom of the jar, indicating that the mixing had taken place only partially. To increase the mixing capacity dislodging sediments in the bottom, the ultrasonic tip was combined with a magnetic stirrer. Before proceeding with the second part of the mixing, the paint was left to cooldown for about 10 min.
2. Five minutes, ultrasonic tip + magnetic stirrer: In the bottom of the jar, there were no sediments, but the paint was still hot. The colour of the painting did not

visibly change from the original colour (but only after the application, you can be assured that there have been no changes). After an hour and a half, sediments were still visible in the bottom of the jar but far fewer than in the first step.

3. Five minutes, ultrasonic tip + magnetic stirrer: There were no sediments at the bottom, the paint was heated, and the colour was apparently unchanged. To speed the cooling and to disperse the heat absorbed by the paint, the jar was placed in a larger bowl containing water at room temperature, using the system in a water bath, till the temperature of the paint has fallen.
4. Five minutes, ultrasonic tip + magnetic stirrer + water bath: After these 5 min, the paint does not present residues at the bottom, the colour was unchanged, and its temperature was not increased. Therefore, it was decided to lengthen the mixing time thanks to the water-bath system.
5. Ten minutes, ultrasonic tip + magnetic stirrer + water bath: After 10 min, the mixture appeared homogeneous, without residues and without colour changes, and its temperature was slightly higher than room temperature, but not significant.

A total mixture time of 30 min was achieved, and the paint was preserved in a test tube to check the possible formation of sediment in the bottom.

After these experiments, new methodologies were performed. Four different procedures were tested, as resumed in Table 7.4, in order to understand which of the procedures could lead to a more homogeneous mixture. Among the various procedures, the order of mixing and the type of applied mixer were changed.

Order of Mixing:

- Sol1: paint + diluent → (paint + diluent) + CNTs
- Sol2: diluent + CNTs → (diluent + CNTs) + paint

Mixer:

- Mix1: magnetic stirrer
- Mix2: ultrasonic bath

The base paint (paint + diluent) was previously prepared. For the Sol1.1, a weight percentage of 0.2% CNTs was added. The mixing started with a magnetic stirrer for 30 min with a control step each 15 min. Figure 7.1 shows a photograph of the mixture Sol1.1; after 30 min of mixing, agglomerates of CNTs were not visible.

Figure 7.2 shows a comparison of the results of painting with Sol1.1 with and without CNTs. It can be seen in the left image (the painting without CNTs) that surface finish is much less erratic than that of the right with CNTs (Sol1.1). The surface of the right is much rougher than the other; in fact, the carbon nanotubes, when stirred, did not disperse in the paint mixture, but it came together in clusters

Table 7.4 Combinations with the respective variants

	Mix1	Mix2
Sol1	Sol1.1	Sol1.2
Sol2	Sol2.1	Sol2.2

Fig. 7.1 Preparation mixture of paint Sol1.1

Fig. 7.2 (*Left*) The surface of a piece coated with the paint without CNTs and (*right*) with Sol1.1

that form in the paint visible bumps. This roughness also tends to change the paint colour, because the protuberances generate tiny light and shadow effects, which vary the appearance of the object painted.

For Sol1.2 the mixing process applied to Sol1.1 was changed. The CNTs were mixed with the diluent before mixing it with the paint. The CNTs were mixed with the diluent with a magnetic stirrer for a total of 30 min with a verification check each 15 min. Figure 7.3 shows the results of the final mixing after 15 min and after 30 min.

As it can be seen in Fig. 7.3, the mixing of the diluent with the CNTs was not successful; in fact, the CNTs are not completely dispersed in the diluent, and some sedimentation are clearly visible on the bottom of the glass jar. This result suggests that CNTs are not soluble into the used diluent for this coating. After mixing the CNTs with the diluent, the paint was added. Such mixture was mixed for 30 min

Fig. 7.3 (*Above*) Result of the mixing of CNTs with the diluent with a magnetic stirrer after 15 min and (*below*) result after 30 min

through a magnetic stirrer. The obtained mixture can be seen in Fig. 7.4. It can be noticed that on the right picture, some dark grey spots appear in the bottom of the jar, indicating possible agglomerates of CNTs. In this case, after painting, the results obtained do not differ much from those of Sol1.1; in fact, as seen in Fig. 7.5, there are obvious protuberances that make the surface very rough. This roughness is due, as in the previous case, to agglomeration of CNTs.

From these results and from the previous coatings, it can be assumed that the mechanical mixing is not the most suitable solution to obtain a uniform paint and with a good surface finish. In addition, the mixing of CNTs with the diluent, before adding the chrome paint, has not yielded positive results as it can be seen in the picture of Fig. 7.3, so it was decided not to proceed with Sol2.2 solution, knowing that the CNTs do not disperse in only thinner. Therefore, it was necessary to continue with the tests using Sol1.2.

Before proceeding with Sol1.2, the CNTs were placed in an oven, for 5 h, at 100 °C and 0% of humidity, in order to remove the possible excess of humidity and enable a better solubility in the paint, since it was verified that the paint was not compatible with water.

Fig. 7.4 Sol2.1 after 30 min of mixing with the magnetic stirrer

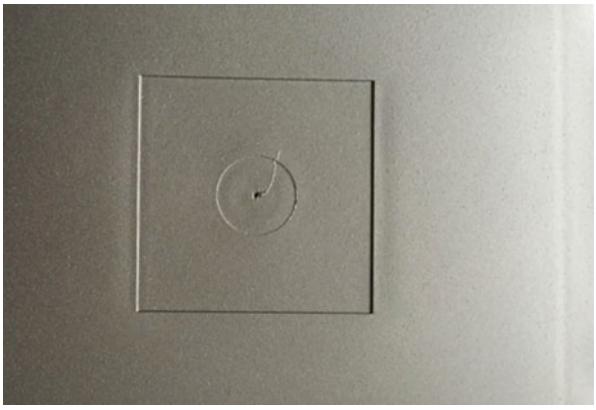

Fig. 7.5 Spray paint with mixing process Sol2.1

Proceeding with the Sol1.2, the CNTs were added to the mixture, and it was used as an ultrasonic bath for a total of 70 min (20-10-10-10-10-10). Figure 7.6 shows the photographs of the bottom of the jar containing the paint at each step. As it can be seen, after 40 min, there are some visible traces of CNTs (images a, b, c); thereon, the agglomerates of CNTs could not be noted on the bottom of the jar. As a precaution, the mixing in ultrasonic bath was conducted for a total of 70 min, in order to disperse the agglomerates, even if not visible. Then it was proceeded with the painting of a piece of plastic, achieving a significantly better result than for Sol1.1 and Sol2.1.

Figure 7.7 shows a part of the painted substrate in which some surface irregularities can be observed as compared with paint without nanoparticles. These irregularities are in much less number than in the two previous cases; in fact, the

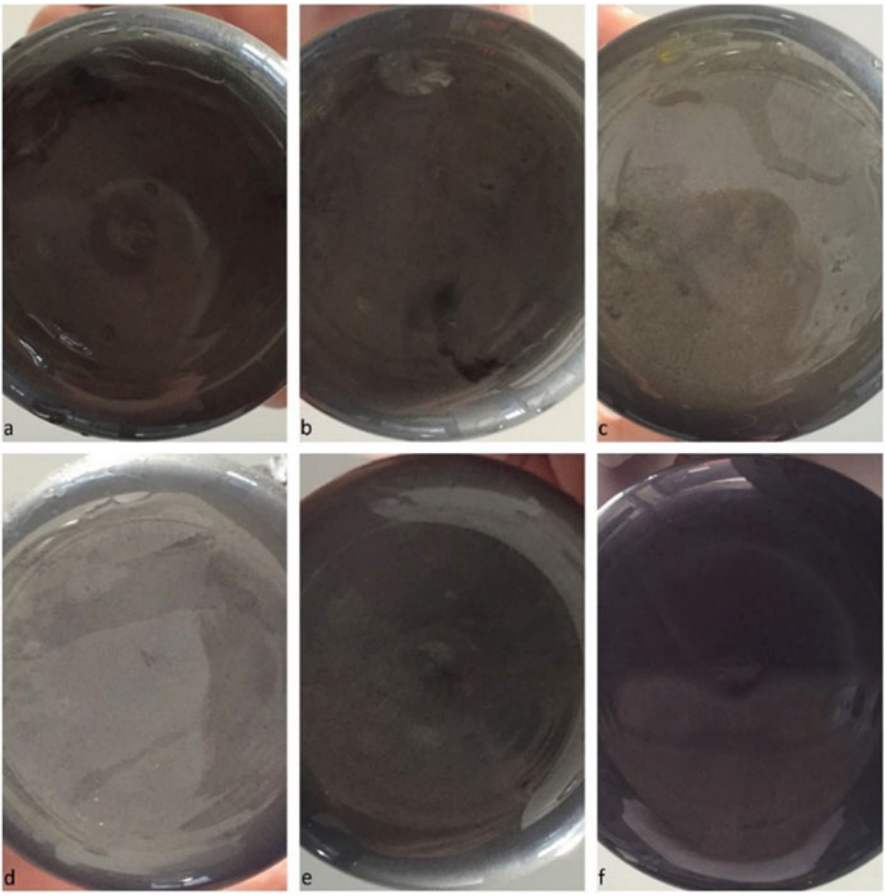

Fig. 7.6 Bottom of the jar with paint Sol1.2: (**a**) 20 min, (**b**) 30 min, (**c**) 40 min, (**d**) 50 min, (**e**) 60 min and (**f**) 70 min

roughness and the matting effect are less. However, satisfactory effects concerning to nacked eye and touch were not achieved; the number and size of the agglomerates of CNTs must be reduced to avoid bumps and surface imperfections.

A new solution Sol1.2 was prepared, with a manual mixture of 0.2 wt% CNTs. To improve the mixing, a stick of polymeric material was used for manual mixing, while the mixture is subjected to the ultrasonic bath. This procedure was adopted to increase the speed of dispersion of the CNTs, as it was believed that manually shaking the mixture agglomerations would break more easily and quickly.

Such "assisted" mixture was performed for a total of 25 min (with intervals at 10, 15, 20, 25 min), changing the water of the tank of the ultrasonic bath to each step, to maintain the paint at a low temperature (room temperature).

Figure 7.8 shows some pictures of the bottom of the jar at each interval, and it can be seen that there are no agglomeration, even for the first 10 min of mixture.

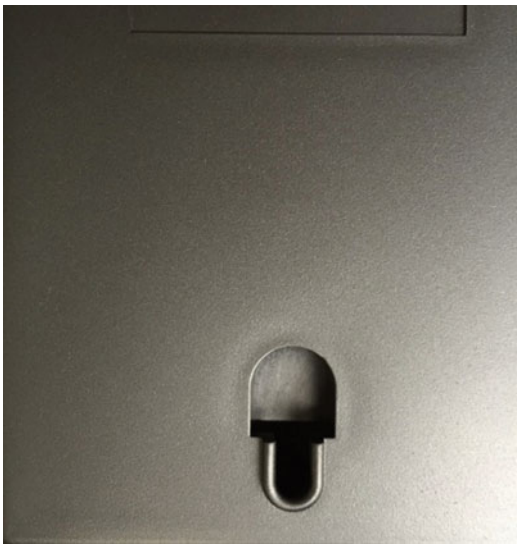

Fig. 7.7 Surface irregularities caused by agglomerates of CNTs (Sol1.2): irregularities are identified looking at the *dark dots* in the light grey background (*bottom right*) and *light dots* in the dark grey background (*top left*)

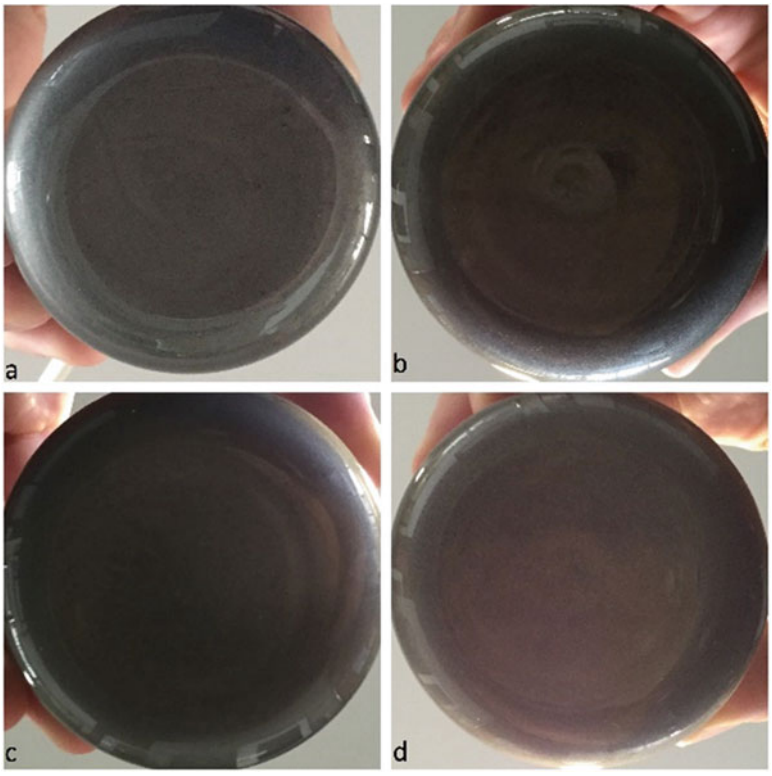

Fig. 7.8 Bottom of the jar of paint Sol1.2 while mixing manually and with ultrasonic bath: (**a**) 10 min, (**b**) 15 min, (**c**) 20 min, (**d**) 25 min

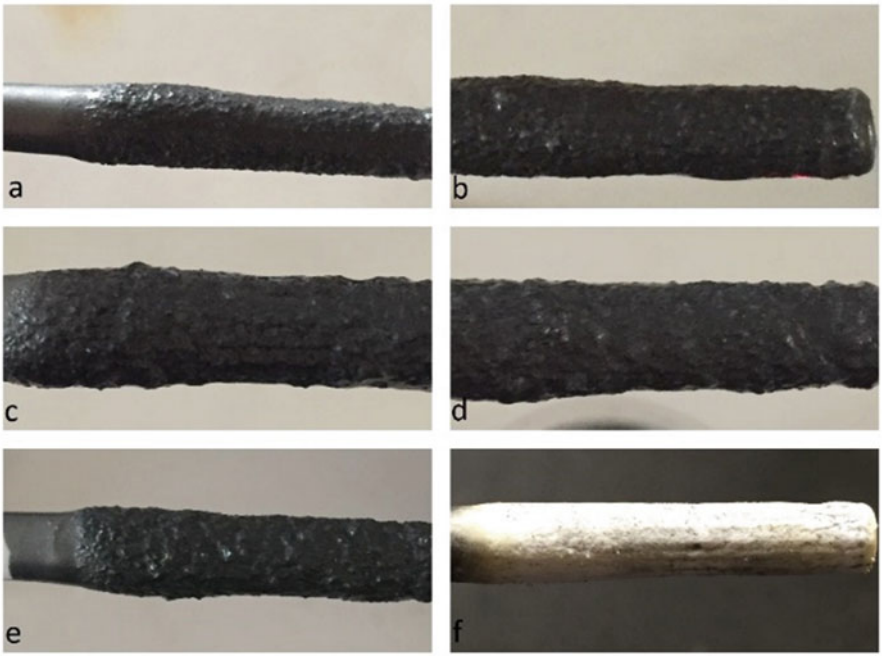

Fig. 7.9 Agglomerates of CNTs on the stick used to mix: photo for each step of the process of ultrasonic bath and (**f**) after cleaning

The mixing was stopped after 25 min because the CNTs agglomerated and tend to attach to the plastic stick, as shown in Fig. 7.9.

It was possible that the stick had attracted the CNTs due to an electrostatic effect, and then it was tried to disperse CNTs leaving the stick immersed in the mixture with the ultrasonic bath. The process continued for 25 min without positive effects because the agglomeration did not come off the stick; therefore it was decided to discard this paint sample and not to proceed with painting because the doses of CNTs would have been changed. During the cleaning of the equipment, it was discovered that, in the bottom of the jar, sediment remained with different texture from that of the paint. The stick had been affected, maybe by the chemical effect of the diluent, combined to the physical effect of ultrasound, and had lost the original shape and texture (Fig. 7.9f). Probably the sediments which remained on the bottom of the jar (Fig. 7.10) were not only agglomerations of CNTs but also particles of polymeric material of the stick. Also for this reason, the sample of chrome paint was unusable. This sample was discarded, and a second one was prepared, using a glass rod stick.

The total time of mixing of this new sample was 30 min, with steps of 5 min to change the water of the bath and to register photos of the bottom of the jar (Fig. 7.11). It can be noted that, since the first 5 min, there are no agglomerates

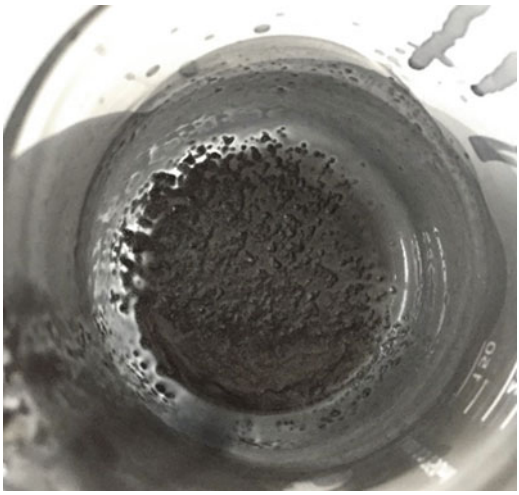

Fig. 7.10 Sediments of CNTs and/or polymeric material of the stick on the bottom of the jar

Fig. 7.11 Bottom of the jar of Sol1.2, while mixing manually with the glass stick and with the ultrasonic bath: (**a**) 5 min, (**b**) 10 min, (**c**) 15 min, (**d**) 20 min, (**e**) 25 min, (**f**) 30 min

Fig. 7.12 Polymeric base painted with Sol1.2

of CNTs at the naked eye and the stick was not affected by the diluent and had not attracted CNTs by electrostatic effect.

After mixing, it was proceeded with the drafting of the first layer of the paint. As it will be explained later, to proceed with the drafting of the second layer, we have waited 15 min for the first to dry enough to catch the second. During the 15 min of drying, the paint was subjected to manual mixing and ultrasonic bath for 10 min, so that there were not any agglomerates fallen to the bottom of the vessel. The coating is shown in Fig. 7.12.

Touching this painting, it was possible to feel the roughness, indicating that the dispersion of the agglomerates was not enough to make acceptable surface finish. At the sight, the piece of plastic is slightly less shiny than that one painted without CNTs.

To get further indication on the mixing quality, it was prepared a test tube containing nanopaint and using Sol1.2 with 0.2 wt% of CNTs. The purpose was to verify possible phase separation and potential sedimentation of the carbon nanotube agglomerates.

The test tube exhibited a distinct division of colours that suggests a phase separation. In Fig. 7.13 (right figure), it is possible to note how the upper part of the tube is of a light grey colour, while the lower part is darker, and, after careful observation, dark grey granules are noticed, which in fact alter the colour of the lower part.

As a first hypothesis for this effect, it can be said that the mixing was not distributed because the nanotubes were concentrated in the lower part after a day of rest. The CNTs have a higher density than the diluted paint, which allowed the separation of the stages vertically. Looking only to the bottom, one could say that the mixing was well distributed, but not much dispersed, because it seemed that nanotubes had formed small but visible grains of nanotubes, which are still too large compared to the nanoscale.

However, a second test tube was filled with paint diluted to 200% without nanoparticles (Fig. 7.13 to the left), to compare the results that would be obtained leaving both paints to rest. In the following days also in the test tube containing the paint without nanoparticles, a vertically phase separation has occurred. This suggested that the cause of this division was not nanoparticles as originally thought, but it was the thinner, which, if left to rest, will separate from the paint and tend to evaporate.

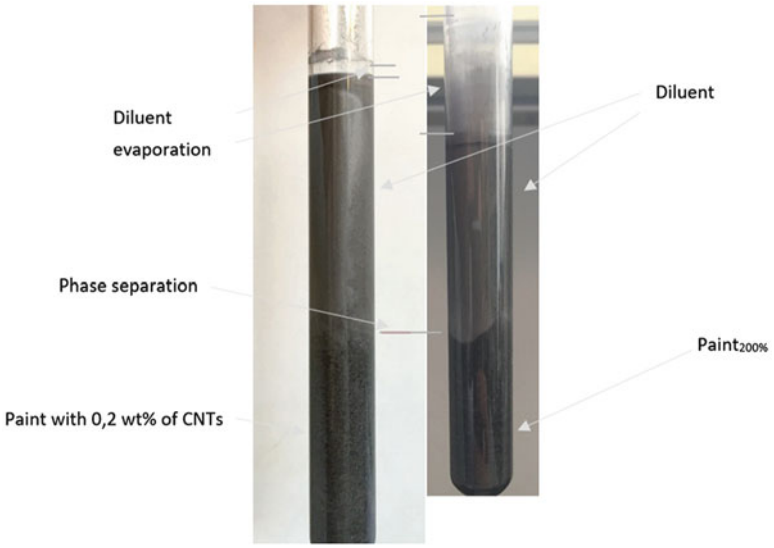

Fig. 7.13 Phase separation in the test tube of paint without nanoparticles (*right*) and in the one mixed with carbon nanotubes (*left*)

7.4.3 Fe_3O_4-Based Nanopaint Production Procedure

After optimizing the procedure to prepare the nanopaints with CNTs, iron oxide nanoparticles (Fe_3O_4) were also tested. The samples were prepared with 0.2 wt% of Fe_3O_4. The first mixture was prepared as the same of Sol1.2:

$$(\text{paint} + \text{diluent}) + Fe_3O_4$$

The procedure was performed in an ultrasonic bath simultaneously assisted by manual mixing with a glass rod. The mixing was stopped every 10 min to check the overheating and to change the water of ultrasonic bath. A total mixing time of 30 min was used. In Fig. 7.14 there are some pictures of the bottom of the jar to check if there was some sedimentation of the Fe_3O_4.

The Fe_3O_4 0.2%, in Fig. 7.15, is the paint with 0.2 wt% of iron oxide and it can be noted that this mixture (Fig. 7.15) presents less erratic particles than the one containing CNTs (Fig. 7.12).

This difference is found also in touch; in fact, the roughness of Fe_3O_4 0.2% is less than that of CNTs with same concentration (CNT0.2%). This result might be attributed to the different shape and size of the nano-iron oxide particles, which have a spherical shape and measure not more than 30 nm. Instead, carbon nanotubes have a cylindrical shape and tend to tangle with each other, making it difficult to desegregate. The intermolecular forces may be greater in the case of CNTs, which would not allow a sufficient separation of the nanoparticles that are grouped

Fig. 7.14 The bottom of the jar when mixing the dye with 0.2 wt% of Fe_3O_4. *Left*, 10 min. *Centre*, 20 min. *Right*, 30 min

Fig. 7.15 Polymeric base painted with Fe_3O_4 0.2%

forming agglomerates. Another factor that may affect this result can be the difference in volumetric proportion of the two types of nanoparticles having different densities: the volume occupied by the nano-Fe_3O_4 is less than that of CNTs, which would allow a dispersion of nanoparticles more effectively for the iron oxide.

To verify the actual nano-dispersion improvement, a solution containing the 0.5 wt% of nano-Fe_3O_4 (Fe_3O_4 0.5%) was prepared, corresponding approximately to the same CNT0.2% volumetric percentage.

In this case the coating is darker than Paint200%, Fe_3O_4 0.2% and CNT0.2%. However, on touch, it seems to be less rough than the paint with CNTs. Its lower roughness would be caused by the shape and the dimension of the nanoparticles, but not by the volumetric percentage. In fact, this sample has about the same volumetric quantity of nano-powder like the CNT's paint.

7.4.4 Application Procedure of the Nanopaints

The paint was applied with a spray gun with a reservoir cup. For the first test, a paint with a diluent/paint ratio equal to 2 was used, to check if the deposition of the layer was homogeneous. The obtained results were satisfactory.

To obtain the painted specimens it was followed the procedures below:

1. Cleaning the surface of the ABS component with ethyl alcohol
2. Application of the coating (two applications)
3. Drying (2 days)
4. Cutting the coated component in a smaller size
5. Peeling off the paint from the ABS substrate

To obtain the specimens with two types of coatings (side by side to compare colour at naked eye), it was followed by the procedures below:

1. Cutting the ABS component in a smaller size
2. Cleaning the surface with ethyl alcohol
3. Partial coverage of the specimen with a paper scotch tape
4. Application of the first type of coating (two applications)
5. Drying (2 days) and tape removal
6. Coverage of the painted surface with a foil of aluminium
7. Application of the second type of paint (two applications)
8. Drying (2 days) and removal of the aluminium foil

In order to obtain adequate thicknesses of the layers for the measurement of the thermal conductivity (at least 25 μm), it was necessary to proceed with four applications of paint.

7.5 Experimental Characterization

Different experimental techniques were utilized to characterize the prepared nanopaints (with CNTs and Fe_3O_4), as well as the base paint. The samples were characterized by means of density, light reflection, thickness, thermal conductivity (of the solid paint, and liquid paint) and electrical conductivity. Table 7.5 lists the different types of paint and nanopaint produced and tested, indicating the respective volumetric percentage of diluent and the weight percentage of nanoparticles.

7.5.1 Density

In order to dose with more precision, it was necessary to know the density of the materials that were going to be used: paint and nanoparticles (CNTs and Fe_3O_4). The density of the nanoparticles was provided by the companies. However, the

Table 7.5 Nomenclature of paints and nanopaints

Name	Diluent vol%	Nanoparticles	Nanoparticles wt%
Paint0%	0	None	0
Paint200%	200	None	0
Paint250%	250	None	0
Paint300%	300	None	0
CNT0.1%	200	CNTs	0.1
CNT0.2%	200	CNTs	0.2
CNT0.3%	200	CNTs	0.3
CNT0.4%	200	CNTs	0.4
CNT0.5%	200	CNTs	0.5
CNT0.7%	200	CNTs	0.7
CNT1.0%	200	CNTs	1.0
Fe_3O_4 0.2%	200	Nano-Fe_3O_4	0.2
Fe_3O_4 0.5%	200	Nano-Fe_3O_4	0.5
Fe_3O_4 1.0%	200	Nano-Fe_3O_4	1.0

Table 7.6 Combinations with the respective variants

Sample	ρ [g/cm^3]	SD [g/cm^3]
Paint with 200%	0.8782	0.0001
Paint with 250%	0.8668	0.0001
Paint with 300%	0.8633	0.0001

density of the paint was not well known, in such a way that the paint was diluted with different amounts of diluent (200, 250 and 300% of diluent). The density was measured with a densimeter Digital Density Meter Model DDM 2910 by Rudolph Research.

Five measurements were completed for each of the three paints, and the average and the standard deviation of the obtained results were calculated. The results are summarized in Table 7.6. As it can be seen, the density decreases with the enhancement of the diluent contents, as it was expected.

7.5.2 Light Reflection

In order to identify the colour variation and the gloss of the different coatings, it was used a UV-Vis-Nir recording spectrophotometer, UV-3100 by Shimadzu. The percentage of reflected light is collected at different wavelengths (from 825 to 200 nm, with steps of 0.2 nm). It was examined three samples for each type of paint (Paint200%, CNT0.2%, Fe_3O_4 0.2%, Fe_3O_4 0.5).

Figure 7.16 presents the graphs of the variation of the reflection percentage with the wavelength for the studied samples. The values entered here are the averages of the results obtained for each type of paint. As the wavelengths approachs the

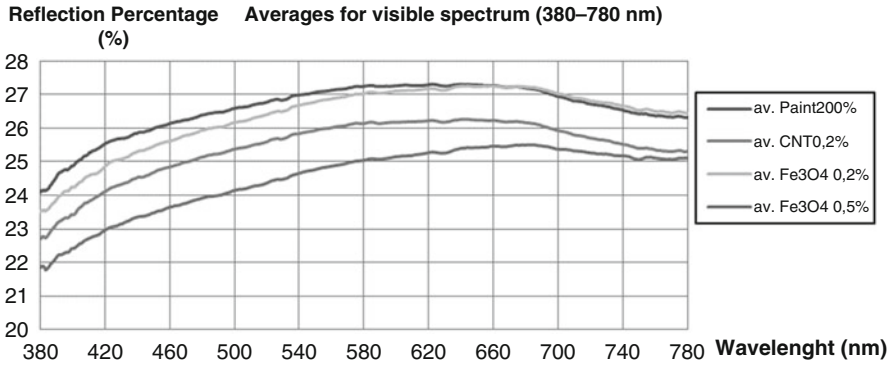

Fig. 7.16 Light reflection in visible spectrum for Paint200%, CNT0.2%, Fe_3O_4 0.2% and Fe_3O_4 0.5%

infrared (towards 700 nm), it can be seen that above 660 nm, the nanopaint Fe_3O_4 0.2% reflects more light than the base paint Paint200%, while the other nanopaints have lower values than that for the Paint200%.

The base paint is the one that possesses better reflectivity values for almost the entire visible spectrum, a result that has already been anticipated in the previous analysis without the aid of instrumentation. In fact, at the naked eye, it was clearly visible that Paint200% had a more gleaming and shiny surface than nanopaints.

7.5.3 Colour Quantification

It was possible to identify the colour of each paint using the obtained values from the measurement of the percentage of the reflected light. The data of the reflection and the wavelength of light (from 200 to 825 nm) were placed in a Matlab programme that gave the values *XYZ*, Lab and *RGB* for each measurement of reflection of light. *XYZ*, Lab and *RGB* represent the colour spaces defined mathematically by the *Commission Internationale de l'Éclairage* (CIE), and the values corresponding to each letter are colour components that, combined together, describe the colour using an abstract mathematical model. Obtained the colour coordinates, it was possible to place them in an online software [22] that receives the *XYZ* values, Lab or RGB and releases the colour image defined by the mathematical coordinates. For the *XYZ*, "*X*", "*Y*" and "*Z*" represent the three primary colours (oversaturated colours) chosen by the CIE to generate all visible colours. For the Lab, "*L*" is the colour brightness from 0 (minimum brightness, black) to 100 (maximum brightness, white), "*a*" expresses the red colour when it is positive (up to $+\infty$) and the green colour when it is negative (up to $-\infty$), and "*b*" expresses the yellow colour when it is positive (up to $+\infty$) and the blue colour when it is negative (up to $-\infty$). "*a*" and "*b*" are chromaticity coordinates. RGB is a model to

Table 7.7 Colour coordinates *XYZ*, Lab and *RGB*

Paint	*X*	*Y*	*Z*	*L*	*a*	*b*	*R*	*G*	*B*
av.Paint200%	25.56	26.96	27.90	58.94	−0.03	1.56	143	142	138
Paint200%	25.56	26.96	27.90	58.94	−0.03	1.56	143	142	138
av.CNT0.2%	24.47	25.82	26.49	57.86	−0.02	1.89	141	140	135
CNT0.2%	24.47	25.82	26.49	57.86	−0.02	1.89	141	139	135
av.Fe_3O_4 0.2%	23.25	24.46	24.98	56.55	0.25	2.05	138	136	132
Fe_3O_4 0.2%	25.27	26.63	27.27	58.63	0.09	1.98	143	142	137
av.Fe_3O_4 0.5%	23.46	24.68	25.21	56.76	0.25	2.05	139	136	132
Fe_3O_4 0.5%	23.66	24.90	25.43	56.98	0.24	2.05	139	137	133

express the colours as percentage of red light (*R*), green light (*G*) and blue light (*B*). Its values range from 0 to 255 and can only be whole number values.

Using the programme previously described, the colour coordinates were obtained (the *RGB* values of these coordinates have been rounded to the nearest whole number as the *RGB)*.

It can be noted in Table 7.7 that the coordinates obtained by various processes, are equal to each other or similar, except for the coordinates of Fe_3O_4 0.2%. Analysing the standard deviation (SD) for the average coordinates of Fe_3O_4 0.2%, it can be noted (Table 7.8) that the averages of the coordinates of the individual samples are more reliable than the coordinate values calculated on the averages of the percentage of light reflection. In fact, the SD Fe_3O_4 0.2% values are lower than those of SD av. Fe_3O_4 0.2% by at least one order of magnitude; therefore, only the values of Fe_3O_4 0.2% (not av. Fe_3O_4 0.2%) were considered.

From table values, colour differences are notable compared to Paint200%, especially the brightness decreases ("*L*" values) with small percentages of nanoparticles. So it cannot use CNTs and nano-Fe_3O_4 to produce nanocoatings with chrome effect, but should use nanoparticles that affect less the colour of the paint.

7.5.4 Thickness

The thickness was an important parameter to be determined because it was an important input for the thermal conductivity evaluation. The thicknesses were determined with a help of an optical microscope (Nikon—Eclipse LV150) with an objective lens, Nikon—LU Plan Fluor 20X/0.45 A ∞/0 BD. In Fig. 7.17 it can be seen how it was determined the thickness of the nanopaints in different place of the layer.

For each type of paint, four samples with a size of 5 × 3 mm^2 (approximately) were prepared, and 25 measurements were made for each sample, at different sites. With this procedure it was possible to derive the mean and standard deviation of the layer thickness. It was analysed the following samples: Paint200%, CNT0.2% and

Table 7.8 Standard deviation of *XYZ*, Lab and *RGB* coordinates of Fe_3O_4 0.2% and av.Fe_3O_4 0.2%

Stand. dev.	*X*	*Y*	*Z*	*L*	*a*	*b*	*R*	*G*	*B*
av.Fe_3O_4 0.2%	2027	2177	2302	2090	0.171	0.064	5354	5686	5066
Fe_3O_4 0.2%	0.216	0.228	0.237	0.213	0.001	0.003	0.471	0.471	0.816

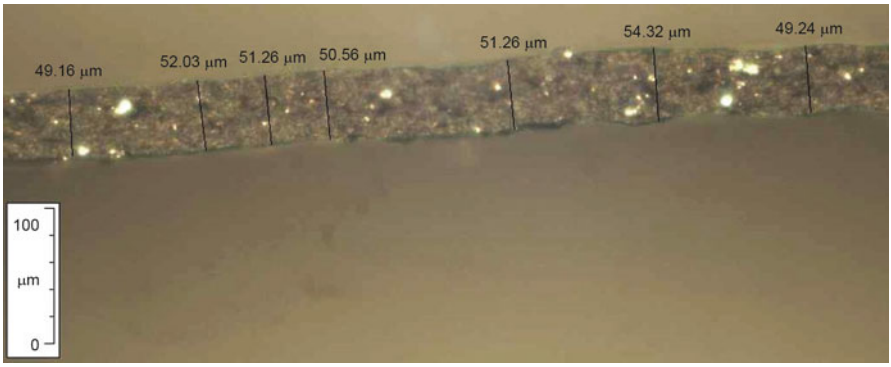

Fig. 7.17 Thickness measurement with the optical microscope "Nikon—Eclipse LV150" and the software "Perfect-Image V7.5"

Table 7.9 Mean and the standard deviation of Paint200%, CNT0.2% and CNT1.0%

Paint	Δ*xav* [µm]	SD Δ*xav* [µm]
Paint200%	41.19	3.99
CNT0.2%	76.71	11.59
CNT1.0%	88.56	8.62

Table 7.10 Averages, standard deviations and uncertainties for paints and nanopaints

Paint	Δ*xav* [µm]	SD Δ*xav* [µm]	*U*(Δ*xav*) [µm]
Paint200%	43.97	2.36	10.03
CNT0.1%	79.16	7.53	10.14
CNT0.2%	88.86	6.87	10.13
CNT0.3%	87.7	6.19	10.11
CNT0.4%	94.45	6.24	10.13
CNT0.5%	88.58	6.37	10.1
CNT0.7%	113.26	10.05	10.23
CNT1.0%	115.93	9	10.22

CNT1.0%. Table 7.9 summarizes the calculated thicknesses of the different samples. The problem of these measurements is the impossibility to measure the thickness in the centre of the specimens without breaking them. The thicknesses at the sides of the specimens were measured, and from the values obtained, the average Δ*xav* and the standard deviation SD Δ*xav* were calculated. To get the averages calculated with values obtained all over the specimen, it was used a micrometre with resolution ±5 µm (Micrometer Mitutoyo). Averages (Δ*xav*), standard deviations (SD Δ*xav*) and uncertainties (*U*(Δ*xav*)) were calculated for Paint200%, CNT0.1%, CNT0.2%, CNT0.3%, CNT0.4%, CNT0.5%, CNT0.7% and CNT1.0%, and are summarized in Table 7.10.

Comparing the values of Paint200%, CNT0.2% and CNT1.0% of Tables 7.9 and 7.10, high differences in values of average are noted above all for the thicknesses of the nanopaints.

7.5.5 Thermal Conductivity of the Solid Paint

The thermal properties were performed using the Gustafsson Probe method (or Hot Disk) with the Thermal Constant Analyzer TPS 2500S. This method uses an electrically conducting pattern (Nickel) element acting both as a temperature sensor and heat source, insulated with two thin layers of Kapton (70 μm). The samples, with the sensor in the middle, are then placed between the substrate halves (Fig. 7.18).

The thermal conductivity, λ_s, of thin samples (the paint was peeled from the substrate) can be extracted from the following formula:

$$\frac{P}{2} = A^* \lambda_s * \frac{\Delta T}{\Delta x} \tag{1.1}$$

where P is the total power output, A is the area of the conducting pattern, λ_s is the thermal conductivity of the thin sample, ΔT is the fully developed temperature difference across one of the insulating layers and Δx is the thickness of the thin sample pieces. The minimum thickness layer is 25 μm, with a resolution of ±0.5 μm.

The measurements were performed for the following paints: Paint200%, CNT0.1%, CNT0.2%, CNT0.3%, CNT0.4%, CNT0.5%, CNT0.7% and CNT1.0%. In Table 7.11, the main results of the thermal conductivity of those

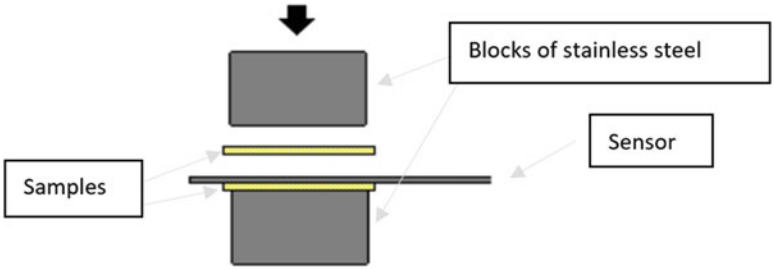

Fig. 7.18 Mounting the samples (*yellow*)

Table 7.11 Averages, standard deviations and uncertainties for paints and nanopaints

Paint	λ_s [W/mK]	$U(\lambda_s)$ [W/mK]	λ_s Enhancement %
Paint200%	0.092	0.021	0
CNT0.1%	0.154	0.02	+67.39
CNT0.2%	0.123	0.014	+33.7
CNT0.3%	0.145	0.017	+57.60
CNT0.4%	0.162	0.017	+76.09
CNT0.5%	0.151	0.017	+64.13
CNT0.7%	0.192	0.017	+108.7
CNT1.0%	0.101	0.009	+9.78

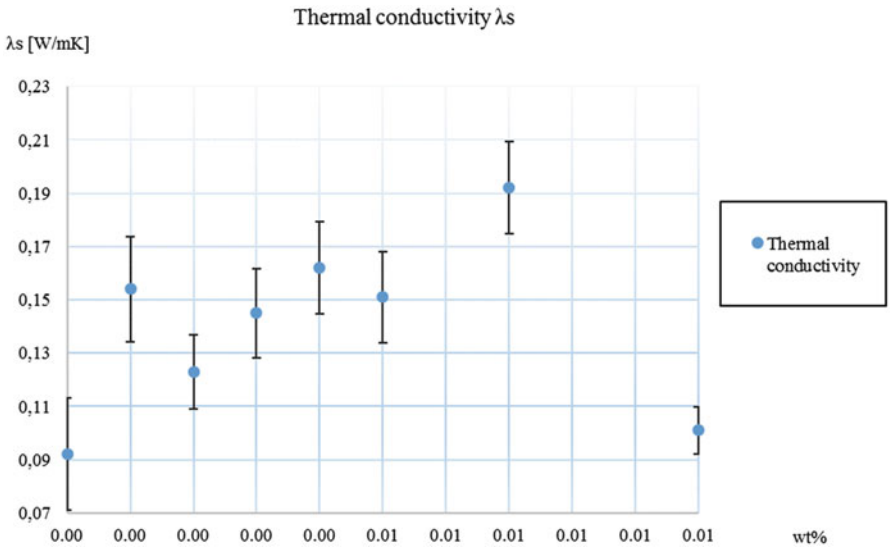

Fig. 7.19 Thermal conductivity varying the mass percentage of CNTs

samples are shown, with the uncertainty $U(\lambda_s)$ that was calculated taking into account the uncertainty of the thickness measured with the micrometre, and it is shown the percentage variation of λ_s related to λ_s of the Paint200%.

As it can be seen from the above presented results, with the addition of the nanoparticle, the thermal conductivity increases till the 0.7% weight concentration of CNTs and then decreases. Figure 7.19 presents the thermal conductivity as function of weight percentage of CNTs. It is possible to fit these values with polynomial curves of different order, however it is necessary to know the exact values of percolation threshold and of the maximum enhancement, and even more values with different wt% are needed to have a complete trend line to justify the choice of the polynomial's order.

It is also worth to mention that as the paint is applied to the substrate (polymeric piece), the diluent evaporates, and for that reason, the weight percentage of the nanoparticles into the nanopaints will increase considerably. Indeed, it can be said that with high values of weight percentages, the nanopaint changed its thermal properties. These specimens were produced by following the same procedures previously used for other tests, but with the difference that the number of paint applications has been doubled to four steps, in order to obtain a thickness greater than the limit for λ_s measurement. The worsening of thermal conductivity by adding the CNTs (over 0.7 wt%) should be justified by the increase of contact resistance resulting from the weak bonds between the CNTs [23].

Table 7.12 Thermal conductivity of paints and nanopaints in liquid phase with measurement's temperature and percentage variation related to Paint200%

Paint	λ_l [W/mK]	$U(\lambda_l)$ [W/mK]	λ_l Enhancement %
Paint200%	0.154	±0.001	18.7
CNT0.1%	0.145	±0.001	18.5
CNT0.2%	0.15	±0.001	19.8
CNT0.3%	0.151	±0.001	19.3
CNT0.4%	0.152	±0.001	19.6
CNT0.5%	0.155	±0.001	19.8
CNT0.7%	0.157	±0.001	19.8
CNT1.0%	0.161	±0.001	18.7

7.5.6 Thermal Conductivity of the Liquid Paint

It was considered useful to measure the thermal conductivity also in the liquid phase (λ_l), to have an index of possible increments of thermal conductivity of the nanopaint solid phase. A thermal analyser KD2 Pro based on the transient wire method to measure the thermal conductivity was used. The instrument collects data every 15 min and at least five measurements of thermal conductivity of each sample were recorded. The results are summarized in Table 7.12, and as it can be observed, the addition of diluent to the base coat (Paint0%) caused a significant decrease of λ_l of about 6.21%. It is useful to compare the paint containing nanoparticles with Paint200%, since the diluent is essential for the application of paints.

The results show that the addition of CNTs clearly increases the thermal conductivity of the base paint. However, the addition of the Fe_3O_4 nanoparticles does not change significantly the thermal conductivity of the nanopaint.

In Fig. 7.20, there is a graph that shows the thermal conductivity of the paint and the nanopaint in the liquid phase, with the respective error bars. For the nanopaint with CNTs, it was possible to add a linear trend line (linear CNTs) to obtain an assessment of the development of the thermal conductivity λ_l. As it can be seen, the values obtained for λ_l do not vary much from the trend line.

7.5.7 Electrical Conductivity Measurements

The DC electrical conductivity (σ_{dc}) of the samples was measured with a Keithley 6517B electrometer, in the temperature range between 170 and 380 K, using a nitrogen bath cryostat setup. During the measurements, the samples were kept in a helium atmosphere to minimize thermal gradients. The σ_{dc} can be calculated, as well as the electrical resistivity (ρ_{dc}):

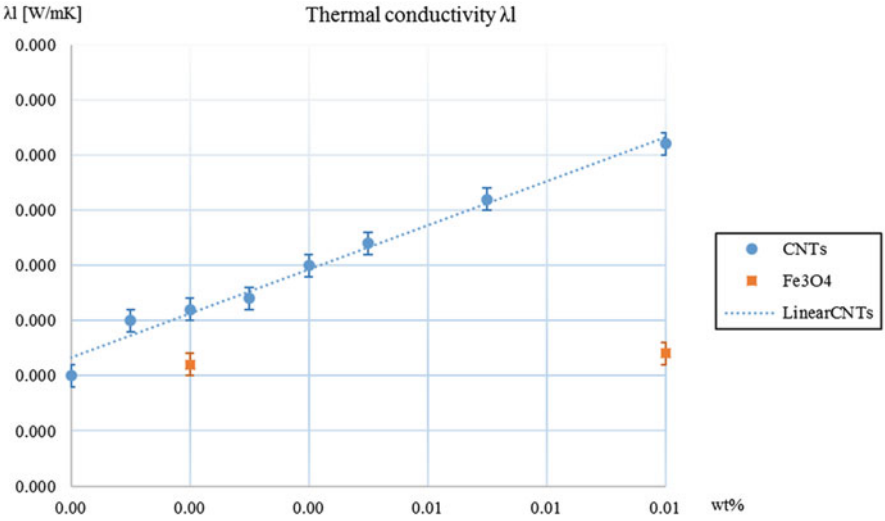

Fig. 7.20 Thermal conductivity for paints and nanopaints in liquid phase

$$\sigma_{dc} = \frac{1}{V} * \frac{d}{A} = \frac{1}{\rho_{dc}} \tag{1.2}$$

$$\rho_{dc} = \frac{A}{d} * R \tag{1.3}$$

V is the electric potential difference, I is the current intensity, d is the distance of the points among which the voltage is measured, A is the section area of the sample perpendicular to the direction of the current, ρ_{dc} is the electrical resistivity (direct current), and R is the electric resistance. The AC electrical conductivity (σ_{ac}) and impedance measurements were also performed in the temperature range of 170–380 K, using the same bath cryostat, with a Network Analyzer, Agilent 4294, operating between 100 Hz and 1 MHz in the Cp-Rp configuration (capacitance in parallel with resistance). In both measurements the temperature of the samples was controlled by an Oxford Research IT-C4.

The real and the complex parts of the permittivity were calculated using the following expressions:

$$\varepsilon' = \frac{d}{S} * \frac{C_p}{\varepsilon_0} \tag{1.4}$$

$$\varepsilon'' = \frac{d}{S} * \frac{1}{\omega R_p \varepsilon_0} \tag{1.5}$$

with C_p as the measured capacitance, R_p the resistance, d the sample thickness, S the electrode area, ω the frequency and ε_0 the vacuum permittivity (8.8542×10^{-12} F/m).

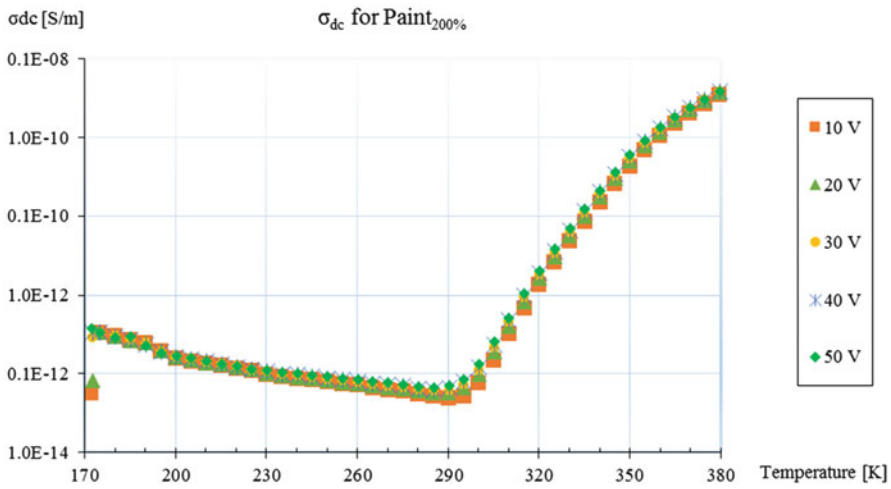

Fig. 7.21 Behaviour of σ_{dc} (Paint200%) changing the temperature between 170 and 380 K. The measurements were done for 10, 20, 30, 40 and 50 V

The AC conductivity, σ_{ac}, was calculated using the relation:

$$\sigma_{ac} = \varepsilon'' \omega \varepsilon_0 \tag{1.6}$$

Figure 7.21 shows the graph of the DC conductivity variation with the temperature, for the base paint, at different voltages. As it can be observed, the DC conductivity decreases with increasing temperature (from 170 to ~290 K), which is a typical behaviour for metallic materials.

For temperatures higher than 300K, the DC conductivity presents a sharp increase. This indicates that at this temperature, there is a structural change in the polymer. Moreover, above this temperature, there must be some charge carriers which become thermally activated and become the predominant conduction type.

Figure 7.22 presents the relation between the current and the applied voltage, for the base paint, at room temperature. It can be seen that the sample follows an ohmic behaviour, so Paint200% can be classified as an ohmic conductor: the potential difference at the terminals of a current-carrying conductor is directly proportional, according to the electric resistance of the conductor, to the intensity of the current.

The DC electrical conductivity analysis was also carried out for nanopaints with CNT0.1%. CNT0.5% and CNT1.0%, and the results are presented in Figs. 7.23, 7.24 and 7.25, respectively. For CNT0.1% there is not a substantial increase of σ_{dc} compared to Paint200%; in fact, the values are within the same orders of magnitude, and the raising of σ_{dc} due to temperatures is similar to that of Paint200%. This suggests that with this percentage of CNTs, there is no percolation effect, while at higher percentages (0.5 and 1.0 wt%), changes of 6 to 8 orders of magnitude can be seen (Figs. 7.24 and 7.25).

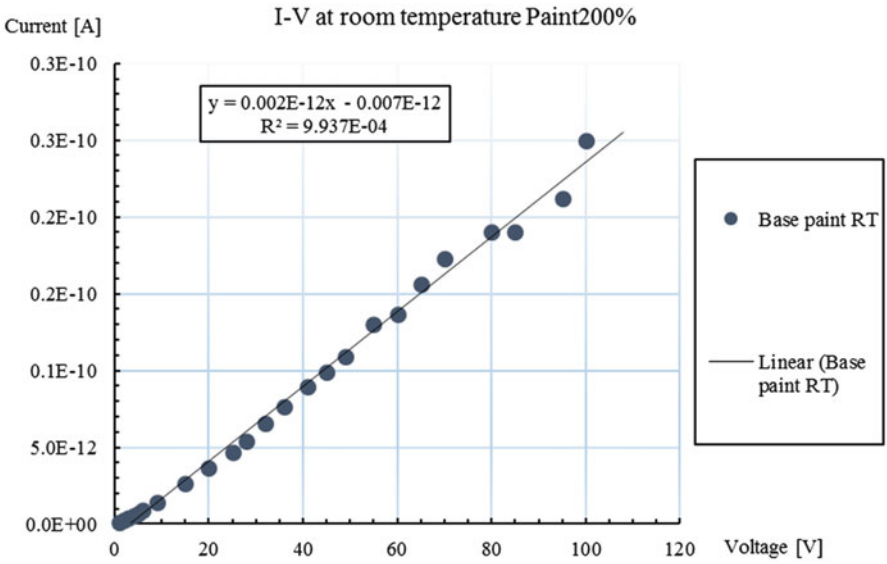

Fig. 7.22 Behaviour of σ_{dc} (Paint200%) changing the temperature between 170 and 380 K. The measurements were done for 10, 20, 30, 40 and 50 V

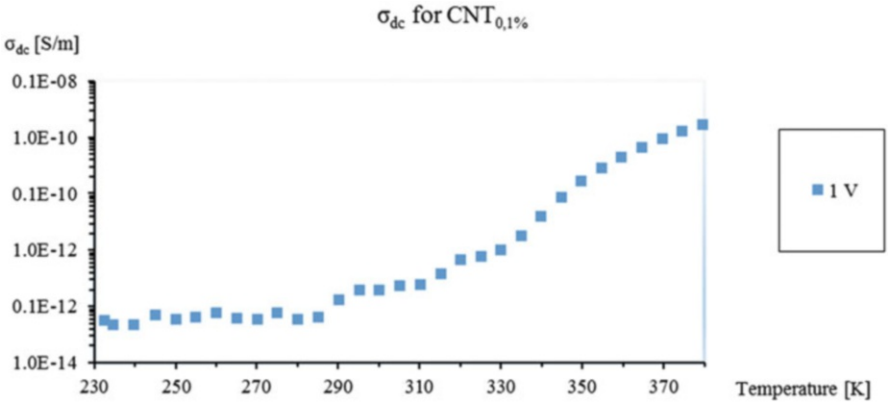

Fig. 7.23 Behaviour of σ_{dc} (CNT0.1%) changing the temperature between 230 and 380 K. The measurements were done for 1 V

From 260 to about 315 K, the DC conductivity is around 10^{-4} S/m, which represents an increase of ~8 orders of magnitude when compared to the base sample (only paint).

Around the temperature of 315 K, the conductivity of the doped paint with 0.5 wt % starts to increase, and at ~360 K the conductivity seems to saturate. At this given temperature, all available charge carriers are in conduction band. The same effect can be seen for the paint with 1.0 wt% but at 305 and ~355 K.

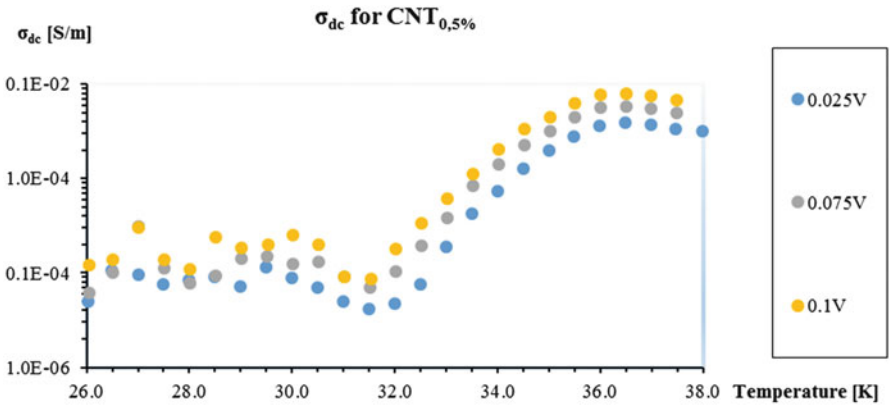

Fig. 7.24 Behaviour of σ_{dc} (CNT0.5%) changing the temperature between 260 and 380 K. The measurements were done for 0.025, 0.075 and 0.1 V

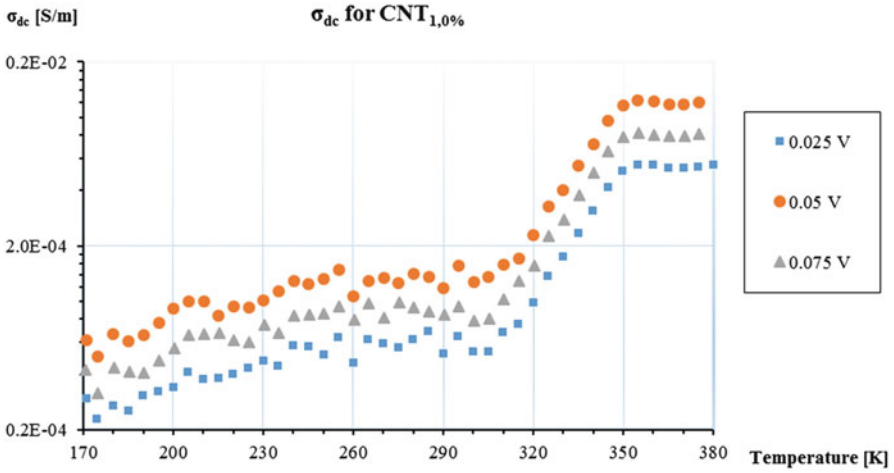

Fig. 7.25 Behaviour of σ_{dc} (CNT1.0%) changing the temperature between 170 and 380 K. The measurements were done for 0.025, 0.05 and 0.075 V

The conductivity dependence of the applied electric field (voltage) is not linear, and the results showed the existence of a maximum around 0.05 V for CNT1.0%, which has a rise in the electric conductivity around 305 K, while around 350 K it saturates.

The raising of σ_{dc} related to temperature for both CNT0.5% and CNT1.0% may be due to the increase of the percolation of CNTs, probably through the softening of the paint at 315 K for 0.5 wt% and at 305 K for that with 1.0 wt%. In fact, a softening of the paint, due to the glass transition temperature, allows the carbon nanotube to move and reorient itself in the matrix, and reach the optimization of

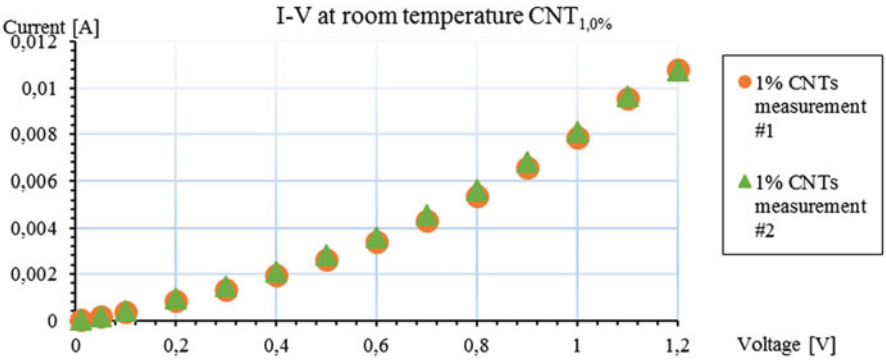

Fig. 7.26 I–V correlation at room temperature for CNT1.0%

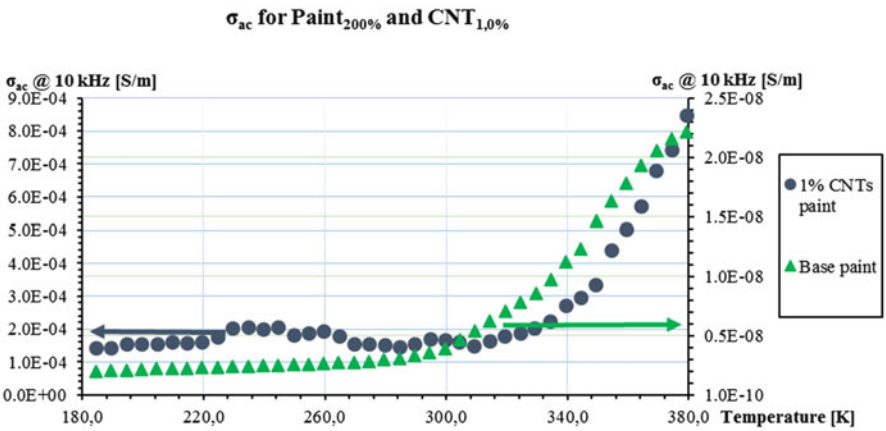

Fig. 7.27 Behaviour of σ_{ac} (*green triangles*, Paint200%; *blue circles*, CNT1.0%) changing the temperature between 170 and 380 K

percolation around 355/360 K. When the maximum percolation is reached, the electric conductivity saturates, and it varies only on the voltage.

The I–V correlation of the CNT1.0%, was performed also at room temperature. Two measurements were made, and their results were very similar as shown in Fig. 7.26. As it can be seen, this sample does not follow an ohmic behaviour because the current is not directly proportional to the potential difference.

The AC conductivity measurements show that, for CNT1.0%, there is a serious increase of the σ_{ac} values (~4 orders of magnitude), as shown in Fig. 7.27. Similarly, to the DC case, for temperatures above 300 K. The dielectric constant of Paint200% decreases with the increase of the frequency and increases with the increase of the temperature, showing that the temperature can activate a polarization mechanism.

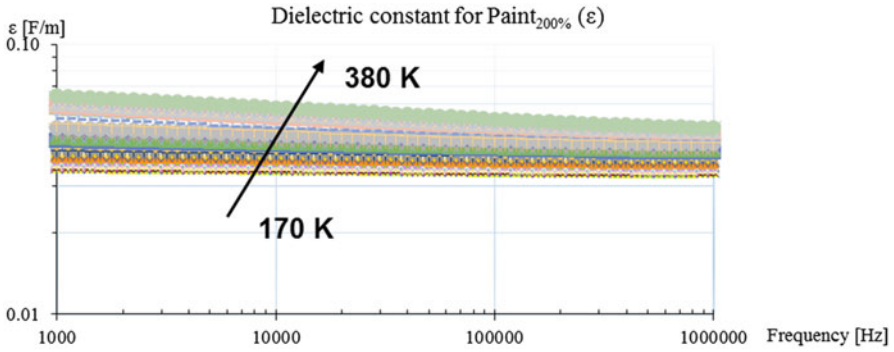

Fig. 7.28 Dielectric constant (ε) of Paint200% varying frequency from 103 to 106 Hz and varying temperature from 170 to 380 K

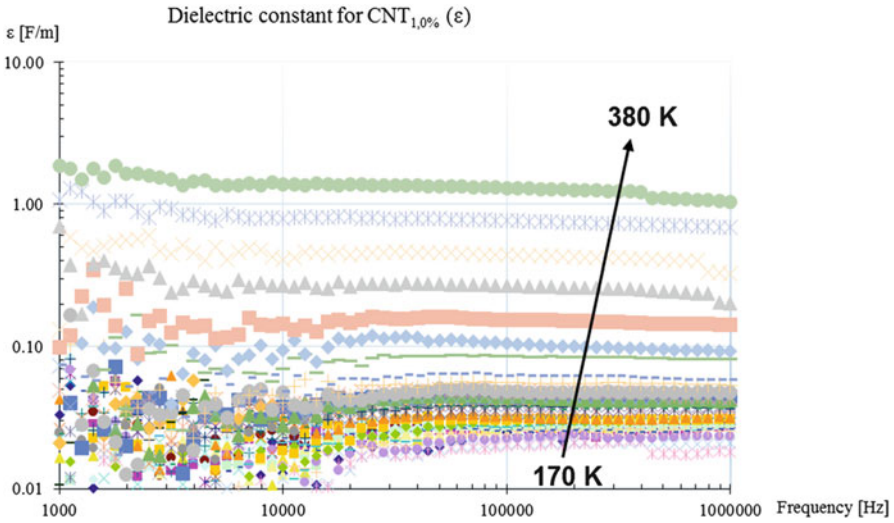

Fig. 7.29 Dielectric constant (ε) of CNT1.0% varying frequency from 103 to 106 Hz and varying temperature from 170 to 380 K

For the base paint, the maximum dielectric constant was ~10, observed at 370 K and 1000 Hz (Fig. 7.28). At the same measurement conditions, the 1% doped sample presented a dielectric constant of ~150 (15× greater).

As shown in Fig. 7.29, the sample with CNTs revealed a higher dispersion for frequencies lower than 1 kHz, which indicates the existence of a strong contribution from electrode polarization or interfacial polarization effects assigned to the presence of CNTs.

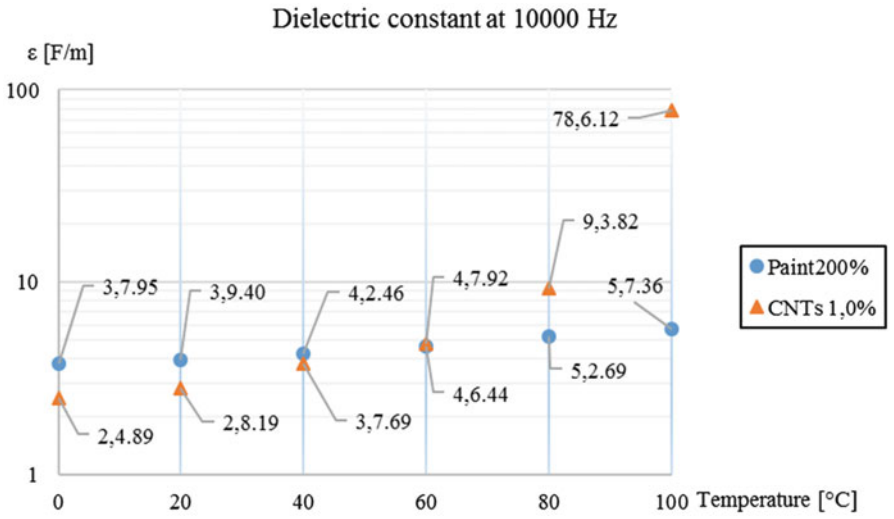

Fig. 7.30 Dielectric constant (ε) of CNT1.0% varying frequency from 10^3 to 10^6 Hz and varying temperature from 170 to 380 K

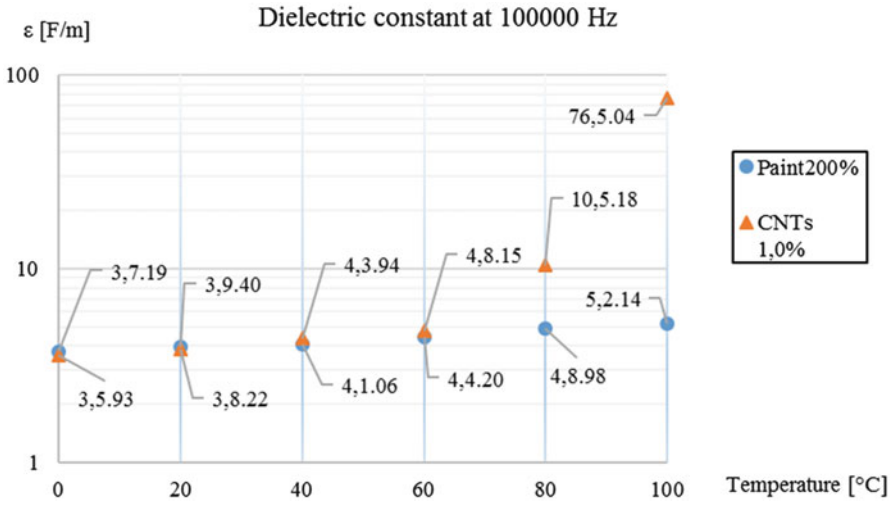

Fig. 7.31 Dielectric constant at 100,000 Hz

In Figs. 7.30 and 7.31, the dielectric constants of Paint200% and CNT1.0% are compared with changes in temperature for the fixed values of 10,000 and 100,000 Hz. It is noted that the dielectric constant increases with temperature and frequency.

7.6 Discussion of the Results

7.6.1 Nanopaint Preparation

The mixing of the nanoparticles is detrimental in the nanopaint preparation; in fact, different tools and different procedures were used to obtain a paint as homogeneous as possible. The first phase, which consists in mixing the base paint with the diluent, may be conducted with a magnetic stirrer for about 30 min. It was not necessary to produce coatings with different amounts of diluent as it evaporates during the application on the substrate, and the percentage of diluent recommended by the manufacturer was used (Paint200%). For the mixing of the nanoparticles, initially an ultrasonic tip was used but tended to overheat the paint with the risk of the diluent to evaporate. To overcome such problem, a water bath was used together with the ultrasonic tip to prevent that effect. Also the incorporation of a magnetic stirrer was used in order to facilitate the mixing and the dispersion of the nanoparticles. However, such procedure was not possible to use with ferromagnetic particles as Fe_3O_4, since the magnetic field generated by the instrument would have limited or prevented proper mixing. As an alternative, an ultrasonic bath was used to mix the nanoparticles, and so it was used the ultrasound without causing overheating of the paint. Furthermore, to improve the dispersion process, during the ultrasonic bath, a glass stick was used to manually assist the mixing of the paint (it was not possible to perform the same process with the ultrasound tip). Therefore, in the preparation of the nanopaint, it was followed by the procedure which included the use of ultrasonic bath with the help of manual mixing for an overall time of mixture of 30 min.

7.6.2 Colour Analysis

It is necessary to take into account the colour change of the paint when the nanoparticles are added to the paint. The use of these paints has the purpose to protect the substrate, but the aesthetic factor is also of utmost importance. In fact, the chrome plating is considered as a process that gives prestige to chromed object, pushing up the price of the finished product. For this reason, the colour changes must be limited as much as possible. Firstly specimens coated with two different types of paint were prepared, as seen in Figs. 7.32, 7.33 and 7.34. In all of the three mentioned figures, in the left part of the specimens, the Paint200% has been applied, while on the right side, paints loaded with nanoparticles have been applied. With a first comparison, it can be seen that paints containing only 0.2% of CNTs and 0.2% of Fe_3O_4 are darker and less bright than Paint200%.

It is evident how the colour changes with the addition of different nanoparticles with different dosages. In Fig. 7.35, the upper part of the samples consists of Paint200% and the lower part by the nanopaint. The specimen on the right presents

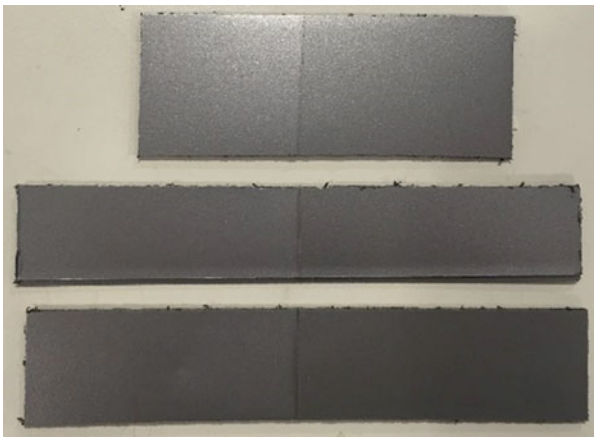

Fig. 7.32 Comparison of Paint200% and Fe_3O_4 0.2%

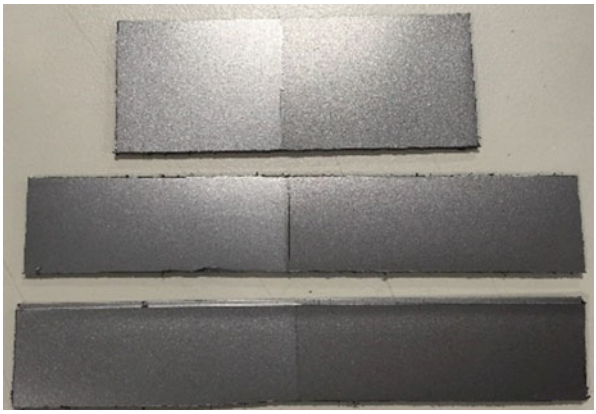

Fig. 7.33 Comparison of Paint200% and Fe_3O_4 0.5%

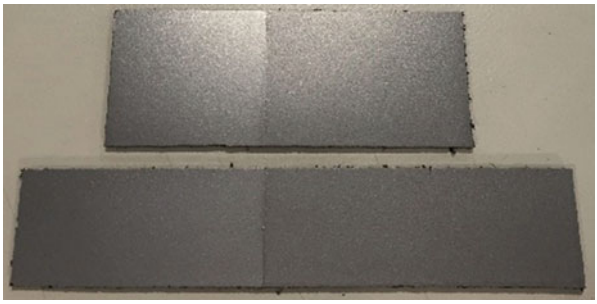

Fig. 7.34 Comparison of Paint200% and CNT0.2%

the duller nanopaint; it is loaded with 0.5 wt% of Fe_3O_4. The colour change is a consequence not acceptable for a paint that is intended for aesthetic use. It is necessary in the future to analyse paint containing nano-powders presenting colours as similar as to grey chrome paint to avoid or at least limit such an evident discolouration.

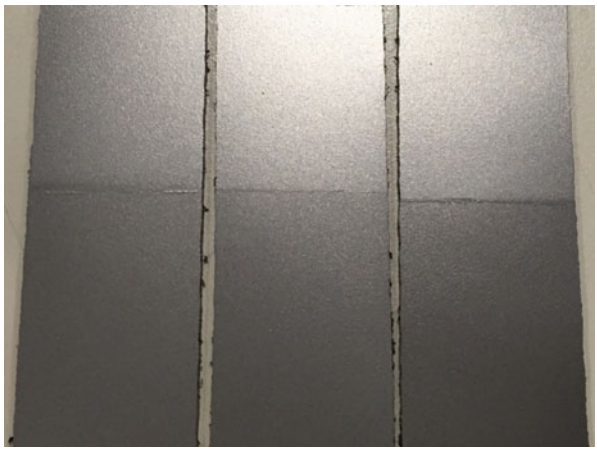

Fig. 7.35 Comparison of Paint200% and nanopaint. *Left*: Paint200% and CNT0.2%. *Centre*: Paint200% and Fe_3O_4 0.2%. *Right*: Paint200% and Fe_3O_4 0.5%

In the analysis of light reflection, a decrease in reflectivity of the paint was found when just 0.2 wt% of CNTs were added. Such colour change was confirmed by RGB/Lab/XYZ analysis. Considering the brightness L of the Lab coordinates, all nanopaints have values of L less than Paint200%, indicating that the brightness is reduced due to of the addition of CNTs. Only the values for the Fe_3O_4 are almost equal to those of Paint200%, but increasing the dose to 0.5 wt% (Fe_3O_4 0.5%), the coordinates of the colour change dramatically. This highlights how nanoparticles used in this work are not suited to the required applications, since they generate substantial colour changes with minimum percentages of nanoparticles. For that reason, in this work we have focused on the production and process of the nanopaint, which can be used in a future work with different nanoparticles that may not alter the colour (e.g. nano-Al).

7.6.3 Thermal Conductivity

As already mentioned, the thermal conductivity of the paints had the same order of magnitude when measured in liquid or solid phase. However, the comparison should be conducted valuating the changes of wt% of nanoparticles after the diluent evaporation. In fact, after drying, the paint in the solid phase is no longer composed of two parts of diluent and a part of pure paint but only pure paint, since the diluent is evaporated to allow solidification. The removal of the diluent is a very decisive factor on the preparation of the nanopaint, as the weight percentage (or volume) of the nanoparticles changes from its initial values. In fact, the nanopaint initially with the 1.0 wt% of CNTs, after solidification, reaches ~3 wt%.

In Fig. 7.36 there is the comparison between λ_s and λ_l of the nanopaint with the CNTs, in which the weight percentages of the solid phase were multiplied per 3 in order to have the approximation of the weight percentage after the diluent evaporation. As it can be seen, the values of solid and liquid phases do not match each

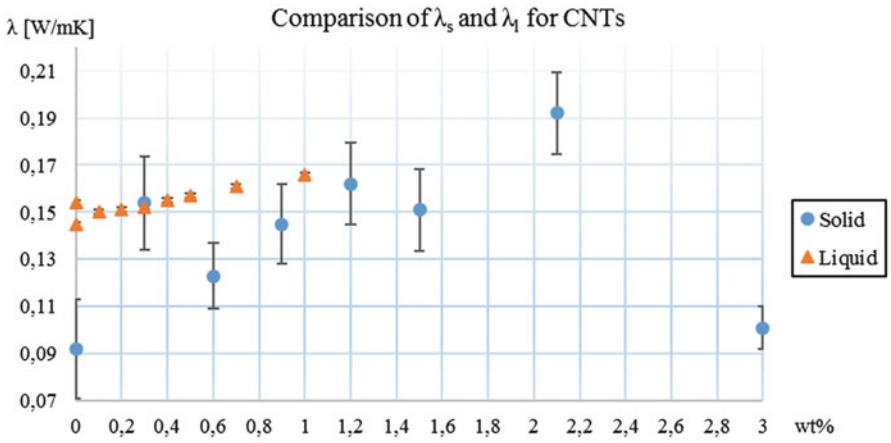

Fig. 7.36 Comparison of λ_s and λ_l for CNTs

Table 7.13 Thermal conductivity of CNTs with different pressure [23]

Sample	Pressure [psi]	λ_s [W/mK]	ϕ [%]
1–2 nm SWCNT	20	0.155	17.2
	50	0.175	18.1
	90	0.194	19.4
<8 nm MWCNT	20	0.154	12.7
	50	0.171	13.7
	90	0.195	15.2
60–100 nm MWCNT	20	0.134	8.9
	50	0.154	10.4
	90	0.170	12.4

other, but the trend of both shows an enhancement of thermal conductivity when the CNTs' weight percentage increases. For λ_l values it is not possible to evaluate a maximum with those wt%, while in solid phase it is possible to estimate a maximum around 0.7 wt%; in fact, that weight percentage corresponds to an enhancement of 108.7%, respectively, to the λ_s of Paint200%.

There is a clear reduction of λ_s between 0.6 and 1.0 wt%, when compared with λ_l, that should be justified in examining some research showing that the addition of CNTs does not result in an improvement of thermal conductivity but in worsening [23]. This phenomenon is due to the fact that the carbon nanotubes have thermal conductivity greater than 3.000 W/mK if they are considered individually, but if they are considered as masses with mono- or bi-dimensional distribution, the thermal conductivity decreases by 1 and 2 orders of magnitude, respectively, while for a three-dimensional distribution, values as lower as 0.2 W/mK are reached, which are typical for an isotropic polymer [23, 24].

In Table 7.13 are presented the thermal conductivity (λ_s) of three types of carbon nanotubes subjected to different pressures; different volume fraction (ϕ) and an

increase of the contact surface between the nanotubes can be observed. It is well known that a large contact resistance limits the transfer of energy in the van der Waals contacts, due to weak intertube bonds. The contact resistance between the tubes decreases with increasing the size of the diameter of the nanotubes, due to a larger area of contact, even if nanotubes with smaller diameters should ensure a greater number of contacts intertube. The thermal resistance also depends on the length and the overlap of the nanotubes and the distances between the junctions. In fact, if the length is greater, if the overlap area of the nanotubes is bigger and if the distance between them is smaller, the intertube thermal resistance will be lower [25]. With the increase of the intertube space, the van der Waals interactions between the tubes are weakened, reducing the heat that, among the nanotubes, may only be transmitted with this mechanism. Instead, when two nanotubes overlap and merge, the energy is transmitted through the bonds between the atoms, by improving the efficiency of heat transfer compared to the exchange mechanism only with van der Waals interactions. A greater length of the nanotubes is helpful to the increase of thermal conductivity, as it allows greater length overlaps and allows the transmission of heat through the molecular bonds for greater distances than those of shorter CNTs, exploiting less van der Waals intertube interactions, which have higher thermal resistance [25].

The heat transmission at the interface between CNTs and the matrix also should be considered, which likely influences the exchange of heat due to the lack of functionalization. In fact, if there is a heat transfer problem between the nanotubes, the same problem may occur again in the interactions between the matrix and CNTs. To overcome this limit, a functionalization of the nanoparticles is necessary, which consists in adding a chemical functional group on the its surface. The goal of functionalization is to coat the surface with a molecule having the appropriate chemical functionality for the desired application [26]. To carry out the functionalization is then necessary to identify the appropriate process for this purpose and the functional group that is chemically compatible with the nanoparticle and with the matrix. The chemical compatibility is necessary to reduce the distance between the atoms and/or to generate the bonds between atoms of the nanoparticles and the matrix, while an automatic organization of CNTs allows a better and faster dispersion.

In this case the presence of agglomerates which were detectable to touch and to the naked eye is an indication of a not-optimal dispersion, which then influences the exchange of heat. Those aggregates are constituted by CNTs, which, randomly dispersed, possess a high thermal resistance in the tube-tube interactions. Moreover, the particle-matrix interface decreases, limiting the heat exchange. Taking into account these phenomena, it is possible to justify the decrease of thermal conductivity with 1.0% of CNTs.

However, the main goal of this work has been partially reached, in the way that it was observed an enhancement on the thermal conductivity with the addition of CNTs, both in liquid and solid phase, confirming the possibility of increasing the thermal conductivity of the paint by adding small percentages of nanoparticles with higher thermal conductivity. The main problem lies in the type of nanoparticle,

because it can greatly vary the aesthetic quality for the colour variations and the presence of agglomerates which vary the surface roughness when a good nano-dispersion is not obtained.

7.6.4 Electrical Conductivity

The electrical behaviour of a nanocomposite, after the addition of CNT, changes from insulator to conductor, as soon as it is established at least one conductive path (percolation phenomenon), dependent on the concentration of nanoparticles (percolation threshold). The percolation threshold has been exceeded with 1.0 wt% of CNTs; in fact, CNT1.0% has electrical conductivity in alternating current (σ_{ac}) about four orders of magnitude higher than that of Paint200%. The improvement in electrical conductivity was obtained also in the case of direct current (σ_{dc}) but about eight orders of magnitude.

This aspect can be considered a relevant factor in reducing the electrostatic charge of the non-conductive polymers. In fact, using chrome-plated plastics as an alternative to metals, the high electrical conductivity of the nanopaint prevents the possible electrostatic discharges when someone touches these elements.

7.6.5 Health and Environmental Aspects

The industrial-scale application of nanoparticles in many areas of daily life, as well as specific health applications, raises the question of the security of these systems. The nanometre size can give rise to concerns in relation to its small size, which could allow to cross the natural barriers, resulting in a potential biological damage. In fact, the nanoparticles are much smaller than most known particulate matter PM10 (PM10, i.e. the atmospheric particulate matter detains a mean aerodynamic diameter of 10 μm), whose percentage in the atmosphere is used as an indicator of pollution. As has been seen, however, the nanoparticles term indicates diverse systems between them. Some nano-systems are used precisely in function of their biocompatibility, for the use in diagnosis, replacing molecules used currently and whose toxicity is ascertained. Therefore, it makes little sense to worry generically of nanoparticles simply because of their size (many nanoparticles are produced spontaneously and are always present in the air or are unknowingly used for centuries). Their properties can depend on many details, the size, the exposed surface and the combination with other nano-systems, and not only from the substance that constitutes them. It is therefore important to make sure that every new system and technology is subjected to focused experiments, in relation to the specific applications. If we process it, we must have a reasonable assurance that the specific nanoparticles used in paint are not harmful to people and to the environment, compared to the expected exposure.

7.7 Conclusions

The study carried out with nanoparticles of Fe_3O_4 has not led to the required solution, since it has failed on two important aspects. Firstly, the paint colour is significantly changed after the addition of the nanoparticles, and especially the brightness is decreased after the addition of low doses (as low as less than 1 wt%). Secondly, the thermal conductivity measurements in the liquid phase do not registered significant increases of λ_l compared to Paint200% (1.8% with 1.0 wt %). This discards the possibility of using such nano-additive for this type of nanopaint.

Regarding the carbon nanotubes, best results were registered for both the thermal conductivity in liquid phase and that one in the solid phase, with a peak of $\lambda_s = 0.192 \pm 0.017$ W/m K for 0.7 wt% of CNTs, corresponding to an enhancement of 108.7% compared to Paint200%. However, despite these improvements, CNTs cannot be used for the purpose of this work because of the brightness variation already registered, even for the weight percentage of 0.2. Excessive reduction in brightness cannot be accepted as this feature is crucial to get a chrome effect, and, with CNTs percentages higher than 0.2 wt%, the colour change is even more evident, tending to a matte dark grey.

The future work may be focused on two main aspects: the determination of the best nanoparticles to be added to the base paint and the optimization of nano-dispersion.

Concerning to the nanoparticles most suitable for the purpose of this work, one must consider the thermal conductivity, the colour and the cost. There are various metals with high thermal conductivity, including gold, silver and copper, to be taken as a reference for the choice of nanoparticles, but they are notoriously precious metals, therefore expensive, or in nano-metric dimensions they take colours that would affect too much the chrome effect (as for CNTs). Comparing the colours of different metals, commercially available in nano-powder, and selecting those with the best thermal conductivity, nano-aluminium particles (nano-Al) would be the best choice to continue this work. In fact, the grey colour of the nano-Al makes to presuppose that they do not significantly vary the colour of the base paint, leaving unchanged the required chrome effect. Furthermore, the thermal conductivity of aluminium is 290 W/m K, around four orders of magnitude higher than that one of the base paint (0.092 W/mK).

However, the RGB analysis must be performed to assess colour changes, thermal analysis in liquid and solid phases and electrical analysis to characterize the new nanopaint containing nano-Al particles.

Other tests are suggested for the evaluation of the quality of the nanopaint, such as the roughness and hardness analyses of the layer after the addition of nanoparticles and pull-off tests of the paint, which, according to other studies on paints, are supposed to show improvement after the addition of nanoparticles [27]. It is also recommended to carry out analyses with a thermographic camera to get photographic results that certify a possible improvement in the thermal

conductivity. Functionalization of nanoparticles will be asked whether it will be necessary to optimize the nano-dispersion to avoid agglomeration for a higher surface quality and to get better percolation of the nanoparticles that improves the thermal and electrical conductivity.

Acknowledgements The authors acknowledge the support of Bruno Silva (Department of Mechanical Engineering of the University of Aveiro), Farzin Mohseni, Bruno Melo, Prof. Vitor Amaral and Dr. Manuel Pedro Graça (Department of Physics of the University of Aveiro), Prof. Augusto Barros Lopes and Artur Sarabando (Department of Materials Engineering) and to CIE STRATIS—Tratamentos, Lda. (Varzea, Barcelos, Portugal).

References

1. Tyler JM (1995) Automotive applications for chromium. Met Finish 93(10):11–14
2. Mandich NV (1999) Practical problems in bright and hard chromium electroplating—Part I. Met Finish 97(6):100–112
3. Interational Agency For Research on Cancer (1990) IARC monographs on the evaluation of carcinogenic risks to humans. IARC 49:208–214
4. Gambelunghe A, Piccinini R, Ambrogi M, Villarini M, Moretti M, Marchetti C, Abbritti G, Muzi G (2003) Primary DNA damage in chrome-plating workers. Toxicology 188 (2–3):187–195
5. Roberti S, Mabilia T, Stocco CF, Sarto F, Merler E (2006) Aumentata mortalità per tumori polmonari tra gli addetti a una cromatura a strato sottile [An increased mortality from lung cancer among workers of a bright electroplating factory]. Epidemiol Prev 30:232–236
6. Mohapatra P, Samantaray SK, Parida K (2005) Photocatalytic reduction of hexavalent chromium in aqueous solution over sulphate modified titania. J Photochem Photobiol A Chem 170 (2):189–194
7. Navinsek B, Panjan P, Milosev I (1999) PVD coatings as an environmentally clean alternative to electroplating and electroless processes. Surf Coat Technol 116–119:476–487
8. Bozyaz E, Ürgen M, Çakr AF (2004) Comparison of reciprocating wear behaviour of electrolytic hard chrome and arc-PVD CrN coatings. Wear 256(7–8):832–839
9. Kuroda S, Kawakita J, Watanabe M, Katanoda H (2008) Warm spraying—a novel coating process based on high-velocity impact of solid particles. Sci Technol Adv Mater 9(3):033002
10. Paint and Coatings Industry Overview—Chemical Economics Handbook (CEH) | IHS [Online]. https://www.ihs.com/products/paint-and-coatings-industry-chemical-economics-handbook.html. Accessed 15 Oct 2015
11. Szeteiová, K. (2010). Automotive materials plastics in automotive markets today. Institute of Production Technologies, Machine Technologies and Materials, Faculty of Material Science and Technology in Trnava, Slovak University of Technology Bratislava.
12. Thermo Fisher Scientific. Chemical Compatibility Guide—The Chemical Resistance Chart. Chem. Resist. Chart Resist, pp 1–7
13. Processo di lavaggio [Online]. http://www.durr-ecoclean.com/it/prodotti/processo-di-lavaggio/. Accessed 2 Mar 2016
14. Pastorelli I (2004) Verniciatura e controllo qualità. Proprietà, tecniche di lavorazione e controllo delle superfici verniciate. Hoepli Editore, Milan
15. Bulla G, Perbellini L (2011) Le nuove tecniche di verniciatura e rischi per la salute. G Ital Med Lav Ergon 33(3):257–263
16. Krishnamoorthy K, Jeyasubramanian K, Premanathan M, Subbiah G, Shin HS, Kim SJ (2014) Graphene oxide nanopaint. Carbon N Y 72:328–337

17. Umwelt Bundes Amt (2013) Use of nanomaterials in textiles, pp 1–12
18. "Linea-surfapore" [Online]. http://www.nanosilv.it
19. Boon T, Shariffa N, Abas F, Mirhosseini H, Arbi I, Ping C (2016) Comparing the formation of lutein nanodispersion prepared by using solvent displacement method and high-pressure valve homogenization: effects of formulation parameters. J Food Eng 177:65–71
20. Juliane F, Desrumaux A, Lardieres J (2000) Effect of high-pressure homogenization on droplet size distributions and rheological properties of model oil-in-water emulsions. Innov Food Sci Emerg Technol 1:127–134
21. Hielscher T (2005) Ens'05, December, pp 14–16
22. EasyRGB—The inimitable RGB and COLOR search engine! [Online]. http://www.easyrgb.com/index.php?X=CALC. Accessed 8 Mar 2016
23. Prasher RS, Hu XJ, Chalopin Y, Mingo N, Lofgreen K, Volz S, Cleri F, Keblinski P (2009) Turning carbon nanotubes from exceptional heat conductors into insulators. Phys Rev Lett 102:105901
24. Hone J, Llaguno MC, Nemes NM, Johnson AT (2000) Electrical and thermal transport properties of magnetically aligned single wall carbon nanotube films. Appl Phys Lett 77 (5):666–668
25. Zhong H (2006) Interfacial thermal resistance between carbon nanotubes: molecular dynamics simulations and analytical thermal modeling. Phys Rev B 74:1–10
26. Subbiah R, Veerapandian M, Yun KS (2010) Nanoparticles: functionalization and multifunctional applications in biomedical sciences nanoparticles: functionalization and multifunctional applications in biomedical sciences. Curr Med Chem 17(36):4559–4577
27. Pham GV, Trinh AT, Xuan T, To H, Nguyen TD (2014) Incorporation of Fe_3O_4/CNTs nanocomposite in an epoxy coating for corrosion protection of carbon steel. Adv Nat Sci Nanosci Nanotechnol 5(3):035016

Chapter 8
Atomic Force Microscopy for Microbial Cell Surfaces

Muhammad Raza Shah and Muhammad Ateeq

8.1 Introduction

Binnig et al. invented atomic force microscope (AFM) in 1986. It is a scanning tool for nanostructure investigations. It is now considered to be one of the landmarks of modern sciences, for citations of the first article increase more than 13,500 times [1]. The AFM has come up as a new addition to macroscopic and microscopic techniques since it has benefits in sample preparation and the ability of high-resolution imaging in both liquid and air environment if compared to standard light microscopy techniques. This sophisticated instrument has successfully been used in all branches of science like material science [2], food science [3], nanofabrication [4], and microbiology, for nearly two decades after its invention [5]. The microbiology field has been revolutionized by AFM. It has enriched the realm of sample preparation and microbial surface analysis in particular during the last two decades [6].

AFM has basically initiated as imaging instrument and provides topographic analysis of microbial surfaces in air with three-dimensional structural details with high resolution [7]. It was reformed in such a way that it can image the microbial surfaces in their natural environmental conditions [8] and to determine the interactive forces of these biological systems within 4 years of AFM invention [9]. For performance optimization, the AFM instrument has been continuously modified

M.R. Shah (✉)
International Center for Chemical and Biological Sciences, HEJ Research Institute of Chemistry, University of Karachi, Karachi 75270, Pakistan
e-mail: raza.shah@iccs.edu

M. Ateeq
Department of Chemistry, Abdul Wali Khan University, Mardan-23200, Pakistan

International Center for Chemical and Biological Sciences, HEJ Research Institute of Chemistry, University of Karachi, Karachi 75270, Pakistan

M.J. Jackson, W. Ahmed (eds.), *Micro and Nanomanufacturing Volume II*,
DOI 10.1007/978-3-319-67132-1_8

with improved sensing and originating features. Its basic purpose is to emerge new techniques like single-molecule force spectroscopy (SMFS), single-cell force spectroscopy (SCFS), and chemical force microscopy (CFM) [10].

It has thoroughly been observed that the AFM-based methods are sensitive enough to allow detection of forces ranging from ~5 pN, that is approximately equal to the bond strength between a single receptor and ligand, to ~100 nN, approximately equal to the force with which cells are stuck together [5, 11]. The spatial resolution of AFM approaches to ~1 nm by using immobilized and extracted cell membranes patches [12], whereas AFM resolution is limited to ~10 nm for dynamic and crenelated microbial surfaces [13].

The morphology and physicochemical properties of microbial systems are important in characterization of microbial interactions with different interfaces and surfaces. The surface morphology of microbial systems is determined with conventional microscopic techniques which require considerable sample preparation as a result of which the sample surface morphology can damage and produce various defects. In addition to it, the macroscopic techniques used for the determination of physicochemical properties of cell surface like contact angle measurements and zeta potential. These techniques provide averaged data on wide assemblages of cells. Fluorescence imaging is influential technique used for localization of single cells in intricate microbial systems [14], but it should be kept in mind that image resolution is dependent to the wavelength of light source. High-resolution images of microbial systems are obtained from electron microscopy techniques. In particular, images of the whole bacterial cells are acquired with three-dimensional electron microscopy or cryo-electron tomography at higher resolution up to two times higher than light microscopy [15]. High-resolution images of microbial systems can also be provided with transmission electron microscopy and scanning electron microscopy techniques, no doubt they are advantageous to some extent, but their limitations may not be neglected ever regarding complex sample preparation including metal coating, dehydration, chemical fixing, and ultrathin section can significantly deteriorate the sample. The above given limitations were mostly required to be elaborated with sophisticated technique so that its consequence may be clear and obvious. It was the need of the researchers to start getting their questions and answers with the invention of AFM. It is known that the AFM images were obtained through direct contact between the sample and the tip, for no or less sample preparation is required. Moreover, true three-dimensional images are provided with AFM, but it only focuses on the limited ranges in heights at one time. AFM is considered to be one of the most important techniques for biological applications, besides the microbial systems can be examined in buffer solution, which are very important for keeping an eye on the live cells in real-time scanning.

Atomic force microscopy has brought great changes in the way the researchers probe the microbial systems. AFM measures the small forces acting between the sample and a sharp tip instead of an incident beam of light [10, 16]. The tip is attached to a cantilever by using a piezoelectric scanner that bends under force and is moved in three dimensions to generate a topographic image. Cantilever's bending

is measured by a laser beam focused on the free end of the cantilever and reflected into a photodiode at the time of scanning the sample surface. In contrast to other microscopy techniques, three-dimensional images of microbial membranes and cells are acquired without fixation, staining, or labeling at high resolution, so in physiological conditions. The microbial systems comprise of highly complex cells which are present in heterogeneous systems. Normally, microbial cells are divided into subclasses which reveal different resistance to stress and growth rate [17]. Furthermore, these subclasses of cells are spatially organized in such a way that they can perform different key functions [18]. To understand such complex microbial systems required single-cell analysis techniques in microbial research. The mechanical and spatial properties of the molecules present on the surface of individual microbial cell are measured by AFM through single-molecule force spectroscopy, in which the cantilever deflection is recorded to be a function of the vertical displacement of the scanner (as the sample is pressed toward the tip) [16]. As a result, it is observed that there is a cantilever deflection versus scanner displacement curve and is transformed into a force distance curve by using suitable modifications. The distinctive adhesive forces between sample and tip are determined during retraction which is used to probe the mechanics and distribution of single molecules like microbial cell surface receptors.

Besides topographic imaging, AFM can also be operated in force spectroscopy mode to determine the physical properties and interactive forces of the microbial systems. A force distance curve is obtained in this operational mode, in which the force signal is determined by recording the cantilever deflection as the AFM tip reaches the sample and then withdraws from it. Furthermore, having generated a force volume image through obtaining force distance curves at different locations, spatial resolution can be accomplished. To study protein folding and unfolding mechanisms and to determine which molecular groups are present on microbial cell surface, functionalized AFM tips are being used [5, 19].

To comprehend cell surface interactions, these innovative AFM techniques are used for analyzing microbial cell walls and providing new opportunities for better understanding of microbial systems. In this chapter, a flavor of the different applications of AFM in microbiology is provided, and the key breakthroughs in pathogen research have been highlighted. This chapter will facilitate the reader and researcher in multidimensional disciplines.

8.2 Atomic Force Microscope: Instrumentation

The AFM instrument comprises of four major parts including a tip, a piezoelectric scanner, an optical deflection system comprising of photo detector and laser diode, and an electrical feedback system. The probing tip (made from silicon or silicon nitride) mounting at adjustable cantilever's end is the heart of the AFM. High-resolution three-dimensional images are obtained by movement of either the sample or the cantilever mounting on a piezoelectric scanner by using AFM.

The basic principle of AFM microscopy technique is a sharp AFM tip raster over the surface during scan, at the time of sensing the interaction between the tip and the sample. The optical deflection system detects the cantilever deflection, and cantilever deflection is a result caused by small interactions forces between the AFM tip and the sample. The backside of the cantilever reflects the laser beam and stored into a four-quadrant photodetector, to record the position of the reflected laser beam. The interactive forces between the tip and the sample are responsible to bring changes in magnitude of deflected laser beam. The deflection signals are automatically administered to restructure an interaction force profile or a topographic image of the sample. To obtain a high-resolution image with simple protocol for sample preparation of the microbial systems, both in liquid and in air environments, AFM topographic analysis has emerged as an essential instrument in addition to standard electron and light microscopy techniques in the past years.

AFM images are generated in three different operational modes like contact, noncontact, and intermittent or tapping modes. The tip movement across the sample during analysis is the only difference among all these operational modes. In the analysis of biological samples, the contact and intermittent or tapping modes are mostly applied. Contact operational mode is most widely used in AFM analysis. In this operational mode, the tip of cantilever directly touches the sample during analysis. Contact mode generates two different types of images, height and deflection. The cantilever deflection is recorded to generate height image when the tip moves across the sample during scanning. Height image gives information about surface roughness and height of the analyzed samples. The sample height is adjusted by using feedback loop in order to keep constant the cantilever deflection when the tip moves across the sample during scanning to generate the deflection image. It is very difficult to keep constant the cantilever deflections as the feedback loop is not perfectly adjusted, so a constant signal error is always present in the deflection image. The deflection image is more sensitive to the fine surface information.

High lateral forces are associated in contact operational mode, as a result soft biological samples can be removed from substrate or damaged. Therefore, to prevent the sample damage, it is necessary to minimize the lateral forces generated from AFM tips. The lateral forces are minimized by using the tapping or intermittent operational mode. In this AFM operational mode, phase and amplitude of the cantilever are administered when the probe of AFM is externally excited around its resonating frequency when AFM tip moves across the sample surface during scanning. In intermittent mode, the tip of AFM comes in contact with surface periodically when the tip moves downward, and as a result sample damage is minimized. The three types of different images can be obtained in intermittent or tapping operational mode including height amplitude, and phase images. Topographic information like contact mode are obtained from height image. Fine structural details and main features of the edges of the sample surface are obtained at the sacrifice of height information in amplitude image which is just like deflection image in contact operational mode [20]. The phase image is generated by recording the phase lagging of cantilever oscillation relative to driving signal. It

provides information about difference in properties and sample composition like adhesion and elasticity [21].

AFM force spectroscopy offers new and exciting opportunities to probe the local properties and ultrastructure of biological samples in physiological environment along with positional precision and high force sensitivity. In this operational mode, deflection of cantilever is monitored as a function when sample is vertically displaced and the tip is pushed forward toward the sample and then pushed back from it. This force curve is useful to gain observations about different surface properties like cell surface charges, cell surface, cell surface hydrophobicity, and cell wall elasticity. Remarkably, the curve between force and distance is recorded at different locations of the x-y plane which gives spatially resolved maps of physicochemical properties of microbial systems with lateral resolution in nanometer scale [22]. The data obtained in this way are then represented either in elasticity maps [22] or in adhesions maps [23].

The force spectroscopy has emerged into three different force modes including single-molecule force spectroscopy (SMFS), chemical force microscopy (CFM), and single-cell force spectroscopy (SCFS) over the years. The AFM tips are functionalized in all these techniques with biological molecules, viruses, chemical groups, or a living cell or replaced by particle. The key parameter which gives information about a specific ligand-receptor interaction (SMFS) [24], on the chemical group's distribution (CFM) [25], about interactional forces which control cell-substrate and cell-cell interrelations (SCFS) [5, 11] is the characteristics force involve in unbinding of AFM tip which is observed during retraction of AFM tip from sample. CFM is used to probe charges of individual cells and local surface hydrophobicity. CFM operational mode of force spectroscopy gives a means for resolution of the interactions of living microorganisms and local chemical properties with nanoscale resolution [26]. The AFM tips chemically functionalized with a specific functional group give naval approaches for better understanding of structure activity relationship of the biological cell surfaces. This technique has also provided new avenues for interactions between the antimicrobial drugs and the microbial cell surfaces [27].

A pivotal provocation in cell biology is to understand how molecules bound to the cell surfaces are organized and interact with their surrounding environment [28]. Answers to these questions are provided by SMFS, which is used to analyze the complex biological systems with individual molecules by simultaneously manipulating and localizing single molecules present in live microbial cells, which then reveal properties and proceedings that on other hand would be unattainable. The AFM tip binds to molecule of interest through the complimentary pair and distensible cross linkers to the substrate in SMFS technique [29]. The force involved in the unbinding of the AFM tip on retraction from attached molecule present in the substrate is recorded in real time [30]. In SMFS the force curve is recorded to show a force with nonlinear elongation which reflects stretching of flexible molecules present on the AFM tip and on the sample, until the "full-off" force of adhesion is observed. The worm-like chain (WLC) [31] model and freely jointed chain (FJC) [32] model from statistical mechanics are used to describe the

elongation force. Polymers are described as an irregular curved filament in WLC model as a linear on the scale of persistence length, which shows the stiffness of molecules. While, as polymers are described in FJC model as an array of rigid independent statistical segments (Kuhn), arranged via flexible-joints [33]. WLC model generally well describes the proteins which function as a continuous deformable rods [34], while FJC model is useful in describing polysaccharides which behave as a series of loosely connected segments [35]. Instead of AFM tip, microbial cell is fixed on cantilever in SCFS technique and force between the cell present on the probe and other cells present in the substrate is determined [36].

8.3 Cell Fixation

One of the most important difficult encounters in the microbial research which limit the AFM application is how to fix microbial cells without changing the variability or surface properties to flat surface. Firm fixation of the live microbial cells on the flat solid surface is obligatory for fruitful AFM topographic analysis and the force determinations. The method used for cell fixation should be selected in such a way that the cells should be fixed strongly enough to tolerate the lateral frictional forces applied by AFM tip without degrading microbial cell surfaces during scanning [37]. Analysis of microbial samples in liquid faces a major problem as microbial cells are flexible and soft, causing an additional hurdle in fixing. In such condition, to ensure firm fixation of microbial sample, surface modification of the substrate is necessary. One of the primary challenges in analysis of microbial sample is therefore microbial cell fixation.

In the beginning studies, AFM images of microbial cells were recorded after drying, as microbial sample preparation was easy in dry condition, but dried microbial cell can generate misleading information. A tremendous progress has been seen in the past two decades, in improving the existing and developing new protocols for cell fixation procedures of microbial cells. One of the most interesting applications of AFM in biological analysis deals with topographic analysis of the living cells in their native liquid environment, where microbial cell interaction with their surrounding environment can be studied [38].

Some of the most commonly used cell fixation techniques which do not require drying of the microbial cells include physical confinement of cells in a porous membrane; aluminum oxide filters; fixation of cells to surfaces coated with positively charged substances including gelatin [39], polyethyleneimine (PEI) [40], or poly-L-lysine [22, 41], by electrostatic interactions which are covalently bound to carboxyl- or amine-terminated surfaces [42]; and adsorption to coated surfaces with adhesively polyphenolic proteins [43]. All these cell fixation methods are used for cell immobilization, but cells attached via electrostatic interactions are generally detached during scanning, whereas reagents used for cross-linking and reactive groups used for covalent binding are known to affect the cells activity. Adsorption

and entrapment techniques are effectively used for viable cell fixation. However, coccoid cells are physically confined in membranes effectively.

In physiological conditions, the living microorganisms are successfully immobilized using adhesively polyphenolic proteins, which strongly fix the microorganism without affecting cells' viability [43]. A universal method for the cell fixation of living microorganism reported by Dague et al., where the living cells are assembled within the arranged microstructured, using capillary/convective deposition with functionalized poly-dimethysiloxane (PDMS) brands. The results of Dague et al. demonstrate the great potential for assemblance of microorganism on microstructure, by using capillary/convective deposition with functionalized PDMS brands for performing precise and accurate experimentations on the living microbial cells using AFM [37].

8.4 Functionalized AFM Tips

Silicon or silicon nitride-made tips are often used as probe in AFM microscopy. The AFM probe may be bare or chemically functionalized and often attached with a fixed cell or particle onto an AFM tip or tipless cantilever. The colloidal probe technique is introduced by Ducker et al. in 1991, consisting of the AFM tipless cantilevers to an attached micron-sized spherical particle, after that it measures the force between the sample and the sphere [44]. Though this protocol provides controlled surface geometry and chemistry, but to get images with high resolution and to map heterogeneous chemical surfaces, application of this large colloidal probes is not useful [45].

Vakarelski and Higashitani used the colloidal probe technique remarkably well by functionalizing the AFM tips with nanoparticles by using wet chemistry application. They successfully submitted a single-gold nanoparticles of the size 10–40 nm at the end of AFM tip, to avoid the limitation applied by either glue contamination or micromanipulation [46]. A new protocol for microbial cells fixation is reported by Razatos et al. involving coating of silicon nitride cantilevers with connecting bacterial layer, followed by covalent crosslinking between the tip and the cells via glutaraldehyde [47].

The bacteria were attached to 3-MPTS-coated glass beads, and furthermore, cell-coated beads were also attached to a tipless cantilever by Lower et al. using epoxy resin [48]. The silicon nitride cantilevers were pretreated with poly-L-lysine, followed by coating these cantilevers with bacterial layer by Touhami et al. [49] Various strategies have been reported for cell probe preparation, to analyze a single cell of bacterium after the pioneer work of above research groups.

It is worth noting that some limitation exists in cell probe method like attachment of cell with AFM probe may either results in denaturation of cell or may change the cell structure and properties which limits high lateral resolution during analysis via AFM [50]. Avoiding these shortcomings, a novel preparation protocol for live single-cell probe using adhesive bioinspired polydopamine is introduced by

Kang and Elimelech [51]. Their findings manipulate that after performing force measurements following the bacterium attachment to tipless cantilevers, bacterium was still alive. Single molecules are fixed to the AFM tips by universally available cross-linkers like polyethylene glycol to prevent denaturation of sample and motional freedom [52]. Primarily, the AFM tips were functionalized with amino groups which were then reacted with benzaldehyde functional groups carrying polyethylene glycol cross-linkers which via lysine residues attach directly to proteins [53].

Self-assembled monolayers (SAMs) of alkanethiols on gold-functionalized AFM tips are attached to single molecules [54]. At molecular level, alkanethiolate SAMs functionalized with gold are well defined structurally. The alkyl chain residues play a vital role in the stabilization through its lateral hydrophobic interactions.

8.5 Microbial Cells Imaging

AFM imaging is an influential supplementary tool if compared to electron microscopy, offering new paradigm for visualization of supramolecular organizations of the microbial systems in liquid or air, in actual time [55].

Primarily, the AFM was used predominantly to encounter the difficulties involved in air, by fixation of delicate samples of microbes on different substrates. In air, the AFM imaging is also useful to minimize the contact area between the substrate and the cell as a result of tumid state of the living cell of bacterium. While scanning, the AFM probe detaches the cell from the substrates [56].

Hayhurst et al. present an interesting AFM imaging of broken sacculi in *Bacillus subtilis* (Fig. 8.1) in air with very high resolution [57].

According to Gillis et al. , air AFM imaging is simpler and more reliable approach than liquid AFM imaging to monitor morphologies of bacterial surfaces and to measure dimensions and densities of bacterial flagella. Figure 8.2 focuses on the deflective images in air of mutant strains of *Bacillus thuringiensis* elaborating different levels of flagellation [58].

Having the ability to image specimen in liquid, a new era has been opened by AFM to observe live cells in the nanoregime, and as a result various structural informations can be achieved surpassing the electron and optical microscopy.

An interesting AFM analysis showing images in real time, in liquid is represented by Plomp et al. in a dynamic way of Bacillus atrophaeus spore germination; which reveals changes in spore coat structure and topography induced by germination as shown in the Fig. 8.3.

Diaz et al. claimed that AFM analysis of *Pseudomonas fluorescens* on organized substrates is a useful tool in air with (70%) humidity contents, to observe orientation of flagella on substrates containing metal without the use of any chemical during the primary level of the biofilm formation. They reported a random

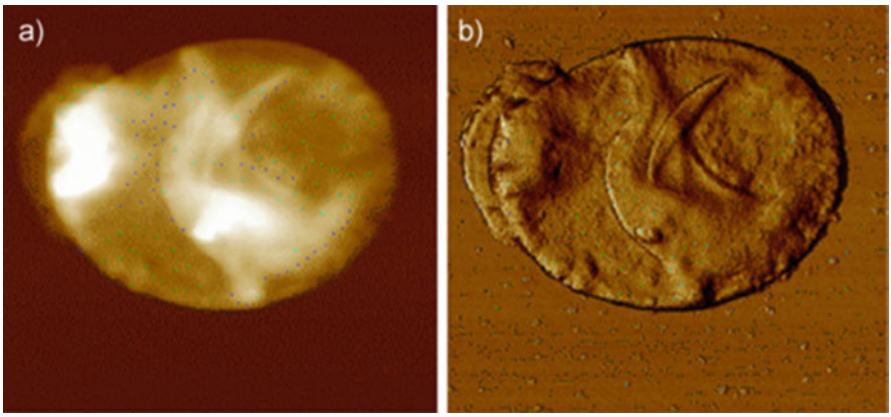

Fig. 8.1 AFM image of *B. subtilis* broken sacculi in air, (**a**) height, and (**b**) phase

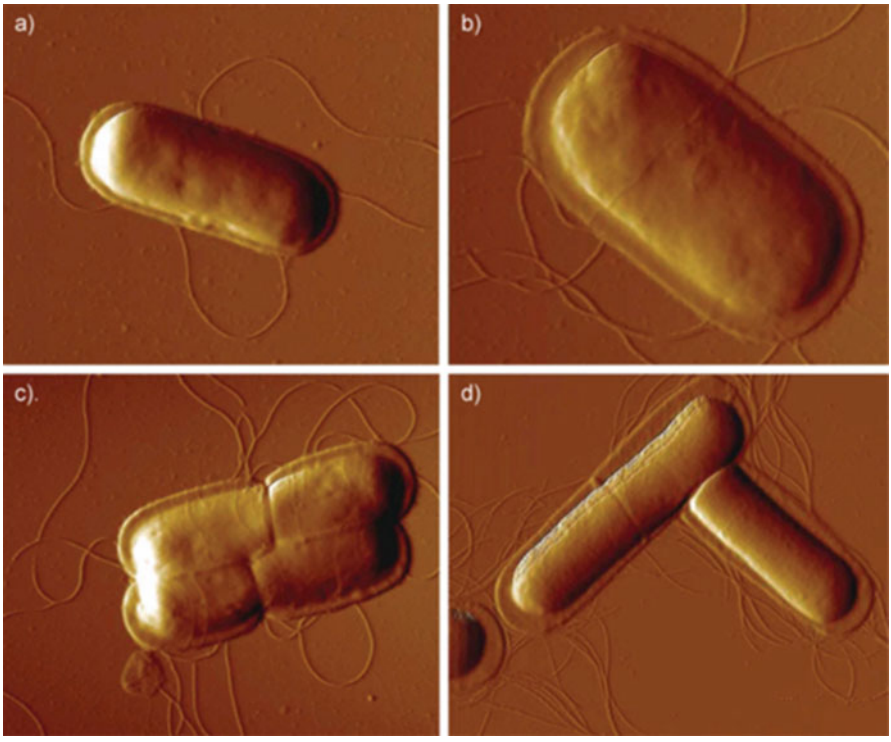

Fig. 8.2 AFM deflection images in air showing different flagellation stages in four *B. thuringiensis* H14 strains

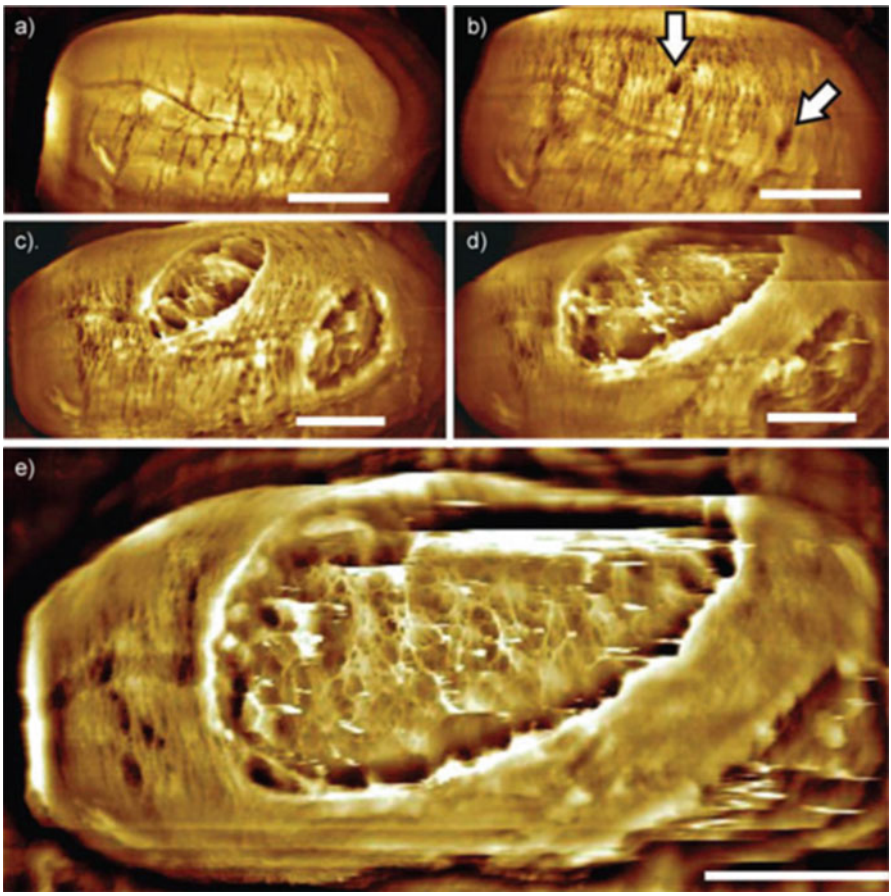

Fig. 8.3 AFM dynamic imaging showing germination of *B. atrophaeus* spores. Initially imaged in water, then germination solution was added to it. Scale bars are equal to 500 nm

orientation of flagella on noble surfaces, like organized gold with sub-microtrenches (Fig. 8.4a) and nano-oriented gold with random arrangements as shown in Fig. 8.4b. Flagella are used for different functions like like movements, keeping cells in contact, oscillating them, possibly involving in signaling functions, and furthermore, it facilitates the accumulating process at initial stage of biofilm formation [59].

Andre et al. have figured out by using AFM topographic imaging in buffers that mutant Lactobacillus plantarum cells lacking in wall-teichoic-acids (WTAs) which reveals rough morphology of cells surfaces (Fig. 8.5 a and b), However, strains of Lactococcus plantarum showing WTAs, the surface morphology was highly polarized, according to AFM images the side walls were less smooth than the pores (Fig. 8.5 d and e) [60].

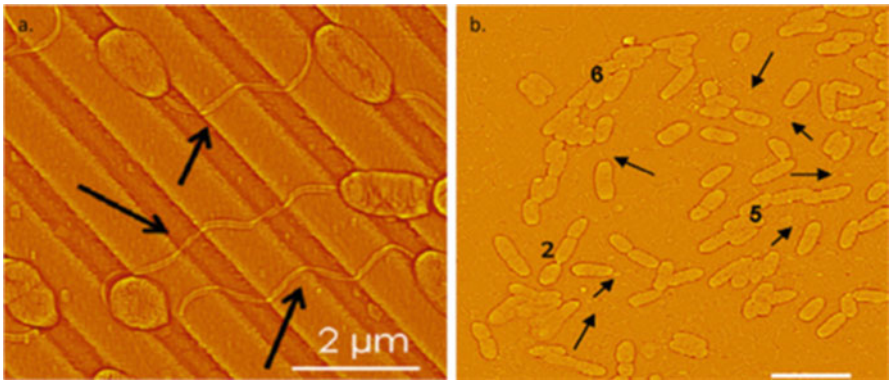

Fig. 8.4 AFM images in contact mode of *P. fluorescens* (**a**) sub-micro-trenches and (**b**) nano-oriented gold substrates. Flagella orientation was shown by arrows pointed toward neighboring microorganisms

Dorobantu et al. pictured the *Acinetobacter venetianus* RAG-1 surface using chemically functionalized AFM tips and AFM imaging terminating in hydrophilic and hydrophobic groups in buffer [42]. It can be witnessed in Fig. 8.6a, obtained with hydrophilic AFM tip, the existence of the cell surrounded by pili that are thin fibrils, in contrast to image shown in Fig. 8.6b, obtained with hydrophobic AFM tip, where no extracellular structure is seen around *A. venetianus* RAG-1 cell.

The thin fibrils (pili) are clearly visible in AFM analysis carried out with hydrophilic AFM tips, but when the AFM analysis is carried out with hydrophobic AFM tips, these thin fibrils are not visible. Such investigations potently propose that these thin fibrils are totally hydrophobic in nature. As soon as the hydrophilic tip reaches near these thin fibrils, their structure remained fixed on substrate, and hydrophilic AFM tips record their morphologies. In opposite to it, as the hydrophobic tip touches the structures, they stick to the hydrophobic AFM tip and move along it. Specially, regarding this case, the AFM tip gets failed to search the presence of these structures [42].

AFM imaging of *Staphylococcus aureus* trapped in filters is used by Turner et al. (etched for 4 h having 990 ± 20 diameters). To draw the AFM image of the division of microorganism with high respect, it is absorbed in brain heart infusion broth (BHI) (Fig. 8.7) [61]. They presented the dynamic way for higher molecular resolution which can be practiced in those cases where microorganisms are fully fixed on the substrate.

The surface of mycobacteria was analyzed by Alsteens et al., with four antimicrobial drugs prior to and after incubation [62].

Shah et al. reported recently the antibacterial potential of silver and gold nanoparticles stabilized with ceftriaxone against *Escherichia coli* ATCC 8739 with respect to kinetics and surface roughness. Conjugation of ceftriaxone with silver and gold nanoparticles improves the kinetics of antibiotics, and cell

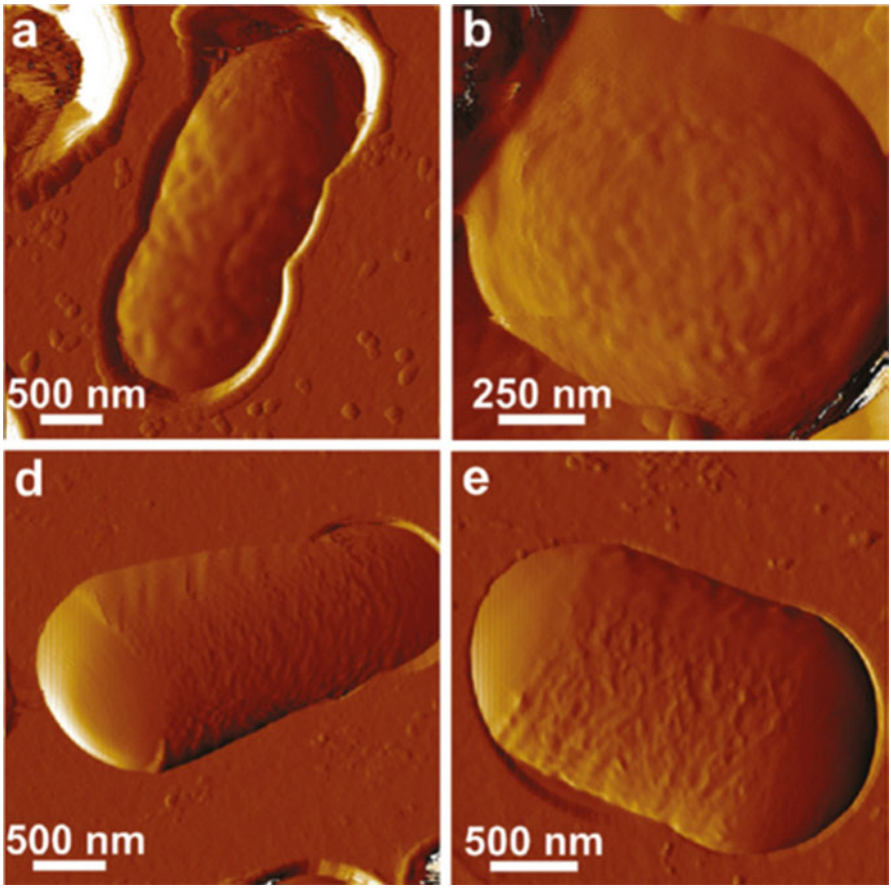

Fig. 8.5 AFM topographic images of cells of mutant *L. plantarum*. (**a**, **b**) Deflection images in sodium acetate buffer of single WTA-deficient cells, showing rough surface morphology, lateral (**a**) and polar (**b**) regions. (**d**, **e**) Deflection images in sodium acetate buffer of cell wall polysaccharide-deficient cells, showing polarized surface morphology

morphologies were completely disrupted in just 2 h of incubation, which was far better than the bare ceftriaxone (Fig. 8.8) [63].

8.6 Force Spectroscopy

The AFM instrument's force measurement potential compounds the importance of AFM spectroscopy; it keeps on going to avail unique visions into the interactions and mechanical property of microbial world.

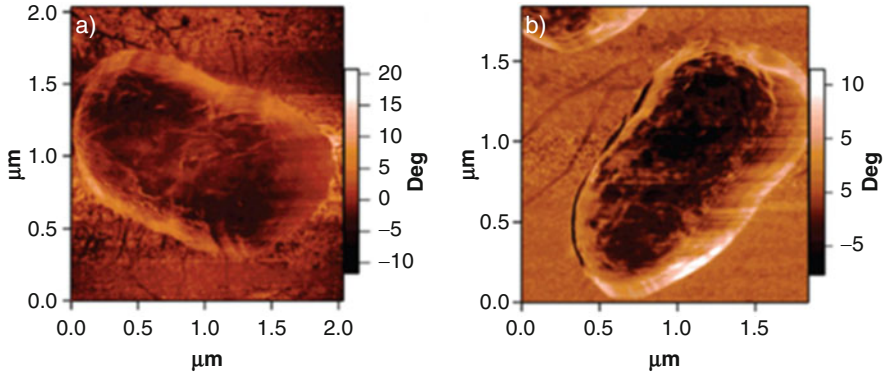

Fig. 8.6 AFM phase images of *A. venetianus* RAG-1 recorded with (**a**) hydrophilic and (**b**) hydrophobic AFM tips in phosphate buffer

SMFS used by Gad et al. for the first time in the domain of research points to specific interaction forces between pairs of receptor ligand. The credit also goes to the research group to draw the position of polysaccharide on the live cell surface of microbes. Gold-coated AFM tips fuctionalized with concanavalin-A made possible to determine binding forces between mannan polymers and concanavalin-A on the yeast *Saccharomyces cerevisiae* surface [64].

Next to them Lower et al. is one of the successful scientists who used SCFS to determine the interactive forces between goethite (a-FeOOH) and *Shewanella oneidensis*: anaerobic and aerobic conditions were used for the above given process. From the force measurements energy value was derived, it showed that in anaerobic conditions *S. oneidensis* gives response to the surface of goethite with the help of rapid developing stronger adhesive allergies at boundary if compared to the aerobic environment [65].

Pseudomonas aeruginosa is attached to AFM tips by Touhami et al. The bacterial cell is fastened on mica surface by thin fibril tethers. Soon after, it was observed by them that interactive forces are associated with elastic properties of thin fibrils between these thin fibrils and hard surfaces of mica. Force extension curves of the thin fibrils obtained from *P. aeruginosa* were qualitatively determined and were found to be similar to the different variety of biopolymers nonlinear stretching curves [49]. To probe complexity in connection with two bacterial surfaces, *Rhodococcus erythropolis* 20S-E1-c and *A. venetianus* RAG-1, Dorobantu et al. practiced AFM tips derivatized with alkanethiols finishing at hydrophobic and hydrophilic functional groups in CFM operational mode [42]. There was no difference in the connection involved for the two different species of bacteria observed at the time of hydrophilic tips that were in action, distribution of interactive forces of a patchy surface was clearly observed between two different cell surfaces, as well as highest forces were collected with hydrophobic AFM tips in one end of cell for *R. erythropolis* 20S-E1-c. In a nut shell, CFM with derivatized hydrophobic AFM tips is allowed to differentiate between microbial surface adhesion differences that

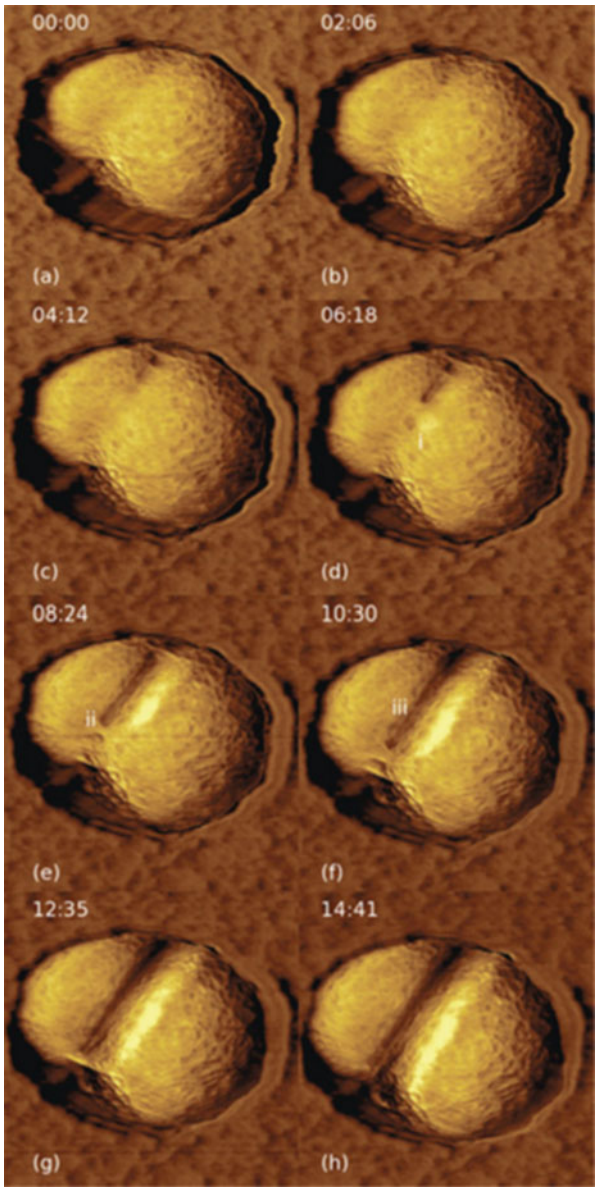

Fig. 8.7 AFM phase images of division of *S. aureus* at room temperature under BHI broth

could have meaningful significance for the cell knitting to hydrophobic interfaces or surfaces.

Recently, Alsteens et al. used single molecule force spectroscopy to unfold single cell adhesion proteins (Als5p), found on Candida albicans surface (Fig. 8.9) [66]. The WLC model elaborates the force extension curve which shows saw-toothed pattern with well-defined force peak signals. The core purpose

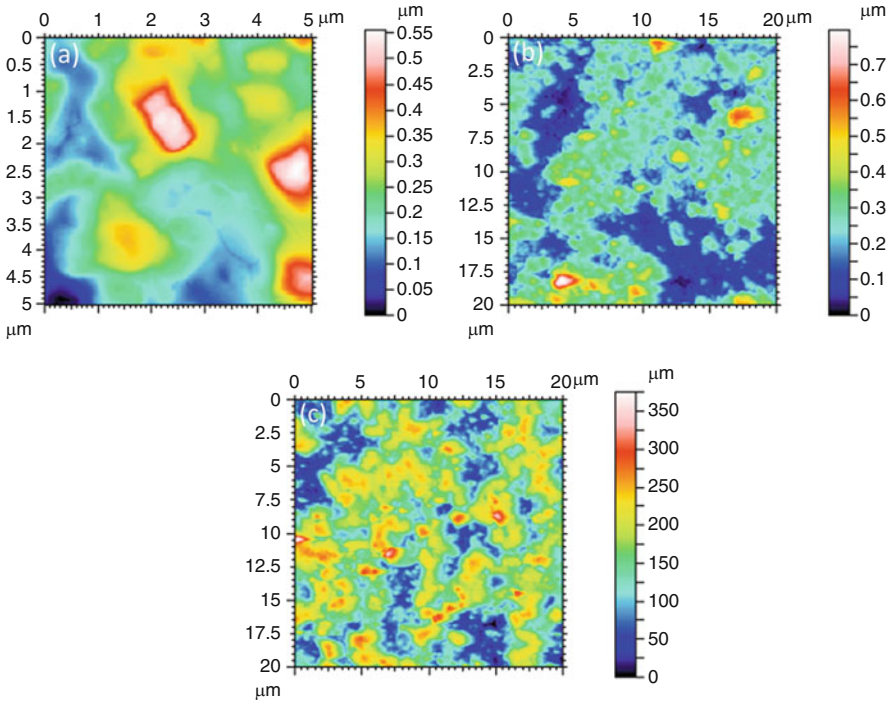

Fig. 8.8 *E.coli* after 2 h treatment with (**a**) 1 mg ceftriaxone, (**b**) 1 mg AgNPs, and (**c**) 1 mg AuNPs

of these single-molecule measurements is to avail inside into mechanical properties of adhesive molecules. It will assist the researchers of the pure scientific community to elaborate and elucidate their potential application and implications in different kind of diseases.

SMFS is used by Andre et al. for the investigations to find out if peptidoglycan is really concealed by polymers present in cell surface of *Lactococcus lactis* wild type (WT) [67]. Andre et al. depict the proof of their hypothesis that *L. lactis* mutants VES5751 and VES5748 which clarify confusion in the domain of research will encode synthesis of polysaccharides present in cell wall. In the synthesis of cell wall, the use of mutant strains is vital; polysaccharides (WPS) made it possible for SMFS to manipulate original architecture of peptidoglycan present in cell wall. Force curves analyzed spatially were obtained across surfaces of *L. lactis* WT cells. Curves associated to interacting forces were obtained spatially by analyzing the surfaces of L. lactis WT cells and the two mutant lacking cells WPS with the help of lysine functionalized AFM tips. Lysin is basically a protein that specifically attached to peptidoglycan in particular (Fig. 8.10).

Adhesion histogram, deflection image, and typical force curve are being showed with the help of Fig. 8.10a–c, drawn on wild-type *L. lactis* with a LysM tip at low applied forces (250 pN). No binding events were showed by most force curves. This

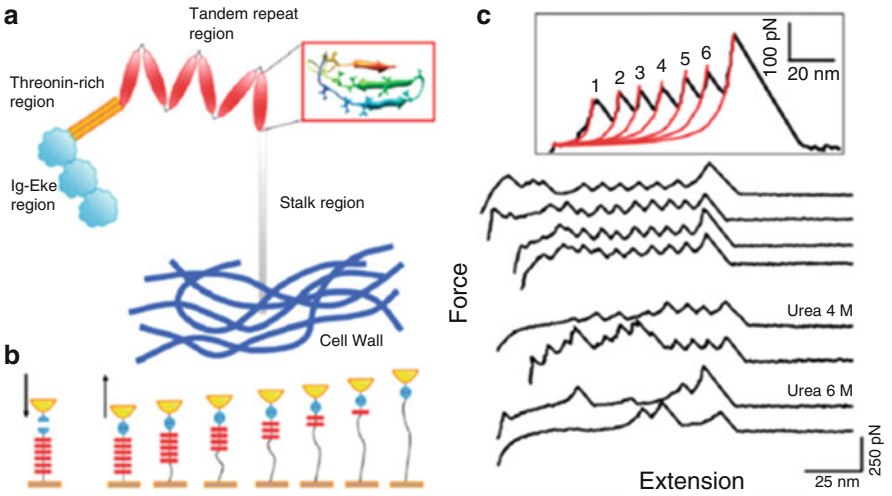

Fig. 8.9 The unfolding mechanism of adhesive cell proteins on *C. albicans* surface. (**a**) Representation of an AlS molecule projecting outward from the *C. albicans* cell wall by means of the stalk region and (**b**) principle of the SMFS experiments. Ig-T-TR6 fragments were attached on a gold surface and stretched via their Ig domains using an Ig-T tip; (**c**) force extension curves obtained by stretching single Ig-T-TR6 showed periodic features reflecting the sequential unfolding of the TR domains (*upper traces*). Force peaks were well described by the WLC model (inset, *red line*). Addition of urea dramatically altered the unfolding peaks (*lower traces*) [66]

experiment affirms that other cell wall components are involved in covering of peptidoglycan. A considerable fractional curve having different behavior is presented by the VES5751 WPS mutant (Fig. 8.10g–i), which shows single well-pronounced maximum at 71 ± 16 pN. The rupture of specific LysM peptidoglycan complexes is reflected by this process.

The analysis of mutant VES5751 WPS shows the same conclusion, but binding forces were regularly observed in 100–200 pN range (Fig. 8.10g–i), predicting that concurrent detection at the same time of two or three molecules was more frequently occurred. Finally, the detection of peptidoglycan on enriched mutant cell surfaces reflects absence of outer polysaccharide layers. From these results, a new era has been opened for understanding the assembly and architecture of peptidoglycan in gram-positive bacteria [67].

For the first time in literature, Park and Abu-Lail used AFM measurements and published heterogeneities in the adhesive energies that can be measured between bacterial cells and silicon nitride model surfaces which represent all species of *Listeria* genus in water. Larger adhesive energies to silicon nitride characterize the pathogenic species of *Listeria* as a result. More heterogeneities can characterize them if compared to the nonpathogenic species [68].

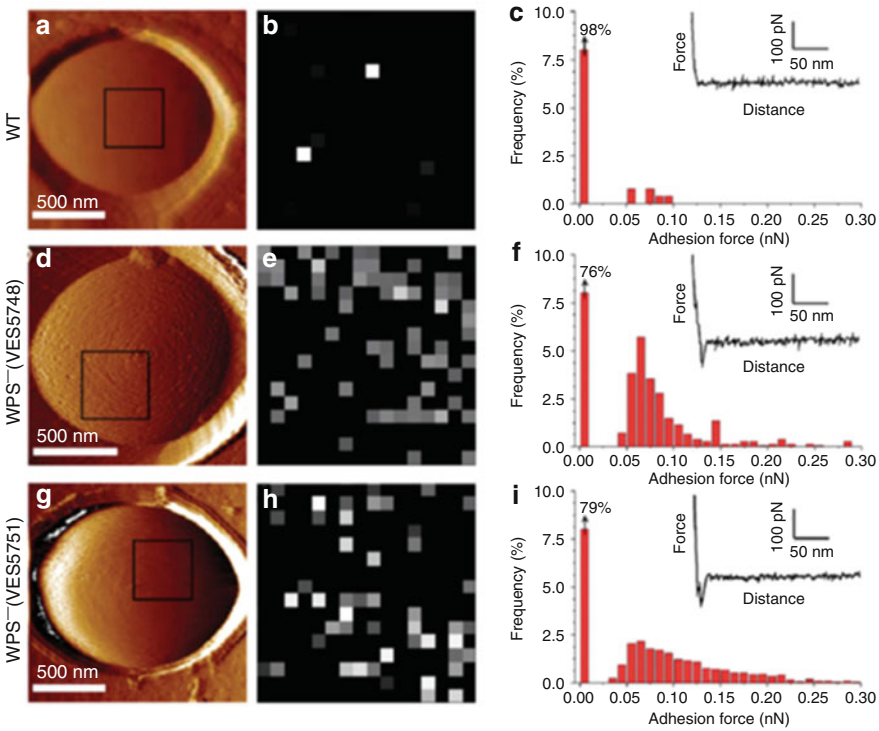

Fig. 8.10 Single-molecule recognition imaging of peptidoglycan. (**a**, **d**, **g**) Deflection images recorded with silicon nitride tips on *L. lactis* WT (**a**), VES5748 WPS mutant, (**d**) and VES5751 WPS mutant (**g**). (**b**, **e**, **b**) Adhesion force maps (400 × 400 nm) recorded on the three strains with LysM tips in the square areas shown in the deflection images, using a maximum applied force of 250 pN. (**c**, **f**, **i**) Force curves along with adhesion histograms

AFM force measurements of two biofilm positive and two nonbiofilm forming strains of *Staphylococcus epidermidis* in the pore confined state were measured directly in aqueous media by Hu et al. To probe adhesion on living cells at the nano-level was their core objective. They used AFM tips functionalized with hydrophobic functional groups in CFM operational mode. Their main objective was to list the minute differences among the four strains of *Staphylococcus epidermidis*. No detectable difference is shown by AFM topographic analysis. Bare hydrophilic silicon nitride tips are used to perform force measurements. They disclose similar adhesive characteristics for every strain; nevertheless, hydrophobic tip showed that hydrophobic interactions are not the main operation in analysis of four different strains of *Staphylococcus epidermidis*.

In a certain degree, the presence of modular proteins is observed as a result of the effect of saw-toothed force distance arrangements on biofilm surface of positive strains registered which may mediate the process of cell adhesion. This observation is considerably remarkable, as the dynamic silent features are shown, which can

offer more confirmation tests for the surface adhesion if compared to the static effect that have been reflected in AFM analysis. [69]

8.7 Conclusion

A treasure of new opportunities is provided by AFM technique for imaging and for using living microbial cells. AFM technique provides innovative intuitions into structure-activity relationship of microbial cells and also images the microbial cell up to single molecular resolution even in physiological environment. Modern development in AFM technology in the field of microbiology has made the scientists able enough to answer related questions concerning microbiology field, like cell signaling and adhesion, shape, tissue and embryonic development, microbial pathogenesis, and cell division [70]. AFM technique has facilitated the direct observations of dynamic structural changes in live microbial systems. In addition to it, the instrumental developments have made possible the dynamic interactions between individual biological macromolecules and cells; they were not getable with other visualization techniques [71].

In this chapter, the principle of AFM is described in detail and discussed in outline; the successes of the present era have been made in AFM spectroscopy regarding topographic analysis of microbial cells and force measurements. Highlighting the core of this chapter is to ask how recent technology has enhanced our view of molecular organization, interaction mechanics, and mechanisms of microbial cell surfaces. The drawbacks and advantages of AFM techniques are also presented in this chapter. Furthermore the challenges will be addressed in the next research of microbial systems.

There is a need for high speed AFM instruments for topographic analysis of microbial cells and to study interactions between the microbial cells in real time with high resolution [72], and their intercommunications in actual time with high resolution will be focused. The AFM ability to pave surface morphology of an individual living cell at the time of growing or interacting with different drugs, for instance, AFM imaging in actual time, discloses new opportunities for studying, remodeling, and assembling of cell walls. It is also worth notable to understand the mode of action of antibiotics [19]. High-speed AFM instrument is therefore expected, which will revolutionize the biological world and will impact physiological process in disease diagnosis and treatments [71].

The applications of SCFS are still under action; it has possessed too much potentiality for betterment. The potential of SCFS is founded on multifunctional applications. It has a magnificent variety of applications in medical as well as in microbiology fields to which it is applicable [36].

The AFM instrumental developments are used to couple with other microscopic techniques or scanning probe microscopy instruments, which will represent a way for instrumental development in the future that will revolutionize the biological sciences in multidimensions [73].

References

1. Binnig G, Quate CF, Gerber C (1986) Atomic force microscope. Phys Rev Lett 56(9):930
2. (a) Bhushan B, Kwak KJ, Palacio M (2008) Nanotribology and nanomechanics of AFM probe-based data recording technology. J Phys Condens Mat 20(36):365207; (b) Johnson LL (2008) Atomic force microscopy (AFM) for rubber. Rubber Chem Technol 81(3):359–383; (c) Withers JR, Aston DE (2006) Nanomechanical measurements with AFM in the elastic limit. Adv Colloid Interface Sci 120(1):57–67
3. Yang H, Wang Y, Lai S, An H, Li Y, Chen F (2007) Application of atomic force microscopy as a nanotechnology tool in food science. J Food Sci 72(4):R65–R75
4. (a) Simeone FC, Albonetti C, Cavallini M (2009) Progress in micro-and nanopatterning via electrochemical lithography. J Phys Chem C 113(44):18987–18994; (b) Tseng AA, Jou S, Notargiacomo A, Chen T (2008) Recent developments in tip-based nanofabrication and its roadmap. J Nanosci Nanotechnol 8(5):2167–2186
5. (a) Cohen SR, Bitler A (2008) Use of AFM in bio-related systems. Curr Opin Colloid Interface Sci 13(5):316–325; (b) Dufrêne YF (2003) Recent progress in the application of atomic force microscopy imaging and force spectroscopy to microbiology. Curr Opin Microbiol 6 (3):317–323; (c) Müller DJ, Krieg M, Alsteens D, Dufrêne YF (2009) New frontiers in atomic force microscopy: analyzing interactions from single-molecules to cells. Curr Opin Biotechnol 20(1):4–13
6. Dufrêne YF (2004) Refining our perception of bacterial surfaces with the atomic force microscope. J Bacteriol 186(11):3283–3285
7. Gould S, Drake B, Prater C, Weisenhorn A, Manne S, Hansma H, Hansma P, Massie J, Longmire M, Elings V (1990) From atoms to integrated circuit chips, blood cells, and bacteria with the atomic force microscope. J Vac Sci Technol A 8(1):369–373
8. Weisenhorn A, Drake B, Prater C, Gould S, Hansma P, Ohnesorge F, Egger M, Heyn S, Gaub H (1990) Immobilized proteins in buffer imaged at molecular resolution by atomic force microscopy. Biophys J 58(5):1251–1258
9. Weisenhorn A, Hansma P, Albrecht T, Quate C (1989) Forces in atomic force microscopy in air and water. Appl Phys Lett 54(26):2651–2653
10. Dorobantu LS, Goss GG, Burrell RE (2012) Atomic force microscopy: a nanoscopic view of microbial cell surfaces. Micron 43(12):1312–1322
11. Müller DJ, Helenius J, Alsteens D, Dufrêne YF (2009) Force probing surfaces of living cells to molecular resolution. Nat Chem Biol 5(6):383–390
12. Müller DJ, Engel A (2007) Atomic force microscopy and spectroscopy of native membrane proteins. Nat Protoc 2(9):2191–2197
13. Plomp M, Leighton TJ, Wheeler KE, Hill HD, Malkin AJ (2007) In vitro high-resolution structural dynamics of single germinating bacterial spores. Proc Natl Acad Sci 104 (23):9644–9649
14. (a) Daniel RA, Errington J (2003) Control of cell morphogenesis in bacteria: two distinct ways to make a rod-shaped cell. Cell 113(6):767–776; (b) Gitai Z (2009) New fluorescence microscopy methods for microbiology: sharper, faster, and quantitative. Curr Opin Microbiol 12(3):341–346
15. Milne JL, Subramaniam S (2009) Cryo-electron tomography of bacteria: progress, challenges and future prospects. Nat Rev Microbiol 7(9):666–675
16. (a) Engel A, Müller DJ (2000) Observing single biomolecules at work with the atomic force microscope. Nat Struct Mol Biol 7(9):715–718; (b) Dufrêne YF (2008) Towards nanomicrobiology using atomic force microscopy. Nat Rev Microbiol 6(9):674–680
17. Lidstrom ME, Konopka MC (2010) The role of physiological heterogeneity in microbial population behavior. Nat Chem Biol 6(10):705–712
18. Campos M, Jacobs-Wagner C (2013) Cellular organization of the transfer of genetic information. Curr Opin Microbiol 16(2):171–176
19. Dufrêne YF (2008) AFM for nanoscale microbe analysis. Analyst 133(3):297–301

20. Vié V, Giocondi M-C, Lesniewska E, Finot E, Goudonnet J-P, Le Grimellec C (2000) Tapping-mode atomic force microscopy on intact cells: optimal adjustment of tapping conditions by using the deflection signal. Ultramicroscopy 82(1):279–288
21. Dorobantu LS, Gray MR (2010) Application of atomic force microscopy in bacterial research. Scanning 32(2):74–96
22. Schaer-Zammaretti P, Ubbink J (2003) Imaging of lactic acid bacteria with AFM—elasticity and adhesion maps and their relationship to biological and structural data. Ultramicroscopy 97 (1):199–208
23. Radmacher M, Cleveland JP, Fritz M, Hansma HG, Hansma PK (1994) Mapping interaction forces with the atomic force microscope. Biophys J 66(6):2159–2165
24. Hinterdorfer P, Dufrêne YF (2006) Detection and localization of single molecular recognition events using atomic force microscopy. Nat Methods 3(5):347–355
25. Frisbie CD, Rozsnyai LF, Noy A, Wrighton MS, Lieber CM (1994) Functional group imaging by chemical force microscopy. Science 265(5181):2071–2074
26. (a) Dorobantu LS, Bhattacharjee S, Foght JM, Gray MR (2009) Analysis of force interactions between AFM tips and hydrophobic bacteria using DLVO theory. Langmuir 25 (12):6968–6976; (b) Noy A (2006) Chemical force microscopy of chemical and biological interactions. Surf Interface Anal 38(11):1429–1441
27. Dague E, Alsteens D, Latgé J-P, Verbelen C, Raze D, Baulard AR, Dufrêne YF (2007) Chemical force microscopy of single live cells. Nano Lett 7(10):3026–3030
28. Dupres V, Alsteens D, Andre G, Verbelen C, Dufrêne YF (2009) Fishing single molecules on live cells. Nano Today 4(3):262–268
29. Francius G, Alsteens D, Dupres V, Lebeer S, De Keersmaecker S, Vanderleyden J, Gruber HJ, Dufrêne YF (2009) Stretching polysaccharides on live cells using single molecule force spectroscopy. Nat Protocols 4(6):939–946
30. Horejs C, Ristl R, Tscheliessnig R, Sleytr UB, Pum D (2011) Single-molecule force spectroscopy reveals the individual mechanical unfolding pathways of a surface layer protein. J Biol Chem 286(31):27416–27424
31. Bustamante C, Bryant Z, Smith SB (2003) Ten years of tension: single-molecule DNA mechanics. Nature 421(6921):423–427
32. Rief M, Oesterhelt F, Heymann B, Gaub HE (1997) Single molecule force spectroscopy on polysaccharides by atomic force microscopy. Science 275(5304):1295–1297
33. Marszalek PE, Dufrêne YF (2012) Stretching single polysaccharides and proteins using atomic force microscopy. Chem Soc Rev 41(9):3523–3534
34. Oberhauser AF, Marszalek PE, Erickson HP, Fernandez JM (1998) The molecular elasticity of the extracellular matrix protein tenascin. Nature 393(6681):181–185
35. Marszalek PE, Oberhauser AF, Pang Y-P, Fernandez JM (1998) Polysaccharide elasticity governed by chair–boat transitions of the glucopyranose ring. Nature 396(6712):661–664
36. Helenius J, Heisenberg C-P, Gaub HE, Muller DJ (2008) Single-cell force spectroscopy. J Cell Sci 121(11):1785–1791
37. Dague E, Jauvert E, Laplatine L, Viallet B, Thibault C, Ressier L (2011) Assembly of live micro-organisms on microstructured PDMS stamps by convective/capillary deposition for AFM bio-experiments. Nanotechnology 22(39):395102
38. Fukuma T, Kobayashi K, Matsushige K, Yamada H (2005) True molecular resolution in liquid by frequency-modulation atomic force microscopy. Appl Phys Lett 86(19):193108
39. (a) Beckmann M, Venkataraman S, Doktycz MJ, Nataro JP, Sullivan CJ, Morrell-Falvey JL, Allison DP (2006) Measuring cell surface elasticity on enteroaggregative *Escherichia coli* wild type and dispersin mutant by AFM. Ultramicroscopy 106(8):695–702; (b) Doktycz M, Sullivan C, Hoyt P, Pelletier D, Wu S, Allison D (2003) AFM imaging of bacteria in liquid media immobilized on gelatin coated mica surfaces. Ultramicroscopy 97(1):209–216
40. (a) D'souza S, Melo J, Deshpande A, Nadkarni G (1986) Immobilization of yeast cells by adhesion to glass surface using polyethylenimine. Biotechnol Lett 8(9):643–648; (b) Velegol

SB, Logan BE (2002) Contributions of bacterial surface polymers, electrostatics, and cell elasticity to the shape of AFM force curves. Langmuir 18(13):5256–5262.
41. Bolshakova A, Kiselyova O, Filonov A, Frolova OY, Lyubchenko YL, Yaminsky I (2001) Comparative studies of bacteria with an atomic force microscopy operating in different modes. Ultramicroscopy 86(1):121–128
42. (a) Camesano TA, Natan MJ, Logan BE (2000) Observation of changes in bacterial cell morphology using tapping mode atomic force microscopy. Langmuir 16(10):4563–4572; (b) Dorobantu LS, Bhattacharjee S, Foght JM, Gray MR (2008) Atomic force microscopy measurement of heterogeneity in bacterial surface hydrophobicity. Langmuir 24 (9):4944–4951
43. Louise Meyer R, Zhou X, Tang L, Arpanaei A, Kingshott P, Besenbacher F (2010) Immobilisation of living bacteria for AFM imaging under physiological conditions. Ultramicroscopy 110(11):1349–1357
44. Ducker WA, Senden TJ, Pashley RM (1991) Direct measurement of colloidal forces using an atomic force microscope. Nature 353(6341):239–241
45. Takano H, Kenseth JR, Wong S-S, O'Brie JC, Porter MD (1999) Chemical and biochemical analysis using scanning force microscopy. Chem Rev 99(10):2845–2890
46. Vakarelski IU, Higashitani K (2006) Single-nanoparticle-terminated tips for scanning probe microscopy. Langmuir 22(7):2931–2934
47. Razatos A, Ong Y-L, Sharma MM, Georgiou G (1998) Molecular determinants of bacterial adhesion monitored by atomic force microscopy. Proc Natl Acad Sci 95(19):11059–11064
48. Lower SK, Tadanier CJ, Hochella MF Jr (2000) Measuring interfacial and adhesion forces between bacteria and mineral surfaces with biological force microscopy. Geochim Cosmochim Acta 64(18):3133–3139
49. Touhami A, Jericho MH, Boyd JM, Beveridge TJ (2006) Nanoscale characterization and determination of adhesion forces of Pseudomonas aeruginosa pili by using atomic force microscopy. J Bacteriol 188(2):370–377
50. Dufrêne YF (2002) Atomic force microscopy, a powerful tool in microbiology. J Bacteriol 184 (19):5205–5213
51. Kang S, Elimelech M (2009) Bioinspired single bacterial cell force spectroscopy. Langmuir 25 (17):9656–9659
52. Verbelen C, Dupres V, Alsteens D, Andre G, Dufrene YF (2011) Single-molecule force spectroscopy of microbial cell envelope proteins. In: Dufrene, Y.F. (Ed.), Life at the Nanoscale – Atomic Force Microscopy of Live Cells. Pan Stanford Publishing Pte. Ltd., Singapore, pp. 317–334
53. Riener CK, Stroh CM, Ebner A, Klampfl C, Gall AA, Romanin C, Lyubchenko YL, Hinterdorfer P, Gruber HJ (2003) Simple test system for single molecule recognition force microscopy. Anal Chim Acta 479(1):59–75
54. Dupres V, Menozzi FD, Locht C, Clare BH, Abbott NL, Cuenot S, Bompard C, Raze D, Dufrêne YF (2005) Nanoscale mapping and functional analysis of individual adhesins on living bacteria. Nat Methods 2(7):515–520
55. Francius G, Lebeer S, Alsteens D, Wildling L, Gruber HJ, Hols P, Keersmaecker SD, Vanderleyden J, Dufrêne YF (2008) Detection, localization, and conformational analysis of single polysaccharide molecules on live bacteria. ACS Nano 2(9):1921–1929
56. Kailas L, Ratcliffe E, Hayhurst E, Walker M, Foster S, Hobbs J (2009) Immobilizing live bacteria for AFM imaging of cellular processes. Ultramicroscopy 109(7):775–780
57. Hayhurst EJ, Kailas L, Hobbs JK, Foster SJ (2008) Cell wall peptidoglycan architecture in Bacillus subtilis. Proc Natl Acad Sci 105(38):14603–14608
58. Gillis A, Dupres V, Delestrait G, Mahillon J, Dufrêne YF (2012) Nanoscale imaging of Bacillus thuringiensis flagella using atomic force microscopy. Nanoscale 4(5):1585–1591
59. Díaz C, Schilardi P, Salvarezza R, Fernández Lorenzo de Mele M (2011) Have flagella a preferred orientation during early stages of biofilm formation?: AFM study using patterned substrates. Colloids Surf B Biointerfaces 82(2):536–542

60. Andre G, Deghorain M, Bron PA, van Swam II, Kleerebezem M, Hols P, Dufrêne YF (2011) Fluorescence and atomic force microscopy imaging of wall teichoic acids in Lactobacillus plantarum. ACS Chem Biol 6(4):366–376
61. Turner R, Thomson N, Kirkham J, Devine D (2010) Improvement of the pore trapping method to immobilize vital coccoid bacteria for high-resolution AFM: a study of Staphylococcus aureus. J Microsc 238(2):102–110
62. Alsteens D, Verbelen C, Dague E, Raze D, Baulard AR, Dufrêne YF (2008) Organization of the mycobacterial cell wall: a nanoscale view. Pflüg Arch Eur J Phys 456(1):117–125
63. Shah MR, Ali S, Ateeq M, Perveen S, Ahmed S, Bertino MF, Ali M (2014) Morphological analysis of the antimicrobial action of silver and gold nanoparticles stabilized with ceftriaxone on Escherichia coli using atomic force microscopy. New J Chem 38(11):5633–5640
64. Gad M, ITOH A, IKAI A (1997) Mapping cell wall polysaccharides of living microbial cells using atomic force microscopy. Cell Biol Int 21(11):697–706
65. Lower BH, Yongsunthon R, Shi L, Wildling L, Gruber HJ, Wigginton NS, Reardon CL, Pinchuk GE, Droubay TC, Boily J-F (2009) Antibody recognition force microscopy shows that outer membrane cytochromes OmcA and MtrC are expressed on the exterior surface of Shewanella oneidensis MR-1. Appl Environ Microbiol 75(9):2931–2935
66. Alsteens D, Dupres V, Klotz SA, Gaur NK, Lipke PN, Dufrêne YF (2009) Unfolding individual Als5p adhesion proteins on live cells. ACS Nano 3(7):1677–1682
67. Andre G, Kulakauskas S, Chapot-Chartier M-P, Navet B, Deghorain M, Bernard E, Hols P, Dufrêne YF (2010) Imaging the nanoscale organization of peptidoglycan in living Lactococcus lactis cells. Nat Commun 1:27
68. Park B-J, Abu-Lail NI (2011) Atomic force microscopy investigations of heterogeneities in the adhesion energies measured between pathogenic and non-pathogenic Listeria species and silicon nitride as they correlate to virulence and adherence. Biofouling 27(5):543–559
69. Hu Y, Ulstrup J, Zhang J, Molin S, Dupres V (2011) Adhesive properties of Staphylococcus epidermidis probed by atomic force microscopy. Phys Chem Chem Phys 13(21):9995–10003
70. Müller DJ, Dufrêne YF (2011) Atomic force microscopy: a nanoscopic window on the cell surface. Trends Cell Biol 21(8):461–469
71. Ando T, Uchihashi T, Fukuma T (2008) High-speed atomic force microscopy for nano-visualization of dynamic biomolecular processes. Prog Surf Sci 83(7):337–437
72. Shibata M, Yamashita H, Uchihashi T, Kandori H, Ando T (2010) High-speed atomic force microscopy shows dynamic molecular processes in photoactivated bacteriorhodopsin. Nat Nanotechnol 5(3):208–212
73. Francis LW, Lewis PD, Wright CJ, Conlan RS (2010) Atomic force microscopy comes of age. Biol Cell 102(2):133–143

Chapter 9
Silicon Micro-/Nanomachining and Applications

Hoang-Phuong Phan, Dzung Viet Dao, and Nam-Trung Nguyen

9.1 Introduction

The invention of silicon (Si)-based diodes and especially the Si bipolar transistors by Shockley, Bardeen, and Brattain seven decades ago has triggered the era of fast-growing information and computer technologies. As a consequence, the development into microelectronic fabrication technologies has also been extensively investigated and progressed to reduce device size and to increase the integration, as well as to enhance their performance. The growing rate of the state-of-the-art microprocessors has reached above Moore's law, which states that the number of transistors on a chip doubles roughly every 2 years. This achievement is largely attributed to the advanced micro- and nanofabrication processing [1].

Taking the great advantages of Si microelectronics fabrication technology, such as miniaturization, integration, high throughput, and high accuracy, micro-/nanofabrication of silicon microelectromechanical systems (MEMS) has also been advancing in the last five decades with established processes such as photolithography, thin-film deposition, etching, and ion diffusion/implantation process [2]. Thanks to the relentless improvement in these fabrication technologies, many MEMS devices, e.g., crash sensors, pressure sensors, micro-mirror arrays, etc., have been developed and widely employed in various fields, playing a key role in automotive, industrial, medical, and aerospace applications. Nowadays, MEMS sensors can be found in smartphones, medical equipment, game controllers, and cars, with their market size being rapidly expanded.

H.-P. Phan (✉) • N.-T. Nguyen
Queensland Micro and Nanotechnology Centre, Griffith University, Brisbane, QLD, Australia
e-mail: hoangphuong.phan@griffithuni.edu.au

D.V. Dao
Queensland Micro and Nanotechnology Centre, Griffith University, Brisbane, QLD, Australia

School of Engineering, Griffith University, Gold Coast, QLD, Australia

M.J. Jackson, W. Ahmed (eds.), *Micro and Nanomanufacturing Volume II*,
DOI 10.1007/978-3-319-67132-1_9

Micromachining technology has been moving toward nanoscale or even atomic level devices, where many interesting properties occur [3]. Unique properties in silicon nanoscale structures (e.g., nanodot, nanowire, nanosheets) include quantum confinement, surface charge effect, field effect, and giant sensing properties. Miniaturization of silicon devices not only enhance their performance but also improve the density of devices per wafer, which significantly bring down the cost.

By providing a general guideline to MEMS technologies, this chapter aims to develop a basic understanding of Si micro-/nanofabrication and their practical applications. Starting with an introduction to the physical properties of Si, the chapter will cover a wide range of fabrication processes, including growth of Si wafer, photolithography, wet and dry etching of Si, and nanolithography (e.g., electron-beam lithography and focused ion beam). Typical MEMS applications such as mechanical sensors and micro-/nanoactuators will also be presented at the end of this chapter.

9.2 Si Material

9.2.1 Si Crystal

Silicon is the most popular material used in MEMS/NEMS applications. The first property which makes Si the first choice of MEMS devices is its worldwide availability. This is due to the fact that over 90% of the Earth's crust is composed of silicate minerals, where Si is the second most abundant element (about 28% by mass) after oxygen. Furthermore, matured fabrication technologies and several excellent properties also make Si preferable material for MEMS devices. This section presents the crystallographic structure of Si, its physical properties, and the fabrication of Si wafers.

Crystalline Si consists of covalent bonds between a Si atom with its four adjacent Si atoms, forming tetrahedrons [4]. The covalent bond between two Si adjacent atoms is formed by two valence electrons, in which each atom contributes one electron to the bond.

The angle between two adjacent bonds is 109.5°. The unit cell of Si crystal is a cubic, and the lattice constant of Si crystal is 5.431 Å, Fig. 9.1. There are eight atoms in one cell; thus, the density of Si atom is 5×10^{22} atoms/cm^3. Si lattice planes and lattice directions are described by a mathematical description known as Miller indices, which are three triples (e.g., *hkl*) that define a vector direction normal to the surface of a particular plane or facet. Figure 9.2 shows the common planes of Si cubic crystal, including (1 0 0), (1 1 0), and (1 1 1) planes. Evidently, as the density of atoms and bond structure in each plane are different, Si crystal possesses anisotropic properties such as orientation dependence of mechanical strength and the different etching rate in different directions.

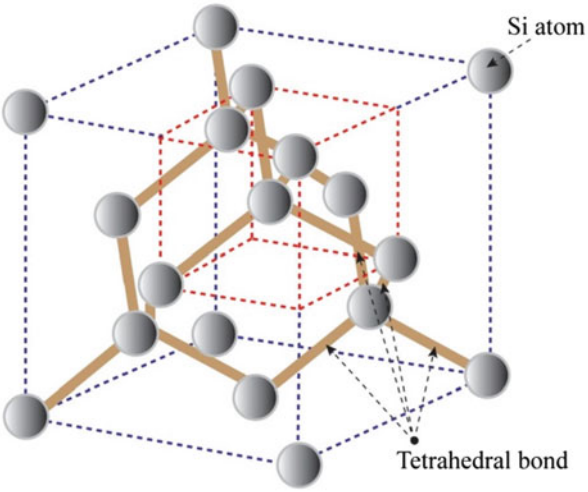

Fig. 9.1 Si crystal

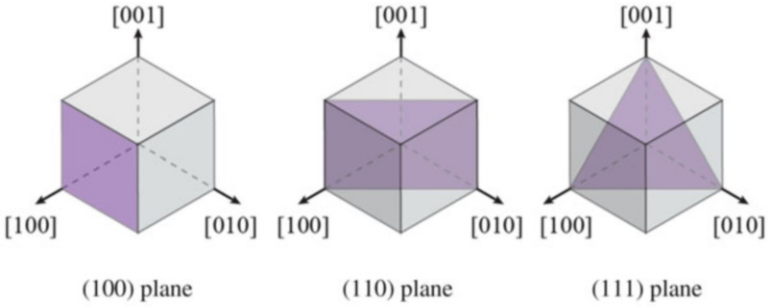

Fig. 9.2 Common planes (1 0 0), (1 1 0), and (1 1 1) in single-crystal Si represented using Miller indices

9.2.2 Properties of Si

Silicon is an excellent material for electronics which can be found in the functional layers of semiconductor devices, as well as in the integrated circuit (IC) chips [5], thanks to its superior electrical and mechanical properties. The energy gap between the conduction band and valence band of Si is 1.12 eV. At a sufficiently high temperature, electrons in the valence band are excited to conduction band, leaving positive charges (holes) in the valance band. These electrons in the conduction band and holes in the valance band are named mobile charge carriers, which can move freely under applied electric fields.

Figure 9.3 shows the electron and hole mobility of Si at different carrier concentrations and temperatures. At room temperature (298 K), the electron and hole concentration of intrinsic Si is approximately 1.4×10^{10} cm^{-3}, and the mobility of electron and hole is 2000 cm^2/V s and 500 cm^2/V s, respectively

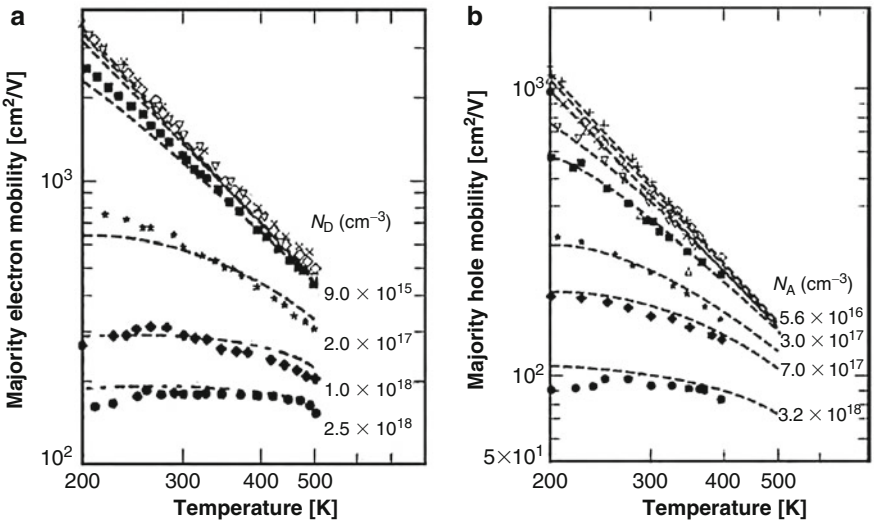

Fig. 9.3 Electron and hole mobility of Si (Reprinted with permission from [7])

[6]. This high mobility makes Si an excellent conductive material, which can be employed in numerous CMOS and MEMS/NEMS devices. The carrier concentration of Si can be improved by introducing impurities such as P, As to form n-type Si and Al, Br to create p-type Si, respectively. However, increasing carrier concentration also leads to a decrease in the mobility of electron and hole (below 100 $cm^2/V\,s$ at concentrations above $2 \times 10^{18}\ cm^{-3}$ [7]. In addition, the mobility of electron and hole also decreases when increasing temperature, which is caused by the carrier-carrier scattering and carrier-phonon scattering phenomena. This temperature dependence property of the carrier mobility in Si has been utilized in numerous thermal-based sensors.

In addition to the excellent electrical and electronic properties, Si also possesses superior mechanical properties [8]. Due to its robustness, Si widely serves as the mechanical support layer for common integrated circuits. Thanks to the large Young's modulus of above 100 GPa and a small mass density of 2.33 g/cm^3, Si offers high frequencies and high-Q factor MEMS resonators. Because Si is an anisotropic material, its mechanical properties (e.g., Young's modulus and Poisson's ratio) vary with crystallographic orientation, Fig. 9.4. For instance, the Young's moduli of Si in [1 0 0] and [1 1 0] directions are 130 GPa and 170 GPa, respectively. Evidently, [1 1 0] direction is preferred for high-frequency applications since it offers larger effective Young's modulus to mass ratio

Another important property for MEMS devices is the thermal conductivity [9]. The thermal conductivity of Si is 168 $W\ m^{-1}\ K^{-1}$, which is approximately twice of that of iron, and about two orders of magnitude larger than that of glass. Therefore, Si substrate can serve as a heat sink which dissipates the heat generated from integrated circuits. Furthermore, Si material is preferable for fast response

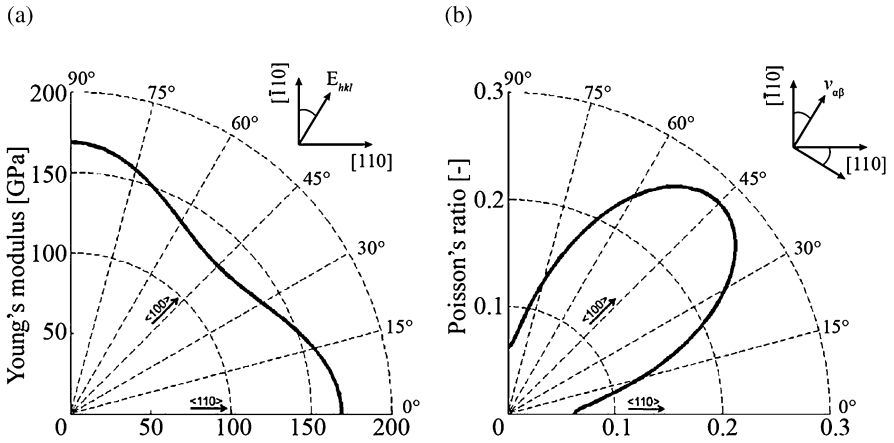

Fig. 9.4 Young's modulus and Poisson's ratio of single-crystal Si in (1 0 0) plane (Reprinted with permission from [8]). (**a**) Young's modulus of Si in (1 0 0) plane. (**b**) Poisson's ratio of Si in (1 0 0) plane

micro- and nanoheaters which are the main components of several thermo-sensors such as gas sensors and anemometers.

9.2.3 Si Wafers

Typically, the fabrication process of a Si device starts from a Si wafer, which is a bulk Si wafer or a Si on insulator (SOI) wafer. The most common technique used to create a bulk Si wafer was invented by Czochralski, as shown in Fig. 9.5. In this process, high-quality polycrystalline silicon nuggets are melted at high temperature of approximately 1400 °C in a quartz crucible [10]. Next, a crystal seed (rod) is dipped into the molten Si and subsequently pulled up and rotated simultaneously. The Si atoms that adhered to the seed will become solid when come out from the molten Si. The adhered Si atoms orient themselves in the same pattern of the Si seed crystal. As a result, a large crystal ingot is formed with its quality and dimension being controlled by the seed crystal quality, temperature gradient, crucible quality, the rate of pulling, and the rotation velocity. The long single-crystal Si ingot is then diced into thinner Si wafers using wire saw. The saw consists of an array of diamond-coated wires, which can cut the ingot into several wafers at the same time, providing a high throughput. The Si wafers are then lapped on both sides to remove the surface silicon which has been cracked or damaged due to the sawing process and to thin down wafer to a desirable thickness. Next, the Si wafers are polished to attain super-flat surfaces with a roughness on atomic scale. Finally, the wafers are cleaned with highly pure chemicals to remove the polishing agents, thereby making them residual free. Figure 9.6 illustrates the evolution of the size of

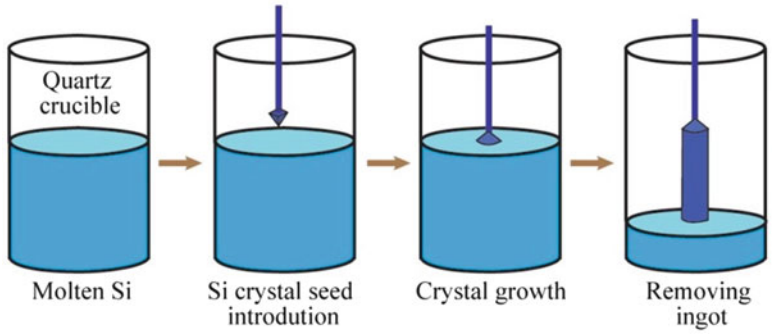

Fig. 9.5 Czochralski process to grow single-crystal Si wafers

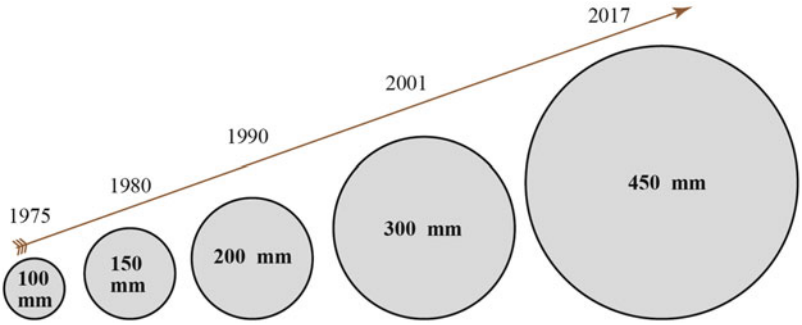

Fig. 9.6 The evolution of Si wafer size

bulk Si wafers since 1975 until recently. Thanks to the relentless effort in the optimization of single-crystal Si wafer growth process, large Si wafers with diameters up to 450 mm have become commercially available. A larger diameter will allow for the production of more semiconductor devices on a wafer and therefore cutting down the cost per chip. These benefits will greatly improve the throughput, enabling cost reduction.

Another widely used wafer for MEMS/NEMS application is the SOI wafer [11, 12]. The buried oxide layer (or BOX layer) sandwiched between two Si layers in a SOI wafer can be employed as an electrically insulator or can function as an etching stop layer in the device fabrication process. These advantages make SOI wafers the most commonly used platform in MEMS and advanced CMOS integrated circuit fabrication.

There are two common techniques to form SOI wafers from bulk Si wafers. The first method is known as SIMOX (separation by implantation of oxygen) process, which is based on the concept of implanting oxygen atoms into bulk Si wafers, Fig. 9.7a. The depth of oxygen penetration in the implantation process can be modified by the implantation energy. Therefore, the thickness of the oxygen-free layer and the thickness of the Si top layer are well controlled. Furthermore,

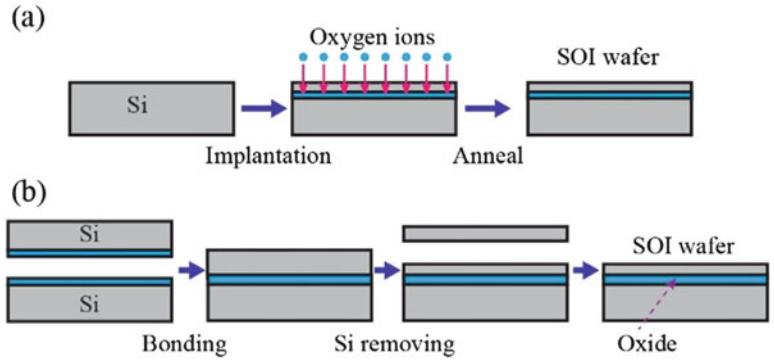

Fig. 9.7 Fabrication process to form SOI wafers from bulk Si wafers. (**a**) Implatation. (**b**) Wafer bonding

following implantation, thermal treatment is carried out to anneal the damage in the active Si layer caused by the implantation, as well as to enforce permanent Si–O bonding in the implanted region. The second approach utilizes wafer bonding technique followed by the removal of excess silicon from one of the wafers. Figure 9.7b shows the bonding approach, where two bulk Si wafers are initially oxidized or deposited with an oxide layer. The oxide layers of these two wafers are then pressed against each other and subsequently permanently bonded. Numerous bonding techniques including anodic and fusion bonding can be utilized to form the permanent glass bond. Finally, the excess silicon in one of the wafers (e.g., device wafer) is removed using Si etching or "smart cut" technique to obtain the desired thickness for the active Si layer. Both methods allow manufacture of wafers up to 200 mm in diameter.

9.2.4 Doping

Intrinsic Si has too high electrical resistivity for most applications. To be used as a functional layer, Si needs to be doped with foreign atoms or dopants. Doping is the technology to introduce impurities (dopants) into a semiconductor (typically intrinsic or low doped) to increase the number of charge carrier concentration, improving the electrical conductivity of the material [13]. To form p-type Si, dopants such as aluminum (Al), boron (Br), and gallium (Ga) are employed, while for n-type Si, nitrogen (N), phosphorous (P), and arsenic (As) are used. Generally, there are three doping techniques, which are in situ, implantation, and thermal diffusion.

The in situ doping method induces the dopants into a semiconductor during its growth process. As such, in the growth of bulk Si wafer using the Czochralski process, dopant impurity atoms (e.g., Br, P) can be added to the molten Si in the crucible, thus changing the Si wafer into p-type or n-type Si. Thermal diffusion utilizes the thermal energy to bring dopants into semiconductors. Typically, Si

wafer is coated with a solution which contains impurities such as Al and P. When the sample is heated at a high temperature, the random motion of dopant atoms becomes faster, allows them to deeply enter into the Si substrate. The diffusion of the impurity from regions of higher concentration (solution) to regions of lower concentration (Si) follows the Fick's law: $F = -D\nabla C$, where F is diffusive flux, D is the diffusivity, and ∇C is the concentration gradient. The main advantage of the thermal diffusion is minimum crystal damage and the capability for batch fabrication. Another doping technique is ion implantation, which has grown to be the principal doping technology used in semiconductor industry including manufacturing of integrated circuits. The implantation technique uses the impact of ion beam (e.g., Br^+, Ga^+) with a Si film to diffuse impurities into the film. After the impact, ions with high kinetic energy can traverse a path known as the ion track until coming to rest in the Si film. By occupying a Si atom in its lattice size, the impurity will introduce extra free carriers, which changes the semiconductor type as well as the total charge carrier concentration.

9.3 Lithography Process

Photolithography is the process to define the patterns on thin film or substrate by using light-sensitive polymers (usually called photoresists) and controlled exposure to UV light [14], as shown in Fig. 9.8. Photoresist is a photosensitive organic material which changes its chemical structure when exposed to ultraviolet light.

Photoresist consists of three main components which are polymer, sensitizer, and solvent. The polymer changes its structure when exposed to radiation, giving the resist its structural properties. The sensitizer controls the reactions in the polymer, while solvent keeps the resist in liquid form. There are two types of photoresist, which are negative and positive. In negative photoresist, the areas exposed to light become polymerized and resist to the develop chemical. Therefore, resultant patterns using this type are opposite to the patterns on the mask. On the other hand, light exposure makes the positive photoresist become soluble to the development solution. Consequently, the printed pattern using positive photoresist is the same as the pattern on the mask. A comparison between positive and negative photoresist is presented in Table 9.1. Typically, positive photoresists offer higher image sharpness and better resolution. The negative photoresist, on the other hand, is less expensive and more tolerant to plasma and chemical etching. In a lithography process, the choice of resist depends on the needs of the specific application, resolution, cost, etch resistance, and ease of use.

The basic steps of a photolithography process include: (1) surface preparation, (2) photoresist application, (3) soft bake, (4) align and expose, (5) development, and (6) hard bake, as illustrated in Fig. 9.9. In the first step, dehydration baking is conducted to remove the moisture absorbed by the substrate from the atmosphere, which improves the adhesion of the photoresist to the substrate. The bake is usually carried out in an enclosed chamber at a high temperature of 200 °C with exhaust,

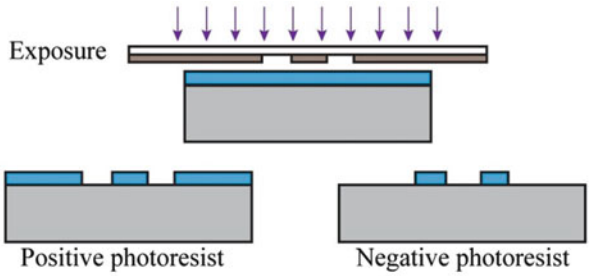

Fig. 9.8 Concept of photolithography to transfer patterns onto a photoresist layer

Table 9.1 Comparison of positive and negative resists

Characteristics	Positive resist	Negative resist
Adhesion to Si	Fair	Excellent
Contrast (image sharpness)	Higher	Lower
Cost	More expensive	Less expensive
Image width to resist thickness	1:1	1:3
Resolution	High ~0.5 μm	Low 2 μm
Plasma etch resistance	Fair	Very good
Wet chemical resistance	Fair	Excellent
Step coverage	Better	Lower

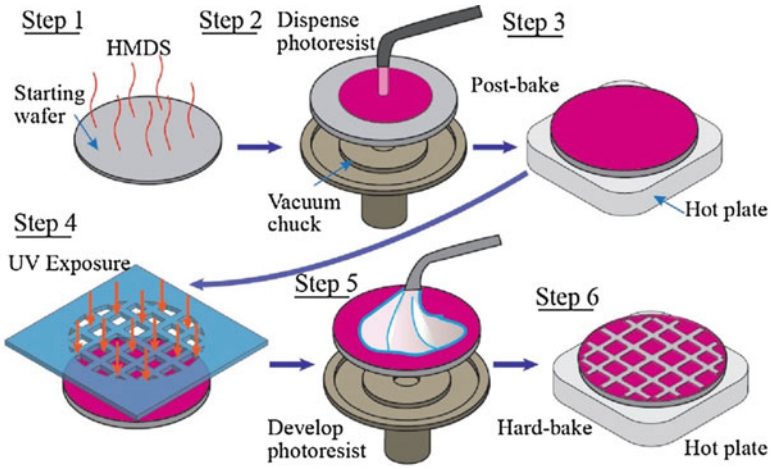

Fig. 9.9 The flow of a photolithography process

along with the evaporation of HMDS (Hexamethyldisilazane) to enhance the adhesion.

In the second step, the photoresist is applied and spin coated on the Si substrate. As shown in Fig. 9.9, the wafer is fixed to a vacuum chuck. A suitable amount of photoresist is dispensed on the substrate using photoresist dispenser. The spin

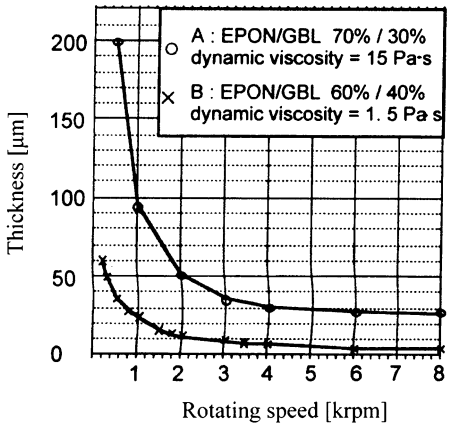

Fig. 9.10 Thickness of SU-8 photoresist under different rotation speeds and viscosity [15]

coater is then slowly sped up to spread the photoresist throughout the wafer. The speed is then ramped up so that the photoresist reaches the desired thickness and uniformity. The thickness of the photoresist (T_p) significantly depends on the concentration of photoresist (C), the viscosity (η), and the rotation speed (ω):

$$T_p = \frac{KC^{\beta}\eta^{\gamma}}{\omega^{\alpha}}$$

where K, α, β, and γ are constants determined from experiments. Once the exponential factors α, β, and γ have been determined, the above equation can be used to predict the thickness of the film that can be spun for various molecular weights and solution concentrations of a given polymer and solvent system. For instance, Fig. 9.10 shows the thickness of a commonly used photoresist SU-8 varying with different rotation speeds and viscosity. Evidently, by increasing the rotation speed and reducing the viscosity of photoresist, a thinner resist layer can be obtained.

After coating, the resulting resist film will contain a certain amount of solvent. At room temperature, an unbaked photoresist film will lose solvent due to evaporation, which may degrade the properties of the film over time. Therefore, following the photoresist application step, the substrate is baked to partially evaporate solvent out of the photoresist. This step is also known as soft bake or prebake, in which the majority of the solvent is removed and the film becomes stable at room temperature. The soft-bake step also aims to enhance the adhesion and etch resistance of the photoresist as well as to improve the uniformity and light-absorbent characteristics of the photoresist. Depending on the type of photoresist, a soft-bake step is typically carried out at approximately 90 °C using a hot plate or a high-temperature oven. When the wafer is removed from the hot plate, baking continues as long as the wafer is hot. Therefore, the wafer is then brought in contact or close proximity to a cool plate to control the cooling of the wafer. Once, the wafer reaches near room temperature, it is ready for the next photolithography exposure process.

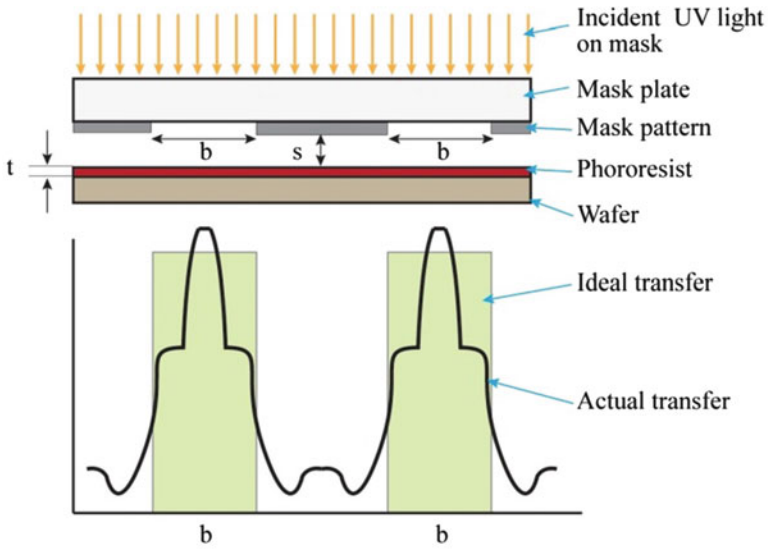

Fig. 9.11 Diffraction limits the resolution

In the fourth step, the mask image is transferred to the resist-coated wafer using UV exposure, which activates photosensitive components of photoresist. The photolithography masks typically have a thin layer of metal (e.g., Cr, Al) patterned on a quartz or soda-lime wafer. The pattern of the photomask is aligned to the Si wafers using a mask aligner. In a mask aligner, optical microscopes are employed to observe the position of alignment marks and to make sure that the position of the alignment marks coincides with that on the wafer underneath. There are three methods to expose a photoresist through a photomask, which are contact, proximity, and project printing. In the contact method, the photomask and the Si wafers are brought into contact, offering a high resolution down to the wavelength of the exposure ultraviolet light. However, this method may also damage the mask due to a direct contact between the wafer and the mask patterns, resulting in a low yield. Therefore, the contact mode is mainly applied for research purpose, as it is not suitable for most practical production environments. Proximity method, on the other hand, keeps the mask a set distance from the wafer (e.g., 10 μm), thus reducing the mask damage. Therefore, the lifetime of the mask is longer, making proximity printing a cost-effective method. Nevertheless, because the distance of the mask and the wafer increases the diffraction of light, the resolution of this photolithography technique is typically limited to 2 μm, which is insufficient for high-resolution patterning. Compared to the former methods, projection printing is by far the most common method of photolithography exposure for industry production. The projection printing is a noncontact method, which employs optical lenses to project the pattern from the photomask to the wafer. The resolution of this technique is down to 0.1–1 μm, while the mask also lasts longer compared to the contact mode. Therefore, this technique has been routinely used in the semiconductor industry.

The resolution of photolithography in contact and proximity modes is limited by the diffraction or bending of the light as it passes through the mask opening and can be expressed by the equation below:

$$2b_{\min} = 3\sqrt{\lambda\left(s + \frac{t}{2}\right)}$$

where $b_{\min}$ is the smallest feature size; λ is the wavelength of light; s is the mask-photoresist spacing; and t is the photoresist thickness. Consequently, to reduce diffraction and achieve the higher resolution, the exposure system can use shorter wavelengths of light (e.g., ArF excimer laser at 193 nm, Hg-vapors lamp, Xe-lamp) and/or high-numerical-aperture lenses to project the light.

Following the photolithography exposure, the photoresist is developed in which the soluble areas of photoresist are dissolved by developer chemicals. The development can be manually done by dipping the photoresist-coated wafer into a beaker which contains resist developer. Another more prevalent method is based on spinning technique, which holds the wafer on a vacuum chuck, and developer is poured onto the rotating wafer. The wafer is then rinsed and dried out while still spinning. The development step is one of the most critical steps in the photoresist process. The characteristics of the resist-developer interactions determine to a large extent the shape of the photoresist profile and, more importantly, the line-width control.

Finally, the substrate is baked at a temperature higher than that of the soft bake to harden the final resist pattern so that it can withstand the harsh environments of the subsequent fabrication processes such as etching. This post-bake process also improves the adhesion of the photoresist to the surface of the wafer, as well as to remove the solvent remaining in the photoresist to prevent solvent-burst effect in the vacuum.

9.4 Etching Processes

Etching is the process to remove thin film or substrate to form functional three-dimensional structures. A schematic sketch of the process used in etching is shown in Fig. 9.12. Prior to the etch process, the wafer (e.g., Si bulk or SOI wafers) are

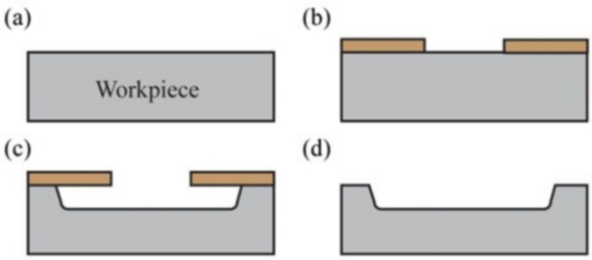

Fig. 9.12 Schematic sketch of a general etching flow. (**a**) Preprocess. (**b**) Masking process. (**c**) Etching process. (**d**) Post-process

cleaned to remove contamination. The residual stress of the wafer may also be released in this step. Next, a mask layer is formed on the top surface of the wafer. The pattern of the mask is created using the photolithography process described in the previous section. Next, etching techniques are applied to remove the areas which are not covered by the mask (e.g., open area). Finally, the mask is removed, leaving the desired structures.

The etching process can be characterized by three parameters: etch rate, etch geometry, and etch selectivity. The etch rate is the rate of material removal in direction perpendicular to the etch surface (μm/min). The etch geometry defines the orientation dependence of the etch rate. For instance, in anisotropic etching, the etching rate varies with Si crystallographic orientation. On the other hand, in isotropic etching, the etching rate is similar in all directions. The third parameter, etch selectivity represents the ratio of the etch rate of the film or substrate to that of the etching mask. Typically, higher etch selectivity is preferred as the mask is more tolerant to the harsh environment of the etching process. Furthermore, etching techniques can be classified as wet chemical etching and dry etching. The following sections present the process and the etching parameters of these techniques.

9.4.1 Wet Etching

Wet etching (i.e., wet chemical etching) uses etchant solutions to remove materials [16, 17]. Etchants are acid or alkaline solutions those can chemically react and etch the target materials. For instance, KOH and TMAH are common etchants employed to etch Si. Figure 9.13 shows the concept of a wet etching process, where a wafer covered by a maskant is dipped into an etchant container (e.g., a glass beaker). Maskants are materials which are chemically resistant to the etchant but dissolved easily by some types of solvent. Common mask materials used in a MEMS process include photoresist (e.g., AZP, ZPN,), SiO_2, and Si_3N_4. Once the wafer is dipped in the etchant, the reactant transported from the etchant solution will be absorbed by the substrate surface, leading to a chemical reaction on the surface. Next, the reaction by-products are desorbed from the substrate surface and then transported into the etching solution. To accelerate the etching rate, the etchant can be heated above room temperature, and agitation (stirring) may also be applied so the reaction

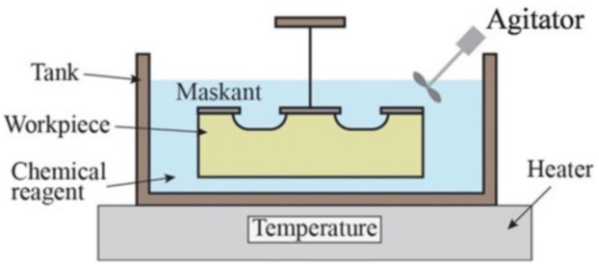

Fig. 9.13 Concept of wet etching process

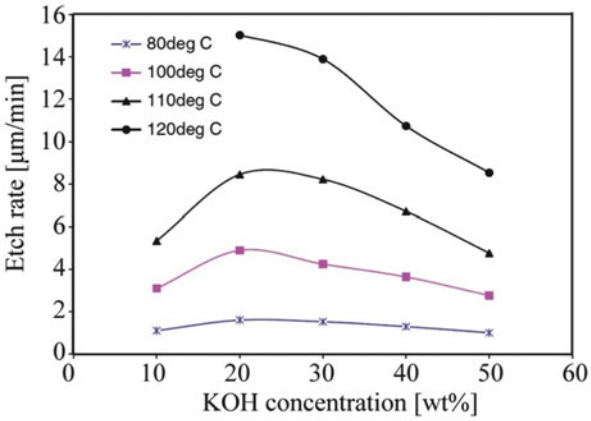

Fig. 9.14 Etch rate of Si (1 1 0) in KOH at different solution concentrations and temperatures (Reprinted with permission from [18])

by-products can be quickly transported into the solution and a new etching solution can move into the etching areas. For instance, in the Si wet etching process using KOH, the chemical reaction is:

$$Si + 2OH^- + 2H_2O \rightarrow SiO_2(OH)_2^{-2} + 2H_2$$

This chemical reaction is dependent on temperature; therefore, changing the temperature of KOH solution will lead to a significant change in the etching rate of Si as shown in Fig. 9.14. Evidently, increasing the temperature of the KOH solution from 80 to 120 °C enhances the etch rate of Si(1 1 0) from 1.52 to 15.06 μm/min. In addition, the etch rate also depends on the concentration of the KOH in the solution as such 20 wt.% of KOH solution provides the maximum Si(1 1 0) etch rate [18].

The KOH-based Si etching process also shows an anisotropic properties, as such the etch rate of (1 0 0) plane to that of (1 1 1) plane is 400:1. The orientation-selective etching of silicon occurring in hydroxide solutions (in this case, KOH) is partly due to the closer packing of some orientations relative to other orientations. For instance, (1 0 0) and (1 1 0) planes have two bonds below surface and two dangling bonds that can react with etchant solutions. Whereas, (1 1 1) plane has three of its bonds below surface and only one dangling bond to react. Therefore, the etch rate along [1 0 0] direction is much faster than [1 1 1] direction. This anisotropic etching property has been widely employed to form Si MEMS three-dimensional micro- and nanostructures such as pyramid and microgroove. Figure 9.15 shows the fabrication of an inverted Si pyramid array for surface plasmon resonance (SPR) applications [19]. The inverted pyramids were formed using Si wet etching where SiO_2 square shapes were used as the etching mask, and KOH was employed as the Si etchant. The anisotropic etching of Si in KOH enabled the formation of the inverted pyramids with their sidewall surface is (1 1 1) plane.

Besides KOH, tetramethylammonium hydroxide (TMAH) is another commonly used etchant to fabricate Si MEMS structure. A comparison between KOH and TMAH is shown in Table 9.2. The main advantages of wet etching over dry etching

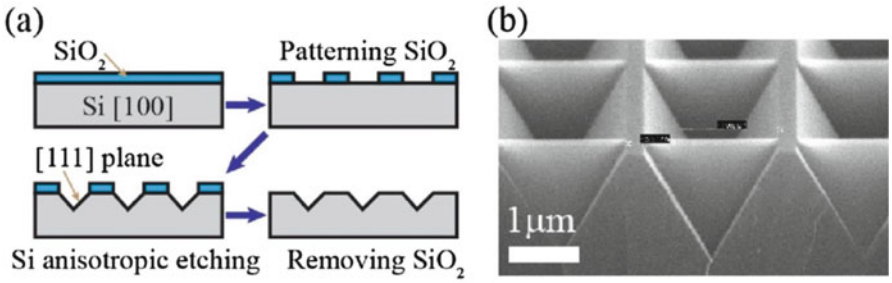

Fig. 9.15 Fabrication of an inverted Si pyramid array using anisotropic wet etching. (**a**) The fabrication process. (**b**) A SEM image of a Si pyramid array (Reprinted with permission from [19])

Table 9.2 Comparison of KOH and TMAH etchants

Etchant	Etch rate (μm/min)	Etch ratio (1 0 0): (1 1 1)	Mask	Remarks
KOH	1.4	400	PR	Good isotropic
			Si_3N_4	Not good for electronic devices
				Low selectivity with oxides
			SiO_2	Dangerous if contact to eyes
				Low etch rate for Br-doped Si
TMAH	1	12.5~50	SiO_2	Compatible for electronics
			Si_3N_4	High selectivity to SiO_2
				Small surface roughness
				Expensive

are low cost and simple technology. Depending on the applications, the users can choose proper etchants with corresponding maskants to obtain the desired structures.

9.4.2 Dry Etching

Dry etching techniques are those that use plasmas (ionized gases) or chemical vapors to initiate chemical reactions or employ energetic ion beams to remove materials. Dry-etching processes yield finer patterns than wet etching because it avoids the large liquid surface tension occurring in wet etching. In addition, dry etching offers greater safety as large quantities of corrosive acids or bases are not required. Furthermore, when a vertical sidewall for deep etchings in the substrate is required, dry etching is the better method in comparison with its counterpart. Dry etching can be classified into three classes, which are physical, chemical, and hybrid (e.g., combining both physical and chemical) processes. These three

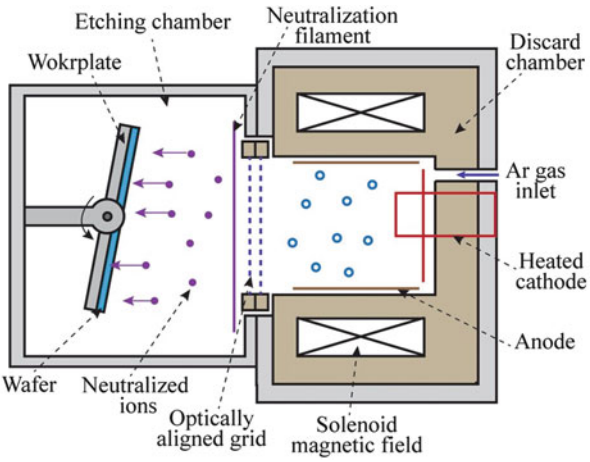

Fig. 9.16 The steps of ion milling

processes are also known as ion etching, plasma etching, and reactive ion etching (RIE). The details of each dry etching technique are presented as follows:

9.4.2.1 Ion Etching

Ion etching is the process to remove atoms from the substrate surface by bombardment with energetic ions (i.e., physical process) [20]. This is an anisotropic etch but selectivity is low. Figure 9.16 shows a simplified view of the function of the ion beam miller. Electrons are emitted from the cathode filament and then accelerated toward the anode. Their path length is increased by the magnetic field, causing impacts and ionization to the gas atoms (e.g., Ar) in the discharge chamber. The ions created in the discharge chamber are extracted and formed into ion beam by a set of grids. Subsequently, an electric potential corresponding to the ion beam energy required for ion milling is applied across a parallel set of grids. Next, the accelerated ions are then neutralized by a neutralization filament to prevent space charge effect. The fully neutralized ions bombard the targeted wafers to remove or etch the target material. The factors determining sputtering yields and consequently ion milling rates are the binding energy of the target material (e.g., Si), the momentum of the bombarding ions, the impact angles, and the mass of the ion. Ion etching is employed when (1) undercutting is not tolerable, (2) chemically inert materials need to be etched (e.g., Pt), and (3) a combination of materials needs to be etched (e.g., alloys).

9.4.2.2 Plasma Etching

Plasma etching uses plasma to generate active species (such as atoms and radicals) from a molecular gas [21]. Plasma is created when the gas source is pumped into the dry etching chamber and then subjected to a strong radio frequency

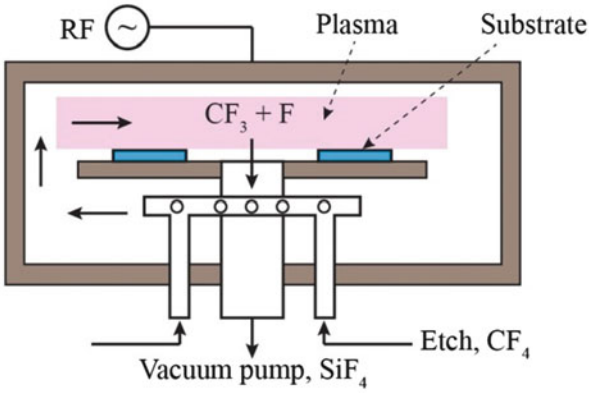

Fig. 9.17 Silicon plasma etching using CF_4

Table 9.3 List of reactive gas used in plasma etching

Material	Kind of gas plasma
Si	CF_4, $CF_4 + O_2$, CCl_2F_2, SF_6, XeF_2
$Si0_2$	CF_4, $CF_4 + O_2$, HF, SF_6, CCl_2F_2, C_3F_8, $C_2F_6 + H_2$
Si_3N_4	CF_4, $CF_4 + O_2$, SF_6
Mo	CF_4, $CF_4 + O_2$
W	CF_4, $CF_4 + O_2$
Au	$C_2Cl_2F_4$
Pt	$CF_4 + O_2$, $C_2Cl_2F_4 + O_2$, $C_2Cl_3F_3 + O_2$
Ti	CF_4
Ta	CF_4
Cr	Cl_2, CCl_4
Cr_2O_3	Cl_2 + Ar, CCl_4 + Ar
Al	CCl_4, CCl_4 + Ar, BCl_3
Al_2O_3	CCl_4, CCl_4 + Ar, BCl_3
GaAs	CCl_2F_2

(RF) electromagnetic field. This results in a decrease or increase in the number of electrons, which forms positive- or negative-charged particles (ions), as well as the dissociate molecular bonds, creating active species. The active species will then react with the substrate to produce volatile by-products and removed the targeted material. An example of Si plasma etching using CF_4 gas is illustrated in Fig. 9.17. Initially, reactive species are generated by plasma ($e + CF_4 \rightarrow CF_3 + F + e$). Next, the generated species diffuse to the targeted surface (e.g., Si). Subsequently, the species are adsorbed by the surface, resulting in chemical reactions, which form volatile by-products ($Si + 4F \rightarrow SiF_4$). Subsequently, the by-products are desorbed from the surface and then diffuse into the gas. The advantages of plasma etching over ion etching are high selectivity and etching rate, while its main disadvantage is the undercut due to isotropic etching. A list of plasma gas for common materials is presented in Table 9.3.

9.4.2.3 Reactive ion Etching

Reactive ion etching (RIE) is the etching process including (1) chemical etching, in which ions react with the substrate and remove the substrate atoms, and (2) physical etching, in which ions impact on the substrate and remove the substrate atoms [22]. By applying an electric field, the reactive gas disassociates, and the chemically reactive gas ions are formed. The ions are then accelerated toward the cathode on which the targeted wafer is held. These ions react with the targeted material, forming another gaseous material. This part is the chemical etching of RIE. Since the ions drift toward the material with high momentum, they can also knock out the material by transferring kinetic energy without chemical reaction. Furthermore, due to the vertical direction of the electric field attracting the ions to the cathode, the ions impinge on the targeted material predominantly in the direction perpendicular to the surface of the material. Therefore, the RIE typically produces anisotropic etch profiles, contrasting with the isotropic profiles of plasma etching. The etch rate of RIE is also typically higher than plasma etching. Moreover, the etch rate and the anisotropic profile of RIE can be further improved by using inductively coupled plasma power sources, as shown in Fig. 9.18. In the ICP system, the plasma is generated with a radio frequency (RF) powered magnetic field of a coil. Therefore, very high plasma densities can be achieved, leading to a high aspect ratio and high etching rate.

Another version of RIE which has been widely employed in today's semiconductor and MEMS industries is deep RIE (DRIE). This technique was pioneered by Robert Bosch Corp., and thus it is well-known as DRIE Bosch process. The idea of DRIE Bosch process is illustrated in Fig. 9.19. The process consists of alternating cycles of etching and passivating layer depositions. Each cycle begins with a passivation step, in which C_4H_8-based plasma is generated to deposit a few monolayers of PTFE (polytetrafluoroethylene)-like fluorocarbon polymer across all surface exposed to the plasma. Following the passivation step, the gas is switched to SF_6 to create chemical reactive plasma that can isotropically etch Si. Through the application of an electric field, ions move toward the wafer, bombarding and removing the passivation polymer. Since the ions almost move in the direction

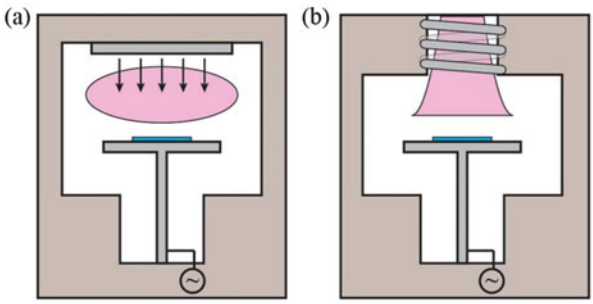

Fig. 9.18 RIE etch system with (**a**) conventional parallel plate system and (**b**) ICP system

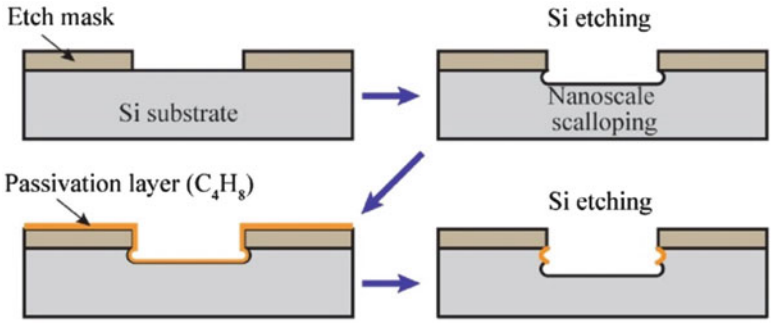

Fig. 9.19 The principle of Bosch DRIE process

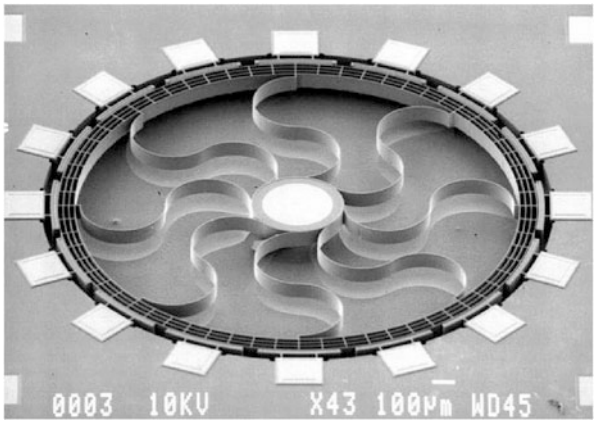

Fig. 9.20 SEM image of an 80 µm thick, 2 mm diameter four-ring gyroscope with meander-shaped springs (Reprinted with permission from [23])

perpendicular to the wafer, the passivation polymer deposited on the horizontal surface will be rapidly removed, while the passivation polymer on the side wall still remains. Furthermore, increasing the ion energy in the vertical direction will result in the exposure of the Si surface of the trench to the reactive fluorine-based species. The exposed Si areas are then removed following the RIE process, while the Si on the sidewall is protected by the remaining C_4H_8 polymer. Therefore, by repeating these steps for several times, etch depths of several hundred microns can be achieved with almost vertical sidewalls.

Figure 9.20 shows an example of the high-aspect-ratio Si microstructure fabricated using a DRIE-based process named HARPSS (high aspect ratio combined poly- and single-crystal silicon).

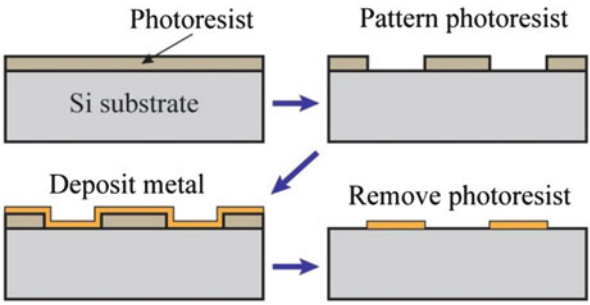

Fig. 9.21 Concept of a lift-off process

9.4.3 Lift-off Process

Besides the etching techniques, lift-off process is another approach used to form micro-/nanostructures [24]. The advantage of this procedure is the ability to work with dielectric layers as well as metallic layers such as platinum or gold which are difficult to pattern by etching directly. In this method, structures of a target material are formed using a sacrificial material such as photoresist. By removing the sacrificial layer (e.g., photoresist) with a solvent that does not attack the device layer (e.g., metals), the material on top of the sacrificial layer is lifted off, leaving the device layer only at the desired areas. Figure 9.21 illustrates an example of the lift-off process used to fabricate micropattern of metals.

In the first step, a photoresist with a thickness of several microns is spin coated on a wafer. Next, the photoresist is patterned using the lithography process. Subsequently, a thin metal layer is then deposited on the wafer coated with the photoresist. Finally, the photoresist is completely striped away, which also remove the metals layer previously deposited on the resist. An important factor for the success of the lift-off procedure is the use of relatively thick photoresist in order to provide a very thin metallic layer on the sidewalls of the opening. This opening allows the solvent (e.g., acetone or IPA) to attack and react with the photoresist from the sidewall. For this reason, negative photoresist is widely used in lift-off process since it offers a larger thickness in comparison to positive photoresist.

9.4.4 Bulk and Surface Micromachining Process

Most of MEMS structures are fabricated using either bulk or surface processes where lithography and etching steps are repeatedly performed until the desired patterns are obtained. Bulk micromachining creates MEMS structures by selectively etching inside a substrate [25]. On the other hand, surface micromachining creates microstructures by depositing and then removing away different layers on top of the substrate, instead of etching the substrate. Figure 9.22 illustrates an example of the bulk process, in which a Si cantilever is fabricated from an SOI

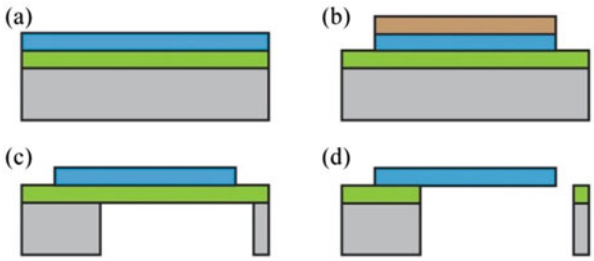

Fig. 9.22 Fabrication flow of a silicon cantilever using bulk micromachining. (**a**) Starting with a SOI wafer. (**b**) Patterning top Si layer. (**c**) Removing the Si at the bottom. (**d**) Etching the BOX layer

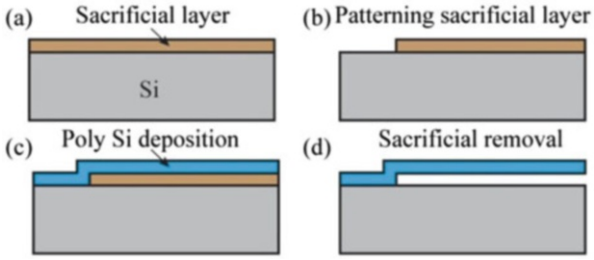

Fig. 9.23 Fabrication flow of a polysilicon cantilever using surface micromachining. (**a**) Sacrificial layer. (**b**) Patterning sacrificial layer. (**c**) Poly Si deposition. (**d**) Sacrificial removal

wafer. In the first step, the Si layer (device layer) is patterned using either dry or wet etching (Fig. 9.22b). Next, the bottom (handling layer) Si layer is selectively etched (Fig. 9.22c). Finally, the BOX layer (SiO_2) is removed to release the cantilever from the substrate (Fig. 9.22d).

Figure 9.23 presents a typical process flow of surface micromachining where a polysilicon structure is fabricated on a Si bulk wafer [26]. Initially, a sacrificial layer such as SiO_2 or S_3N_4 is deposited on top of the Si wafer. Next, the sacrificial layer is patterned using lithography and etching. Subsequently, a device layer (polysilicon) is deposited (e.g., using chemical vapor deposition). Finally, the sacrificial layer is removed leaving the free-standing polysilicon cantilever. In some case, to avoid the stiction of the cantilever to the Si substrate after removing the sacrificial layer, isotropic dry etching is more preferable than wet etching.

9.5 Nanomachining Techniques

While the resolution of the conventional photolithography process is limited to ~0.5 μm, advanced nanolithography allows the dimension of MEMS devices to scale down to below 100 nm. The devices in nanoscales offer several advantages including high density of functional chips per wafer, large surface area to volume ratio, and numerous interesting physical properties. Nanolithography process also shows its high potential for NEMS in comparison to the bottom up process, as it is compatible with conventional lithography fabrication, as well as makes the direct

integration of MEMS/NEMS devices with ICs possible. The common nanolithography processes include X-ray lithography, electron beam lithography (EBL), focused ion beam, and scanning probe nanolithography.

9.5.1 X-ray Lithography

As presented in Sect. 9.3, the resolution of UV lithography is limited to microscale due to the large wavelength of several hundred nanometers, causing a significant light diffraction effect. Consequently, the idea that diffraction effects in photolithography could be effectively neutralized by employing photons with extremely short wavelengths has motivated the use for wavelengths in the X-ray portion of the electromagnetic spectrum [27]. Therefore, by employing X-ray with wavelength in nanometer scale, the X-ray lithography allows the fabrication of MEMS devices with smallest feature size of approximately 50 nm. The principle of X-ray lithography is similar to that of UV lithography. However, since most materials used to make image-forming lenses or mirrors are not suitable for X-ray, the projection printing method is not relevant to X-ray nanolithography. As a result the other noncontact approach—the proximity printing method—has been widely applied to X-ray lithography systems. In addition, X-ray masks are made of low-atomic-number materials, on which the circuit patterns are placed in the form of high-atomic-number material. X-ray passes through the low-atomic-number areas and is mostly absorbed by the high-atomic-number material, as a result forming the desired pattern on the photoresist-coated wafer. Furthermore, to enhance the X-ray transmission, the mask is typically made of thin silicon carbide membrane with thickness of below 2 μm. Silicon carbide is widely employed due to its superior mechanical properties as well as excellent tolerance to long exposure to X-ray [28, 29].

One of the most well-known nanolithographies using X-ray is the LIGA process, whose name stands for lithography, electroplating, and molding (German acronym for Lithographie, Galvanoformung, and Abformung) [30], as presented in Fig. 9.24. X-ray LIGA was one of the first major techniques which provides high-aspect-ratio structures with the lateral precision in order of nanometer. In the process, an X-ray-sensitive photoresist such as typically PMMA (polymethyl methacrylate) or Su-8 is initially coated onto a wafer. PMMA and Su-8 are preferable due to their large thickness of up to hundred microns. The photoresist is then exposed to high-energy X-rays from a synchrotron radiation source and subsequently developed to form a three-dimensional (3D) structure. Next, the 3D structure is filled by the electrodeposition of metal. Afterward, by applying the lift-off process, the PMMA resist is chemically stripped away, producing a metallic mold insert. This mold can be employed to fabricate parts in polymers or ceramics through injection molding. Beside the high aspect ratio up to 100:1, X-ray LIGA also offers excellent features such as parallel side walls with a flank angle nearly 90° and smooth side walls with a surface roughness in the order of 10 nm.

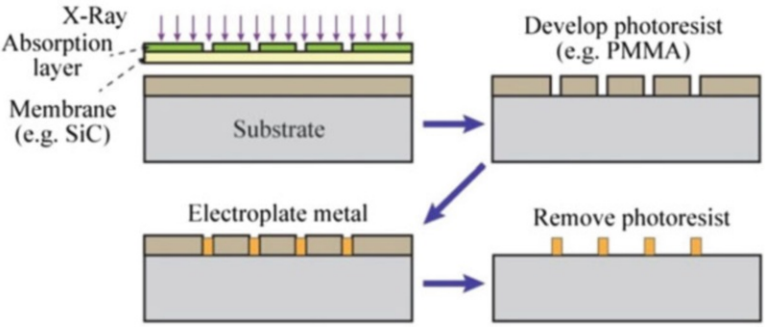

Fig. 9.24 The concept of an X-ray LIGA process used to fabricate high-aspect-ratio metal structures or precision molds

9.5.2 Electron Beam Lithography

The principle of employing extremely short wavelength to improve resolution is also applied in electron beam (EB) lithography for nanoscale fabrication [31]. The wavelength of an electron is defined using the de Broglie equation: $\lambda = h/p$, where h is the Planck constant and p is the momentum of the electron. By applying a high electric field (e.g., in several kV), the electron receives a large momentum, resulting in an extremely small wavelength. Typically, the wavelengths of electron beam are in the order of picometers, thus providing ultra-fine lateral feature sizes, which is much better than X-ray and UV lithography. The first electron beam lithography (EBL) was developed in the 1960s by modifying the scanning electron microscope. An EBL system consists of an electron gun, electron column, and sample holder, as presented in Fig. 9.25. The electron gun (electron source) is an electrical component in vacuum tubes that produces a narrow electron beam that has a precise kinetic energy. Generally, there are two types of electron gun which are thermionic emitter and field emitter. In thermionic gun, electron which received sufficiently high thermal energy will overcome the barrier to emit from the hot cathode. The electric field between cathode and anode accelerates and further focuses the electron. Meanwhile, the field emitter utilizes high electric field to narrow a surface barrier so that electron can tunnel through the barrier. Although the field emission source provides higher resolution, the thermionic gun offers better stability over a long electron beam writing time. The electron beam column consists of electrostatic (capacitance) and magnetic (coil) lenses as well as blank. The blank is used to switch electron beam writing or non-writing statuses. The leases are used to shape and focus the electron beam by utilizing the electrostatic and magnetic (Lorentz) force: $F = q(E + v \times B)$, where F is the force exerted on electron, E and B are the applied electric field to the capacitance and coil, respectively, and v is the velocity of electron. The electron beam will focus on an EB resist coated on the wafer which is placed on the sample holder to make an exposure.

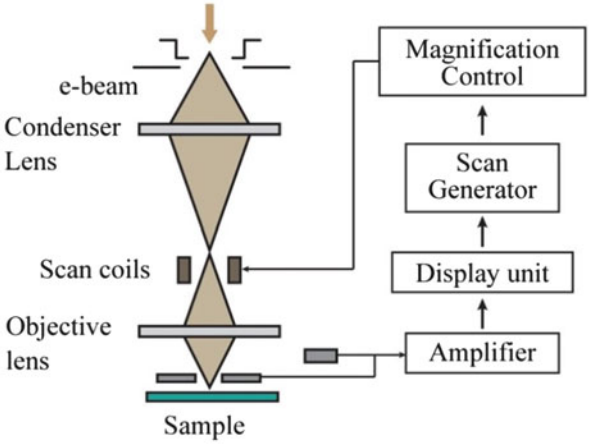

Fig. 9.25 Electron beam lithography system

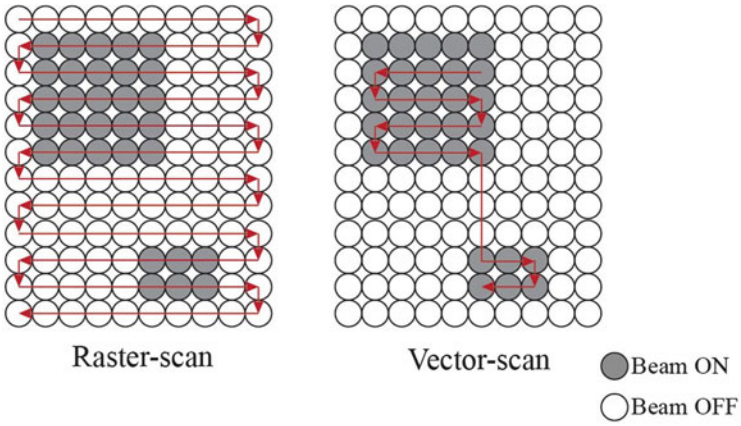

Fig. 9.26 Scan methods of EB lithography

There are two approaches to transfer the pattern image to the wafer which are raster scan and vector scan, as shown in Fig. 9.26. In the raster scan, the EB moves back and forth, while the EB is switched to on state when it meets the areas containing desired patterns and switched to off state on the other areas, using the blank. The raster scan method is simple but relatively time-consuming since the beam has to scan spot by spot throughout the whole wafer. The vector scan, on the other hand, moves the EB only on the area where it needs to be exposed. Therefore this method is less time-consuming and thus more effective. The resolution of electron beam is dominated by the spot size of electron beam, the electron scattering to the resist and substrate, and electron-electron repulsion. By optimizing these parameters, fabrication of nanostructures with the smallest lateral size of 10 nm is achievable.

9.5.3 *Focused Ion Beam*

Along with the electron beam lithography, focus ion beam is among the most popular nanomachining tools for MEMS/NEMS devices [32]. The FIB systems have been initially developed in the 1970s and commercialized for more than two decades ago. The FIB is relatively similar to that of the EBL systems. Instead of electron emitter in the EBL, ion source is employed to bombard the targeted area. The most common ion type used in FIB is Ga^+, which is generated from a Ga containing liquid-metal ion source (LMIS) under a strong electric field. The emitted electron beam is then refined and condensed when passing through electrostatic and magnetic lenses. The ion beam energy typically varies from 10 to 50 keV, and its beam currents ranging from 1 pA to 10 nA. The beam current is controlled to obtain specific requirement such as a fine beam for high-resolution imaging on sensitive samples or a heavy beam for fast and rough milling.

When the Ga^+ ions hit the targeted wafer, they sputter the material and lose energy to the electrons of the surface as well as to its atoms. This impact will lead to the generation of secondary ions, neutral atoms, and secondary electrons. When the ion beam scans on the sample surface, the signal from the sputtered ions or secondary electrons is collected to form an image. Therefore, using FIB with low energy, it is possible to obtain image with high resolution of up to 5 nm. The sputtering impact also causes the milling and deposition effect. As such, with high ion energy, the ion bombardment can remove the material to form desired structures. This direct milling capability is considered a significant advantage of FIB as it can fabricate nanostructures without requiring a resist layer like X-ray and EB lithography. Another important effect in FIB is implantation, that is, the penetration of high-energy ions into a deep layer ranging from a few nanometer to several tens nanometer of the substrate material. Table 9.4 shows a typical implantation depth for Ga^+ ions in Si, SiO_2, and Al. In addition, for the case of single-crystal substrate, the penetration of ions into substrate can also amorphize the material, since the implanted ions will knock out the crystal atom from its lattice. The amorphization impact has also been widely employed in maskless fabrication as presented in Fig. 9.27. In the first step, Ga^+ ion beam is locally scanned on a single-crystal Si to form nanopatterns [33]. The exposed areas become amorphous Si, while the other areas remain single-crystal Si. As the etching rate of amorphous Si is much lower than single-crystal Si, the Si layer surrounding and underneath of the amorphized layer can be completely striped away using wet etching (e.g.,

Table 9.4 Typical implantation depth (nm) of Ga+ in Si, SiO_2, and Al estimated using Monte Carlo simulation

Ga^+ ion energy (keV)	Si	SiO_2	Al
10	13 ± 5	12 ± 4	11 ± 4
20	20 ± 7	19 ± 6	17 ± 6
30	27 ± 9	25 ± 8	23 ± 8
40	33 ± 11	31 ± 10	29 ± 10
50	39 ± 14	38 ± 11	35 ± 12

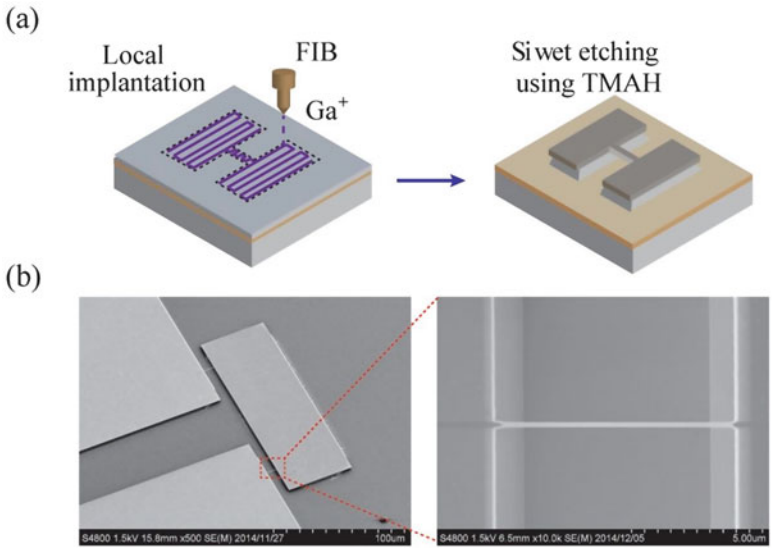

Fig. 9.27 A demonstration of a maskless fabrication using FIB. (**a**) Fabrication process. (**b**) SEM images of Si nanowires (Reprinted with permission from [33])

TMAH) without significantly attacking the amorphous layer. Finally, the amorphous Si can be re-crystalized by employing thermal annealing process.

9.5.4 Scanning Probe Lithography

Along with the well-known function for imaging and microscopy, scanning probe has also showed its potential for nanoscale fabrication [34]. Utilizing advanced technologies developed for scanning microscopy systems, scanning probe lithography (SPL) can directly induce selective modifications on a surface with a precise localization of the defined pattern. An SPL system basically runs based on the principle of either scanning tunneling microscopy (STM) or atomic force microscopy (AFM). In scanning tunneling microscopy lithography (STML), a large bias voltage is applied between the sharpened conducting tip (typically within atomic range ~1 nm) and the target sample [35], Fig. 9.28. When the distance between the tip and the sample is sufficiently small, electrons begin to tunnel from the tip through the gap to the sample or vice versa. The generated tunneling current can be considered as a miniaturized electron beam to achieve most direct writing functions at diminishing scales, which is similar to the electron beam lithography. Consequently, like EBL, STML can exposure the photoresist coated on the sample, changing its properties for subsequent resist development. Furthermore, as the applied voltage in STML is several orders of magnitude smaller than that of the EBL, STML can significantly reduce the effect of electron back scattering, thus

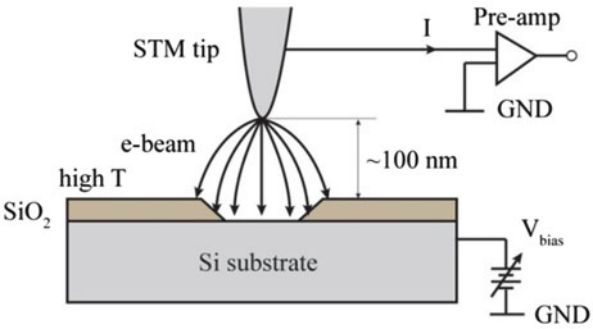

Fig. 9.28 A concept of STML used to decompose a SiO_2 layer [34]

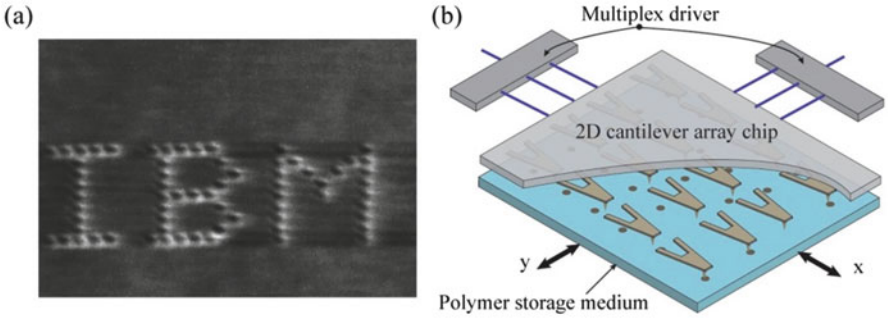

Fig. 9.29 Direct material removal/etching using AFML. (**a**) Nanostructures of polycarbonate patterned using thermomechanical writing process (Reprinted with permission from [37]). (**b**) The concept of a millipede system for data storage [38]

improving the resolution of EB exposure. Nevertheless, the low applied voltage in STML also limits its application to very thin photoresist films. In addition, STML in an ambient condition can be implemented for oxidation of material such as metals or silicon with spatial feature size of a few nanometers. Furthermore, STML has been employed for direct material deposition which the STM tip acts as a miniature emission source because under a bias voltage, atoms or nanoparticles from the tip can also be emitted and adsorbed the target surface. Another function of STML is direct etching. As such, the field emitted electron beam extracted from the STM tip can remove SiO_2 through thermal desorption.

The other type of SPL is based on atomic force microscopic lithography (AFML), in which the nanofabrication process is performed using both electrical and mechanical interaction between the AFM tip and the targeted materials [36]. For photoresist exposure, a large voltage is applied to the tip, which generates an electric field, providing an electron source for exposing ultrathin resists. The AFML methods can perform photoresist exposure, direct etching and deposition like STML, Fig. 9.29. AFML direct patterning utilizes thermal-induced modification, in which the AFM tip is heated at high temperature by applying a high voltage [37]. The hot AFM tip is then pressed again the target substrate to form desired

structures. This concept is named millipede, which can also be applied for data storage system, where the heated AFM tool is used for data writing, while the atomic force is utilized for data reading. Millipedes which have 15 nm bit pitch, leading to a storage density of more than 1 Tb per inch, have also been realized [38]. Other functions such as oxidation and deposition are also equipped in AFML, where the electronic field is utilized to oxidize a conductive material in ambient environment and to transfer atoms from the tip to the substrate. Compared to STML, the AFML-based techniques are less restrictive, since AFML can be conducted in a normal room environment and is also applicable to nonconductive materials. Furthermore, similar to the features of microscopies, AFML can fabricate nanostructures with higher scan speeds but lower resolution in comparison to STML.

9.6 MEMS/NEMS Applications

This section provides a general introduction to the applications of MEMS/NEMS devices, especially sensors and actuators, fabricated using the micro- and nanomachining techniques presented in the previous sections. In addition, in light with the scope of this chapter, most devices presented here employ Si as the functional material [39, 40].

9.6.1 Sensors

Utilizing the advancement of micro- and nanofabrication technology, MEMS/NEMS sensors have been extensively developed and commercialized for more than five decades. This section presents some examples of Si-based sensors including mechanical, thermal, and optical transducers, which are fabricated using the micro- and nanomachining technologies.

9.6.1.1 Si Piezoresistive Sensors

The piezoresistive effect is defined as the change of electrical resistivity in a material under the application of a strain or stress [41, 42]. The effect is also quantified by a parameter named gauge factor (GF) which is the ratio of the relative resistance change to the applied strain. Typically, a large gauge factor is preferable for MEMS mechanical sensor. Among several semiconductors, single-crystal Si possesses one of the most significant piezoresistive effects with maximum GFs of above 100 in both p-type and n-type. Using the piezoresistive effect, mechanical quantities such as strain, force, mass, acceleration, and pressure can be detected by

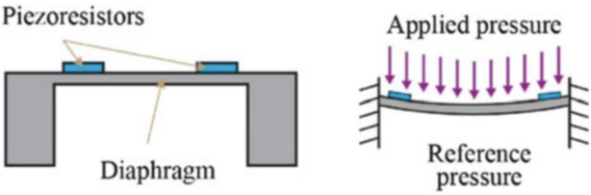

Fig. 9.30 Concept of a piezoresistive pressure sensor

measuring the resistance change. Among these mechanical sensors, pressure sensor is one of the most successful MEMS applications.

Figure 9.30 shows concept of MEMS piezoresistive sensors. The sensor consists of a diaphragm with a piezoresistive layer fabricated on its surface and a sealed gas cavity underneath [43]. A change in pressure will lead to the deformation of the diaphragm. The deflection of the diaphragm (ω) can be calculated using the Timoshenko's plate and shell model:

$$\omega(r) = \frac{Pa^4}{64D}\left[1 - \left(\frac{r}{a}\right)r\right]^2$$

where r, a, and P are the radial distance from the center of the diaphragm, diaphragm radius, and applied pressure, respectively. D is the flexural rigidity, given by:

$$D = \frac{Eh^3}{12(1-\nu)}$$

where E, h, and ν are the Young's modulus, thickness, and Poisson's ratio of the diaphragm, respectively. It is clear that the amount of deflection is directly proportional to the applied pressure. Furthermore, the deflection of the rigid diaphragm will cause the piezoresistive elements to change their resistances. In most pressure sensors, to enhance the sensitivity, piezoresistive elements are typically fabricated at the edge of the diaphragm where stresses are concentrated.

9.6.1.2 Si Thermal Sensors

Thermal sensors basically employ the modification of the properties of materials due to the change in temperature. Commonly employed thermal properties include thermoresistive (i.e., change in resistance caused by temperature change). Thermal sensors basically employ the modification of the properties of materials due to the change in temperature. Commonly employed thermal properties include thermoresistive (i.e., change in resistance cause by temperature change), thermoelectric (i.e., the generation of a voltage in a thermal gradient), and thermal expansion (change in geometry when varying temperature).

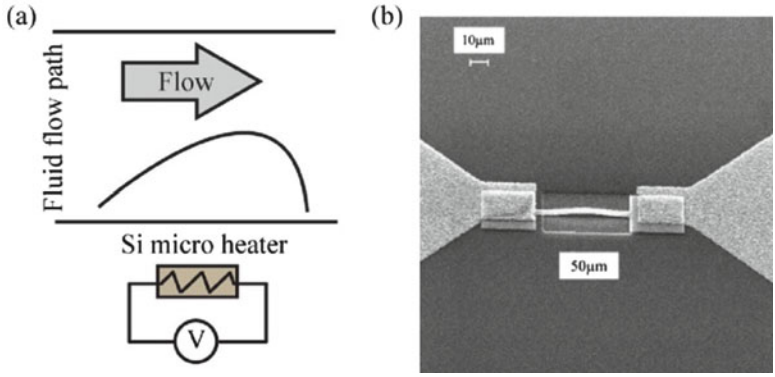

Fig. 9.31 (**a**) Concept of a hot wire airflow sensor. (**b**) SEM image of a suspended Si hot wire sensor (Reprinted with permission from [44])

Figure 9.31a shows a Si airflow sensor which operates by heat transfer from a heated element to the surrounding cooler fluid. The thermal flow sensor is basically a hot wire, which is heated and subjected to fluid flow. When a sufficiently high electrical power is applied to the wire, its temperature will increase due to the Joule heating effect with a heating power of $P = U \times I$, where U and I are the applied voltage and current, respectively. When a fluid flow is applied, convective heat loss increases from the heated element, resulting in a change of the resistance of the wire due to the thermoresistive effect [45, 46]. In the constant current mode, the differential output voltage ΔV and flow velocity v follow King's law:

$$\Delta V = a + bv^n$$

where a, b, and n are constant. Consequently, by measuring the change in output voltage (or resistance change: $\Delta R = \Delta V/I$), the fluid flow rate is obtained. A SEM image of a hot wire airflow sensor utilizing polysilicon is shown in Fig. 9.31b. The fabrication of this hot wire sensor used three-mask photolithography steps, flowing the etching methods described in the previous section.

9.6.1.3 Si Photonic Crystal Sensors

Photonic crystals (PhCs) are a periodic distribution of one material within a different host material having different refractive index. PhCs show a variety of band dispersions and artificial photonic band gaps in which wave propagation is restricted for a certain range of wavelengths. By using different materials and adjusting geometrical parameters, the propagation of light can be modified in numerous ways. In the last two decades, the PhCs in Si have been the subject of intense international research efforts, particularly for light flow control applications, as well as sensing devices such as pressure, and biosensors [47]. Figure 9.32a

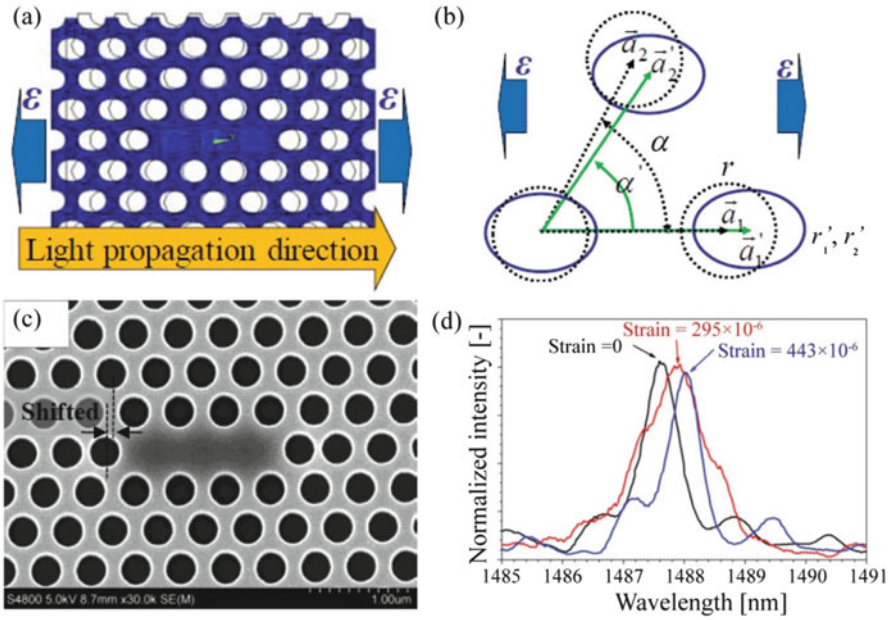

Fig. 9.32 Si photonic crystal for strain sensors. (**a**) Concept of a 2D Si photonic crystal structures. (**b**) The deformation of nanoholes under strain. (**c**) A SEM image of a Si photonic crystal array. (**d**) The optical band gap under strain (Reprinted with permission from [48])

shows concept of strain sensors based on Si PhCs [48]. The sensor consists of an air-hole lattice with a particular diameter and pitch. When a mechanical stress or strain is applied to the Si PhC structure, the geometry of the air-hole lattice will be changed, resulting in a change in its optical properties including the resonance wavelength, Fig. 9.32b. Therefore, by measuring the shifting in resonance wavelength of the transmission spectrum, high-resolution strain sensing can be achieved. Figure 9.32c shows a SEM image of Si PhCs strain sensor fabricated from a SOI wafer, in which the pattern of nanoscale hole was fabricated using EBL, and Si was etched using RIE. Experimental data showed that resonance wavelength significantly increased when increasing the applied tensile strain Fig. 9.32d. This result indicates the potential of Si PhCs for mechanical sensors.

9.6.2 Actuators

Common MEMS/NEMS actuators implement mechanism such as electrostatic, magnetic, thermal expansion, and piezoelectric effect. While the last mechanism requires piezoelectric material such as PZT, ZnO, and AlN, the former approaches

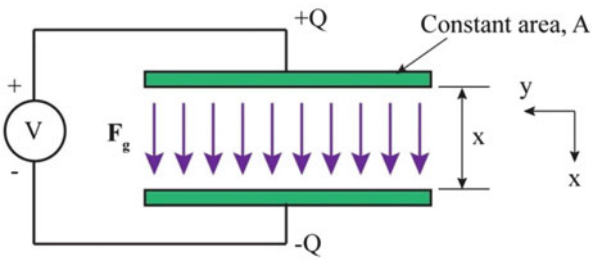

Fig. 9.33 Principle of electrostatic actuator based on a parallel capacitor

can be performed using Si material. The following are the basic concept and example of Si-based actuators and resonators.

9.6.2.1 Electrostatic Actuators

Silicon comb-drive electrostatic actuators are among the most frequently utilized in MEMS since they were first reported about 20 years ago. The advantages of these actuators include the simple and mass fabrication process, accuracy, easy control, and large displacement [49]. The working principle of electrostatic actuator is based on electrostatic force, which can be simply explained using the parallel plate capacitance structure, Fig. 9.33. The energy (W) stored in a parallel-plate capacitor is given by:

$$W = \frac{1}{2}CV^2 = \frac{\varepsilon_r \varepsilon_0 A}{x}V^2$$

where V is applied voltage, C is the capacitance, A is the surface area of each conductive plate, x is the distance between two plates, and ε_o and ε_r are the permittivity of space and the relative permittivity of the dielectric material between the plates. Consequently, the electrostatic force attracting the two plates is:

$$F = \frac{dW}{dx} = -\frac{\varepsilon_r \varepsilon_0 A}{x^2}V^2$$

By controlling the applied voltage, the electrostatic force can be modified, moving the electrodes to the desired position. Employing this simple principle and smart design structures, complex electrostatic actuators with several degrees of freedom (DOF) motion can be obtained. For instance, as shown in Fig. 9.34, a micro-transportation system comprising of rackets and a container was developed based on an SOI platform. When the electrostatic comb-drive is actuated, the induced force will push the ratchet racks inward, causing the driving wings to move inward. Subsequently, following the motion of the wings, the container is moved forward. When the force is removed, the container will maintain its position due to the anti-reverse wings of the ratchet mechanism. Repeating this cycle, the container can be transported to the targeted position.

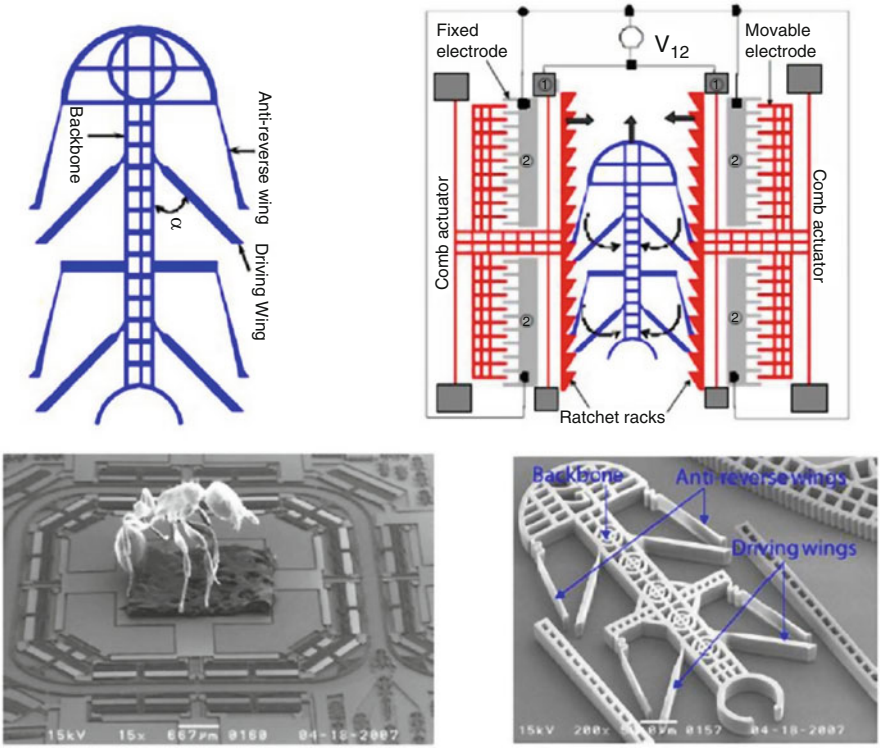

Fig. 9.34 Structure of a micro-container and a schematic view showing the working principle of the system (Reprinted with permission from [49])

9.6.2.2 Thermal Actuators

Thermal actuation has been proved as a compact, stable, and high-force actuation technique with several advantages over electrostatic actuation [50]. The application of thermal actuation can be found in linear and rotary microengines, nanopositioners, optical benches, and instrumentation for material property characterization. The principle of thermal actuators lies on the thermal expansion and heat transfer in materials at high temperature. One of the most well-known mechanisms is the hot arm and cool arm structure shown in Fig. 9.35.

In this flexural actuator, the hot arm (narrow arms) is positioned parallel to the cool arm (wider section), and their roots are connected to two electrodes. Due to the ratio of the width of these two arms, most of electrical resistance concentrates at the narrow area (hot arm). Therefore, when a sufficiently high voltage is applied, both arms will be heated by the Joule heating effect. Since the surface area of the hot arm is much smaller than the cool arm and so its heat loss to convection, the temperature of the narrow arm significantly increases. Whereas, the temperature of the wide arm

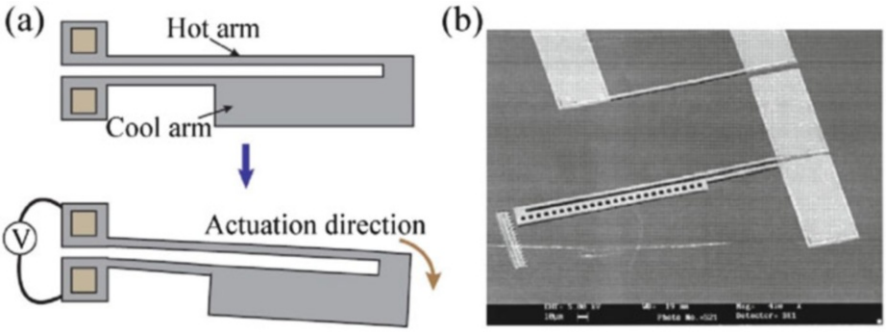

Fig. 9.35 (**a**) Concept of a hot arm and cool arm thermal actuator. (**b**) SEM image of a Si microthermal actuator (Reprinted with permission from [50])

remains relatively low. The change in temperature causes the arm to be expanded following thermal expansion:

$$\varepsilon = \lambda \Delta T$$

where ε, λ, and ΔT are thermal strain, thermal expansion coefficient, and the temperature change, respectively. Clearly, the hot arm has a larger expansion than that of cool arm, which results in the lateral bending of the whole structure. A SEM image of a MEMS Si flexural actuator using the hot arm and cool arm structure is shown in Fig. 9.35b.

9.6.2.3 Magnetic Actuators

One of the most common mechanisms used in magnetic actuator is the implementation of the Lorentz force. Because the Lorentz force is perpendicular to the direction of the directions of current and magnetic field, the vibration modes (e.g., in plane and out plane) of a magnetic actuator are tunable by changing the direction of the applied magnetic field. In addition, since the Lorentz force is independent on the surface area, magnetic actuator is scalable down to nanometer orders [51].

Figure 9.36 shows a magnetic-driven Si nanowires resonator [52]. When passing a current I through the Si nanowire with a length L, in the presence of an applied magnetic field B, the Lorentz force F inserted to the nanowire is:

$$F = LI \times B$$

If the driven force is supplied in an AC mode, it will induce a vibration into the nanowire. Furthermore, when the frequency of the current matches that of the natural frequency of the Si nanowires, it will cause a resonance in the nanowire,

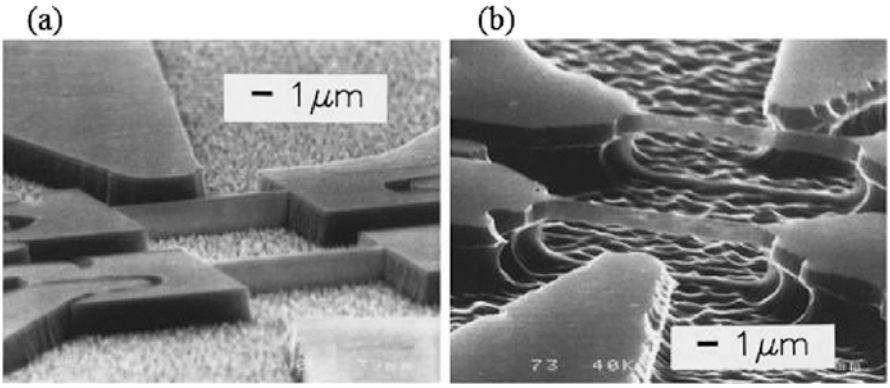

Fig. 9.36 SEM micrographs of magnetic resonator (**a**) non-released structures following the anisotropic Si etch; (**b**) undercut Si nanowire magnetic resonators (Reprinted with permission from [52])

providing noticeably large amplitude of vibration. The resonance frequency (f_r) of nanowires is given by:

$$f_r \sim \frac{d}{L^2}\sqrt{E/\rho}$$

where d, L, E, and ρ are the thickness, length, Young's modulus, and density of the Si nanowire, respectively. Evidently, by choosing proper dimensions for the nanowire, a very high resonance frequency (VHF) up to several GHz is achievable. The high-frequency resonators can be used for the numerous applications including ultrahigh-resolution mass detection, quantum electromechanics, electromechanical signal generation and processing, and high-speed logic and computation.

References

1. Venema L (2011) Silicon electronics and beyond. Nature 479(7373):309–309
2. Gad-el-Hak M (ed) (2001) The MEMS handbook. CRC Press, Boca Raton
3. Mnyusiwalla A, Daar AS, Singer PA (2003) Mind the gap': science and ethics in nanotechnology. Nanotechnology 14(3):R9
4. Shimura F (ed) (2012) Semiconductor silicon crystal technology. Elsevier, Amsterdam
5. Sze SM, Ng KK (2006) Physics of semiconductor devices. Wiley, Hoboken
6. Ghibaudo G, Rafhay Q (2014) Electron and hole mobility in semiconductor devices. Wiley Encyclopedia of Electrical and Electronics Engineering
7. Klaassen DBM (1992) A unified mobility model for device simulation -II. Temperature dependence of carrier mobility and lifetime. Solid-State Electron 35(7):961–967
8. Hopcroft MA, Nix WD, Kenny TW (2010) What is the Young's modulus of silicon? J Microelectromech Syst 19(2):229–238

9. Shanks HR et al (1963) Thermal conductivity of silicon from 300 to 1400 K. Phys Rev 130 (5):1743
10. Plummer JD (2009) Silicon VLSI technology: fundamentals, practice, and modeling. Pearson Education India, London
11. Maleville C et al (1997) Wafer bonding and H-implantation mechanisms involved in the Smart-cut technology. Mater Sci Eng B 46(1):14–19
12. Mark Noworolski J et al (1996) Fabrication of SOI wafers with buried cavities using silicon fusion bonding and electrochemical etch back. Sens Actuat A Phys 54(1):709–713
13. Sparks DR et al (1995) Method of micromachining an integrated sensor on the surface of a silicon wafer .US Patent No. 5, pp 427–975
14. Mack C (2007) Fundamental principles of optical lithography: the science of microfabrication. Wiley, Hoboken
15. Lorenz H, Despont M, Fahrni N, LaBianca N, Renaud P, Vet- tiger P (1997) SU-8: a low-cost negative resist for MEMS. J Micromech Microeng 7(3):121
16. Thong JTL, Choi WK, Chong CW (1997) TMAH etching of silicon and the interaction of etching parameters. Sens Actuat A Phys 63(3):243–249
17. Tanaka H et al (2004) Fast etching of silicon with a smooth surface in high temperature ranges near the boiling point of KOH solution. Sens Actuat A Phys 114(2):516–520
18. Dutta S, Md I, Kumar P, Pal R, Datta P, Chatterjee R (2011) Comparison of etch characteristics of KOH, TMAH and EDP for bulk micromachining of silicon (110). Microsyst Technol 17:1621–1628
19. Nicolas M, Perney B, Baumberg JJ, Zoorob ME, Charlton MDB, Mahnkopf S, Netti CM (2006) Tuning localized plasmons in nanostructured substrates for surface-enhanced Raman scattering. Opt Express 14(2):847857
20. Klaassen EH et al (1996) Silicon fusion bonding and deep reactive ion etching: a new technology for microstructures. Sens Actuat A Phys 52(1):132–139
21. Manos DM, Flamm DL (eds) (1989) Plasma etching: an introduction. Elsevier, Amsterdam
22. Jansen H et al (1996) A survey on the reactive ion etching of silicon in microtechnology. J Micromech Microeng 6(1):14
23. Ayazi F, Najafi K (2000) High aspect-ratio combined poly and single-crystal silicon (HARPSS) MEMS technology. J Microelectromech Syst 9(3):288–294
24. Usenko AY (2002) Process for lift-off of a layer from a substrate. US Patent No. 6352909
25. Yazdi N, Khalil N (2000) An all-silicon single-wafer micro-g accelerometer with a combined surface and bulk micromachining process. J Microelectromech Syst 9(4):544–550
26. Howe RT (1988) Surface micromachining for microsensors and microactuators. J Vac Sci Technol B 6(6):1809–1813
27. Smith HI, Flanders DC (1980) X-ray lithography—a review and assessment of future applications. J Vac Sci Technol 171:533–535
28. Phan H-P et al (2016) Piezoresistive effect in p-type 3C-SiC at high temperatures characterized using Joule heating. Sci Rep 6:28499
29. Neukermans AP et al (1986) Silicon carbide film for X-ray masks and vacuum windows. US Patent No. 4608326
30. Hruby J (2001) LIGA technologies and applications. MRS Bull 26(4):337–340
31. Tseng AA et al (2003) Electron beam lithography in nanoscale fabrication: recent development. IEEE Trans Electron Packag Manufact 26(2):141–149
32. Tseng AA (2005) Recent developments in nanofabrication using focused ion beams. Small 1 (10):924–939
33. Phan H-P et al (2015) Piezoresistive effect of p-type silicon nanowires fabricated by a top-down process using FIB implantation and wet etching. RSC Adv 5(100):82121–82126
34. Tseng AA, Notargiacomo A, Chen TP (2005) Nanofabrication by scanning probe microscope lithography: a review. J Vac Sci Technol B 23(3):877–894
35. McCord MA, Pease RFW (1986) Lithography with the scanning tunneling microscope. J Vac Sci Technol B41:86–88

36. Hu S et al (1998) Fabrication of silicon and metal nanowires and dots using mechanical atomic force lithography. J Vac Sci Technol B 16(5):2822–2824
37. Terris BD, Mamin HJ, Best ME, Logan JA, Rugar D, Rishton SA (1996) Nanoscale replication for scanning probe data storage. Appl Phys Lett 69:4262
38. Eleftheriou E, Antonakopoulos T, Binnig GK, Cherubini G, Despont M, Dholakia A, Durig U et al (2003) Millipede—a MEMS-based scanning-probe datastorage system. IEEE Trans Magn 39(2):938–945
39. Phan H-P et al (2015) The piezoresistive effect of SiC for MEMS sensors at high temperatures: a review. J Microelectromech Syst 24(6):1663–1677
40. Bell DJ et al (2005) MEMS actuators and sensors: observations on their performance and selection for purpose. J Micromech Microeng 15(7):S153
41. Minh-Dung N et al (2013) A sensitive liquid-cantilever diaphragm for pressure sensor. In: 2013 I.E. 26th International Conference on Micro Electro Mechanical Systems (MEMS). IEEE
42. Minh-Dung N et al (2013) A hydrophone using liquid to bridge the gap of a piezo-resistive cantilever. In: 2013 Transducers & Eurosensors XXVII: The 17th International Conference on Solid-State Sensors, Actuators and Microsystems (Transducers & Eurosensors XXVII). IEEE
43. Eaton WP, Smith JH (1997) Micromachined pressure sensors: review and recent developments. Smart Mater Struct 6(5):530
44. Laghrouche M, Adane A, Boussey J, Ameur S, Meunier D, Tardu S (2005) A miniature silicon hot wire sensor for automatic wind speed measurements. Renew Energy 30(12):1881–1896
45. Kuo JT, Yu L, Meng E (2012) Micromachined thermal flow sensors—a review. Micromachines 3(3):550–573
46. Dinh T et al (2015) Graphite on paper as material for sensitive thermoresistive sensors. J Mater Chem C 3(34):8776–8779
47. Birner A et al (2001) Silicon-based photonic crystals. Adv Mater 13(6):377388
48. Bui TT, Dao DV et al (2011) Investigation of strain sensing effect in modified single-defect photonic crystal nanocavity. Opt Express 19(9):8821–8829
49. Dao DV et al (2010) Micro/nano-mechanical sensors and actuators based on SOI-MEMS technology. Adv Nat Sci Nanosci Nanotechnol 1(1):013001
50. Huang Q-A, Lee NKS (1999) Analysis and design of polysilicon thermal flexure actuator. J Micromech Microeng 9(1):64
51. Feng XL et al (2007) Very high frequency silicon nanowire electromechanical resonators. Nano Lett 7(7):1953–1959
52. Cleland AN, Roukes ML (1996) Fabrication of high frequency nanometer scale mechanical resonators from bulk Si crystals. Appl Phys Lett 6918:2653–2655

Chapter 10
Solid-State Micropores for Living Cell Detection and Discrimination

Muhammad Hammad Ijaz, Muhammad Usman Raza, Syeda Momina Mahmood, and Samir M. Iqbal

10.1 Introduction

Coulter counter is a standard for cell counting. Cells suspended in an ionic solution pass through apertures that are tens to hundreds of micrometers in diameter. Ionic current is measured across the aperture. Cell passage is sensed when the current values drop below certain levels due to ion blocking through the aperture. Taking this a step further, with exactly defined orifices in nanoscale thin membranes and high-resolution and precision electronic measurements, we have the field of solid-state micropores.

Blood contains a number of cells which can give us plenty of information about the condition of a living body. The cells that are abundant in blood are red blood cells (RBCs). These cells can be easily removed from blood by lysis techniques. There are also white blood cells (WBCs) in the blood which are hard to separate.

M.H. Ijaz • M.U. Raza
Nano-Bio Lab, Department of Electrical Engineering, Nanotechnology Research Center
University of Texas at Arlington, Arlington, TX 76019, USA

S.M. Mahmood
Chemical Engineering, University of California San Diego, La Jolla, CA 92093, USA

S.M. Iqbal (✉)
Nano-Bio Lab, Department of Electrical Engineering, Nanotechnology Research Center
University of Texas at Arlington, Arlington, TX 76019, USA

Nano-Bio Lab, Department of Bioengineering, Nanotechnology Research Center,
University of Texas at Arlington, Arlington, TX 76019, USA

Department of Urology, University of Texas Southwestern Medical Center at Dallas,
Dallas, TX 75235, USA

Department of Electrical Engineering, The University of Texas Rio Grande Valley,
Edinburg, TX 78539, USA
e-mail: smiqbal@ieee.org

M.J. Jackson, W. Ahmed (eds.), *Micro and Nanomanufacturing Volume II*,
DOI 10.1007/978-3-319-67132-1_10

The cells that are important for cancer detection are also present in blood and are called circulating tumor cells (CTCs).

CTCs detach from the primary tumor and enter into bloodstream. They cause secondary tumors in distant sites leading to metastasis [1–3]. The early detection of CTCs is very important for the early diagnosis of cancer [4]. In other words, CTCs can act as a marker to predict the cancer disease in a patient [5]. They are low in number, so it is difficult and challenging to detect them [6–10]. If CTCs are detected at the initial stage of cancer or before the metastasis, it can give us the idea about the tumor growth [11, 12] which in turn can increase the chances of curing the cancer.

Studies have shown that cancer cells have distinctly different physical and mechanical properties than normal cells [13]. They are larger in size than RBCs and WBCs, and hence their physical properties can be used to differentiate and detect from normal cells in a blood sample. A number of techniques are being used for the detection of CTCs. Some of these techniques include using array of activated micro-posts to separate CTCs, use of laser scanning cytometry, use of centrifugal force for isolation of cells, cell sorting from fluorescence signals, etc. [14–22]. These techniques have their shortcomings. Some are limited by their low throughput, and some are either complex or expensive to be used as point-of-care device.

The use of micropores for cancer cell detection from a blood sample is not only simple but also very efficient. The use of micropores for cancer detection uses the fact that CTCs have different physical properties than other cells present in blood. Their larger size and different pliability can be used for their distinction from other cells.

When a blood sample is passed through the micropore, CTCs, being larger in size, interact with the micropore periphery differently than WBCs and RBCs. In other words, they block the flow of ionic current through the micropore in a distinctly different way. If this blockage can be detected, the tumor cells can be detected from the sample. The micropore chip is placed between two reservoirs filled with electrolytes, and electrodes are placed in each reservoir of electrolyte for detecting the ionic current. When voltage is applied across the micropore, the ionic current starts to flow through the micropore. The micropore current blocked by cells causes increase in the resistance to the flow of ions and the current drops. The current blockages show up as pulses in the current trace. If the current is monitored, each drop in current gives us indication about the presence of tumor cells in the sample. This is the basis of cancer detection using micropores.

The number of CTCs in a blood sample can be as few as 1 in 100 million. The chances of detecting the cancer cell from blood sample are very low. Blood thus needs to be first processed to get rid of unnecessary cells. RBCs have the highest concentration in blood. The lysis of RBCs dramatically increases the chances of detecting CTCs from blood samples. The number of WBCs can also be decreased by using different techniques such as spiral microfluidics [19, 20]. Processing of blood before injecting the sample in the micropore assembly can be helpful in detection of CTCs.

10.2 Micropore Fabrication

The micropores can be made in a number of ways. One way is to microfabricate these by drilling thin suspended solid-state membranes in silicon chips. The drilling is usually done with focused ion beam (FIB). The duration of drilling time and dose of ions determine the size of the micropores. Optical lithography followed by wet or dry etching can also be employed to create micropores in membranes of various materials. Micropore chips can be fabricated in a desired dimension depending on their intended use. The most commonly used micropores are the ones with fixed diameters [18, 23–26]. The micropores with tunable diameters have also been fabricated which makes it easier to detect cells of different size with a single device [27].

10.2.1 Fixed Diameter Micropores

The basic fabrication process of micropores starts with a silicon wafer. Double-sided polished silicon wafer is used for this purpose. Silicon wafer is cleaned first to get rid of residual impurities. The wafer is then oxidized (Fig. 10.1a). The thickness of oxide layer depends on the time for which the wafer is placed in the furnace and oxidation conditions. A 200 nm thin oxide has been used for cancer detection work [18, 25]. Depending on the application, the thickness of oxide can be changed.

After oxidation, the wafer is cleaned with Piranha solution, and photoresist is applied on both sides of the wafer. Photolithography is then used to form square window pattern in the photoresist (Fig. 10.1b). This square window in photoresist is used to etch the oxide layer underneath the resist.

The buffered hydrofluoric acid (BHF) is used to etch the exposed silicon dioxide (referred to as oxide) through the square window in photoresist. The pattern is transferred to the underneath oxide layer. The photoresist applied to the other side of the wafer protects the oxide layer during the BHF etch. After opening a square window in the oxide on one side, the remaining photoresist is removed from both sides of wafer. Now, we have oxide layer completely covering one side of the wafer and oxide layer with square windows pattern in it on the other side (Fig. 10.1c).

Diluted tetramethylammonium hydroxide (TMAH) is used for anisotropic etching of silicon, which is done to etch the silicon wafer all the way through [18, 28]. The etch stops automatically once it hits SiO_2 layer on the other side. Thus we get a silicon dioxide membrane. After TMAH etch, freestanding silicon dioxide membranes are achieved in which micropores are drilled.

For drilling the micropore, FIB is used. The size/diameter of the micropore depends on the dose of FIB and the time for which the oxide membrane is exposed to the beam [23]. After the hole is drilled, we get a silicon chip with freestanding silicon dioxide membrane and a micropore in it (Fig. 10.1d).

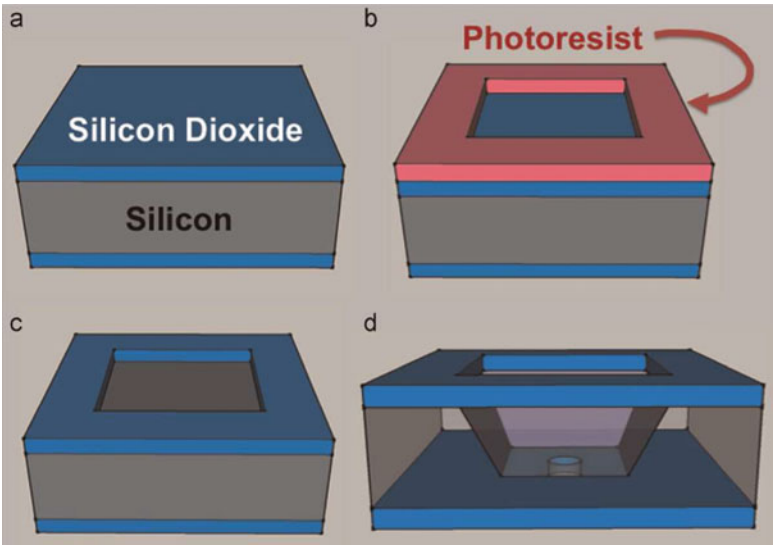

Fig. 10.1 Fabrication of solid-state fixed diameter micropores. (**a**) Oxide layer is thermally grown on both sides of silicon wafer. (**b**) Photolithography is done to transfer a square window on oxide layer on one side of wafer. (**c**) Wafer after oxide etch and removal of photoresist. (**d**) Wafer after anisotropic etching of silicon with tetramethylammonium hydroxide (TMAH) and FIB drilling [18] (Reprinted with permission)

The walls of the FIB-drilled micropores are rough from the inside. It can damage the cells flowing through the micropores. In order to smoothen the walls, the micropore chips are placed in a furnace at high temperature for a few minutes. This smoothens the walls of the micropore [25]. The chip is then taken out of the furnace and is now ready for use in the experiment assembly.

Other materials than silicon dioxide can also be used to create membranes for micropore drilling. Researchers have used silicon nitride instead of silicon dioxide as well [23].

Another fabrication technique to create micropores starts with drilling or etching a small hole in the silicon chip. After a hole is created, the silicon wafer is placed inside the furnace for oxidation. A layer of silicon dioxide is grown on top of the wafer as well as inside the micropore. This layer decreases the diameter or size of the hole initially drilled [24, 29, 30]. The oxidation is usually done at high temperature for a long time depending on how much oxide layer is needed inside the hole to reach the desired micropore size (Fig. 10.2). This method has its shortcomings. The most important is that it takes a long time for oxidation. Also, the diameter of micropore is dependent on precise oxidation. The oxidation time and temperature have to be thus closely monitored.

The thickness of oxide layer/membrane grown plays an important role in the translocation of cells through the micropore. If the thickness of membrane is more, it increases the chances of blockage of micropore. This is because as thickness is increased, the physical area of contact for cells with the inner walls of micropore

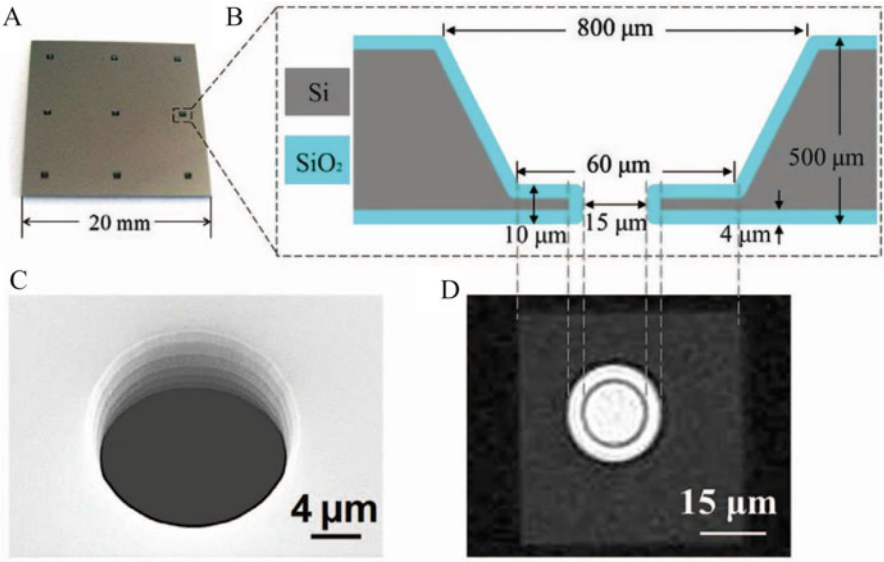

Fig. 10.2 Cross section of micropore in silicon chip with oxide layer grown on top and inside the micropore [24] (Reprinted with permission)

also increases. The probability of cells attaching to the micropore walls also increases. This can lead to micropore blockage. In thin membrane, the chances of blockage are very less because usually just one cell passes through the membrane at a time and a very small area of the translocating cell comes in contact with the micropore periphery [25].

10.2.2 Tunable/Resizable Micropores

Fixed size micropores are very efficient and depict high throughput, but these have a limitation. A separate micropore chip, of very specific size, has to be fabricated depending on the size of the cell to be studied or separated from a mixture. In order to overcome this shortcoming, in experiments in which cells of different sizes are being separated, some researchers are using the tunable micropores.

One of the examples of tunable/resizable micropore is the one used by Roberts et al. for particle detection and discrimination [27]. In that device, the micropore is mechanically fabricated on a thick polyurethane membrane by puncturing it (Fig. 10.3). This puncturing produces a conical pore in the membrane. The diameter of the pore depends on the puncturing process [27, 31, 32].

Now, the size of the micropore can be varied by placing the membrane in a fluid cell and then attaching four adjustable jaws to it [27]. The size of the micropore can be varied by adjusting the jaws. When the jaws are opened, macroscopic strain is

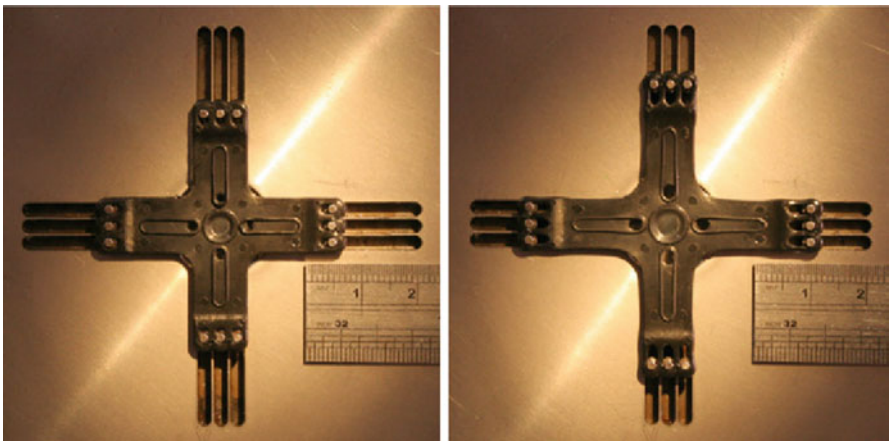

Fig. 10.3 Tunable micropore assembly [31] (Reprinted with permission)

applied on the membrane. This strain changes the pore size [27, 31, 32]. This way, the micropore can be used to discriminate particle or cells of different sizes from a mixture by changing the size of the micropore.

10.3 Micropore Measurements

The flow of ionic current through the micropore is measured as a temporal current trace. The passage of each cell is detected as a transient decrease of ionic current. The duration of the transient decrease, also called a pulse, or an event, is proportional to the size or mechanical properties of cells [18, 23, 25]. This resistive-pulse technique in micropores has been used for cell discrimination for many years. This technique was used by Kasisnowicz et al. in 1996 for measuring DNA translocation through nanopores [33]. The number of pulses can tell the concentration of cells from the frequency of the translocation events [34–36].

Resistive-pulse technique in micropores for cell detection is based on the fact that when nonconducting cells are passed through the micropore, they block the micropore if their size is comparable to the size of micropore. Thus there is a drop in ionic current measured by the electrodes [18, 25]. The resistance of a micropore can be modeled as a resistance (R) such that,

$$R = \frac{\rho L}{A}$$

where

ρ = resistivity of the solution
A = area of micropore
L = thickness of the micropore chip

The resistivity can be calculated theoretically or can be found experimentally for a given micropore setup. Theoretically $\rho = {}^{1}/_{\sigma}$ and $\sigma = n_{\mathrm{KCl}}(\mu_{\mathrm{K}} + \mu_{\mathrm{Cl}})e$, where σ is the conductivity of the solution. Considering an electrolyte solution of KCl, n_{KCl} is the number density of potassium or chloride ions, and e is the elementary charge. The electrophoretic mobilities of potassium and chloride ions are depicted by μ_{K} and μ_{Cl}, respectively. During the cell translocation, some or all area of micropore is blocked; hence the resistance to the flow of current increases. The measurements of these current variations give an idea about the size and frequency of cells that are present in the mixture. This is the key to cancer cell detection using micropores.

Blood samples contain many cell types. The cells that are of interest to us here are CTCs. If we use the blood sample as it is, the chances of getting CTC will be one in a billion. It is efficient to get rid of cells that are of no use for us before passing the blood through the micropore. RBCs can be easily removed by using lysis byffer. Just the removal of RBC increases the chances of detecting CTCs manyfold. Techniques using centrifugal force have also been used to get rid of WBCs from blood and in increasing concentration of CTCs in a given sample [19, 20].

After getting rid of as many undesired cells as possible, the sample is passed through the micropore. CTCs are larger in size than RBCs and WBCs [15]. When RBCs and WBCs pass through the micropore, they offer very less resistance to the flow of current as compared to CTCs. The CTC translocation through the micropore gives a larger drop in current which is measured by the electrodes. The frequency of current drops by the passage of cells is noted. This gives us the idea about the presence and concentration of CTCs in blood sample. Example pulses stemming from the drop in ionic current by the flow of RBCs, WBCs, and CTCs are shown in Fig. 10.4.

It can be seen in the above figure that the drop in current in the case of cancer cell translocation is much larger than those in the cases of RBCs and WBCs. This is because of larger size of cancer cells. Each incident of current drop gives us information about the translocation of a single cancer cell from the micropore. By analyzing the frequency of current drops, we can get the idea about the concentration of cancer cells in the blood sample. This can directly indicate the stage of the primary tumor.

10.4 Experiment Assembly

The resistive-pulse technique is ideally suited for cell detection with micropores. The assembly used by Iqbal and coworkers for cancer cell discrimination is described below [18, 25]. Similar setups have also been used by others [23].

Micropore chip was sandwiched between two blocks made of Teflon (Fig. 10.5). One block was the inlet block, and the other was designated as the outlet block. A small hole was drilled in both blocks for the passage of biological fluid. Micropore chip was aligned between the two blocks such that the micropore membrane was in

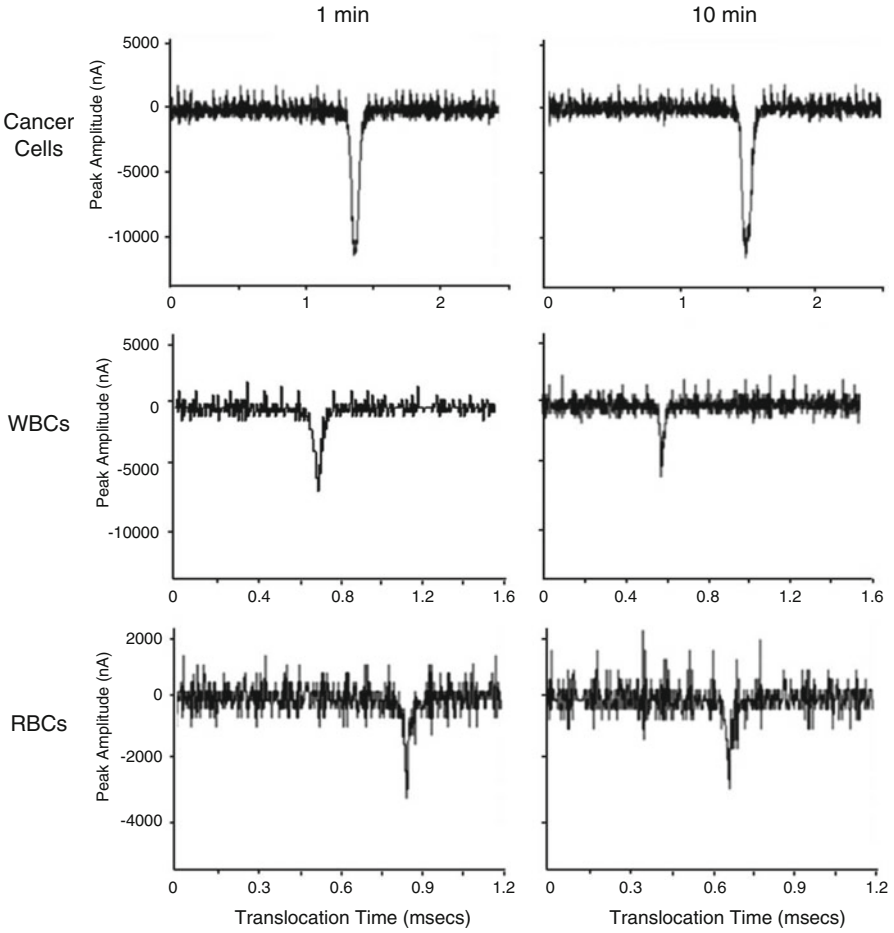

Fig. 10.4 Drop in ionic current through micropore due to blockage by RBCs, WBCs and cancer cells [25]. The micropore performance does not change over extended period of time (Reprinted with permission)

front of the holes in the Teflon blocks. Gaskets made of polydimethylsiloxane (PDMS) were used to hold the microchip between the blocks on both sides [18, 25].

Inlet and outlet blocks were filled with electrolyte solution (NaCl or KCl). Blood spiked with cancer cells was centrifuged, the cell pellet was suspended in the electrolyte solution, and the suspension was pushed from the inlet block. Ag/AgCl electrodes were used to measure ionic current across the micropore (Fig. 10.6). As the cells were injected, variations in current through the micropore were measured by the electrodes.

When cells passed through the micropore, they offered resistance to the flow of current which was measured as drop in the ionic current by the electrodes. The number of instances of current drop gave the concentration of the cells in the

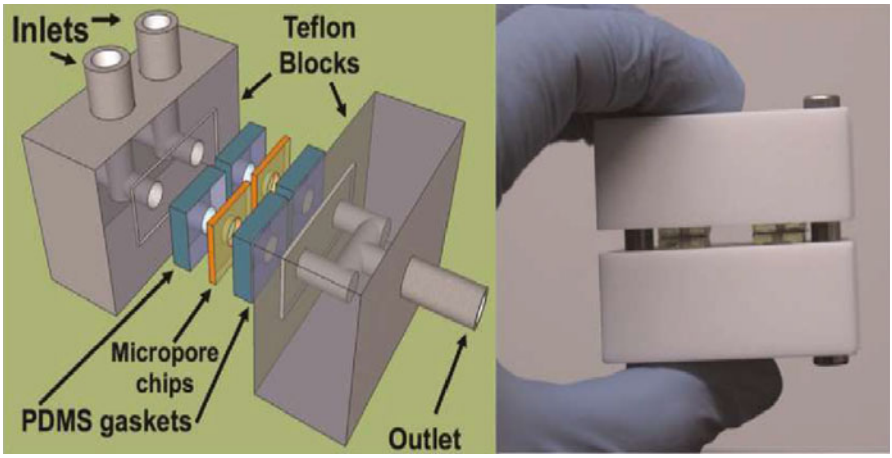

Fig. 10.5 Two micropore chips sandwiched between Teflon blocks for cancer cell detection [18] (Reprinted with permission)

solution. The pulse time gave the size of the cells. In this way, different cell types could be discriminated from a biological solution.

Liu et al. used a similar assembly for their experiments on nanopore-micropore hybrid chips [23]. They used two separate blocks filled with KCl, and micropore was sandwiched between them. Cells were added in the KCl solution, and electric field was applied to both sides of the chips (Fig. 10.7). The current was detected. The difference in the current because of the blockage of micropores by the cells was detected, and this gave the size and length of the cells that were being detected.

10.5 Chemically Activated Micropores

Circulating tumor cells are key to cancer detection, but these are very low in number in blood at the onset of the disease, making it very challenging to detect their presence in blood [6–9, 37, 38]. Also, the resistive-pulse technique doesn't work well for discrimination when the cells that are being detected are of the same size as some other cells present in the biological fluid [24]. It requires engineering other factors to increase the differentiation of cancer cells from blood samples. One way of doing that is using chemically activated micropores by covering the walls of the micropore with ligands specific to the cell to be captured [39–41]. These activated micropores can isolate the signals of the target cells from the fluid during their translocation through the micropore [24]. Another approach has been to graft micropore walls with aptamer molecules [42].

The ligands that are used in activating the micropores depend on which type of cancer cell we are detecting. Bellah et al. used biomarker-specific aptamers in the micropores to slow down the tumor cells for functional analysis [42]. In their

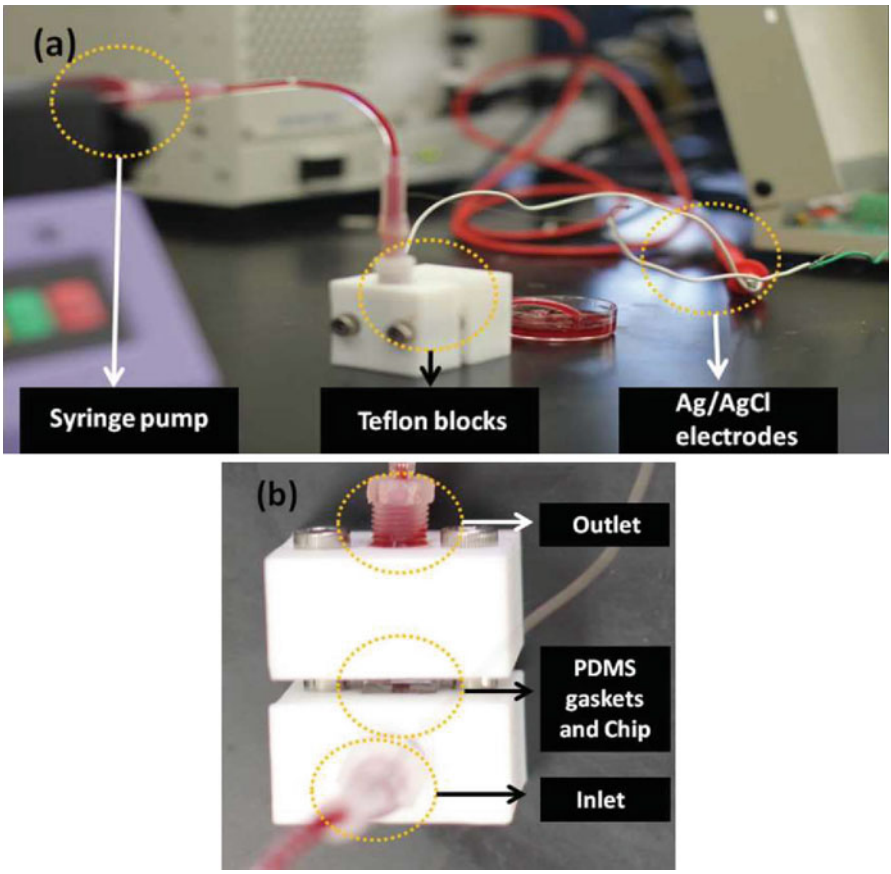

Fig. 10.6 (**a**) Experimental assembly for measuring current variations. (**b**) Micropore chip between the inlet and outlet Teflon blocks having inlet and outlet [25] (Reprinted with permission)

experiments, they used a differential solid-state micropore approach. They functionalized one micropore with the aptamer molecule that was specific to epidermal growth factor receptor (EGFR). EGFR is a known biomarker overexpressed on cancer cell surfaces. The other micropore had no functionalization. The translocation behavior of tumor cells through two micropores was distinctly different. The differentiation putatively stemmed from the selective interactions of cell-surface based EGFR and the aptamer molecules.

In a similar approach, Talasaz et al. used monoclonal antibody to trap single cells in an array of chemically functionalized micropores [43]. The fabrication process for micropore array is shown in Fig. 10.8. The size of the micropores was less than the size of the cells to be trapped. A thin layer of Au/Cr was sputtered on silicon nitride membrane that contained the micropores. The micropore array was functionalized by inserting the probe molecules from backside of the array and then cleaning off the excessive probe molecules. The suspension of cells was spread on

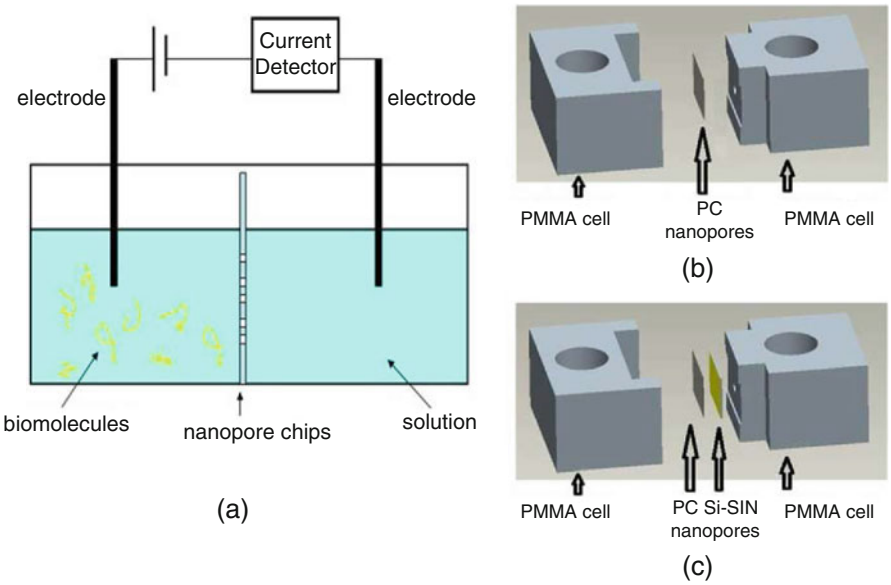

Fig. 10.7 (**a**) Prototype of experiment assembly. (**b**) and (**c**) Nanopore chips are sandwiched between two blocks [23] (Reprinted with permission)

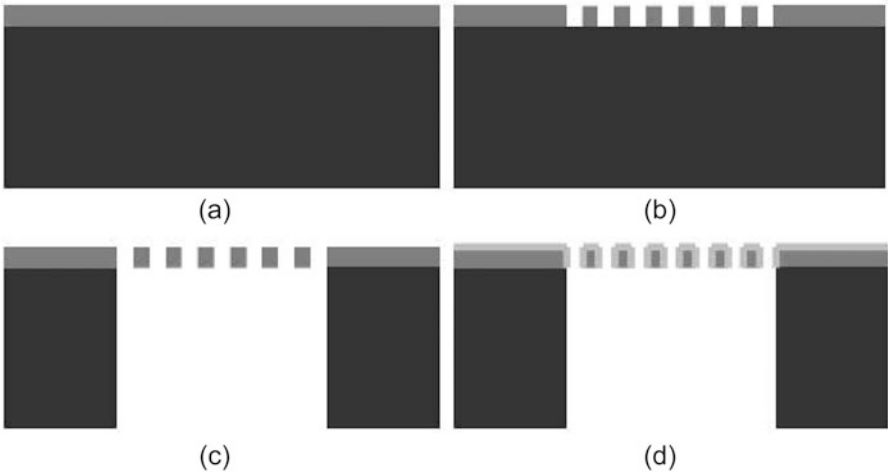

Fig. 10.8 Fabrication of a micropore membrane. (**a**) Silicon nitride is deposited on silicon wafer. (**b**) Micropores are patterned on silicon nitride. (**c**) Silicon is etched from backside of wafer. (**d**) Micropores are coated with desired material depending on experiment [43] (Reprinted with permission)

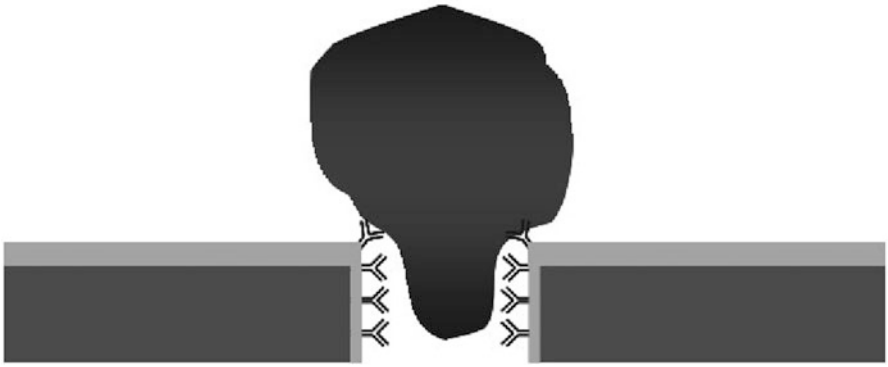

Fig. 10.9 A cell captured and trapped in one micropore of the array [43] (Reprinted with permission)

the top side of the micropore array, and suction was applied from the back. The size of cells to be captured was less than the size of micropores; hence the cells were stuck inside the micropores as shown in Fig. 10.9.

The same experiment, when performed without functionalizing the micropores with antibodies, gave different results. In that case, most of the micropores were not filled with the cells to be captured, while in the case of functionalized micropores, almost all the micropores were filled with cells [43]. This was not a translocation device with flow through resistive-pulse measurements.

Chemically activated micropores can be used in parallel with resistive-pulse technique even if the cells in biological fluid have similar dimensions. For example, B and T lymphocytes have similar dimensions [24, 44]. These cannot be detected in a biological fluid if we just use simple resistive-pulse technique. The ionic current drop in case of translocation of similarly sized cells, e.g., B or T lymphocytes, some CTCs, WBCs, etc., will be the same, and we can't differentiate between the two. That's where chemically activating the micropores with antibodies or aptamers specific to cell surface receptors of interest comes in handy [24, 40].

Chemically activated micropores using aptamers and antibodies increase the chances of detecting the cancer cells [16404143], but they have a few limitation. Aptamers or antibodies are not available for all cancer cells, and also depositing them inside the walls of micropores is a difficult and time-taking process [38].

10.6 Nano-textured Microfluidic Channels

Studies have shown that micro- or nano-level roughness on the surface can result in better cell adhesion, differentiation, and growth [45–49]. Cells have more chances of adherence on a nanotextured surface than on a plain surface which increases their time of translocation through the micropore, thus increasing the chances of

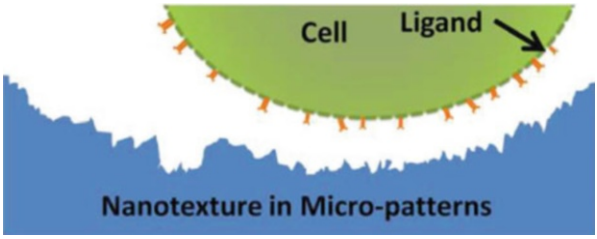

Fig. 10.10 Schematic of micro-patterns and nanotexture for enhanced cell adhesion [46] (Reprinted with permission)

detection of CTCs from a blood sample. Nano-textured microfluidic channels have been used for this purpose [38, 46, 50].

There are a number of techniques for creating textured surfaces. Some of them include chemical etching, micro-contact printing, stencil-assisted patterning, and electro-spinning [47, 49, 51–53]. But these methods are complex and time-consuming. One simple method of getting nanotextured microfluidic channel is to use reactive-ion etching (RIE) (Fig. 10.10). Oxygen and carbon tetrafluoride are usually used for the etching process [38].

10.7 Multichannel Micropore Array

The single micropore chip fabrication and cell detection is efficient, but it has low throughput and thus requires long processing of samples. The throughput can be increased if multiple micropores can be added in the assembly.

Same fabrication process can be followed for making micropore array as that for making a single micropore chip. The only difference would be that now instead of one square window in silicon wafer, multiple windows would need to be etched and thus multiple freestanding membranes can be achieved on the wafer. Holes can be drilled in each membrane, and the chip can be connected to the experiment assembly [24, 43]. A micropore array chip was shown in Fig. 10.3.

The only disadvantage of using this type of array is that damage to a single membrane would result in the loss of the whole array. This can be overcome by using multiple single micropore chips and joining them together in one experiment assembly (Fig. 10.5) [18]. An array of two micropore chips can process a sample in half the time. Now, if one of the micropore chips is damaged, it can be replaced easily or electrically isolated without affecting the other micropore chips. We will not have to discard the whole array of micropores.

Another way of increasing the mechanical strength of micropore array is to divide the whole chip in different compartments and drilling equal number of holes in each compartment as shown in Fig. 10.11 [43]. The problem here is again that of single-cell measurement. Even if we can address each micropore individually for resistive-pulse measurements, the physical break at the site of one micropore can make the whole chip unusable.

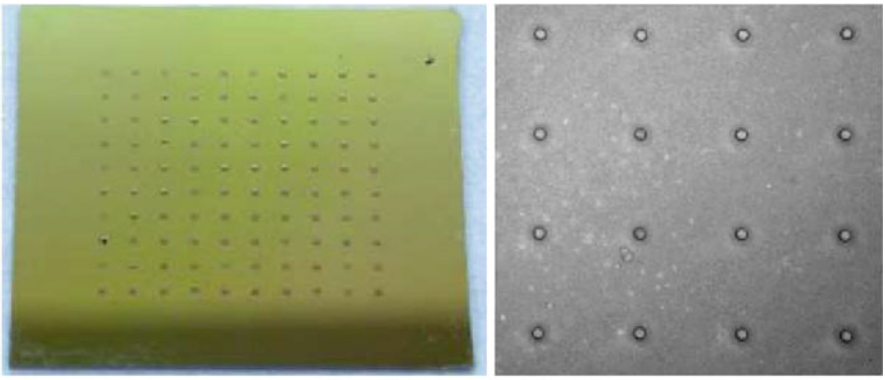

Fig. 10.11 (**a**) A silicon nitride membrane with one hundred compartments. There are 100 micropores in each compartment. (**b**) A close-up view of the 2 μm micropores. [43] (Reprinted with permission)

10.8 Conclusions

This chapter introduced the solid-state micropores and their use for living cell interrogation. The use of micropores was compared and contrasted especially with respect to their sensitivity to cellular properties. The functionalized micropores were also explained. Their use to capture, isolate, and target tumor cells carries high potential in disease diagnostics due to the power of affinity-based interaction between ligands and the tumor cells.

References

1. Ghossein RA, Bhattacharya S, Rosai J (1999) Molecular detection of micrometastases and circulating tumor cells in solid tumors. Clin Cancer Res 5:1950–1960
2. Steeg PS (2006) Tumor metastasis: mechanistic insights and clinical challenges. Nat Med 12:895–904
3. Cristofanilli M, Budd GT, Ellis MJ, Stopeck A, Matera J, Miller MC, Reuben JM, Doyle GV, Allard WJ, Terstappen L (2004) Circulating tumor cells, disease progression, and survival in metastatic breast cancer. N Engl J Med 351:781–791
4. Kohn EC, Liotta LA (1995) Molecular Insights into Cancer Invasion: Strategies for Prevention and Intervention. Cancer Res 55:1856–1862
5. Cristofanilli M, Budd GT, Ellis MJ, Stopeck A, Matera J, Miller MC et al (2004) Circulating tumor cells, disease progression, and survival in metastatic breast cancer. N Engl J Med 351:781–791
6. Rolle A, Günzel R, Pachmann U, Willen B, Höffken K, Pachmann K (2005) Increase in number of circulating disseminated epithelial cells after surgery for non-small cell lung cancer monitored by MAINTRAC® is a predictor for relapse: a preliminary report. World J Surg Oncol 3:1

7. Zieglschmid V, Hollmann C, Böcher O (2005) Detection of disseminated tumor cells in peripheral blood. Crit Rev Clin Lab Sci 42:155–196
8. Kahn HJ, Presta A, Yang L-Y, Blondal J, Trudeau M, Lickley L et al (2004) Enumeration of circulating tumor cells in the blood of breast cancer patients after filtration enrichment: correlation with disease stage. Breast Cancer Res Treat 86:237–247
9. Krivacic RT, Ladanyi A, Curry DN, Hsieh H, Kuhn P, Bergsrud DE et al (2004) A rare-cell detector for cancer. Proc Natl Acad Sci U S A 101:10501–10504
10. Racila E, Euhus D, Weiss AJ, Rao C, McConnell J, Terstappen LW et al (1998) Detection and characterization of carcinoma cells in the blood. Proc Natl Acad Sci 95:4589–4594
11. Cohen SJ, Punt CJ, Iannotti N, Saidman BH, Sabbath KD, Gabrail NY et al (2008) Relationship of circulating tumor cells to tumor response, progression-free survival, and overall survival in patients with metastatic colorectal cancer. J Clin Oncol 26:3213–3221
12. de Bono JS, Scher HI, Montgomery RB, Parker C, Miller MC, Tissing H et al (2008) Circulating tumor cells predict survival benefit from treatment in metastatic castration-resistant prostate cancer. Clin Cancer Res 14:6302–6309
13. Suresh S (2007) Biomechanics and biophysics of cancer cells. Acta Mater 55:3989–4014
14. Nagrath S, Sequist LV, Maheswaran S, Bell DW, Irimia D, Ulkus L et al (2007) Isolation of rare circulating tumour cells in cancer patients by microchip technology. Nature 450:1235–1239
15. Vona G, Sabile A, Louha M, Sitruk V, Romana S, Schütze K et al (2000) Isolation by size of epithelial tumor cells: a new method for the immunomorphological and molecular characterization of circulating tumor cells. Am J Pathol 156:57–63
16. Zabaglo L, Ormerod MG, Parton M, Ring A, Smith IE, Dowsett M (2003) Cell filtration-laser scanning cytometry for the characterisation of circulating breast cancer cells. Cytometry A 55A:102–108
17. Fu AY, Spence C, Scherer A, Arnold FH, Quake SR (1999) A microfabricated fluorescence-activated cell sorter. Nat Biotechnol 17:1109–1111
18. Ilyas A, Asghar W, Kim YT, Iqbal SM (2014) Parallel recognition of cancer cells using an addressable array of solid-state micropores. Biosens Bioelectron 62:343–349
19. Warkiani ME, Khoo BL, Wu L, Tay AKP, Bhagat AAS, Han J et al (2016) Ultra-fast, label-free isolation of circulating tumor cells from blood using spiral microfluidics. Nat Protoc 11:134–148
20. Hou HW, Warkiani ME, Khoo BL, Li ZR, Soo RA, Tan DS-W et al (2013) Isolation and retrieval of circulating tumor cells using centrifugal forces. Sci Rep 3:1259
21. Liu M, Sun X-T, Yang C-G, Xu Z-R (2016) On-chip preparation of calcium alginate particles based on droplet templates formed by using a centrifugal microfluidic technique. J Colloid Interface Sci 466:20–27
22. Warkiani ME, Guan G, Luan KB, Lee WC, Bhagat AAS, Chaudhuri PK et al (2014) Slanted spiral microfluidics for the ultra-fast, label-free isolation of circulating tumor cells. Lab Chip 14:128–137
23. Liu L, Zhu L, Ni Z, Chen Y (2013) Detecting a single molecule using a micropore-nanopore hybrid chip. Nanoscale Res Lett 8:1–7
24. Liu J, Bombera R, Leroy L, Roupioz Y, Baganizi DR, Marche PN et al (2013) Selective individual primary cell capture using locally bio-functionalized micropores. PLoS One 8: e57717
25. Asghar W, Wan Y, Ilyas A, Bachoo R, Kim YT, Iqbal SM (2012) Electrical fingerprinting, 3D profiling and detection of tumor cells with solid-state micropores. Lab Chip 12:2345–2352
26. Ali W, Moghaddam FJ, Raza MU, Bui L, Sayles B, Kim YT et al (2016) Electromechanical transducer for rapid detection, discrimination and quantification of lung cancer cells. Nanotechnology 27:195101
27. Roberts GS, Kozak D, Anderson W, Broom MF, Vogel R, Trau M (2010) Tunable nano/micropores for particle detection and discrimination: scanning ion occlusion spectroscopy. Small 6:2653–2658

28. Bean KE (1978) Anisotropic etching of silicon. IEEE Tran Electron Dev 25:1185–1193
29. Liu J, Pham P, Haguet V, Sauter-Starace F, Leroy L, Roget A et al (2012) Polarization-induced local pore-wall functionalization for biosensing: from micropore to nanopore. Anal Chem 84:3254–3261
30. Picollet-Dhahan N, Sordel T, Garnier-Raveaud S, Sauter F, Ricoul F, Pudda C et al (2004) A silicon-based "multi patch" device for ion channel current sensing. Sensor Lett 2:91–94
31. Sowerby SJ, Broom MF, Petersen GB (2007) Dynamically resizable nanometre-scale apertures for molecular sensing. Sensor Actuat B Chem 123:325–330
32. Willmott GR, Moore PW (2008) Reversible mechanical actuation of elastomeric nanopores. Nanotechnology 19:475504
33. Kasianowicz JJ, Brandin E, Branton D, Deamer DW (1996) Characterization of individual polynucleotide molecules using a membrane channel. Proc Natl Acad Sci U S A 93:13770–13773
34. DeBlois R, Bean C (1970) Counting and sizing of submicron particles by the resistive pulse technique. Rev Sci Instrum 41:909–916
35. DeBlois RW, Bean CP, Wesley RK (1977) Electrokinetic measurements with submicron particles and pores by the resistive pulse technique. J Colloid Interface Sci 61:323–335
36. DeBlois RW, Wesley R (1977) Sizes and concentrations of several type C oncornaviruses and bacteriophage T2 by the resistive-pulse technique. J Virol 23:227–233
37. Pelkey T, Frierson H, Bruns D (1996) Molecular and immunological detection of circulating tumor cells and micrometastases from solid tumors. Clin Chem 42:1369–1381
38. Islam M, Bellah MM, Sajid A, Hasan MR, Kim Y-t, Iqbal SM (2015) Effects of nanotexture on electrical profiling of single tumor cell and detection of cancer from blood in microfluidic channels. Sci Rep 5:13031
39. Gyurcsányi RE (2008) Chemically-modified nanopores for sensing. TrAC Trends Anal Chem 27:627–639
40. Xu Y, Phillips JA, Yan J, Li Q, Fan ZH, Tan W (2009) Aptamer-based microfluidic device for enrichment, sorting, and detection of multiple cancer cells. Anal Chem 81:7436–7442
41. Dharmasiri U, Balamurugan S, Adams AA, Okagbare PI, Obubuafo A, Soper SA (2009) Highly efficient capture and enumeration of low abundance prostate cancer cells using prostate-specific membrane antigen aptamers immobilized to a polymeric microfluidic device. Electrophoresis 30:3289–3300
42. Bellah MM, Iqbal SM, Kim Y-T (2014) Differential behavior of EGFR-overexpressing cancer cells through aptamer-functionalized micropores. Microfluid Nanofluid 17:983–992
43. Talasaz AH, Powell AA, Stahl P, Ronaghi M, Jeffrey SS, Mindrinos M et al (2006) Cell trapping in activated micropores for functional analysis. Conf Proc IEEE Eng Med Biol Soc 1:1838–1841
44. Rembaum A, Dreyer W (1980) Immunomicrospheres: reagents for cell labeling and separation. Science 208:364–368
45. Cheng MM-C, Cuda G, Bunimovich YL, Gaspari M, Heath JR, Hill HD et al (2006) Nanotechnologies for biomolecular detection and medical diagnostics. Curr Opin Chem Biol 10:11–19
46. Mahmood MAI, Wan Y, Islam M, Ali W, Hanif M, Kim Y-T et al (2014) Micro+nanotexturing of substrates to enhance ligand-assisted cancer cell isolation. Nanotechnology 25:475102
47. Wan Y, Kim Y-t, Li N, Cho SK, Bachoo R, Ellington AD et al (2010) Surface-immobilized aptamers for cancer cell isolation and microscopic cytology. Cancer Res 70:9371–9380
48. Asghar W, Kim Y-T, Ilyas A, Sankaran J, Wan Y, Iqbal SM (2012) Synthesis of nano-textured biocompatible scaffolds from chicken eggshells. Nanotechnology 23:475601
49. Bacakova L, Filova E, Parizek M, Ruml T, Svorcik V (2011) Modulation of cell adhesion, proliferation and differentiation on materials designed for body implants. Biotechnol Adv 29:739–767

50. Islam M, Sajid A, Mahmood MAI, Bellah MM, Allen PB, Kim Y-T et al (2015) Nanotextured polymer substrates show enhanced cancer cell isolation and cell culture. Nanotechnology 26:225101
51. Chen W, Weng S, Zhang F, Allen S, Li X, Bao L et al (2012) Nanoroughened surfaces for efficient capture of circulating tumor cells without using capture antibodies. ACS Nano 7:566–575
52. Kim DH, Lee H, Lee YK, Nam JM, Levchenko A (2010) Biomimetic nanopatterns as enabling tools for analysis and control of live cells. Adv Mater 22:4551–4566
53. Park TH, Shuler ML (2003) Integration of cell culture and microfabrication technology. Biotechnol Prog 19:243–253

Chapter 11
Iron Pyrite (FeS_2): Sustainable Photovoltaic Material

Sadia Khalid, E. Ahmed, Yaqoob Khan, Saima Nawaz, M. Ramzan, N.R. Khalid, and W. Ahmed

11.1 Introduction

Iron–sulfur system constitutes a range of Fe–S phases which play critical role in marine systems particularly in biogeochemical processes. On the other hand, Fe–S system is a keystone for the interpretation of thermal kinetics and phase relationships of numerous significant ternary systems together with Zn–Fe–S, Ni–Fe–S, and Fe–As–S systems. The phases of iron sulfide are mackinawite (FeS_{1-x}), troilite (FeS_t), greigite (Fe_3S_{4g}), pyrrhotite ($Fe_{1-x}S$), marcasite (FeS_{2m}), pyrite (FeS_2), etc. [1]. The only stable binary phases in Fe–S system at >200 °C or near ambient temperature are pyrrhotites and pyrite. The evaluation of the Earth's surface

S. Khalid (✉)
Department of Physics, Bahauddin Zakariya University, Multan 60800, Pakistan

Nano Science and Technology Department, National Centre for Physics, Shahdra Valley Road, Quaid-i-Azam University Campus, Islamabad 45320, Pakistan
e-mail: sadiabzu@gmail.com

E. Ahmed • M. Ramzan
Department of Physics, Bahauddin Zakariya University, Multan 60800, Pakistan

Y. Khan
Nano Science and Technology Department, National Centre for Physics, Shahdra Valley Road, Quaid-i-Azam University Campus, Islamabad 45320, Pakistan

S. Nawaz
Nano Science and Technology Department, National Centre for Physics, Shahdra Valley Road, Quaid-i-Azam University Campus, Islamabad 45320, Pakistan

Department of Chemistry, Quaid-i-Azam University, Islamabad 45320, Pakistan

N. Khalid
Department of Physics, University of Gujrat, Gujrat, Pakistan

W. Ahmed
School of Mathematics and Physics, University of Lincoln, Lincoln, UK

M.J. Jackson, W. Ahmed (eds.), *Micro and Nanomanufacturing Volume II*,
DOI 10.1007/978-3-319-67132-1_11

environment is primarily based on the analysis of iron sulfides mainly pyrite (FeS_2). Wadia et al. [2] investigated 23 promising semiconducting materials in detail and identified some unconventional photovoltaic materials including pyrite (FeS_2), tenorite (CuO), and zinc phosphide (Zn_3P_2) on the basis of their availability and use. Iron disulfide has two polymorphs, e.g., pyrite and marcasite. Pyrite (FeS_2) is an inexpensive and the most earth-abundant semiconductor material among transition metal disulfides (TMS_2), e.g., MnS_2, FeS_2, CoS_2, NiS_2, CuS_2, or ZnS_2. Its exceptional properties make it an appealing material for large-scale and sustainable photovoltaic (PV) and photoelectrochemical (PEC) applications [3].

Iron pyrite (FeS_2) has NaC1-like structure of space group T_h^6,($Pa\bar{3}$) with a face-centered cubic sublattice of diamagnetic Fe^{2+} ions that occupy the Na positions and <1 1 1> oriented S-S dimers occupying the anion (Cl) positions. Fe atoms are octahedrally coordinated at corners and face centers of the cubic unit cell, while the disulfide dumbbell (dimers) atoms S_2^{2-} lie at the center of the cube and the midpoints of the cubic unit cell. The axis of the S_2^{2-} dimers is parallel to four intersecting diagonals of the cubic space lattice, thus giving pyrite hemihedral symmetry [4]. The lattice parameter a is 0.54175 nm and Wyckoff parameter u is 0.3868 (Fig. 11.1).

Top of the valence band (VB) of pyrite primarily comprises of nonbonding Fe 3d t_{2g} states that lie above a bonding S 3p-Fe 3d e_g band. The bottom of the conduction band (CB) is usually explained with reference to a blend of Fe 3d e_g^* and S 3p states (Fig. 11.2).

Pyrite is diamagnetic in nature [6] and has six-paired d electrons completely filling the t_{2g} orbitals. Fe^{2+} stays in a low-spin state in pyrite which indicates the

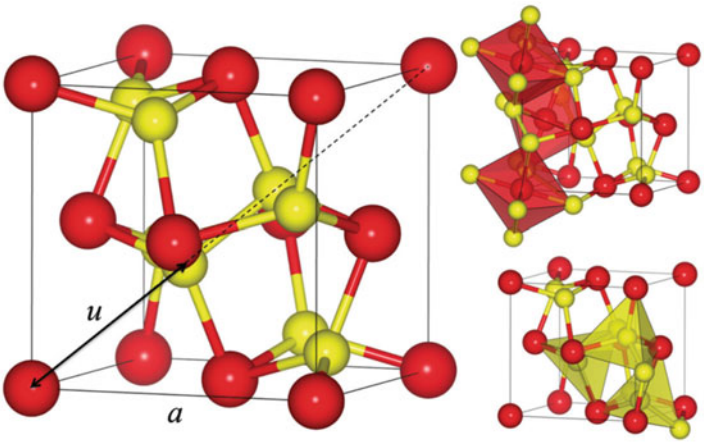

Fig. 11.1 The iron pyrite structure with the S atoms indicated as light-gray (*yellow*) spheres and the Fe atoms in dark-gray (*red*) color. In the right panel, the (almost) octahedral and tetrahedral coordinations of the Fe and S atoms are displayed. The octahedrons share their corners. In the tetrahedrons, the characteristic S dimers are clearly visible. The lattice constant a and the Wyckoff parameter u are the structural parameters mentioned in the text (Reproduced from Ref. [4] with permission from the American Physical Society)

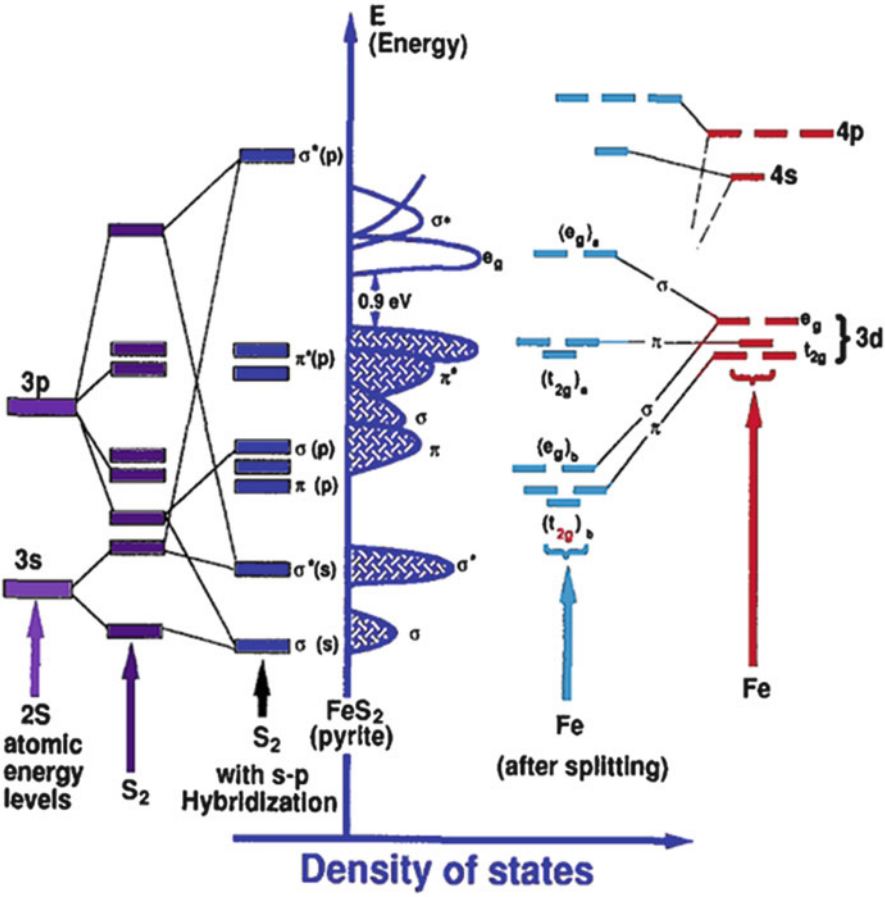

Fig. 11.2 Qualitative electronic structure of FeS_2 (Reproduced from Ref. [5] with permission from The Electrochemical Society)

strength of the ligand field due to S_2^{2-} anions [7]. Semiconducting properties of pyrite arise due to existing free charge carriers in the crystal structure. Free charge carriers generate due to deviation from stoichiometric composition, impurity elements in solid solution, and thermal excitation across the energy gap [8].

11.2 Promising Aspects of Iron Pyrite

Direct and indirect bandgap of pyrite are 1.2 and 0.95 eV, respectively. Its high absorption coefficient of $\alpha = 6 \times 10^5$ cm^{-1} (for $\lambda > 700$ nm) makes it an attractive candidate for solar absorber layers [5]. High-electron carrier mobility of 360 cm^2 V^{-1} s^{-1} has been reported as single-crystal n-type pyrite and an estimated minority carrier

diffusion length of 0.1–1 μm [9]. High photocurrent of 42 mA cm^{-2} has been observed from n-type single-crystal pyrite in liquid junction PEC solar cells [10]. Conductivity of natural pyrite ranges between 0.02 and 562 $(\Omega\ cm)^{-1}$ [11]. Usually, p-type conductivity arises in pyrite with S/Fe ratio >2, while n-type conductivity due to sulfur deficiency. Defects are always present as defect formation requires only a small amount of energy [12]. A donor defect is created by sulfur deficiency, and an acceptor defect is created by sulfur excess [13]. Sun et al. reported that intrinsic p-type conductivity is induced by oxygen [14]. Solar cells incorporating pyrite would be more efficient and preferable due to less material toxicity and more economic as compared to cadmium compounds. Theoretical efficiency of pyrite is ~31% slightly less than 33.7% limit for an ideal bandgap of 1.34 eV, and 20 nm of it can absorb as much light as 300 μm of silicon. Because it has excellent absorption of light (penetration depth: $\delta = \sim 15$ nm in the visible) [15], less raw material is required for thin film solar cells. Recent advances in nanotechnology have enabled the fabrication of economic photovoltaic devices. Synthetic techniques to various nanostructured materials are potentially worthwhile in photovoltaic applications. In previous 10 years, colloidal (solution-processed) pyrite thin films comprising of nanocrystals (NCs) have revealed exceptional optoelectronic performance because of the quantum confinement effect. Mostly, pyrite films show low concentration of majority carriers ~10^{18} cm^{-3}. Therefore, pyrite thin film photovoltaic cells should be highly doped with carrier concentration of 10^{19} cm^{-3}. Instead, it is tricky to save these nanocrystals for a longer time due to faster oxidation. So there should be a simple and inexpensive experimental methodology that can be used for the preparation of quality pyrite thin films.

11.3 Synthetic Routes to Pyrite

Both physical and chemical methods (Table 11.1) have been employed for growth of pyrite thin films. Pyrite thin films have been synthesized directly (single-step growth) by evaporating pyrite or sulfur and iron as targets under vacuum and indirectly (two-step growth) by sulfuration of iron (Fe) [16], hematite (Fe_2O_3)

Table 11.1 Pyrite thin film growth methods

Physical vapor deposition	Chemical vapor deposition	Misc. deposition methods
Flash evaporation [31]	MOCVD [32]	Electrodeposition [33]
Sequential evaporation [34]	LPMOCVD [35]	Chemical bath deposition [22]
MBE [36]	APCVD [37, 38]	Spray pyrolysis [39, 40]
Sputtering [41]	AACVD [42, 43]	Solgel [44]
Thermal evaporation [45, 46]	Pulsed PECVD [47]	Hydrothermal/solvothermal [48, 49]
Laser or pulsed electron ablation [50, 51]		Hot injection method [52, 53]

[17, 18], magnetite (Fe_3O_4) [19], troilite (FeS) [20], greigite (Fe_3S_4) [21], and Fe–O–S [22] thin films pre-deposited by various physical vapor deposition methods and numerous chemical synthetic techniques. Annealing of precursor films in sulfur atmosphere has several ways including H_2S reactive annealing [23], plasma-assisted sulfuration [24], irradiation by helium-neon (HeNe) laser (wavelength, 632.8 nm; intensity, 6×10^4 W cm^{-2}) [25], and neodymium-doped yttrium aluminum garnet (Nd:YAG) laser annealing [26]. Optimization of experimental conditions such as deposition temperature, Ar/H_2S pressure ratio, and total working gas pressure insights into deposition mechanism of pure phase polycrystalline with low roughness iron pyrite films by reactive sputtering of iron target (Fig. 11.3) [27].

But the major problem associated with pyrite thin films is the stoichiometry and purity. By doping pyrite, properties can be improved as well as impurity issue can be resolved. Designing the appropriate precursors for fabrication of the pyrite layers plays a crucial role [28]. Iron pyrite thin films have been grown by atmospheric- or low-pressure metal-organic chemical vapor deposition (AP or LPMOCVD) by the using precursors iron pentacarbonyl [$Fe(CO)_5$] or iron acetate $Fe(acac)_3$ and hydrogen sulfide (H_2S), tert-butyl sulfide (TBS) or tert-butyl disulfide (TBDS) as iron source, and the sulfur source, respectively [29]. Single-source precursors, e.g., iron complexes of dithiocarbamates or thiobiurets, provide single-step synthesis of nanocrystals and nanocrystalline pyrite thin films [30].

In recent few years, trend has changed from micro thin films to nano thin films and from polycrystalline thin films to nanocrystalline (nanocrystals) thin films, so as the synthetic routes have also changed to hydrothermal/solvothermal and hot injection methods. Both experimental techniques utilize two-step nanocrystals/nano thin film growth (with a few exceptions that utilize hydrothermal/solvothermal approach to synthesize in situ thin film growth). The first step is the synthesis of nanocrystals of pyrite, and the second step is the synthesis of thin films by spin [54], spray [52], or dip [55] coating methods. Recently, Jasion et al. [56] created hyperthin iron sulfide nanostructures (2D discs) with atomic layer thickness by solution hot injection method (Fig. 11.4). Similar to the earlier reports, they synthesized an octadecylamine (ODA) ligand in the first step that was added to a Fe^{2+} solution resulting to ~3–5 nm iron nanoparticles as seen in the transmission electron microscopy (TEM) (Fig. 11.4a, e). The ODA ligand acts as both a reducing agent for the Fe^{2+} (Eq. (11.1)) and as a capping layer on the subsequent nanocrystal formation. Sulfur injection into the iron seed particles oxidizes to form Fe^{2+} and S_x^{2-} moieties (Eq. (11.2)), and these species form the FeS_2 nanostructures via Eqs. (11.3) and (11.4).

$$Fe^{2+} + 2e^- \xrightarrow{L} Fe^0 \tag{11.1}$$

$$Fe^0 + S_x \rightarrow Fe^{2+} + S_x^{2-} \tag{11.2}$$

$$Fe^{2+} + S_x^{2-} \rightarrow FeS + S_{x-1} \tag{11.3}$$

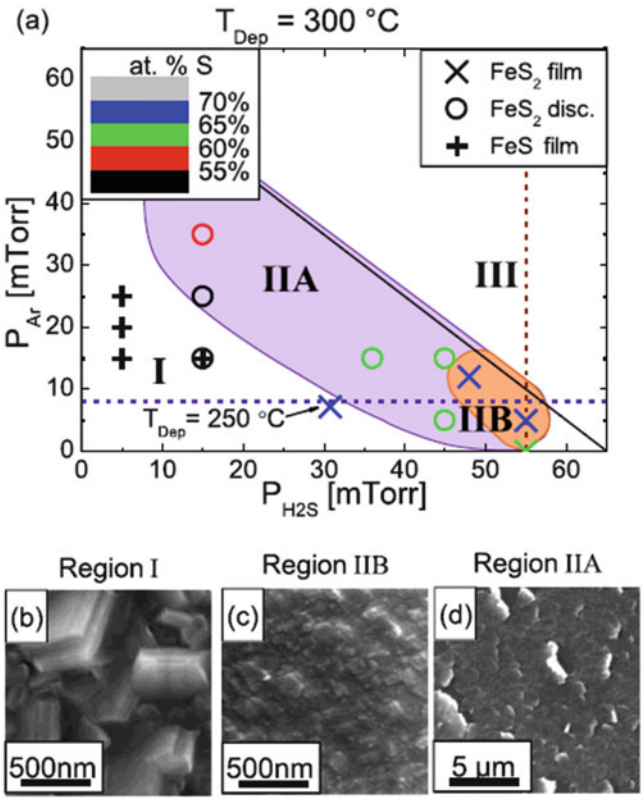

Fig. 11.3 "Phase diagram" of observed Fe_xS_y phases and associated S contents as a function of P_{Ar} and PH_2S at a fixed T_{Dep} of 300 °C. The thicknesses ranged from 19 to 66 nm for continuous films (strongly dependent on P_{Tot}). The Fe_xS_y phases are represented by symbols: crosses for continuous FeS_2 films, circles for discontinuous FeS_2 films, and plus signs for FeS. The atomic % S is represented by color, according to the scale shown on the top left. The diagram is split into regions I, IIA (*purple*), IIB (*orange*), and III based on phase and morphology. Note the additional 250 °C data point indicated on the figure. Representative secondary electron SEM images in regions I, IIB, and IIA are shown in (**b**), (**c**), and (**d**), respectively (Reproduced from Ref. [27] with permission from the American Institute of Physics)

$$FeS + S_x^{2-} \rightarrow FeS_2 + S_{x-1}^{2-} \tag{11.4}$$

Li et al. [57] used similar approach using Fe_3O_4 nanoparticles (NPs) to synthesize ultrathin FeS_2 nanosheets on the basis of oriented attachment (OA) growth. They prepared small-size uniform Fe_3O_4 NPs seeds for FeS_2 nuclei formation through the anion exchange of O in Fe_3O_4 by S. Then FeS_2 nanosheets were grown from FeS_2 nuclei by OA mechanism (Scheme 11.1). The morphology and stoichiometry of the FeS_2 could be tuned by the initial sulfur concentration. These 2D FeS_2 materials displayed excellent stability and electrocatalytic activity as

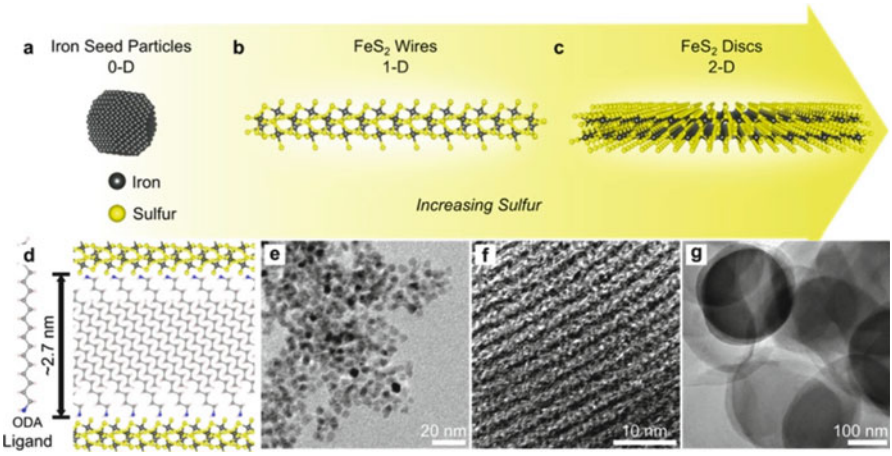

Fig. 11.4 Schematic representation and TEM images of the 1D and 2D FeS_2 structure formation. (**a**, **e**) Fe^0 nanoparticles that are formed in the absence of sulfur. (**b**, **f**) FeS_2 wires formed from 1:6 Fe:S precursor solution. (**c**, **g**) FeS_2 discs formed in the 1:24 Fe:S precursor. (**d**) Schematic of 2.7 nm wide ligand interstitial layer that separates both wires and discs to form their respective bulk structures (Reproduced from Ref. [56] with permission from the American Chemical Society)

catalysts for hydrogen evolution reaction (HER). This seed-mediated OA strategy opens new horizons for ultrathin semiconductor nanostructure preparation from materials with inherent non-layered host crystals.

Paul O'Brien research group has main focus on single-source precursors especially on a variety of complexes for the preparation of transition metal chalcogenides (nanoparticles and thin films) [58]. They are pioneer in fabrication of pyrite thin films by AACVD [42]. Their recent work has explored the fabrication of transition metal-doped pyrite thin films by AACVD [43]. The typical AACVD experimental kit is shown in Fig. 11.5.

They also fabricated good-quality thin films of pyrite (FeS_2) from mixed alkyl dithiocarbamate complexes of iron(III) $[Fe(S_2CNnBu_2)_3]$ and $[Fe(S_2CNMe^iPr)_3]$ as a single-source precursor by LPMOCVD and AACVD in temperature range of 350–500 °C. Ramasamy et al. [59] used iron thiobiuret complexes with 1,1,5,5,-tetraalkyl-2-thiobiurete (alkyl = methyl, ethyl, and isopropyl) as a single-source precursor for the deposition of iron sulfide (FeS and FeS_2) thin films by aerosol-assisted chemical vapor deposition (AACVD). Akhtar et al. [60] prepared iron sulfide nanocrystals (NCs) by thermal decomposition of iron(III) thiocarbamate complexes including $[Fe(S_2CNEt^iPr)_3]$, $[Fe(S_2CN(Hex)_2)_3]$, $[Fe(S_2CNEtMe)_3]$, and $[Fe(S_2CN(Et)_2)_3]$ complexes in oleylamine (OA), hexadecylamine (HDA), and octadecene (OD) at different growth temperatures (170, 230, and 300 °C). Pyrite was obtained as dominant phase by AACVD of the symmetrical complex $[Fe(S_2CN(Et)_2)_3]$ having shorter alkyl chains 350 °C while pyrrhotite at higher temperatures (400 and 450 °C). Pyrite (FeS_2) phase is dominant in all thin films fabricated from unsymmetrical iron(III) dithiocarbamate complexes; however, the

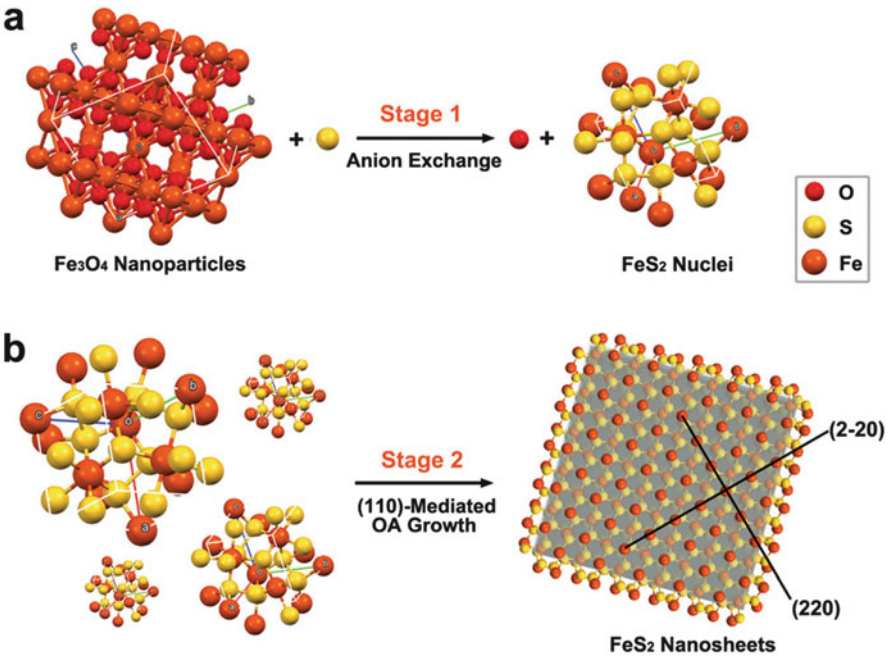

Scheme 11.1 The schematic illustration of the formation of FeS_2 nuclei from preformed Fe_3O_4 NPs (**a**) and FeS_2 nanosheets through (1 1 0) facet-mediated OA growth from FeS_2 nuclei (**b**) (Reproduced from Ref. [57] with permission from The Royal Society of Chemistry)

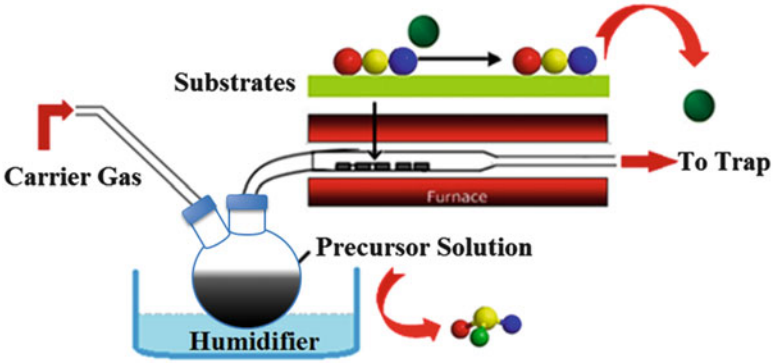

Fig. 11.5 Aerosol-assisted chemical vapor deposition (AACVD) kit

pyrrhotite is dominant for all thin films fabricated from symmetrical complexes [42].

11.4 Modification of Pyrite Properties

Properties of pyrite can be modified by the following:

1. Nanostructures (quantum dots (0D), nanowires (1D), nanosheets (2D), nanocrystals (3-D), etc. [61]) can improve various electric and electronic properties particularly photovoltaic properties (Fig. 11.6) [62].
2. Alloying: Alloying refers to a compound having elements in higher quantities that may be used to modify the mechanical, physical, or chemical properties. The alloyed compound needs not to be single phase. Alloying agents may result in formation of new phases. Photovoltaic properties of pyrite can be improved by tuning the bandgap through alloying. The alloying of iron pyrite (FeS_2) would involve the random replacement of either Fe or S atoms with another cation ($M_xFe_{1-x}S_2$) or anion (FeA_xS_{2-x}) where M is for metal and A for anion, respectively. As the degree of alloying increases, the material begins to take on more of the electronic and physical properties associated with the alloying material [63].
3. Doping: Doping refers to adding an element in very small quantities (ppm or ppb) in a material. Dopant concentrations may vary usually <1000 ppm. Doping may be interstitial or substitutional into the host crystal structure maintaining the same phase. Dopants are typically taken into solid solution. The purpose of doping is to modify the electric, magnetic, or electronic properties of materials [64]. The Co-doped pyrite displayed higher absorption in visible-light region with enhanced photocatalytic activity (Fig. 11.7). The cobalt-doped pyrite ($Co_{0.333}Fe_{0.667}S_2$) decomposed 48.9% methylene blue (MB) within 210 min that was 36.5% higher than that of the pristine pyrite [65].
4. Composites: Composites of pyrite with various materials are through different approaches to increase energy/power density for energy storage and conversion

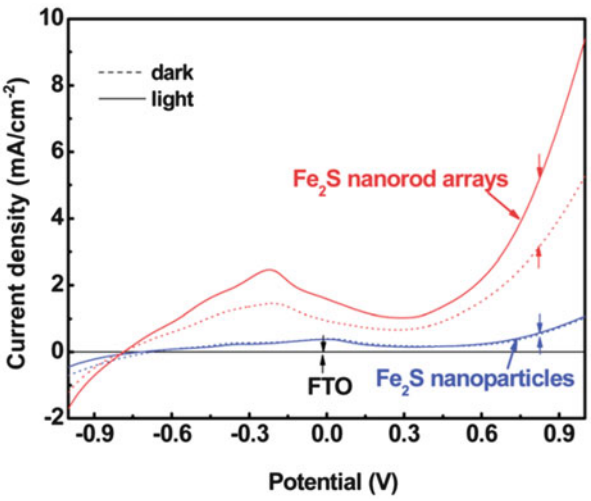

Fig. 11.6 Photocurrent-potential behavior of FeS_2 films under dark and light conditions. The data were collected as a single sweep from negative to positive potentials ranging from −1.0 to 1.0 V. The anode was irradiated using a xenon lamp at an intensity of 500 mW cm^{-2} in a three-electrode system in 0.5 M sodium sulfate solution (Reproduced from Ref. [62] with permission from The Royal Society of Chemistry)

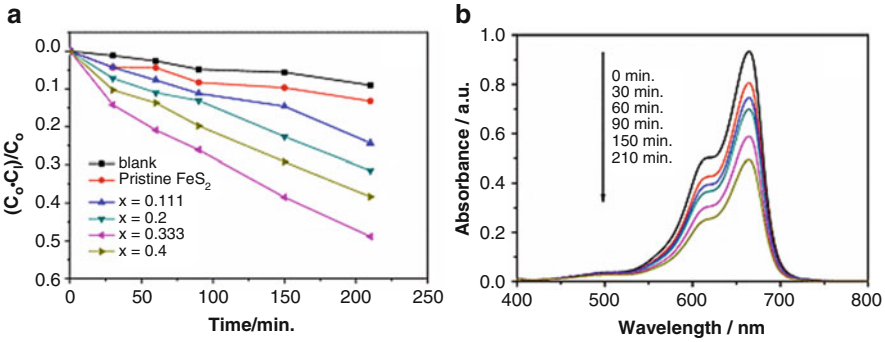

Fig. 11.7 (**a**) UV-vis spectral changes of MB (10 mg/L) in aqueous photocatalyst dispersions as a function of irradiation time. Blank test was carried out without catalyst under the same conditions; (**b**) the temporal evolution of the spectra during the photodegradation of MB mediated by $Co_{0.333}Fe_{0.667}S_2$ catalyst under visible-light illumination ($\lambda > 420$ nm) (Reproduced from Ref. [65] with permission from Springer)

devices [66, 67]. Symmetric charge storage device of nano pyrite consists of (H_3PO_4)/polyvinyl alcohol (PVA) electrolyte gel sandwiched between two similar electrodes made up of FeS_2/polyaniline (PA), upon which graphite sheets are used as current collectors (Fig. 11.8). The device exhibited a charge storage capacity of approximately 20 mAh, and the maximum discharging current is 30 mA (device dimension, 2 cm^2). The pseudo-octahedral or flower-like FeS_2 nanostructures (diameter = 400–500 nm) in the conducting polymer matrix of rod or tubular PA (average thickness = 20–30 nm) offer better electrochemical activity/conductivity. The increase of device size can increase discharge carrying capacity to run a DC motor, stepper motor, etc. Additionally, the device is flexible, lightweight, and portable [67]. FeS_2@carbon fiber electrode coated with a thin layer of Al_2O_3 enhances the cycling stability of the Li–FeS_2 system with high discharge energy densities at both the material level (~1300 Wh/kg – FeS_2) and the electrode level (~1000 Wh/kg—FeS_2 electrode) in the voltage range of 1.0–3.0 V [68].

11.5 Doped Pyrite

Introducing dopant atoms into nanocrystals by synthetic control improves physical and chemical properties of materials by triggering energy levels at nanolevel [69]. Substituting cations or anions with isovalent elements or compensated dimers is an extensively used methodology for tuning the bandgaps of semiconductors. Recent advancement in nanotechnology has proved that nanostructural metal chalcogenides (MCs) are promising candidates for efficient energy conversion and

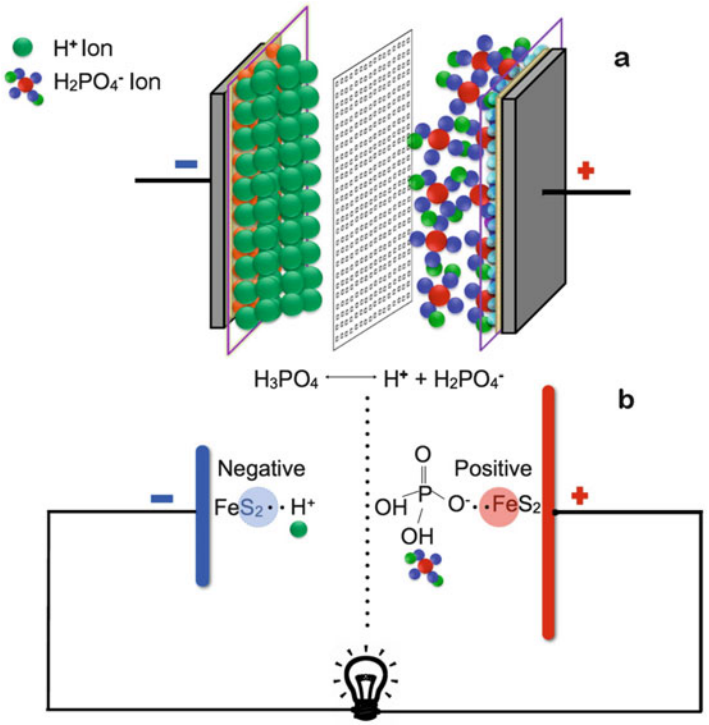

Fig. 11.8 Proposed charge storage mechanism of the device. (**a**) Electrical double-layer formation during charging. The electrolyte (H_3PO_4) dissociates and H^+ ions migrate toward the cathode, and $H_2PO_4^-$ ions migrate toward the anode. (**b**) Possible pseudo-capacitive effects occur at the electrode surface, since sulfur atom is a nucleophile having enough electron density, which will easily create an adduct with H^+ and, thus possibly forming H–S hydrogen bonding. Whereas Fe center has enough positive character, so it can act as an electrophile, where it can create a loose electrostatic bond with oxo donor group of phospho ion. In summary, these features of nano FeS_2 offer it a bifunctional electrode character (Reproduced from Ref. [67] with permission from The Royal Society of Chemistry)

storage (ECS) systems centered on their extraordinary physical and chemical properties [70]. Ternary metal chalcogenides systems have been widely applied in organic and inorganic p-n junctions as TMS_2 such as $CuInS_2$, $AgInS_2$, $AgBiS_2$, etc. thin films where they show improved properties [71] than undoped metal sulfide thin films. Hu et al. [63] investigated theoretically alloying pyrite (FeS_2) with oxygen for bandgap tuning by using density functional theory (DFT) (Fig. 11.9). Bandgap of pyrite can be improved by replacing some Fe by ruthenium (Ru) or oxygen (O) to form $Fe_{1-x}Ru_xS_2$ and $Fe_{1-x}O_xS_2$ compounds or by alkaline earth metal elements (Be, Mg, Ca, Sr, Ba, and Cd). Ruthenium- and oxygen-alloyed pyrite systems revealed bandgap enhancement practically; nevertheless, their incorporation into pyrite may be restricted by the large positive enthalpy of mixing.

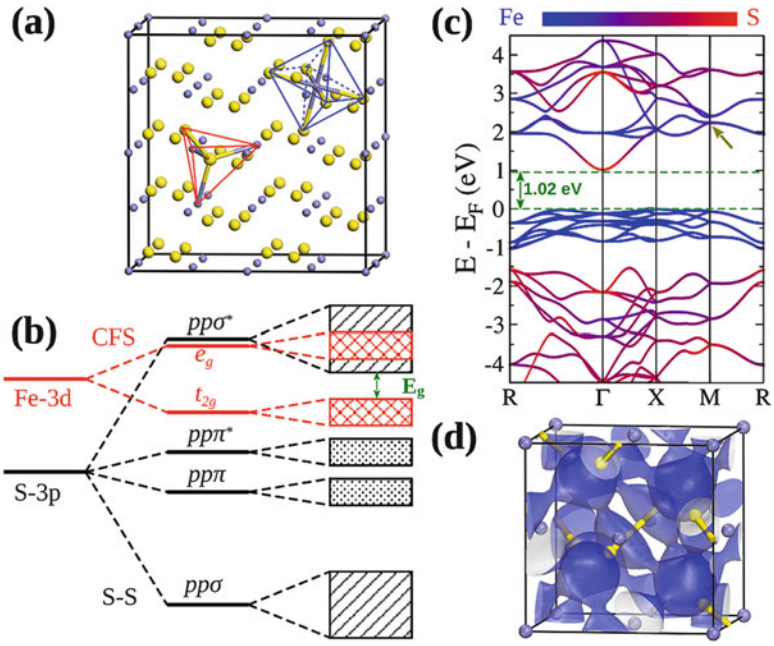

Fig. 11.9 Crystal structure and electronic properties of bulk iron pyrite. (**a**) $2 \times 2 \times 2$ supercell of bulk pyrite (96 atoms). The *yellow* and *purple* spheres denote S and Fe atoms, respectively. The local symmetries around the Fe and S atoms are indicated by the *blue* octahedron and the *red* tetrahedron, respectively. (**b**) Sketch of the energy diagram for the Fe 3d and S 3p orbitals of bulk pyrite under the influences of crystal-field splitting (CFS) and S-S dimerization. The green arrow denotes the bandgap (E_g). (**c**) Band structure of bulk pyrite with a color scale indicating the contributions from Fe and S atoms. Atomic contributions were computed by projecting the Bloch wave functions of pyrite into atomic orbitals of Fe and S atoms. It should be noted that the conduction band minimum (CBM) consists almost completely of S ppσ* orbitals, as shown also in (**b**). The horizontal *dashed green lines* indicate the energy positions of the valence band maximum (VBM) and the CBM. The *brown arrow marks* the degenerate Fe e_g levels that split in the presence of O_S, as highlighted in Fig. 11.2. (**d**) Single-state charge density of the CBM at 0.016 e/Å^3 for a conventional pyrite unit cell (Reproduced from Ref. [63] with permission from the American Chemical Society)

Alongside, they found bandgap narrowing by substitutional incorporation of zinc in $Z_xFe_{1-x}S_2$ alloys [72].

Up till now, numerous dopants have been investigated (Ru [73], Mn [74], Co [75], Ni [76], Cu [77], Zn [78], Ti [79], Se [80], Sn [81], Al, P [82], As [83], Si, Sb [84], Cr, Au [85], Nd [86]) for modification and improvement of iron pyrite properties. $M_xFe_{1-x}S_2$ ternaries exhibit enhanced properties than pure FeS_2 that can make it captivative as window material for photovoltaic applications: pyrite organic, inorganic, and hybrid solar cells. Recently, Mao et al. [87] observed more than five times reduction of dark currents in the $Z_xFe_{1-x}S_2$ photoconductor.

11.6 Transition Metal (TM)-Doped Pyrite

Transition metal dichalcogenides (TMDCs) have a great potential use in quantum dots, photovoltaics, dilute magnetic semiconductors, superconductors, electronics, thermoelectric, sensors, heterogeneous catalysis, and oxygen reduction reaction (ORR) catalysts [70]. Electrical and magnetic properties of TMDCs depend on their electronic configuration, i.e., d electrons. In TMDCs, valence and conduction band energy levels are comprised of metal and sulfur s and p orbitals with d orbital energy levels added by metal. The relative energy of the d orbital levels may vary widely. Secondly the d orbitals may overlap with sulfur orbitals or d orbitals of adjacent metal to form a band (or bands) or may not overlap at all (remained localized). In this section, we discuss properties of transition metal (Co, Ni, Cu, Zn)-doped pyrite ($M_xFe_{1-x}S_2$).

11.6.1 Electrical and Magnetic Properties

Electrical and magnetic properties in pyrite group of minerals vary from FeS_2 to ZnS_2. Pyrite is diamagnetic and has six-paired d electrons and completely filling the t_{2g} orbitals. Fe^{2+} in a low-spin state in pyrite indicates the strength of the ligand field due to S_2^{2-} anions. Semiconducting properties of pyrite are due to the e_g^* levels that overlap to form a bond. It exhibits n-type or p-type of electrical conductivity depending on the impurities present in it. The p-type of pyrite is usually iron deficient, while n-type conductivity arises due to sulfur deficiency.

CoS_2 shows a d electron configuration of $(t_{2g})^6(e_g)^1$. It is metallic in nature and shows n-type conductivity. CoS_2 exhibits ferromagnetic ordering at low temperature along with temperature-dependent paramagnetism above the Curie temperature due to very narrow e_g^* bandwidth. Solid solutions of FeS_2 and CoS_2 constitute a mixed crystal system $Fe_{1-x}Co_xS_2$ for $0 < x < 1$ [88–90]. $Fe_{1-x}Co_xS_2$ system has been extensively studied for spintronic applications [91–103]. Electronic structure of $Fe_{1-x}Co_xS_2$ system was studied by Umemoto et al. for spintronic devices [104]. Tomm et al. [85] synthesized single crystals of $Fe_{1-x}Co_xS_2$ by chemical vapor transport (CVT). Carrier concentration by doping Co was found to be in the range of 2×10^{17}–3×10^{19} cm^{-3}. High carrier concentration (10^{20} cm^{-3}) and the low Seebeck coefficients (<70 μV/K) were observed in n-type cobalt-doped (0.3 at %) pyrite ($Fe_{1-x}Co_xS_2$) thin films (100 nm) fabricated by metal-organic chemical vapor deposition (MOCVD) on glass and Si substrates. The potential barrier heights (7–37 meV) with trap density (2×10^{13} cm^{-2}) in the grain barriers are determined from temperature-dependent Hall mobility. Di-tert-butyl disulfide ($[(CH_3)_3C]_2S_2$, TBDS), iron pentacarbonyl ($Fe(CO)_5$, IPC), and tricarbonyl nitrosyl cobalt ($Co(CO)_3NO$, TCNCo) were utilized as organometallic sources for sulfur (S), iron (Fe), and cobalt (Co), respectively. Lattice expansion was observed by peak shifting (up to 0.02°) toward smaller angles. The resistivity of $Fe_{1-x}Co_xS_2$ thin films (50 nm

thickness) deposited on Si substrate decreases from 0.2 Ω cm at $x = 1.8 \times 10^{-3}$ to 0.005 Ω cm at $x = 7.7 \times 10^{-2}$ as compared to 0.4 Ω cm resistivity of undoped FeS_2 thin films (100 nm thickness) [105]. Thomas et al. prepared $Fe_{1-x}Co_xS_2$ films by indiffusion of a thin cobalt layer into a FeS_2 film deposited on corning glass substrates by low-pressure metal-organic chemical vapor deposition (LPMOCVD) at 475 °C. $Fe_{1-x}Co_xS_2$ films showed enhanced photoactivity with charge carrier concentration of about 10^{20} cm^{-3} and a Hall mobility of about 1.5 $cm^2/(V\ s)$ [106]. Lehner et al. measured low resistivity (0.009–0.02 Ω cm) at room temperature for $Fe_{1-x}Co_xS_2$ thin films using a Van der Pauw method as compared to resistivity (15–85 Ω cm) of undoped FeS_2 thin films. Carrier concentration was $10^{18.7}$–$10^{19.3}$ cm^{-3}. Hall mobility of 60–270 $cm^2\ V^{-1}\ s^{-1}$ was observed for doped pyrite, whereas for undoped pyrite, it was 8–70 $cm^2\ V^{-1}\ s^{-1}$ [83]. Díaz-Chao et al. [107] prepared cobalt-doped FeS_2 thin films by direct sulfuration of metallic Fe-Co bilayers (Fe/Co ~ 2.5) at temperature 250–500 °C. Structural analysis was done by X-ray diffraction (XRD). Rutherford backscattering spectroscopy (RBS) composition depth profile revealed three zones: a cobalt-rich FeS_2 layer on the surface, a FeS_2 layer with homogeneous diffusion of Co, and a nondiffused Co layer near the substrate. The resistivity and Seebeck coefficient varied from $(3.7 \pm 0.2) \times 10^{-3}$ to $(2.1 \pm 0.1) \times 10^{-2}$ Ω cm and from -17.4 ± 0.9 μV/K to -67 ± 4 μV/K, respectively. Jiao et al. [64] synthesized cobalt-doped FeS_2 thin films on iron substrates by solvothermal method with the aid of supercritical carbon dioxide (CO_2). Enhanced photocurrent response photolysis was revealed by films. Sodium triphosphate ($Na_5P_3O_{10}$), sodium thiosulfate ($Na_2S_2O_3{\cdot}5H_2O$), cobalt (II) chloride ($CoCl_2{\cdot}6H_2O$), and sulfur (S) were used as reactants in a mixture of ethylene glycol deionized water ($V_{\text{ethylene glycol}}$: $V_{\text{deionized water}} = 1$: 9). For cobalt-doped FeS_2 thin film reaction, conditions were maintained at reaction time 24 h, reaction temperature 180 °C, and pressure 11 MPa. Recently, Clamagirand et al. [108] reported nanocrystalline Co-doped FeS_2 thin films synthesized by sulfuration ($T = 300$ °C, $P = 1.33$ mPa, $t = 20$ h) of Co/Fe bilayers prepared by consecutive thermal evaporations of cobalt and iron. Co doping leads to a semiconductor (FeS_2) to semimetal (CoS_2) conversion apparent in the change of sign of Seebeck coefficient (+80 to −80 μV/K) and decrease in resistivity ($8.4 \pm 0.5\ 10^{-2}$ to $4.2 \pm 0.1\ 10^{-4}$) evolution at RT.

NiS_2 exhibits semiconducting properties that are related to the spin splitting of the t_{2g} and e_g^* levels. It shows paramagnetic behavior at room temperature. Ferrer et al. [109] prepared $Fe_{1-x}Ni_xS_2$ ($0 < x < 1$) thin films by sulfuration of pre-deposited Fe–Ni layers. As previously observed in cobalt-doped FeS_2 thin films, Ni incorporation in FeS_2 lattice increases the dimensions of the unit cell. $Fe_{1-x}Ni_xS_2$ single crystals grown by chemical vapor transport (CVT) method are determined to be single phase and isostructural. Energy red shift behavior in $Fe_{1-x}Ni_xS_2$ single crystals with the increase of the Ni dopant was observed in Raman spectra measured at room temperature of the Ni-doped FeS_2 crystals. The resistivity of the $Fe_{1-x}Ni_xS_2$ single crystals decreased with the increased doping concentration of Ni. Moreover, Ni doping destroyed the photoconductive sensitivity of FeS_2 [110]. Ni–Fe donor levels at 0.37 and 0.42 eV below the conduction

band minimum (CBM) were also observed in $Fe_{1-x}Ni_xS_2$ single crystals [111]. Alongside, Ni-doped FeS_2 showed a high charge/discharge capacity of 320–285 mAh/g for over 20 cycles due to enhanced electronic conductivity [76].

CuS_2 exhibits temperature-independent Pauli paramagnetism that is the result of delocalization of electrons in the e_g^* band. There is a great contribution of Ferrer et al. [112] research group in the improvement of undoped and doped FeS_2 thin film research. They prepared a series of n-type $Fe_{1-x}Cu_xS_2$ thin films by sulfuration (sulfur pressure of 600 Torr) of Fe-Cu at different temperatures (200–500 °C). The resistivity and optical absorption edge of the films change with the sulfuration temperature from 0.002 to 3.28 Ω cm and 0.8 to 1.1 eV, respectively. N-type $FeXS_2$ (X = Al, Cu, Ni) thin films are prepared by sulfuration of flash-evaporated Fe-X (X = AI, Cu, Ni) layers at 350 °C. Room temperature dark resistivity of the films varies from 0.21 to 7×10^{-4} Ω cm depending on the impurity concentration. Hall mobilities are between 1 and 10^4 cm^2/V s, and resistivity lowers from 0.210 to 0.053 Ω cm, lowest for 2.0 atom % Ni-doped samples. Optical bandgap is modified by doping ranging 0.54–1.55 eV, largest for 10 atom % Al-doped samples. Bandgap of copper was found to be 1.12/0.90 eV [113]. Recently, bandgap ($E_g = 0.47$ eV) of Cu-doped FeS_2 was theoretically calculated by the first principle plane wave pseudo-potential theory by Fan et al. [114]. Ding et al. [77] solvothermally synthesized Cu-doped FeS_2 with improved electrochemical properties. Cu-doped FeS_2 revealed two discharge plateaus, at 1.6 and 1.4 V in the charge/discharge measurements with specific discharge capacity of 866 mAh/g at current density of 90 mA/g which is approximately 11% higher than that of the undoped FeS_2. The initial discharge capacity at a current density of 2700 mA/g was 518 mAh/g, and its cyclic discharge capacity exceeded 105 mAh/g at the 20th cycle. Cyclic voltammetry and resistance measurements revealed that Cu doping reduces both the internal resistance and polarization of Li/FeS_2 batteries.

ZnS_2 is a diamagnetic insulator with four e_g electrons [115, 116]. Incorporation of small quantities of Zn ($<5 \times 10^{20}$ cm^{-3}) into FeS_2 leads to a significant change of relevant photoelectrochemical properties: the width of the forbidden energy gap, the quantum efficiency for the generation of photocurrents, and the photocurrent spectrum [78].

11.6.2 Structural Properties

O'Brien and co-workers [117] synthesized transition metal diethyldithiocarbamate complexes with the general formula $[M(S_2CN(Et)_2)_n]$ [M = Fe(III), Co(III), Ni(II), Cu(II), Zn(II), and n = 2, 3] and used them as single-source precursors for the deposition of iron pyrite (FeS_2) and transition metal-doped iron pyrite ($M_xFe_{1-x}S_2$) thin films over glass, silicon (Si(1 0 0)), and indium tin oxide (ITO)-coated glass substrates by aerosol-assisted chemical vapor deposition (AACVD). The transition metal doping did not change the cubic crystal structure of FeS_2 but caused a peak shift in all $M_xFe_{1-x}S_2$ thin films. Divalent cations with ionic radius larger than Fe^{2+}

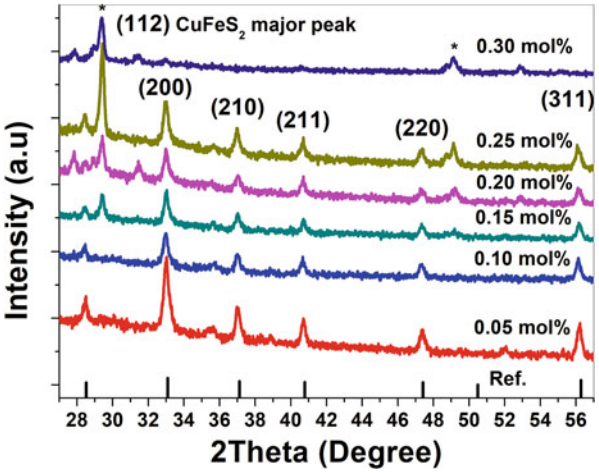

Fig. 11.10 p-XRD patterns of copper-doped iron sulfide $Cu_xFe_{1-x}S_2$ thin films deposited from complexes **(1)** and **(4)** at 350 °C on glass substrate by AACVD, showing the effect of varying mol% of copper complex (**4**) in the precursor solution (Reproduced from Ref. [43] with permission from The Royal Society of Chemistry)

incorporated into the FeS_2 structure form substitutional solid solutions, and the lattice parameter should be increased. The calculated lattice parameter "*a*" of films was 0.5420 nm for undoped FeS_2 and 0.5419–0.5444 nm ($Co_xFe_{1-x}S_2$), 0.5422–0.5427 nm ($Ni_xFe_{1-x}S_2$), 0.5428–0.5435 nm ($Cu_xFe_{1-x}S_2$), and 0.5421–0.5422 nm ($Zn_xFe_{1-x}S_2$). The increase of the lattice parameter suggested an increase of the interplanar crystal spacing. The average lattice distortion degree was found to be greatest in copper-doped pyrite thin films greater than the values already reported for pyrite thin films where $\delta < 0$ [118]. The average value of dislocation density was found to be maximum in zinc-doped and minimum in copper-doped pyrite thin films. The most pronounced structural changes observed with p-XRD were observed in the case of copper-doped pyrite thin films where the lattice changes from cubic (pyrite—ICDD No. 01-073-8127) to tetragonal (chalcopyrite—ICDD No. 01-083-0984) as evidenced by the appearance of a peak at $2\theta = 29.5°$ (Fig. 11.10). This deviation in structural parameters varied from cobalt- to zinc-doped pyrite thin films. The preferred orientation was observed along (2 0 0) crystal plane for all dopants except copper-doped pyrite thin films where phase transformation from pyrite to chalcopyrite at $x = 0.30$ mol% developed preferred orientation along (1 1 2) plane. Some diffraction peaks were too weak to be observed at higher concentration of zinc precursor ($x = 0.30$ mol%), and p-XRD pattern was observed as for amorphous material [43]. It is also inferred that the value of the lattice distortion of transition metal-doped iron pyrite thin films increases with the dopant concentration. Consequently, cation substitution in pyrite provokes lattice strain [11, 109].

Recent studies of XRD diffraction patterns of cobalt-doped pyrite thin films (Co atomic concentration of 0.16 ± 0.02 and 0.40 ± 0.05) revealed a distinctive phase with a cubic structure (Pmnm). No segregation of Co or Fe was observed displaying the full solubility of Co in FeS_2. EDX measurements indicated the S/(Fe + Co) ratio equal to 2.2 ± 0.1 proposing that $Fe_{1-x}Co_xS_{2.2}$

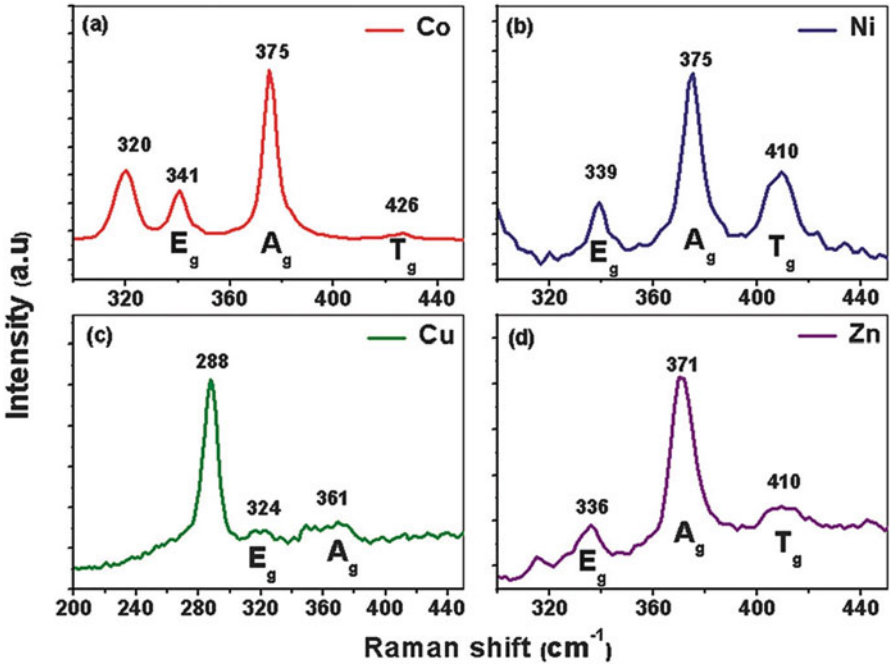

Fig. 11.11 Raman spectra of transition metal-doped pyrite $M_xFe_{1-x}S_2$ thin films at $x = 0.10$ mol % deposited from complexes (**1**) and (**2**), (**3**), (**4**), and (**5**) at 350 1C on ITO substrate deposited by AACVD (Reproduced from Ref. [117] with permission from The Royal Society of Chemistry)

($x = 0.16 \pm 0.02$ and 0.40 ± 0.05) is the unique formed crystalline phase. The crystallite size was between 20 and 50 nm calculated by Scherrer formulae revealing its nanocrystalline character [108].

The Raman spectrum of $M_xFe_{1-x}S_2$ ($x = 0.10$ mol%) thin films synthesized by AACVD at 350 °C on indium tin oxide (ITO) substrates exhibits three vibration bands that are characteristic pyrite (FeS_2) active modes for S_2 dumbbell libration (E_g), S-S inphase stretch (A_g), and coupled libration and stretch (T_g) modes [117]. The Raman spectrum for the $Co_xFe_{1-x}S_2$ revealed the stoichiometric substitution of Co^{2+} for Fe^{2+} in pyrite lattice as evidenced by the band at 320 cm^{-1} (Fig. 11.11).

11.6.3 Surface Properties

AFM analysis of transition metal-doped pyrite ($M_xFe_{1-x}S_2$) thin films showed the presence of uniform and crack-free surfaces (Fig. 11.12). Overall surface morphology of thin films showed adherent, compact, and crack/fracture-free surfaces. Adherence is a chemical-physical phenomenon depending on the method of thin

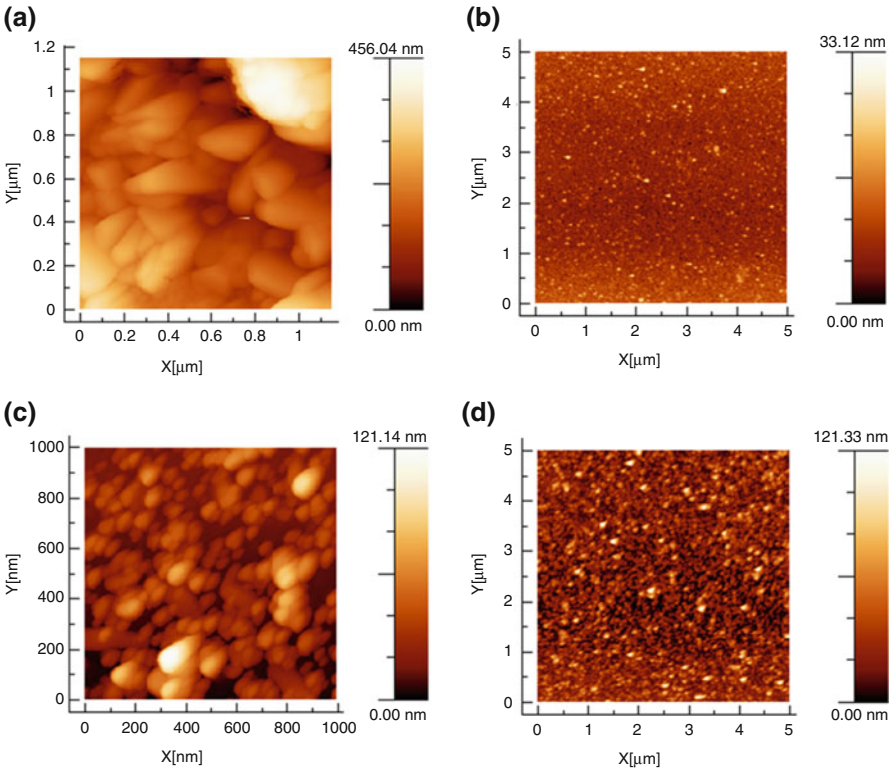

Fig. 11.12 Height-profile AFM images of transition metal-doped pyrite ($M_xFe_{1-x}S_2$) thin films deposited at 350 °C on glass substrates by AACVD from complexes (**a**) (**1**) and (**2**), (**b**) (**1**) and (**3**), and (**c**, **d**) (**1**) and (**5**) (Reproduced from Ref. [43] with permission from The Royal Society of Chemistry)

film fabrication, and the adhesion at nanoscale decreases with increasing surface roughness. Thin films fabricated by chemical vapor deposition method are typically adherent. Average roughness values for $M_xFe_{1-x}S_2$ thin films varied as 13.9, 7.9, 6.8, and 6.1 nm [117]. Variation in crystallite size and growth with doping has been discussed previously. The average crystallite heights were observed as 200–400 nm, 33–182 nm, 130–100 nm, and 120–140 nm for 0.05 mol% and 0.30 mol% transition metal (Co, Ni, Cu, Zn)-doped pyrite ($M_xFe_{1-x}S_2$) thin films prepared by using transition metal precursors. Their analysis also revealed the formation of nanocrystalline material in 0.30 mol%-doped zinc pyrite thin films with an average diameter of 3–60 nm. AFM images of transition metal-doped pyrite ($M_xFe_{1-x}S_2$) thin films showed well-interconnected crystallites with uniform distribution of particles [43].

X-ray photoelectron spectroscopy (XPS) analysis of the Sn^{4+}-doped FeS_2 films was carried out to investigate the surface electronic states of doped pyrite [81]. The broad scan of the sample consisted of iron, tin, sulfur, oxygen, and carbon

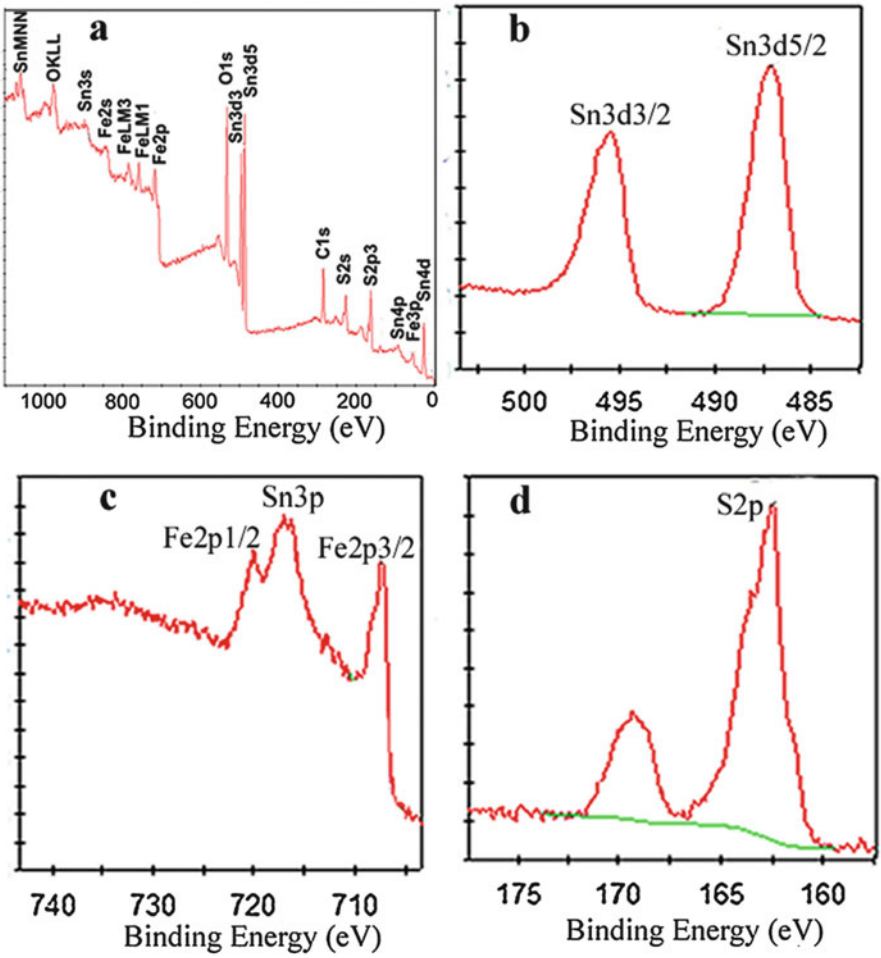

Fig. 11.13 XPS analysis of the prepared Sn^{4+}-doped FeS_2 films: (**a**) survey scan and high-resolution scans of (**b**) Sn region, (**c**) Fe region, and (**d**) S region (Reproduced from Ref. [81] with permission from Elsevier Ltd.)

(Fig. 11.13). The weak C1s and O1s peaks originate from the adsorbed reactants and gaseous molecules in the atmosphere. Two strong peaks at 487.1 and 495.5 eV can be indexed to Sn3d3/2 and Sn3d5/2, respectively. The peaks located at 707.4 eV and 720 eV correspond to Fe2p3/2 and Fe2p1/2 relates to the values of bulk FeS_2. The middle peak at 717 eV is the feature of electronic states of Sn3p. The maximum peak at 162.3 eV can be attributed to the pyritic sulfur (S_2^{2-}). The peak appearing at 168 eV may be attributed to the SO_4^{2-} on the surface of the film. The results verified the formation of Sn^{4+}-doped FeS_2. X-ray photoelectron spectroscopy (XPS) of selected transition metal-doped pyrite ($M_xFe_{1-x}S_2$) thin films are

prepared by AACVD using precursors (**1**) and the dopant precursors (**2**–**5**) of concentration 0.30 mol%. Integration and comparison of the Fe 2p, Co 2p, Ni 2p, Cu 2p, and Zn 2p signals revealed compositions of transition metal-doped pyrite thin films ($M_xFe_{1-x}S_2$) [117]. XPS analysis revealed phase transformation of pyrite to doped pyrite with an approximate surface composition of $M_xFe_{1-x}S_2$ (discounting other inconsequential species that may be present) [119–121]. - Copper-doped pyrite thin film at $x = 0.30$ mol% revealed transformation from pyrite (FeS_2) to chalcopyrite ($CuFeS_2$) at binding energy 161.3 eV of $S2p_{3/2}$ and 74.65 eV for Cu $3p_{3/2}$. Density functional theory (DFT) calculation revealed that the interaction of impure pyrite (impurities like As, Co, and Ni) with oxygen can enhance the oxidation of pyrite [13]. Pyrite containing impurities is observed to be more reactive than undoped pyrite [122, 123]. XPS studies of the oxidized transition metal-doped pyrite revealed the shifting of binding energies of surface components toward higher binding energies as compared to pure pyrite [120]. This observation is in accordance with the results from XPS studies suggesting that bulk defect states introduced in doped pyrite increase the density of occupied surface states which mediate charge transfer and thus oxidation [124]. Accordingly, surface study reveals the influence of doping on oxidation processes related to the surface defects.

11.6.4 Optical and Photovoltaic Properties

Typically, iron pyrite thin films show substantial optical absorption lower than bandgap energy. The sub-bandgap optical absorption in semiconductors arises from disorder based on defects such as vacancies, non-impurity lattice substitutions, nonstoichiometric composition, and impurities. Bandgap broadening by zinc alloying of FeS_2 nanocrystals (NCs) was explored by Mao et al. [87]. Thirty times higher zinc incorporation up to 6 at% was achieved than previously reported. A more than five times reduction of dark current in $Fe_{1-x}Zn_xS_2$ photoconductor was perceived to be attributed to the increased bandgap (Fig. 11.14).

Recently, Rana et al. [125] reported fabrication of $Cu_xFe_{1-x}S_2$ (CFS) thin films by two-step method using chemical spray pyrolysis followed by post-sulfurization. The sulfur-deficient CFS films were driven to chalcopyrite CFS (CH-CFS) structure, while the sulfur-cured CFS films were grown with Cu-incorporated pyrite CFS (P-CFS) structure. The bandgaps of sulfur-deficient CH-CFS films were estimated to be 0.885–0.949 eV whereas those of sulfur-cured P-CFS films were found to be 1.062–1.156 eV, and pure FS films were measured to be around 1 eV. The blue shift in optical absorption band edge of films shows formation of solid solution. The enhancement in bandgap was also reported in transition metal-doped pyrite thin films ($M_xFe_{1-x}S_2$) deposited by AACVD at 350 °C [117]. Kinner et al. [126] reported that optical absorption by $Co_{0.5}Fe_{0.5}S_2$ nanocrystals approaches zero

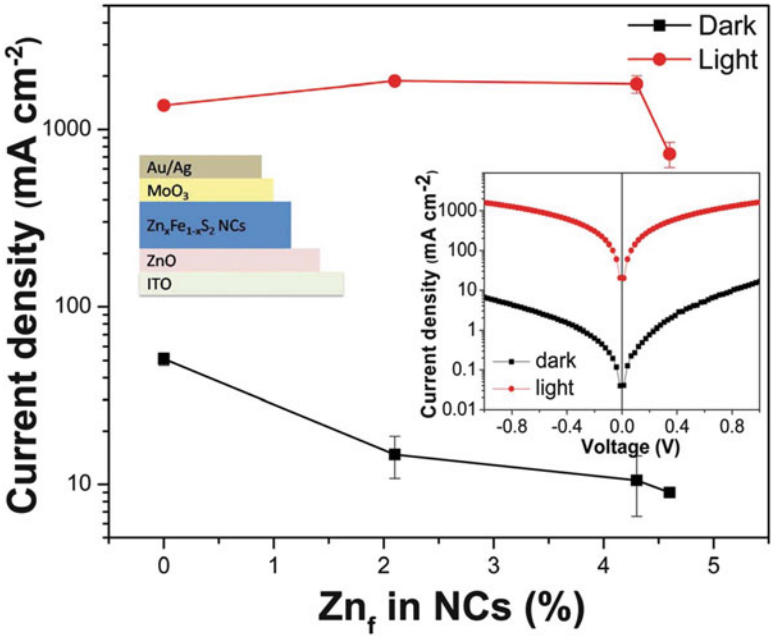

Fig. 11.14 Photocurrent and dark current changes of the $Zn_xFe_{1-x}S_2$ NC photodetector devices with different zinc alloying levels with the structure of ITO/ZnO/ $Zn_xFe_{1-x}S_2/MoO_3$/Au/Ag with a bias of −1 V. The insets show a schematic structure of the $Zn_xFe_{1-x}S_2$ photodetector devices (*left*) and typical dark current and photocurrent curves of a $Zn_{0.043}Fe_{0.957}S_2$ NC device (*right*) (Reproduced from Ref. [87] with permission from The Royal Society of Chemistry)

only at ∼2000 nm (Fig. 11.15). Most of the theoretical studies regarding bandgap enhancement of doped pyrite propose that transition metals (Ni, Cu) introduce new defect states within pyrite structure [11]. Density functional theory (DFT) calculations show that oxygen alloying in pyrite can increase its bandgap 1.0–1.5 eV without introducing electronic states within the bandgap [63]. Alloying pyrite with different elements involves issues like differences in electronegativity, size, bandgap bowing, and miscibility [72]. Bandgap bowing effect was observed in $Fe_xM_{1-x}S_2$ thin films. Increment in bandgap of $Fe_xM_{1-x}S_2$ thin films might be attributed to transition metal doping, oxygen alloying, and quantum confinement effect. Recently, first principle calculations investigated by Xiao et al. [127] explored that biaxial strain can also increase bandgap of pyrite. Synthesis of doped pyrite NCs and nanocrystalline thin films encourages the use of pyrite nanocrystalline materials in photovoltaic, optoelectronic, and energy conversion devices.

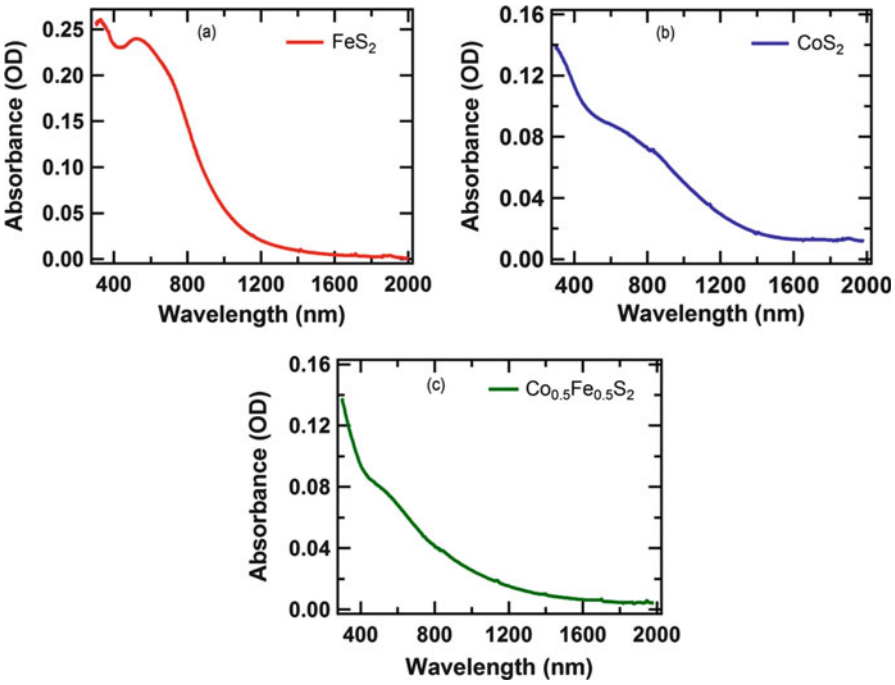

Fig. 11.15 Absorbance spectra (optical density, OD) for the as-synthesized NCs capped with TOPO. The figure shows absorbance for nanocrystalline samples consisting of (**a**) FeS_2, (**b**) CoS_2, and (**c**) $Co_{0.5}Fe_{0.5}S_2$. In all cases, the solvent was chloroform, and the path length of the cuvette was 2 mm (Reproduced from Ref. [126] with permission from the American Chemical Society)

11.7 Pyrite (FeS_2) Photovoltaics: Current Status

11.7.1 Inorganic Solar Cell (ISC)

Ferrer et al. [9] reported carrier mobility to be between 200 and 0.07 $cm^2\ V^{-1}\ s^{-1}$ and density of majority charge carriers for undoped p-type pyrite thin films. Carrier mobility varied from 200 to 0.1 $cm^2\ V^{-1}\ s^{-1}$ in doped n-type films with carrier densities from 2×10^{18} to 10^{22} cm^3 (p-type films) and from 6×10^{17} to 10^{21} cm^3 (n-type films). From these results, the modeling of pyrite solar cells based on p-n junction, parameters were established as (Table 11.2):

Recently, Bhandari et al. [128] developed FeS_2 nanocrystals (NCs) as a low-barrier back contact to CdTe thin film solar cells within a Cu-free architecture due to high work function ($\varphi = 5.0$–5.45 eV) and the high free hole concentration of FeS_2. An optimal device performance for FeS_2 NC layer thickness of ~0.7 μm with an efficiency of ~13% below that of the champion Cu/Au back contact device was achieved (Fig. 11.16).

Table 11.2 Pyrite thin film solar cell parameters [9]

Parameter	Symbol	Value
Bandgap	E_g	1 eV
Thickness	D	1 μm
Carrier concentration	N	10^{19} cm^{-3}
Diffusion lengths	L	0.1 μm
Carrier lifetimes	T	10^{-7} s
Short-circuit current	I_{SC}	40–50 mA cm^{-2}
Open-circuit voltage	V_{OC}	500 mV
Efficiency	η	20%

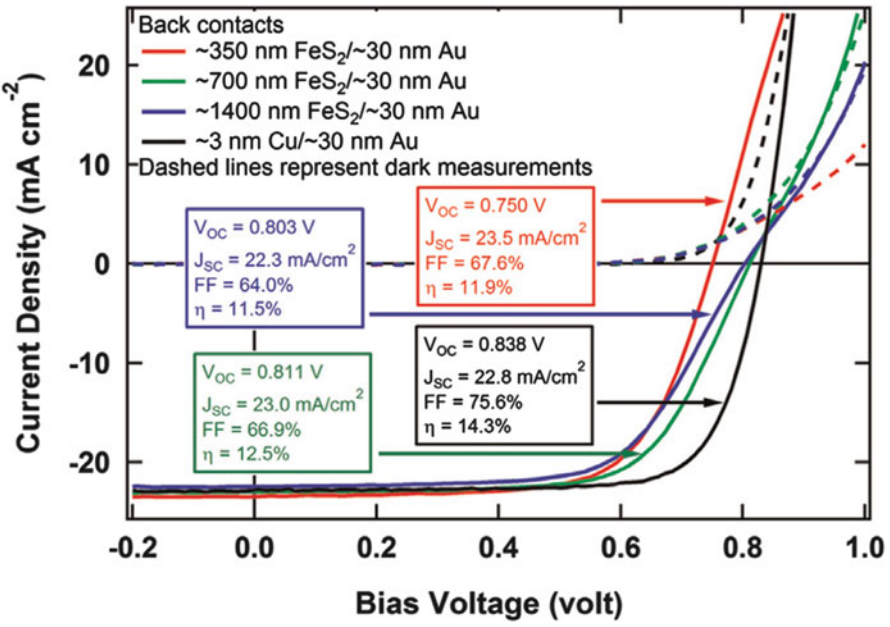

Fig. 11.16 J-V curves for CSS-deposited CdTe devices when the FeS_2-NC contact layer thickness was varied from 0.35 to 1.4 μm. Performance parameters for each device are shown in the boxes (Reproduced from Ref. [128] with permission from Elsevier B.V.)

11.7.2 Dye-Sensitized Solar Cell (DSSC)

The dye-sensitized solar cell with the low-cost counter electrode via the solution-processable method and partially transparent FeS_2 NC thin film (100 nm) exhibits promising energy conversion efficiency (η) of 7.31% as compared to Pt-CE (7.52%). FeS_2 NC also exhibits significant electrochemical stability more than 500 successive cycle scans. Solution-processable FeS_2 NC ink will be able to print on numerous substrates such as ITO/PET that are heat sensitive preferentially flexible for large-area roll-to-roll fabrication [129]. Recently, Wei et al. [130]

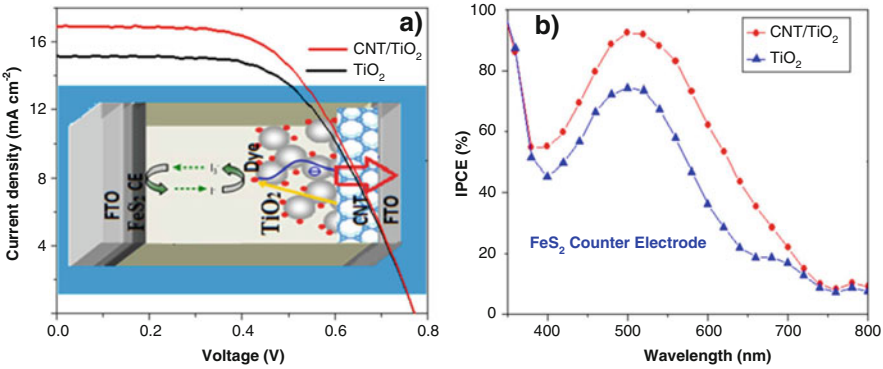

Fig. 11.17 (**a**) Current density–voltage (*J–V*) characteristics of MWCNT/TiO_2 and TiO_2 WEs DSSCs with FeS_2 thin films as CE. (FeS2 film thickness is about 1 μm.) Inset: schematic diagram of a device with MWCNT/TiO_2 WE. *J–V* characteristics were obtained under 1-sun AM 1.5 G solar irradiance, (**b**) IPCE spectra of the devices (Reproduced from Ref. [131] with permission from the Macmillan Publishers Limited, part of Springer Nature)

demonstrated FeS_2 nanochain networks as efficient CE with high power conversion (η) (6.26 (on PET-ITO)—7.16% (on FTO)) for DSSCs. As-prepared pyrite nanochain network exhibited high catalytic activity with no significant decay even after 2000 cycles.

Multiwalled carbon nanotube with mesoporous titania networks (MWCNT)/TiO_2 can be a new substitute in DSSCs as photoanode. Its large specific surface area and efficient electrochemical activity make it a favorable alternative to standard FTO/TiO_2 mesoporous-based DSSC. MWCNT/TiO_2 mesoporous-based DSSCs with FeS_2 CE achieved a high photon-to-electron conversion efficiency of 7.27% under 100 mW cm^{-2} under simulated solar irradiance of AM 1.5G 1-Sun (Fig. 11.17) [131].

Similarly, FeS_2-sensitized ZnO@ZnS nanorod arrays displayed an improved optical absorption that extended from visible to near-infrared region. This combination made a gradient energy-level structure that revealed a high photocurrent density at 1.0 V much larger than that of ZnO@ZnS nanorods with high irradiation stability. Pyrite can be further employed with wide bandgap materials as an efficient sensitizer for enhanced light absorption and photoresponse [132].

11.7.3 Tandem Dye-Sensitized Solar Cell (TDSSC)

To reduce degradation effects and low efficiency of DSSCs, the tandem DSSCs could be attractive devices for the improved energy conversion efficiency of solar modules. In tandem dye-sensitized solar cells (TDSSCs), Pt cathode is replaced by photocathode to absorb more solar energy [133, 134]. The fill factor (FF) [135] and photovoltaic efficiency (η) [136] are given by Eqs. (11.5) and (11.6):

$$\mathrm{FF} = \frac{I_{\max} V_{\max}}{I_{\mathrm{SC}} V_{\mathrm{OC}}} \tag{11.5}$$

$$\eta(\%) = \frac{I_{\max} V_{\max}}{P_h} \tag{11.6}$$

where $I_{\max}$ and $V_{\max}$ are current and voltage at maximum power point on the power output curve, I_{SC} is short-circuit current, V_{OC} is open-circuit voltage, and P_h is the power density of incident light. TiO_2-FeS_2 based tandem solar cell with thin n-type FeS_2 nanosheets (thicknesses 30–50 nm and flower-like morphology) as photocathode and n-type TiO_2 nanorod film as the photoanode was investigated. The photovoltaic parameters were calculated using the above equations are $I_{\mathrm{SC}} = 2.04 \frac{\mathrm{mA}}{\mathrm{cm}^2}$, $V_{\mathrm{OC}} = 0.38$ V, FF = 0.40, and $\eta = 0.93\%$ for TiO_2–FeS_2 tandem DSSC [137].

11.7.4 Bulk Heterojunction Solar Cell (BHJ)

A typical organic-inorganic hybrid solar cell or bulk heterojunction (BHJ) solar cell consists of conjugated polymers (poly-3-hexylthiophene (P3HT), phenyl-C_{61}-butyric acid methyl ester (PCBM), etc.) incorporated with semiconductor nanocrystals (TiO_2, ZnO, PbS, CdS, etc.) inserted between a transparent metal electrode, usually indium tin oxide (ITO), and a low work function metal, usually aluminum (Al) [138].

Pyrite nanocrystals (10 nm) were used in a polymer poly-(3-hexylthiophene) (P3HT) based polymer/inorganic bulk heterojunction hybrid photovoltaic device. Absorption edge shifted from 650 to 900 nm as compared to pristine P3HT. A high photoresponse with PCE 0.16% was observed in this polymer-based pyrite solar cell [54].

The blending of FeS_2 NCs (nanocubes of size 80 ± 5 nm and quantum dots of size 15 ± 3 nm) with cadmium sulfide (CdS) quantum dots (QDs) results in the controllable dispersion of FeS_2 NCs within the CdS QD matrix. Strong interfacial interaction was found between FeS_2 NCs and CdS QDs due to the formation of bicontinuous donor/acceptor phases at interface. Bipolar heterojunction photoactive thin film, layer by layer along with sequential ligand exchange mechanism, can significantly increase charge separation and carrier transport efficiency that are important for inorganic bipolar heterojunction photovoltaic cells as compared to the FeS_2/CdS bilayer heterostructures. Amplified charge separation efficiency and the improved charge collection efficiency are supported by the bicontinuous percolated nanomorphology that imparts additional dynamic transport paths for both electrons and holes [139]. Steinhagen et al. [52] have explored various device architectures for pyrite nanocrystals, as well as Schottky junction, heterojunction, and hybrid organic/nanocrystal devices. But not one of the devices showed photovoltaic response that seems to originate from the extremely conductive surface-associated defects in pyrite [140, 141]. Wang et al. demonstrated a

photodiode device based on pyrite FeS_2 NCs/metal oxide heterojunctions with ITO/ZnO (80 nm)/FeS_2 NC (100 nm)/MoO_3 (15 nm)/Au structure. Exceptional photoresponse, high ratio of photocurrent to dark current, and spectral response extending from visible (390–700 nm) to near-infrared region (750–1150 nm) of solution-processable FeS_2 NCs suggest wide potential for the growth of photovoltaic industry.

A blue shift was observed in the absorption edge of TiO_2 (20 nm), ZnO nanoparticulate (diameter, 2–5 nm), and ZnO nanorod (length of 8 μm and diameter of 300 nm) electrodes sensitized with FeS_2 (pyrite) nanoparticles (50–70 nm). Quantum size effect is manifested in both absorption (bandgap 1.6–2.0 eV) and photocurrent action spectra. The photo-induced absorption (PIA) spectra indicated long life charge separation state arising in the quantum dot (QD)-sensitized wide bandgap metal oxides. Highest long-lived charge separation was observed for FeS_2-modified ZnO nanorods. However, multiphase FeS_2 affects performance of the electrodes, so there is a need to develop phase-pure and stoichiometric pyrite for promising quantum dot solar cells [142].

11.7.5 Inverted Organic Solar Cell (IOSC)

Buffer layer of acidic PEDOT/PSS (poly-3,4-ethylenedioxythiophene/polystyrene sulfonate) layer proves to be unfavorable to active polymer layer P3HT/PCBM (poly-3-hexylthiophene/phenyl-C61-butyric acid methyl ester), and oxidation and degradation of the low work function metal cathode (Al) are the major instability problem of OSCs. It is dynamically more promising to contact a coating of a metal such as Ag or Au that is less air sensitive [143]. Inverted organic solar cell structure was discovered to overcome the above deficiencies. Inverted organic solar cells (IOSCs) consist of metal or metal oxide of high work function as the top electrode and metal of low work function in place of the bottom anode. These inverted configuration OSCs have improved OSCs' lifetime by controlling oxidation of the top electrode with an impressive PCE of 4.4% [144].

FeS_2 nanocrystals with an average radius of 27 nm (concentration varied from 0 to ~4 wt%) were utilized to form inverted ternary hybrid BHJ solar (Fig. 11.18). Photocurrent enhancement up to 20% was observed by adding FeS_2 NCs up to ~0.5 wt% in the films. Pyrite (FeS_2) NCs improve the film morphology by growing charge generation and transportation. Fill factor (FF), open-circuit voltage (V_{OC}), and PCE up to 28% enhanced after 28 days of exposure of these hybrid devices to air as compared to control device without FeS_2 NCs [145].

FeS_2 NCs/polymer solid solar cells in inverted structure: FTO/TiO_2 layer/active layer (FeS_2:P3HT:PCBM)/PEDOT:PSS layer/Ag electrode displayed a *PCE* of 3.0% having high stability in the range of 20–80 °C retaining 83.3% of its initial efficiency after 15 weeks of exposure in the air. The *PCE* fluctuation magnitudes were also found smaller than QDSSC under the same condition [146].

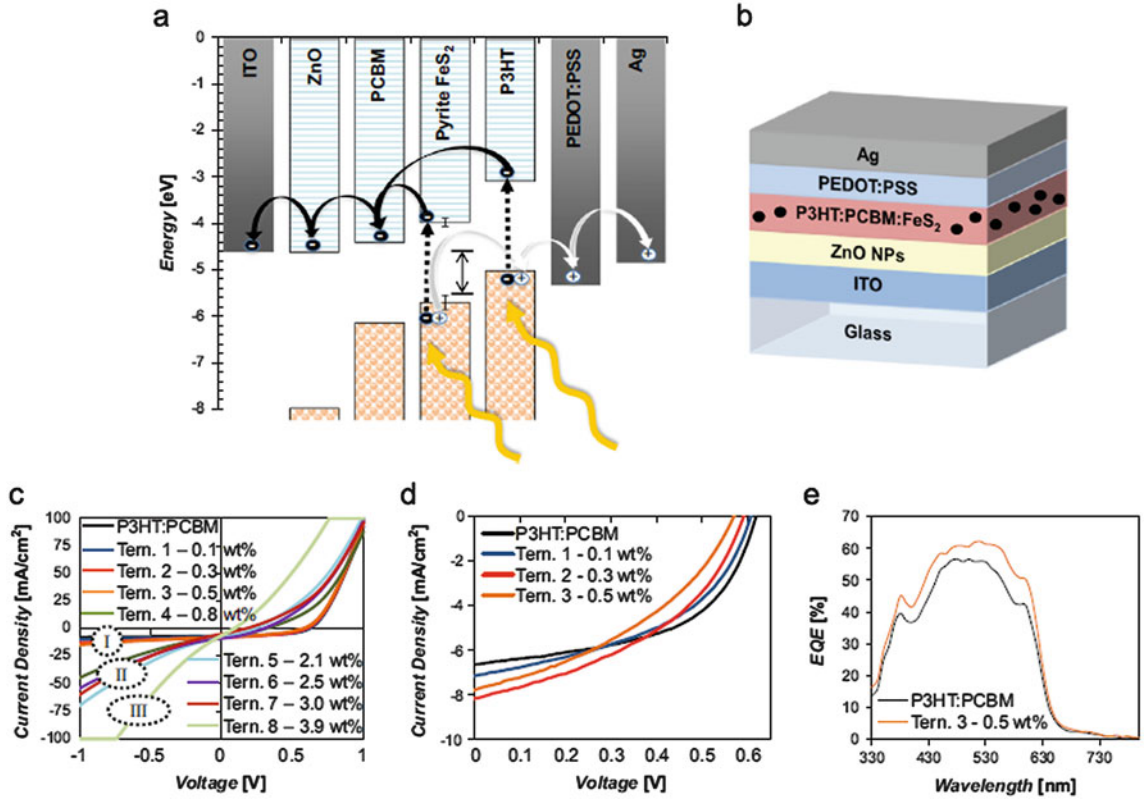

Fig. 11.18 (**a**) Energy band diagram of the materials used in the inverted ternary hybrid BHJ solar cell. The average EVB (−5.6 eV) and ECB (−3.9 eV) measured from CV are shown along with error bars. In comparison, the literature values of EVB (−5.4 eV) and ECB (−4.5 eV) are also shown as the short horizontal black lines. (**b**) Schematic of an inverted ternary hybrid BHJ solar cell incorporating pyrite FeS_2 NCs. (**c**) The *J*–*V* curves in the voltage range of −1 to +1 V for all ternary devices showing three distinct performance regimes. (**d**) The *J*–*V* curves in the voltage range of 0 to +0.6 V for the devices exhibiting "regime I" behavior showing enhanced photocurrents upon addition of FeS_2 NCs. (**e**) EQE spectra of a control P3HT:PCBM device compared to a ternary device with 0.5 wt% FeS_2 NCs (Reproduced from Ref. [145] with permission from Elsevier B.V.)

11.7.6 Inverted Inorganic Bulk Heterojunction Solar Cell (IIBHJSC)

Recently, Nam et al. demonstrated FeS_2 NCs-based inverted-type all-inorganic BHJ solar cells. The optimized device displayed a good PV performance under AM 1.5G illumination with FeS_2 NCs:CdSe QDs at a weight ratio of 1:1 and a polymeric hole transport material (HTM) between the photoactive layer and the top electrode. This colloidal FeS_2 NCs-based inverted device showed better air stability than conventional structure (Fig. 11.19) [147].

11.7.7 Photoelectrochemical (PEC) Solar Cells

By engineering size of quantum dot, higher absorption coefficient, high carrier mobilities, and multiple carrier generation can together play a role beyond the Schottky-Queisser (SQ) limit [148]. Surface modification of titania (TiO_2) with pyrite (FeS_2) quantum dots for photoelectrochemical cell yielded maximum

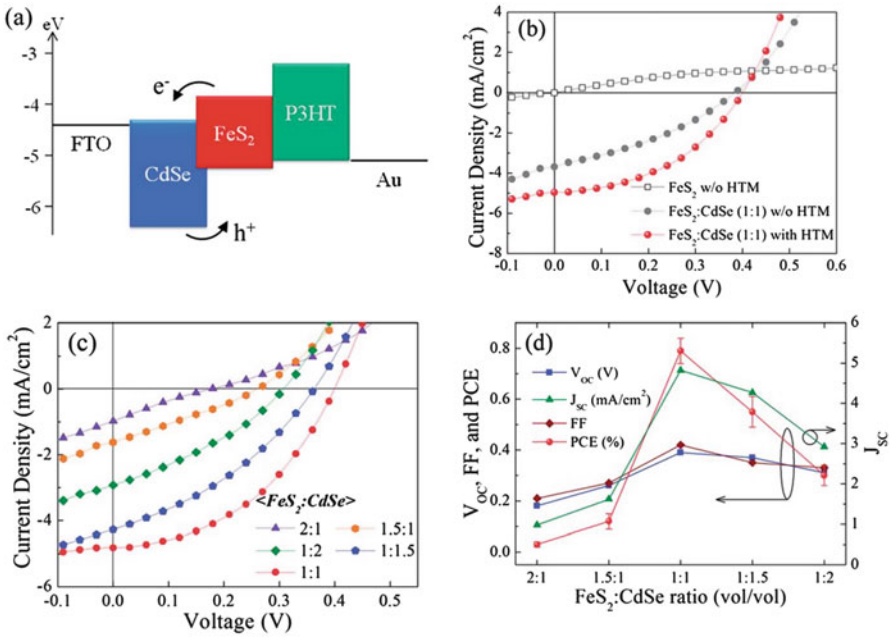

Fig. 11.19 (**a**) Energy band diagram of the solar cell. (**b**) Representative *J–V* characteristics of the inverted solar cells consisting of FeS_2 NCs without an HTM and the FeS2 NCs:CdSe QD (1:1) blend with or without an HTM. (**c**) *J–V* characteristics and (**d**) photovoltaic parameters of the devices as a function of FeS_2–CdSe ratio in the presence of the HTM (Reproduced from Ref. [147] with permission from The Royal Society of Chemistry)

incident of photon-to-photocurrent efficiency (IPCE) (Eq. (11.7)) of about 23% at 400 nm excitation determined from Eq. 13 where I_{sc} is the short-circuit current (A/cm^2), I_{inc} is the incident light intensity (W/cm^2), and λ is the excitation wavelength (nm) [149].

$$\text{IPCE}\ (\%) = 100 \cdot \frac{1240\, I_{SC}}{I_{inc}\lambda} \tag{11.7}$$

The photocurrent and open-circuit voltage measurements under the AM 1.5 light illumination revealed excessive light-harvesting efficiency of pyrite (FeS_2)-sensitized titania (TiO_2) nanotube (NT) arrays. The titania nanotubes (TNTs) with inner diameter ca. 100 nm and wall thickness ca. 15 nm were used [150].

Recently, Jin research group [151] has investigated electrochemical properties of transition metal pyrites (FeS_2, CoS_2, NiS_2) and their alloys. They have explored these earth-abundant transition metal disulfides as potential alternative counter electrode materials in photoelectrochemical (PEC) solar cells.

The FeS_2/TiO_2 photoanode exhibited improved photoresponse ranging from visible to NIR region for PEC hydrogen generation. The proper sulfurization eliminated the FeS_2 surface defect and enhanced the interface charge transfer between FeS_2 and TiO_2 (Fig. 11.20) [152].

Well-aligned 1D FeS_2 nanotube arrays (average outer diameter of 150 ± 20 nm with wall thickness of 50 ± 5 nm) on ZnO nanorod arrays possessed high corrosion resistance and electrochemical stability. The J–V curves of FeS_2 nanotube arrays displayed the five times larger photocurrent at 1.0 V than FeS_2 NPs. This indicates the better photoresponse of 1D FeS_2 nanotube arrays with rapid charge transfer [153].

11.8 Low-Cost Photodetectors

The efficient optoelectronic properties of FeS_2 NCs demonstrated a great potential for low-cost photodetector devices. FeS_2 QDs and cubes exhibited a better photoresponse in the visible and NIR region, respectively. The FeS_2/CdS thin film devices displayed a very fast response time of 10 ms with high responsivity of (174.9 A/W) under a very low bias voltage. The magnetic field affected the photocurrent by 72.6% due to interfacial magnetic-diluted semiconductor CdFeS phase [154].

The nano gap FeS_2 NC photodetector displayed a spectral response in the UV-vis region with a very high photocurrent in the range of 10^{-2} to 1 μA for approximately 1 μm^2 gap area [155]. Recently, Yang et al. studied ZnO-CuI p-n, ZnO-FeS_2, and ZnO-FeS_2-CuI p-i-n photodiodes. Among them, ZnO-FeS_2-CuI p-i-n photodiode displayed the highest rectifying ratio of 197 at ±1 V under AM 1.5 illumination with J_{sc} of 0.5 mA/cm^2 and on-off current ratio of 371 at zero bias voltage (Fig. 11.21). This performance indicated the feasibility of self-power mode

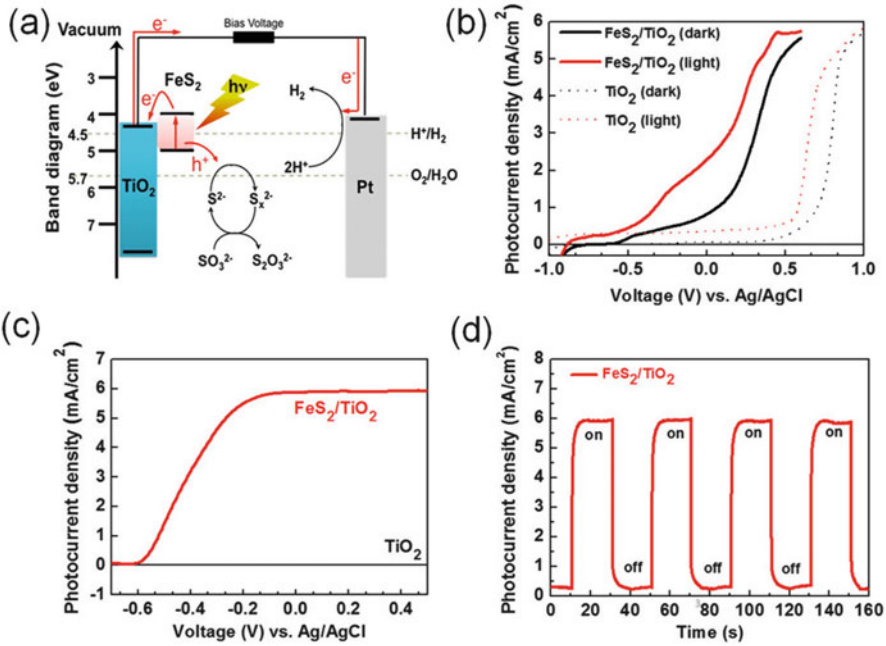

Fig. 11.20 (**a**) Schematic illustration of the PEC device with a FeS_2/TiO_2 photoanode and a passive Pt cathode, for light-driven water splitting in aqueous solution. (**b**) The photocurrent-potential (I–V) responses of FeS_2/ TiO_2 photoanode and pure TiO_2 in the alkaline electrolyte (pH 13.5) with $SO_3^{2-}/S_2O_3^{2-}$ as sacrificial agent under simulated AM 1.5 illumination (100 mW/cm^2). (**c**) The photocurrent-potential (I–V) responses of FeS_2/ TiO_2 and TiO_2 photoanodes in the alkaline electrolyte (pH 13.5) with $SO_3^{2-}/S_2O_3^{2-}$ as sacrificial agent under NIR laser (808 nm) illumination (300 mW/cm^2). (**d**) Light chopping photocurrent measurements in a three-electrode cell using FeS_2/TiO_2 photoanode as working electrode (Reproduced from Ref. [152] with permission from Macmillan Publishers Limited, part of Springer Nature)

of this device. The maximum responsivity (17 mA/W at 400 nm) and high responsivity around 900 nm display the potential for NIR photodetectors systems. These results are attributed to the efficient extraction of photogenerated electrons and holes due to the built-in electric field in increased depletion layer width for p-i-n structure. The low V_{oc} could be carrier recombination from the trap states within FeS_2 NC film due to defects [156].

11.9 Emerging Era of Pyrite: Clean Hydrogen Production

Hydrogen evolution reaction (HER) from water through electrocatalysis using cost-effective materials to replace precious Pt catalysts holds great promise for clean energy technologies. Earth-abundant iron pyrite NPs can efficiently activate molecular hydrogen under mild conditions [157].

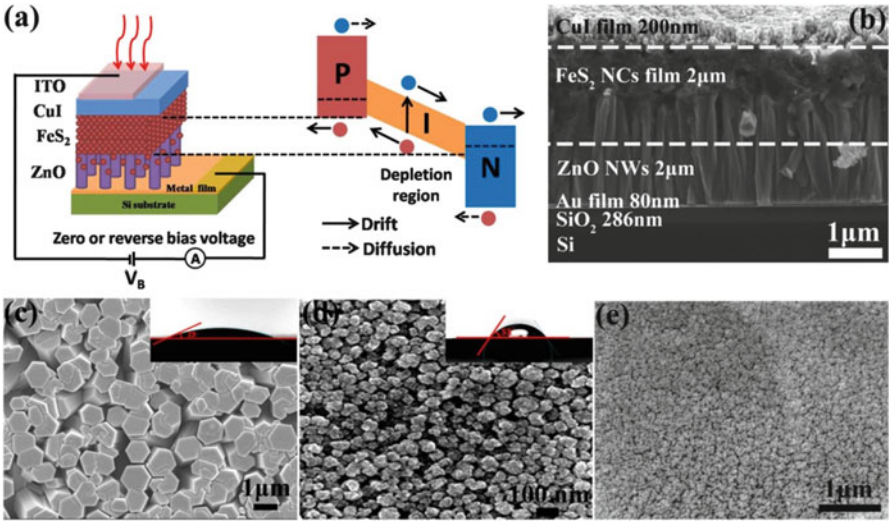

Fig. 11.21 (**a**) Schematic diagram of ZnO-FeS_2-CuI p-i-n photodiode. The device can work at zero or reverse bias voltage. The drift and diffusion process of electron and hole are shown here. SEM images of typical photodiode device: (**b**) cross section, the thickness of each layer is shown here. Plane view of each layer, (**c**) ZnO micro/nanowire arrays, (**d**) FeS_2 NCs film, and (**e**) CuI film. The insets of (**c**) and (**d**) are corresponding water contact angles (Reproduced from Ref. [156] with permission from Macmillan Publishers Limited, part of Springer Nature)

Recently, Wang et al. reported a hybrid, highly active and stable catalyst of Co-doped pyrite hybridized with carbon nanotubes ($Fe_{1-x}Co_xS_2$/CNT) for HER in acidic medium. $Fe_{1-x}Co_xS_2$/CNT is a cost-effective, scalable and efficient catalyst for hydrogen production. It exhibited a low overpotential of ~0.12 V at 20 mA/cm^2, small Tafel slope of ~46 mV/decade, and long-term durability over 40 h of HER operation using bulk quantities of $Fe_{0.9}Co_{0.1}S_2$/CNT hybrid catalysts at high loadings (~7 mg/cm^2) [158].

Titanium-doped pyrite films have been recently used as photoanode in a PEC for hydrogen photogeneration for solar hydrogen photogeneration. Flat band potential of Ti-FeS_2 was determined as $V_{fb} = -0.55 \pm 0.02$ V vs. NHE presenting a suitable position of the FeS_2/electrolyte interface in the energy-level diagram for HER (Fig. 11.22). Hydrogen photogeneration efficiencies using Ti-FeS_2 films were estimated to be up to ~8% [159].

11.10 Challenges for Sustainable Pyrite (FeS_2) Photovoltaics

Pyrite has numerous applications including energy conversion and storage devices. Pyrite photovoltaics is the most attractive field of technology for researchers, however, the pyrite-based solar devices revealed very low solar conversion

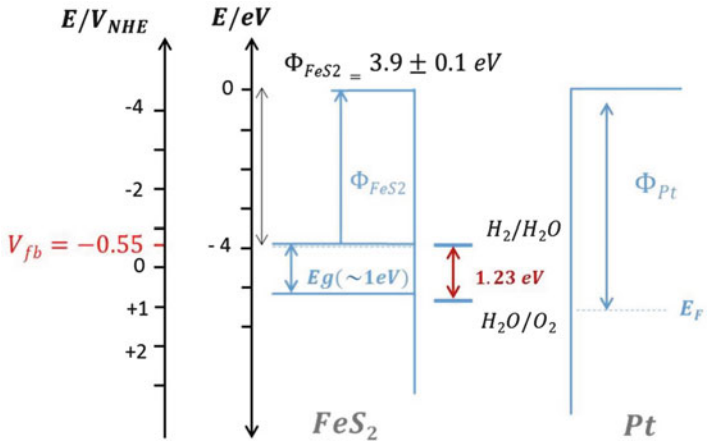

Fig. 11.22 Energy-level diagram at the Ti-FeS_2/Na_2SO_3 interface (pH 9.0) (Reproduced from Ref. [159] with permission from the American Chemical Society)

efficiency of <3%. Currently, the performance of pyrite photovoltaic devices is limited by high recombination losses and dark current high density of deep defect states that cause low open-circuit voltages (V_{OC}) $\leq$ 200 mV with low fill factor (~50%) (Fig. 11.23). The high carrier losses in iron pyrite arise due to fast localization and recombination assisted by intermediate gap states (Scheme 11.2).

More precisely, there are multistep experimental procedures with expensive and cautious experimental methods to synthesize phase-pure pyrite. Also, starting materials are typically environment unfriendly. Oxidation of pyrite thin films remains a problem for large-area, green and sustainable photovoltaics. Therefore, it requires synchronization between theoretical and experimental research work to categorize pyrite issues. It involves the consistency between computational and experimental measurements. Efficiency of pyrite-based solar devices can be improved by bandgap engineering of pyrite that is one of the applicable practices. Doping pyrite with various elements using quality experimental techniques can provide a practical approach for efficient pyrite photovoltaics.

11.11 Conclusion and Perspective

Iron pyrite and doped iron pyrite hold great potential for being used as photovoltaic material. In this chapter, the current status of the synthesis techniques for pyrite and doped pyrite is discussed. Also their properties and application in various configurations for solar cells are summarized. The incorporation of transition metal into FeS_2 can efficiently improve its properties, particularly extended light harvesting,

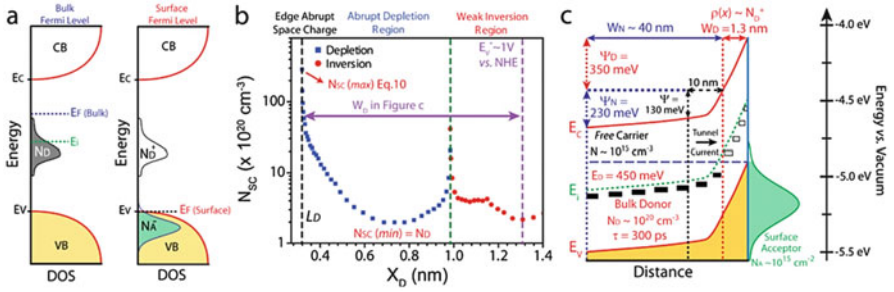

Fig. 11.23 Space charge region properties of the iron pyrite single crystals. (**a**) Occupancy of the deep donor (ND) density of states (DOS) relative to the bulk and surface Fermi level, as determined from the EIS measurements. Surface states (NA) are plotted for the purpose of illustrating their occupancy under surface Fermi level pinning. (**b**) Experimental profile for the apparent charge density in the abrupt space charge region (NSC) as a function of the variable abrupt space charge depth (XD), as determined from the fitting results for CSC vs. V under dark conditions. The total width of the abrupt space charge region (WD) under surface Fermi level pinning condition is shown using a purple double-sided arrow and was calculated using the estimated valence band edge potential (EV*). (**c**) Proposed energy band scheme for {1 0 0}-faceted iron pyrite single crystal with various values determined experimentally herein (Reproduced from Ref. [160] with permission from the American Chemical Society)

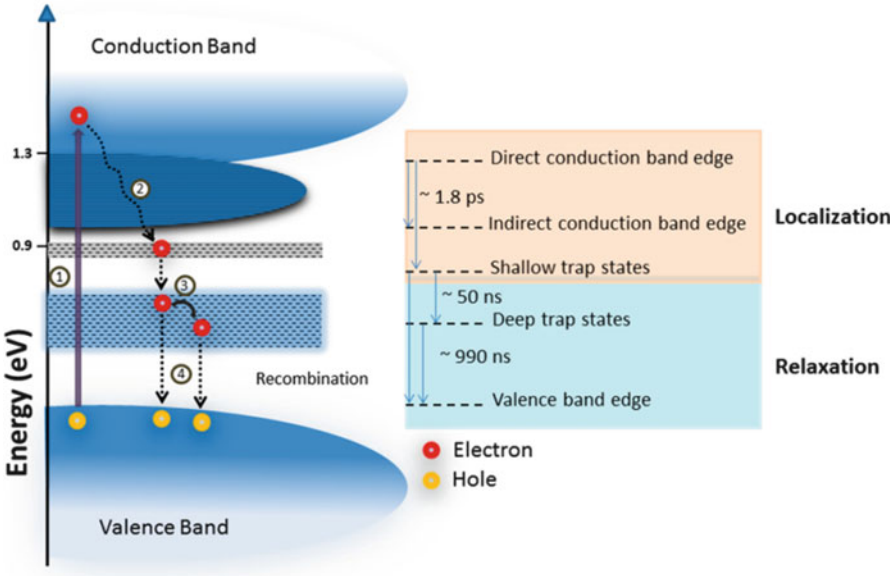

Scheme 11.2 Representative schematic of the photophysical processes involved in iron pyrite based on optical pump probe spectroscopy (Reproduced from Ref. [161] with permission from the American Chemical Society). *Note*: (*1*) Optical excitation of electron from valence to conduction band, (*2*) rapid carrier localization of the excited carrier to indirect band edge and low-lying shallow defect states, (*3*) slower electron relaxation to midgap deep defect states/band (long-lived trap states), and (*4*) electron recombination process with the valence band holes

enhanced absorption, and excellent electron conductivity. Despite the demonstrated advances, the research in this field is still at an early stage of development.

Unlike the conventional deposition methods, deposition of undoped and doped pyrite thin films using the solution-based process like aerosol-assisted chemical vapor deposition (AACVD) provides a simple and economical way. Additionally, it is challenging to sustain the pyrite phase at the same time while varying dopants under similar experimental conditions using various experimental techniques. Consequently, pyrite cannot simply be compared with and developed along the line of classical semiconductor compounds. So, systematic work is required to establish the role of impurities in doped pyrite to improve its properties.

References

1. Rickard D, Luther GW (2007) Chem Rev 107:514–562
2. Wadia C, Alivisatos AP, Kammen DM (2009) Environ Sci Technol 43:2072–2077
3. Vaughan DJ, Craig JR (1978) Mineral chemistry of metal sulfides, vol 493. Cambridge University Press, Cambridge
4. Schena T, Bihlmayer G, Blügel S (2013) Phys Rev B 88:235203
5. Ennaoui A, Fiechter S, Jaegermann W, Tributsch H (1986) J Electrochem Soc 133:97–106
6. Kuvandikov O, Shakarov KO, Shodiev Z, Rabbimova G (2007) J Commun Technol Electron 52:1062–1064
7. Ho C, Huang Y, Tiong K (2006) J Alloy Compd 422:321–327
8. Pridmore D, Shuey R (1976) Am Mineral 61:248–259
9. Ferrer I, Ares J, Sanchez C (2003) Sol Energy Mater Sol Cells 76:183–188
10. Ennaoui A, Fiechter S, Pettenkofer C, Alonso-Vante N, Büker K, Bronold M, Höpfner C, Tributsch H (1993) Sol Energy Mater Sol Cells 29:289–370
11. Abraitis P, Pattrick R, Vaughan D (2004) Int J Miner Process 74:41–59
12. Birkholz M, Fiechter S, Hartmann A, Tributsch H (1991) Phys Rev B 43:11926
13. Li Y-Q, Chen J-H, Chen Y, Guo J (2011) Trans Nonferrous Met Soc Chin 21:1887–1895
14. Sun R, Chan M, Kang S, Ceder G (2011) Phys Rev B 84:035212
15. Ferrer I, Nevskaia D, De las Heras C, Sanchez C (1990) Solid State Commun 74:913–916
16. Meng L, Liu YH, Tian L (2003) J Cryst Growth 253:530–538
17. Luan Z, Huang L, Wang F, Meng L (2011) Appl Surf Sci 258:1505–1509
18. Yonemoto BT, Hutchings GS, Jiao F (2014) J Am Chem Soc 136:8895–8898
19. Smestad G, Ennaoui A, Fiechter S, Tributsch H, Hofmann W, Birkholz M, Kautek W (1990) Solar Energy Mater 20:149–165
20. Wang X, Wang G, Chen J, Zhu X, Tian J, Jiang C, Zhang Y, Liu X, Wang R (2013) Mater Lett 110:144–147
21. Liu H, Chi D (2012) J Vac Sci Technol A 30:04D102
22. Mazón-Montijo D, Nair M, Nair P (2013) ECS J Solid State Sci Technol 2:P465–P470
23. Pimenta G, Kautek W (1994) Thin Solid Films 238:213–217
24. Bausch S, Sailer B, Keppner H, Willeke G, Bucher E, Frommeyer G (1990) Appl Phys Lett 57:25–27
25. Teo M, Kulinich S, Plaksin O, Zhu A (2010) Chem A Eur J 114:4173–4180
26. Umehara M, Takeda Y, Azuma H, Motohiro T (2012) Jpn J Appl Phys 51:02BP10
27. Baruth A, Manno M, Narasimhan D, Shankar A, Zhang X, Johnson M, Aydil ES, Leighton C (2012) J Appl Phys 112:054328
28. Bessergenev V, Pereira R, Botelho do Rego A (2007) Surf Coat Technol 201:9141–9145

29. Adusumilli SP, Dhakal TP, Westgate CR (2012) Synthesis of iron pyrite film through low temperature atmospheric pressure chemical vapor deposition. In: MRS Proceedings. Cambridge University Press, Cambridge
30. Malik MA, Revaprasadu N, Ramasamy K (2012) Nanoscience: nanostructures through chemistry, vol 1. RSC Publishing, Cambridge, UK, p 29
31. De las Heras C, Ferrer I, Sanchez C (1993) J Appl Phys 74:4551–4556
32. Clayton A, Irvine S, Barrioz V, Brooks W, Zoppi G, Forbes I, Rogers KD, Lane DW, Hutchings K, Roncallo S (2011) Thin Solid Films 519:7360–7363
33. Luan Z, Wang Y, Wang F, Huang L, Meng L (2011) Thin Solid Films 519:7830–7835
34. Vahidi M, Lehner S, Buseck P, Newman N (2013) Acta Mater 61:7392–7398
35. Meester B, Reijnen L, Goossens A, Schoonman J (2000) Chem Vapor Depos 6:121–128
36. Bronold M, Kubala S, Pettenkofer C, Jaegermann W (1997) Thin Solid Films 304:178–182
37. Berry N, Cheng M, Perkins CL, Limpinsel M, Hemminger JC, Law M (2012) Adv Energy Mater 2:1124–1135
38. Samad L, Cabán-Acevedo M, Shearer MJ, Park K, Hamers RJ, Jin S (2015) Chem Mater 27:3108–3114
39. Yamamoto A, Nakamura M, Seki A, Li E, Hashimoto A, Nakamura S (2003) Sol Energy Mater Sol Cells 75:451–456
40. Moon DG, Cho A, Park JH, Ahn S, Kwon H, Cho YS, Ahn S (2014) J Mater Chem A 2:17779–17786
41. Zhang X, Scott T, Socha T, Nielsen D, Manno M, Johnson M, Yan Y, Losovyj Y, Dowben P, Aydil ES (2015) ACS Appl Mater Interfaces 7:14130–14139
42. Akhtar M, Abdelhady AL, Azad MM, O'Brien P (2012) J Cryst Growth 346:106–112
43. Khalid S, Ahmed E, Azad MM, Lewis DJ, Abu BS, Khan Y, O'Brien P (2015) New J Chem 39:1013–1021
44. Luan Z, Wang F, Yao D, Huang L, Meng L (2011) Mater Res Bull 46:1577–1581
45. Clamagirand J, Ares J, Ferrer I, Sánchez C (2012) Near room temperature power factor of metal sulfides films. In: 9th European conference on thermoelectrics: ECT2011. American Institute of Physics
46. Pascual A, Yoda S, Barawi M, Clamagirand JM, Ares JR, Ferrer IJ, Sánchez C (2014) J Phys Chem C 118:26440–26446
47. Sentman CD, O'Brien M, Wolden CA (2013) J Vac Sci Technol A 32:021201
48. Layek A, Middya S, Ray PP (2013) J Renew Sustain Energy 5:031601
49. Sajimol AM, Anand PB, Anilkumar KM, Jayalekshmi S (2013) Polym Int 62:670–675
50. Yokoyama D, Namiki K, Yamada Y (2006) J Radioanal Nucl Chem 268:283–288
51. Henda R, Al-Shareeda O, McDonald A, Pratt A (2012) Appl Phys A 108:967–974
52. Steinhagen C, Harvey TB, Stolle CJ, Harris J, Korgel BA (2012) J Phys Chem Lett 3:2352–2356
53. Zhu L, Richardson BJ, Yu Q (2015) Chem Mater 27:3516–3525
54. Lin Y-Y, Wang D-Y, Yen H-C, Chen H-L, Chen C-C, Chen C-M, Tang C-Y, Chen C-W (2009) Nanotechnology 20:405207
55. Bi Y, Yuan Y, Exstrom CL, Darveau SA, Huang J (2011) Nano Lett 11:4953–4957
56. Jasion D, Barforoush JM, Qiao Q, Zhu Y, Ren S, Leonard KC (2015) ACS Catal 5:6653–6657
57. Li T, Liu H, Wu Z, Liu Y, Guo Z, Zhang H (2016) Nanoscale 8:11792–11796
58. O'Brien P, Otway DJ, Park J-H (1999) Iron sulfide (FeS_2) thin films from single-source precursors by aerosol-assisted chemical vapor deposition (AACVD). In: MRS proceedings. Cambridge University Press, Cambridge
59. Ramasamy K, Malik MA, Helliwell M, Tuna F, O'Brien P (2010) Inorg Chem 49:8495–8503
60. Akhtar M, Akhter J, Malik MA, O'Brien P, Tuna F, Raftery J, Helliwell M (2011) J Mater Chem 21:9737–9745
61. Middya S, Layek A, Dey A, Ray PP (2014) J Mater Sci Technol 30:770–775
62. Wang M, Xing C, Cao K, Zhang L, Liu J, Meng L (2014) J Mater Chem A 2:9496–9505

63. Hu J, Zhang Y, Law M, Wu R (2012) J Am Chem Soc 134:13216–13219
64. Jiao J, Chen L, Kuang D, Gao W, Feng H, Xia J (2011) RSC Adv 1:255–261
65. Long F, He J, Zhang M, Wu X, Mo S, Zou Z, Zhou Y (2015) J Mater Sci 50:1848–1854
66. Golsheikh AM, Huang N, Lim H, Chia C, Harrison I, Muhamad M (2013) Chem Eng J 218:276–284
67. Dubey A, Singh SK, Tulachan B, Roy M, Srivastava G, Philip D, Sarkar S, Das M (2016) RSC Adv 6:16859–16867
68. Zhu Y, Fan X, Suo L, Luo C, Gao T, Wang C (2016) ACS Nano 10:1529–1538
69. Buonsanti R, Milliron DJ (2013) Chem Mater 25:1305–1317
70. Gao M-R, Xu Y-F, Jiang J, Yu S-H (2013) Chem Soc Rev 42:2986–3017
71. Deng M, Shen S, Zhang Y, Xu H, Wang Q (2014) New J Chem 38:77–83
72. Sun R, Ceder G (2011) Phys Rev B 84:245211
73. Smestad G, Da Silva A, Tributsch H, Fiechter S, Kunst M, Meziani N, Birkholz M (1989) Sol Energy Mater 18:299–313
74. Liu L, Yuan Z, Qiu C, Liu J (2013) Solid State Ion 241:25–29
75. Díaz-Chao P, Ares J, Ferrer I, Sánchez C (2013) J Mater Sci 48:4914–4924
76. Liu X, Kim H-S, Hong J-H, Xu Z, Xiao H, Ahn I-S, Kim K-W (2014) Powder Technol 256:545–552
77. Ding W, Wang X, Peng H, Peng Z, Dong B (2013) Mater Res Bull 48:4704–4710
78. Büker K, Fiechter S, Eyert V, Tributsch H (1999) J Electrochem Soc 146:261–265
79. Ferrer IJ, Ares J, Sánchez C (2001) Solid State Phenomena 80:281–286
80. Diener A, Neumann T, Kramar U, Schild D (2012) J Contam Hydrol 133:30–39
81. Xia J, Lu X, Gao W, Jiao J, Feng H, Chen L (2011) Electrochim Acta 56:6932–6939
82. Blenk O, Bucher E, Willeke G (1993) Appl Phys Lett 62:2093–2095
83. Lehner S, Savage K, Ayers J (2006) J Cryst Growth 286:306–317
84. Schieck R, Hartmann A, Fiechter S, Könenkamp R, Wetzel H (1990) J Mater Res 5:1567–1572
85. Tomm Y, Schieck R, Ellmer K, Fiechter S (1995) J Cryst Growth 146:271–276
86. De las Heras C, Bausá L (1997) J Phys Condens Mat 9:9483
87. Mao B, Dong Q, Xiao Z, Exstrom CL, Darveau SA, Webber TE, Lund BD, Huang H, Kang Z, Huang J (2013) J Mater Chem A 1:12060–12065
88. Bouchard R (1968) Mater Res Bull 3:563–570
89. Ogawa S, Teranishi T (1972) Phys Lett A 42:147–148
90. Jarrett H, Cloud W, Bouchard R, Butler S, Frederick C, Gillson J (1968) Phys Rev Lett 21:617
91. Guo S, Young DP, Macaluso RT, Browne DA, Henderson NL, Chan JY, Henry LL, DiTusa JF (2008) Phys Rev Lett 100:017209
92. Zhang X, Wu N, Manno M, Leighton C, Vescovo E, Dowben P (2012) J Phys Condens Mat 25:012001
93. Kaster BC (2011) Magnetic properties of $Co_{1-x}Fe_xS_2$. Miami University
94. Guo S, Young D, Macaluso R, Browne D, Henderson N, Chan J, Henry L, DiTusa J (2010) Phys Rev B 81:144423
95. Utfeld C, Giblin S, Taylor J, Duffy J, Shenton-Taylor C, Laverock J, Dugdale S, Manno M, Leighton C, Itou M (2009) Phys Rev Lett 103:226403
96. Manno M, Frakie R, Leighton C (2009) J Appl Phys 105:093912
97. Chandra U, Zuburtikudis I, Parthasarathy G, Sreedhar B (2014) Phase Transitions 87:477–490
98. Leighton C, Manno M, Cady A, Freeland J, Wang L, Umemoto K, Wentzcovitch R, Chen T, Chien C, Kuhns P (2007) J Phys Condens Mat 19:315219
99. Guo S (2006) Magnetic, thermodynamic and transport properties of the magnetic semiconductor $Fe_{1-x}Co_xS_2$ and superconducting LaSb2. Louisiana State University
100. Han J-T, Huang Y-H, Huang W (2006) Mater Lett 60:1805–1808

101. Wang L, Chen T, Chien C, Checkelsky J, Eckert J, Dahlberg E, Umemoto K, Wentzcovitch R, Leighton C (2006) Phys Rev B 73:144402
102. Mazin I (2000) Appl Phys Lett 77:3000–3002
103. Guo S, Young D, Macaluso R, Browne D, Henderson N, Chan J, Henry L, DiTusa J (2010) Phys Rev B 81:144424
104. Umemoto K, Wentzcovitch RM, Wang L, Leighton C (2006) Phys Stat Solidi B 243:2117–2121
105. Oertel J, Ellmer K, Bohne W, Röhrich J, Tributsch H (1999) J Cryst Growth 198:1205–1210
106. Thomas B, Ellmer K, Bohne W, Röhrich J, Kunst M, Tributsch H (1999) Solid State Commun 111:235–240
107. Díaz-Chao P, Ferrer I, Sánchez C (2008) Thin Solid Films 516:7116–7119
108. Clamagirand JM, Ares JR, Flores E, Diaz-Chao P, Leardini F, Ferrer IJ, Sánchez C (2016) Thin Solid Films 600:19–24
109. Ferrer I, de la Heras C, Sanchez C (1995) J Phys Condens Mat 7:2115
110. Ho C, Huang C, Wu C (2004) J Cryst Growth 270:535–541
111. Lehner S, Newman N, Van Schilfgaarde M, Bandyopadhyay S, Savage K, Buseck P (2012) J Appl Phys 111:083717
112. Ferrer I, De las Heras C, Sánchez C (1993) Appl Surf Sci 70:588–592
113. Ferrer I, Caballero F, De las Heras C, Sánchez C (1994) Solid State Commun 89:349–352
114. Fan JL, Lu SK (2013) First-principles calculation of electronic structure of the Cu-doped Pyrite FeS_2. Adv Mater Res 652–654:590–593
115. Pearce CI, Pattrick RA, Vaughan DJ (2006) Rev Mineral Geochem 61:127–180
116. Folkerts W, Sawatzky G, Haas C, De Groot R, Hillebrecht F (1987) J Phys C Solid State Phys 20:4135
117. Khalid S, Malik MA, Lewis DJ, Kevin P, Ahmed E, Khan Y, O'Brien P (2015) J Mater Chem C 3:12068–12076
118. Huang L, Meng L (2007) Mater Sci Eng B 137:310–314
119. Mattila S, Leiro J, Laajalehto K (2003) Appl Surf Sci 212:97–100
120. Mattila S, Leiro J, Heinonen M (2004) Surf Sci 566:1097–1101
121. Schaufuß AG, Nesbitt HW, Kartio I, Laajalehto K, Bancroft GM, Szargan R (1998) Surf Sci 411:321–328
122. Lehner S, Savage K, Ciobanu M, Cliffel DE (2007) Geochim Cosmochim Acta 71:2491–2509
123. Lehner S, Savage K (2008) Geochim Cosmochim Acta 72:1788–1800
124. Savage KS, Stefan D, Lehner SW (2008) Appl Geochem 23:103–120
125. Rana TR, Khadka DB, Kim J (2015) Mater Sci Semicond Process 40:325–330
126. Kinner T, Bhandari KP, Bastola E, Monahan BM, Haugen NO, Roland PJ, Bigioni TP, Ellingson RJ (2016) J Phys Chem C 120:5706–5713
127. Xiao P, Fan X-L, Liu L-M, Lau W-M (2014) Phys Chem Chem Phys 16:24466–24472
128. Bhandari KP, Koirala P, Paudel NR, Khanal RR, Phillips AB, Yan Y, Collins RW, Heben MJ, Ellingson RJ (2015) Sol Energy Mater Sol Cells 140:108–114
129. Wang YC, Wang DY, Jiang YT, Chen HA, Chen CC, Ho KC, Chou HL, Chen CW (2013) Angew Chem Int Ed 52:6694–6698
130. Wei Z, Qiu Y, Chen H, Yan K, Zhu Z, Kuang Q, Yang S (2014) J Mater Chem A 2:5508–5515
131. Kilic B, Turkdogan S, Astam A, Ozer OC, Asgin M, Cebeci H, Urk D, Mucur SP (2016) Sci Rep 6:27052
132. Wang M, Chen C, Qin H, Zhang L, Fang Y, Liu J, Meng L (2015) Adv Mater Interfaces 2: 1500163
133. Ameri T, Li N, Brabec CJ (2013) Energ Environ Sci 6:2390–2413
134. Balasingam SK, Lee M, Kang MG, Jun Y (2013) Chem Commun 49:1471–1487
135. Lade S, Uplane M, Lokhande C (2001) Mater Chem Phys 68:36–41

136. Rincón M, Jiménez A, Orihuela A, Martınez G (2001) Sol Energy Mater Sol Cells 70:163–173
137. Hu Y, Zheng Z, Jia H, Tang Y, Zhang L (2008) J Phys Chem C 112:13037–13042
138. Goubard F, Wantz G (2013) Polym Int 63(8):1362–1367
139. Kirkeminde A, Ruzicka BA, Wang R, Puna S, Zhao H, Ren S (2012) ACS Appl Mater Interfaces 4:1174–1177
140. Murphy R, Strongin DR (2009) Surf Sci Rep 64:1–45
141. Herbert F, Krishnamoorthy A, Van Vliet K, Yildiz B (2013) Surf Sci 618:53–61
142. Bedja I, Hagfeldt A (2011) Adv OptoElectron 2011:824927
143. Cai W, Gong X, Cao Y (2010) Sol Energy Mater Sol Cells 94:114–127
144. Zhang F, Xu X, Tang W, Zhang J, Zhuo Z, Wang J, Wang J, Xu Z, Wang Y (2011) Sol Energy Mater Sol Cells 95:1785–1799
145. Richardson BJ, Zhu L, Yu Q (2013) Sol Energy Mater Sol Cells 116:252–261
146. Yan J, Shamim T, Chou SK, Li H, Luo L, Luan W, Yuan B, Zhang C, Jin L (2015) Energy Procedia 75:2181–2186
147. Nam M, Choi D, Kim S, Lee S, Lee K, Kim S-W (2014) J Mater Chem A 2:9758–9763
148. Choi H, Nahm C, Kim J, Kim C, Kang S, Hwang T, Park B (2013) Curr Appl Phys 13:S2–S13
149. Bedja I (2011) Mater Sci Poland 29:171–176
150. Song XM, Wu JM, Meng L, Yan M (2010) J Am Ceram Soc 93:2068–2073
151. Faber MS, Lukowski MA, Ding Q, Kaiser NS, Jin S (2014) J Phys Chem C 118:21347–21356
152. Wang D-Y, Li C-H, Li S-S, Kuo T-R, Tsai C-M, Chen T-R, Wang Y-C, Chen C-W, Chen C-C (2016) Sci Rep 6:20397
153. Wang M, Xue D, Qin H, Zhang L, Ling G, Liu J, Fang Y, Meng L (2016) Mater Sci Eng B 204:38–44
154. Gong M, Kirkeminde A, Xie Y, Lu R, Liu J, Wu JZ, Ren S (2013) Adv Opt Mater 1:78–83
155. Liu S, Wu J, Yu P, Ding Q, Zhou Z, Li H, Lai C-c, Chueh Y-L, Wang ZM (2014) Nanoscale Res Lett 9:1–7
156. Yang Z, Wang M, Shukla S, Zhu Y, Deng J, Ge H, Wang X, Xiong Q (2015) Sci Rep 5:11377
157. Ma B, Tong X, Guo C, Guo X, Guo X, Keil FJ (2016) RSC Adv 6:55220–55224
158. Wang D-Y, Gong M, Chou H-L, Pan C-J, Chen H-A, Wu Y, Lin M-C, Guan M, Yang J, Chen C-W, Wang Y-L, Hwang B-J, Chen C-C, Dai H (2015) J Am Chem Soc 137:1587–1592
159. Barawi M, Ferrer IJ, Flores E, Yoda S, Ares JR, Sánchez C (2016) J Phys Chem C 120:9547–9552
160. Cabán-Acevedo M, Kaiser NS, English CR, Liang D, Thompson BJ, Chen H-E, Czech KJ, Wright JC, Hamers RJ, Jin S (2014) J Am Chem Soc 136:17163–17179
161. Shukla S, Xing G, Ge H, Prabhakar RR, Mathew S, Su Z, Nalla V, Venkatesan T, Mathews N, Sritharan T, Sum TC, Xiong Q (2016) ACS Nano 10:4431–4440

Chapter 12
Application of Nanomaterials in Dentistry

Saad Bin Qasim and Ihtesham Ur Rehman

12.1 Introduction

Over the past few years, focus on the clinical application of nanobiomaterials in dentistry has been an area of interest to researchers worldwide. Nanotechnology is currently driving dental materials industry to substantial growth [1]. The advent of nanotechnology in dentistry seems to have answers to the mysteries or problems associated with conventional materials, as they have the tendency to mimic surface and interface properties of natural tissues. Nanotechnology has as a principle the ambitious challenge of precisely controlling individual particles in nanometer range. Some of the results are very relevant and have a major impact on human life and have already been adapted [2]. While the fields of tissue engineering and regenerative medicine have hinted at much promise over the last few decades, significant amount of research is still required with the field of nanotechnology to innovate new exciting materials that can overcome drawbacks of the existing biomaterials. Nanodentistry is still considered as an emerging field with a huge potential to yield new innovative generation of technologically advanced biomaterials in prosthodontics, orthodontics, periodontics, operatives, or restorative dental sciences. It is expected that nanodentistry will eventually give rise to highly efficient, effective, and personalized dental treatment [2].

S.B. Qasim
Department of Restorative and Prosthetic Dental Sciences, College of Dentistry, Dar Al Uloom University, Riyadh, Saudi Arabia

I.U. Rehman (✉)
Department of Materials Science and Engineering, Kroto Research Institute, University of Sheffield, Sheffield, UK
e-mail: i.u.rehman@sheffield.ac.uk

M.J. Jackson, W. Ahmed (eds.), *Micro and Nanomanufacturing Volume II*,
DOI 10.1007/978-3-319-67132-1_12

12.2 Dental Nanocomposites

Dental composites are among the most popular restorative materials for direct-filling capabilities. Composite resins are made up of a resin polymer matrix, coupling agent, inorganic filler, coloring agent, and initiator. Considering the variety of nanocomposites and resin-based dental materials containing nanoparticles currently has the highest feasibility for clinical use. Using nanoparticles allows the addition of larger amounts of fillers into dental resin composite compared to those containing microparticles (Fig. 12.1) [1].

Three pivotal attributes of composite resins are mechanical properties, physical nature, and aesthetics; all of these are affected by silica. Resin-based composites containing nanoparticles and nanoclusters exhibit a higher surface free energy that exerts differential behavior in terms of mechanical and physiochemical properties, such as excellent color density, low polymerization shrinkage, adequate surface brightness, low surface roughness, resistance to fracture, and excellent adherence to dental tissues [1, 3, 4]. Silica-based filler particles have been studied at nanoscale to enhance mainly the mechanical properties, thermal stability, and other physical properties. Studies conducted in the past have focused on issues related to polymerization shrinkage, resin and filler particles, nanoleakage, postoperative sensitivity, and secondary caries [5]. More recently novel nanoparticle of amorphous calcium phosphate (nACP) synthesized via spray drying technique and calcium fluoride nanoparticles were reinforced into composites. The addition of these nanoparticles in a ratio of 1.5 made the existing composite a SMART filling material. The release of Ca and P ions in acidic pH was enhanced, thereby affecting the carious activity [6].

In another study, nanogel particles have been used that were based on polymers with high molecular weight to address polymerization shrinkage and cavity wall stresses associated with polymerization of dental composites without changing other functional properties of the resins [7, 8]. A recent review by Melo and co-workers focused on the use of nanotechnology-based restorative materials for dental caries management. They mentioned that nanomaterials have great potential to decrease biofilm accumulation, to inhibit the demineralization process, to be used for remineralization tooth structure, and to combat caries-related bacteria. Agents such as silver, zinc oxide, calcium fluoride, calcium phosphate, quaternary ammonium polyethylenimine, nanohydroxyapatite (nHA), and/or nanofluorohydroxyapatite have been incorporated into various commercial and experimental restorative materials [9]. The antimicrobial potential of silver (Ag), zinc (Zn), and copper (Cu) to some extent has been well documented in the past. These metals and their oxides have been incorporated in a number of dental applications either alone or in combination with other ingredients, and the interest lies in replacing traditional micron-sized antimicrobial metal powders with their nanoscale counterparts. The superior properties of engineered nanomaterials are attributed to their enhanced surface area as well as their potential to interact directly with the bacterial cell wall. The choice of engineering nanoparticles depends on the final clinical application. For example, silver, zinc, and

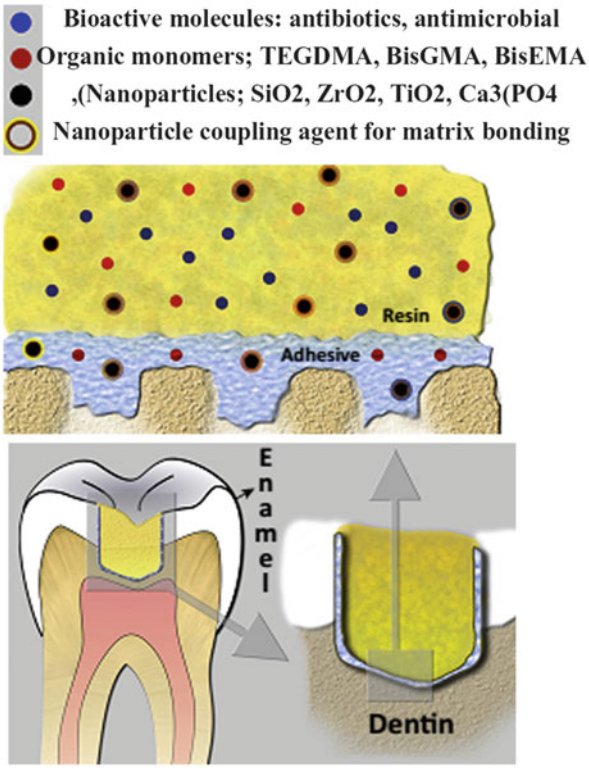

Fig. 12.1 The basic composition of new nanotechnological resin-based composite comprises of (1) inorganic nanoparticles that provide mechanical, aesthetics, antimicrobial remineralization, and drug delivery properties; (2) coupling agents (e.g., organosilanes) that increase nanoparticle bonding to the polymeric matrix; (3) organic monomers for the generation of the polymeric matrix; and (4) other possible bioactive molecules with the antimicrobial, anti-inflammatory, or antibiotic properties [1]

titanium dioxide nanoparticles are incorporated into resin-based composites or used as coating with antimicrobial properties for dental materials, while other bioactive glass nanopowders are used for root canal disinfectant [10].

12.3 Resin Modified Nano-glass Ionomer Cements

Glass ionomer cement (GIC) was invented by Wilson and Kent in 1969 and is based on a reaction of an acidic polymer and basic glass formulation [9]. The mixture of polyacrylic acid and an ion-leachable calcium fluoroaluminosilicate glass results in an acid-base reaction that forms a highly cross-linked structure that adheres to tooth structure. The advent of nanotechnology in glass ionomer cements has led to the development of nanofilled resin-modified GIC (RMGIC) originally developed by 3M ESPE-Ketac™ (KN). The nanoparticle range from 100 nm compared to 30 μm in conventional GIC.

A timeline reported by Khurshid et al. shown in Fig. 12.2 mentions about the evolution of glass ionomer cements [11]. According to 3M ESPE, using nanosized

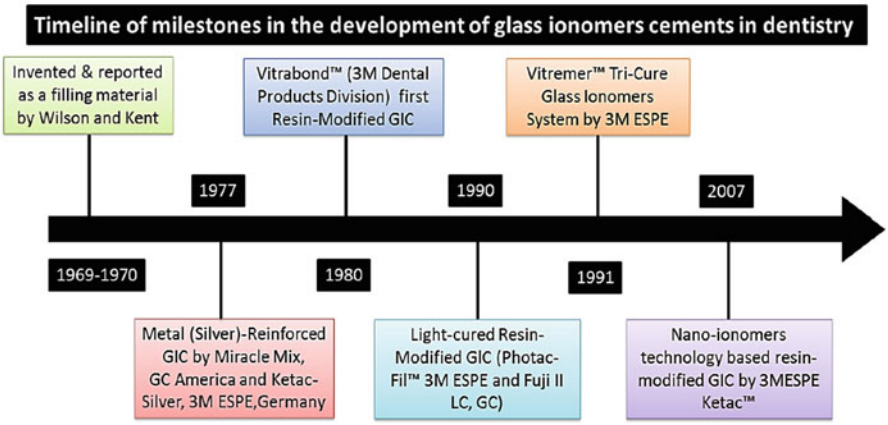

Fig. 12.2 A timeline of the milestones achieved to date on the development of glass ionomer cements for dental applications [11]

filler and clusters results in improved aesthetics; fluoride release is rechargeable after being exposed to topical fluoride source. However, studies have shown that the cumulative F release from KN was lesser than conventional GIC [12]. More recently, another nanofilled RMGIC (Equia system) has been developed. The fillers are composed of silica powder with an average size of 40 nm. The nanofillers tend to agglutinate in the resin matrix, which is used to develop a layer (35–40 μm thick) that seals and protects the surface of the restoration and adhesive interface between resin and tooth structure. Rehman and co-workers synthesized N-vinylpyrrolidone-containing polymer and altered the monomer sequence and incorporated into GIC liquid formulations. They used nanoparticle ranging from 50 to 100 nm for both HA and fluoroapatite; mechanical tests were suggestive of increased compressive and diametrical tensile strength [13].

In an attempt to enhance the mechanical and biophysical properties of powder liquid formulations of glass ionomer cements, various types of nanosized powders have been incorporated into the glass powder component. Some of the mechanical properties have been summarized in the Table 12.1.

12.4 Nanotech in Orthodontics

Arch wires play a critical role during the orthodontic treatment. Their primary goal is to generate mechanical force that are transmitted through the brackets to move the teeth in correct occlusion to relieve crowding or spacing. Currently stainless steel (SS) and nickel titanium (NiTi) arch wires are commonly used. Friction occurring when the wire slides in between the bracket slots are the primary factor

Table 12.1 Few powder modification of glass ionomer cements and their reported properties: *HA* hydroxyapatite, *FA* fluorohydroxyapatite, *FAS* fluoroaluminosilicate glass, TiO_2 titanium oxide, ZrO_2 zirconium oxide [14]

GIC formulation			Mechanical properties			
Liquid	Powder	Nanofiller percentage and size	Compressive strength (MPa)	Tensile strength (MPa)	Flexural strength (MPa)	Reference (s)
Polyacrylic acid copolymer	Unmodified FAS glass	No nanofillers, glass size: 3.34–9.6 μm	161	11.8	14.8	[15]
Polyacrylic acid copolymer	FAS Glass + HA	5 wt.%, 100–200 nm	178	19	31	[13]
Polyacrylic acid copolymer	FAS Glass + FA	5 wt.%, 100–200 nm	179	23	33	[13]
Polymer of AA, NVP, IA (8:1:1)	FAS Glass + HA	5 wt.%, 100–200 nm	183.8	23.5	36	[13]
Polyacrylic acid copolymer	FAS Glass + TiO_2	3%, size variable	176.27	–	23.17	[16, 17]
Polyacrylic acid copolymer	FAS Glass + HA/ ZrO_2	4 vol. %, particle dimension: 20 × 200 nm	176.30	12.67	–	[18]

influencing tooth movement. Recently nanoparticles have been used as a component of dry lubricants. Dry lubricants are aimed at reducing friction in between the two sliding surfaces. Biocompatible nanoparticles have been coated on SS wires. Inorganic fullerene like nanoparticles of tungsten disulfide, which are effective dry lubricants, has been assessed for self-lubricating coatings on orthodontic SS wires [19]. Another area where nanotechnology is used is the orthodontic elastomeric ligatures. These ligature wires have been used to place the arch wire securely in place during the treatment process. There potential to be used as a carrier scaffold to carry nanoparticles that are anticariogenic, anti-inflammatory, and/or drug-embedded molecules has also been looked into. Fluoride release from ligature wires reported an initial burst during the first and second day, followed by a logarithmic decrease [20]. Although the applications of nanotechnology in orthodontics are still in its infancy stage, the future looks very promising in terms of (1) nanodesigned orthodontic bonding materials, (2) nanovector for gene delivery for mandibular growth stimulation, and (3) nanomechanical sensors. In addition, these can be fabricated into the base of the orthodontic brackets and tubes to give real-time feedback about the applied orthodontic force being applied to the clinician and manage the treatment [21].

12.5 Endodontics (Pulp Regeneration)

Root canal disinfection is considered as the most critical and clinically acceptable step in regenerative or revascularization procedures. Regenerative endodontics aim to replace inflamed necrotic pulp tissues with regenerated pulp-like tissues to revitalize and improve life quality [22]. The most current regenerative endodontic strategy uses either triple or as an alternative a double antibiotic paste for approximately 1 month [23]. Subsequently the tooth is reinserted and irrigated, and the periapical tissues are lacerated with an endodontic file to induce bleeding. With bleeding growth factors and stem cells from the apical region repopulate the natural fibrin-based scaffold, triggering pulp-dentine complex regeneration [24].

It has been proposed by Kanaparthy and Kanaparthy that nanobots could be developed from parts with dimensions ranging from 1 to 1000 nm. These bots combined with nanosensors can be used for delivery of precise amount of therapeutic agents or drugs for delivery in pulp capping procedures [25]. The use of nanorobotic dentifrices when delivered by either mouthwash or toothpaste can cover all subgingival surfaces, thereby metabolizing all trapped organic matters into harmless and odorless vapors. However, there are conflicting views that remain with respect to the use of nanobots in vivo, which need to be addressed before nanotechnology can be absorbed in modern clinical dentistry [26]. The images of the first ever nanorobots were made by Peter S. Solarz, which showed a nanorobot performing dental restorative procedure on the occlusal surface of a molar (Fig. 12.3) as an aid to visualization; the artist depicted its size as 1000 times larger

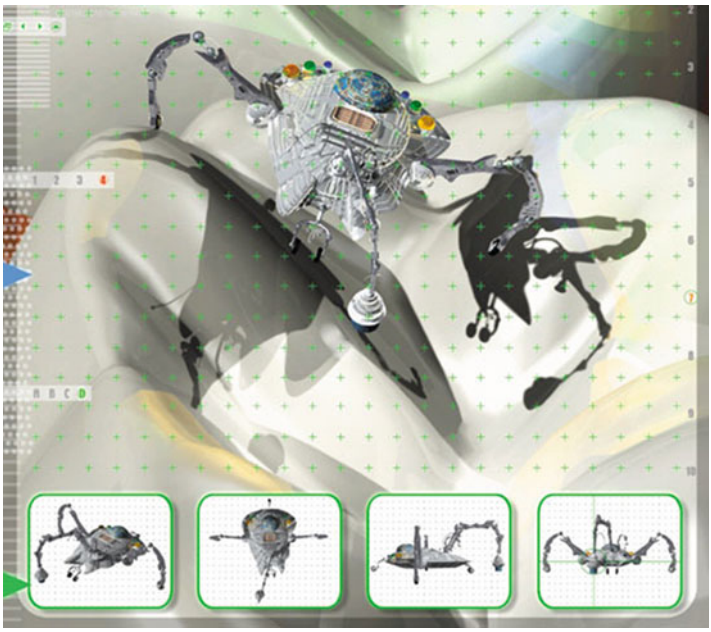

Fig. 12.3 Concept of nanorobots as proposed by Freitas Jr. [27] who mentioned about the use of micrometer-sized dental nanorobots that were reported to be constructed with the next 10–20 years in 2000, to allow precisely controlled oral analgesia, dentition replacement therapy using biologically autologous whole replacement teeth manufactured during a single dental office visit

than the actual size [27]. The dentifrobots are invisibly small (1–10 μm) with 103 to 105 nanodevices/oral cavity crawling at 1–10 μm/s [25].

Recently Bottino et al. reported the use of bioactive nanofibrous scaffolds for regenerative endodontics. They fabricated a fibrous composite scaffold using polydioxanone (PDS), metronidazole, or ciprofloxacin by electrospinning and proposed that the nano-/microfibrous scaffolds could potentially be used as a drug delivery system for root canal disinfection prior to regenerative endodontics [28]. In another study conducted by Bottino et al., they fabricated a 3D nanocomposite scaffold composed of PDS II and halloysite nanotubes (HNTs) by electrospinning. They reported that these scaffolds could potentially be good candidates for encapsulation of distinct bioactive molecules [29]. A technical hurdle to complete pulpal regeneration still remains as efforts made till now report the use of synthetic materials with biologic mechanism to achieve functional tissue regeneration. Future studies using infected root canals in vivo should be conducted to prove clinical relevance. Nevertheless an ideal regenerative therapy could possibly include root decontamination with an antimicrobial solution, followed by a cell-free bioactive scaffold to release its bioactive ingredients. Once a bacteria-free canal is created, scaffolds containing stem cells or growth factors could be placed to trigger development of pulpal tissue that will eventually form dentine-like tissue [30].

12.6 Nanoparticles in Adhesive Dentistry

Interest in the field of adhesive dentistry to improve and enhance the bond strength between the tooth and restorative material has excelled over the past decade or so. The incorporation of TiO_2 nanoparticles in dental adhesives was reported by Welch and co-workers; this work was aimed at achieving combined effect of bioactivity and on-demand bactericidal effect. Photocatalytic activity of adhesive incorporated with TiO_2 proved to interfere with the bacterial acidity and was found to have a positive effect on tooth remineralization in simulated body fluid [31]. The concept of self-healing adhesives is another very interesting aspect in adhesive dentistry. The concept of self-healing polymer relies on encapsulation of monomers and catalyst and reinforcing these encapsulated healing precursors into polymer. As the cracks are triggered, these capsules rupture and healing monomers fill the crack to polymerize the space, thereby allowing healing of the crack site. To allow for the healing agents in dental adhesives to reach the submicron spaces formed after acid etching, the dire need for nanoencapsulating agent is required. The incorporation of polyurethane nanocapsule loaded with the core materials of triethylene glycol dimethacrylate (TEGDMA) for use as a major ingredient in the self-healing bonding resin have been reported by Ouyang and co-workers. This nanoencapsulated monomers in dental adhesives have shown to enhance bond strength and could also improve bond strength in between the resin and tooth surface [32].

12.7 Impact of Nanotechnology on Dental Implants

Dental implants are now advised as an alternate to restoring teeth via crowns and bridges in clinical dentistry. The advent of nanotechnology in the field of implant dentistry has promised to produce surfaces with controlled architectural geometry and chemistry that would help in understanding the biological interactions and develop interfaces with predictable tissue-integrative properties [33, 34]. Surface and interface properties play a vital role in determining the biological interactions, specifically nanosized roughness, and chemistry has a critical role in the interactions of proteins and cells [35, 36]. Techniques such as grit blasting, anodization, acid etching, chemical grafting, and ionic implantation have been reported earlier as being able to alter the surface of metal implants [37]. Anodization has been commonly used to obtain nanoscale oxides on metal including titanium [38]. The OsseoSpeed surface (Astra Tech, AB, Molndal, Sweden) bears a nanotopography created by TiO_2 blasting followed by a hydrofluoric acid treatment, and over a micron rough titanium surface, 50–100 nm surface accretions of TiO_2 can be seen under a scanning electron microscopy (SEM) image [39]. Another nanoscale implant clinically available involves a calcium phosphate (CaP) nanoparticle modification of a minimally rough titanium alloy implant (Nanotite, 3i Implant Innovations, Florida, USA). This surface is achieved by particulate sol-gel deposition

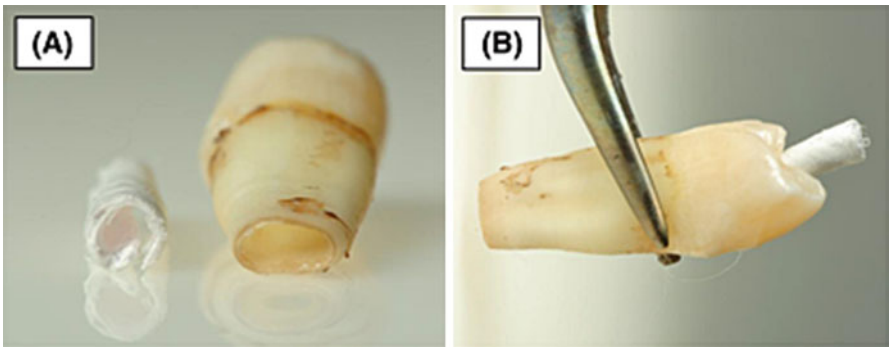

Fig. 12.4 Image illustrating how an electrospun tube can be inserted in the canal for regenerative endodontic possibilities. (**a** and **b**) Transverse and lateral views of extracted premolar tooth with a tubular electrospun scaffold placed adjacent (**a**) and inserted inside the tooth (**b**)

method using discrete crystalline deposition of CaP (size 20 nm) with surface coverage of around 50% [36]. A study conducted by Stavroullakis and co-workers was aimed at studying the in vitro effect of different implant treatments on cytokine production by human gingival fibroblasts. Different commercially available implants with nanotopographies were tested (Fig. 12.4). They concluded that sandblasted and turned implants significantly enhanced the secretion of interleukin [40] (Fig. 12.5).

12.8 Nanoparticles in Periodontal Regeneration

The regeneration of periodontal tissues lost as a consequence of destructive periodontal diseases still remains a major challenge for clinicians worldwide [41]. Tissue engineering approaches have been adapted to restore and reconstruct functionality of impaired tissues for decades [42]. A range of treatment options are adapted to regenerate lost periodontal ligaments, alveolar bone, and cementum. However, the outcomes of existing treatments are variable and unpredictable [41]. For these reasons, there has been much interest in developing methods for regenerating the lost tissues in order to restore dental function and aesthetics. This has been met by using biologically active agents and guided tissue regeneration (GTR) or guided bone regeneration (GBR) [43]. Adapting a functionally graded approach toward fabricating a bioactive trilayered membrane with structural and functional gradients that vary in morphology and composition has also been investigated by a number of researchers [28, 41–44]. Among these, Qasim and co-workers adapted a naturally derived biopolymer chitosan and synthetic hydroxyapatite (HA) to synthesize porous templates via freeze gelation and fibers in aligned and random orientation (Figs. 12.6 and 12.7) by electrospinning chitosan composite solution with ultrahigh molecular weight polyethylene oxide that could be used as a

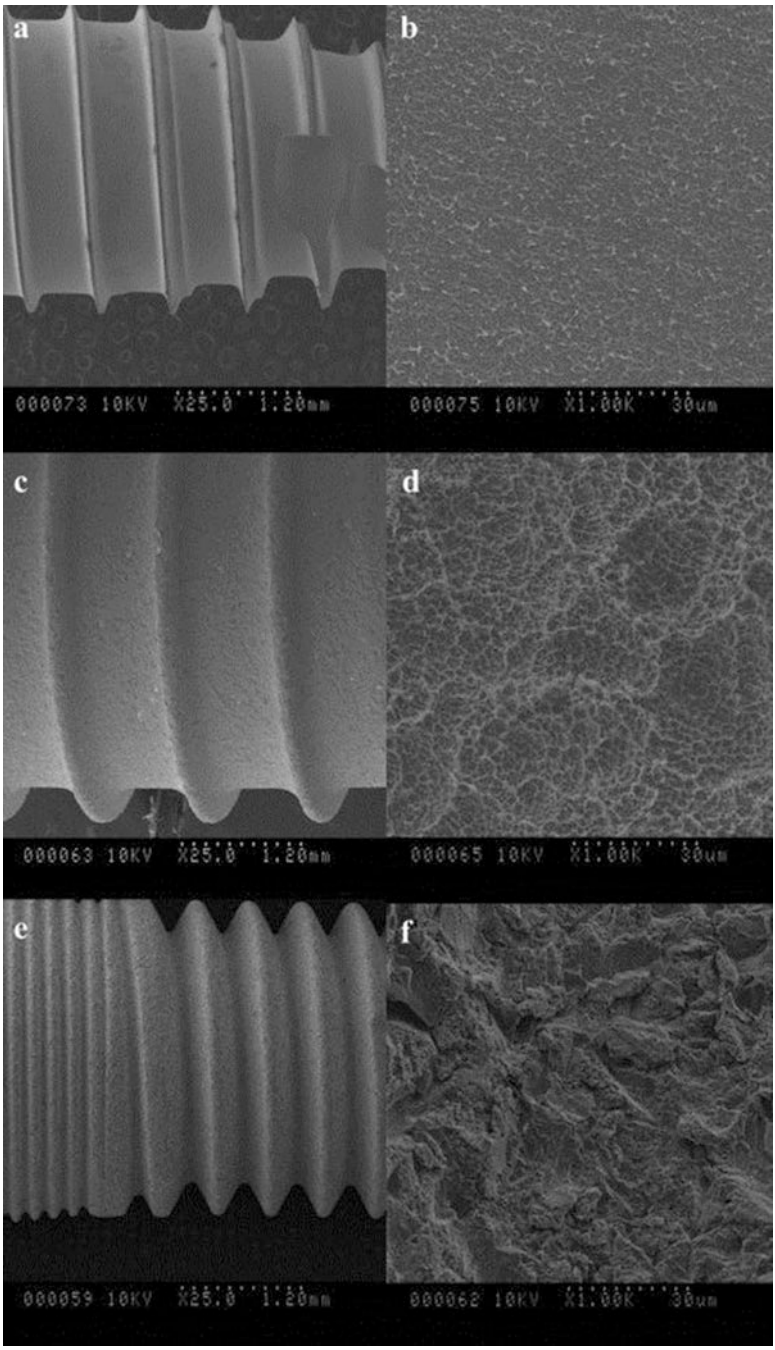

Fig. 12.5 SEM images of acid-etched commercial dental implants with nanotopographies. SEM: (**a**, **b**) correspond to 3i NanoTiteV R implant; (**c**, **d**) correspond to StraumannV R Standard implant; and (**e**, **f**) correspond to OsseoSpeedTM implant [40]

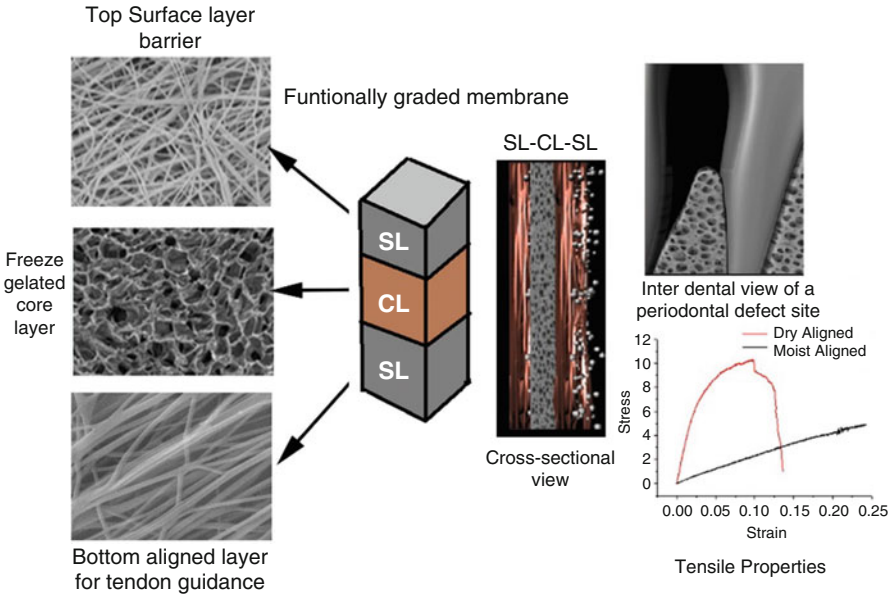

Fig. 12.6 Diagrammatic illustration by Qasim and co-workers of the functionally graded membrane using chitosan electrospun fibers for periodontal regeneration, also depicting a core layer of freeze gelated chitosan. Fibers have the potential to be loaded with bioactive ingredients for enhancing bone regeneration. Adapted with permission from Elsevier [41]

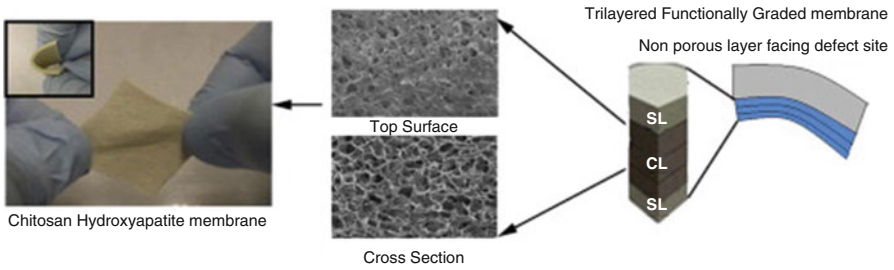

Fig. 12.7 Porous templates fabricated via freeze gelation to fulfill the criteria of a core layer in a trilayered membrane for periodontal regeneration as reported by Qasim and co-workers. Surface layer (SL), core layer (CL). Image showing handling capability of the synthesized membranes as well. Adapted with permission from Elsevier [43]

surface and core layer in a trilayered membrane for periodontal regeneration. The biological results reported showed that human embryonic stem cell-derived mesenchymal progenitor cells (hESMPs) not only exhibited attachment and proliferation but also promoted mineralized matrix deposition on both templates [41, 43]. Using nanosized hydroxyapatite and other bioactive agents such as alpha (α) tricalcium phosphate (TCP), beta (β) TCP, or even nanobioglasses can

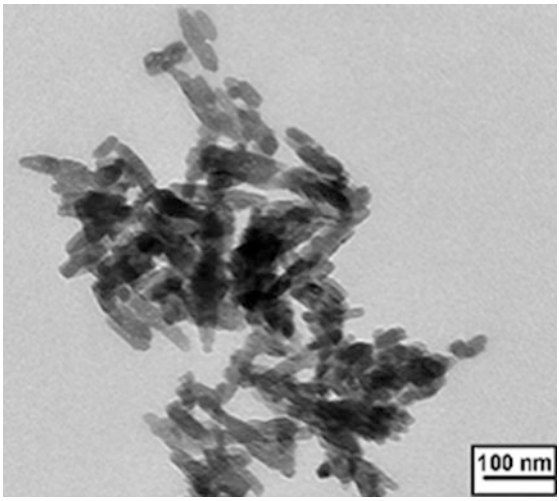

Fig. 12.8 A transmission electron microscopy micrograph depicting rod-shaped nanobioglass with an average size below 100 nm as reported by Peter and co-workers [47]

have an added advantage for regeneration of the lost bone microarchitecture. A similar work was also conducted by Siddiqui and Pramanik using micro- and nano-β-TCP [45].

The use of bioactive glass nanoparticles in dentistry alone and in composite formulations to act as scaffolds for periodontal tissue engineering has been gaining attention due to their reported superior bioactivity when compared with conventional micron-sized bioactive glass materials. Evidence from the literature suggests a more rapid mineralization in bones and teeth when in contact with nanosized bioactive glass [43, 46]. This rapid mineralization is attributed to the larger surface area and enhanced bioactivity.

The unique feature of bioactive glasses is that when they come in contact with the body a layer of carbonated apatite is developed which interacts with the mineralized tissue to form a strong bone. Peter et al. synthesized a composite scaffold with nanobioactive glass, chitosan, and gelatin using lyophilization and freezing techniques (Figs. 12.8 and 12.9). They reported that the swelling and degradation rate of the composite scaffolds decrease with addition of nanobioactive glass, and protein adsorption was enhanced simultaneously. Furthermore, the composite scaffolds showed good bioactivity and cellular attachment and spread compared to the control specimens [47].

The decrease size of these materials promotes cellular adhesion, enhances osteoblast proliferation and differentiation, and increases the biomineralization process. Moreover, using nanosized particles may provide a base for a more rapid release of calcium and phosphate. Zahid and co-workers conducted an extensive review of the biological properties of bioactive glasses and their composites. They reported that demerits of brittleness and low fracture toughness of conventional bioglasses can be addressed by designing scaffolds from micro- to nanoscale with ideal properties. Additions of inorganic metal oxides such as calcium oxide, potassium oxide, sodium oxide, and magnesium oxide can adjust the bioactivity

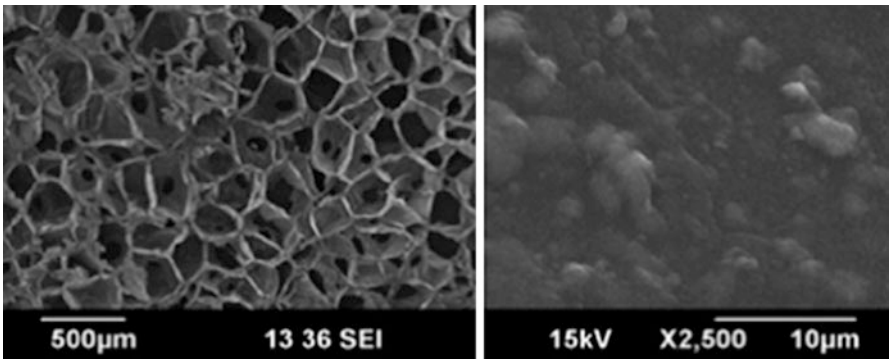

Fig. 12.9 Scanning electron micrographs of macroporous microstructure of composite scaffolds showing pores ranging from 150 to 300 µm as reported by Peter et al. [47]

rate. In addition to inclusions of zinc (ZnO), copper (CuO) and silver (AgO) can impart antibacterial properties. Zinc (Zn) and magnesium (Mg) can trigger osteoblast proliferation, differentiation, and bone mineralization. Strontium (Sr) reduces bone resorption and enhances bone healing [48].

Nanotechnology has also been adapted for drug delivery for treating periodontal diseases. Triclosan-loaded nanoparticles were reported by Pinon-Segundo and co-workers, prepared by emulsification process using poly-DL-lactide-co-glycolide, poly-D,L-lactide, and cellulose acetate polyvinyl alcohol (PVA) for use as a stabilizer. These triclosan-loaded nanoparticles were about 500 nm in size, and release profile study revealed that the depletion zone moved toward the center of the device as the drug was eluted. An in vivo study was conducted using these particles in dogs, with only gingival index and bleeding on probing being determined. Results showed that nanoparticles were able to effect the reduction of inflammation of experimental sites [46, 49]. Another example of the use of nanotechnology is the development of Arestin® in which tetracycline is incorporated into microspheres for drug delivery by local means to periodontal pocket [49, 50]. Nanofibers, nanorods, nanoplatelets, nanotubes, nanofibrils, and quantum wires are other major nanomaterials being widely explored for various applications of which management of periodontal disease could be a prime target [51].

12.9 Craniofacial Bone Tissue Engineering Approaches Using Nanoceramics

Bone tissue engineering approaches are used in clinical procedures such as restoration of alveolar bone after a chronic periodontal episode, peri-implantitis, sinus augmentation or lift, reconstructive surgery after a traumatic incident, or even after oral cancer. Nanobiomaterials have played a significant role in fabricating materials

with properties that are supportive of cellular attachment, proliferation, and differentiation. These innovative materials mimic natural tissue structure and function. Bone is an ideal example of naturally nanostructured composite material. It is composed of closely connected inorganic (bone apatite) and organic component, mainly collagen, due to to this functionally graded hierarchial nature of bone with the lowest level of osseous materials in nanoscale range, biomaterials with nanometer structure are logically natural choices for fabrication of bone implants and graft materials for bone osseous regeneration [52]. Surprisingly, even after four decades of research on bioactive glasses by numerous research clusters, no other bioactive glass composition has been found to have better biological properties than that of the original composition of Bioglass® 45S5. Traditionally glass fabrication was done either by sol–gel or melt-quenching route. Nanoparticles of silica can be formed using sol–gel route at room temperature. The physical difference between sol–gel and melt-derived glasses is that sol–gel glasses tend to have inherent nanoporosity. These porosities at nanolevel can enhance the cellular response and specific surface area [53]. More recently, a number of other techniques, such as unidirectional freezing of suspensions, solid free-form fabrication, polymer foam replication, and microemulsion techniques, have been employed to create nanostructured bioactive glass-based materials. The increased surface area of these nanoscale bioactive glasses has two significant effects, faster dissolution and therefore release of ions and higher protein adsorption. These products can eventually lead to enhanced bioactivity as well [54].

Other aspects of regeneration have also been explored using biomimetic scaffold with aligned porosity by Panseri et al. Calcium phosphate (Ca/P)-based ceramics are well known to mimic the natural mineralized phase of tooth and are a very promising solution to be used in dental reconstructive surgeries as well. Furthermore, they provide a suitable template for dental pulp stem cell growth and odontogenic differentiation. Magnesium-doped hydroxyapatite nanoparticles were synthesized on gelatin templates. The scaffolds were aimed at dentine regeneration. These scaffolds were blended with alginate, and the process of freeze-drying was adapted (Fig. 12.10). The processing parameters were harnessed in such a way that microscopic aligned channels were created which were suitable for tissue engineering applications [55].

12.10 Conclusion

Although the use of nanotechnology in dentistry is expanding continuously (Fig. 12.11), pragmatic challenges have hindered the clinical applications of new and emerging nanobiomaterials. A number of research groups and clusters are working tirelessly in this domain to enhance the versatility of this technology. On the other hand, the increase in development of nanotech products in dentistry requires a complete analysis and full appraisal before they can be added to the armory of clinicians. The ultimate fate of using nanobiomaterials is strongly

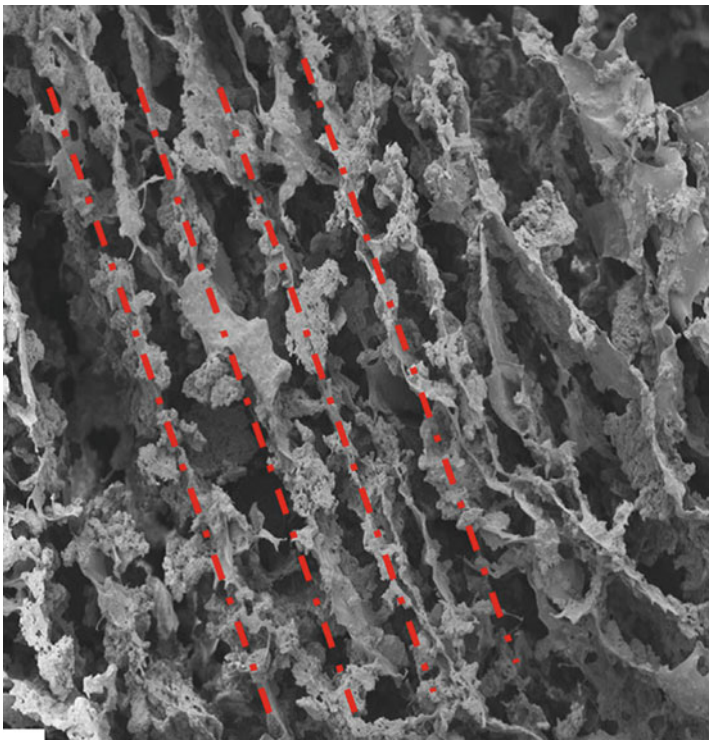

Fig. 12.10 Scanning electron microscopy of a biomimetic scaffold with aligned microporosity for dentine regeneration as reported by Panseri and co-workers [55]. The *dashed lines* depict the aligned porosity. Adapted with permission from Elsevier

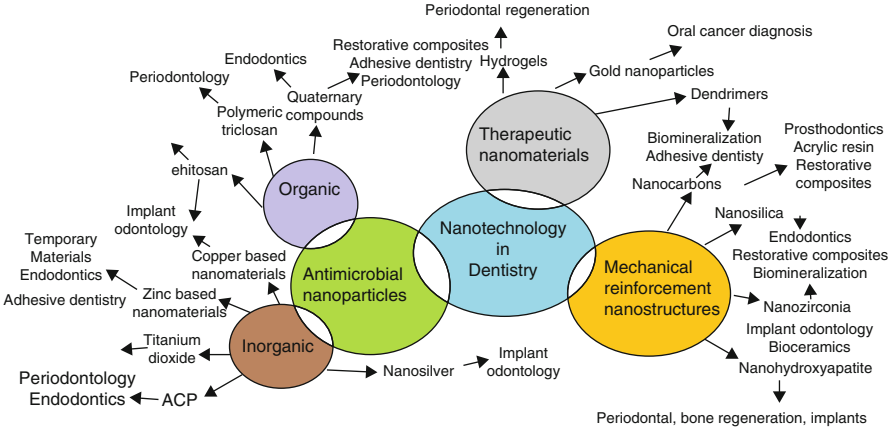

Fig. 12.11 Diagrammatic illustration of the uses of nanotechnology in dentistry

dependent on the precise selection of preclinical models suitable to evaluate the safety and efficacy of developing therapies in humans. Predictable tools such as "lab on a chip" may utilize saliva as a media to diagnose dental or other physical anomalies.

The scientific hurdle for nanobiomaterials in dentistry lies in understanding the interaction of materials being developed at the nanolevel with oral and maxillofacial tissues. Moreover, nanotechnology research will make way for development of tools and techniques that will allow clinicians to predict, diagnose, treat, and/or manage oral conditions at their earliest. These ideas may seem impossible at this stage; however, inventions have always been the brainchildren of outrageous ideas of both the clinicians and non-clinicians working in partnership to find new applications.

12.11 Research Recommendations

Although the potential benefits of engineered nanomaterials tend to overcome the drawbacks associated with them in dentistry, there are still several scientific aspects that need further exploration, which will ultimately improve the current knowledge and understanding of clinical interactions. Mechanistic research into how nanomaterials can strengthen tooth structure and further exploration of adding physiological function to nanoehnanced dental materials will deliver a paradigm shift in clinical dentisty. Further targeted investigations into the interactions of nanoparticles with oral biofilms are also the current need of time.

References

1. Padovani GC et al (2015) Advances in dental materials through nanotechnology: facts, perspectives and toxicological aspects. Trends Biotechnol 33:621–636
2. Subramani K, Ahmed W, Hartsfield JK (2012) Nanobiomaterials in clinical dentistry. William Andrew, Norwich
3. Curtis AR, Shortall AC, Marquis PM, Palin WM (2008) Water uptake and strength characteristics of a nanofilled resin-based composite. J Dent 36:186–193
4. Kim YS, Kwon HK, Kim BI (2011) Effect of nano-carbonate apatite to prevent re-stain after dental bleaching in vitro. J Dent 39:636–642
5. Ferracane JL (2011) Resin composite-state of the art. Dent Mater 27:29–38
6. Xu HHK et al (2010) Strong nanocomposites with Ca, PO_4, and F release for caries inhibition. J Dent Res 89:19–28
7. Moraes RR et al (2012) Improved dental adhesive formulations based on reactive nanogel additives. J Dent Res 91:179–184
8. Moraes RR et al (2011) Control of polymerization shrinkage and stress in nanogel-modified monomer and composite materials. Dent Mater 27:509–519
9. Melo MAS, Guedes SFF, Xu HHK, Rodrigues LKA (2013) Nanotechnology-based restorative materials for dental caries management. Trends Biotechnol 31:459–467

10. Besinis A, De Peralta T, Tredwin CJ, Handy RD (2015) Review of nanomaterials in dentistry: interactions with the oral microenvironment, clinical applications, hazards, and benefits. ACS Nano 9:2255–2289
11. Khurshid Z et al (2015) Advances in nanotechnology for restorative dentistry. Materials (Basel) 8:717–731
12. Paschoal MA et al (2011) Fluoride release profile of a nanofilled resin-modified glass ionomer cement. Braz Dent J 22:275–279
13. Moshaverinia A et al (2008) Modification of conventional glass-ionomer cements with N-vinylpyrrolidone containing polyacids, nano-hydroxy and fluoroapatite to improve mechanical properties. Dent Mater 24:1381–1390
14. Najeeb S et al (2016) Modifications in glass ionomer cements: Nano-sized fillers and bioactive nanoceramics. Int J Mol Sci 17(**7**):1134
15. Moshaverinia A et al (2008) Effects of incorporation of hydroxyapatite and fluoroapatite nanobioceramics into conventional glass ionomer cements (GIC). Acta Biomater 4:432–440
16. Elsaka SE, Hamouda IM, Swain MV (2011) Titanium dioxide nanoparticles addition to a conventional glass-ionomer restorative: Influence on physical and antibacterial properties. J Dent 39:589–598
17. Garcia-Contreras R et al (2015) Mechanical, antibacterial and bond strength properties of nano-titanium-enriched glass ionomer cement. J Appl Oral Sci 23:321–328
18. Gu YW, Yap AUJ, Cheang P, Khor KA (2005) Effects of incorporation of HA/ZrO_2 into glass ionomer cement (GIC). Biomaterials 26:713–720
19. Katz A, Redlich M, Rapoport L, Wagner HD, Tenne R (2006) Self-lubricating coatings containing fullerene-like WS2 nanoparticles for orthodontic wires and other possible medical applications. Tribol Lett 21:135–139
20. Wiltshire WA (1996) Determination of fluoride from fluoride-releasing elastomeric ligature ties. Am J Orthod Dentofac Orthop 110:383–387
21. Lapatki BG, Bartholomeyczik J, Ruther P, Jonas IE, Paul O (2007) Smart bracket for multidimensional force and moment measurement. J Dent Res 86:73–78
22. Yang J, Yuan G, Chen Z (2016) Pulp regeneration: Current approaches and future challenges. Front Physiol 7:58
23. Yassen GH, Chu TMG, Eckert G, Platt JA (2013) Effect of medicaments used in endodontic regeneration technique on the chemical structure of human immature radicular dentin: an in vitro study. J Endod 39:269–273
24. Murray PE, Garcia-Godoy F, Hargreaves KM (2007) Regenerative endodontics: a review of current status and a call for action. J Endod 33:377–390
25. Kanaparthy R, Kanaparthy A (2011) The changing face of dentistry: nanotechnology. Int J Nanomedicine 6:2799–2804
26. Shetty NJ, Swati P, David K (2013) Nanorobots: future in dentistry. Saudi Dent J 25:49–52
27. Freitas RAJ (2000) Nanodentistry. J Am Dent Assoc 131:1559–1565
28. Bottino MC et al (2013) A novel three-dimensional scaffold for regenerative endodontics: materials and biological characterizations. J Tissue Eng Regen Med. https://doi.org/10.1002/term.1712
29. Bottino MC et al (2012) Recent advances in the development of GTR/GBR membranes for periodontal regeneration—a materials perspective. Dent Mater 28:703–721
30. Albuquerque MT, Valera MC, Nakashima M, Nor JE, Bottino MC (2014) Tissue-engineering-based strategies for regenerative endodontics. J Dent Res 93:1222–1231
31. Welch K, Cai YL, Engqvist H, Stromme M (2010) Dental adhesives with bioactive and on-demand bactericidal properties. Dent Mater 26:491–499
32. Ouyang XB et al (2011) Synthesis and characterization of triethylene glycol dimethacrylate nanocapsules used in a self-healing bonding resin. J Dent 39:825–833
33. Tomsia AP, Lee JS, Wegst UGK, Saiz E (2013) Nanotechnology for dental implants. Int J Oral Maxillofac Implants 28:E535–E546

34. Tomsia AP et al (2011) Nanotechnology approaches to improve dental implants. Int J Oral Maxillofac Implants 26:25–44
35. Le Guehennec L, Soueidan A, Layrolle P, Amouriq Y (2007) Surface treatments of titanium dental implants for rapid osseointegration. Dent Mater 23:844–854
36. Mendonca G, Mendonca DBS, Aragao FJL, Cooper LF (2008) Advancing dental implant surface technology - From micron- to nanotopography. Biomaterials 29:3822–3835
37. Shokuhfar T (2014) Recent progress toward surface modification of bone/dental implants with titanium and zirconia dioxide nanotubes. J Nanotech Smart Mater 1:1–14
38. Zhang L, Han Y (2010) Effect of nanostructured titanium on anodization growth of self-organized TiO_2 nanotubes. Nanotechnology 21(5):055602
39. Cooper LF et al (2006) Fluoride modification effects on osteoblast behavior and bone formation at TiO_2 grit-blasted c.p. titanium endosseous implants. Biomaterials 27:926–936
40. Stavroullakis A et al (2015) Dental implant surface treatments may modulate cytokine secretion in Porphyromonas gingivalis-stimulated human gingival fibroblasts: a comparative study. J Biomed Mater Res A 103:1131–1140
41. Qasim SB, Najeeb S, Delaine-Smith RM, Rawlinson A, Ur Rehman I (2016) Potential of electrospun chitosan fibers as a surface layer in functionally graded GTR membrane for periodontal regeneration. Dent Mater 33:71–83
42. Qasim SB et al (2016) In-vitro and in-vivo degradation studies of freeze gelated porous chitosan composite scaffolds for tissue engineering applications. Polym Degrad Stab. https://doi.org/10.1016/j.polymdegradstab.2016.11.018
43. Qasim SB, Delaine-Smith RM, Fey T, Rawlinson A, Rehman IU (2015) Freeze gelated porous membranes for periodontal tissue regeneration. Acta Biomater 23:317–328
44. Bottino MC et al (2013) Bioactive nanofibrous scaffolds for regenerative endodontics. J Dent Res 92:963–969
45. Siddiqui N, Pramanik K (2014) Effects of micro and nano β-TCP fillers in freeze-gelled chitosan scaffolds for bone tissue engineering. J Appl Polym Sci 131. doi: 10.1002/app.41025
46. Hong Z et al (2010) Mono-dispersed bioactive glass nanospheres: Preparation and effects on biomechanics of mammalian cells. J Biomed Mater Res A 95:747–754
47. Baino F, Novajra G, Vitale-Brovarone C (2015) Bioceramics and scaffolds: a winning combination for tissue engineering. Front Bioeng Biotechnol 3:202
48. Zahid S et al (2016) Biological behavior of bioactive glasses and their composites. RSC Adv 6 (74):70197
49. Piñón-Segundo E, Ganem-Quintanar A, Alonso-Pérez V, Quintanar-Guerrero D (2005) Preparation and characterization of triclosan nanoparticles for periodontal treatment. Int J Pharm 294:217–232
50. Paquette DW, Hanlon A, Lessem J, Williams RC (2004) Clinical relevance of adjunctive minocycline microspheres in patients with chronic periodontitis: secondary analysis of a phase 3 trial. J Periodontol 75:531–536
51. Kong LX, Peng Z, Li SD, Bartold PM (2000) Nanotechnology and its role in the management of periodontal diseases. Periodontology 40:184–196
52. Tran N, Webster TJ (2009) Nanotechnology for bone materials. Wiley Interdiscip Rev Nanomed Nanobiotechnol 1:336–351
53. Jones JR (2013) Review of bioactive glass: from Hench to hybrids. Acta Biomater 9:4457–4486
54. Polini A, Bai H, Tomsia AP (2013) Dental applications of nanostructured bioactive glass and its composites. Wiley Interdiscip Rev Nanomed Nanobiotechnol 5:399–410
55. Panseri S et al (2016) Biomimetic scaffold with aligned microporosity designed for dentin regeneration. Front Bioeng Biotechnol 4:48

Chapter 13
Electrical Conductivity of CVD Diamond Thin Films

Mahtab Ullah, R.A. Manzoor, and E. Ahmed

13.1 Introduction

For semiconductor applications, low resistivity, smooth, and good-quality diamond films with nanograins are highly desirable. Considerable research has been conducted to increase the growth rate of diamond by varying many parameters such as deposition pressure, gas flow rate, substrate temperature, etc. Rau and Picht [1] showed that the mass transport in the gas phase plays an important role during diamond growth. Nucleation and growth of diamond films can be controlled by the mass transport rate at high substrate temperatures instead of any chemical reaction rate occurring on the surface at these temperatures. In the past decade, various researchers reported different results by varying gas flow rates in the deposition chamber. For instance, Fan et al. [2] reported no effect of gas flow on the growth rate. In another study, Yu et al. [3] have demonstrated that growth rate increases by increasing the gas flow rate, while Celii et al. [4] reported that the gas flow had little effect on the growth rate. Thus, in order to depict the effects caused by various gas flow rates in the deposition chamber, more research is needed.

The transport of diverse gas species (formed during deposition inside the HFCVD system) to the substrate plays a significant role in diamond film growth [1]. These species are affected by various factors such as deposition pressure, filament temperature, composition of the incoming gases, etc. Influence of deposition pressure among all of the abovementioned parameters is very important for the growth of diamond, because it changes both the gas phase chemical reaction

M. Ullah (✉)
Department of Physics, Government College University Faisalabad Layyah Campus, Layyah, Pakistan
e-mail: mahtabullah@yahoo.com

R.A. Manzoor • E. Ahmed
Department of Physics, Bahauddin Zakariya University, Multan, Pakistan

M.J. Jackson, W. Ahmed (eds.), *Micro and Nanomanufacturing Volume II*,
DOI 10.1007/978-3-319-67132-1_13

kinetics and the gas phase fluid dynamics among diverse gas species in a chemical vapor deposition chamber [5]. The deposition pressure for diamond film growth used in HFCVD is in the range from numerous tens to quite a few hundred mbar, which directs diamond nucleation density of 10^7–10^8 cm^{-2} [6, 7]. By applying negative bias to the substrate, Makris et al. [8] and Pecoraro et al. [9] have obtained diamond films with high nucleation density 10^{10}–10^{11} cm^{-2} at 30 mbar and 15 mbar, respectively. Lee et al. [10] and Jiang et al. [11] noted high diamond nucleation density 10^{10}–10^{11} cm^{-2} on Si substrates under very low pressure (0.13 mbar, 1.3 mbar). Yang et al. [12] have deposited diamond thin film by graphite etching through hydrogen as carbon source in HFCVD reactor without plasma discharge. High-quality diamond films have also been deposited at temperatures as low as 250 °C using microwave plasma reactor [13].

Preparation and characterization of nanocrystalline diamond films have been of great interest in the last few years. Many researchers [14–16] have studied the role of oxygen addition into ($CH_4 + H_2$) plasma polycrystalline diamond growth and have investigated that O_2 addition reduces impurity incorporation and improve quality of the diamond [15, 16]. Many researchers have found that CH_x and C_2H_x radicals are main contributors to the characteristics of diamond synthesized using gas phases [17–24]. CH_x radicals are the precursors of diamond, and C_2H_x radicals are those of non-diamond components. As a result, as the ratio C_2/CH decreases, high-quality diamond is formed [22, 23]. So the decrement of C^o radicals in the plasma is significant for high-quality diamond. Adding O_2 to the feed gas can decrease C^o radicals in the plasma and generates O and OH radicals in the chamber. These two species (O and OH) can etch the non-diamond component more rapidly than atomic H [23, 24]. Hence, it is considered that the increase of OH radicals and the decrease of C^o radicals in the plasma cause the enhancement of diamond quality in the $CH_4/H_2/O_2$ systems. In the HFCVD chamber, the dissociation of feeding gases H_2, CH_4, and O_2 is very effective. Many additional reaction species containing O_2 are created with the addition of O_2 in the CH_4/H_2 plasma. These additional O_2 species absolutely vary the gas phase chemistry and effect the formation of grains in diamond thin films with various morphologies and mixed textures. However, very little work is found on the influence of O_2 addition on the resistivity and growth rate of diamond films in HFCVD system.

Diamond films grown by HFCVD are polycrystalline and highly defective, and properties of these films differ from perfect diamond [25]. The doping and various deposition conditions may be responsible for defects such as dislocations, line defects, self-interstitial point defects, stacking faults, and species of grain boundaries, which show significant effects on the properties of diamond films [26]. Such doped diamond films can be made attractive for semiconducting applications [27]. The p-type and n-type conductivity in diamond can be obtained either by doping of boron [28] or nitrogen [25]. These doped p-type and n-type diamond films have some limitations, and it is challenging to achieve effective conductivity

[29, 30]. Effects of nitrogen and oxygen (O_2) accumulation on the growth and morphology of polycrystalline diamond films have been investigated by some researchers [31–33]. Ahmed et al. [34] have used nitrogen to control the surface morphology of diamond thin film using CVD system. Ando et al. [35] have found that growth parameters and film properties for conventional HFCVD reactor are different from that for a MPCVD system. It is expected that the source of nitrogen impurities, which are unintentionally incorporated into the diamond film, is mainly from the leaking of atmospheric air into the deposition chamber [26]. As covalent radius of nitrogen is comparable to that of carbon ($r_C = 0.77$ Å, $r_N = 0.75$ Å), it has been observed, at low concentration, that it occupies the diamond lattice sites producing substitution nitrogen-doped semiconducting and superconducting diamond films [36]. However, at high-nitrogen concentration, it may be incorporated in cluster form that may produce changes in bonding and morphological structure of the films [37]. Ma et al. [38] observed a shrink in grain size from 15 ± 0.02 to 9 ± 0.02 nm of nitrogen-incorporated NCD films synthesized by MP CVD in a gas mixture of $CH_4/H_2/N_2$ with varying nitrogen concentration in a wide range (0–75%). In contrast, some researchers observed that grain size increases with the addition of nitrogen gas (up to 25%) in the DC arc plasma jet CVD diamond films [39], ultrananocrystalline diamond (UNCD) films and nano-wires [40, 41] synthesized by microwave plasma CVD. Current status of understanding nitrogen doping of diamond remains unclear, and the subject still requires a thorough and systematic study.

In previous decade, researchers started to add boron dopants in the diamond films, making them p-type semiconductors [42]. High boron doping can change insulating diamond films into films with metallic character and hence make them potential materials for their applications in electrical appliances. That is why, preparing high-quality boron-doped diamond (BDD) films is very important. Due to smaller atomic radius of boron as compared to other potential dopants, it is easy to synthesize the electrical conducting diamond with higher-doping levels [43]. However, B-containing gases such as B_2H_6 and BCl_3 used for the deposition of diamond films are potentially hazardous. A very simple and effective way to produce B-doped diamond films by an ex situ heat treatment procedure can be applied instead of an in situ doping using volatile gases [44]. In a novel deposition technique, boron carbide (B_4C) block (3×3 in.) was positioned close to the film at a temperature of around 2300 °C for 20 h during CVD diamond growth. It is expected that this B_4C may act as a suitable boriding agent for diamond in the same way as it does for metals [44].

The main focus of this investigation was to elaborate and demonstrate the effect of varying methane (CH_4) concentration and/or changing pressure in the reaction chamber as well as to characterize diamond films by adding various gaseous species

such as oxygen (O_2) and nitrogen (N_2) or by incorporating boron, tantalum, etc. on film growth, crystal quality, grain size, and surface morphology of diamond films grown by HFCVD technique.

13.2 Fabrication of Diamond Thin Films

Microcrystalline diamond films were deposited onto silicon (Si) substrate using HFCVD. Circular Si(1 0 0) wafers ($\varphi = 10$ cm) with smooth and plane surface were used as substrates, prior to deposition, the wafers were ultrasonically cleaned in ethanol, deionized water and hydrofluoric acid (HF) to remove the oxide layer. Silicon substrates on 8 cm molybdenum holder were placed into the reaction chamber. Hydrogen and 1% methane in N_2 were introduced simultaneously into the reaction chamber at various flow rates (Table 13.2). The pressure in the chamber was maintained at 30 mbar or as described in Table 13.2. The source gases ($CH_4 + H_2$) were thermally activated by 0.5 mm thick eight coplanar tungsten filaments separated by 5 mm spacing. Gas flow rates were controlled by using a precision mass flow controller. Deposition time was about 20 h. Temperature of filament and substrate was ~2800 °C and 900 °C, respectively, measured by thermocouples placed close to them. As grown films were examined using SEM (LEO 1550 with acceleration voltage of 10 kV), X-ray diffraction spectroscopy (D500, Cu Kα, $\lambda = 0.1541$ nm) and Raman spectroscopy with visible excitation [97] at room temperature. Raman spectra were analyzed with a backscattering geometry using 514 nm lines of an Ar + laser. Spectra were collected using Renishaw 2000 micro-Raman system. A laser output of 10 mW was used, and the laser spot was focused on the sample surface using a 20× objective with short-focus working distance. The resistivity was investigated using a 4-point probe current/voltage in van der Pauw (1958) geometry at room temperature with maximum voltage of ±100 V. The current and voltage were measured using a semiconductor device analyzer (Agilent B1500A).

A summary of the deposition parameters/conditions set during the fabrication of diamond films is shown in Tables 13.1 and 13.2.

Table 13.1 HFCVD parameters used/set for diamond film deposition

Process variables	Operating parameters
Tungsten filament diameter (mm)	0.5
Deposition time (h)	20
Gas mixture (vol.%)	1% CH_4 and 99% H_2
Gas pressure (mbar)	30 (or varied from 10 to 50 as required)
Substrate temperature (°C)	900 ± 10
Filament temperature (°C)	2800 ± 50
Inter-wire distance of filament (mm)	5
Distance from filament to substrate (mm)	Varied from 5 to 20 as required

Table 13.2 Other growth parameters used for doped or un-doped diamond films

Condition/ doping	Sample	H_2 (sccm)	CH_4 (sccm)	O_2 (sccm)	Time (h)	Pressure (mbar)	Content (vol. %)
Oxygen doping	(a)	300	3	0.00	20	30	0.000
	(b)	300	3	0.01	20	30	0.003
	(c)	300	3	0.02	20	30	0.007
	(d)	300	3	0.03	20	30	0.010
	(e)	300	3	0.04	20	30	0.013
Nitrogen doping	N_2						
	(a)	300	3	0.00	20	30	0.000
	(b)	300	3	0.04	20	30	0.013
	(c)	300	3	0.08	20	30	0.026
	(d)	300	3	0.32	20	30	0.105
	(e)	300	3	0.64	20	30	0.210
Boron doping	*B*						
	(a)	300	3	–	20	20	0.000
	(b)	300	3	–	20	30	0.000
	(c)	300	3	–	20	40	0.000
	(d)	300	3	–	20	20	0.64
	(e)	300	3	–	20	30	1.77
	(f)	300	3	–	20	40	2.05
CH_4	(a)	300	20	–	20	30	6.25
	(b)	300	30	–	20	30	9.09
	(c)	300	40	–	20	30	11.76
	(d)	300	50	–	20	30	14.29
Pressure effect	(a)	300	3	–	20	10	–
	(b)	300	3	–	20	20	–
	(c)	300	3	–	20	30	–
	(d)	300	3	–	20	40	–
	(e)	300	3	–	20	50	–

13.2.1 Low Resistance Polycrystalline Diamond Thin Films Deposited by Hot Filament Chemical Vapor Deposition

For semiconductor applications, low resistivity, smooth, and good-quality diamond films with nanograins are highly desirable.

Considerable research has been conducted to increase the growth rate of diamond by varying many parameters such as deposition pressure, gas flow rate, substrate temperature, etc.

Rau et al. [1] showed that the mass transport in the gas phase plays an important role during diamond growth. Nucleation and growth of diamond films can be controlled by the mass transport rate at high substrate temperatures instead of any chemical reaction rate occurring on the surface at these temperatures. In the past decade, various researches reported different results by varying gas flow rates in the deposition chamber. For instance, Fan et al. [2] reported no effect of gas flow on the growth rate.

In another study, Yu et al. [3] have demonstrated that growth rate increases by increasing the gas flow rate, while Celii et al. [4] reported that the gas flow had little effect on the growth rate. Thus, in order to depict the effects caused by various gas flow rates in the deposition chamber, more research is needed. This research was carried out to understand the changes caused by methane concentration on the growth rate of diamond.

13.2.1.1 Structural Studies

Figure 13.1 shows representative spectra of diamond thin films with a typical diamond (cubic) structure. The characteristic (1 1 1), (2 2 0), (3 1 1), and (2 2 2) peaks of diamond structure are clearly visible at 2θ values of 43°, 75°, 91°, and 95°. Few weak silicon (carbide) peaks [JCPDS Card Nos. 77-2111 (Si), 74-1302 (SiC)] are also present, and their presence may be justified since silicon was used as the substrate material for the deposition of diamond thin films. The FWHM of the diamond (1 1 1) or (2 2 2) XRD peak observed at 2θ angles of ~43° (or ~95°) can be used as a qualitative measure of the degree of crystallinity within the diamond deposit. The FWHM is dependent on both the grain size and the crystallinity and usually has a tendency to become narrow when the grain size becomes large. A comparison of (1 1 1) diamond peak for a series of depositions at various gas

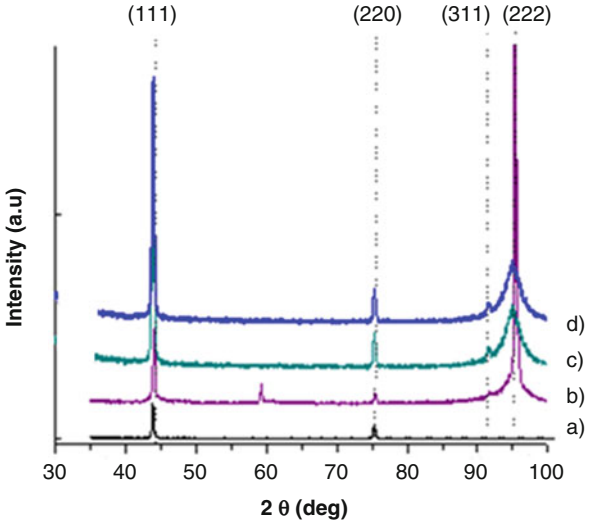

Fig. 13.1 XRD patterns of four diamond films with various methane concentrations (vol.%), (**a**) 6.25, (**b**) 9.09, (**c**) 11.76, (**d**) 14.29

concentration revealed an increase in intensity (see Fig. 13.1). Higher-gas concentrations lead to a considerable variation in the intensity of all (1 1 1), (2 2 0), (3 1 1), and (2 2 2) signals. FWHM of the XRD (1 1 1) peak clearly demonstrates improvements in terms of grain size of the diamond polycrystals with the gas concentration, while higher concentration leads to degradation in grain size due to high nucleation rate with some outgrowth (2 2 2) peak in Fig. 13.1. This morphological trend is in agreement with those of Yu et al. and Chen et al. [45, 46]. From these experimental findings, it can be said that an appropriate gas concentration can improve the quality of diamond crystals.

13.2.1.2 Effect on Morphology

In SEM micrographs Fig. 13.2c, d, some outgrowth has been observed, which can be related with the carbon conversion efficiency. It is calculated mathematically using formula explained by Bataineh et al. [47]:

$$\begin{aligned}
&\text{Carbon supplied (atoms/h)} \\
&\quad = \frac{D(\text{sccm}) \times \left(60(\text{min/h}) \times \text{No.of atoms in one mole of gas}\right.}{\text{Volume of one mole of gas (cc)}} \\
&\quad = \frac{D\ (\text{sccm}) \times \left(60(\text{min/h}) \times 6.024 \times 10^{23}(\text{atoms})\right.}{22,400(\text{cc})} \\
&\quad = 1.61 \times 10^{21}\text{D(in gasous state)} \\
&\text{Carbon added to the film (atoms/h)} \\
&\quad = \frac{C(\text{g/h}) \times \text{No.of C atoms per cm}^3}{\text{Density of diamond (g/cm}^3)} \\
&\quad = \frac{C(\text{g/h}) \times 1.79 \times 10^{23}(\text{atoms})}{3.515(\text{g/cm}^3) \times 1(\text{cm}^3)} \\
&\quad = 5.0925 \times 10^{22}\ \text{C (solid phase)} \\
&\%\text{Carbon conversion efficiency} \\
&\quad = \frac{\text{carbon added to the film}}{\text{carbon supplied by gas}} \times 100 \\
&\quad = 3156 \times \left(\frac{C}{D}\right)\%
\end{aligned} \tag{13.1}$$

where C (g/h) is the amount of carbon that is added to the film and D (sccm) is the carbon that is supplied by mixture of gases ($CH_4 + H_2$). When methane content is very high, carbon to diamond conversion efficiency shows an increase for a moment and then it becomes normal. Behavior of carbon conversion efficiency for present polycrystalline films is comparable to that of Bataineh et al. [47].

SEM micrographs in Fig. 13.2 show that with increasing gas flow rate, film surface morphology gradually changes from small grain size to enhanced growth/grain size. At low methane concentration (6.25 vol.%), highly oriented and well-faceted microcrystalline diamond films (average grain size 2.5 ± 0.02 μm) were

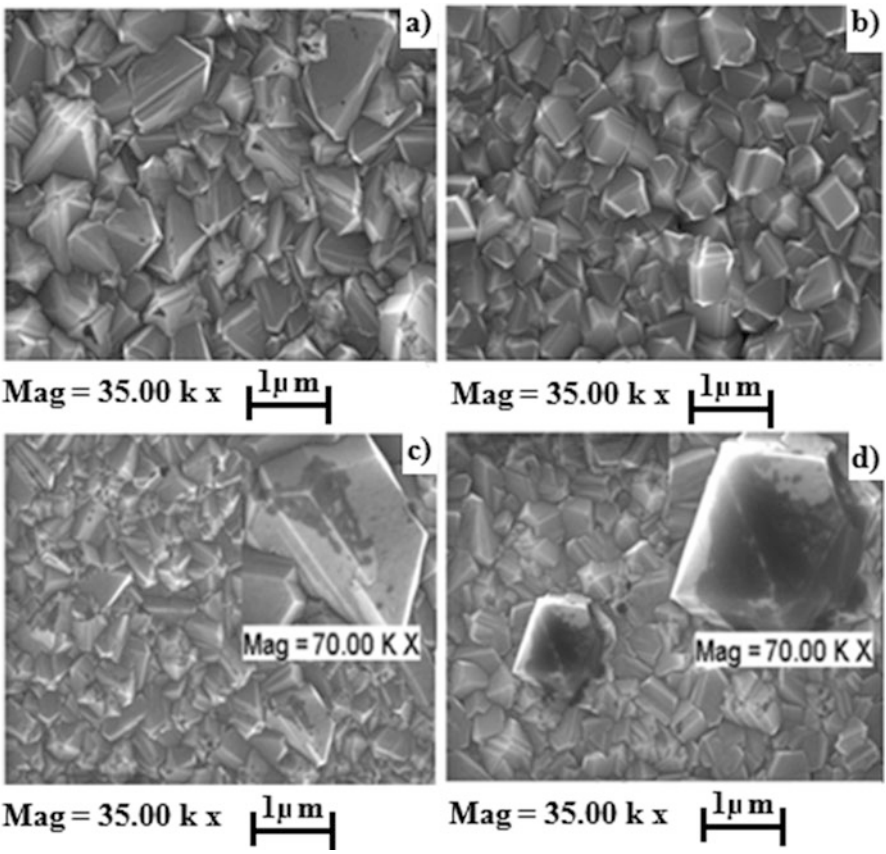

Fig. 13.2 SEM micrographs of four diamond films at various methane concentrations (vol.%), (**a**) 6.25, (**b**) 9.09, (**c**) 11.76, (**d**) 14.29. Insets in Figures **d** and **e** are their corresponding SEM images at 70 K× magnifications

deposited (Fig. 13.2a). On increasing methane concentration to 9.09 vol.%, grain size reduced to 1.3 ± 0.02 μm with well-faceted grain orientations (Fig. 13.2b). Further increase in the methane content from 11.76 to 14.29 vol.% (Fig. 13.2c, d) resulted overgrowth of diamond grains (2.9 μm) with some amorphous spot on them. This indicates prevailing effects of gas flow rate on diamond growth rate. This behavior of diamond growth is totally opposite to that observed by Yu et al. [45]. Its reason may be the conversion efficiency at high methane content as explained by Bataineh et al. [47].

13.2.1.3 Effect on Crystal Quality

Micro-Raman spectroscopy was applied in the wave number range 100–2000 cm^{-1} to compare the quality of diamond crystals grown at different methane concentrations. At low methane concentration Fig.13.3 depicts a sharp peak at 1332 cm^{-1}

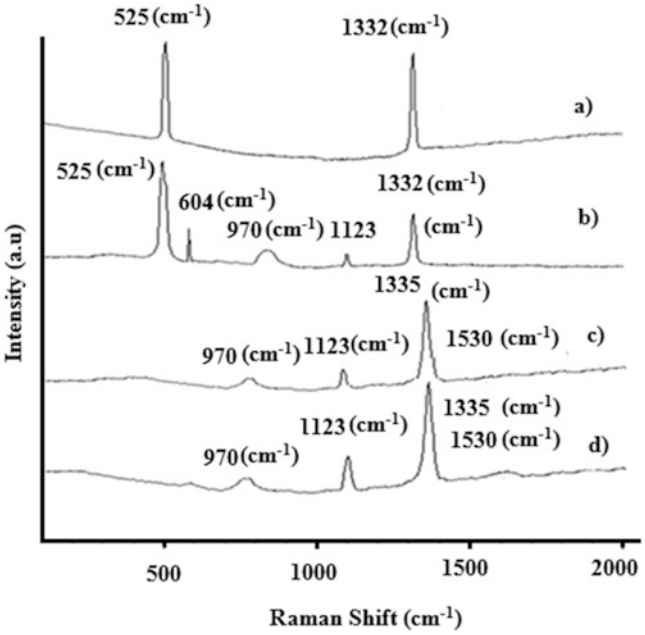

Fig. 13.3 Raman spectra of four diamond films at various methane concentrations (vol.%), (**a**) 6.25, (**b**) 9.09, (**c**) 11.76, (**d**) 14.29

linked to natural diamond. At comparatively high concentration of methane, this peak shifts to 1335 cm^{-1}, which might be due to compressive stresses originated by higher methane content. Local outgrowth in the diamond crystals increases simultaneously with rise of methane concentration at a pressure ~30 mbar (Figs. 13.3c, d). This outgrowth in local diamond raises the internal stresses and appears to be responsible for down grading of diamond quality as calculated by Eq. (13.1).

This unwanted snoozing can be minimized by optimizing the methane concentration. Shifting of diamond peak and outgrowth has also been observed by Schwarz et al. [48] at pressures of 30 and 50 mbar. Another peak around 1530 cm^{-1} (G band) originating from disordered and glassy amorphous carbon in the vicinity of grains did not appear at low methane concentration but appeared at high methane concentration. The peak observed at 1123 cm^{-1} is ascribed to amorphous networks/nanocrystalline diamond [48].

Two extra peaks around 525 and 604 cm^{-1} induced by local disorder [49] at low methane concentration disappeared at high concentration. Moreover, FWHM of diamond peak at 1332/1335 cm^{-1} is increasing with increasing methane concentration. The area under diamond peak increases with increasing methane concentration as noted by Silva et al. [50] and others [51–53].

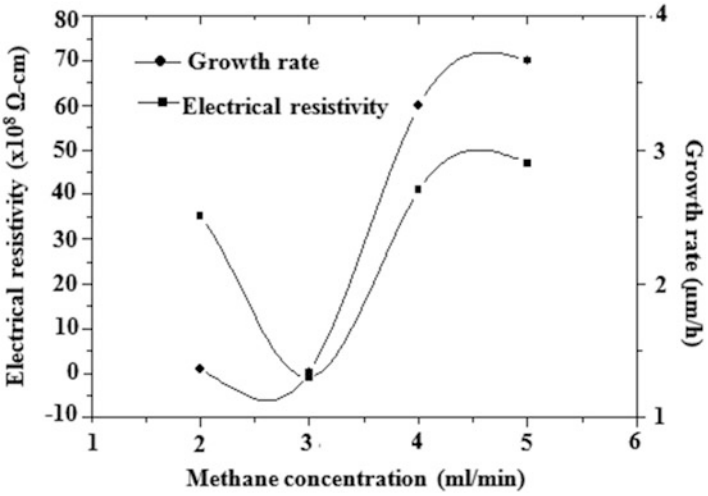

Fig. 13.4 Electrical resistivity (*left*) and growth rate (*right*) as a function of methane concentration

13.2.1.4 Effect on Growth Rate

Effect of methane concentration on diamond growth rate as determined from different cross-sectional SEM measurements is depicted in Fig. 13.4 (right), which indicates in general an increase with rise of methane concentration. Diamond growth rate increases as a consequence of increasing amount of atomic hydrogen and diamond precursors on the substrate. Similar results were observed by others [54–57]. Electrical resistivity (Fig. 13.4 (left)) is low at low methane concentration but increases at higher methane concentrations. Lower resistivity may be due to rise of sp^2/sp^3 ratio at low methane concentration [38] as observed in Raman spectra (Fig. 13.3). A minimum in resistivity (1.79×10^7 Ω cm) is obtained at CH_4 concentration of 9.09 vol.%. The rise of electrical resistivity at high methane concentrations may be due to outgrowth of local diamond.

13.2.2 Effect of Reactor Pressure on Electrical and Structural Properties of Diamond Films Grown by Hot Filament CVD

The transport of diverse gas species (formed during deposition inside the HFCVD system) to the substrate plays a significant role in diamond film growth [1]. These species are affected by various factors such as deposition pressure, filament temperature, composition of the incoming gases, etc. Influence of deposition pressure among all of the abovementioned parameters is very important for the growth of

diamond, because it changes both the gas phase chemical reaction kinetics and the gas phase fluid dynamics among diverse gas species in a chemical vapor deposition chamber [19]5]. The deposition pressure for diamond film growth used in HFCVD is in the range from numerous tens to quite a few hundred mbar, which directs diamond nucleation density of 10^7–10^8 cm^{-2} [6, 7]. By applying negative bias to the substrate, Makris et al. [8] and Pecoraro et al. [9] have obtained diamond films with high nucleation density 10^{10}–10^{11} cm^{-2} at 30 mbar and 15 mbar, respectively. Lee et al. [10] and Jiang et al. [11] noted high diamond nucleation density 10^{10}–10^{11} cm^{-2} on Si substrates under very low pressure (0.13 mbar, 1.3 mbar). Yang et al. [12] have deposited diamond thin film by graphite etching through hydrogen as carbon source in HFCVD reactor without plasma discharge. High-quality diamond films have also been deposited at temperatures as low as 250 °C using microwave plasma reactor [13]. In this work, a study of polycrystalline diamond growth on (1 0 0) silicon substrates deposited in a HFCVD system at various pressures (up to 50 mbar) using 1% methane in hydrogen is reported.

13.2.2.1 Structural Studies

Figure 13.5 shows representative spectra of diamond thin films with a typical diamond (cubic) structure. The characteristic (1 1 1) and (2 2 2) peaks of diamond structure are clearly visible at 2θ values of 43.9° and 94.96°. The FWHM of the

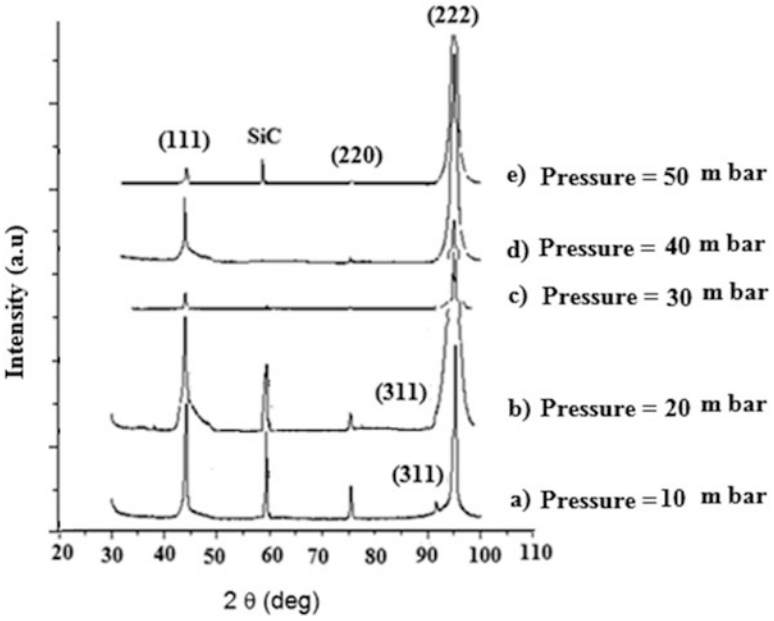

Fig. 13.5 XRD patterns of five diamond films at various pressures, (**a**) 10 mbar, (**b**) 20 mbar, (**c**) 30 mbar, (**d**) 40 mbar, (**e**) 50 mbar

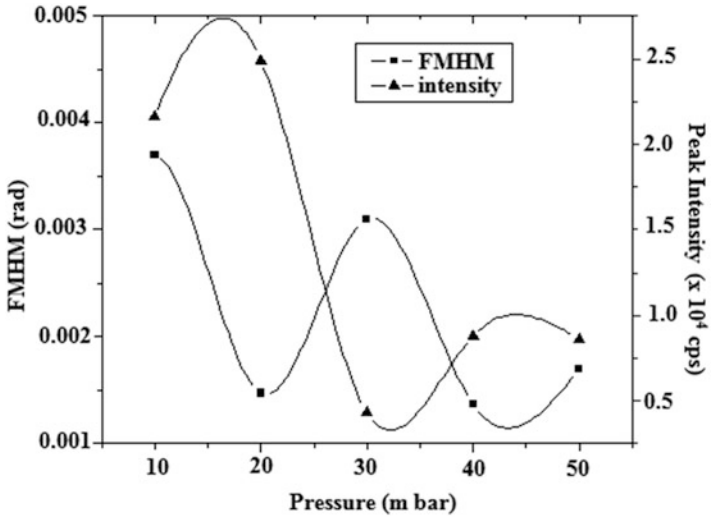

Fig. 13.6 FWHM and peak intensity of (1 1 1) plane for HFCVD diamond films at various pressures as determined from XRD patterns

diamond (1 1 1) or (2 2 2) XRD peak observed at 2θ angles of ~44° (or ~95°) can be used as a qualitative measure of the degree of crystallinity within the diamond deposit. The FWHM is dependent on both the grain size and the crystallinity and usually has a tendency to become narrow when the grain size becomes large. A comparison of (2 2 2) diamond peak for a series of depositions at various pressures revealed a decrease in intensity with some oscillatory trend (see Fig. 13.6). Higher pressures lead to a considerable decrease in the intensity of the (3 1 1) signal with no peak being observed at pressures $\geq$30 mbar (see Fig. 13.5). Figure 13.6 shows FWHM of the XRD (2 2 2) peak as a function of deposition pressure and clearly demonstrates the improvements in terms of grain size of the diamond polycrystals with the pressure, while greater pressure leads to degradation in grain size due to high nucleation rate but low growth rate. The findings here are very much consistent with that of Yang et al. [58]. From these experimental findings, it can be said that an appropriate pressure can improve the quality of diamond crystals.

13.2.2.2 Effect on Morphology

SEM micrographs of five different samples grown at various pressures for quality and internal structure analysis are shown in Fig. 13.7. At very low pressure of 10 mbar, randomly oriented diamond crystals with rough surface and mean crystallite size of ~0.9 μm were detected. Figure 13.7b shows ~2.5 μm diameter some isolated and some connected crystals with (1 1 1) facet dominant grown at 20 mbar. The presence of isolated and disconnected crystals may have appeared due to not proper etching of Si wafer surface prior to CVD. But with the rise of pressure from

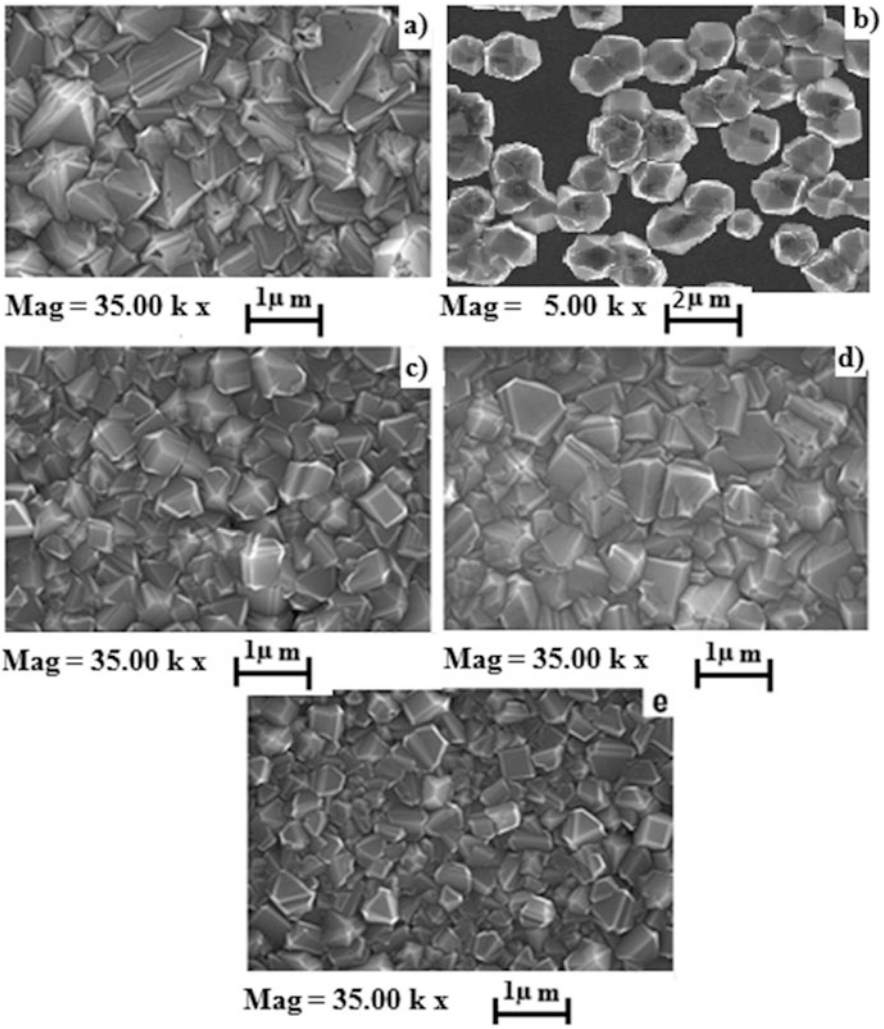

Fig. 13.7 SEM micrographs of five diamond samples at various pressures, (**a**) 10 mbar, (**b**) 20 mbar, (**c**) 30 mbar, (**d**) 40 mbar, (**e**) 50 mbar

30 to 50 mbar, uniform and smooth films of polycrystalline grains were obtained having well-facetted shape with average grain size in the range from 0.7 ± 0.02 to 1.0 ± 0.02 μm (Fig. 13.7c–e). Figure 13.8 depicts the behavior of diamond grain size and grain density as a function of chamber pressure. In both cases an oscillatory but opposite behavior is noticed as both are reciprocal to each other. The grain density was calculated using the relation [59]:

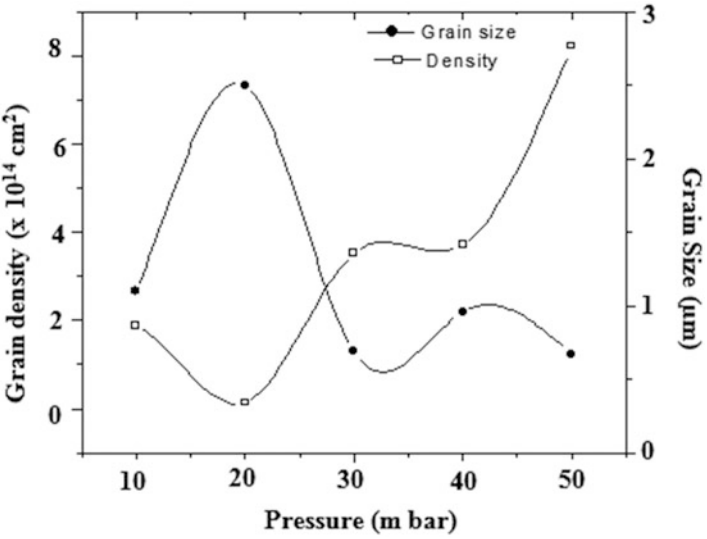

Fig. 13.8 Diamond crystallite size and density as a function of chamber pressure as determined from SEM micrographs

$$N_v = \left(2.4150\sqrt{\bar{a}} - 1.4552\,\bar{l}\right) \tag{13.2}$$

where $\bar{a}$ is the average grain area on a random two-dimensional section and $\bar{l}$ gives the average intercept length of a random test line with grain surface. Figure 13.8 shows that except at 20 mbar pressure, diamond grain density almost shows an increasing trend with rise of pressure. It means that diamond growth rate is relatively high at low pressures up to 20 mbar (demonstrating single and isolated crystals as seen in Fig. 13.7b), but pressures greater than 20 mbar suppress the diamond growth rate but increase the nucleation rate that's why diamond grains density is higher with relatively smaller and fine crystallite sizes at these pressures. The larger crystals obtained at 20 mbar pressure may be caused by lateral impingement of diamond crystallites as the diamond nucleation is small since the Si wafer (substrate) was not properly etched. On the basis of above-cited facts, it can be concluded that pressure poses large effects on the diamond morphology and grain size. This behavior of diamond growth is in agreement with that of Hirakuri et al. [55]. Moreover, almost all the films were noticed to grow uniformly and smoothly at all pressures with polycrystalline grains so that such polycrystalline films can be grown using HFCVD system at relatively large substrate areas.

13.2.2.3 Effect on Crystal Quality

Raman spectra of diamond films for the comparison of crystal quality and study of any impurities present in the diamond films deposited at different pressures are shown in Fig. 13.9. In the spectra for film deposited at 10 mbar, a diamond peak exists at 1339 cm^{-1}. The Raman peak at 1339 cm^{-1} indicates a shift as compared to the natural diamond peak (1332 cm^{-1}), and this shift may be due to the presence of compressive stresses at low pressure. The weak G and D peaks of graphite are situated at 1350 cm^{-1} and 1475 cm^{-1}, respectively. Two further peaks at 1140 and 963 cm^{-1} are observed among which 1140 cm^{-1} peak can be associated with amorphous network in the literature [60, 61] or may be due to Ne lamp, and 963 cm^{-1} may be a second-order silicon peak. The spectrum observed at 10 mbar is similar

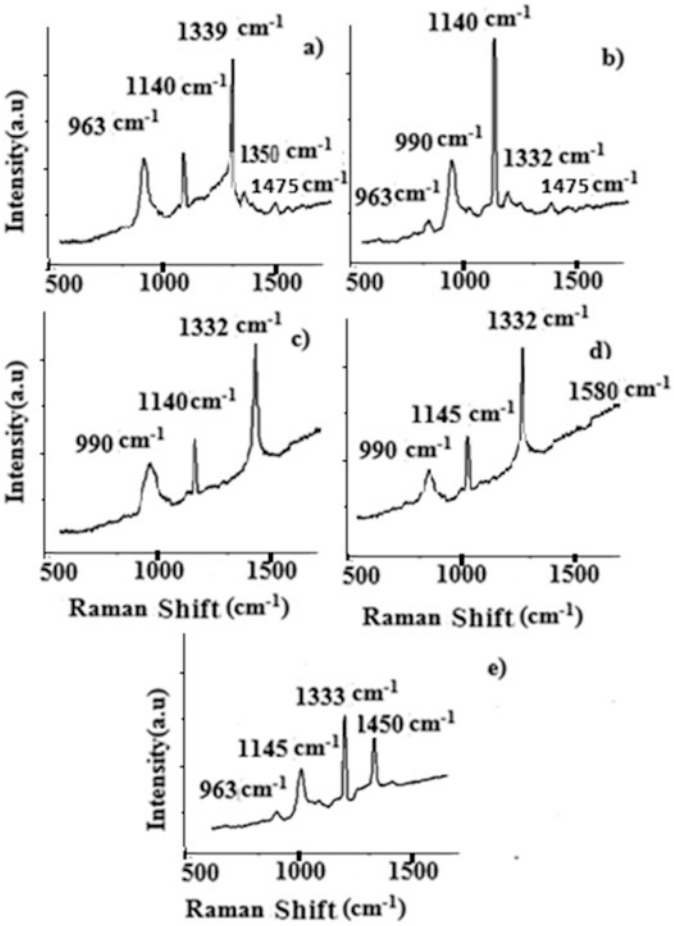

Fig. 13.9 Raman spectra of five diamond films grown at various pressures, (**a**) 10 mbar, (**b**) 20 mbar, (**c**) 30 mbar, (**d**) 40 mbar, (**e**) 50 mbar.

to that of Schwarz et al. [48] observed at 3 mbar. At 20 mbar pressure, diamond peak is shifted back to its natural position, i.e., 1332 cm^{-1}, but with low intensity. Moreover, the G and D peaks are absent at this pressure. This may be due to the increasing generation of atomic hydrogen caused by the extension of residence time, which is capable of enhancing the removal of non-diamond components [62]. The amorphous peak is at the same position, while second-order silicon peak is shifted to 990 cm^{-1} (Fig.13.9b). Such behavior may be caused by the isolated diamond crystals observed only at this pressure as most of the surface is Si and is in agreement with that of Yang et al. [58]. At pressures of 30 and 40 mbar, the diamond peak remains at its natural position. This is possibly due to etching by which amorphous carbon peak is strongly reduced as shown in Fig. 13.9d–e. However, an extra weak peak at 1580 cm^{-1} is observed at a pressure of 40 mbar, also noticed by Schwarz et al. [48] at 3 mbar pressure. This is actually the G peak related to the highly oriented graphite phase (HOPG). The diamond peak at pressure of 50 mbar is again slightly shifted to 1333 cm^{-1} (Fig. 13.9e). From the above results, it can be concluded that Raman spectra also support the fact that the quality of diamond strongly depends on chamber pressure, because the generation of atomic hydrogen sharply decreases with increasing pressure [55]. The FWHM values obtained for Raman 1332 cm^{-1} peak presented in Table 13.3 also support our results of the crystal quality with increasing pressure. It is noticed that where the growth rate is higher, FWHM values are lower and so diamond crystals have relatively larger sizes. But the pressures where FWHM values are higher, good-quality diamond crystals are the results.

13.2.2.4 Effect on Electrical Resistivity

Figure 13.10 shows electrical resistivity measured by four-point probe *I–V* in van der Pauw geometry at room temperature with maximum voltage of ±100 V. From the results presented in Table 13.3 and Fig. 13.10, it is clear that resistivity decreases rapidly up to a pressure of 30 mbar and then slowly with further increase of chamber pressure. The decrease of resistivity might be due to the causes of grain edge and contamination scattering at lower deposition pressures [63]. But as diamond grain density increases at pressures ≥30 mbar see Fig. 13.7, increasing the grain boundary area, consequently reducing the conductivity and causing the

Table 13.3 Diamond film parameters

Deposition pressure (mbar)	Resistivity ($\times 10^7$ Ω cm)	Growth rate (μm/h)	FWHM of Raman 1332 cm^{-1} peak
10	105.00	0.054	10.54
20	72.40	0.125	09.52
30	01.17	0.035	14.36
40	00.29	0.048	10.21
50	01.57	0.034	14.32

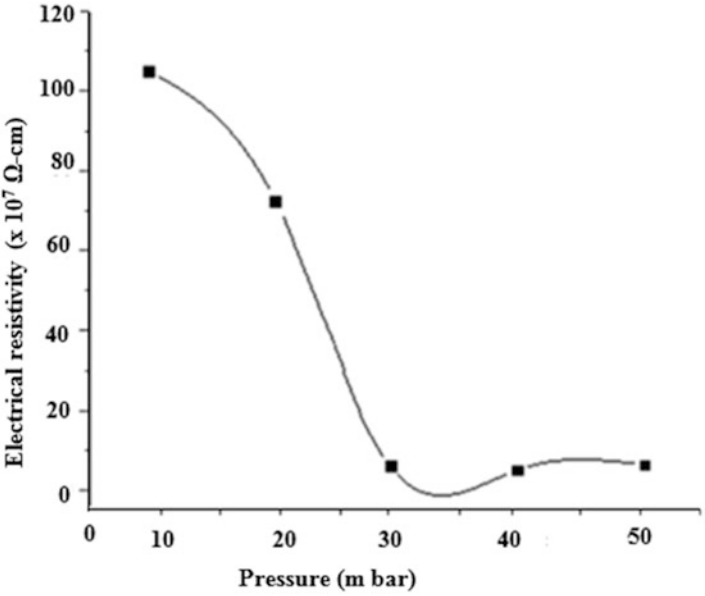

Fig. 13.10 Electrical resistivity as a function of reactor pressure

observed slow decrease of resistivity with pressure. The behavior of resistivity with pressure also supports the findings obtained using SEM, XRD, and Raman spectroscopy.

13.2.2.5 Effect on Growth Rate

The pressure dependence of growth rate (as determined from the cross-sectional view using SEM) of diamond crystals is displayed in Fig. 13.11 at a substrate temperature of 900 °C and indicates that growth rate increases strongly with increasing pressure up to 20 mbar and then decreases with further rise of pressure. The growth rate shows a maximum at 20 mbar (0.125 μm/h) and a minimum at 50 mbar (0.034 μm/h). Thus, the highest growth rate (at 20 mbar) is almost four times the slowest growth rate (at 50 mbar). Behavior of growth rate for pressures >20 mbar is in agreement with that observed by Schwarz et al. [48]; however, magnitudes of growth rate differ significantly. The reason for such a high growth rate has already been discussed in Sect. 13.2.2.2. Schwarz et al. [48] found the fastest growth rate (0.7 μm/h) at 3 mbar, while growth rate at 50 mbar was only 0.2 μm/h. Brunsteiner et al. [64] found maximum growth rate at 27 mbar with a slightly slower growth rate at a pressure of 7 mbar. These results disagree with growth rates observed in the present investigations.

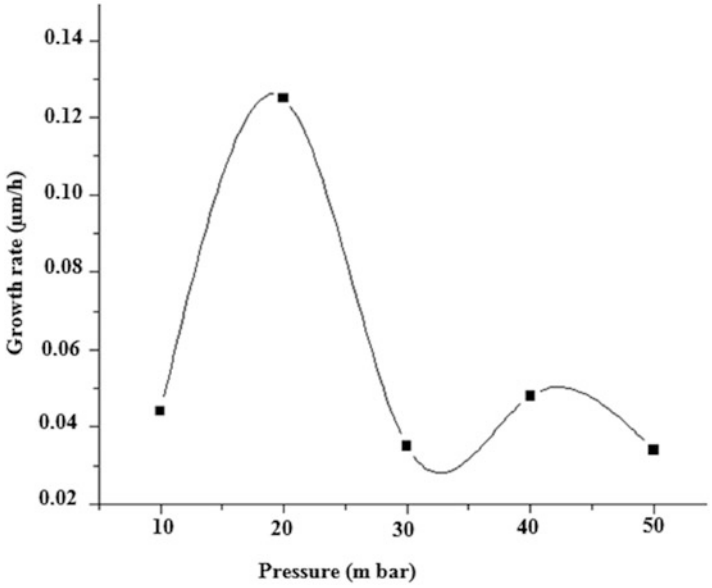

Fig. 13.11 Diamond polycrystals growth rate as a function of pressure

A possible explanation of this disagreement could be different deposition conditions based on experimental setup such as use of 8 W (tungsten) filaments ($\Phi = 0.5$ mm), filament temperature, filament-substrate distance, gas flow rate, etc. The FWHM values obtained for Raman 1332 cm^{-1} peak presented in Table 13.3 also support the results of the growth rate with increasing pressure. Therefore, where the growth rate is higher, the lower is the FWHM value and so on.

13.2.3 Controlling Properties of Microcrystalline Diamond Films Using Oxygen in a Hot Filament Chemical Vapor Deposition System

Preparation and characterization of nanocrystalline diamond films have been of great interest in the last few years. Many researchers [14–16] have studied the role of oxygen addition into ($CH_4 + H_2$) plasma polycrystalline diamond growth and have investigated that O_2 addition reduces impurity incorporation and improve quality of the diamond [15, 16].

Effects of nitrogen and oxygen (O_2) accumulation on the growth and morphology of polycrystalline diamond films have been investigated by some researchers [31–33]. Ahmed et al. [34] have used nitrogen to control the surface morphology of diamond thin film using CVD system. Ando et al. [35] have found that growth

parameters and film properties for conventional HFCVD a reactor is different from that for a MPCVD system.

Many researchers have found that CH_x and C_2H_x radicals are main contributors to the characteristics of diamond synthesized using gas phases [17–24]. CH_x radicals are the precursors of diamond, and C_2H_x radicals are those of non-diamond components. As a result, as the ratio C_2/CH decreases, high-quality diamond is formed [23, 24]. So the decrement of C^o radicals in the plasma is significant for high-quality diamond. Adding O_2 to the feed gas can decrease C^o radicals in the plasma and generates O and OH radicals in the chamber. These two species (O and OH) can etch the non-diamond component more rapidly than atomic H [23, 24]. Hence, it is considered that the increase of OH radicals and the decrease of C^o radicals in the plasma cause the enhancement of diamond quality in the CH_4/H_2/O_2 systems. In the HFCVD chamber, the dissociation of feeding gases H_2, CH_4, and O_2 is very effective. Many additional reaction species containing O_2 are created with the addition of O_2 in the CH_4/H_2 plasma. These additional O_2 species absolutely vary the gas phase chemistry and effect the formation of grains of diamond films with various morphologies and mixed textures. However, very little work is found on the influence of O_2 addition on the resistivity and growth rate of diamond films in HFCVD system. In this work, the effect of O_2 addition on resistivity and growth rate of diamond films in HFCVD system is investigated.

13.2.3.1 Structural Studies

XRD patterns of five various samples for texture analysis are taken and are shown in Fig. 13.12. Three randomly oriented diamond peaks (1 1 1), (2 2 0), and (3 1 1) with diverse intensities are observed. These three diffraction peaks confirm the diamond nature of the films. For all samples the (1 1 1) lines are much stronger than (2 2 0) and (3 1 1). For samples b and d in Fig. 13.12, (2 2 0) and (3 1 1) are weaker indicating the one type of pattern, i.e., (1 1 1). For sample e, all three diffraction peaks reappear confirming that these films have mixed textures. The strongest peak observed in all the as-grown samples at approximately 2θ value of 75° is due to the silicon substrate.

13.2.3.2 Effect on Morphology

Morphology of diamond films grown at various oxygen concentrations is shown in Fig. 13.13. From these micrographs there seems a significant change in the film morphology when oxygen is added to methane/hydrogen gas mixture. Without oxygen, film is found to be polycrystalline in nature with mixed {1 1 1}, {2 2 0}, and {3 1 1} texture having an average grain size of about 1.5 ± 0.02 μm (see Figs. 13.12a and 13.13a and Table 13.2). With small amount of oxygen addition (O_2 = 0.003 vol.%), pyramid-like structure is seen, and average crystal size increases to 1.6 ± 0.02 μm (see Fig. 13.13b and Table 13.4) with {1 1 1} facet

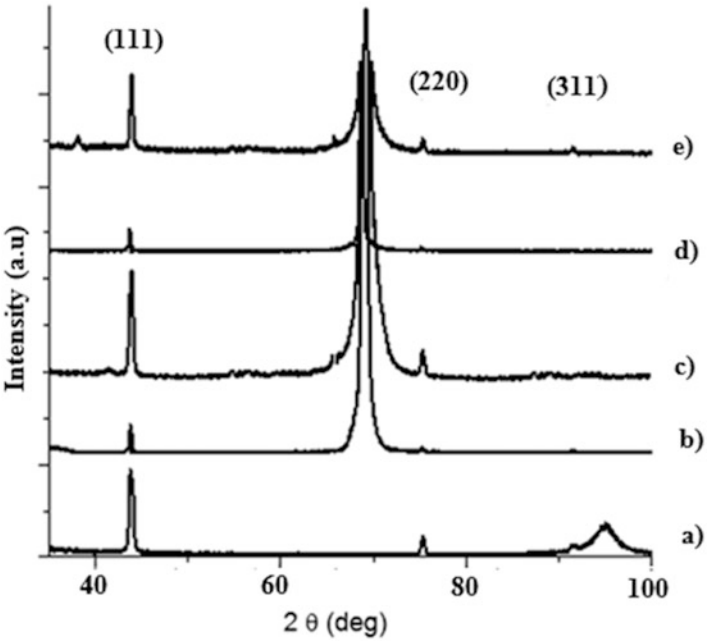

Fig. 13.12 XRD patterns of diamond films grown at substrate temperature of 900 °C with various O_2 contents, (**a**) $O_2 = 0.000$, (**b**) 0.003, (**c**) 0.007, (**d**) 0.010, and (**e**) 0.013 vol.%

dominant. For further increase of oxygen content ($O_2 = 0.007$–0.010 vol.%), crystal size is increased more with better crystal quality involving mixed {1 1 1},{2 2 0}, and {3 1 1} texture (see Fig. 13.13c). With higher addition of oxygen ($O_2 = 0.010$–0.013 vol.%), grain size further enhanced from 1.65 ± 0.02 to 1.8 ± 0.02 μm; moreover grain boundaries are very clear and sharp (see Fig.13.13d, e).

Some small crystallites formed on the surface of large crystallites are seen in almost all the samples. These small crystallites are caused by secondary nucleation. The number of these secondary nuclei is decreasing as the oxygen concentration is increasing. This provides evidence that the crystal quality is improving due to decrease of secondary nucleation as clear Figs.13.13a–e. Some black spots are also obvious in the films, which might be the graphite particles and/or a small amount of amorphous carbon has been retained in the film. This is consistent with the Raman spectrum where the weak G peaks were (see Fig 13.14c) observed. These results favor those of Hara et al. [65].

The formation of pyramid-like morphology originated by addition of O_2 in the film Fig. 13.13c can be explained by twinning occurring at (1 1 1) planes. This leads to the film formation with {1 1 1} morphology as studied by the other scientists [16]. Recording morphology changes, it is noted that small amount of O_2 does not change texture and grain size, but as O_2 concentration is increased, an improvement in the quality of grain as well as its size with {1 1 1} facet becoming dominant. This

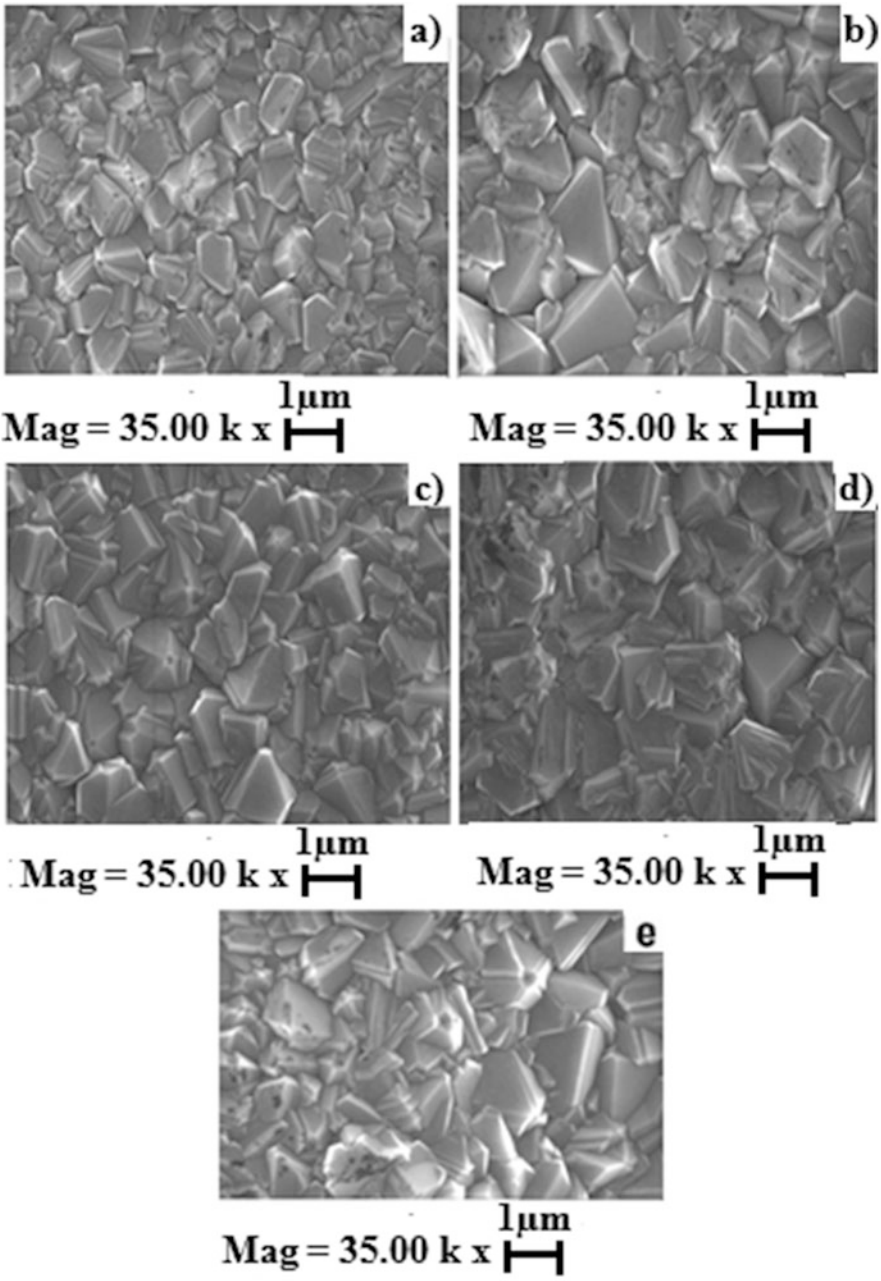

Fig. 13.13 SEM micrographs of diamond samples, (**a**) $O_2 = 0.000$, (**b**) 0.003, (**c**) 0.007, (**d**) 0.010, and (**e**) 0.013 vol.%

Table 13.4 Growth parameters of oxygen-doped diamond films

Sample	H_2 (sccm)	CH_4 (sccm)	O_2 (sccm)	Time (h)	Growth rate (μm/h)	FWHM of 1332 cm^{-1} peak	Average grain size (±0.02 μm)	Resistivity ($\times 10^9$ Ω cm)
(a)	300	3	0.00	20	2.0	14.36	1.50	6.56
(b)	300	3	0.01	20	2.1	14.30	1.60	5.06
(c)	300	3	0.02	20	2.0	13.92	1.65	0.30
(d)	300	3	0.03	20	2.0	10.67	1.70	0.03
(e)	300	3	0.04	20	2.5	09.91	1.80	1.05

result is in good agreement with those of Neto [33] and Yu et al. [31], i.e., O_2 concentration affects the morphology and promotes the formation of {1 1 1} texture of polycrystalline diamond films grown using HFCVD.

13.2.3.3 Effect on Crystal Quality

To verify the nature and crystalline quality of diamond observed in SEM and XRD patterns, Raman spectra of different specimen with various oxygen concentrations are recorded and presented in Fig. 13.14. For all concentration of oxygen, a strong and sharp peak around 1333 cm^{-1} is observed. This is associated with the bulk diamond and attributes to sp^3 C–C bonding [66]. The peak at 1121 cm^{-1} originates due to oxygen impurities as they form C–O bond in the graphite state [67]. Moreover these peaks contribute a possible decrease in resistivity [38]. Peaks appearing at 961 cm^{-1} correspond to second-order Si peaks; their intensities do not link film characteristics.

A non-diamond broad G peak at about 1550 cm^{-1} appears in the spectrum, which indicates relatively poor quality of diamond compared to samples a, d, and e. These G peaks are due to amorphous carbon as shown in Fig. 13.14a, c. Increase of oxygen concentration may cause the non-diamond peaks to disappear and improve the sharpness of diamond peaks (1333 cm^{-1}) [65].

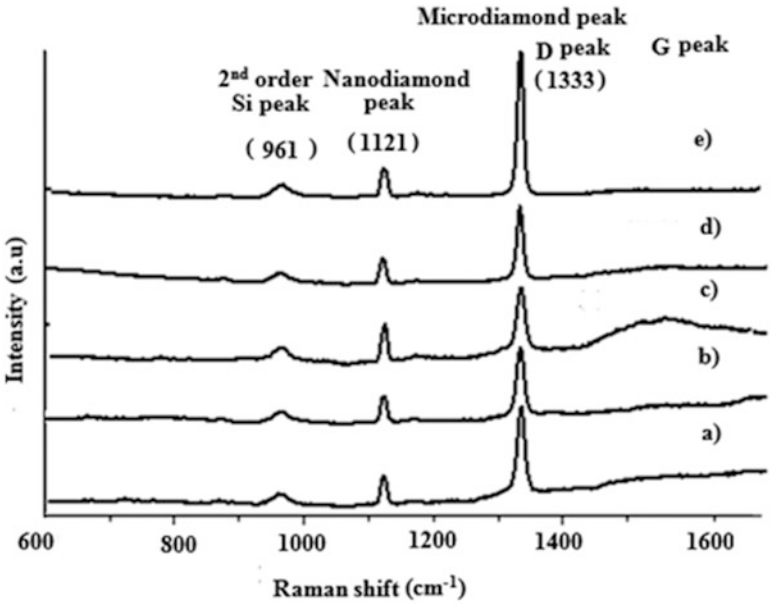

Fig. 13.14 Raman spectra of diamond films with varying oxygen contents, (**a**) $O_2 = 0.000$, (**b**) 0.003, (**c**) 0.007, (**d**) 0.010, and (**e**) 0.013 vol.%

The above finding can be explained as follows: The non-diamond peak around 1550 cm^{-1} appears only when oxygen concentration is 0.007 vol.%. This may be due to the reason that oxygen reacts with H and reduces the formation of diamond phase by increasing the formation of graphite at the interface [33], and its disappearance on diamond growth with rising oxygen (Fig.13.14b, c). The disappearance of this peak with rising oxygen contents (Fig. 13.14d, e) indicates that the added oxygen had etched away the amorphous carbon component and suppressed its formation during the long deposition period [16]. These Raman spectra are in excellent agreement with the SEM morphology observations. The FWHM values obtained for Raman 1333 cm^{-1} peak presented in Table 13.4 also support our results of the crystal quality with increasing oxygen content in the diamond films. It is noticed that FWHM values are decreasing with rising oxygen content in diamond films and so diamond crystals have relatively larger sizes, reducing secondary growth and hence yielding good-quality diamond crystals.

13.2.3.4 Effect on Growth Rate

In order to investigate the effect of oxygen on growth rate of diamond films, different cross-sectional SEM measurements as a function of oxygen addition were made and are shown in Fig. 13.15.

The data is given in Table 13.4. It is clear from the images and data (Table 13.4) that growth rate decreases with small addition of oxygen (Fig. 13.15a–c) but increases with higher amounts of oxygen (Fig. 13.15e). The growth rate as function of oxygen concentration is shown in Fig. 13.16. The observed rise and fall in growth rate can be explained by the following way: The rise in growth rate for large amount of oxygen is due to surface activation by oxygen, either as OH or O, which presumably produces radical sites by H atom abstraction.

And the decline in growth rate due to smaller amount of oxygen is due to the enhanced oxidation rate of solid carbon at the surface of growing diamond film and the depletion of gas phase hydrocarbons in the plasma due to Co formation [17, 67–74].

Generally the decrease is explained by etching process shown in Fig. 13.17. Howard et al. [75] suggested that atomic oxygen can make the growth of the film more difficult by forming carbon bridge or double bonds with surface carbon atoms [75]. According to Chen et al. [76], addition of oxygen to the methane/oxygen gas mixture causes a decrease in the nucleation density of the film.

13.2.3.5 Effect on Grain Size

Grain sizes of five different samples were calculated by analyzing SEM micrographs (Fig.13.18) and by X-ray diffraction patterns (Fig. 13.12) using Sherrer's eq. [35]:

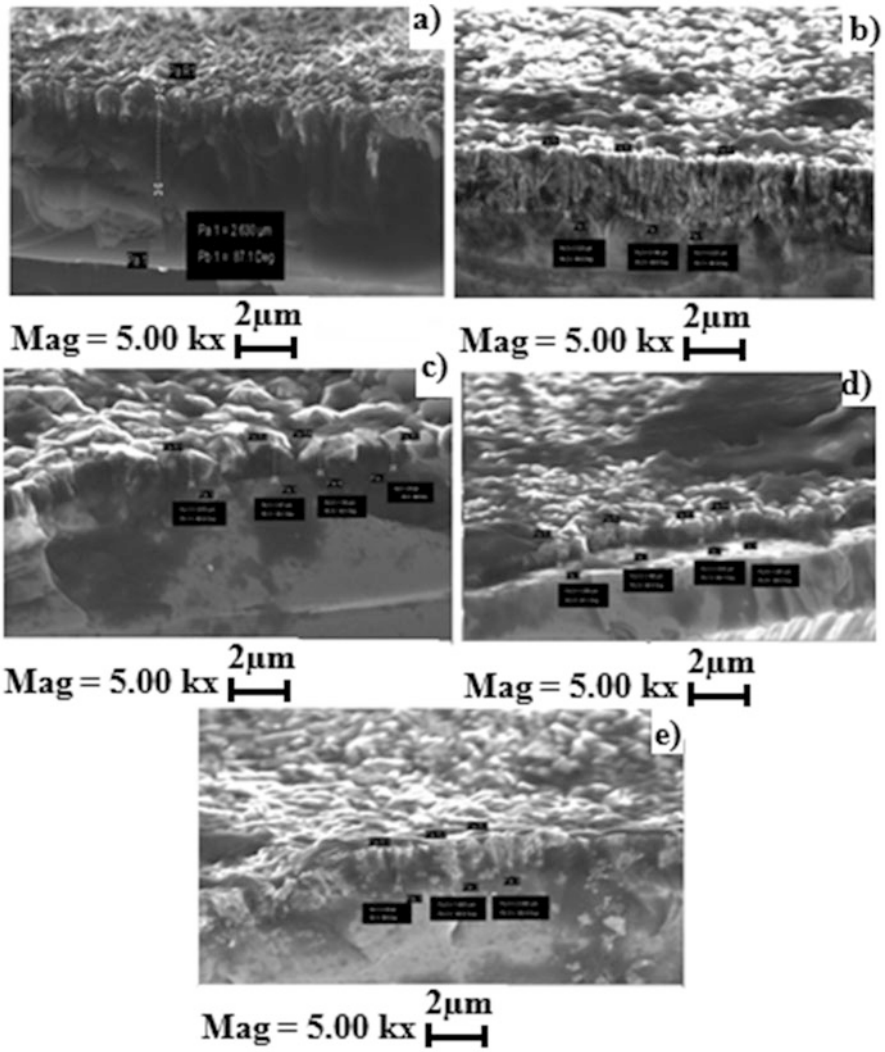

Fig. 13.15 SEM cross-sectional view of diamond films with varying oxygen content: (**a**) $O_2 = 0.000$, (**b**) 0.003, (**c**) 0.007, (**d**) 0.010, and (**e**) 0.013 vol.%

$$\mathbf{S}_{hkl} = \frac{0.9\lambda}{B\cos\theta} \tag{13.3}$$

where $\lambda = 1.5418$ Å and B is the full width at half maximum (FWHM) of the (1 1 1) diffraction peak. The average crystallite size $\mathbf{S}_{hkl}$ as determined from Eq. (13.3) and shown in Fig. 13.19 indicates an increase from 1.5 ± 0.02 to 1.8 ± 0.02 μm as the oxygen concentration increases from 0.0 to 0.013 vol.% in the reaction chamber. Similar results are also observed from SEM micrographs as seen in Fig. 13.18 with

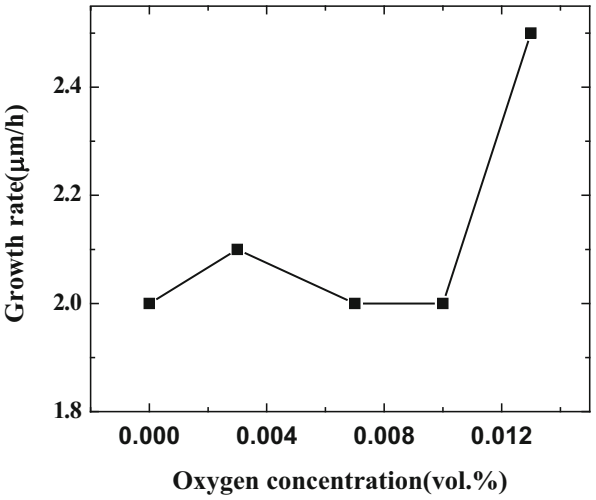

Fig. 13.16 Growth rate as function of oxygen concentration

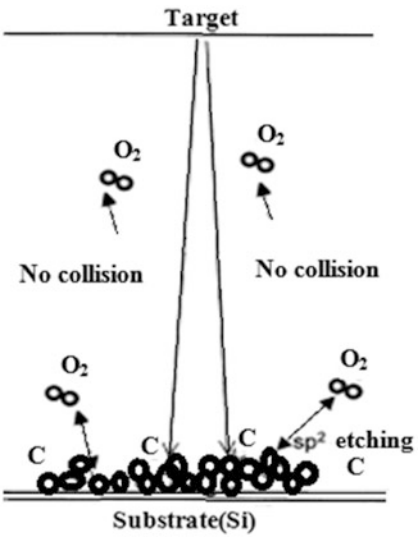

Fig. 13.17 Etching process of sp^2 bonding fraction during film growth in oxygen atmosphere

only a slight variation. Thus addition of oxygen reduces the defects sp^2 and increases sp^3. This increase in average grain size may be explicated by the lack of carbide formation of non-diamond carbon phases particularly graphite that grow on the edge and hence enhance the grain size [33].

13.2.3.6 Effect on Electrical Resistivity

Electrical resistivity (Fig. 13.20) decreases by adding oxygen content to diamond films. This fall of resistivity can be explained as: on top diamond layer some black spots were observed which have much lower electrical resistivity. The numbers of

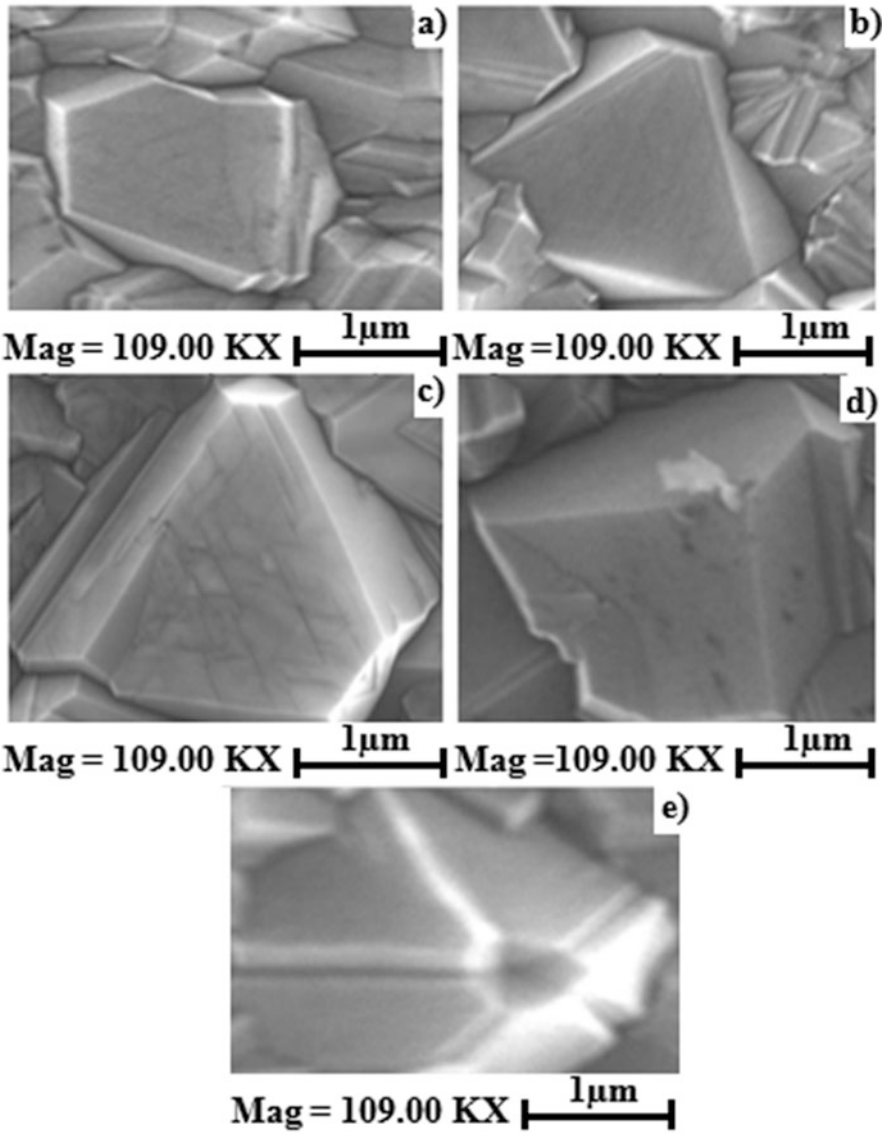

Fig. 13.18 SEM grain size view of five diamond films with different oxygen concentrations, (**a**) $O_2 = 0.000$, (**b**) 0.003, (**c**) 0.007, (**d**) 0.010, and (**e**) 0.013 vol.%

these defects were noted to increase with the rise of oxygen concentration since these defects depend on diamond growth conditions. As a result electrical resistivity decreases as shown in Fig. 13.20 and Table 13.4; these results are in good agreement with the results observed by Lux [77].

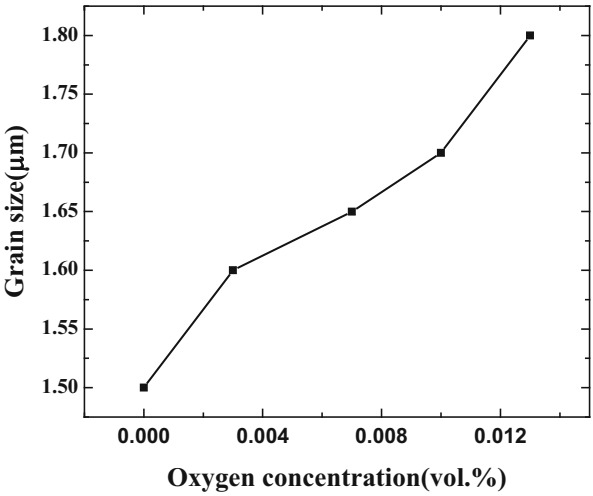

Fig. 13.19 Diamond grain size as a function of oxygen concentration

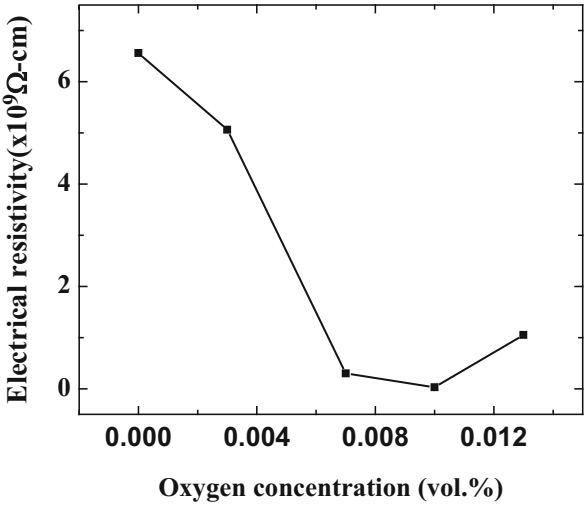

Fig. 13.20 Resistivity as a function of oxygen concentration in diamond films

13.2.4 Influence of Boron on Properties of CVD Diamond Thin Films at Various Deposition Pressures

In previous decade, researchers started to add boron dopants in the diamond films, making them p-type semiconductors [42]. High boron doping can change insulating diamond films into metallic and increase their applications in electrical appliances. So preparing high-quality boron-doped diamond (BDD) films is very important for their applications. Due to smaller boron atomic radius compared to other potential

dopants, it is easy to synthesize the electrical conducting diamond with higher doping levels [43]. However, B-containing gases such as B_2H_6 and BCl_3 used for the deposition of diamond films are potentially hazardous. A very simple and effective way to produce B-doped diamond films by an ex situ heat treatment procedure can be applied instead of an in situ doping using volatile gases [44]. In this technique a boron carbide (B_4C) block (3 × 3 in.) was positioned close to the film at a temperature of around 2300 °C for 20 h during CVD diamond growth. The B_4C may act as suitable boriding agent for diamond in the same way as it does for metals [44].

13.2.4.1 Structural Studies

As depicted in Fig. 13.21, three diffraction peaks (1 1 1), (2 2 0), and (3 1 1) in addition to a strong reflection corresponding to (2 2 2) plane were noticed. The 1st sharp peak around 43.91° is a characteristic reflection of (1 1 1) plane, second peak at 75.27° is related to (2 2 0) plane, and third one of low intensity at 91.46° corresponds to (3 1 1) plane confirming the crystalline nature of these diamond films. In all samples (2 2 2) reflection at 96° is much stronger than (1 1 1), (2 2 0), and (3 1 1) reflections. Intensity of (1 1 1) and (2 2 0) peaks decreases with the increase of deposition pressure. For samples a, b, and c, (3 1 1) reflections have almost been disappeared (Fig. 13.21). For samples d, e, and f which are fabricated in the presence of B_4C, (3 1 1) peak has appeared, but (2 2 2) reflections are still sharp and dominant confirming the transfer of texture from (1 1 1) to (2 2 2). It is noted that diamond texture changes from (1 1 1) to (2 2 0) and (3 1 1) in the presence of B_4C. An obvious difference of peak intensities at 43.91° without B_4C and at 75.27° at various pressures with B_4C can be observed (Fig. 13.21). Therefore, it can be concluded from the above analyses that introduction of B_4C vapors into the reactive gases not only changes the crystal orientation but also improves the crystal quality of boron-doped diamond films as shown in Fig. 13.21d, f. Wang et al. [78] used $B(OCH_3)_3$ vapors into reactive gases instead of solid B_4C (the present case) keeping pressure constant at 30 mbar and noted not only the change of crystal orientation (analogous to present results) but also the degradation of diamond crystals by excessive introduction of boron (B/C ratio greater than 4:4). However, present results show an improvement in the crystal quality perhaps due to change of pressure and use of different boron compound (solid B_4C not vapors), which may be responsible for relatively lower concentration of activated boron atoms in the reactive gases, since lesser number of boron atoms show weaker affinity to affect the diamond growth process. From the above experimental findings, it can be seen that an appropriate deposition pressure can improve the quality of diamond films.

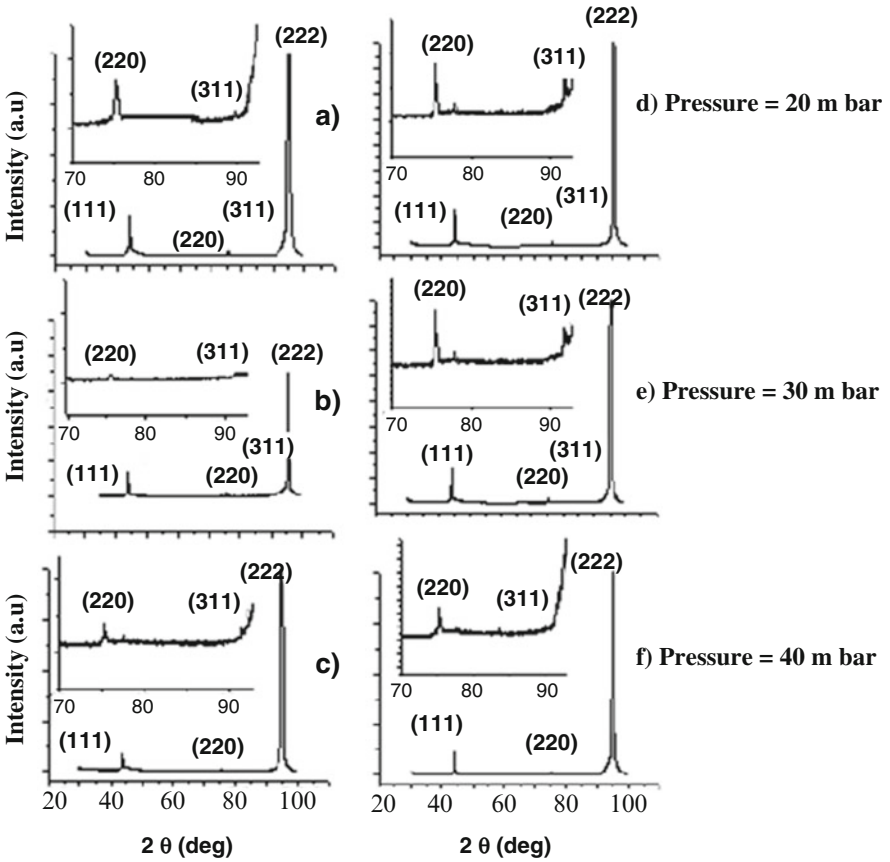

Fig. 13.21 XRD patterns of diamond films grown at substrate temperature of 900 °C at various pressures and without boron: (**a**) 20 mbar, (**b**) 30 mbar, (**c**) 40 mbar, with boron: (**d**) 20 mbar, (**e**) 30 mbar, (**f**) 40 mbar, Insets depict the intensity of (2 2 0) and (3 1 1) reflections

13.2.4.2 Effect on Morphology

Morphology of diamond films grown at various deposition pressures for 20 h with and without B_4C is recorded by SEM and presented in Fig. 13.22. From these micrographs it seems a significant change in the film morphology when pressure is changed in the presence of B_4C. Without B_4C and at pressure of 20 mbar, film is found to be single crystalline in nature with {1 1 1} and {2 2 2} texture having an average crystal size of about 1.9 μm with very low nucleation rate and high growth rate (see Fig. 13.21a). At pressure of 30 mbar, polycrystalline structure is seen with relatively larger nucleation rate and lower growth rate. This causes average crystal size to decrease from 1.9 to 0.6 μm (see Fig. 13.21b and Table 13.5) with (2 2 2) facets dominant. For further increase of pressure, average crystal size is reduced more with the largest nucleation rate and finer crystal quality (see Fig 13.21c). This

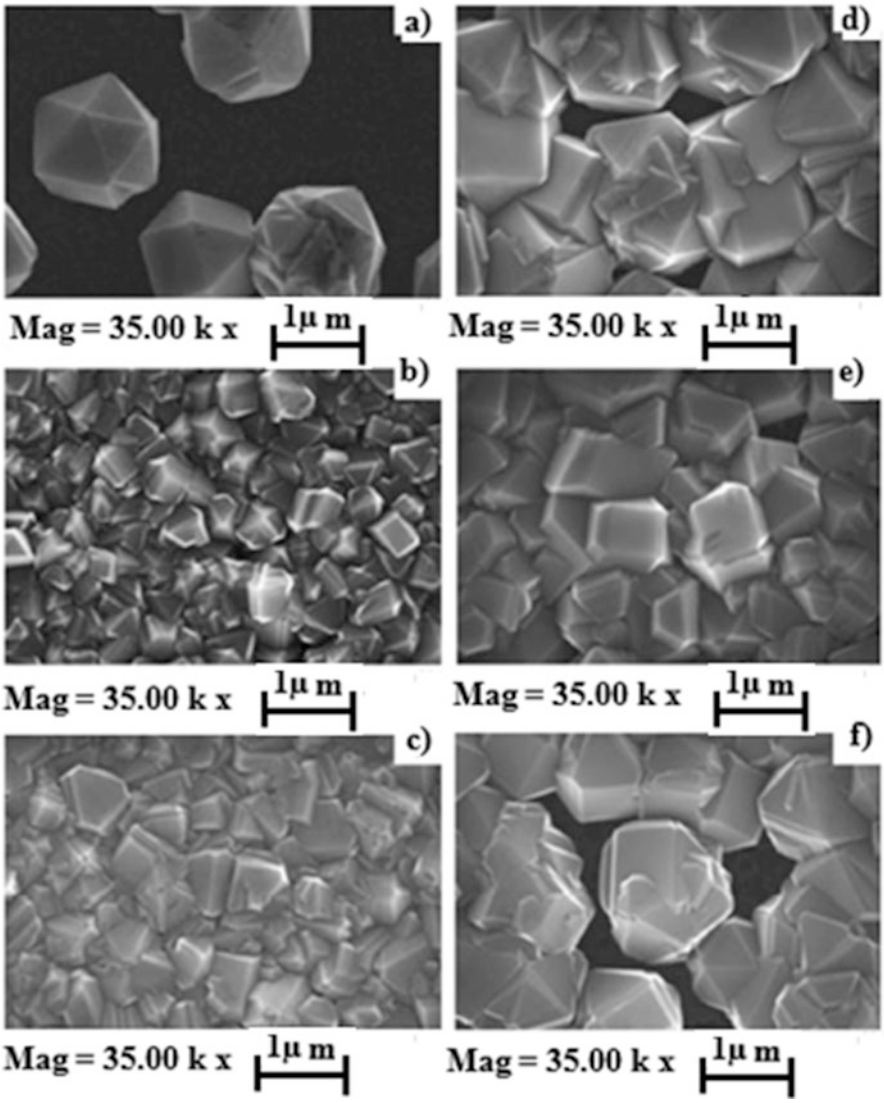

Fig. 13.22 Surface morphology of the coating prepared at various pressures: without boron: (**a**) 20 mbar, (**b**) 30 mbar, (**c**) 40 mbar, with boron: (**d**) 20 mbar, (**e**) 30 mbar, (**f**) 40 mbar

trend of decreasing growth rate is analogous to that presented in Ref. [58], where it is observed that growth rate is high at low pressures. However, this trend is opposite to that of Kweon et al. [5]. When B_4C is introduced in the deposition chamber, it is noticed that diamond crystal quality is improved with sharp and clear crystal edges involving mixed {1 1 1}, {2 2 0}, {3 1 1}, and {2 2 2} textures (see Fig. 13.21d, e, and f). Nucleation rate has improved by adding B_4C in the reactive gases making

Table 13.5 Growth parameters without B

Sample	Pressure (mbar)	Resistivity ($\times 10^7$ Ω cm)	Average grain size (±0.02 μm)
(a)	20	72.40	1.9
(b)	30	1.17	0.6
(c)	40	0.285	0.5

Table 13.6 Growth parameters with B

Sample	Pressure (mbar)	Boron content (%)	Resistivity ($\times 10^5$ Ω cm)	Average grain size (±0.02 μm)
(d)	20	0.64	9.82	1.0
(e)	30	1.77	7.62	1.2
(f)	40	2.05	6.33	1.3

growth rate to decrease with diamond polycrystals of about 1 μm size (compare Fig. 13.22a, d). With increasing pressure in the presence of B_4C, average grain size further enhanced from 1.0 to 1.3 μm (Table 13.6). Moreover grain boundaries are very clear and sharp (see Fig. 13.21d, e, and f). Some small crystallites on the surfaces of large crystallites are also visible in Figs. 13.21d and 13.22f. These small crystallites are caused by secondary nucleation on adding B_4C. The extent of this secondary nucleation is decreasing as pressure is increasing. At pressure of 30 mbar, secondary nucleation is almost negligible providing evidence for better crystal quality as clear from Fig. 13.21e. These changes indicate that as pressure increases from 20 to 40 mbar, both the grain size and the crystal quality of as-grown diamond films are highly enhanced with (3 1 1) and (2 2 2) facets being dominant (Figs. 13.21d–f). It can be concluded that appropriate amount of boron doping and gas pressure is crucial for improving the structural properties of diamond films. This result is in good agreement with those of Jia et al. [63], who has shown that when boron doping in the diamond is low, boron replaces C-atoms and does not accumulate at the grain boundaries. On the other hand, when a large number of B-atoms enter into the diamond structure, they not only replace C-atoms but also accumulate themselves at grain boundaries. As a consequence, B-atoms induce structural defects and damage the crystal integrity. Analogous behavior is observed in the present samples as clear from SEM micrograph (Figs. 13.22a–f).

13.2.4.3 Effect on Crystal Quality

Raman spectra of different diamond films with various deposition pressures with and without B_4C are recorded and presented in Fig. 13.23. In the absence of B_4C, strong and sharp natural diamond peak around 1332 cm^{-1} is observed Figs. 13.23a–c. At wave number of 1140 cm^{-1}, another strong peak can be found, which decreases in intensity with increasing pressure. This peak is ascribed to amorphous network [48]. Peaks appearing at 990 cm^{-1} correspond to second-order Si peak. In the presence

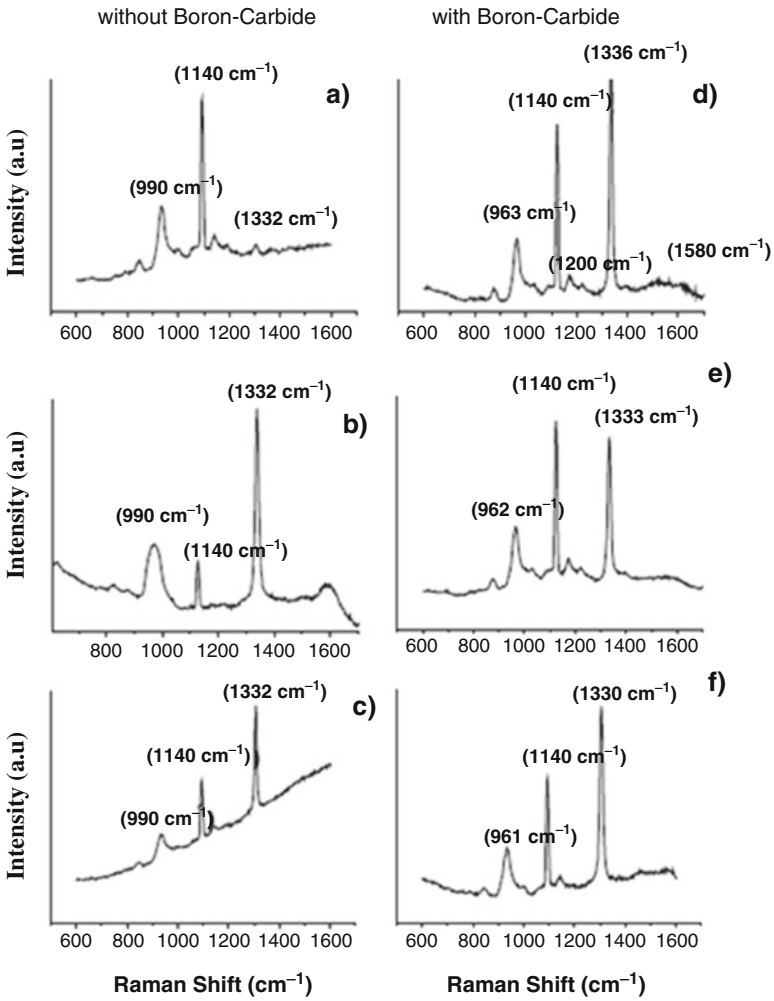

Fig. 13.23 Raman spectra of six diamond films at various pressures without boron: (**a**) 20 mbar, (**b**) 30 mbar, (**c**) 40 mbar and with boron: (**d**) 20 mbar, (**e**) 30 mbar, (**f**) 40 mbar

of B_4C characteristics, diamond peak at 1332 cm^{-1} shifts to 1336 cm^{-1} and then to lower frequency at 1333 cm^{-1} as shown in Fig. 13.23d, f. Boron doping also induces a wide peak around 1200 cm^{-1}. The two peaks at 1336 and 1333 cm^{-1} associated with bulk diamond [79] are attributed to sp^3 C–C bonding. Raman peak at ~961 cm^{-1} may be related to Si substrate; however, it may also be due to the effect of boron doping [80]. The intensity of this peak increases with increasing pressure, and it shifts toward low frequencies (Fig. 13.23d–f). The downshift may be due to the following reasons: First, Raman photons may interact with the defects induced by boron doping. This interaction may decrease the energy of photons. Second, there exist internal stresses in the films. The effect of tensile stresses may cause the shift of diamond peak to lower

frequencies. Similar results were noted by other workers [81, 82]. Third, in line with kinetic theory of gases, at low pressures the mean free paths are much longer; as a result more and more active species (H atoms and CH_3, C_2H_2 radicals, etc.) can survive collisions and reach the substrate surface. At high pressures tensile stresses are decreased; hence, the magnitude of shifting to low frequency becomes smaller [11, 83, 84]. Fourth, phonon bands at 1336 and 1333 cm^{-1} and signal at 1200 cm^{-1} are thought to be caused by the Fano interference induced by quantum mechanical interference between the discrete phonon states and electronic continuum [85, 86]. The Raman signal at 1200 cm^{-1} may be correlated with peak at 1220 cm^{-1} as reported by Krivchenko et al. [80] and around 1225 cm^{-1} as reported by Wang et al. [87]. Such peak is likely to be due to the effect of boron addition and looks to be independent of the presence of sp^2 phase. A non-diamond broad G peak at about 1588 cm^{-1} appears in the spectrum. This G peak is disappearing as the pressure increases proving the high quality of diamond as shown in Fig. 13.23d. Presence of B_4C may cause the non-diamond peaks to disappear and improves the sharpness of diamond peaks 1333 cm^{-1}. The above finding can be explained as follows: The non-diamond peak around 1588 cm^{-1} appears only when pressure is 20 mbar in the presence of B_4C. The disappearance of this peak with rising pressure (Fig. 13.23d, e) indicates that the added B_4C had etched away the amorphous carbon component and suppressed its formation during the long deposition pressure. These Raman spectra are in excellent agreement with the SEM morphology observations. These Raman spectra are also used to roughly estimate the boron content in the doped films through area under the Raman peaks of diamond at 1332, 961, and 1200 cm^{-1}. The results obtained are shown in Fig. 13.24 and tabulated in Table 13.4. Moreover, the intensity and FWHM of Raman 1333 cm^{-1} peak almost decrease with an increase in pressure, which leads to relatively larger crystallite size (Table 13.4) and better quality of diamond crystals.

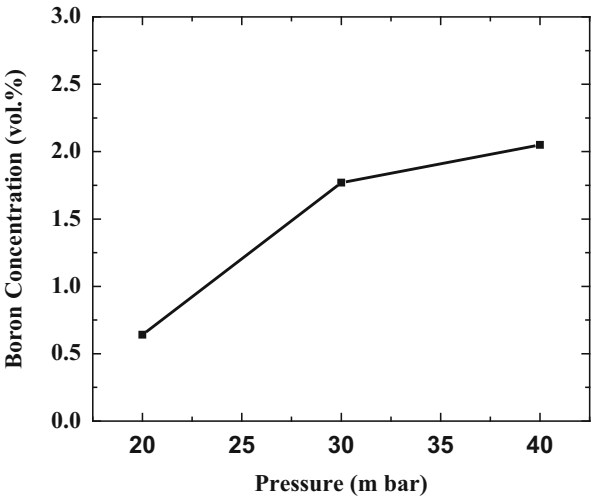

Fig. 13.24 Boron concentration as a function of pressure determined from Raman spectra

13.2.4.4 Effect on Electrical Resistivity

Electrical properties of boron-doped diamond films are examined by four-point measurements. Figure 13.25 shows that resistivity of the diamond films without boron content decreases rapidly when pressure increases from 20 mbar to 30 mbar, while resistivity reduction becomes rather very slow as pressure exceeds up to 40 mbar. On the addition of B_4C into the reactive gases, resistivity shows a sudden drop of approximately three orders of magnitude, i.e., from 7.24×10^8 to 9.82×10^5 Ω cm. Fig. 13.25 also depicts the behavior of resistivity of boron-doped diamond films as a function of pressure. It is seen that resistivity decreases with increasing pressure; however, this decrease of resistivity is rather much slower as compared to diamond films without boron. Similar results are reported in [88]. It is found that a critical value of B/C ratio and deposition pressure is necessary at which boron-doped diamond film with least film resistivity can be obtained. At the highest pressure, the resistivity of BDD films reaches 6.3×10^5 Ω cm, which satisfies the requirement of electrical device applications [89, 90]. The variation of film resistivity with pressure can be explained as: at high pressures under high temperatures near the substrate, the B_4C vapors are usually decomposed into activated boron ions and carbon ions. At very low boron concentration, the boron ions can be easily added into the diamond films during the deposition process; as a result, concentration of hole carriers is increasing. Consequently, resistivity of the diamond film lowers by raising B/C ratio. When the B/C ratio exceeds, the B_4C vapor will be in a saturated state, leading to a saturation of hole carrier concentration. Secondly at high-deposition pressure, the effects of grain boundary and impurity scattering will be enhanced, which may deter the electron conductivity giving rise to a slow decrease of resistivity. This picture is

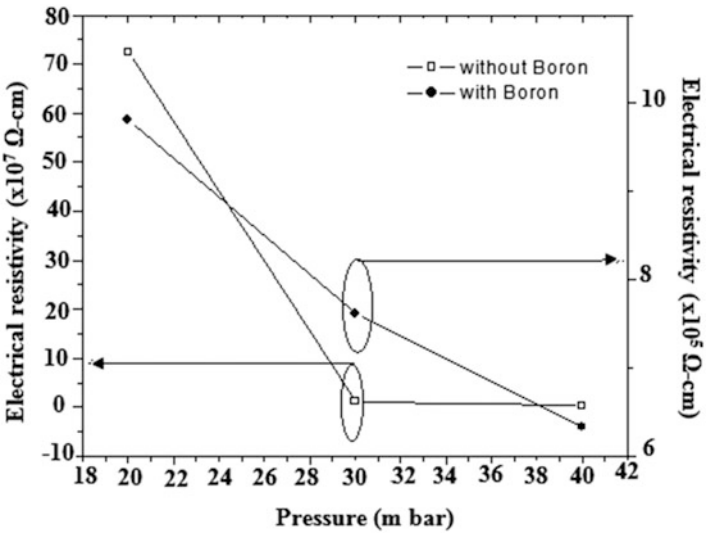

Fig. 13.25 Electrical resistivity as a function of pressure

partially supported by our experimental results from SEM and Raman analyses. Regarding Raman analyses, it is noted that with increasing pressure in the chamber, B-content in the film increases (Table 13.6). Moreover, the intensity and FWHM of Raman 1333 cm^{-1} peak almost decrease with an increase in pressure, which leads to relatively larger crystallite size (Table 13.6), relatively lesser grain boundaries and hence lesser resistance in the flow of charge carriers, that enhances conductivity.

13.2.4.5 Effect on Grain Size

The SEM cross-sectional view of boron-doped diamond films is shown in Fig. 13.26. For low pressure no continuous film is formed on the substrate showing voids. The growth behavior observed in these micrographs is analogous to Fig. 13.22d–f. Figure 13.27 shows that average grain size of the diamond films

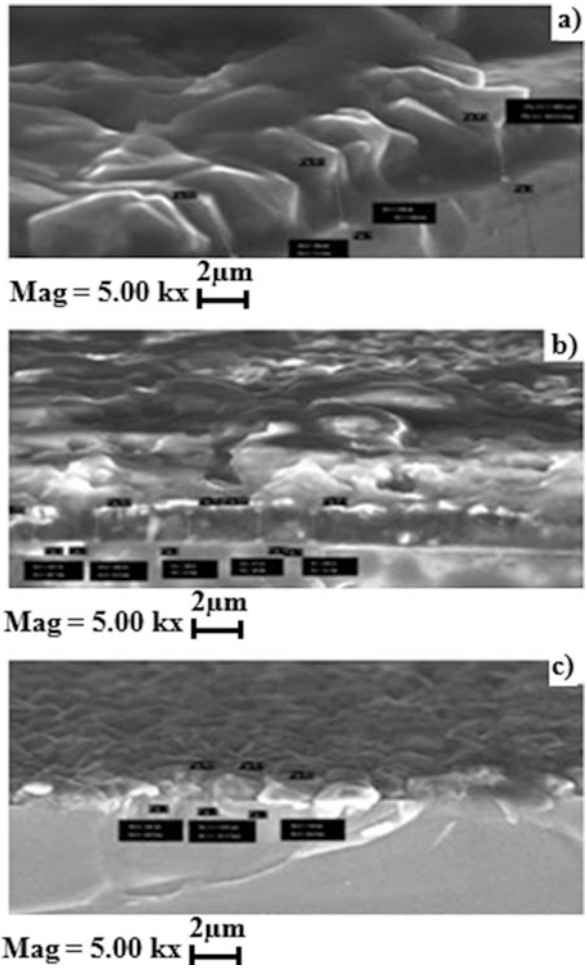

Fig. 13.26 SEM cross-sectional view of three diamond films at various pressures containing boron: (**a**) 20 mbar, (**b**) 30 mbar, (**c**) 40 mbar

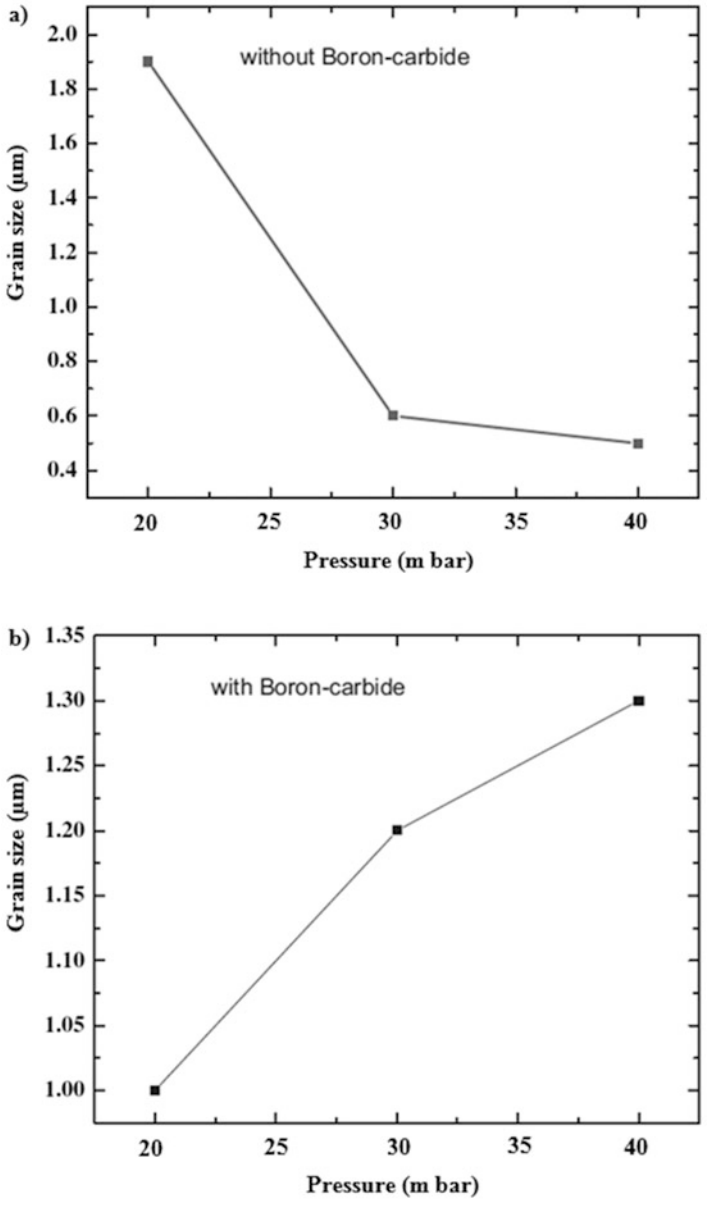

Fig. 13.27 Average grain size as a function of pressure: (**a**) without B, (**b**) with B

without boron content decreases rapidly when pressure increases from 20 to 30 mbar, while this reduction becomes almost constant as pressure exceeds to 40 mbar. On the addition of B_4C into the reactive gases, average grain size decreases from 1.9 ± 0.02 to 1.0 ± 0.02 µm. Figure 13.27 also depicts the behavior

of grain size of boron-doped diamond films as a function of pressure. It is seen that average grain size increases with increasing pressure from about 1 ± 0.02 to 1.3 ± 0.02 μm as discussed earlier in Sect. 3.2. However this behavior of grain size is opposite to that of diamond films without boron. Similar results were observed by Lu et al. [91], who noted that roughing step will bring defects on the Si substrates which are favorable for the nucleation of diamond.

13.2.5 Growth of Nitrogen-Incorporated Diamond Films Using Hot Filament Chemical Vapor Deposition Technique

Diamond films grown by HFCVD are polycrystalline and highly defective, and properties of these films differ from perfect diamond [25]. The doping and various deposition conditions may be responsible for defects such as dislocations, line defects, self-interstitial point defects, stacking faults, and species of grain boundaries, which show significant effects on the properties of diamond films [26]. Such doped diamond films can be made attractive for semiconducting applications [27]. The p-type and n-type conductivity in diamond can be obtained either by doping of boron [28] or nitrogen [38]. These doped p-type and n-type diamond films have some limitations, and it is challenging to achieve effective conductivity [29, 30]. The source of nitrogen impurities, which are unintentionally incorporated into the diamond film, is mainly from the leaking of atmospheric air into the deposition chamber [26]. Since the covalent radius of nitrogen is comparable to that of carbon ($r_C = 0.77$ Å, $r_N = 0.75$ Å), it has been observed, at low concentration, that it occupies the diamond lattice sites producing the substitution nitrogen-doped semiconducting and superconducting diamond films [36]. However, for high concentration of nitrogen, it may become incorporated in cluster form that may also produce changes in bonding and morphological structure of the films [37]. Ma et al. [38] observed a shrink in grain size from 15 ± 0.02 to 9 ± 0.02 nm of nitrogen-incorporated NCD films synthesized by MP CVD in a gas mixture of $CH_4/H_2/N_2$ with varying nitrogen concentration in a wide range (0–75%). In contrast, some researchers observed that grain size in the DC arc plasma jet CVD diamond films [39], ultrananocrystalline diamond (UNCD) films, and nano-wires [40, 41], synthesized by microwave plasma CVD, increases with the addition of nitrogen gas (up to 25%). Current status of understanding nitrogen doping of diamond remains unclear, and the subject still requires a thorough and systematic study.

The focus of this investigation is to elaborate the effect of nitrogen on film growth, grain size, and surface morphology of diamond films grown by HFCVD.

13.2.5.1 Structural Studies

Figure 13.28 shows representative patterns with typical polycrystalline structure. Two diamond peaks (1 1 1) and (2 2 0) were observed for all samples. While (3 1 1) diamond peak is present only when there is no nitrogen, the absence of (3 1 1) peak is strongly affected by crystal defect density. It might be considered as a result of increase of defect densities introduced by the increased nitrogen concentration [27]. The characteristic (1 1 1) peak of diamond structure is clearly visible at 2θ value of 43.9°. The FWHM of the diamond (1 1 1) XRD peak observed at 2θ angles of ~44° can be used as a qualitative measure of the degree of crystallinity. The FWHM is dependent on both the grain size and the crystallinity and usually has a tendency to become narrow when grain size becomes large [92]. The contraction of (1 1 1) peaks reveals an increase in crystal size for lower concentration of nitrogen (Fig. 13.28b, c), and its broadening exposes the decrease of crystal size for higher nitrogen concentrations (0.105 and 0.210 vol.%), which is shown in Fig. 13.28d, e. Similar results were observed by Yong et al. [93]. Figure 13.28 shows that diamond films grow preferably along (1 1 1) direction. This behavior is similar to the earlier results published in the scientific literature [93, 94].

13.2.5.2 Effect on Morphology

The morphology of diamond films grown at various nitrogen additions is shown in Fig. 13.29 by SEM micrographs. From these micrographs it is clear that there is a significant change in the film morphology when nitrogen is added to ($CH_4 + H_2$) gas mixture. Surface of the film without nitrogen consists of crystallites with randomly oriented {1 1 1} facets lying parallel to the substrate plane (Fig. 13.29a). For low concentration of nitrogen (i.e., nitrogen = 0.013 vol.%),

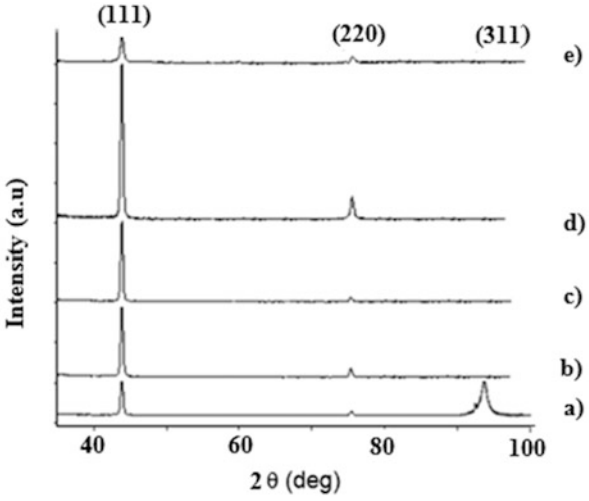

Fig. 13.28 XRD patterns of diamond films grown at substrate temperature of 900 °C with various nitrogen concentration (**a**) $N_2 = 0.000$, (**b**) 0.013, (**c**) 0.026, (**d**) 0.105, and (**e**) 0.210 vol.%

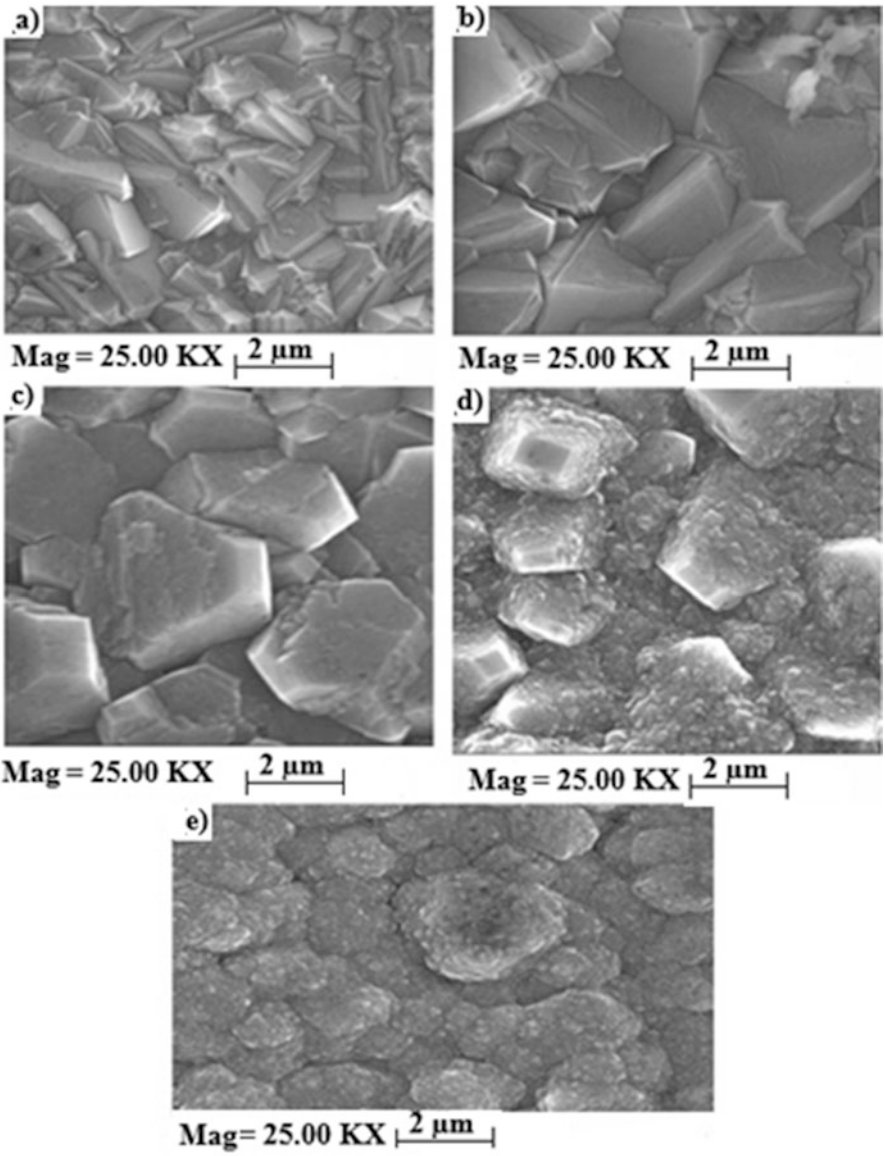

Fig. 13.29 Surface morphology of the coating prepared with various nitrogen concentration (**a**) $N_2 = 0.000$, (**b**) 0.013, (**c**) 0.026, (**d**) 0.105, and (**e**) 0.210 vol.%

the crystallites have well-defined edges, and there is no reasonable change in crystallite size (Fig. 13.29b). With further addition of nitrogen (i.e., nitrogen = 0.026 vol.%), the morphology is seen to involve secondary nucleation with slight increase in grain growth. Grain boundaries are very clear and sharp; upward growth with square surface is evident (Fig. 13.29c). This over/upward growth of

diamond grains may be due to sp^2-bounded graphitic carbon. For additional nitrogen concentration (i.e., nitrogen = 0.105 vol.%), observe a superposition of two grain populations, smaller (nano-sized) and bigger (micro-sized) ones, and multiple nucleation with excess growth and bigger top square edges (Fig. 13.29d). It can be noted that nucleation of nano-sized grains is higher than the microcrystallites; as a result average grain size abruptly decreases to nano. Similar results were observed by other researchers [27, 28, 38]. With more addition of nitrogen (i.e., nitrogen = 0.210 vol.%), cauliflower-like morphology is obtained (Fig. 13.29e). This type of morphology is very usual for nanocrystalline diamond films [39].

The superposition of two grain populations and excessive growth of secondary nucleation may be due to the following mechanisms: During diamond growth, atomic species (i.e., C^o, H^o) do not find sufficient time to move around to add well-defined crystallite sites and hence form secondary crystallites that grow rapidly with respect to microcrystallites. This may reduce the sharpness of crystallites edges (as clear from Fig. 13.29d to e) in the same way as it happens in case of dendritic growth [39]. Nitrogen is the well-known major impurity in natural and single crystal diamond [26, 36, 37]. It can easily be added into the diamond films as an impurity during the growth process as evidenced by nitrogen-related infrared absorption studies in nanocrystalline diamond films grown with nitrogen addition [95] and theoretical studies by density functional tight-binding simulations [96]. On reaching the tolerance limit of lattice imperfections due to N_2 impurity, the diamond lattice collapses and ceases further growth of diamond grains, hence leading to nanocrystalline diamond formation [92]. The extra growth and secondary population may be related to the unique large distortion along (1 1 1) direction of the C–N bond [37]. In the presence of large distortion along the (1 1 1) direction, it is difficult to grow along the same direction, because it is energetically favorable for the growth to proceed along another crystallographic direction [37].

13.2.5.3 Effect on Crystal Quality

The HFCVD grown films show the following features of Raman spectra as depicted in Fig. 13.30:

Si mode: Small peaks around wave numbers 964.9–994.5 cm^{-1} in the Raman spectra originate due to second-order phonon scattering from silicon substrate [97, 98], and therefore, their intensities are linked with substrate material.

Disorder (D) diamond: The strongest Raman feature around wave numbers 1345.2–1362.0 cm^{-1} is due to disorder D peak usually found in the spectra of diamond-like carbon at 1350 cm^{-1} [38, 94, 99], for various concentrations of nitrogen. This peak has been shifted from 1350 cm^{-1} to higher wave numbers, i.e., 1361 or 1362 cm^{-1} (Fig. 13.30b, c), due to compressive stresses caused by interstitial defects in the films [100] and toward lower wave numbers, i.e., 1345.2 cm^{-1} (Fig. 13.30d), due to tensile stresses in the film by the addition of nitrogen. The peak around wave number 1361 or 1362 cm^{-1} may also involve

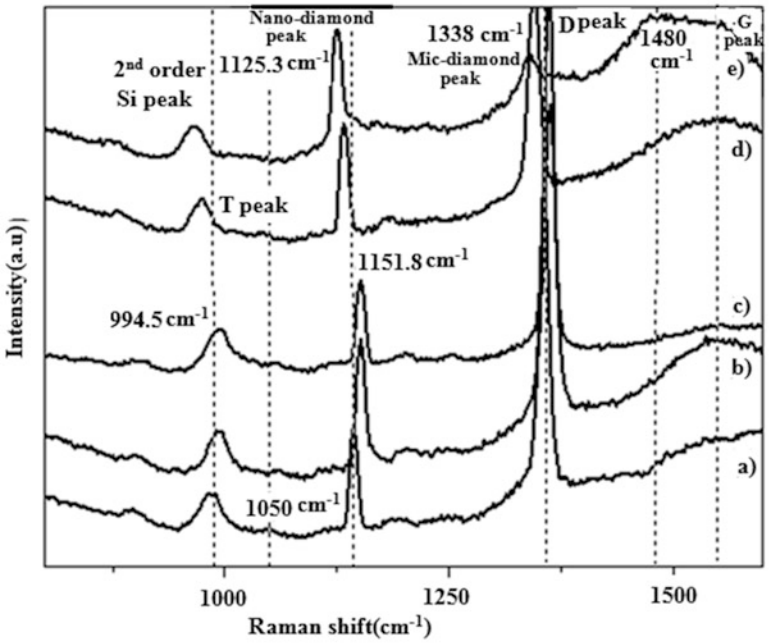

Fig. 13.30 Raman spectra of five diamond films with various nitrogen concentration (**a**) $N_2 = 0.000$, (**b**) 0.013, (**c**) 0.026, (**d**) 0.105, and (**e**) 0.210 vol.%

contributions due to the vibrational density of states (VDOS) of graphite [96]. In this region graphite has a higher VDOS band limits than diamond because the sp^2 sites have stronger, slightly shorter bond than sp^3 sites. The D peak at wave number 1357.4 cm^{-1} observed for film without nitrogen has been split into two new peaks with wave numbers 1340.2 and 1362.0 cm^{-1} (broad) at nitrogen content of 0.210 vol.% (Fig. 13.30e). The sharp peak at 1340.2 cm^{-1} may be due to the bulk diamond feature and represents the microcrystalline diamond [48]. This behavior is consistent with the SEM micrograph (Fig. 13.30e). No narrow diamond peak at 1332 cm^{-1} was detected in any of the films, although Fig. 13.30 shows clearly diamond XRD peaks. This can be explained as follows: in addition to the crystalline diamond phase in present films, there is still a component of non-diamond phase involving amorphous, diamond-like, or graphitic carbon structure.

T peaks: A weak and broad peak at wave number 1050 cm^{-1} originates due to small amount of diamond crystalline domain indicating that it could be precursor structure. This feature occurs in a region that might be expected for amorphous or microcrystalline diamond in polytype structure [97]. This peak also contributes to the C–C sp^3 vibrations [98]. This peak shifts toward higher wave numbers with nitrogen concentration up to 0.08 sccm, but for further rise of nitrogen content in the $CH_4 + H_2$ mixture, the peaks shift toward lower wave numbers, and at nitrogen content of 0.210 vol.%, it disappears due to the higher sp^2 and lesser sp^3 bonds [38, 97].

Amorphous network/nanoband: The peak at wave number 1125.3 cm^{-1} or 1133.1 cm^{-1} is associated with amorphous network [49]102 but often named nanocrystalline diamond in the literature [60, 101]. Similarly, sharp peaks in between 1144.0 and 1151.8 cm^{-1} wave numbers are attributed to C–H bonds [55] 38 and may provide direct evidence of nano-sized diamond crystals. Such peak was earlier considered disordered-activated but now believed to arise from sp^2 hybridized structure [97, 102]. Moreover peak around wave number 1480.0 cm^{-1} is due to C–H bonds [38] observed only in the film with the highest concentration of nitrogen (0.210 vol.%) as shown in Fig. 13.30e. This peak along with peak at 1125.3 cm^{-1} can be considered an indication of the presence of nano-diamond structure. This behavior is consistent with that observed through SEM (Fig. 13.29e).

Non-diamond band: Broad peaks around wave numbers of 1548.9–1553.6 cm^{-1} for various concentrations of nitrogen originate due to the bond stretching of all pairs of sp^2 sites only named as G peaks [101]. With the addition of nitrogen, intensity of this broad sp^2 feature is found to increase (except for film with nitrogen concentration of 0.026 vol.%), and the width is found to decrease. The presence of this non-diamond phase is a result of the deterioration of the crystal growth, most probably by nitrogen-induced multiple nucleation and overgrowth which finally lead to the deposition of layers with an amorphous appearance [100]. The smallest amount of non-diamond phase is noticed in the film with nitrogen content = 0.026 vol.% providing good-quality diamond crystallites (Figs. 13.29c and 13.30c). The Raman spectra of the graphitic regions appear somewhat similar to that of carbon nanotubes but significantly different from highly oriented pyrolytic graphite [99].

Within the scope described above, it could be concluded that spectra features indicate composite behavior. Such Raman feature possessing many vibrational modes is caused by the breakdown of the solid-state Raman selection rules since nanocrystalline or highly disordered films allow more vibrational modes to become Raman active [97]. This situation can be responsible for the shifting and asymmetric broadening of existing peaks and/or appearance of new signals [97]. Almost all peaks shift toward higher wave numbers with nitrogen concentration up to 0.026 vol.%, but for further rise of nitrogen content in the $(CH_4 + H_2)$ mixture, these peaks shift toward lower wave numbers. Some weak and broad peaks are also visible in spectra induced by local disorder [49]. The intensity of peak around wave number 1125 cm^{-1} increase with the increase of nitrogen indicating that the precursor area decreases with the increase of nitrogen content [97]. Moreover, it is a sign of reduction in the size of nanoparticles.

13.2.5.4 Effect on Grain Size

The average grain size obtained by SEM and conventional FWHM technique XRD is shown in Fig. 13.31, which indicates that it increases from 1.3 ± 0.02 to 1.4 ± 0.02 μm when nitrogen flow increased from 0.0 to 0.013 vol.%. For further increase of nitrogen to 0.026 vol.%, grain size further increased up to

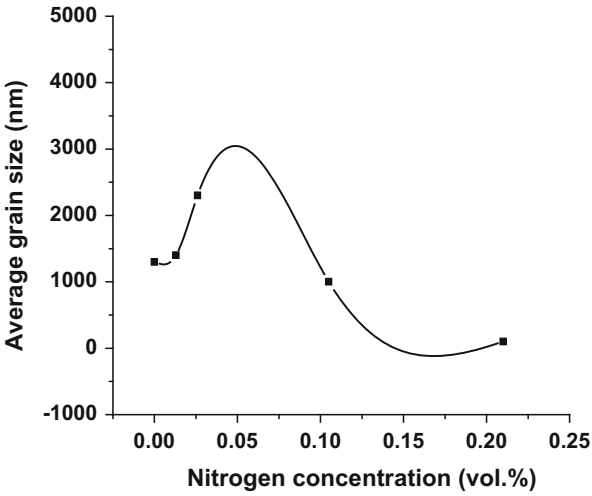

Fig. 13.31 Average grain size as a function of N_2 concentration

2.3 ± 0.02 μm. This type of nitrogen effect on diamond grain size is not in line with the published work on the topic as Ma et al. [38] detected a decrease in grain size from 15 ± 0.02 to ~7 ± 0.02 nm of nitrogen-incorporated NCD films synthesized by microwave plasma-enhanced CVD with rising nitrogen concentration in a wide range (0–75%) due to increasing defect density. However, present results follow the trend as observed in the DC arc plasma jet CVD diamond films [39]. On increasing nitrogen content in ($CH_4 + H_2$) mixture from 0.105 to 0.210 vol.%, grain size starts decreasing from microns to nanometers and reduces up to 100 ± 0.02 nm (Fig. 13.31). Variation of grain size as a function of nitrogen concentration shows opposite trend when compared with the published work [36–41]. As shown in Fig. 13.31, addition of nitrogen up to certain extent (0.013–0.026 vol.%) reduces the graphitic phase and enhances the diamond phase, but by further increase in nitrogen concentration from 0.105 to 0.210 vol.% leads to boost up the graphitic phase and defect sp^2 rings [97]. The variation in grain size with nitrogen concentration may be due to the following reasons:

At low concentrations, nitrogen incorporates into the diamond lattice producing semiconducting diamond [30]. This phenomenon might be responsible for the increase of grain size. On the other hand, the reduction of grain size may be due to the efficient etching mechanism of sp^2 and sp^3 carbon induced by nitrogen atoms [101]. This is also possible due to the reduction of defects in crystal, since at high concentration, nitrogen produces changes in bonding and morphological structure of the film [37].

13.2.5.5 Effect on Electrical Resistivity

The electrical resistivity was investigated by four-point probe *I–V* in van der Pauw geometry at room temperature with maximum applied voltage of ±100 V. Results

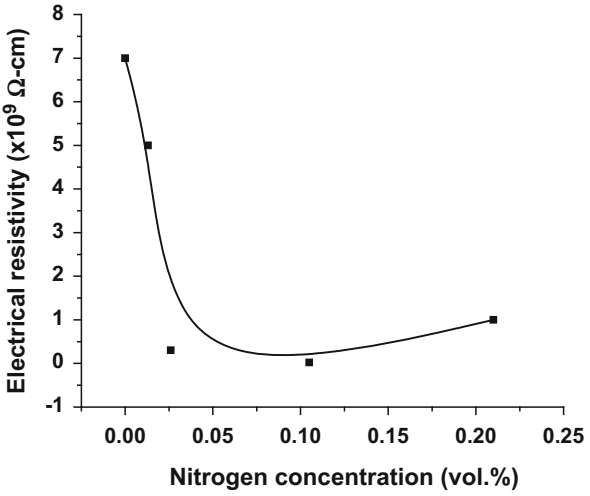

Fig. 13.32 Resistivity as a function of N_2 concentration

are depicted in Fig. 13.32 as a function of nitrogen concentration. It can be seen that the presence of nitrogen in the $(CH_4 + H_2)$ mixture significantly reduces the resistivity of diamond films from 7×10^9 to 2×10^7 Ω cm. The decrease of resistivity may be due to the increase of sp^2/sp^3 ratio [38] as observed in Raman spectra (Fig. 13.30) and significant changes in the microstructure [37]. Note that resistivity is minimum at nitrogen concentration (0.105 vol.%) and increases slightly for nitrogen content of 0.210 vol.% due to increasing disorder, showing an interrelation to the strong and relatively narrow G peak of the corresponding samples (Fig. 13.30d, e). The fall of resistivity may also be hypothesized by increasing the ordered phase (micro-diamond) than disordered phase (amorphous) of carbon on the top surface of the film [38].

13.2.6 Modeling of Doped Diamond Films

This chapter describes the theoretical modeling of diamond and diamond thin films on doping with various elements such as transition metals including Cu, Cd, Hg, Zn, and B and nonmetals involving various gases such as oxygen, nitrogen, etc. These theoretical results are based on density functional theory calculations and first-principle calculations performed by software such as VASP, etc. These calculations involve band structure determinations, density of states, formation energy, etc. of pure diamond and by doping diamond with various elements.

13.2.6.1 On Theoretical Study of Magnetic Behavior of Diamond Doped with Transition Metals

The interesting thing about properties of diamond is that it shows promising properties that underlies many interesting phenomenon of physics. However, it is distinguished in the sense that it exhibits optical, thermal, electronic, and magnetic properties.

Naturally occurring diamond does not show magnetism, but results are encouraging upon doping [103–107]. Nanocrystalline diamond films [108] improve performance of many electronic devices, and their magnetic behavior can be referred as the point to study spintronics [109, 110]. Spintronics is a spin-based concept of modifying technology which is very useful in physics. Using defects in diamond to probe magnetic properties at nanoscale has attracted many physicists in the area of the computer-based simulation [111–113]. These experimental and theoretical research monitor ferromagnetism (FM) in carbon-based materials [113–117] and theoretical predictions about the existence of ferromagnetism in carbon-based materials induced by disorder [118, 119] initialized the present studies. In this paper, we are interested in the role of substitution of transition metals (TMs) as dopant in bulk diamond crystal. In this scenario diamond lattice served to be the host and the TMs takes the place in diamond lattice as the primary substituted atom. Upon doping together, their happy relationship subjects magnetism in material sciences. The TMs are assumed to be symmetrically doped in the host. When substitutional TMs occupy cation sites, the d states of the TMs hybridize with the p states of the neighboring host anions (carbon atom). This p-d hybridization results in strong magnetic interactions between localized spins and carriers in the host's valence band [120]. As a result, the system exhibits stable ferromagnetism, and the spin-polarized carriers are used for spin manipulation. We choose to study the effect of TMs metal substitution into diamond bulk. From theoretical point of view, although TMs do not have magnetic complications, hence one can avoid possible magnetic ground states at low temperatures. In the present study we elaborate and encourage the importance of TMs doping in diamond to check out its magnetic behavior in terms of ferromagnetism.

13.2.6.2 DFT Picture

For each crystal structure, total energy can be calculated using density functional theory as described by Hohenberg and Kohn [121]. The electronic configuration of various TMs such as Cu, Cd, Hg, and Zn are reliably dependent upon different orbitals which specify the distribution of electrons. The shell configurations of these TMs are shown in Table 13.7 given below:

Among the modern simulation techniques, the projected augmented wave (PAW) method has proved to be an effective and accurate process of calculating electronic structure and semi-local functions. This is due to its accurate determination of interaction integrals by controlling multiple moments. Its mathematical

Table 13.7 The electronic configurations of various transition metals

Metal	Symbol	Atomic No.	Atomic radii (pm)	Electronic configurations
Carbon	C	6	67	$1s^2, 2s^2, 2p^2$
Copper	Cu	29	145	$1s^2, 2s^2, 2p^6, 3s^2, 3p^6, 3d^{10}, 4s^1$
Zinc	Zn	30	142	$1s^2, 2s^2, 2p^6, 3s^2, 3p^6, 3d^{10}, 4s^2$
Cadmium	Cd	48	161	$1s^2, 2s^2, 2p^6, 3s^2, 3p^6, 3d^{10}, 4s^2, 4p^6, 4d^{10}, 5s^2$
Mercury	Hg	80	171	$1s^2, 2s^2, 2p^6, 3s^2, 3p^6, 3d^{10}, 4s^2, 4p^6, 4d^{10}, 5s^2, 5p^6, 4f^{14}, 5d^{10}, 6s^2$

beauty is that it links the physical wave function to an auxiliary one. The wave function is divided into two parts:

$$\psi(r) = \psi_c(r) + \psi_v(r) \tag{13.4}$$

The subscripts "c" and "v" correspond to the states in core and valence shell, respectively. The metallic p orbital further splits into three orbitals which are responsible for most of the properties when material is doped with other metals. This phenomenon is referred as the hybridization of orbitals. Theoretical description of electronic properties can be stated with reference to Eq. 13.5 and the above-cited facts. Empirically, electrical conductivity in semiconductors depends upon transition of electrons from valence to conduction band and hence upon the band gap E_g:

$$E_g = E_c - E_v \tag{13.5}$$

where E_c and E_v are the respective energies of the conduction and valence band edges [122]. The schematic diagram (Fig. 13.33) illustrates the band gap in semiconductors by plotting valence (V_B) and conduction (C_B) bands as $E(k)$ diagram.

For carbon atoms, band gap energy is found to show variations because different research workers tried different approximations [107, 123, 124] for its determination. Remediakis and Kaxiras [124] have determined band gap of carbon using GDFT/LDA to be 4.718 eV, while they found the value of 5.48 eV experimentally. Present calculations determined the value of band gap of virgin diamond to be 4.71 eV using DFT/GGA, whereas it has the respective values of 2.23, 2.25, 2.26, and 2.92 due to the doping of Cu, Cd, Hg, and Zn into diamond lattice. These values of diamond band gap for each doped metal are given in Table 13.8.

13.2.6.3 Magnetic Behavior of Doped Atoms

To observe the magnetic behavior of diamond films, diamond structure was first optimized to find out the optimized lattice parameters. A carbon atom in the diamond lattice was then substituted by one TM atom. This substitution causes

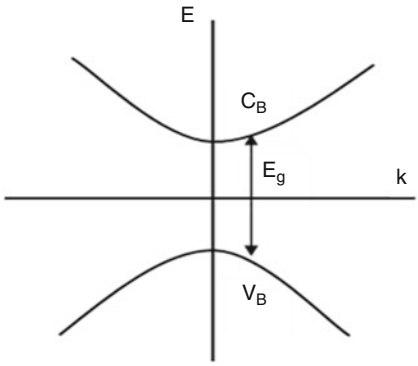

Fig. 13.33 Schematic diagram of the band gap

Table 13.8 Band gap of diamond films upon doping of different metals

Sr. No.	Material	Band gap (eV)
1	Diamond without doping	4.71
2	Diamond with Cu doping	2.23
3	Diamond with Cd doping	2.25
4	Diamond with Hg doping	2.26
5	Diamond with Zn doping	2.92

only a slight change of −0.005 Å in the lattice parameter *a* after performing the structural optimization. In fact, this difference occurred due to the differences in atomic radii of carbon and TMs atoms as well as any change observed in bond lengths of each transition metal atom with its four nearest neighbor carbon atoms (TMs-C_4 system), such bond length is around 1.54 Å. The spin-polarized states that possess energies of 557, 563, 557, and 554 eV, respectively, for Cu, Cd, Hg, and Zn doping in diamond are noticed to be lower than those of non-spin-polarized state energies. The total magnetic moments determined have values of 2.89, 1.99, 1.96, and 1.80μ_B per Cu, Cd, Hg, and Zn atoms in the doped diamond, respectively. The magnetization observed in doped diamonds is found to be well consistent with that determined by Wu et al. [122] with the exception that present doped diamonds acquired slightly larger magnetic moments. The spin charge densities of these TMs-3d and C-2p are shown in Fig. 13.34, whereas the spin-resolved density of states of the TM-doped diamond system is shown in Fig. 13.35. It can be seen from that majority spin is semiconducting with a gap, and the minority spin shows metallic behavior with adequate unfilled states above the Fermi level, suggesting a half metallic behavior which is also reported in [125]. These unfilled states are very useful in charging a conduction carrier, which is required in spin injection where sufficient polarized spin current is required [122], so it is proposed that TM-doped diamond can be used as spin injection charge carriers. In the present study we used same techniques for magnetic coupling as used in [122]. For ferromagnetic and antiferromagnetic (AFM) coupling, we substitute two TMs atoms separated with the largest possible distance 7.92 **Å**. The total energy is calculated for both cases along *c*-direction, and it is found that FM state is the ground state than that of AFM state.

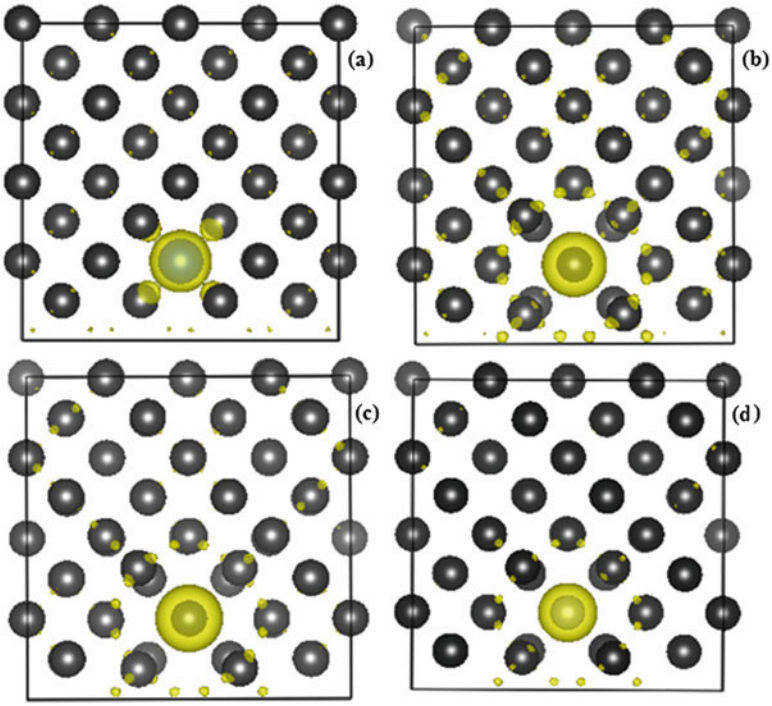

Fig. 13.34 Isosurface of spin charge density of NDFs system doped with 1.56% (**a**) Cu, (**b**) Cd, (**c**) Hg, (**d**) Zn

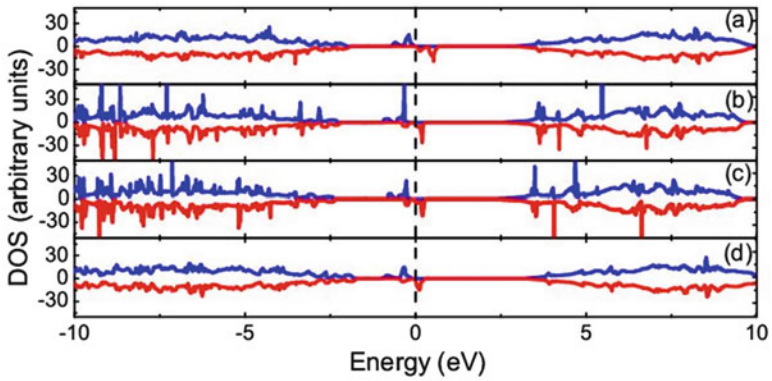

Fig. 13.35 Spin-polarized DOSs of (**a**) Cu, (**b**) Cd, (**c**) Hg, (**d**) Zn show semiconducting behavior at Fermi level

13.2.6.4 Electronics Properties

The spin-resolved band structures of the doped diamond are shown in Fig. 13.36. It can be seen from the majority spin channel being semiconductor, and red line shows the Fermi level in both majority and minority spin-polarized band structures. The minority spin-polarized band structure shows metallic behavior with adequate unfilled states above the Fermi level which is also reported in [122]. It is also observed that majority of spin-polarized channel of Cu-doped diamond shows more semiconducting behavior and thus larger spin polarization as compared to other TMs, so the Cu is more favorable for this purpose.

In density of state, blue and red curves correspond to d and p orbitals, respectively, for TM-doped diamond as in Fig. 13.35; it shows the half metallic behavior which is also reported in [126]. It is observed from the results of DOS of each species having different values of curve from valence to conduction band at the Fermi level that Cu has higher value, and this band also splits near the Fermi level (−18.86), whereas Zn carries the lowest value (−13.46). The Cd and Hg consist of intermediate values. In order to understand the mechanism of stabilized FM state in TM-doped diamond, projected spin densities of states (PDOSs) of the TMs atom and its four mutual nearest neighboring C-atoms are investigated which are shown in Fig. 13.37. (Cu-$C_{4)}$. It can be seen from majority spin channel the strong coupling between Cu 3d and C 2p; the interaction peak is observed at −2.56 eV for Cu-3d overlaps with that of 2p of the C-atoms in Cu-C_4, and the second peak of Cu-3d at −0.861 eV also overlaps with that of 2p of C-atom with smaller magnetization. It is also observed from the valance band channel that there is splitting of states that occurred in case of Cu atom due to d–d hybridizations. In the minority spin channel, the 2p state of the four connecting C-atoms contributes significantly to the unoccupied states, and this kind of similar trend can also be found for Cd, Hg, and Zn which are shown in Figs. 13.38, 13.39, and 13.40, respectively. These attributes indicate a strong hybridization between TMs and its four neighboring C-atoms. This strong hybridization induces finite magnetization on TMs atom as well as the neighboring C-atoms, as shown in Fig. 13.34. Each C-atom carrying magnetization and the magnitude of the magnetization in due to all these TMs dopant in diamond are present in Table 13.9.

13.2.6.5 Formation Energy

In almost all materials, some kind of defect is always present, and they prominently affect the electronics and magnetic properties of the host material. Theoretically, these defects can be defined topologically [127–129]. Formation energy is the difference in the total crystal energy before and after the defect arises. They are often formed as compensation sources when dopants are introduced, or as a result of nonstoichiometric growth or annealing. Defect formation energy varies animally with Fermi energy and the chemical potential of the atomic species [130].

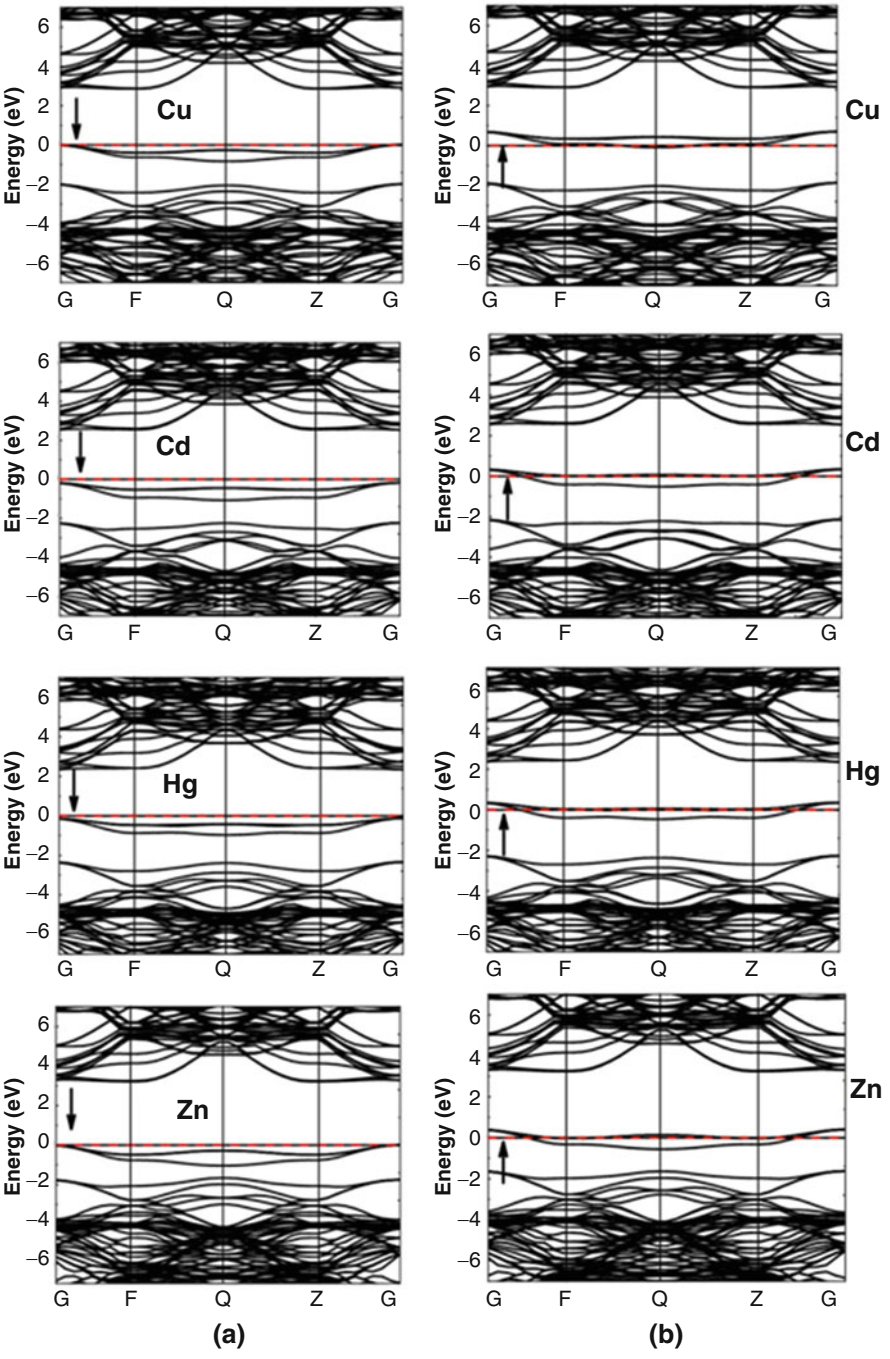

Fig. 13.36 Band structure of (**a**) minority spin and (**b**) majority spin of NDFs with 1.56% of TMs doped and *red dotted line* show the Fermi level

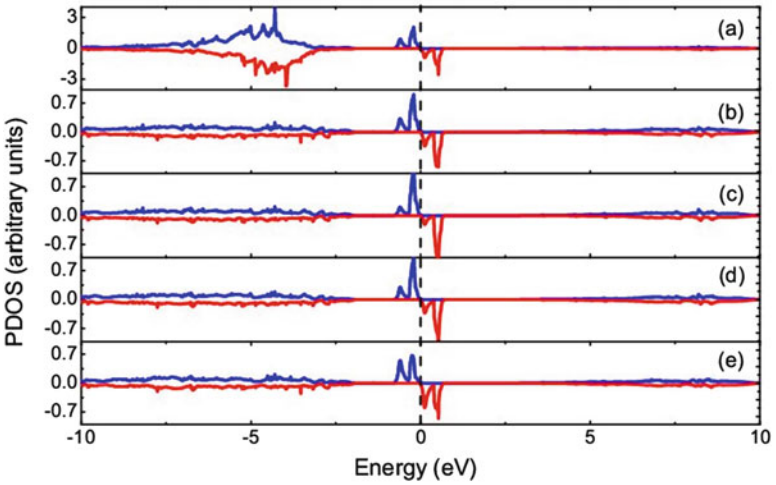

Fig. 13.37 Spin PDOSs of Cu-3d (**a**) and C-2p of the C-atoms in Cu-C_4 structure (**b**)–(**e**)

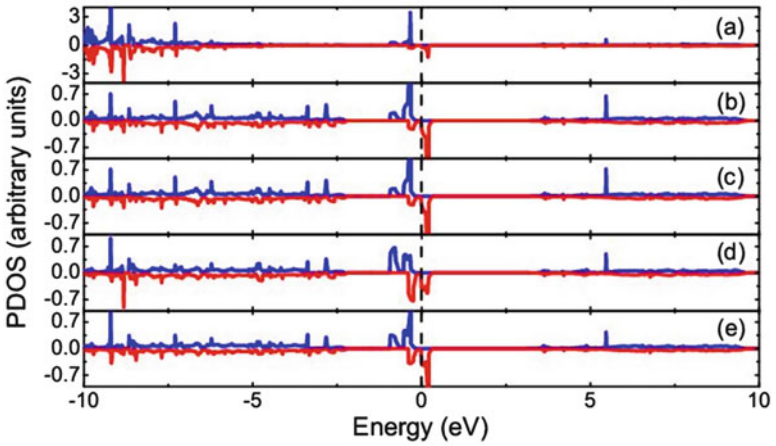

Fig. 13.38 Spin PDOSs of Cd-3d (**a**) and C-2p of the C-atoms in Cd-C_4 structure (**b**)–(**e**)

The formation energy is defined as:

$$E_f = E_{tot} - E^0_{tot} + n_+\mu_+ \tag{13.6}$$

where E_{tot} is the total energy of the system containing the defect, is the total energy of the system, n_+ is the number of the defects atoms introduced into the host E^0_{tot} system, and μ_+ is its chemical potential. In the present study, the formation energy of carbon cadmium-doped system is smaller (−24.16 eV) as compared to the

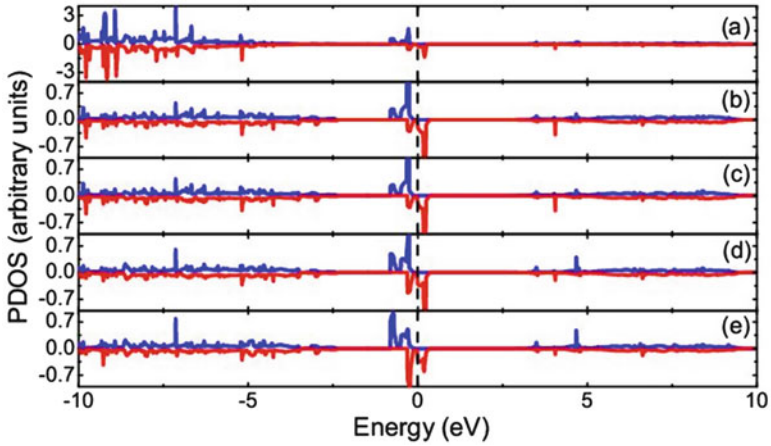

Fig. 13.39. Spin PDOSs of Hg-3d (**a**) and C-2p of the C-atoms in Hg-C_4 structure (**b**)–(**e**)

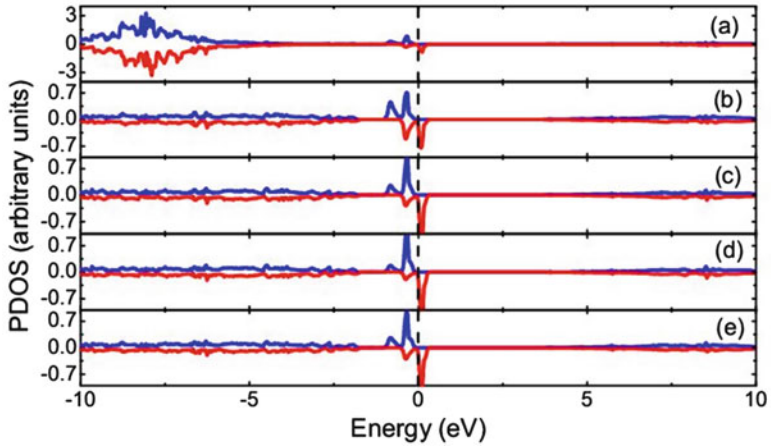

Fig. 13.40 Spin PDOSs of Zn-3d (**a**) and C-2p of C-atoms in Zn-C_4 structure (**b**)–(**e**)

carbon copper-doped system (−17.31 eV), and formation energy of Hg and Zn lies in between −21.12 eV and −18.16 eV, respectively.

13.2.6.6 Analysis of Bond Length and Bond Angle

When non-TM atom is incorporated into diamond, impurity atoms can form bond with carbon. This bond lengths and bond angle of the nearest neighbor of TMs with carbon are shown in Table 13.10. The bond length of Cu–C_4 system is less as compared to the other dopant; it is due to the difference of their atomic radii size.

Table 13.9 Magnetic moments of different doped system in diamond

Species	Magnetic moment (μ_B)
Cu–C	
Cu	0.796
C_4	0.242 (each carbon)
Cd–C	
Cd	0.303
C_4	0.223 (each carbon)
Hg–C	
Hg	0.395
C_4	0.213 (each carbon)
Zn–C	
Zn	0.371
C_4	0.197 (each carbon)

Table 13.10 Bond lengths and the bond angle among the nearest non-TM atoms doped in various doped diamond

Species	Atomic radii (Pm)	Length (Å)	Bond angle (°)
$Cu–C_4$	128	1.539	109.47
$Cd–C_4$	161	1.912	109.47
$Hg–C_4$	171	1.929	109.47
$Zn–C_4$	142	1.801	109.47

From above analysis, doping concentration has a great impact on bond lengths of TMs with carbon bond.

13.2.7 Electrical Conductivity Enhancement by Boron Doping in Diamond Using First-Principle Calculations

Diamond and its thin films have acquired an extraordinary attractiveness and large potential industrial applications because of their highly valuable characteristics such as high-carrier mobility, the highest hardness, chemical inertness, and large energy gap (~5.5 eV) making them highly insulating materials with high thermal conductivity [131, 137]. Moreover, doping of various elements such as boron, nitrogen, oxygen, and phosphorus in diamond further enhances its usefulness into applications of electronics and electrochemical devices [132, 133, 138, 139]. It is known that doping of small amounts of boron in diamond makes it a material with p-type character having activation energy of ~0.37 eV [134–136, 140–142]. On the other hand, heavily boron-doped diamond usually demonstrates metallic behavior [91]. Recently heavily boron-doped diamond has shown superconducting behavior. Such interesting characteristics have significantly attracted the attention of researchers and opened new ways for handling superconductivity issue caused by impurity-induced metallization in semiconductors [143–147]. However, the

fabrication and characterization of p-type diamond thin films with small amounts of boron doping could not show much progress; as a result the development of diamond-based p-type semiconductor devices was diminished.

In recent years, a few researchers tried to explore B-doping in diamond experimentally [91, 143, 147–151] and somewhat theoretically [143, 144, 152, 153] through computer simulations without much success. Nakamura et al. [137] tried experimentally to explore electronic structure of B-doped diamond using soft X-ray absorption and emission spectroscopy near B and C *K* edges. According to them electronic structure of C, 2s 2p near Fermi level, is responsible for electronic properties of B-doped diamonds. However, Xiang et al. [152] and Blasé et al. [153] investigated the electronic structure of B-doped diamond through computer simulations using density functional theory (DFT) and illustrated superconductivity in highly B-doped diamond to be caused by electron-phonon coupling (EPC). Ashcheulov et al. [144] have recently shown that boron defects concentration and their location play key roles in the conductivity of diamond. In addition, we have already demonstrated experimentally that boron doping in diamond thin films enhances its electrical conductivity with the increase of chamber pressure in hot filament chemical vapor deposition (HFCVD) system, since a rise of chamber pressure resulted in enhancement of boron concentration in diamond films [148]. It is also noticeable that when B-doping in diamond films is low, boron replaces C-atoms (substitutional defects) and do not accumulate at the grain boundaries. On the other hand, when large number of B-atoms diffuses into the diamond structure, they not only replace C-atoms in the matrix but also accumulate themselves at grain boundaries (interstitial defects). As a result, B-atoms not only increase conductivity but also induce structural defects and so high concentration of B-doping can damage the crystal structure integrity. Moreover, high B-content in diamond ($>10^{20}$ atoms cm^{-3}) may result in metallic-like conductivity, while low B-content ($\sim10^{17}$ atoms cm^{-3}) produces hole conduction in the valence band caused by ionized substitutional B-atoms [91, 144]. That's why in order to maintain the conductivity and the integrity of crystal structure of B-doped diamond thin films, it looks significantly useful to study theoretically the crystal and electronic structure of diamond at low and high concentrations of B-doping by considering total/partial density of states (T/P DOS) of B: 2s 2p and C: 2s 2p structures through computer simulations. Determination of total/partial density of states and charge distributions are found to be more reliable ways to study and explain electronic properties of semiconducting materials in comparison with conventional Bardeen, Cooper, and Schrieffer (BCS) theory [131, 137].

In this study, the experimental results obtained for B-doping in diamond thin films [148] are further analyzed in detail with the aid of first-principle calculations in terms of B-atoms contribution to the continuum of diamond electronic states. In this regard, the electronic structure of both B: 2s 2p and C: 2s 2p in B-doped diamond has been explored by applying the density functional theory (DFT) simulations. Because electrical conductivity of doped diamond is mainly attributed to C: 2p, electronic structure near the Fermi level and any variation in its electronic

structure caused by impurity/defects are expected to be responsible for enhancement/decrement in electrical conductivity. TDOS and PDOS have been determined for various B-concentrations in B-doped diamond films in order to study the influence of B-content on the electronic states of the diamond lattice. Moreover, the electronic structures are analyzed to determine bonding properties and charge distributions among boron and carbon atoms and their impact on the electronic properties of B-doped diamond thin films. The main aim of these DFT calculations was to create a relationship between fundamental properties such as B–B, B–C bonds, charge, and the electronic states of B-incorporated in B-doped polycrystalline diamond films and explanation of possible mechanism for the enhancement in electrical conductivity.

13.2.7.1 Electron Density of States

In order to analyze the electronic structure, determination of partial and total electron density of states has been made for the case of diamond films doped with different boron concentrations. Just for comparison the well-known TDOS and PDOS of pristine diamond films are presented in Fig. 13.41. This diagram clearly illustrates the electron density of states in the valence and conduction bands separated by an energy band gap (~4.61 eV) and also the Fermi energy E_F (the *dotted line*). It is noticed that the valence band of pure diamond consists of two

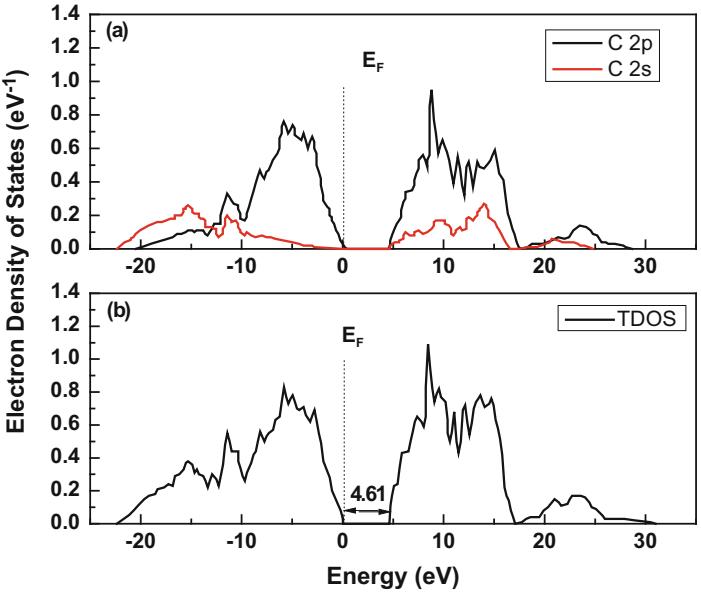

Fig. 13.41 (**a**) PDOS and (**b**) TDOS of pristine diamond depicting the electrical charge distribution of C: 2s and C: 2p orbits

regions showing high and low energies. These high- and low-energy regions are mainly occupied by C: 2p and C: 2s states, respectively, as clear from Fig. 13.31a, whereas C: 2p electron states are found to be dominant in the conduction band of diamond. Moreover, the PDOS measurements in the conduction band region depict that ratio of the areas under the curves for C: 2s and C: 2p states is approximately 1:3 (Fig. 13.41a).

In addition, combined effect of these two energy states is presented in Fig. 13.41b as total density of states (TDOSs). The data presented in Fig. 13.41 for pure diamond films has been compared with total density of states of the B-doped diamond films as illustrated in Fig. 13.42. It can be noticed from Fig. 13.42 that both the conduction and the valence bands have been shifted toward lower energies in the case of weak B-doped diamond (~1.54% B, TDOS for $n = 64$) films yielding a decrease in the band gap energy (~2.61 eV). The Fermi level is now found almost in the middle of the valence and conduction bands; it was close to top of valance band edge in pure diamond. It means that the addition of boron atoms to diamond films generates few localized states close to the top of valence band edge as demonstrated in Fig. 13.43 (the acceptor levels lie at small energy interval of

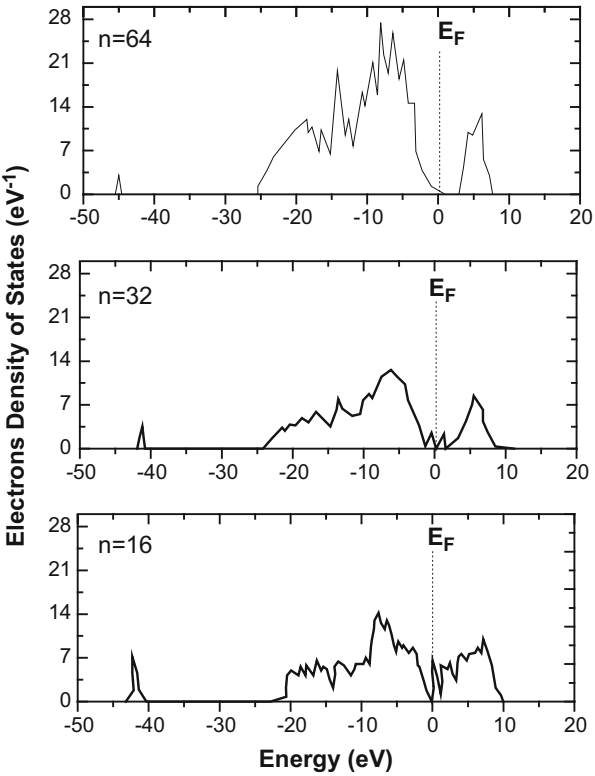

Fig. 13.42 TDOS of B-doped diamond films. Here n is the total number of C-atoms along with one boron atom in each cell

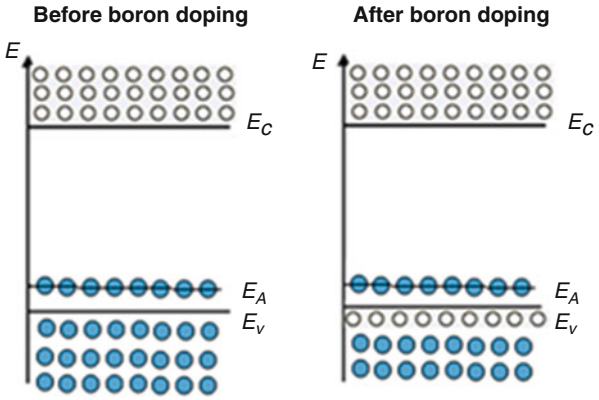

Fig. 13.43 Schematic diagram of energy levels in B-doped diamond

$E_A \sim 0.065$ eV). In addition, the valence band peak for boron atoms appears and is centered at -45.0 eV having a width of ~1.5 eV. This boron peak also seems to contribute to reduce the band gap energy and an increase in the conductivity of B-doped diamond. When boron concentration becomes relatively high (~3.03% B, TDOS for $n = 32$ as shown in Fig. 13.42), Fermi level shifts slightly toward top of the valence band, and some localized states (acceptor levels) are formed inside the energy band gap as well as close to the bottom of the conduction band. As a result, energy gap of such a doped diamond suddenly falls to very small value as compared to that of un-doped diamond films (Fig. 13.42 for $n = 32$), and hence B-doped diamond films behave like a good semiconductor. Moreover, the valence band peak for boron atoms has now been shifted toward higher energies and is centered at -41.10 eV (having almost the same width as observed for low B-doping, $n = 64$). The shifting of boron valence band peak toward higher energies might also be a cause of reduction in the band gap energy and an enhancement in the conductivity. Similar types of results have already been observed by Shao et al. [154] for Li- and P-doping in diamond. Further rise of boron concentration (~5.88% B, TDOS for $n = 16$ as in Fig. 13.44) in diamond creates a high density of acceptor level states in the energy gap which overlaps with the conduction band. That's why Fermi level coincides with the top of valence band, yielding a significant reduction in the energy band gap to have almost zero magnitude. This behavior of TDOS signifies the conductive nature of highly B-doped diamond films. The valence band peak for boron atoms has now been shifted slightly toward lower energies and is centered at -42.26 eV, but now it has almost twice the width as observed for low B-doping; it also depicts a significant rise in TDOS. The shifting of boron valence band toward higher energies with rising B-doping in diamond films is very much analogous to that observed for Li- and P-doping in diamonds [154]. This behavior might be related with widening of impurity level states in such a way that they can create an impurity band [155], which almost completely fills the energy gap region, and hence highly B-doped diamond behaves as a conductor. In addition, hopping conduction in B-doped diamond using the excited states of B-atoms also plays a key role in enhancing conductivity. With the increase of B-content in diamond, the

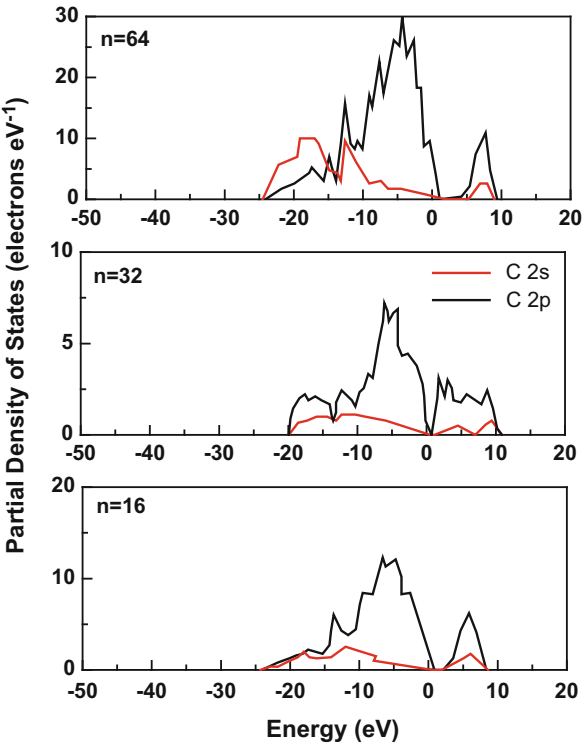

Fig. 13.44 PDOS of B-doped diamond depicting the electric charge distributions of C: 2s and C: 2p orbits of the carbon atoms

wave functions of B-excited states overlap and create an impurity band leading to a variable-range hopping mechanism [144]. For highly concentrated B-doped diamond, impurity band accesses the top of valence band yielding metallic-like behavior. All the abovementioned facts illustrate that when acceptor impurity atoms are incorporated into diamond, impurity (acceptor) level hole states appear at top of the valence band enabling B-doped diamond films to act as a semiconductor. But on further increasing the concentration of boron atoms in the diamond lattice, more and more impurity states are created inside the energy gap at top of the valence as well as bottom of conduction bands, widening the acceptor levels and converting them into an impurity band, or even extending them to the entire energy gap region. Hence, semiconducting behavior of B-doped diamond films changes to that of a conductor. This result may lead to metal-insulator transition of B-doped diamond.

13.2.7.2 Partial Density of States

For more detailed analysis of the electronic properties of B-doped diamond films, partial density of states (PDOS) is also determined for varying concentrations of B-atoms. Such calculated PDOS for B-doped diamond are shown in Fig. 13.44.

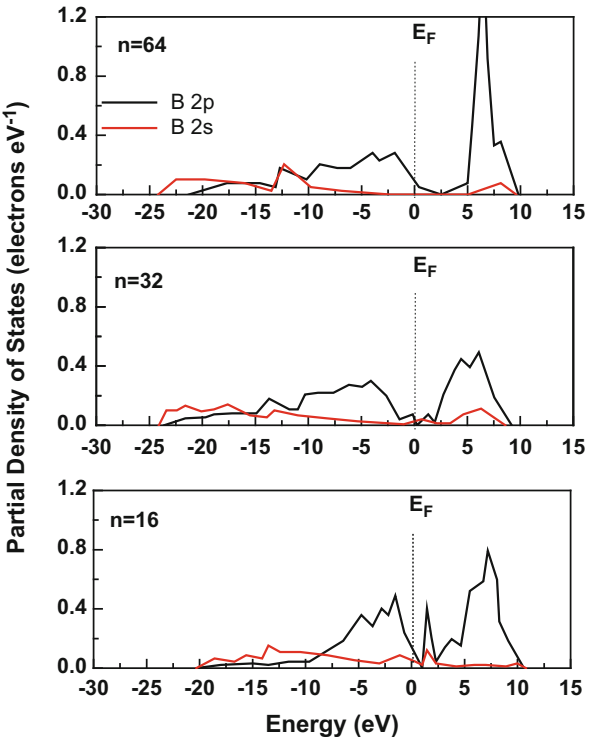

Fig. 13.45 PDOS of B-doped diamond depicting the electric charge distributions of B: 2s and B: 2p orbits of the boron atoms

From these plots, it is clear that contributions of carbon atoms 2s orbit in the valence band decreases as the concentration of boron atoms increases. Moreover the density of states of C: 2p orbit shows a decrease in magnitude with rising boron content. In addition, the most part of valence band near Fermi level and whole conduction band mainly comes from contributions of carbon atoms 2p orbit. However, a little contribution of C: 2s orbit in the conduction band of B-doped carbon is also obvious from Fig. 13.44. At low doping concentration, area of PDOS of conduction band is large, while at high B-doping concentration, conduction band area of PDOS becomes small. On the other hand, PDOS plots drawn in Fig. 13.45 clearly demonstrate a significant rise in contributions of B: 2s orbit for both valence as well as conduction bands in contrast to C: 2s orbit (Fig. 13.44) with rising B-doping in diamond. In addition, Fig. 13.45 also illustrates that because of increasing B-content in diamond films, both B: 2s and B: 2p orbits involve themselves to create impurity levels in the region of band gap energy, and their density increases with increasing B-content. It is also noticed that the band gap energy of B-doped diamond decreases with increasing B-doping. Furthermore, area under PDOS plots of conduction band portion looks to be directly proportional to the doping concentration because as doping concentration increases, area under PDOS (boron) plots of conduction band region also depicts an increase as obvious from Fig. 13.45. Hence, as a B-atom is incorporated into diamond lattice, covalent

bonds near the B-atom will be wiped out, and energy bands of carbon and boron atoms will split near Fermi level. This splitting of energy bands near Fermi level increases with increasing boron concentration. This may be due to the interactions between outer shell electrons of B-atom and carbon atoms [154]. Such splitting of energy bands near the Fermi level is very much favorable in enhancing the conducting properties of a semiconductor [154].

13.2.7.3 Orbital Charge Distribution

In order to understand orbital electron distributions of each atom in B-doped diamond films and to know how bonding exists among different atoms, orbital charge distribution was determined and results obtained from such calculations are shown in Table 13.11. It is seen that both s and p orbital charge numbers are positive and show only slight variations. It means that when B-atoms combine with other atoms they lose nearly the same charge in the vicinity of carbon atoms with rising B-atoms concentration in the diamond lattice. How B-atoms are bonded to C-atoms and how electrical charge is distributed among various atoms in B-doped diamond are clearly illustrated in Fig. 13.46. Our DFT calculations have shown that at higher concentration of boron atoms in diamond lattice, atomic charge of B-atom is

Table 13.11 Orbital charge distributions of B-atoms in B-doped diamond films

Number of carbon atoms	s (orbital charge after atom combined with another atom)	p (orbital charge after atom combined with another atom)	Total charge (eV)	Charge that an atom gains/losses after it combined with another atom (eV)
16	1.21	2.36	3.57	−1.90
32	1.22	2.34	3.56	−0.87
64	1.24	2.28	3.52	1.89

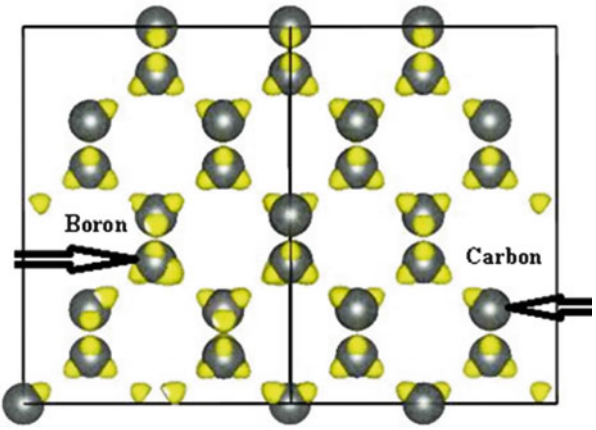

Fig. 13.46 Representation of the electrical charge distributions of boron-doped diamond

negative indicating that some charge of C-atom has transferred to boron atom (Table 13.7). Moreover, it is also obvious from Table 13.11 that at higher concentration of B-atoms, total change in s and p orbital charge numbers of boron atom increases slightly from 3.56 to 3.57; however, the atomic charge decreases significantly, i.e., from −0.87 to −1.90 which boron atom gains after it combines with another atom. This negative charge may be caused by low vibrational modes induced by boron atoms that occupy interstitial spaces in diamond lattice [131, 137], since it is known that boron atoms yield much localized vibrational modes which contribute to half of electron-phonon coupling [152, 153]. At lower boron content in B-doped diamond ($n = 64$ leading to ~1.54% B), atomic charge of boron atom is positive indicating that some charge of B-atom has transferred to the vicinity of carbon atoms (Table 13.11). In this case, the s orbital charge number is the highest, and p orbital charge number is the lowest, yielding a total change in s and p orbital charge numbers of boron atom of 3.52, and the atomic charge becomes positive, i.e., 1.89, which boron atom loses after it combines with another atom. The above-cited facts indicate that when doping concentration is low, B-atom contributes charge to bonding, but on increasing its content in diamond lattice, it gains charge after bonding with other atoms. As a consequence, it can be said that B-atoms induce structural defects, which are helpful in improving conductivity but may damage the integrity of diamond crystals at much higher concentration of boron atoms [144, 154].

13.2.7.4 Analysis of Bond Length

When boron atoms are incorporated into diamond lattice, they can form B–C bonds. The bond lengths and bond populations of such nearest neighbor B–C bonds have been calculated, and results are presented in Table 13.12. At low doping concentrations of B-atoms ($n = 64$ leading to ~1.54% B), bond population of B-C-atoms is −0.11 indicating that B–C bonds demonstrate antibonding state. But as doping content of B-atoms increases, bond population values become positive indicating that the antibonding state has now been transferred to an acceptable bonding state. By looking at the magnitudes of B–C bond lengths (Table 13.12), it can be concluded that when boron content in the diamond lattice is low (i.e., when $n = 64$), length of B–C bond is about 2.54 Å. However, results display a slight reduction of about 0.04 Å in the average value of B–C bond length when $n \leq 32$. From above analysis, it can be inferred that the studied concentration of B-doping in the diamond lattice has not posed much significant impact on bond lengths of B–C bonds.

Table 13.12 Bond lengths and bond populations among the nearest neighbor B–C-atoms in B-doped diamond films

Number of carbon atoms	Population	Length (Å)
16	0.14	2.50
32	0.61	2.53
64	−0.11	2.54

13.2.8 *Electronic Structure Calculations of Oxygen-Doped Diamond Using DFT Technique*

The global aim of this study is to understand the mechanism of oxygen incorporation into diamond crystals by quantum mechanical methods and density functional theory (DFT) calculations. Using DFT calculations, the lattice distortion and depth of donor level of the O-doping in diamond will be compared with those given in literature.

13.2.8.1 Structural Optimization

A model structure of oxygen-doped diamond shown in Fig. 13.47 is constructed using a 64-atoms 2 × 2 × 2 supercell of diamond containing 1 O and 63 C-atoms. Figure 13.47 illustrates that dopant oxygen replaces C-atom to form a substitutional defect. All atoms in the supercell are allowed to move freely and also to change the position of oxygen atom in the second as well as in the third layer in order to minimize the energy and hence to achieve a stable and the most probable configuration. Results presented here have been obtained for the optimized structure with minimum global. The optimized C–O bond lengths (1.54 Å) for substituted oxygen atom having bond angles of 109.47° are also shown in Fig. 13.48. It is also obvious from this figure that equilibrium lengths of all the C–O bonds are the same. It means equilibrium configuration of oxygen becomes C_4–O. In general it is known that the highest occupied molecular orbital is localized at the substituted atom; on the other hand, a node is usually created in the longer bond. Due to equivalent bond lengths, no such nodes are noticed, and all C–O bonds are equally stronger. Moreover, it is noticed that the C_4–O bond lengths are almost the same as observed for C–C bond lengths in diamond lattice (1.54 Å). As a result no lattice distortions are seen in the oxygen-doped diamond.

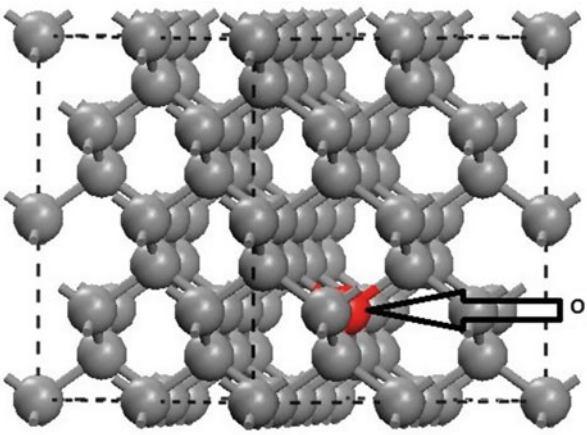

Fig. 13.47 Model structure of oxygen-doped diamond

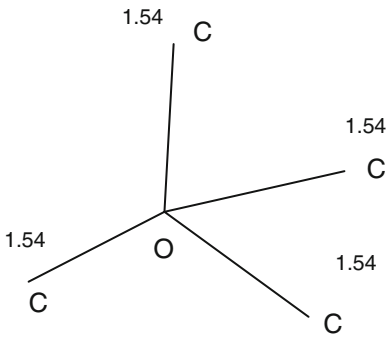

Fig. 13.48 Equilibrium geometry of O-doped diamond around the substituted atom (unit: Å)

13.2.8.2 Formation Energy of Oxygen Defect

Energy required to form an oxygen substitutional site in diamond is defined as [156]:

$$E_f = E_{tot} - E^o_{tot} + n_+\mu_C - \mu_O \tag{13.7}$$

where E_{tot} (−581 eV) is the total energy of diamond containing an oxygen defect, E^o_{tot} (−572 eV), the total energy of diamond lattice, $n_+(=1)$, the number of oxygen atoms substituted into diamond lattice, and μ_C (−156.22 eV [157]) and μ_O are respective chemical potentials of diamond and oxygen $\left(\mu_O = \frac{1}{2}\mu_{O_2} = 0\right)$ [156]. The oxygen doping in diamond is found to be thermodynamically favorable because of the negative formation energy. This result is in good agreement with that of Riedel et al. [158]. A remarkable fact responsible for a shift in energy bands is the electro negativity which leads to polarization. Thus when diamond is doped by an impurity such as oxygen, $C^{\delta+} - O^{\delta-}$ dipole may be formed due to a difference of electro negativities [161] between C (2.55) and O (3.44) atoms. This causes polarization of CAO bond. Due to its higher electro negativity (3.44), oxygen atom carries negative charge received from C-atoms since electrons can easily transfer from C- to O-atoms [161]. This is why the C–O bond is polarized toward O-atom. This behavior causes a systematic shift in the energy bands, which are responsible for any change in the electronic properties of oxygen-doped diamond.

13.2.8.3 Band Structures

Band structures (BSs) of oxygen-doped diamond films have been determined to elaborate their electronic properties. Figure 13.49 illustrates the BSs of diamond films doped with oxygen substitutional impurity. Just for comparison, BS of pure diamond having band gap ~4.4 eV [159] is also shown in Fig. 13.49a. Figure 13.49b, c shows BSs of 1.56% oxygen-doped diamond films for majority (↑) and minority (↓) spins, respectively, and demonstrates the creation of impurity levels inside the

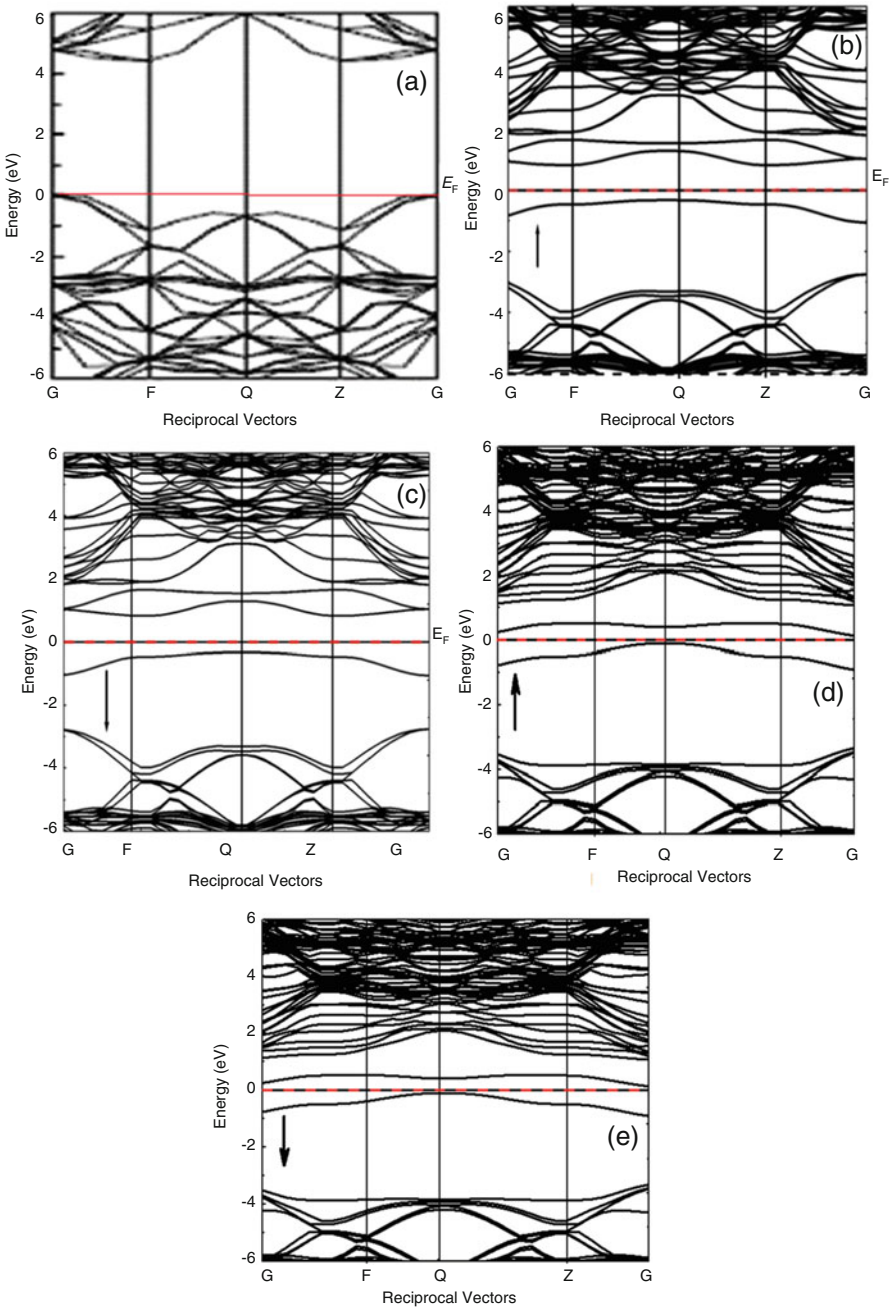

Fig. 13.49 Band structure of (**a**) pure diamond taken from [162], (**b**) majority spin (↑), (**c**) minority spin (↓) of diamond with 1.56% of oxygen doping, (**d**) majority spin (↑), and (**e**) minority spin (↓) of diamond with 3.12% of oxygen doping. *Red line* shows Fermi level

band gap region but close to the conduction band minimum (CBM). Moreover, Fermi level (E_F) lies below the CBM; hence, oxygen defect/substitution acts as a donor in diamond, which means that oxygen atom donates electrons to diamond structure. In addition, it is also notable that oxygen doping in diamond has shifted the band structure (relative to that of pure diamond) downward. The donor level of oxygen-doped diamond is slightly deeper generating an energy gap of ~1.34 eV for majority spin (↑) and ~1.10 eV for minority spin (↓) as illustrated in Fig. 13.49b, c. In order to see the effect of increasing oxygen content in diamond lattice, energy band structure of 3.12% oxygen-doped diamond is also illustrated in Fig. 13.49d, e for spin up (↑) and spin down (↓) charge carriers. These plots also demonstrate the creation of impurity levels near the CBM as well as in the valence band maximum (VBM). Due to this reason, CBM extends toward Fermi level; consequently there is a further decrease in band gap energy to ~0.46 eV for spin up (↑) and ~0.44 eV for spin down (↓) carriers as demonstrated in Fig. 13.49d, e. So due to reduction in band gap energy, the electrical conductivity of oxygen-doped diamond films increases so that these films behave like good semiconductors. Analogous trend has been observed by Zhou et al. [155]; however, the magnitudes of band gap energy are different which might be related with the different concentrations of oxygen doping. Moreover, present DFT results verify our experimental findings that with the addition of oxygen into diamond lattice increases its conductivity so that oxygen-doped diamond films behave like a semiconductor [160].

13.2.8.4 Density of States

The total and partial density of states of oxygen-doped diamonds is shown in Fig. 13.50. The valence and conduction bands are mostly occupied by the C 2p states (Fig. 13.50a). It is noticeable that impurity level states exist in the band gap region and extend the CBM toward the Fermi level. This results in a decrease of band gap, and the oxygen-doped diamond behaves as a semiconductor. The calculated partial density of states of oxygen-doped diamond films (as shown in Fig. 13.50b) clearly indicate that valence and conduction bands are mostly occupied by O 2p states. Also the CBM has been shifted to Fermi level because of the formation of a band localized at ~55 eV. This behavior indicates the role of oxygen as a donor. Present results are in contrast to those of Long et al. [161] who expressed the acceptor role of oxygen in diamond by creating impurity levels near the VBM. However, our results are in good agreement with those of Zhou et al. [155]. It is notable that Long et al. [161] studied oxygen absorption at the surface only which involves either C–O–C or C=O bonding but not the C_4–O configuration, and this fact is mainly responsible for the two different behaviors (donor or acceptor) of oxygen-doped diamonds.

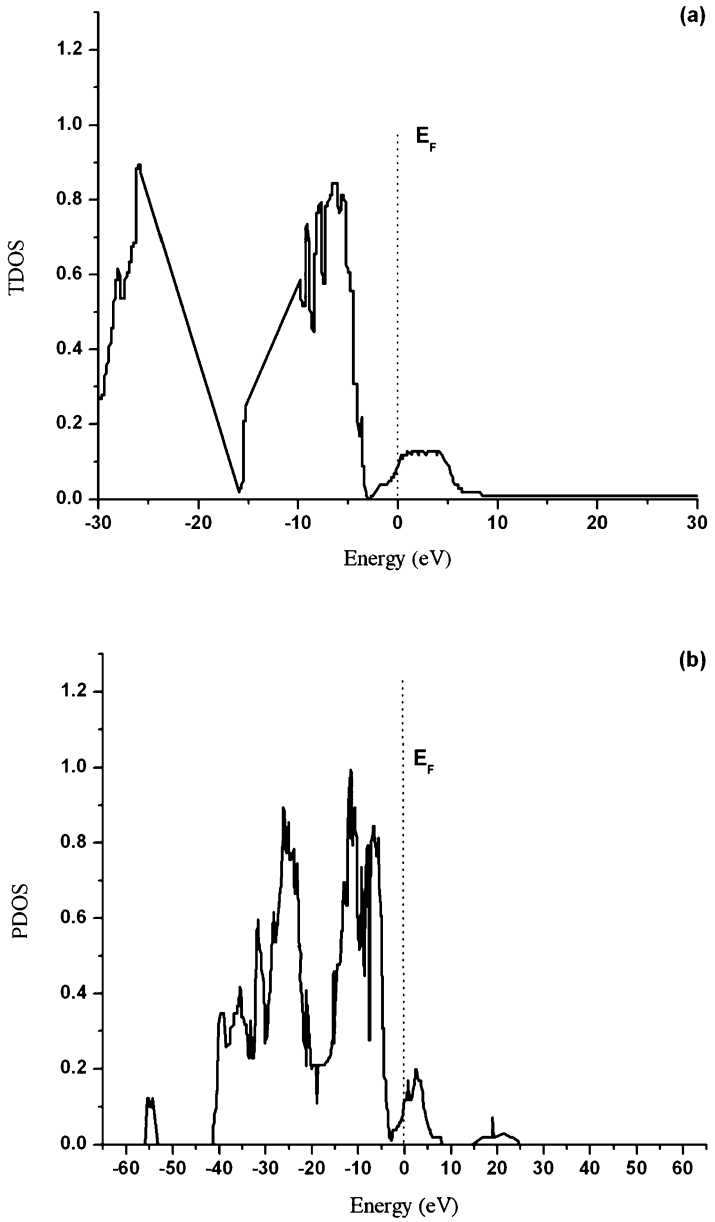

Fig. 13.50 (**a**) Total density of states in oxygen-doped diamond, (**b**) partial density of states of O 2p. *The dash line* represents Fermi level

13.2.8.5 Projected Spin Densities of States

To provide a deep insight into the electronic/magnetic structure of oxygen-doped diamond films, projected spin density of states are also determined through DFT calculations and are displayed in Fig.13.51I for a structure containing single O-atom along with its four mutual nearest neighbor C-atoms. The system remains conducting throughout all the calculations with the significant contributions from O 2p states at the Fermi level. The appearance of specific O 2p band with the energy

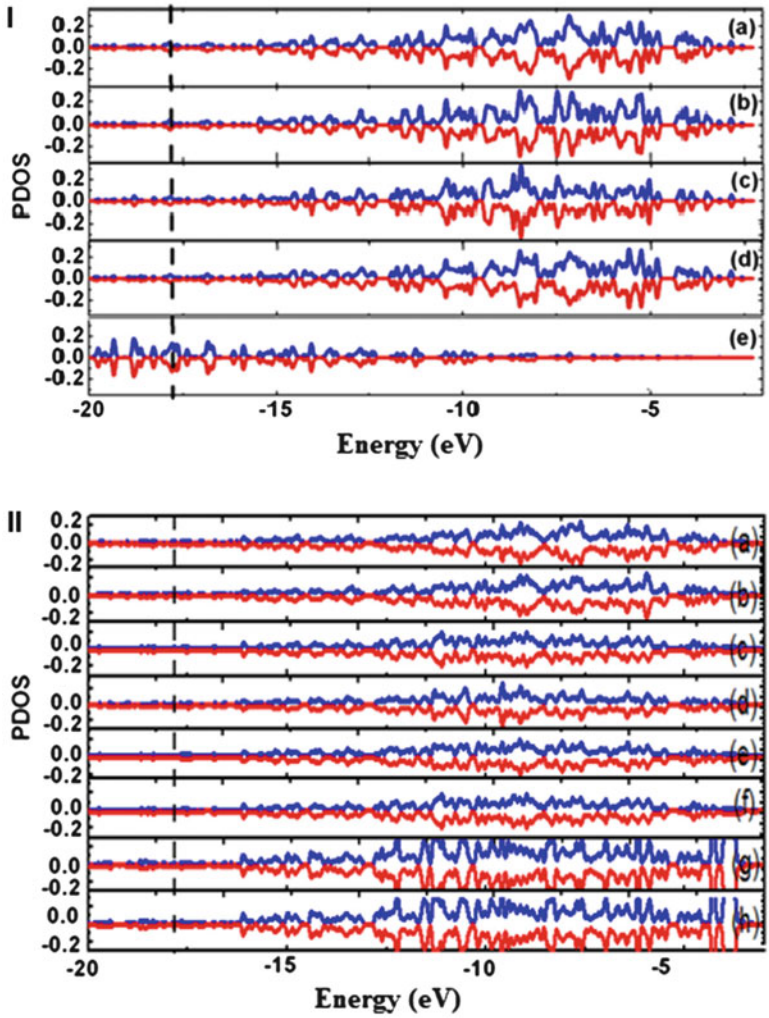

Fig. 13.51 Spin-projected density of states (PDOSs) for single O-atom doping; (**a**)–(**d**) C 2p of carbon atoms in O–C_4 structure, and (**e**) oxygen O 2p, and (II) PDOSs for double O-atoms doping; (**a**)–(**f**) C 2p of carbon atoms for O–C bonding with nearest neighbors and (**g**) and (**h**) oxygen O 2p

peak at −17.75 eV is observed. Position of the O 2p band is insensitive to the presence of O-atoms and lies within energy range of −17.75 and −5 eV. Moreover, no appreciable magnetic moments appear in these systems on oxygen as well as on carbon atoms for all C1-C4 configurations (Fig. 13.51a–e). From these findings it can be stated that oxygen-doped diamond behaves as a nonmagnetic semiconductor with zero density of carriers at the Fermi level for both spin projections; O↓↑ (EF) = 0. To further analyze the effect of higher concentration of O-atoms in the diamond lattice, PDOSs are illustrated in Fig. 13.51II for a structure involving two O-atoms along with their nearest neighbor C-atoms. It is noticed that no O 2p band appears at −17.75 eV as seen in Fig.13.51I(e)) involving single O-atom. Instead such band appears close to VBM, i.e., −2 to −4 eV (Fig. 13.51IIg, h). The appearance of such a band leads to further decrease of band gap energy as described above.

13.2.8.6 Charge Density of Oxygen Defects

Figure 13.52 demonstrates charge density distributions for the oxygen substitution into the diamond lattice. Different colors (online) observed in Fig. 13.52 indicate distribution of charge density at different regions. The excess (positive) charge density is noticed around atoms (blue) which decreases as the distance from the center is increased by the change of colors from purple to pink to orange (which depicts deficit (negative) charge density). The blue color depicts the formation of single bond by the sharing of electrons between two atoms. It is obvious from Fig.13.52 that charges between C- and O-atoms are relatively larger than those between C- and C-atoms. This leads to relatively stronger C–O chemical bonding with respect to that of C–C bonds. The larger value of charges between C- and O-atoms shows that the incorporation of oxygen defect can exhibit some kind of vacancy character of defect states associated with C-atom bonds. The similar types

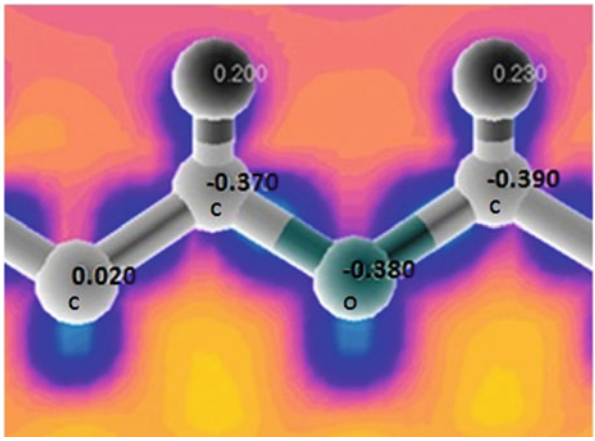

Fig. 13.52 Electron-density distributions of oxygen in diamond. Due to higher electro negativity of oxygen, excess negative charge has been accumulated around O-atom leading to $C^{\delta+} - O^{\delta-}$ dipole.

of results have been observed by Long et al. [155] but different from that of Gali et al. [162], who associated their results to the weaker nature of C–O chemical bonds caused by longer C–O bond lengths as compared to those of C–C bonds which lead to lattice distortion in the oxygen-doped diamond.

13.3 Conclusions

Based on the experimental and theoretical results, following conclusions can be drawn:

1. Growth rate decreases at low concentrations of methane but increases at high methane concentrations by a factor of about 3. Optimized methane concentration for well-faceted diamond is 3.0 mL/min. Outgrowth is observed when excess amount of methane is added to deposition chamber. Electrical resistivity generally increases with rise of methane concentration having a minimum (1.79×10^7 Ω cm) at methane concentration of 3.0 mL/min. This result enables diamond films to behave as a semiconductor.
2. Diamond films of uniform thickness and relatively large film areas are successfully grown on Si substrates with single/polycrystalline grains at various deposition pressures using HFCVD system. Growth rate generally decreases with the increase of pressure due to high-nucleation rate at high pressures. The quality of diamond crystals gradually improves with increase of pressure resulting in well-faceted diamond at 40 mbar. Grain size, grain density, FWHM, and growth rate all show an oscillatory behavior with the increase of pressure. Resistivity decreases rapidly up to 2×10^6 Ω cm at low pressures. SEM, XRD, Raman spectroscopy, and resistivity results almost support each other.
3. Addition of O_2 into the deposition chamber results in high-quality diamond polycrystals with large grain size, low resistivity (2×10^7 Ω cm), and (1 1 1) dominant facets. Growth rate rises with the addition of O_2. Low-resistive polycrystalline diamond film with large grain size is achievable at very low O_2 content.
4. The SEM and XRD results indicate that as-grown boron-doped polycrystalline diamond films are of (1 1 1) preferred orientation and better crystal quality. Film resistivity falls abruptly (i.e., from 10^8 to 10^5 Ω cm) with rise in grain size which is observed at elevated pressures. Diamond polycrystalline films grown at appropriate B-content and elevated pressures behave as good semiconductors finding their applications in electronic devices.
5. Morphology/microstructure shows significant variations on adding nitrogen into diamond films. At low N_2 concentrations, good-quality polycrystalline micro-diamond grains grow with sharp and smooth edges. However, at higher N_2 concentrations (i.e., 0.32 and 0.64 sccm), superposition of two grain populations, nano- and micro-sized ones, is noticed, i.e., nano-sized grains grow with respect to microcrystallites. Such nano-sized diamond grains have rarely been produced

with nitrogen addition using the conventional and cheap HFCVD technique. The shifting and asymmetric broadening of peaks and/or appearance of new signals in Raman spectra with the addition of nitrogen is attributed to highly disordered or nanocrystalline films. Such films allow more vibrational modes to become Raman active by breaking solid-state selection rules. Electrical resistivity of nitrogen-doped diamond films decreases significantly from 10^9 to 10^7 Ω cm due to ordered diamond grains and increased sp^2 bonds. Threshold flow rate (0.08 sccm) of N_2 opens a new window in the development of diamond for diverse electronic applications.

6. Calculations of electronic properties of B-doped diamond thin films using DFT methods show that B-atoms can support split of diamond energy band near/at Fermi level and hence enhance electron conductivities of B-doped diamond thin films. Boron doping shows significant effect only on atomic charge, positive (1.89 eV) at low B-content but negative at higher B-concentrations. This orbital charge distribution of B-atom shows trend similar to that of electron conductivity enhancement. These theoretical findings support our experimental results of B-doped diamond polycrystalline films showing a sudden fall in resistivity (10^5 Ω cm) at high b-content making it a good semiconductor for its applications in electrical devices.
7. The O_2 and TM dopants become spin polarized on doping into diamond by magnetizing p electrons of C-atoms through s-p and p-d hybridization, respectively. The p-d hybridization is very strong for Cu as compared to other TM dopants and prefers FM coupling state among all dopants rather than that of AFM coupling. Thus TMs are promising nonmagnetic dopants for diamond to fabricate magnetic materials with reduced size and free from magnetic precipitates. The s-p hybridization is very weak in O-doped diamond. The appearance of specific O (2p) band with the energy peak at −18 eV looks to be insensitive to the presence of O-atoms and lies within energy range of −18 and −5 eV. Small lattice distortion indicates that oxygen is relatively unstable in diamond because of higher binding energy of the O-doped diamond (4.94 eV). The donor level of O-doped diamond is very deep and found between the valence and conduction bands yielding energy gap of ~0.865 eV. In summary, our calculations revealed that the incorporation of the oxygen atoms into the diamond (1 0 0) surface is partially favorable.

The *best experimental results* obtained under various deposition conditions, such as deposition pressure, addition of impurities, and different gases are presented in Table 13.13. However, from the DFT calculations based on a spin-polarized GGA-PW91 functional and plane wave basis set using VASP codes, results are summarized in Table 13.14.

Table 13.13 Experimental results

Condition	Morphology	Maximum growth rate (μm/h)	Minimum grain size (μm)	Minimum electrical resistivity ($\times 10^6$ Ω cm)
Methane	Outgrowth (snoozing)	3.6	1.3	17
Pressure	Isolated	1.7	2.5	2
Oxygen doping	Pyramids-like	2.5	1.8	20
Boron doping	Sharp diamond	Decreased	1.0	0.1
Nitrogen doping	Cauliflower	Increased	0.1	20

Table 13.14 Theoretical results

Doped species	Spin polarized	Magnetic moment (μB)	Bond length (Å)	Conductivity	Bond population	Incorporation into diamond
Boron	–	–	Little effect	Increases	Little effect	Favorable
Oxygen	Yes	Small	Increases	Small	–	Partially Favorable
Transition metal doping						
Cu	Yes	High	Small	Increases	High	Favorable
Hg	Yes	Middle	Low	Decreases	Middle	Favorable
Zn	Yes	Low	High	Decreases	Low	Favorable
Cd	Yes	Very low	Low	Decreases	Very low	Favorable

13.4 Objectives of This Chapter

The most favorable result obtained from our experiments and theoretical calculations is that B-doped diamond can be deposited and used as a good semiconductor in computer and biomedical applications because it possesses minimum resistivity (1×10^5 Ω cm) as compared to other dopants. This was one of our required objectives of this chapter.

References

1. Rau H, Picht F (1992) J Mater Res 7:934
2. Fan QH, Pereira E, Cracio J (1999) J Mater Sci 34:1353
3. Yu J, Huang R, Wen L, Shi C (1998) J Mater Sci Lett 17:1011
4. Celii FG, White D Jr, Purdes AJ (1991) J Appl Phys 70:5636
5. Kweon D-W, Lee J-Y, Kim D (1991) J Appl Phys 69:8329
6. Larijani MM, Navinrooz A, Le Normand F (2006) Thin Solid Films 501:206

7. Wang SF, Wang Y-R, Pu J-C, Sung JC (2006) Thin Solid Films 498:224
8. Makris TD, Giorgi R, Lisi N, Pilloni L, Salernitano E (2005) Diam Relat Mater 14:318
9. Pecoraro S, Arnault JC, Werckmann J (2005) Diam Relat Mater 14:137
10. Lee ST, Lam YW, Lin Z, Chen Y, Chen Q (1997) Phys Rev B 55:15937
11. Kang J, Xiao C, Xiong Y, Wang Y, Meng Q, Lin Z, Feng K-A (2000) Diam Relat Mater 9:1691
12. Yang Q, Xiao C, Chen W, Hirose A (2005) Carbon 43:748
13. Yang Q, Chen W, Xiao C, Hirose A (2005) Carbon 43:2618
14. Chang JJ, Mantei TD (1992) J Appl Phys 71:2918
15. Ruan J, Kobashi K, Choyke WJ (1992) Appl Phys Lett 60:1884
16. Tang CJ, Neves AJ, Fernandes AJS (2004) Diam Relat Mater 13:3448
17. Mucha JA, Flamm DL, Ibbotson DE (1989) J Appl Phys 65:3448
18. Wu CH, Tamor MA, Potter TJ, Kaiser EW (1990) Thin Solid Films 68:4825
19. Harris SJ, Weiner AM (1989) Appl Phys Lett 55:2179
20. Johnson CE, Weimer WA, Cerio FM (1992) J Mater Res 7:1427
21. Chu CJ, Evelyn MPD, Hauge RH, Margrave JL (1990) J Mater Res 5:2405
22. Kim YK, Jung JH, Ahn HJ, Lee JY (1995) J Mater Sci Mater Electron 6:28
23. Takeuchi K, Yoshida T (1992) J Appl Phys 71:2636
24. Rosner DE, Strakey JP (1973) J Phys Chem 77:69
25. Robins LH, Cook LP, Farabaugh E-N, Feldman A (1989) Phys Rev B 39:13367
26. Musale DV, Sainkar SR, Kshirsagar ST (2002) Diam Relat Mater 11:75
27. Rakha SA, Xintai Z, Zhu D, Guojun Y (2010) Curr Appl Phys 10:171
28. Poferl DJ, Gardner N-C, Angus J-C (1973) J Appl Phys 1428:171
29. Kohn E, Adamschik M, Schmid P, Denisenko A, Aleksov A, Ebert W (2001) Prospects of diamond devices. J Phys D Appl Phys 34:77
30. Yu BD, Miyamoto Y, Sugino O (2005) Appl Phys Lett 97:103514
31. Yu Z, Karlsson U, Flodström A (1999) Thin Solid Films 342:74
32. Seo S-H, Lee T-H, Kim Y-D, Park C-K, Park J-S (2004) Thin Solid Films 212:447
33. Neto MA, Pereira E (2006) Diam Relat Mater 15:465
34. Ahmed W, Rego CA, Cherry R, Afzal A, Ali N, Hassan IU (2000) Vacuum 56:153
35. Ando Y, Tachibana T, Kobashi K (2001) Diam Relat Mater 10:312
36. Collins AT, Lightowler E-C (1979) In: Field J-E (ed) Properties of diamond. Academic Press, San Diego
37. Jin S, Moustakas T-D (1994) Appl Phys Lett 65:404
38. Ma KL, Zhang WJ, Zou YS, Chong YM, Leung KM, Bello I, Lee ST (2006) Diam Relat Mater 15:626
39. Badzian A, Tong Lee T (1993) Appl Phys Lett 62:3432
40. Arenal R, Bruno P, Miller D-J, Bleuel M, Lal J, Gruen D-M (2007) Phys Ther Rev 75:195431
41. Vlasov II, Lebedev OI, Ralchenko VG, Goovaerts E, Bertoni G, Tendeloo GV, Konov VI (2007) Adv Mater 19:4058–4062
42. Man WD, Wang JH, Wang CX (2002) New Carbon Mater 17(1):62
43. Tanko Y, Takenouchi T, Ishii S (2007) Diam Relat Mater 16:911
44. May PW, Rosser KN, Fox NA, Younes CM, Beardmore G (1997) Diam Relat Mater 6:450
45. Yu J, Huang R, Wen L, Shi C (1997) Mater Lett 32:143
46. Chen W, Lu X, Yang Q, Xiao C, Sammynaiken R, Maley J (2006) Thin Solid Films 515:1970
47. Bataineh M, Khatami S, Asmussen J Jr (2005) J Mater Process Technol 169:26
48. Schwarz S, Rosiwal SM, Frank M, Breidt D, Singer RF (2002) Diam Relat Mater 11:589
49. Buckley G, Moustakas TD, Ye L, Voiron J (1989) J Appl Phys 66:3595
50. Silva F, Gicquel A, Tardieu A, Cledat P, Chauveau T (1996) Diam Relat Mater 5:338
51. Goodwin DG (1993) J Appl Phys 74:6888
52. Wada N, Solin SA (1988) Physica B 105(353):6888
53. Shroder RE, Nemanich RJ, Glass JT (1990) Phys Rev B41:3738
54. Ralchenko V, Sychov I, Vlasov I (1999) Diam Relat Mater 8:189

55. Hirakuri KK, Kobayashi T, Nakamura E, Mutsukura N, Friedbacher G, Machi Y (2001) Vacuum 63:449
56. Lu X, Yang Q, Xiao C, Hirose A (2007) Diam Relat Mater 16:1623
57. Li X, Perkin J, Collazo R, Nimanich RJ, Sitar Z (2006) Diam Relat Mater 15:1784
58. Yang S, He Z, Li Q, Zhu D, Gong J (2008) Diam Relat Mater 17:2075–2079
59. Hanson KL (1979) Acta Metall 27:515
60. Hirakuri KK, Yoshii M, Friedbacher G, Grasserbauer M (1997) Diam Relat Mater 6:1031
61. Leeds SM, Davis TJ, May PW, Pickard CDO, Ashfold MNR (1998) Diam Relat Mater 7:233
62. Kobayashi T, Hirakuri KK, Mutsukura N, Machi Y (1999) Diam Relat Mater 8:1057
63. Jia F, Bai Y, Qu F, Zhao J, Zhuang C, Jiang X (2010) Vacuum 84:930
64. Brunsteiner R, Haubner R, Lux B (1993) Diam Relat Mater 2:1263
65. Hara T, Yoshitake T, Fukugawa T, Zhu LY, Itakura M, Kuwano N, Tomkiyo Y, Nagayama K (2004) Diam Relat Mater 13:622
66. Lewis IR, Edwards HGM (2001) Handbook of Raman spectroscopy: from the research laboratory to the process line. CRC Press, Boca Raton
67. Hart ES, Priest RG (1997) Thin Solid Films 310:39
68. Ken Kim Y, Han J, Lee J-Y, Ahn H-J (1995) J Mater Sci Mater Electron 6:28
69. Weimer WA, Cerio FM, Johnson CE (1991) J Mater Res 6:2134
70. Sfinchez O, Grnez-Aleixandre C, Agultd F, Albella JM (1994) Diam Relat Mater 3:1183
71. Han YS, Reaney IM, Trolier-Mckinstry S (1997) Thin Solid Films 310:39
72. Gomez-Alexiander C, Garcla MM, Finchez OS, Albellaet JM (1997) Thin Solid Films 303:34
73. Muranaka Y, Yamashita H, Sato K, Miyadera H (1990) J Appl Phys 67:6247
74. Yoshitake T (2000) Diam Relat Mater 9:689
75. Howard WN, Spear KE, Frenklach M (1993) Appl Phys Lett 63:2641
76. Chen C-F, Hong T-M, Chen S-H (1993) J Appl Phys 74:4483
77. Lux H (2003) Appl Surf Lett 1040:27
78. Wang ZL, Lu C, Li JJ, Gu CZ (2009) Diam Relat Mater 18:132
79. Feng Y, Lva J, Liua J, Gaoa N, Pengb H, Chen Y (2011) Appl Surf Sci 257:3433
80. Krivchenko VA, Lopaev DV, Minakov PV, Pirogov VG, Rakhimov AT, Suetin NV (2007) Tech Phys 55(11):1471–1474
81. Kim JG, Yu J (1998) Scr Mater 39(6):807
82. Jin ZS, Jiang ZG, Hu H (2003) New Carbon Mater 18(1):65
83. Liang X, Wang L, Zhu H, Yang D (2007) Surf Coat Technol 202:261
84. Chao JF, Zhen BY, Fang Q, Jian S, Jun ZJ, Xin J (2010) New Carbon Mater 25(5):357
85. Abstreiter G, Cardona M, Pinczuk A (1984) Light Scatter Solids IV 54:5
86. Cerdeira F, Fjeldly TA, Cardona M (1973) Phys Rev B 8:4734
87. Wang YG, Lau SP, Tay BK, Zhang XH (2002) J Appl Phys 92:7253
88. Li L, Li H, Lu X, Cheng S, Wang Q, Ren S, Liu J, Zou G (2010) Appl Surf Sci 256:1764
89. Wang ZL, Luo Q, Liu LW, Li CY, Yang HX, Yang HF, Li JJ, Lu XY, Jin ZS, Lu L, Gu CZ (2006) Diam Relat Mater 15:659
90. Giustino F, Yates JR, Souza I, Cohen ML, Louie SG (2006) Phys Rev Lett 98:47005
91. Lu C, Tian SB, Gu CZ, Li JJ (2011) Diam Relat Mater 20:217
92. Tang CJ, Neves AJ, Pereira S, Fernandes AJS, Grácio J, Carmo MC (2008) Diam Relat Mater 17:72
93. Yong JX, Zhang H-D, Li CM, Chen G-C, Lu F-X, Tang W-Z, Tong Y-M (2004) Diam Relat Mater 13:139
94. Zhang Q, Yoon SF, Ahn J, Rusli, Guo Y-P (1998) Microelectron J 29:875
95. Tang CJ, Neves AJ, Carmo MC (2005) Appl Phys Lett 86:223107
96. Barnard AS, Sternberg M (2007) Nanotechnology 18:025702
97. Filik J (2005) Spectro Eur 17(5):10
98. Wasyluk J, Perva T-S, Lau D-WM, Taylor MB, Mcculloch D-G, Stopford J (2010) Diam Relat Mater 19:514
99. Lee JK, John P (2010) Thin Solid Films 519:625

100. Cao GZ, Schemer J-J, Van Enckevort WJ-P, Elst W-ALM, Gilling L-J (1996) J Appl Phys 79:1357
101. Fu YQ, Sun C-Q, Du H-J, Yan B-B (2001) J Phys D Appl Phys 34:1430
102. Ali M, Urgen M (2011) Appl Surf Sci 257:8420
103. Lombardi EB (2008) Diam Relat Mater 17:1345
104. Li LA, Cheng SH, Li HD, Yu Q, Liu JW, Lv XY (2010) Nano-Micro Lett 2:154
105. Gao H-X, Li J-B, Xia J-B (2012) Condens Matter 407:2347
106. Kalish R (1999) Carbon 37:781
107. Perdew JP, Yue W (1986) Phys Rev B 33:8800
108. Gruen DM (1999) Ann Rev Mater Sci 29:211
109. Ohno H (1998) Science 281:951
110. Wolf SA, Awschalom DD, Buhrman RA, Daughton JM, von Molnár S, Roukes ML, Chtchelkanova AY, Treger DM (2001) Science 294:1488
111. Chernozatonskii LA, Sorokin PB, Kvashnin AG, Kvashnin DG (2009) JETP Lett 90:134
112. Ruoff R (2008) Nat Nanotechnol 3:10
113. Höhne R, Esquinazi P, Heera V, Weishart H (2007) Diam Relat Mater 16:1589
114. Murata K, Ushijima H, Ueda H, Kawaguchi K (1991) J Chem Soc Chem Commun 18:1265
115. Turek P, Nozawa K, Shiomi D, Awaga K, Inabe T, Maruyama Y, Kinoshita M (1991) Chem Phys Lett 180:327
116. Allemand P-M, Khemani KC, Koch A, Wudl F, Holczer K, Donovan S, Gruner G, Thompson JD (1991) Science 253:301
117. Esquinazi P, Setzer A, Höhne R, Semmelhack C, Kopelevich Y, Spemann D, Butz T, Kohlstrunk B, Lösche M (2002) Phys Rev B 66:024429
118. Esquinazi P, Höhne R (2005) J Magn Magn Mater 290–291:20
119. Ovchinnikov AA, Shamovsky IL (1991) J Mol Struc Theochem 251:133
120. González J, Guinea F, Vozmediano MAH (2001) Phys Rev B 63:134421
121. Dergan A (2010) A seminar on "Electronic and transport properties of carbon nanotubes". Department of Physics, University of Ljubljana
122. Sander MHD, Tans J, Dai H, Thess A, Smalley RE, Geerligs LJ, Dekker C (1997) Nature 386:474
123. Segui A, Khan MJI, Saidi EH, Belhaj A (2013) Inter J Geom Methods Mod Phys 10:1250090
124. Gein AK, MacDonald AH (2007) Phys Today 60:35
125. Susskind L (2001) The quantum hall fluid and nanocommutative chern-simons theory. arXiv: hep-th/0101029
126. Boubaker K (2013) Adv Phys Chem 2013:5
127. Hohenberg P, Kohn W (1964) Phys Ther Rev 136:864
128. Gabrysch M (2008) Electronic properties of diamond. PhD thesis, Department of Engineering Sciences, Uppsala Universitet, Uppsala, p 15
129. Johnson KA, Ashcroft NW (1998) Phys Rev B 58:15548
130. Remediakis IN, Kaxiras E (1999) Phys Rev B 59:5536
131. Wu RQ, Peng GW, Liu L, Feng YP, Huang ZG, Wu QY (2006) Appl Phys Lett 89:142501
132. Partner HL, Nigmatullin R, Burgermeister T, Pyka K, Keller J, Retzker A, Plenio MB, Mehlstäubler TE (2013) New J Phys 15:103013
133. Ohno DKY, Beschoten B, Matsukura F, Ohno H, Awschalom DD (1999) Nature 402:790
134. Fiederling MKR, Reuscher G, Ossau W, Schmidt G, Waag A, Molenkamp LW (1999) Nature 402:787
135. Fishman S, De Chiara G, Calarco T, Morigi G (2008) Phys Rev B 77:064111
136. Dong W, Wang A, Zhao M (2013) Sci Rep 3:1
137. Nakamura J, Kabasawa E, Yamada N, Einaga Y, Saito D, Ishiki H, Yugo S, Perera RCC (2004) Phys Rev B 70:245111
138. Gildenblat GS, Grot SA, Badzian A (1991) Proc IEEE 79:647
139. Glesener JW (1994) Appl Phys Lett 64:217
140. Shimomi H, Nishibayashi Y, Fujimori N (1991) Jpn J Appl Phys 130:1363

141. Ekimov EA, Sidorov VA, Bauer ED, Melnik NN, Curro NJ, Thompson JD, Stishov SM (2004) Nature 428:542
142. Koizumi S, Nebel C, Nesladek M (2008) Physics and applications of CVD diamond. Wiley-VCH Verlag GmbH & Co KGaA, Weinheim
143. Lu C, Wang ZL, Xu LF, Yang HX, Li JJ, Gu CZ (2010) Diam Relat Mater 19:824
144. Ashcheulov P, Sebera J, Lovalenko A, Petrak V, Fendrych F, Nesladek M, Taylor A, Zivcova ZV, Frank O, Kavan L, Dracinsky M, Hubik P, Vacik J, Kraus I, Kratochvilova I (2013) Eur Phys J B 86:443
145. Sopik B (2009) New J Phys 11:103026
146. Mandal S, Naud C, Williams OA, Bustarret E, Omnes F, Rodiere P, Meunier T, Saminadayar L, Bauerle C (2010) Nanotechnology 21:195303
147. Oki N, Kagayama T, Shimizu K, Kawarada H (2010) J Phys Conf Ser 215:012143
148. Ullah M, Ahmed E (2012) Curr Appl Phys 12:945
149. Chen YH, Hu CT, Lin IN (1999) Appl Phys Lett 75:2857
150. Thonke K (2003) Semicond Sci Technol 18:20
151. Werner M, Job R, Zaitzev A, Fahrer WR, Seifert W, Johnston C, Chalker PR (1996) Phys Stat Sol A 154:385
152. Xiang HJ, Li Z, Yang J, Hou JG, Zhu Q (2004) Phys Rev B 70:504
153. Blasé X, Adessi C, Connetable D (2004) Phys Rev Lett 93:237004
154. Shao QY, Wang GW, Zhang J, Zhu KG (2013) Condens Matter Phys 16:1
155. Zhou H, Yokoi Y, Tamura H, Takami S, Kubo M, Miyamoto A, Gamo MN, Ando T (2001) Jpn J Appl Phys 40:2830
156. Yan CX, Dai Y, Huang BB (2009) J Phys D Appl Phys 42:14407
157. Faccio R, Werner LF, Pardo H, Goyenola C, Ventura ON, Mombru AW (2010) J Phys Chem C 114:18961–18971
158. Riedel M, Ristein J, Ley L (2004) Phys Rev B 69:125338
159. Batista RJC, Chacham H, Carara SS, de Oliveira AB (2014) J Phys Chem C. doi:10.1021/jp503470r
160. Ullah M, Ahmed E, Hassan IU, Jackson MJ, Ahmed W (2011) J Manufact Technol Res 3/4:153
161. Long R, Dai Y, Yu L (2007) J Phys Chem C 111:855
162. Gali A, Lowther JE, Deak P (2001) J Phys Condens Mat 13:11607–11613

Chapter 14
Synthesis and Characterisation of Magnetic Nanoparticles in Medicine

A. Majid, W. Ahmed, Y. Patil-Sen, and T. Sen

14.1 Introduction

Superparamagnetic iron oxide nanoparticles (SPIONs) have received significant attention (Fig. 14.1), due to superparamagnetic features and tunable physicochemical properties such as size, shape and constituent of materials. Additionally, iron oxide is known as biocompatible iron ions with biological systems. Size may be controlled from several to hundreds of nanometres, smaller than living cells (10–100 μm) being more comparable to viruses (20–450 nm) or proteins (5–50 nm). SPIONs, due to the iron oxide cores, can be targeted to desired area using external magnet. They have promising properties such as superparamagnetism, irreversibility, greater saturation magnetisation values and increased anisotropy. These particles without applied magnetic field do not show magnetic interactions. SPIONs generally are classified into two groups: magnetite Fe_3O_4 and maghemite γ-Fe_2O_3 [1–4].

Magnetites are naturally occurring minerals, black in colour with strong magnetic properties. Magnetite crystals have also been found in certain bacteria, birds and human brain [5]. Magnetite is inverse spinel in cubic structural configuration, which is closely packed with oxygen and iron in both tetra- and octahedral fashion. Thus, magnetite possesses interesting magnetic properties from iron spins in both tetra- and octahedral interaction sites. In bulk form, magnetite possesses higher Curie temperature and is ferromagnetic at room temperature. In their nanoscale size

A. Majid
Department of Biochemistry, Shah Abdul Latif University, Khairpur, Pakistan

W. Ahmed (✉)
School of Mathematics and Physics, University of Lincoln, Lincoln, UK
e-mail: wahmed@lincoln.ac.uk

Y. Patil-Sen • T. Sen
School of Physical Sciences and Computing, University of Central Lancashire, Preston, UK

M.J. Jackson, W. Ahmed (eds.), *Micro and Nanomanufacturing Volume II*,
DOI 10.1007/978-3-319-67132-1_14

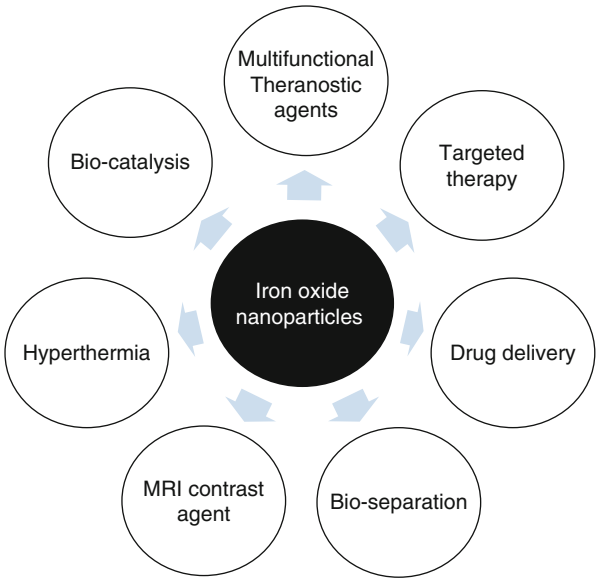

Fig. 14.1 Biomedical applications of iron oxide nanoparticles

distribution, they possess superparamagnetic behaviour. The arrangement of ferric and ferrous ions in both sites creates electron transfer via applied magnetic field. If the particle size is <50 nm, the individual particle has a single randomly oriented domain that caused superparamagnetism. The size and shape influence the coercivity and remanence effect [6]. The nanomagnetite has a high surface-to-volume ratio. Therefore, they tend to aggregate while decreasing their surface energy. During synthesis or storage, magnetite oxidises to maghemite. One of the important roles of coating materials is to prevent aggregation and oxidation of magnetite. The superparamagnetic behaviour remains stable, when modified with biocompatible materials making them an ideal candidate for biomedical applications. Alongside the above applications, the nanomagnetite has been used in other applications, such as magnetic seals, contrast agents, bio-separation, catalysis, hyperthermia and applied external field directed targeting (see Fig. 14.1) [2, 7].

14.2 Synthesis Routes of Magnetite Nanoparticles

14.2.1 Co-precipitation

This method is comparably simple, quick and cost-effective for the preparation of magnetite and maghemite nanomaterials. Co-precipitation method is involved in mixing of ferric and ferrous ions (usually 1:2 or 1:1.5, respectively) in alkaline medium. However, the acidic medium can also be used. Ideally, the solution is heated below 80 °C (or at room temperature). To avoid the oxidation of magnetite

to maghemite, inert gas environment is ideal. The parameters such as temperature, pH and molar ratio affect the size, shape and type (magnetite or maghemite) of resulting products.

Though this is the easiest method for the iron oxide nanoparticle synthesis in aqueous solution, some researchers also have used the surfactant to the solution to avoid the aggregation and obtain narrow-size distributed nanoparticles [2].

14.2.2 Thermal Decomposition Method

This method involves in thermal decomposition of iron (III) (dodecacarbonyl) or iron (III) (acetylacetonate) source in absolute ethanol using temperature up to 280 °C. This method though a bit complicated yields monodispersed nanoparticles. The nanoparticles cannot be dispersed in aqueous medium but only be dissolved in organic solvent along the use of surfactant [8, 9].

14.2.3 Microemulsion Method

This method involves a more complex system comprising three main components: polar, nonpolar and amphiphilic mediums. The amphiphilic substances (surfactants) reduce the surface tension of both immiscible mediums and produce the transparent medium. The water nanodroplets in bulk oily medium provide the "nanoreactors" for the synthesis of resulting iron oxide nanoparticles. The shape of water nanodroplets is spherical thus providing spherical nanoparticle; meanwhile, the size of these nanodroplets influences the size of resulting nanoparticles. Thus, the size and shape of nanoparticles can be tuned according to the size and shape of water nanodroplets [10].

14.2.4 Hydrothermal Method

This method involves the high pressure and temperature to hydrolyse the dehydrated salt resulting in the supersaturation of metal salts. The high temperature and pressure are used to achieve increased dehydration with good diffusivity of salts in water. In this approach, higher supersaturation can be obtained with fine grains having good crystallinity. The reaction parameters such as time, temperature, pressure and iron source can be tuned to obtain the desired size and shape of nanoparticles. This process does not involve the use of organic solvent or surfactant [11].

14.2.5 Sonochemical Method

This method involves the use of ultrasound waves that arise from acoustic cavitation. The formation, growth and implosive collapse of bubble occur in the aqueous medium. The implosive collapse creates a confined hotspot through shock wave within the bubbles. This hotspot creates extreme conditions in which nanoparticles are formed. The nanoparticle formed with this method usually has undefined shapes and sizes.

14.3 Silica-Coated Superparamagnetic Iron Oxide Nanoparticles

Ideal nanoparticles should have good dispersion in an aqueous environment to achieve desired results. The biomedical applications of magnetic nanoparticles require coatings with minimal toxicity and maximum loading capacity during targeting and tracking in the desired area. To achieve nanoparticle dispersions, numerous studies have been performed with water-soluble polymers (polysaccharide) [12], dendritic stabilisers (poly-amidoamine) [13], thiols (siloxanes) [14] and proteins [15]. However, due to high cost, complicated synthesis and further modifications, processes and commercial scale productions have limited their applications.

Among all these polymers, mesoporous silica got great attention as stabilisers due to their range of desired properties, such as mesoporosity, stability and binding ability to different bioactive molecules for effective cellular communications.

Silica-based spheres also showed to be stimuli responsive to pH and electrolyte concentration and a novel adaptive encapsulation property for functional inorganic materials [16]. Based on the adaptability to hybrid materials, the silica had opened new horizons for a variety of guest materials. These hybrid materials include charged or uncharged, hydrophilic to hydrophobic inorganic materials. This approach can be extended to a variety of bioactive molecules and functional inorganic materials to design multifunctional biomaterials. The adaptation of functional materials as core materials in the hybrid structures possibly will lead to the new avenues for encapsulation of functional inorganic materials into bioactive and biocompatible materials. The flexible biocompatible inorganic hybrid materials with novel functionalities will help in solving problems associated with biocompatibility, aggregation, solubility and bioavailability in drug delivery system. It is crucial to understand how to control and regulate the self-assemblies of hybrid materials.

This chapter has focused on spherical silica and iron oxide to understand the synthesis and structural properties of silica-coated iron oxide nanoparticles as core-shell materials. This section presented the study of a silica-coated nanoparticle as

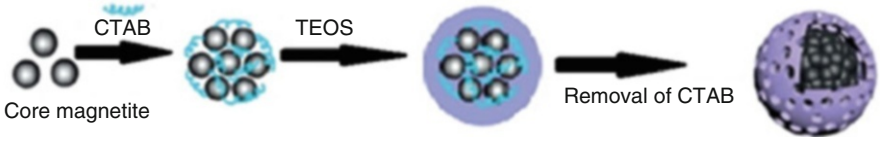

Fig. 14.2 Silica coating on bare SPIONs modified from Barbosa et al. 2016

model core-shell materials. The model consists of superparamagnetic iron oxide cores, which were coated with the mesoporous silica.

14.3.1 Synthesis of Mesoporous Silica-Coated Superparamagnetic Iron Oxide Nanoparticles

The methods of mesoporous silica-coated SPIONs were published in [1, 3, 17, 18]. Briefly, 1 g of SPIONs is dispersed in ethanol-water (1:1). 30 mL of 28% ammonium hydroxide is then added to the solution and stirred for 10 min. Subsequently, 20 g of hexadecyltrimethylammonium bromide (CTAB) powder was added to the mixture. It was stirred for a further 5 min and sonicated in an ultrasonic bath for 15 min, and the solution was heated to 60 °C in a nitrogen flow. Silica precursor tetraethyl orthosilicate (TEOS) of 12 mL was added dropwise under continuous stirring for 2 h. The brownish product obtained was transferred to the 1 L conical flask. The material was then washed initially with 500 mL of deionised water (two cycles) using slab magnet separation, two cycles of acidic ethanol using ultrasonic bath and then several cycles of water until the pH of the mixture was reached to 7.0. A schematic depiction of mesoporous Si-SPIONs is given in Fig. 14.2.

14.4 Characterisation of Superparamagnetic Iron Oxide Cores and Silica-Coated Core-Shell Nanoparticles

SPION by changing the different synthetic conditions could provide different magnetic properties. A variety of techniques can be utilised to study the size distribution of nanoparticles. The "size" in SPIONs is some way unclear due to the difference in different parts of nanoparticles, the whole iron oxide (crystalline and amorphous), the presence of hydrated layer in solution and the polydispersity of almost all SPIONs. The SPION size was measured with TEM images. TEM reveals the total nanoparticle size of the SPIONs (crystalline and amorphous parts) (Fig. 14.3). Moreover, it displays the details of size distribution and the morphology of nanoparticles. Meanwhile, the method of sample preparation can also induce the

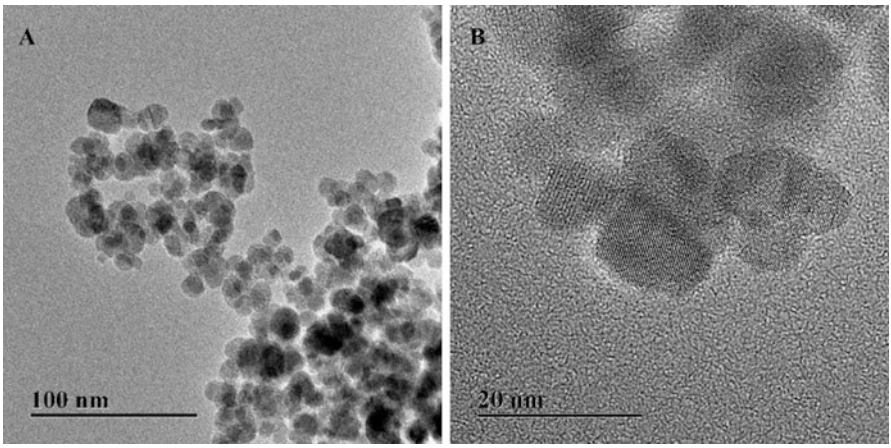

Fig. 14.3 TEM images of SPIONs, (***a***) low magnification and (**b**) higher magnification showing atomic arrangement of nanoparticles

aggregation of nanoparticles, where the TEM measurements may consequently not reflect the actual size distribution.

HRTEM displays the atomic arrangement of nanoparticles. It can be used to further study the crystallinity of nanoparticle structures (such as lattice vacancies and defects) and surface atomic arrangement.

TEM analysis of bare SPIONs achieved using co-precipitation shows the spherical shapes with a mean diameter in the range of ~10–25 nm (Fig. 14.3). The shape and size distribution is narrow for bare SPIONs. After sonication for 15–30 min in ultrasonic bath, they showed good stability and reduced aggregation.

Bare SPIONs are coated with a thin layer of silica on magnetite particle seeds, forming the Fe_3O_4 composites with spherical core-shell pattern. This layer was important for further coating of mesoporous silica. Briefly, it facilitates the interaction between CTAB and silicate materials. Hence, it favours the deposition of CTAB and then SiO_2. In addition, it reduces the chances of Fe_3O_4 core from being rapidly etched under alkaline environment. It protects the Fe_3O_4 magnetite cores to oxidise as maghemite by retaining its magnetic property in the final step of the removal of CTAB templates. After removal of CTAB, discrete mesoporous core-shell structured nanospheres with size ~200 nm were obtained (see Fig. 14.4).

XRD is performed to obtain the crystalline structure of the particles. XRD pattern of the SPIONs is shown in Fig. 14.5. The lattice constant values (a) were obtained, and spectra can be matched with PDF database to predict the type of the nanoparticles. The data from Fig. 14.5 were used for interplanar spacing (d) calculation in the atomic lattice and the lattice constant (a) calculations for the identification of crystal structure using software (DIFFRAC.EVA, Bruker, UK).

The lattice constant value (a) is used to identify the magnetic type of the iron oxide nanoparticles. For maghemite, this value is 0.833 nm, and for magnetite, it is 0.839 nm (mineralogy database accessible from Bruker software). From the data in

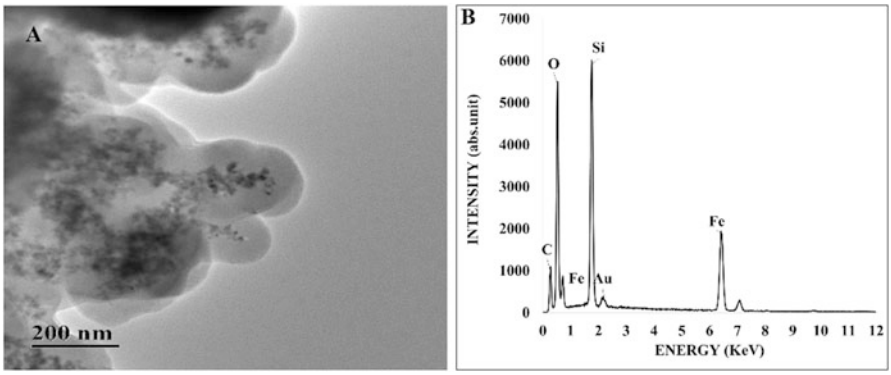

Fig. 14.4 (**a**) TEM image (**b**) EDXS analysis of silica-coated SPIONs

Fig. 14.5, the calculated value of SPIONs was 0.839 nm. The resulting core magnetic nanoparticles were magnetite (Fe_3O_4) possessing cubic spinel structures. The bare magnetite produced multiple peaks with *hkl* value of 220, 311, 400, 511 and 440 in the 2θ (PDF 04005-4319, 01-086-1362), showing good agreement with published data [1, 3, 4, 17, 18]. Meanwhile, there was no evidence of impurities observed in the XRD pattern.

XRD pattern of SPIONs shows the low intensity corresponding to very small size of magnetite nanoparticles. The average particle diameter can be calculated from the XRD pattern of the wide intense peak (3 1 1). Scherrer equation can be used to measure the size of the nanoparticle. The equation is presented in Eq. (14.1) [19–21]:

$$D = \frac{K\lambda}{(B\cos\theta)} \tag{14.1}$$

where factor K is 0.9 (as spherical), B structural = B observed—B standard (where B is the full width at half maximum in radians), θ is half of the Bragg angle (in radians) and λ is the wavelength of the X-rays (1.5418 Å) used. This will indicate the diameter of magnetite.

Figure 14.5 shows the XRD patterns where six diffraction peaks (220, 311, 400, 442, 511 and 440) are seen in the wide-angle region 2 θ (5–80). The peaks are indexed to the crystalline structure of pure magnetite nanoparticles along with the wide, intense peak (circle) of amorphous silica. The XRD pattern confirms amorphous nature of silica spheres with a similar diffraction pattern. The major diffraction peak at 35.5°(311), along with others at 30.5°(220), 43.5°(400) and 57.5°(511), and minor at 63°(440) confirm the presence of magnetic core in silica matrix [22].

Elemental analysis using energy dispersive X-ray spectroscopy (EDXS) confirmed the presence of constituent elements. Figure. 14.4b shows the elemental analysis of silica-coated SPIONs. As expected iron and oxygen peaks were observed on the collected spectrum along with carbon and gold peaks, eliminating

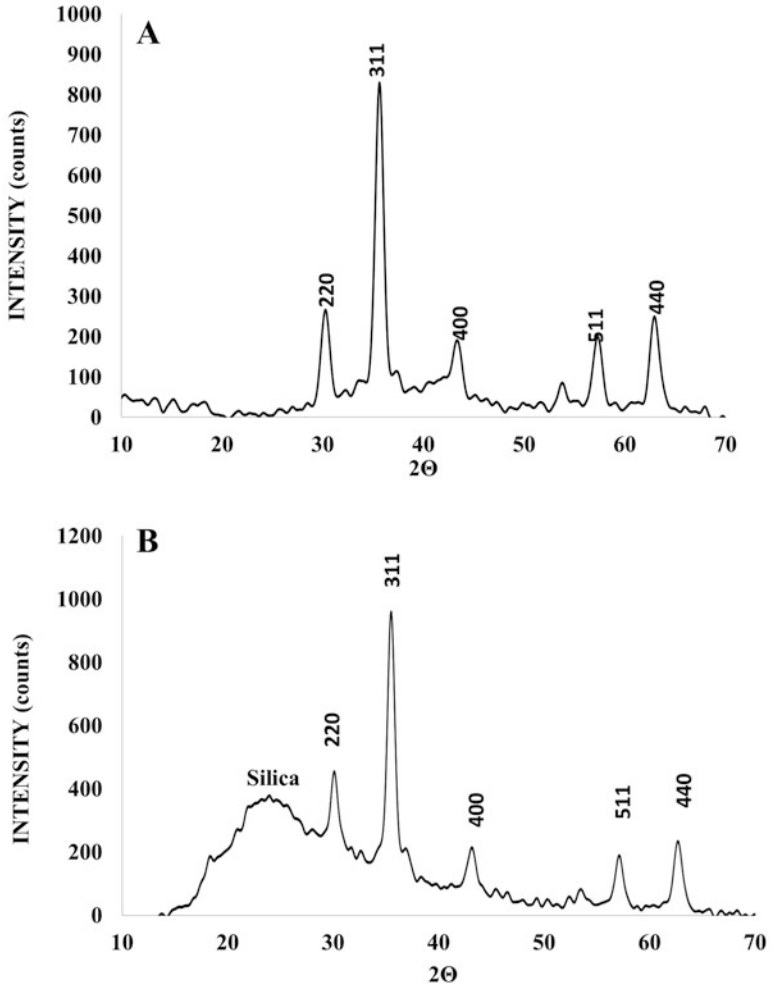

Fig. 14.5 (**a**) XRD pattern of SPIONs, (**b**) EDAX analysis of SPIONs

from the carbon tape and gold coating, respectively. For each sample, EDXS spectra should be taken from various representative areas, and the averaged results are displayed for each element identified. EDXS can reveal the detected elemental compositions in mass per cent; however, these results could not reflect the stoichiometry of formulated elements due to the interference of atmospheric oxygen and gold coating.

Vibrating sample magnetometer (VSM) can be used to analyse the magnetic behaviour of magnetite materials. A typical magnetisation hysteresis loop depicts the magnetic behaviour of a magnetic nanoparticle corresponding to the applied external magnetic field. There are various factors, which can alter the hysteresis loop of magnetic materials. These include the size, shape, interaction and chemical

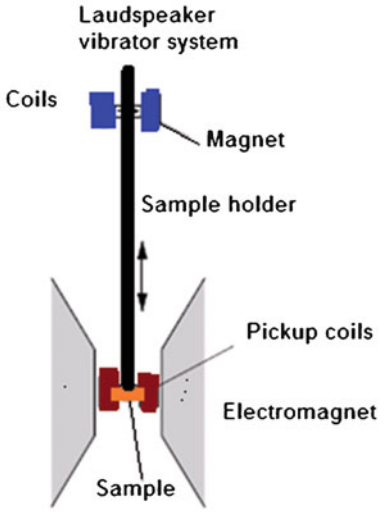

Fig. 14.6 Instrument setup of VSM

structure of sample and also the orientation of the magnetising field [23, 24]. The parameters used to express the magnetic capacity of materials include the saturation magnetisation (M_s) and the saturation field (H_{sat}) (see Fig. 14.6).

The application of moderate magnetic field H, magnetic moment of particle energy control over the anisotropy energy [25]. This change in energy reciprocally rotates the magnetic moment of domains into the new orientation; these orientations are moving with exposure of applied external magnetic field. The changes in magnetic moment of domain walls are somewhat comparable to the anisotropy energy. Thereafter, as applied external magnetic field modifies the balance of energies causing the moment's reorientation, increased magnetic field led to achieve saturation magnetisation (M_s) of magnetic materials (Fig. 14.7). The magnetic moment reversed and slowly aligned with applied magnetic field amplitude direction that causes the hysteresis of sample of single domain [24]. Hence, M_s value for microscale materials is different compared to nanoscale materials. The observed experiment M_s values for nanosize magnetic materials were in range of 30–60 emu·g^{-1}, compared to bulk magnetic materials, where M_s value was reported up to 90 emu g^{-1} [25]. The nanosize magnetic particles containing single domain of less than 35 nm were called superparamagnetic iron oxide nanoparticles (SPIONs). In SPIONs, the higher magnetic moment and lower potential energy in volume are significantly smaller compared to their thermal energy. Therefore, thermal energy itself creates the magnetic moment of nanoparticles with applied magnetic field [26]. This behaviour of iron oxide materials causes the lack of hysteresis losses. Where coercive fields do not reach to zero, the lack of hysteresis loss creates the heat release within nanosize magnetic materials.

Zero remanence value indicated superparamagnetic nature of bare SPIONs and silica-coated SPIONs; they become magnetised when external magnetic field is applied and nonmagnetic once the field is removed. Hysteresis loop pattern of

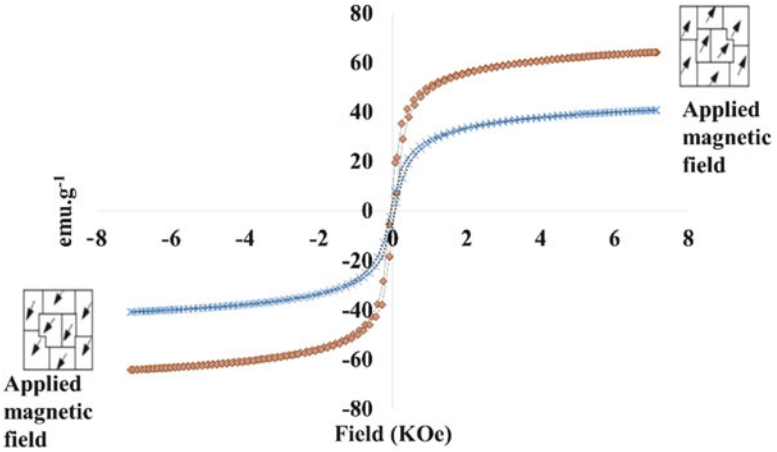

Fig. 14.7 Hysteresis curves of superparamagnetic nanoparticles

silica-coated SPIONs is similar to the core magnetite indicating the magnetic properties are retained during the procedure of silica coating and precipitation. This desired behaviour of SPIONs is making them an ideal candidate for biomedical applications [27–30]. As observed from the hysteresis curves for bare SPIONs and silica-coated SPIONs, both materials reached magnetisation saturation at around 2 kOe of the applied field.

Figure 14.7 shows zero magnetisation ($M = 0$). When external field is applied (arrows), these materials aligned with magnetic field until they reach to M_s (saturation magnetisation) plateau. The M_s is defined as in the following equation:

$$M_s = \frac{M}{p} \quad \left[\frac{\text{emu}}{g}\right] \tag{14.2}$$

where p is the density of magnetised materials and M is applied magnetic field.

The saturation magnetisation of magnetite is shown in Fig. 14.7. VSM technique involves Faraday's law of induction, where changes in the magnetic field produce the electric field. The electric field is then measured, which provides the information regarding the magnetic behaviour of magnetic particles. Measurements were performed at room temperature using 7 kOe magnetic field. Samples need to be dried and ground into a fine powder and then packed into plastic tubes of length ~10 mm and internal diameter ~1.9 mm. For each measurement, ~150 mg of magnetite materials are enough to achieve reliable results. The saturation magnetisation values are expressed as electromagnetic units per gramme (emu g^{-1}).

The magnetisation properties of SPIONs can be achieved using medium- to high-frequency 2–20 kOe magnetic field. The saturation magnetisation (M_s) of SPIONs prepared using co-precipitation method is 64 emu g^{-1} (Fig. 14.7). These values are in good agreement with the literature [31–33]. However, the saturation

magnetisation was significantly lower compared to 92 emu g^{-1} for bulky bare magnetite [34]. The lower size distribution of the nanoparticle displays the lower saturation magnetisation value [35, 36].

Surface area analyses were obtained using nitrogen gas adsorption techniques using BET. The mesoporous silica-coated magnetite silica nanoparticles exhibited very high specific surface area of 791.3154 m^2 g^{-1} compared to bare magnetite of 85.8505 m^2 g^{-1}. The adsorption-desorption isotherm for the silica-coated iron oxide nanoparticles shows hysteresis curve, which is IUPAC 4 isotherm. This hysteresis isotherm is characteristic of the behaviour of mesoporous materials. No such hysteresis was seen in the adsorption-desorption isotherms of bare SPIONs. Hysteresis behaviour only occurs in porous materials, where pores cause the adsorption and desorption of gas which reveals the type of isotherms to have different path [37].

TGA analysis of bare SPIONs and silica-coated SPIONs is useful for qualitative and quantitative purposes of volatile elements of the nanocomposite. The TGA curve (Fig. 14.8) depicts the weight loss of bare magnetite over the temperature range from 25 to 500 °C which is ~3.5%, possibly due to the loss of residual water from the sample. TGA was also performed to measure the relative mass proportion of the silica-coated materials. It is worth knowing the amount of water adsorbed, which can be useful in the design of drug carriers. The removal of water from silica material was accomplished at 120 °C and remained the losing of CTAB molecules until 250 °C from porous silica materials. CTAB weight loss appeared at 30–500 °C via decomposition (see Fig. 14.8). Thermal profile of CTAB alone showed complete degradation at 400 °C [38]. Hence, it could be possible that CTAB degradation happened gradually by shifting to higher temperature up to 500 °C.

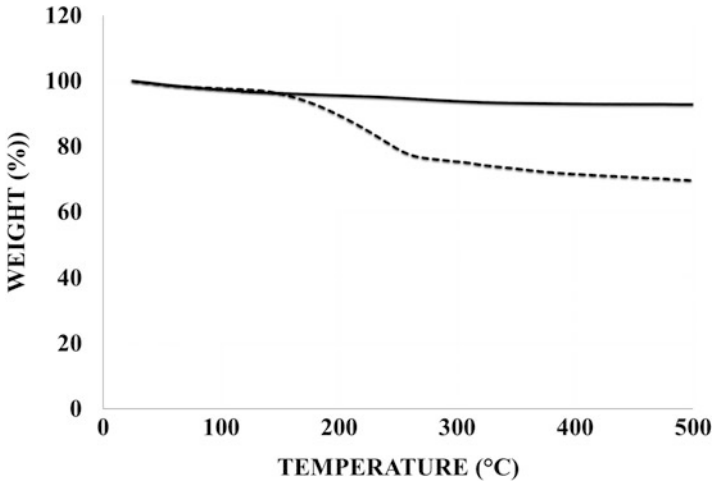

Fig. 14.8 Thermogravimetric analysis of bare SPIONs (*solid line*) and silica-coated SPIONs (*dotted line*)

Bare SPIONs and silica-coated SPIONs were also characterised using FTIR to confirm the bonding of Fe–O. The FTIR spectrum of both core and core-shell materials is depicted in Fig. 14.9.

In Fig. 14.9a, the peaks at 545 and 440 cm^{-1} are assigned to the Fe–O bond of Fe_3O_4. However, the characteristic bands for a Fe–O bond of bulk Fe_3O_4 are stated as 570 and 400 cm^{-1}; a shift in the bands of the Fe–O that were around 545 and 440 cm^{-1}, respectively, is also reported for the Fe_3O_4 nanoparticles [39]. This shift is probably due to the nanosize of materials, where certain bonds of surface atoms are broken, causing the rearrangement of electrons on the particle surface. The successful deposition of silica on the bare magnetite material, namely, mesoporous silica-coated iron oxide nanoparticles (silica-coated SPIONs), was also confirmed by FTIR analysis. The silica-coated material was compared to bare magnetite

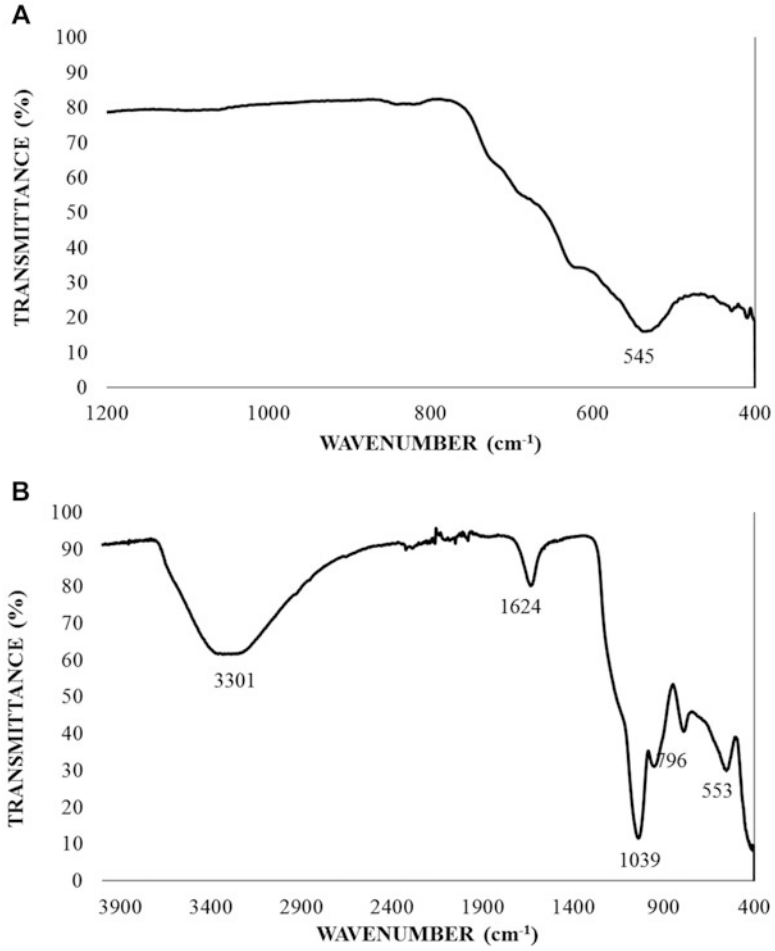

Fig. 14.9 FTIR spectrum of (**a**) bare SPION and (**b**) silica-coated SPION nanocomposites

Table 14.1 FTIR spectrum band assignment of iron oxide nanoparticles

Wavenumber (cm^{-1})	Possible assignment
570	Fe–O–Fe bending
800, 802	Si–O bending
939, 932	Si–OH stretching
1083, 1089	Si–O–Si stretching
1630, 1628	C–O bending
3200–3400	. . .–OH stretching

nanoparticles from the literature findings, the FTIR spectrum of silica-coated magnetic nanoparticles and the assignment of the bands shown in Table 14.1. The characteristic bands nearly at 1085, 800 and 550 cm^{-1} are corresponding to the stretching and bending of Si–O and Fe–O bonds, respectively. The main sharp peak of the Si–O vibrational band at 1085 cm^{-1} shows a stoichiometric arrangement of the silicon dioxide structure. Some impurity vibrational bands are also seen in the FTIR spectrum shown in Table 14.1. These are small compared to the main peaks. The peaks at 1600 and 2300 cm^{-1} are corresponding to vibrations of carbon impurity atoms. The FTIR spectrum (see Fig. 14.9) for the deposited silica also showed a wide peak of OH groups at around 3200–3400 cm^{-1}. These results reveal the presence of OH molecules on the surface of the mesoporous silica-coated iron oxide nanoparticles.

14.4.1 Heat Induction from Magnetic Nanoparticles in Alternating Magnetic Field

The heat induction from magnetic nanoparticles is caused by either hysteresis loss, Nėel relaxation or Brownian relaxation phenomenon. The relative strength of these mechanisms depends on the different factors such as size, shape, chemical composition and density of the nanoparticles.

Large-size particles that contain more than one domain reduce the magnetostatic energy. This energy comes up from magnets' own field. The magnetostatic energy (ME) is defined in the following terms:

$$\mathrm{ME} = \left(\frac{1}{2}\right) f H^2 dv \tag{14.3}$$

where dv denotes the volume and H defines the applied magnetic field.

Figure 2–6 explains the materials of numerous domains reducing the magnetic field H. As the domain volume increases, the north and south poles attracted and reduced the space; hence, it reduces magnetostatic energy of particles. The domains are separated with a domain wall. A huge amount of magnetic movement m is produced from each domain (Fig. 14.10).

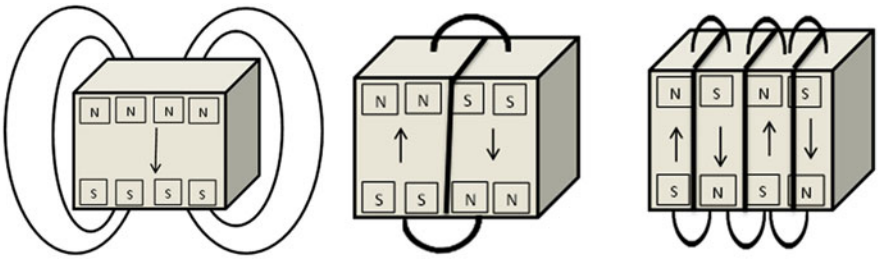

Fig. 14.10 Schematic diagram of magnetostatic energy reduction as the number of domains increases

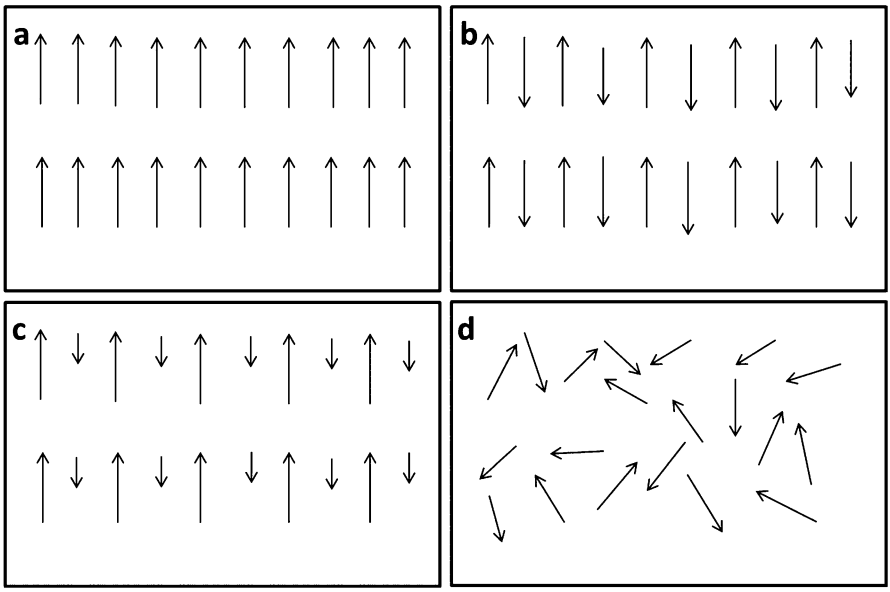

Fig. 14.11 Schematic diagram of magnetic moment orientation of different magnetic materials: (**a**) ferromagnetic, (**b**) antiferromagnetic, (**c**) ferrimagnetic and (**d**) paramagnetic materials

The magnetic materials then can be classified such as ferrimagnetic, ferromagnetic, antiferromagnetic and paramagnetic according to the orientation of their magnetic moment. The theory and mechanism for formation of these magnetic materials could not be possibly explained in this section; however, Fig. 14.11 displays the magnetic moment orientation of different magnetic materials. The magnetic moment orientation of ferrimagnetism, ferromagnetism and antiferromagnetism is aligned in one direction under the Curie temperature. Magnetic moment orientation varies from domain to domain; however, the domains are aligned in one orientation, and when external field is not applied, this orientation is called “easy axis”.

SPIONs showed the zero coercivity and remanence in the hysteresis loops, confirming the SPIONs made via co-precipitation methods are superparamagnetic.

14.4.2 Different Types of Hyperthermia

(a) *Diathermia*: In this type of hyperthermia treatment, temperature usually be kept lower than 41 °C. This type of treatment is used for physical and occupational therapies. The heat is induced from ultrasound, microwave and shortwave.
(b) *Moderated hyperthermia*: This applies to the treatment with temperature ranges from 40 to 45 °C. This range of temperature is ideal of killing of cancer cells [40].
(c) *Thermal ablation*: In this hyperthermia-based treatment, the temperature reaches up to 55 °C. This temperature causes the necrosis of cells and coagulation of body proteins and other biomolecules. The hyperthermia can be used into localised area, regional or organ based thermal ablation [41].

Different techniques can induce the hyperthermia-localised temperatures, including IR radiation, ultrasound, microwave, magnetic-based materials and administration of heated liquids or direct heating from chamber. The hyperthermia-based treatments of cancers, however, proved effective in initial clinical trials [42]. The molecular mechanism behind the cells' killing is still not fully understood. Several studies have revealed the intracellular mechanism of heat-induced cell damages. The hyperthermia activate the energy for protein coagulation [43]. The proteins in nucleus are more sensitive to hypothermia-induced coagulation compared to other intracellular biomolecules [44]. Moreover, the nucleus is a more efficient place for heat-induced protein denaturation [45]. Meanwhile, studies have revealed the good correlation of heat-induced cell damaging and nuclear protein denaturation [43, 46].

The relation between immune system and hyperthermia was studied [47]. According to these studies, hyperthermia was assumed to have increased the whole body temperature after applying the localised hyperthermia. However, it promotes the defence system by inducing the immune system. The killing of cells starts at 40 °C. In vivo studies confirmed the accumulation of dead cells in cancer sites after localised hyperthermia [48]. Another important application of magnetic field triggered drug release and targeted region (localised hyperthermia), which also triggers the drug release to specific sites.

14.5 Methods for Induction of Hyperthermia

(a) *Heated water circulations:* This is the oldest technique used for induction of hyperthermia, in which the whole body is kept in insulated chamber where circulating warm water increases the heat inside the body. This technique was

initially used in replacement of chemotherapy or radiotherapy. To achieve the hyperthermia, different instruments were designed in a systematic way, where the patient's whole body is kept inside the chamber except its head [49]. This type of hyperthermia approach is recommended to high-risk patients after surgery. This technique has a drawback of the non-uniform distribution of heat inside the body, which causes the lesions and surface burning. The computer simulation studies were performed to solve this problem [50]. Still, this approach could not reach to the patients because of its side effects such as cardiac arrest, RBC and platelet deficiency and biomolecule coagulations. In general, this approach has led to the investigation of localised hyperthermia.

(b) *Non-invasive wireless-induced hyperthermia*: In this approach, localised regions are targeted via applying waves; these waves cause heat generation over the targeted region. The various applicators are studied and commercially available for treatment of localised cancers. Such heat-inducing applicators include high-energy focused ultrasound waves, non-invasive electromagnetic radiofrequency waves, infrared frequency-based microwave, electromagnetic frequency waves based on inserting the antennas to avoid the uneven distribution of heating in localised hyperthermia, macroscopic radio frequencies electrode-induced heating for localised hyperthermia, few centimetres ferromagnetic seed implantation in a magnetic field and nanoparticle-based hyperthermia [51–54].

(c) *Nanoparticle-induced hyperthermia*: In nanoparticle-induced hyperthermia, heat is produced from loss of hysteresis or relaxation over applied alternate current magnetic field. This approach of hyperthermia-based treatment is more precise, where nanoparticles are systematically administered to the body and can be targeted via magnetic field or attachment of selective moieties or by exploiting enhanced permeability and retention effect. Nanoparticles upon systematic administration in the body can be directed and excited via applying external magnetic field. In comparison, other studied approaches such as radiofrequency electromagnetic waves, microwaves and high-energy focused ultrasound could not be directed by any means to the desired sites [55]. Magnetic nanoparticles also are MRI contrast materials, hence can be tracked and visualised for their localised distribution inside the targeted sites before starting the hyperthermia treatment [56].

Systematic hyperthermia-triggered controlled-release drug systems were designed, where magnetic nanoparticles were coated with certain thermos-sensitive biocompatible polymers and drug molecules. For this purpose, biocompatible gels were used to coat the magnetic materials. These gels have shown morphological alteration when exposed to different temperatures [57]. In addition, gels also work as sponge material for controlled release of payloads. In a drug delivery application, magnetic nanoparticles via thrust force can be propelled to targeted sites, where they can increase the temperature of hydrogel, thereby releasing the cargo molecules inside.

14.6 Magnetic Field-Induced Hyperthermia and Magnetic Field-Triggered Drug Release

Magnetic hyperthermia involves the transformation of magnetic energy into heat generated from the thermal fluctuation of magnetic nanoparticles in an AC magnetic field. The heat may be utilised both for the destruction of tumour cell directly (thermal ablation) and in combination with chemotherapy (Fig. 14.13).

Specific power absorption (SPA) of SPIONs can be determined in a commercial AC field applicator commonly available (see Fig. 14.12). The frequency and magnetic field strength varied from $f = 2.35$–418.5 kHz and 100–300 G, respectively. The measurements are performed within a thermally insulated working space.

The term hyperthermia indicates the increased temperature-based precise therapy of body tissues. In cancer applications, hyperthermia is the treatment of cancer exploiting the increased temperature. According to initial studies, increased precise heating can cook the cancer cells [59, 60]. The hyperthermia-based treatment could be divided in three categories based on the temperature utilisations.

Magnetic nanoparticles have been investigated as promising tools for hyperthermia treatment in cancerous tissues in vitro studies and animal models. The initial positive results of magnetic nanoparticle-induced hyperthermia have provided the impetus for the Phase I human experiments [61]. In hyperthermia, body temperature is increased to change the structural characteristics of cellular functions. In localised hyperthermia treatment, the temperature may rise up to 42 °C; tumour cells do not resist this temperature with sudden changes compared to normal cells leading to tumour cell destruction [62]. The change in the temperature alters the

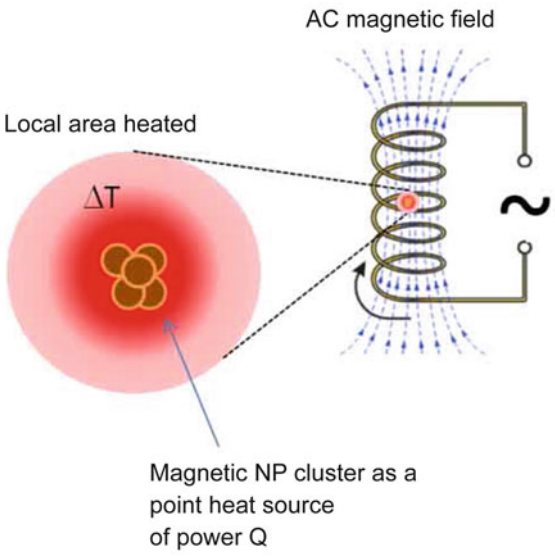

Fig. 14.12 Schematic diagram of magnetic hyperthermia-based treatment adapted from [58]

structure-function relationship of enzymes and proteins, causing cell apoptosis via deregulating the cell growth and differentiation [63]. Hyperthermia-triggered alteration of cell membranes caused changes in the transporting mechanism of membrane permeability. Cellular studies demonstrated that the sudden increase in the temperature altered the synthesis and structural conformation of nucleic acids and also inhibited DNA repair enzymes [64, 65]. The induction of hyperthermia can be achieved via numerous techniques, such as microwave or electromagnetic radiations [66, 67], focused high ultrasound waves [68] or electrical energy [69]. Even though these techniques generate sufficient heat however, they failed to provide uniform distribution and deep penetration of heat for therapeutic applications in tumour sites. Hence, insufficient or nonhomogeneous distribution of heat in tumour sites causes a temperature rise in only surface sites. Another important factor is excessive and uncontrolled heat induction that causes the peritumoural cell damage. Nanoparticle-induced magnetic hyperthermia has somewhat addressed these issues.

Magnetic-induced hyperthermia applications were initially reported in 1957 [70]. A series of research papers were published for studying the potential application of hyperthermia ablation therapy. However, consistent studies for therapeutic-based applications were published after the 1990s. Still fewer studies are available in animal models [71–73]. More studies are needed to address the limitations, toxicity, selectivity and efficiency for effective and safe treatment of tumours. The mechanism of magnetic hyperthermia involves the systematic administration of magnetic materials. After applying external magnetic field, magnetic materials can increase temperature in targeted region [74]. Currently, magnetic hyperthermia stands for the non-invasive, effective and comparable uniform and deeply penetrating technique for regions where accessibility is limited and specific to targeted regions and has enhanced rate of heat transfer.

Magnetic hyperthermia efficiency depends on the various properties of nanoparticles such as size, shape, saturation magnetisation value and Curie point (Tc). Curie point is critical which provides the control of heat transfer to avoid excess heating [75]. Another important factor for controlling the desired temperature is the tunable strength and frequency of the magnetic field. The efficiency of induced heat of magnetic materials was measured as the specific absorption rate (SAR). SAR reflects the heat transformation from magnetic energy, which is characteristic of Brownian rotation and Néel relaxation phenomenon. In Brownian rotation, the particles rotate physically within the dispersion medium. In Néel relaxation mechanism, particle's magnetic moment at atomic level rotates within the particles. The Brownian rotation and Néel rotation processes are revealed as relaxation times (T_B and T_N), respectively. In hyperthermia studies, SAR values are dependent on the particles' internal (Néel) characteristics (such as size, shape, elemental composition, functional modifications and additives), and the external (Brownian) characteristics reflect the strength (H) and frequency of the magnetic field. The following equation can define the SAR:

$$SAR = \frac{c}{M\text{mnp}}\left(\frac{\Delta T}{\Delta t}\right) \tag{14.3}$$

where c is the specific heat capacity of the medium and $\frac{\Delta T}{\Delta t}$ reflects the initial slope of temperature change during the heat induction and M_{mnp} is mass of nanoparticles (mg) [76].

The initial study of magnetic hyperthermia-based treatment in vivo was performed using dextran-coated SPIONs with a core size of approximately 3 nm [77]. Dextran-coated SPIONs were systematically administered into tumour tissues and subsequently the magnetic field was applied. Applied magnetic field frequency and strength and tissues selection and conductivity should be taken into consideration to avoid possible harmful effects. The magnetic field frequency of 0.1–1.5 MHz and 0–300 G strength are considered safe for in vivo application [78]. A variety of trials have been conducted by different companies such as MagForce Nanotechnologies (Germany) and NanoTherm (UK), showing the efficiencies of magnetic hyperthermia-based treatments of localised solid tumours by reducing the discomfort or harms to normal cells [79]. This treatment involved killing cells using induction heating. Heating was generated by SPIONs via Brownian rotation or Nėel relaxation on subsequent applied magnetic field. This mechanism comprises different modules: SPIONs, magnetic field and incorporated drugs. Due to the SPIONs' ultrasmall size and exposure to the applied magnetic field, they are localised inside the tumours and generate concentrated and uniform heat in selected sites (see Fig. 8.1).

The concept of engineering of hyperthermia-responsive drug loaded iron oxide nanoparticles, which can increase the internal temperature when exposed to external magnetic field and trigger drug release. The different iron oxide nanoparticle concentrations on the hyperthermia of bare SPIONs are needed to be optimised. The magnetic field-triggered drug release system may provide an ideal system in cancer treatment by simultaneously exploiting both chemotherapy and hyperthermia ablation therapy (Fig. 14.13).

SPIONs synthesised via co-precipitation method were studied to investigate the concentration effects in water. Four different concentrations (2.5, 5, 7.5 and 10 mg mL^{-1}) were used. Magnetic field with a frequency of 406 kHz and strength of 200 G was kept constant in all of the experiments. SPIONs of different concentrations from 2.5 to 10 mg mL^{-1} showed slowest and fastest induced heating rate, respectively, upon exposure to the alternate magnetic field (Fig. 8.2). The results of magnetic field-induced hyperthermia were highly concentration dependent. The 2.5 mg mL^{-1} showed slowest temperature increase and reached 42 °C in 20 min of exposure to the AC magnetic field. In the 5 mg mL^{-1} solution, the temperature was increased sharply compared to 2.5 mg mL^{-1}. It reached 50 °C in approximately 10 min. Similarly, 7.5 mg mL^{-1} took only 4 min to achieve 50 °C. The fastest heating pattern was seen for 10 mg mL^{-1} of B-SPION-SS, taking only 3.5 min to reach 50 °C. These results were consistent with previous studies [80, 81], where they found a sharp increase in the temperature using constant magnetic field

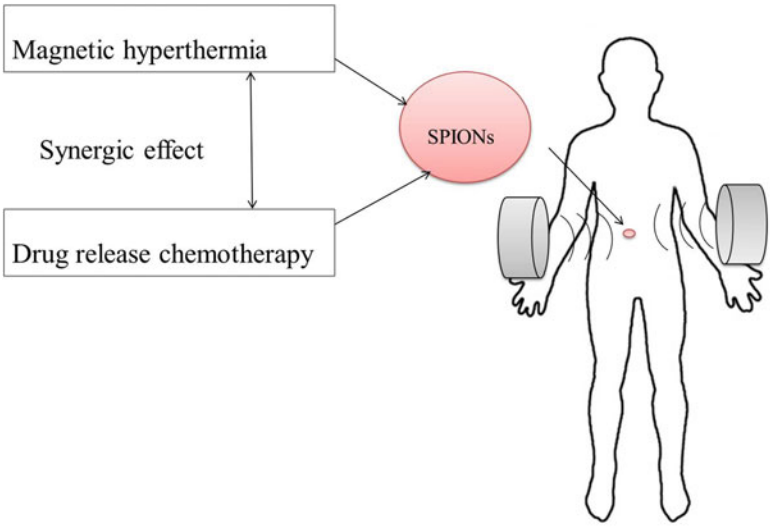

Fig. 14.13 Depiction of localised magnetic field-triggered nanoparticles thermo-chemotherapy

strength and frequency. The mechanism of heat induction from synthesised nanoparticles could be due to the Brownian rotation and Nėel relaxation of Fe_3O_4 nature of the nanoparticles with low conductivity ($\rho = 10^2\ \Omega$ cm, resistivity); hence, Eddy current heat induction may be negligible [81]. VSM and XRD data also confirmed the superparamagnetic nature of the nanoparticles; the heat induction from hysteresis loss may also be negligible. The main source of heat induction will only be contributed to the Brownian rotation or Nėel relaxation.

The specific absorption rate (SAR) was measured using Eq. 8.1. For all studies (Figure 8.2a–d), initial slope $\frac{\Delta T}{\Delta t}$ was calculated from the first minute of applied magnetic field. The calculated SAR values are shown in Table 8.1 for all concentrations. The highest SAR value (63 W g^{-1}) was found for the 2.5 mg mL^{-1} with the magnetic field strength and frequency. However, this value was higher compared to the previous study [82], where the size-dependent effect of SAR calculation was studied. For iron oxide with size of approximately 20 nm, SAR value was 40 W g^{-1}. In a similar SPION size distribution of as this study the SAR value was 63 W g^{-1}. The minimum SAR value found in this study was 22 W g^{-1}. These results were consistent with previous studies [80, 83–85].

The kinetic studies on the effects of temperature showed a sharp increase for higher concentrations. The SAR values were in reverse in order to the concentration. The highest SAR value was obtained for lowest concentration. The possible reason behind the fast increase of temperature and lower SAR value is the retention of the Brownian particles and relaxation effect in lower concentrations. Higher concentrations of bare SPIONs facilitated the formation of large aggregates. Other studies confirmed the good dispersions of bare SPIONs showing higher SAR value via better

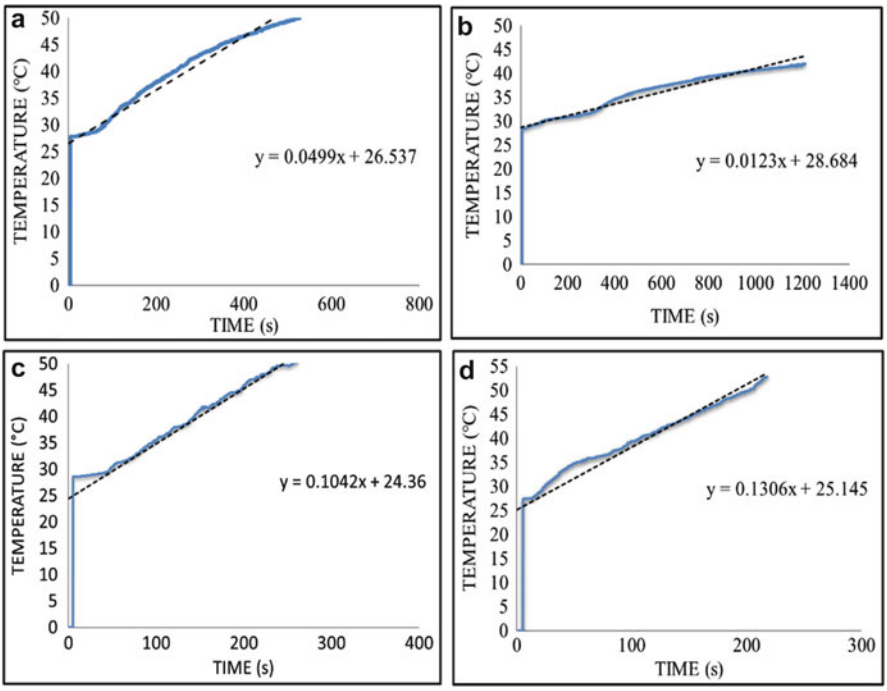

Fig. 14.14 Bare SPION temperature increased curves after exposure to AC magnetic field on (**a**) 2.5 mg mL^{-1}, (**b**) 5 mg mL^{-1}, (**c**) 7.5 mg mL^{-1} and (**d**) 10 mg mL^{-1}

Brownian rotation and Nèel relaxation effects [86, 87]. The 5–10 mg mL^{-1} of bare SPIONs were found to be effective and safe for hyperthermia treatment of tumour tissues [88]. Figure 14.14a–d shows concentration-dependent heat induction of bare SPIONs where the temperatures were set in between a minimum of 42 °C and a maximum of 55 °C in water as a medium of dispersion. These results confirmed that the concentration from 2.5 to 10 mg mL^{-1} could increase the temperature to 42–55 °C using 406 kHz frequency and 200 G. Table 14.2 shows the SAR values as a function of the concentration of bare SPIONs. SAR trend followed the results obtained via computer simulation [89], where SAR values were found higher in lower concentration compared to higher concentration (lower SAR values). This was also somewhat common for lower concentration, where lower concentration particles in suspension were expected as individuals rather than as aggregates after the application of a magnetic field in the suspension. However, larger aggregates tended to sediment and less exposed to the magnetic field. A similar study, where SAR was calculated using different volume vials, showed that lower volume vials have three times higher SAR values than the value obtained with larger volume vials [89]. This difference may be attributed to exposure of applied magnetic field to individual nanoparticles in a suspension.

Table 14.2 Experimental SAR values calculated for spherical iron oxide nanoparticle

Concentration (mg mL^{-1})	SAR (W g^{-1})
2.5	63
5	36
7.5	30
10	22

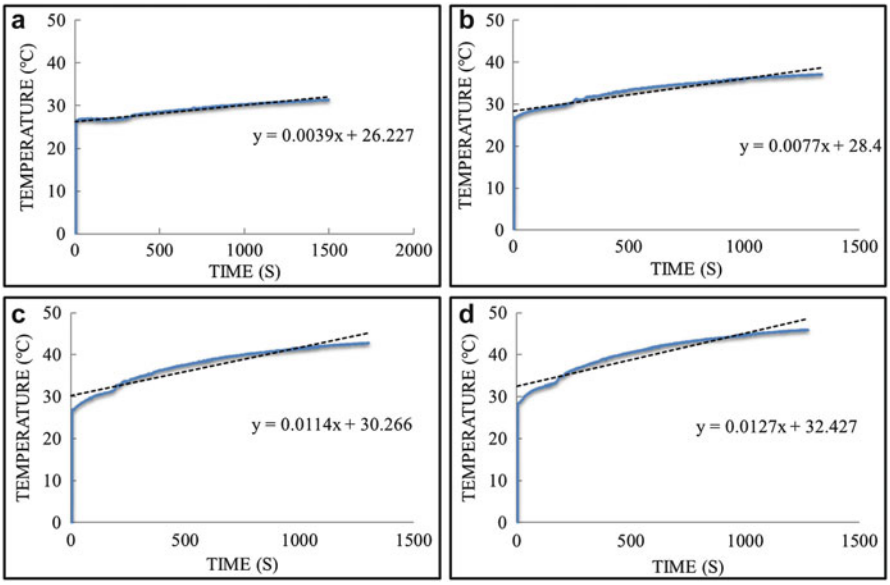

Fig. 14.15 Si-SPION hyperthermia effect after exposure to AC magnetic field: (**a**) 2.5 mg mL^{-1}, (**b**) 5 mg mL^{-1}, (**c**) 7.5 mg $mL^{-}1$ and (**d**) 10 mg mL^{-1}

14.7 Magnetic Field-Induced Hyperthermia of Silica-Coated Iron Oxide Nanoparticles

Figure 14.15 reveals the silica-coated magnetic nanoparticles (Si-SPIONs) induced heating curves of four concentrations in water of 2.5, 5, 7.5 and 10 mg mL^{-1} using a frequency of 406 kHz and a magnetic field strength of 200 G. The higher concentration of silica-coated iron oxide nanoparticles showed a sharp increase and higher maximum temperature compared to lower concentrations. Each formulation reached a plateau temperature within 25 min of exposure of magnetic field. In 2.5 mg mL^{-1}, the graph did not display the temperature increase in the first 4–5 min. This time possibly indicates a lag phase where Si-SPIONs heating occurs firstly in the cores and then dissipates to the shell and finally to the medium, where temperature probe was attached. After this time, heating could be seen clearly, requiring 23 min to raise 5 °C (Fig. 14.15a). In Fig. 14.15c, d, heating curves (5–10 mg mL^{-1}) showed the sharp temperature increase from the first minute of

Table 14.3 Experimental SAR values calculated for spherical silica-coated iron oxide nanoparticle

Concentration (mg mL^{-1})	SAR (W g^{-1})
2.5	131
5	117
7.5	54
10	30

exposure of the magnetic field; however, in first 4 min, the heating trend was somewhat slower than in later time up to 20 or 23 min. This trend also confirmed the presence of coating, where initial heat dissipation occurred in the shell, and then it transferred to the medium, where temperature probe was located. 5 mg mL^{-1} solutions took 23 min to raise 9 °C reaching 37 °C (Fig. 14.15b). Higher concentration of 7.5 mg mL^{-1} showed an increase in the temperature up to 43 °C by raising 15 °C in 20 min (Fig 14.15c). However, the fastest and maximum heat induction was seen for 10 mg mL^{-1} concentration, where a maximum temperature was observed at 46 °C by raising 18 °C, over exposure of 20 min of magnetic field (Fig. 14.15d, Table 14.3).

14.8 Magnetic Field-Triggered Drug Release from Bare Superparamagnetic Iron Oxide Nanoparticles

Doxorubicin (DOX) release profile was also generated under an AC magnetic field (DM100, nB nanoscale Biomagnetics, Spain) to investigate the temperature-triggered DOX release. DOX-loaded iron oxide nanoparticles (1 mL of PBS buffer) were kept in an AC field applicator using a frequency of 406 KHz and magnetic field strength of 200 G for 15 min. A schematic diagram is depicted in Fig. 14.16. The DOX release profile was obtained by measuring UV absorbance at λ_{485} nm of supernatant via magnetic separation. DOX content was measured using the standard curve in PBS. The results have been plotted as percentage DOX release over time and temperature.

DOX was loaded into the bare SPIONs to investigate magnetic field-triggered release properties. DOX was loaded into bare SPIONs, where SPION cores induced hyperthermia via Brownian rotation and Nėel relaxation mechanism. DOX-loaded nanoparticle solution was placed in between the magnetic field coils; thermal insulation jacket was used to reduce the effects of the surrounded temperature. Additionally, water circulation was used to control environmental and thermal effect of the coils. The magnetic field strength and frequency were set to 200 G and 406 kHz, respectively, for all the experiments conducted. The colour of DOX was seen clearly after release experiments as free DOX after exposure of applied magnetic field. Figure 14.17 shows the DOX release behaviour under applied magnetic field and without the magnetic field. The release values were dependent on bare SPION concentration; this was possibly due to the higher heating influence of bare SPIONs; a similar pattern was also reported in Bi et al. [90]. Figure 14.17

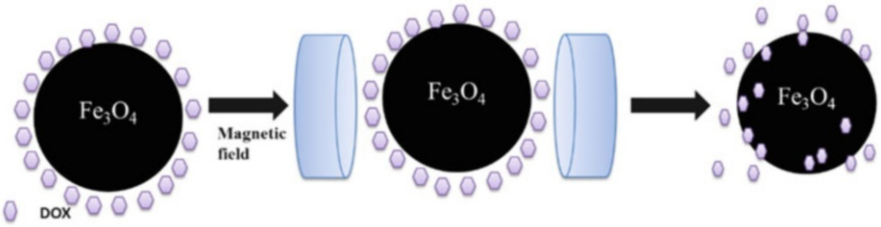

Fig. 14.16 Schematic diagram of DOX release after exposure to magnetic field

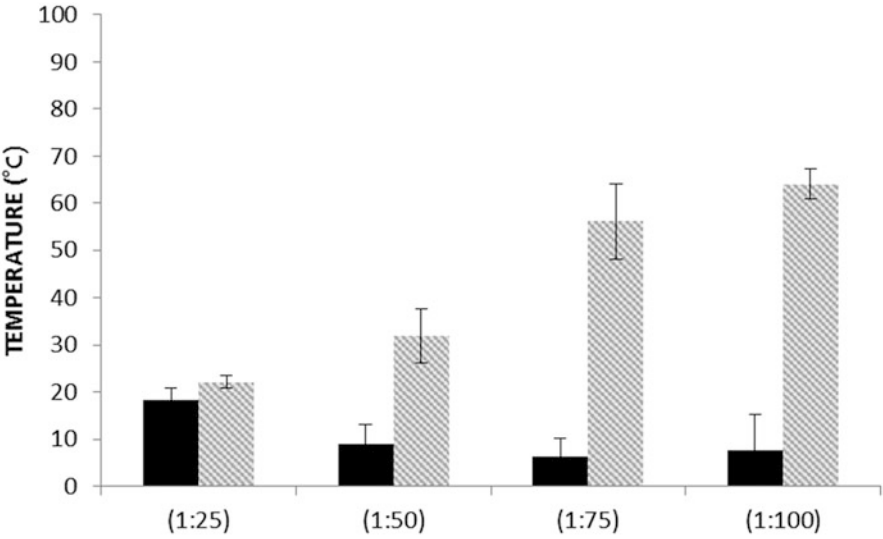

Fig. 14.17 Magnetic field-triggered drug release from bare SPIONs without magnetic field exposure (*black*) and applied magnetic field (*grey*)

demonstrates different concentrations of 2.5, 5, 7.5 and 10 mg mL^{-1} used to investigate the release behaviour. The release percentage reached up to 60% for 10 mg mL^{-1}. The presence of greater amount of particles induces more and rapid heat, which ultimately enhances the DOX release.

14.9 Magnetic Field-Triggered Drug Release from Silica-Coated Superparamagnetic Iron Oxide Nanoparticles

Silica-coated SPION (Si-SPION) DOX release behaviour was investigated in the presence and absence of magnetic field. Figure 14.18 shows increase trend of DOX release after exposure of magnetic field in all samples. This release behaviour was

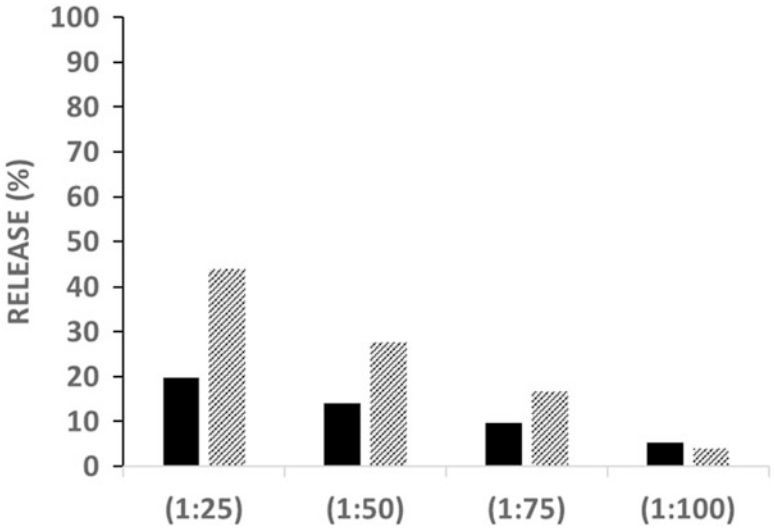

Fig. 14.18 Magnetic field-triggered drug release Si-SPIONs without magnetic field exposure (*black*) and applied magnetic field (*grey*)

in good agreement with previously published studies for poly(trimethylene carbonate) poly(l-glutamate)-coated SPIONs [91], poly(propylacrylamide)-coated SPIONs [92], PEG-capped silica-coated SPIONs [93] and bare SPIONs [94]. In all of the above studies, different polymer-coated SPIONs could increase the drug-releasing efficiency up to twofold on applied magnetic field strength. As shown in Fig. 14.18 in lower concentrations of 2.5, 5 and 7.5 mg mL^{-1}, the release behaviour was reduced, possibly reflecting the sustained release of drug from mesoporous silica shell.

References

1. Bruce IJ, Taylor J, Todd M, Davies MJ, Borioni E, Sangregorio C, Sen T (2004) Synthesis, characterisation and application of silica-magnetite nanocomposites. J Magn Magn Mater 284:145–160
2. Mahmoudi M, Sant S, Wang B, Laurent S, Sen T (2011) Superparamagnetic iron oxide nanoparticles (SPIONs): development, surface modification and applications in chemotherapy. Adv Drug Deliv Rev 63(1–2):24–46
3. Sen T, Bruce IJ (2009) Mesoporous silica–magnetite Nanocomposites: fabrication, characterisation and applications in biosciences. Microporous Mesoporous Mater 120(3):246–251
4. Sen T, Sheppard SJ, Mercer T, Eizadi-sharifabad M, Mahmoudi M, Elhissi A (2012) Simple one-pot fabrication of ultra-stable core-shell superparamagnetic nanoparticles for potential application in drug delivery. RSC Adv 2(12):5221

5. Kirschvink JL, Kobayashi-Kirschvink A, Diaz-Ricci JC, Kirschvink SJ (1992) Magnetite in human tissues: a mechanism for the biological effects of weak ELF magnetic fields. Bioelectromagnetics 13(S1):101–113
6. Hergt R, Andra W, d'Ambly CG, Hilger I, Kaiser WA, Richter U, Schmidt H-G (1998) Physical limits of hyperthermia using magnetite fine particles. IEEE Trans Magn 34 (5):3745–3754
7. Santhosh PB, Ulrih NP (2013) Multifunctional superparamagnetic iron oxide nanoparticles: promising tools in cancer theranostics. Cancer Lett 336(1):8–17
8. Maity D, Kale SN, Kaul-Ghanekar R, Xue J-M, Ding J (2009) Studies of magnetite nanoparticles synthesized by thermal decomposition of iron (III) acetylacetonate in tri (ethylene glycol). J Magn Magn Mater 321(19):3093–3098
9. Amara D, Felner I, Nowik I, Margel S (2009) Synthesis and characterization of Fe and Fe 3 O 4 nanoparticles by thermal decomposition of triiron dodecacarbonyl. Colloids Surf A Physicochem Eng Asp 339(1):106–110
10. Laurent S, Henoumont C, Stanicki D, Boutry S, Lipani E, Belaid S, Muller RN, Vander Elst L (2017) Superparamagnetic iron oxide nanoparticles. In: MRI contrast agents. Springer, Singapore, pp 55–109
11. Cai H, An X, Cui J, Li J, Wen S, Li K, Shen M, Zheng L, Zhang G, Shi X (2013) Facile hydrothermal synthesis and surface functionalization of polyethyleneimine-coated iron oxide nanoparticles for biomedical applications. ACS Appl Mater Interfaces 5(5):1722–1731
12. Guardia P, Di Corato R, Lartigue L, Wilhelm C, Espinosa A, Garcia-Hernandez M, Gazeau F, Manna L, Pellegrino T (2012) Water-soluble iron oxide nanocubes with high values of specific absorption rate for cancer cell hyperthermia treatment. ACS Nano 6(4):3080–3091
13. Nordmeyer D, Stumpf P, Gröger D, Hofmann A, Enders S, Riese SB, Dernedde J, Taupitz M, Rauch U, Haag R (2014) Iron oxide nanoparticles stabilized with dendritic polyglycerols as selective MRI contrast agents. Nanoscale 6(16):9646–9654
14. Rajabi F, Kakeshpour T, Saidi MR (2013) Supported iron oxide nanoparticles: recoverable and efficient catalyst for oxidative SS coupling of Thiols to disulfides. Catal Commun 40:13–17
15. Sakulkhu U, Mahmoudi M, Maurizi L, Salaklang J, Hofmann H (2014) Protein corona composition of superparamagnetic iron oxide nanoparticles with various physico-chemical properties and coatings. Sci Rep 4:5020
16. Yan X, Zhu P, Li J (2010) Self-assembly and application of diphenylalanine-based nanostructures. Chem Soc Rev 39(6):1877
17. Sharifabad ME, Hodgson B, Jellite M, Mercer T, Sen T (2014) Enzyme immobilised novel core-shell superparamagnetic nanocomposites for enantioselective formation of 4-(R)-hydroxycyclopent-2-en-1-(S)-acetate. Chem Commun 50(76):11185–11187
18. Sen T, Sebastianelli A, Bruce IJ (2006) Mesoporous silica−magnetite nanocomposite: fabrication and applications in magnetic bioseparations. J Am Chem Soc 128(22):7130–7131
19. Holzwarth U, Gibson N (2011) The Scherrer equation versus the'Debye-Scherrer equation. Nat Nanotechnol 6(9):534
20. Monshi A, Foroughi MR, Monshi MR (2012) Modified Scherrer equation to estimate more accurately nano-crystallite size using XRD. World J Nano Sci Eng 2(03):154
21. Burton AW, Ong K, Rea T, Chan IY (2009) On the estimation of average crystallite size of zeolites from the Scherrer equation: a critical evaluation of its application to zeolites with one-dimensional pore systems. Microporous Mesoporous Mater 117(1):75–90
22. El Mendili Y, Bardeau J-F, Randrianantoandro N, Greneche J-M, Grasset F (2016) Structural behavior of laser-irradiated γ-Fe2O3 nanocrystals dispersed in porous silica matrix : γ-Fe2O3 to α-Fe2O3 phase transition and formation of ε-Fe2O3. Sci Technol Adv Mater 17(1):597–609
23. Simeonidis K, Martinez-Boubeta C, Balcells L, Monty C, Stavropoulos G, Mitrakas M, Matsakidou A, Vourlias G, Angelakeris M (2013) Fe-based nanoparticles as tunable magnetic particle hyperthermia agents. J Appl Phys 114(10):103904
24. Jiles D (2015) Introduction to magnetism and magnetic materials. CRC Press

25. Harris LA (2002) Polymer stabilized magnetite nanoparticles and poly (propylene oxide) modified styrene-dimethacrylate networks.
26. Brown WF Jr (1963) Thermal fluctuations of a single-domain particle. Phys Rev 130(5):1677
27. Graczyk H, Bryan LC, Lewinski N, Suarez G, Coullerez G, Bowen P, Riediker M (2015) Physicochemical characterization of nebulized superparamagnetic iron oxide nanoparticles (SPIONs). J Aerosol Med Pulm Drug Deliv 28(1):43–51
28. Ling D, Lee N, Hyeon T (2015) Chemical synthesis and assembly of uniformly sized iron oxide nanoparticles for medical applications. Acc Chem Res 48(5):1276–1285
29. Karimzadeh I, Aghazadeh M, Ganjali MR, Norouzi P, Shirvani-Arani S, Doroudi T, Kolivand PH, Marashi SA, Gharailou D (2016) A novel method for preparation of bare and poly (vinylpyrrolidone) coated superparamagnetic iron oxide nanoparticles for biomedical applications. Mater Lett 179:5–8
30. Kandasamy G, Surendran S, Chakrabarty A, Kale SN, Maity D (2016) Facile synthesis of novel hydrophilic and carboxyl-amine functionalized superparamagnetic iron oxide nanoparticles for biomedical applications. RSC Adv 6(102):99948–99959
31. Feng B, Hong RY, Wang L, Guo L, Li HZ, Ding J, Zheng Y, Wei DG (2008) Synthesis of Fe 3 O 4/APTES/PEG diacid functionalized magnetic nanoparticles for MR imaging. Colloids Surf A Physicochem Eng Asp 328(1):52–59
32. Banaei A, Vojoudi H, Karimi S, Bahar S, Pourbasheer E (2015) Synthesis and characterization of new modified silica coated magnetite nanoparticles with bisaldehyde as selective adsorbents of Ag(i) from aqueous samples. RSC Adv 5(101):83304–83313
33. Greene D, Serrano-Garcia R, Govan J, Gun'ko YK (2014) Synthesis characterization and photocatalytic studies of cobalt ferrite-silica-titania nanocomposites. Nanomaterials 4 (2):331–343
34. Qu L, Tie S (2009) Mesoporous silica-coated superparamagnetic magnetite functionalized with CuO and its application as a desulfurizer. Microporous Mesoporous Mater 117 (1):402–405
35. Chatterjee J, Haik Y, Chen C-J (2003) Size dependent magnetic properties of iron oxide nanoparticles. J Magn Magn Mater 257(1):113–118
36. Maaz K, Duan JL, Karim S, Chen YH, Zhai PF, Xu LJ, Yao HJ, Liu J (2016) Fabrication and size dependent magnetic studies of Ni X Mn 1− X Fe 2 O 4 (X= 0.2) cubic nanoplates. J Alloys Compd 684:656–662
37. Knežević NŽ, Lin VS-Y (2013) A magnetic mesoporous silica nanoparticle-based drug delivery system for photosensitive cooperative treatment of cancer with a mesopore-capping agent and mesopore-loaded drug. Nanoscale 5(4):1544–1551
38. Wang YD, Zhang S, Ma CL, Li HD (2007) Synthesis and room temperature photoluminescence of ZnO/CTAB ordered layered nanocomposite with flake-like architecture. JOL 126(2):661–664
39. Bordbar AK, Rastegari AA, Amiri R, Ranjbakhsh E, Abbasi M, Khosropour AR (2014) Characterization of modified magnetite nanoparticles for albumin immobilization. Biotechnol Res Int 2014:705068
40. Nikam DS, Jadhav SV, Khot VM, Phadatare MR, Pawar SH (2014) Study of AC magnetic heating characteristics of co 0.5 Zn 0.5 Fe 2 O 4 nanoparticles for magnetic hyperthermia therapy. J Magn Magn Mater 349:208–213
41. Majeed J, Pradhan L, Ningthoujam RS, Vatsa RK, Bahadur D, Tyagi AK (2014) Enhanced specific absorption rate in silanol functionalized Fe 3 O 4 CORE–shell nanoparticles: study of Fe leaching in Fe 3 O 4 and hyperthermia in L929 and HeLa cells. Colloids Surf B Biointerfaces 122:396–403
42. Cihoric N, Tsikkinis A, van Rhoon G, Crezee H, Aebersold DM, Bodis S, Beck M, Nadobny J, Budach V, Wust P (2015) Hyperthermia-related clinical trials on cancer treatment within the ClinicalTrials. Gov registry. Int J Hyperthermia 31(6):609–614
43. Kampinga HH (2006) Cell biological effects of hyperthermia alone or combined with radiation or drugs: a short introduction to newcomers in the field. Int J Hyperthermia 22(3):191–196

44. Lepock JR (2004) Role of nuclear protein denaturation and aggregation in thermal radiosensitization. Int J Hyperthermia 20(2):115–130
45. Nishita M, Inoue S, Tsuda M, Tateda C, Miyashita T (1998) Nuclear translocation and increased expression of Bax and disturbance in cell cycle progression without prominent apoptosis induced by hyperthermia. Exp Cell Res 244(1):357–366
46. Kampinga HH, Dikomey E (2001) Hyperthermic radiosensitization: mode of action and clinical relevance. Int J Radiat Biol 77(4):399–408
47. Shen R-N, Lu L, Young P, Shidnia H, Hornback NB, Broxmeyer HE (1994) Influence of elevated temperature on natural killer cell activity, lymphokine-activated killer cell activity and lectin-dependent cytotoxicity of human umbilical cord blood and adult blood cells. Int J Radiat Oncol Biol Phys 29(4):821–826
48. Burd R, Dziedzic TS, Xu Y, Caligiuri MA, Subjeck JR, Repasky EA (1998) Tumor cell apoptosis, lymphocyte recruitment and tumor vascular changes are induced by low temperature, long duration (fever-like) whole body hyperthermia. J Cell Physiol 177(1):137–147
49. Pettigrew RT, Galt JM, Ludgate CM, Smith AN (1974) Clinical effects of whole-body hyperthermia in advanced malignancy. Br Med J 4(5946):679–682
50. Paulides MM, Stauffer PR, Neufeld E, Maccarini PF, Kyriakou A, Canters RAM, Diederich CJ, Bakker JF, Van Rhoon GC (2013) Simulation techniques in hyperthermia treatment planning. Int J Hyperthermia 29(4):346–357
51. Varon J, Acosta P (2008) Therapeutic hypothermia: past, present, and future. Chest J 133 (5):1267–1274
52. Vaupel P, Kallinowski F, Okunieff P (1989) Blood flow, oxygen and nutrient supply, and metabolic microenvironment of human tumors: a review. Cancer Res 49(23):6449–6465
53. Wust P, Hildebrandt B, Sreenivasa G, Rau B, Gellermann J, Riess H, Felix R, Schlag PM (2002) Hyperthermia in combined treatment of cancer. Lancet Oncol 3(8):487–497
54. Lele PP (1990) Electronically-controlled variable focus ultrasound hyperthermia system.
55. Jordan A, Scholz R, Wust P, Fähling H, Felix R (1999) Magnetic fluid hyperthermia (MFH): cancer treatment with AC magnetic field induced excitation of biocompatible superparamagnetic nanoparticles. J Magn Magn Mater 201(1):413–419
56. Mornet S, Vasseur S, Grasset F, Duguet E (2004) Magnetic nanoparticle design for medical diagnosis and therapy. J Mater Chem 14(14):2161–2175
57. Ang KL, Venkatraman S, Ramanujan RV (2007) Magnetic PNIPA hydrogels for hyperthermia applications in cancer therapy. Mater Sci Eng C 27(3):347–351
58. INL (2017) International Iberian Nanotechnology.
59. Hahn GM (1974) Metabolic aspects of the role of hyperthermia in mammalian cell inactivation and their possible relevance to cancer treatment. Cancer Res 34(11):3117–3123
60. Quinto CA, Mohindra P, Tong S, Bao G (2015) Multifunctional superparamagnetic iron oxide nanoparticles for combined chemotherapy and hyperthermia cancer treatment. Nanoscale 7 (29):12728–12736
61. Shevtsov M, Multhoff G (2016) Recent developments of magnetic nanoparticles for theranostics of brain tumor. Curr Drug Metab 17(8):737–744
62. Cavaliere R, Giogatto BC, Giovanella BC (1967) Selective heat sensitivity of cancer cells. Cancer 20(9):1351–1381
63. Sellins KS, Cohen JJ (1991) Hyperthermia induces apoptosis in thymocytes. Radiat Res 126 (1):88–95
64. Paolini A, Guarch CP, Ramos-López D, Lapuente J, Lascialfari A, Guari Y, Larionova J, Long J, Nano R (2016) Rhamnose-coated superparamagnetic iron-oxide nanoparticles: an evaluation of their in vitro cytotoxicity, genotoxicity and carcinogenicity. J Appl Toxicol 36 (4):510–520
65. Wong RSL, Kapp LN, Krishnaswamy G, Dewey WC (1993) Critical steps for induction of chromosomal aberrations in CHO cells heated in S phase. Radiat Res 133(1):52–59
66. Stahl H, Wust P, Maier-Hauff K, Seebass M, Mischel M, Gremmler M, Golde G, Löffel J, Felix R (1995) The use of an early postoperative interstitial-hyperthermia combination therapy

in malignant gliomas. Strahlentherapie und Onkol. Organ der Dtsch. Rontgengesellschaft... [et al] 171(9):510–524
67. Sneed PK, Stauffer PR, McDermott MW, Diederich CJ, Lamborn KR, Prados MD, Chang S, Weaver KA, Spry L, Malec MK (1998) Survival benefit of hyperthermia in a prospective randomized trial of brachytherapy boost±hyperthermia for glioblastoma multiforme. Int J Radiat Oncol Biol Phys 40(2):287–295
68. Mitsumori M, Hiraoka M, Okuno Y, Nishimura Y, Li YP, Fujishiro S, Nagata Y, Abe M, Koishi M, Sano T (1996) A phase I and II clinical trial of a newly developed ultrasound hyperthermia system with an improved planar transducer. Int J Radiat Oncol Biol Phys 36 (5):1169–1175
69. Wismeth C, Dudel C, Pascher C, Ramm P, Pietsch T, Hirschmann B, Reinert C, Proescholdt M, Rümmele P, Schuierer G (2010) Transcranial electro-hyperthermia combined with alkylating chemotherapy in patients with relapsed high-grade gliomas: phase I clinical results. J Neurooncol 98(3):395–405
70. Gilchrist RK, Medal R, Shorey WD, Hanselman RC, Parrott JC, Taylor CB (1957) Selective inductive heating of lymph nodes. Ann Surg 146(4):596
71. Hoopes PJ, Petryk AA, Misra A, Kastner EJ, Pearce JA, Ryan TP (2015) Utility and translatability of mathematical modeling, cell culture and small and large animal models in magnetic nanoparticle hyperthermia cancer treatment research. *SPIE BiOS*, International Society for Optics and Photodermatol, p. 932604
72. Thiesen B, Jordan A (2008) Clinical applications of magnetic nanoparticles for hyperthermia. Int J Hyperthermia 24(6):467–474
73. Attaluri A, Kandala SK, Wabler M, Zhou H, Cornejo C, Armour M, Hedayati M, Zhang Y, DeWeese TL, Herman C (2015) Magnetic nanoparticle hyperthermia enhances radiation therapy: a study in mouse models of human prostate cancer. Int J Hyperthermia 31(4):359–374
74. Kashevsky BE, Kashevsky SB, Korenkov VS, Istomin YP, Terpinskaya TI, Ulashchik VS (2015) Magnetic hyperthermia with hard-magnetic nanoparticles. J Magn Magn Mater 380:335–340
75. Tang Y, Flesch RCC, Jin T (2017) A method for increasing the homogeneity of the temperature distribution during magnetic fluid hyperthermia with a Fe-Cr-Nb-B alloy in the presence of blood vessels. J Magn Magn Mater 432:330–335
76. Hervault A, Thanh NTK (2014) Magnetic nanoparticle-based therapeutic agents for thermo-chemotherapy treatment of cancer. Nanoscale 6(20):11553–11573
77. Jordan A, Scholz R, Wust P, Fähling H, Krause J, Wlodarczyk W, Sander B, Vogl T, Felix R (1997) Effects of magnetic fluid hyperthermia (MFH) on C3H mammary carcinoma in vivo. Int J Hyperthermia 13(6):587–605
78. Schmid G (2011) Nanoparticles: from theory to application. Wiley, Somerset
79. Maier-Hauff K, Ulrich F, Nestler D, Niehoff H, Wust P, Thiesen B, Orawa H, Budach V, Jordan A (2011) Efficacy and safety of intratumoral thermotherapy using magnetic iron-oxide nanoparticles combined with external beam radiotherapy on patients with recurrent glioblastoma multiforme. J Neurooncol 103(2):317–324
80. Frimpong RA, Dou J, Pechan M, Hilt JZ (2010) Enhancing remote controlled heating characteristics in hydrophilic magnetite nanoparticles via facile co-precipitation. J Magn Magn Mater 322(3):326–331
81. Ghosh R, Pradhan L, Devi YP, Meena SS, Tewari R, Kumar A, Sharma S, Gajbhiye NS, Vatsa RK, Pandey BN, Ningthoujam RS (2011) Induction heating studies of Fe3O4 magnetic nanoparticles capped with oleic acid and polyethylene glycol for hyperthermia. J Mater Chem 21(35):13388–13398
82. Ma M, Wu Y, Zhou J, Sun Y, Zhang Y, Gu N (2004) Size dependence of specific power absorption of Fe 3 O 4 particles in AC magnetic field. J Magn Magn Mater 268(1):33–39
83. Zhang L-Y, Gu H-C, Wang X-M (2007) Magnetite ferrofluid with high specific absorption rate for application in hyperthermia. J Magn Magn Mater 311(1):228–233

84. Müller R, Hergt R, Zeisberger M, Gawalek W (2005) Preparation of magnetic nanoparticles with large specific loss power for heating applications. J Magn Magn Mater 289:13–16
85. Behdadfar B, Kermanpur A, Sadeghi-Aliabadi H, del Puerto Morales M, Mozaffari M (2012) Synthesis of high intrinsic loss power aqueous ferrofluids of iron oxide nanoparticles by citric acid-assisted hydrothermal-reduction route. J Solid State Chem 187:20–26
86. Surendra MK, Dutta R, Ramachandra Rao MS (2014) Realization of highest specific absorption rate near superparamagnetic limit of CoFe 2 O 4 colloids for magnetic hyperthermia applications. Mater Res Express 1(2):26107
87. Thorat ND, Khot VM, Salunkhe AB, Prasad AI, Ningthoujam RS, Pawar SH (2013) Surface functionalized LSMO nanoparticles with improved colloidal stability for hyperthermia applications. J Phys D Appl Phys 46(10):105003
88. Pankhurst QA, Connolly J, Jones SK, Dobson J (2003) Applications of magnetic nanoparticles in biomedicine. J Phys D Appl Phys 36(13):R167
89. Huang S, Wang S-Y, Gupta A, Borca-Tasciuc D-A, Salon SJ (2012) On the measurement technique for specific absorption rate of nanoparticles in an alternating electromagnetic field. Meas Sci Technol 23(3):35701
90. Bi H, Ma S, Li Q, Han X (2016) Magnetically triggered drug release from biocompatible microcapsules for potential cancer therapeutics. J Mater Chem B 4(19):3269–3277
91. Sanson C, Diou O, Thevenot J, Ibarboure E, Soum A, Brûlet A, Miraux S, Thiaudière E, Tan S, Brisson A (2011) Doxorubicin loaded magnetic polymersomes: theranostic nanocarriers for MR imaging and magneto-chemotherapy. ACS Nano 5(2):1122–1140
92. Thévenot J, Oliveira H, Sandre O, Lecommandoux S (2013) Magnetic responsive polymer composite materials. Chem Soc Rev 42(17):7099–7116
93. Saint-Cricq P, Deshayes S, Zink JI, Kasko AM (2015) Magnetic field activated drug delivery using thermodegradable Azo-functionalised PEG-coated core–shell mesoporous silica nanoparticles. Nanoscale 7(31):13168–13172
94. Oliveira H, Pérez-Andrés E, Thevenot J, Sandre O, Berra E, Lecommandoux S (2013) Magnetic field triggered drug release from polymersomes for cancer therapeutics. J Control Release 169(3):165–170

Chapter 15
A Review on the Application of Nanofluids in Coiled Tube Heat Exchangers

A.M. Fsadni, J.P.M. Whitty, A.A. Adeniyi, J. Simo, and H.L. Brooks

15.1 Introduction

Due to their compact design, ease of manufacture and high efficiency in heat and mass transfer, helically coiled tubes are widely used in a number of industries and processes such as in the food, nuclear, aerospace and power generation industries and in heat recovery, refrigeration, space heating and air-conditioning processes. Due to the formation of a secondary flow, which inherently enhances the mixing of the fluid, helically coiled tubes are known to yield enhanced heat transfer characteristics when compared to straight tube heat exchangers. The secondary flow is perpendicular to the axial fluid direction and reduces the thickness of the thermal boundary layer. Goering et al. [1] estimated the secondary flow to account for circa 16–20% of the mean fluid flow velocity.

This phenomenon finds its origins in the centrifugal force which is a function of the curvature of the coil structure. A number of active and passive methods have also been applied to helically coiled tube heat exchangers to further enhance their heat transfer performance and reduce the system size and costs. Typical passive methods are the variation of the coil and tube design through the incorporation of ribs and corrugations [2] and the use of propellers [3], fins [4] and internal springs [5]. More recently, numerical and experimental investigations on the dispersion of nanoparticle additives to the base fluid have yielded enhanced heat exchanger performance characteristics.

Nanoparticles improve the thermal conductivity without significant changes to the chemical and physical properties of the base fluid [6, 7]. Moreover, the thermal boundary layer thickness is reduced due to the non-uniform distribution of the

A.M. Fsadni (✉) • J.P.M. Whitty • A.A. Adeniyi • J. Simo • H.L. Brooks
Computational Mechanics Research Group, University of Central Lancashire, Preston PR1 2HE, UK
e-mail: afsadni@uclan.ac.uk

M.J. Jackson, W. Ahmed (eds.), *Micro and Nanomanufacturing Volume II*,
DOI 10.1007/978-3-319-67132-1_15

thermal conductivity and viscosity resulting from the Brownian motion of the nanoparticles [8]. Consequently, enhanced convective heat transfer coefficients characterise the application of nanofluids in heat exchangers. However, in coiled tube heat exchangers, the secondary flow and the higher nanofluid viscosities (in relation to the base fluid) could also result in an undesirable increase in the frictional pressure drop over that of straight tubes. Mukesh Kumar et al. [9] reported frictional pressure drops in the range of 3–9% higher than those of water, ceteris paribus. Therefore, due to the higher pumping power required, the performance of helically coiled tubes is also a strong function of the resultant frictional pressure drop [10].

The aim of the current study is to provide an overview of the various experimental and numerical investigations on the applications of nanofluids in helically coiled tubes. This work is by no means meant to be an authoritative writing on the studies of nanofluids in coiled tubes. For this purpose, the reader is directed to the comprehensive reviews on the heat transfer [6] and pressure drop characteristics [11] in helically coiled tubes. It is the authors' hope that this chapter will be useful to both academics and industry-based engineers through the provision of a concise report on the most recent developments in this field of study.

15.2 Nanofluids

Nanofluids are an offshoot of the recent developments in nanotechnology and are prepared through the dispersion of nanoparticles in a base fluid, typically water. This preparation is done through the sonication of the particles in water (using an ultrasonic bath) which ensures a homogenous distribution of particles in the base fluid. Nanoparticle diameters are in the range of 1–100 nm and are typically a metal or a metal oxide whose thermal conductivity is significantly higher than that of the base fluid. Serrano et al. [12] presented the comparative diagram given in Fig. 15.1 to help the reader appreciate the size of nanoparticles in relation to widely known examples of millimetre or micrometre size.

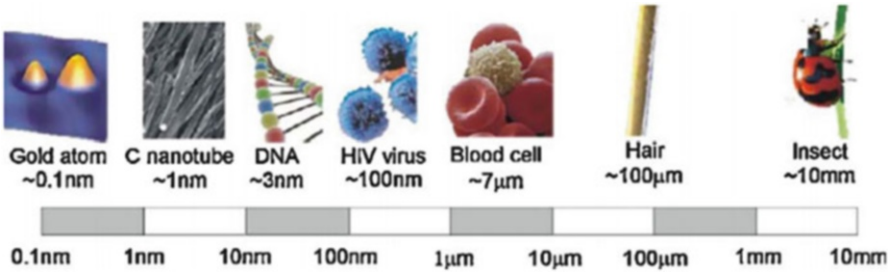

Fig. 15.1 Comparative length scale and some related examples ([12], Fig. 1)

Some widely used oxides are alumina (Al_2O_3), copper oxide (CuO) and silicon dioxide (SiO_2) [13]. Hence, Saidur et al. [14] concisely describe nanofluids as a suspension of nanoparticles in a base fluid. When compared to conventional solid-liquid suspensions for the enhancement of the thermo-physical properties of water, nanofluids result in the following distinct advantages:

- High dispersion stability with predominant Brownian motion of particles
- High specific area and therefore more heat transfer surface between particles and fluids
- Reduced pumping power when compared to pure liquid to achieve equivalent heat transfer characteristics
- Reduced particle clogging when compared to conventional slurries
- Can be used in miniature systems, such as microchannels
- Adjustable thermo-physical properties such as thermal conductivity and surface wettability by varying particle concentrations to suit different applications

Due to the advantages elucidated above, nanotechnology is finding its way in numerous applications for cleaner, low-carbon energy supplies and uses. Hence, the use of high-performance coolants in heat exchangers potentially diminishes the requirements for traditional energy supplies such as electricity, petroleum fuel or natural gas. Saidur et al. [14] listed the following pertinent technological areas where nanotechnology maybe integrated:

- Engine cooling
- Engine transmission oil
- Diesel electric generator as jacket water coolant
- Boiler exhaust flue gas recovery
- Heating and cooling of buildings
- Cooling of electronics
- Cooling of welding processes
- Electrical transformer cooling oil
- Nuclear systems cooling
- Solar water heating
- Nanofluids in drilling
- Refrigeration systems
- High-power lasers
- Biomedical applications
- Thermal storage

15.2.1 Thermo-Physical Properties of Nanofluids

The fluid effective thermal conductivity, dynamic viscosity, mass density and specific heat are modified to simulate the impact of the nanoparticle concentration on the base fluid. The latter is typically specified as a volume concentration. The

density and specific heat of the nanofluid are given by Eqs. (15.1) and (15.2) [15] which are based on the theory of mixtures. These correlations are valid for a nanoparticle volume concentration in the range of 1–10% [16]:

$$\rho_{nf} = (1-\varphi)\rho_{bf} + \varphi\rho_{np} \tag{15.1}$$

where ρ_{nf}, ρ_{np} and ρ_{bf} are the densities of the nanofluid, nanoparticles and the base fluid, respectively, whilst φ is the nanoparticle volumetric concentration.

$$\left(\rho C_p\right)_{nf} = (1-\varphi)\left(\rho C_p\right)_{bf} + \varphi\left(\rho C_p\right)_{np} \tag{15.2}$$

where $C_{p,nf}$, $C_{p,bf}$ and $C_{p,np}$ are the specific heats for the nanofluid, base fluid and the nanoparticles, respectively.

The effective thermal conductivity of the nanofluids (Eq. 15.3) is calculated through the addition of the static and the dynamic components [17]. The latter considers the Brownian motion of the nanoparticles:

$$k_{eff,nf} = k_{\text{static}} + k_{\text{Brownian}} \tag{15.3}$$

The static thermal conductivity is given in Eq. (15.4):

$$k_{\text{static}} = k_{bf}\left[\frac{k_{np} + 2k_{bf} - 2\left(k_{bf} - k_{np}\right)\varphi}{k_{np} + 2k_{bf} + \left(k_{bf} - k_{np}\right)\varphi}\right] \tag{15.4}$$

where k_{bf} and k_{np} are the thermal conductivities of the base fluid and the nanoparticles, respectively.

The Brownian thermal conductivity is given in Eq. (15.5):

$$k_{\text{Brownian}} = 5\times10^4\beta\varphi\rho_{bf}C_{p,bf}\sqrt{\frac{\kappa T}{\rho_{np}di_{np}}f(T,\varphi)} \tag{15.5}$$

where the Boltzmann constant $\kappa = 1.3807\times10^{-23}$ J/K, β is an empirically derived equation dependent on the nanoparticle volumetric concentration, and di_{np} is the equivalent diameter of the nanoparticle. β is case dependent. For alumina (Al_2O_3) in the range of $1\% \le \varphi \le 10\%$, β is given in Eq. (15.6) [16]:

$$\beta = 8.4407(100\varphi)^{-1.07304} \tag{15.6}$$

$f(T,\varphi)$ is given in Eq. (15.7) [16]:

$$f(T,\varphi) = (0.028217\varphi + 0.003917)\left(\frac{T}{T_o}\right) - (0.030699\varphi + 0.00391123) \tag{15.7}$$

To calculate the effective dynamic viscosity for the nanofluid, many recent investigations used the empirical equation given in Eq. (15.8) [18–22]:

$$\frac{\mu_{nf}}{\mu_{bf}} = \frac{1}{1 - 34.87\left(\frac{di_{np}}{di_{bf}}\right)^{-0.3}\varphi^{1.03}} \tag{15.8}$$

where μ_{nf} and μ_{bf} are the dynamic viscosities for the nanofluid and the base fluid, respectively, and di_{bf} is the equivalent diameter of the base fluid molecules, calculated through Eq. (15.9):

$$di_{bf} = \left(\frac{6M_{bf}}{N\pi\rho_{bf}}\right)^{1/3} \tag{15.9}$$

where M is the molecular weight of the base fluid and N is the Avogadro constant.

Figure 15.2a–d presents the thermo-physical properties of four widely used nanofluids with the nanoparticle volume concentration in relation to the base fluid. Evidently, the addition of nanoparticles (Table 15.1) to water yields higher densities, viscosities and thermal conductivities which in turn increase with the nanoparticle volume concentration. For example, at a concentration of 4%, the nanofluids are 39% more viscous than the base fluid (Fig. 15.7b). Despite the numerous studies which appraised the effects of the nanoparticle concentration as a sole function of the Reynolds number [23, 24], consideration should be taken of the thermo-physical relations elucidated in Fig. 15.2. Higher nanofluid viscosities require higher fluid velocities to maintain the same Reynolds number, and therefore, the thermo-hydrodynamic performance of nanofluids should be investigated against other pertinent system parameters, such as the volume and mass flow rates and the pumping power.

15.3 Flow Characteristics in Coiled Tubes

For single and multiphase flows, the secondary flow in coiled tubes yields a substantial increase in the frictional pressure drop, which often results in diminished system efficiencies (due to enhanced pumping power requirements). For air-water two-phase bubbly flow in helically coiled tubes, Akagawa et al. [25] reported frictional pressure drops in the range of 1.1–1.5 times higher than those in straight tubes, ceteris paribus. With the use of nanofluids, such a penalty could nullify the enhanced efficiencies gained with the dispersion of nanoparticles in the base fluid [26].

Moreover, due to the secondary flow (Fig. 15.3), the thermo-hydrodynamic characteristics are significantly different to those in straight tubes. Figure 15.4 presents the localised heat transfer coefficient following a numerical study on the

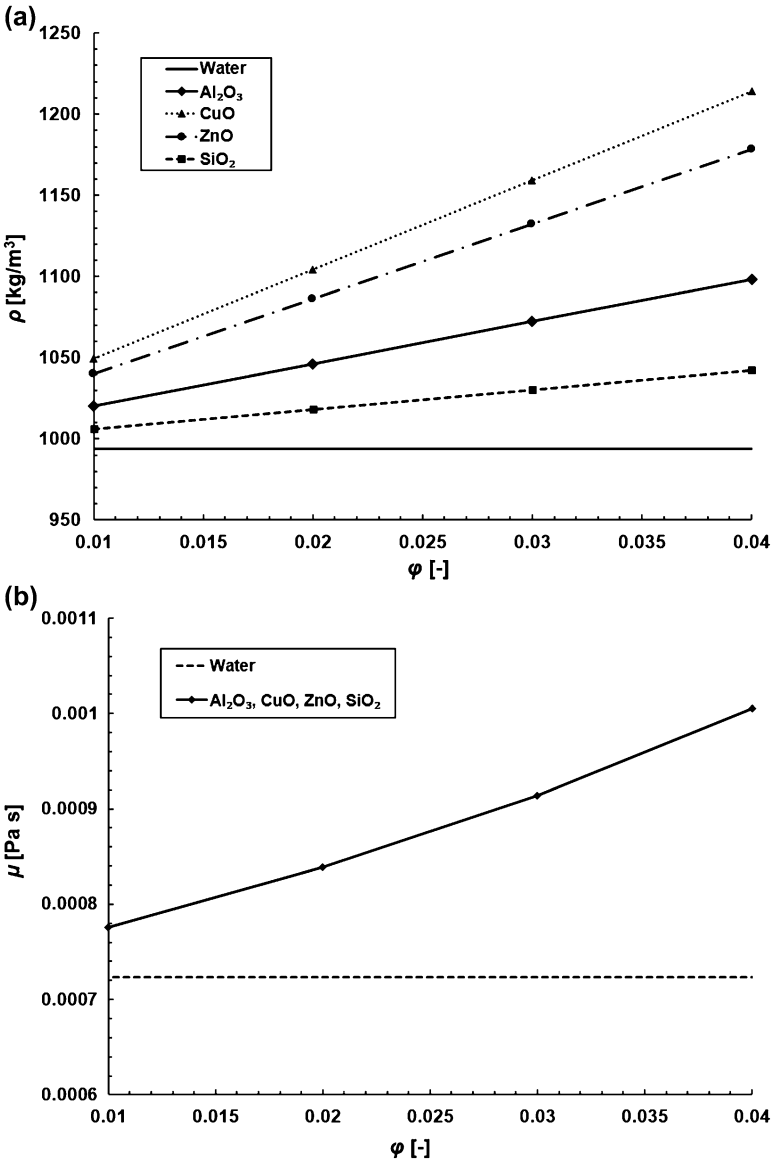

Fig. 15.2 Density (**a**), viscosity (**b**), thermal conductivity (**c**) and specific heat (**d**) of nanofluids with nanoparticle concentration at 308 K

use of Al_2O_3-water nanofluids in coiled rectangular-circular tubes as reported by Fsadni et al. [13]. The influence of the coil curvature and the consequent hydrodynamic characteristics is elucidated in the fact that the localised heat transfer coefficients on the inner tube wall are significantly diminished in relation to those

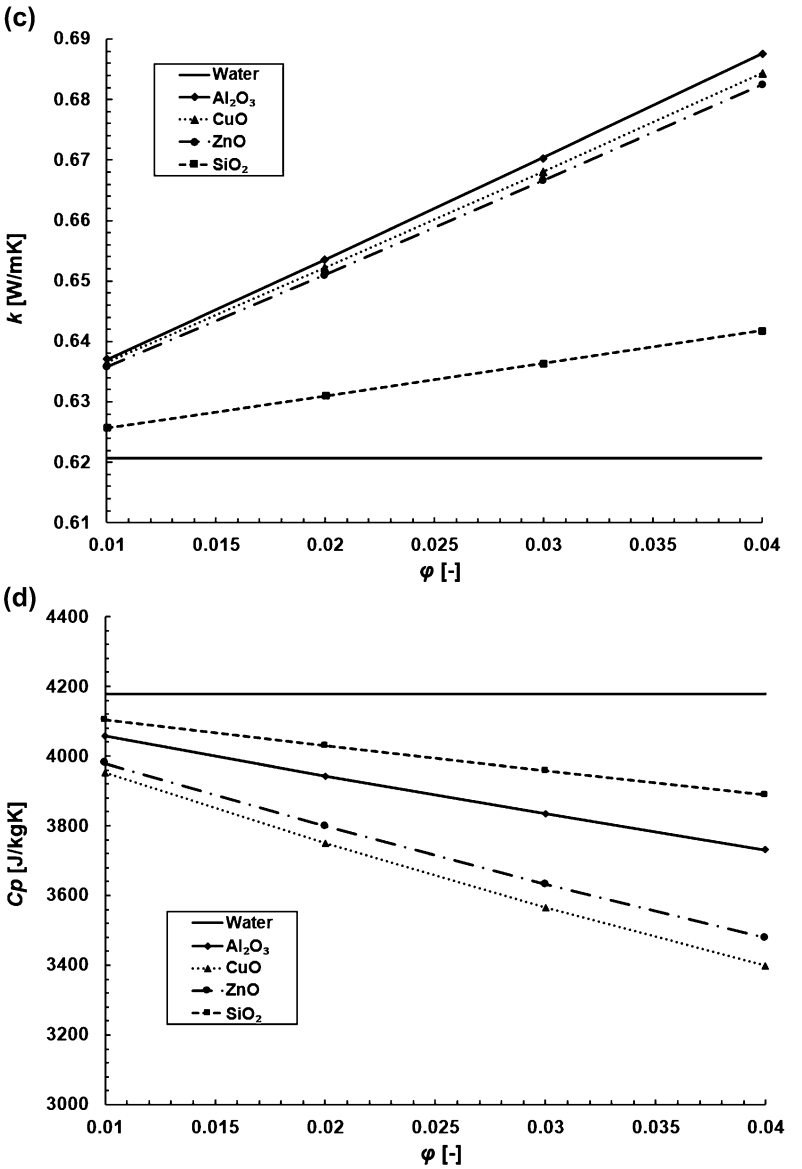

Fig. 15.2 (continued)

Table 15.1 Thermo-physical properties of nanoparticles at $T = 300$ K [19]

Material	ρ (kg/m^3)	k (W/m K)	Cp (J/kg K)
Al_2O_3	3600	36.00	765.0
CuO	6500	17.65	533.0
ZnO	5600	13.00	495.2
SiO_2	2200	1.40	745.0

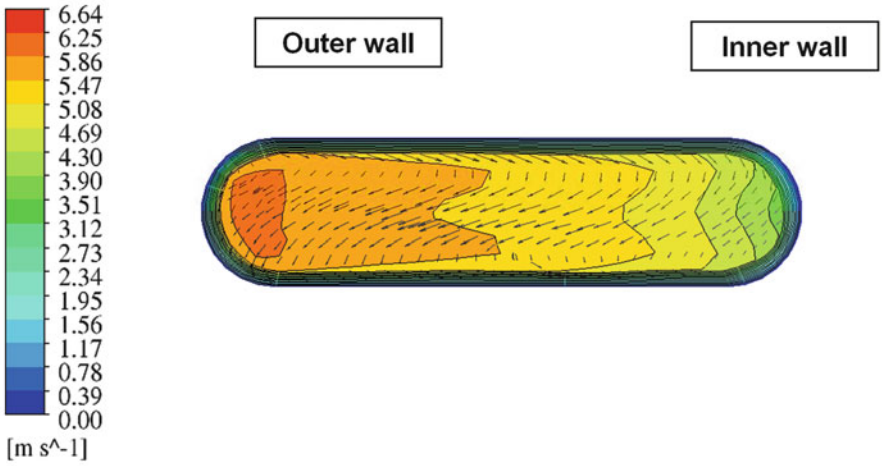

Fig. 15.3 Velocity profiles and vectors for a coiled tube with an oval cross-sectional design

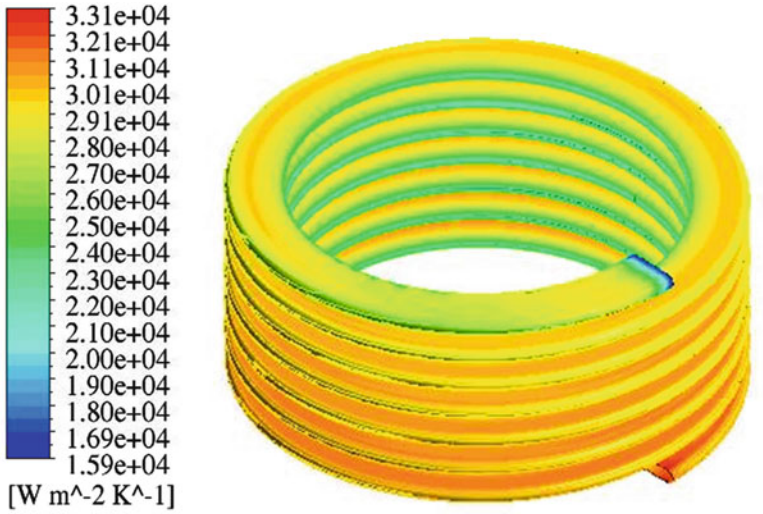

Fig. 15.4 Mean heat transfer coefficient for Al_2O_3-water nanofluids ($\varphi = 4\%$) in a coiled tube ([13], Fig. 15)

at the outer wall. This phenomenon can be attributed to the centrifugal force and the resultant secondary flow which reduces the thickness of the thermal boundary layer at the outer wall region [21]. Moreover, whereas in straight tubes the transition from laminar to turbulent flow occurs at Reynolds numbers in the region of 2500, the transition in curved tubes takes place at higher Reynolds numbers. The critical

Reynolds number (Eq. 15.10) is used to determine the transition of the flow from laminar to turbulent flow [27]:

$$Re_{\text{crit}} = 2 \times 10^4 \delta^{0.32} \tag{15.10}$$

where δ is the curvature ratio defined through Eq. (15.11):

$$\delta = \frac{d_{tb}}{D_c} \tag{15.11}$$

For $\delta^{-1} < 860$ whilst for $\delta^{-1} > 860$, Re_{crit} for a curved tube is equal to that for a straight pipe.

Another dimensionless number, unique to coiled tubes, is the Dean number, given in Eq. (15.12). It is used to characterise the flow in curved tubes and quantifies the magnitude of the secondary flow due to the centrifugal force [28]:

$$De = \text{Re}\sqrt{\delta} \tag{15.12}$$

The pertinent literatures present various methods for the calculation of a system performance index. This index is used to analyse the thermo-hydrodynamic performance of heat transfer enhancement methods. Amongst these methods are those reported by Hashemi and Akhavan-Behabadi [29] Eq. (15.13). The performance index balances the advantages gained with optimised heat transfer regimes against the disadvantages due to higher frictional pressure drops and, therefore, can be analysed as a function of the *Re* number. A performance index greater than unity suggests that the benefits gained through optimised heat transfer coefficients outweigh the impact of higher frictional pressure drops. The performance of coiled tubes is a complex function of the coil design parameters (Fig. 15.5) as well as the resultant pressure drop. Moreover, drag reduction techniques could also be beneficial for coiled tube heat exchangers [30]:

$$\eta_c = \frac{\left(\frac{h_{c,nf}}{h_{s,bf}}\right)}{\left(\frac{\Delta P_{f,c,nf}}{\Delta P_{f,s,bf}}\right)} \tag{15.13}$$

where $h_{c,nf}$ is the mean heat transfer coefficient after the application of heat transfer enhancement techniques, $h_{s,bf}$ is the mean heat transfer coefficient in a straight tube with the base fluid only, $\Delta P_{f,c,nf}$ is the frictional pressure drop after the application of enhancement techniques and $\Delta P_{f,s,bf}$ is the frictional pressure drop in a straight tube with the base fluid only.

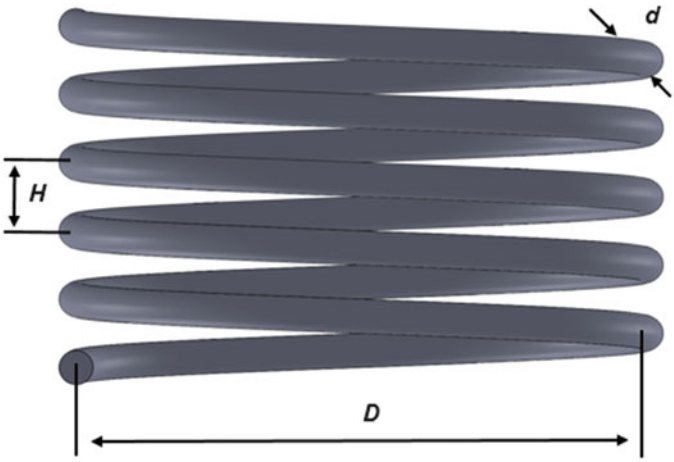

Fig. 15.5 Schematic representation of helical pipe characteristics

15.4 Experimental Work in Literature

15.4.1 Heat Transfer Characteristics

Recent work reported by [31] investigated the application of nanofluids in helically coiled tube heat exchangers. Their research investigated the pressure drop and convective heat transfer performance of Al_2O_3-water nanofluids under laminar and turbulent flow conditions. They reported that the effect of nanoparticles on the Reynolds number, pressure drop and heat transfer performance is negligible. These findings were mainly attributed to the mitigation of the secondary flow as a result of the higher viscosity and density of the nanofluid. In fact, the highest heat transfer improvement with nanofluids over pure water was measured at 3%. Intriguingly, Wu et al. also eliminated the possibility of Brownian motion due to the nanoparticles. Other studies have reported significantly different results.

Mukesh Kumar et al. [9] reported that a volumetric concentration of 0.8% Al_2O_3 nanoparticles with water at turbulent flow conditions resulted in a 28% increase in the convective heat transfer coefficient. In contrast to the conclusions made by Wu et al. [31], Mukesh Kumar et al. [9] attributed the improved heat transfer coefficient to the enhancement of the intensity of the secondary flow and the induced fluid mixing due to Brownian motion. These conflicting results could be attributed to the smaller curvature ratios used by Wu et al., thus reducing the centrifugal force acting on the two phases. Kannadasan et al. [32] also reported an increase in the heat transfer performance and the friction factor with CuO nanoparticles under turbulent flow conditions. As illustrated in Fig. 15.6, they reported enhanced heat transfer rates with vertically orientated coils which they attributed to the rapidly developing secondary flows. Correlations were also presented for the calculation of the Nusselt number and the friction factor, both of which are a function of the Dean number, the

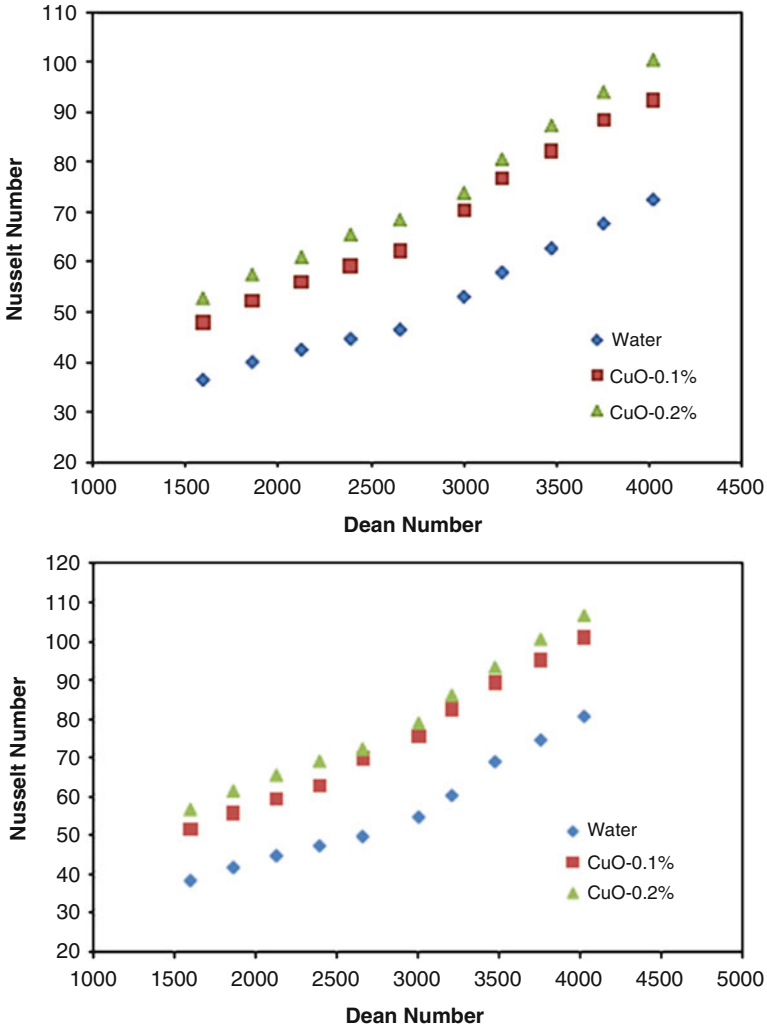

Fig. 15.6 Variation of the Nusselt number with the Dean number in turbulent flow horizontal (*left*) and vertical orientations ([32], Figs. 4 and 5)

ratio of the internal tube radius to the mean coil radius and the volume concentration. Similarly, Kahani et al. [33] reported a significant enhancement to the heat transfer rate through the use of Al_2O_3 and TiO_2 nanoparticles at 1% volume concentration under laminar and turbulent flow conditions, whilst Akhavan-Behabadi et al. [34] reported a 60% increase in the Nusselt number with the application of multiwalled carbon nanotube nanoparticles to the oil base fluid in helical coils.

Akhavan-Behabadi et al. [34] and Akbaridoust et al. [35] also reported that the geometrical variables such as the reduction of the coil-to-tube diameter ratio and

the increase of the pitch-to-tube diameter ratio resulted in enhanced heat transfer rates for both the base fluid and nanofluids. However, Kahani et al. [33] suggested that the latter had a weaker effect on the heat transfer rate when compared to the coil-to-tube diameter ratio. Akhavan-Behabadi et al. [34] also reported that the Reynolds number increment resulted in the strongest impact on the heat transfer rate at the highest concentration of nanoparticles, this being 0.4% by weight. They attributed this result to the higher viscosity of the base fluid (oil) at lower Reynolds numbers, thus limiting the freedom of movement of the nanoparticles.

Suresh et al. [36] investigated the use of CuO nanofluids with water in horizontally placed smooth tubes as well as with tubes equipped with dimple protrusions of 0.6 mm added as a passive enhancement to the performance of the heat exchangers. They reported that at higher Reynolds numbers, the dimples, combined with 3% CuO nanoparticles, resulted in an increase of up to 39% in the measured Nusselt number. However, such geometrical features resulted in an increase in the tube friction factor in the range of 2–10%.

15.4.2 Frictional Pressure Drop

There is a significant paucity of studies on the pressure drop characteristics of nanofluids in helically coiled or curved tube heat exchangers. Fakoor-Pakdaman et al. [10] reported that the few studies reported on the investigation of nanofluid flow in helically coiled tubes were mainly focused at investigating the heat transfer characteristics with the system parameters. In fact, their study, published in 2013, was the first study to comprehensively investigate the isothermal pressure drop with nanofluids in helically coiled tubes.

Most of the investigations reviewed in this chapter have reported an increase in the nanofluid frictional pressure drop with the nanoparticle concentration and the Reynolds number. This is mainly attributed to the resultant higher relative mixture densities and viscosities [9, 10, 29]. However, most researchers agreed that at low fluid velocities, the rate of increase in the pressure drop with the nanoparticle volume concentration was smaller than that at higher fluid velocities. Mukesh Kumar et al. [9] attributed this result to the dominance of the viscosity effects at low Dean numbers. Furthermore, Hashemi and Akhavan-Behabadi [29] and Rakhsha et al. [21] reported that the higher rate of chaotic motion and migration of the nanoparticles at increased Reynolds numbers could be the reason for the different rates of pressure drop increases. There are no experimental studies which investigated the pressure drop characteristics of the principle nanofluids, these being the oxides of aluminium and copper dispersed in water, at identical system parameters. However, Hashemi and Akhavan-Behabadi [29] reported that due to the spherical properties of CuO nanoparticles, reduced levels of friction could result

when compared to other nanofluids. This is due to the rolling effect (instead of sliding) between the oil and solid phases.

There is an agreement amongst authors [31, 32] that the transitional velocity and hence the critical Reynolds number of nanofluids will be higher than that of the base fluid. This is due to the higher viscosity of the former fluid. Some controversies characterise the studies on nanofluid flow in coiled tubes. The majority of investigations reviewed in the present study reported a significant appreciation in the frictional pressure drop with nanofluids over that of the base fluid only. Furthermore, the increment in the pressure drop for helically coiled tubes was reported to be higher than that for straight pipes. In view of this, Suresh et al. [36], Fakoor-Pakdaman et al. [10] and Kahani et al. [33] presented correlations for the calculation of the friction factor and pressure drop with nanofluids. These correlations are principally a function of the coil geometry, Dean or Reynolds numbers and the nanoparticle concentration. With a 2% weight concentration of CuO nanoparticles in oil, flowing through a helically coiled tube, Hashemi and Akhavan-Behabadi [29] reported an increase in the pressure drop of 20.3% over that of the base fluid only, whilst for a straight tube, this was measured as 13.2%. Similarly, for 2% volume concentration of CuO in water, Kannadasan et al. [32] reported that the friction factor, when compared to water flow only, increased by 24% and 23% for horizontal and vertical orientations, respectively. However, in contrast to these findings, Suresh et al. [36] and Wu et al. [31] reported that the resultant pressure drop increment with a wide range of nanoparticle concentrations was marginal when compared to that of the base fluid alone. In fact, Wu et al.'s pressure drop results were reasonably predicted by the Ito [27] and Seban and McLaughlin [37] equations for single-phase flow in helically coiled tubes. Suresh et al. attributed these results to the nanoscale size of the additive nanoparticles. Furthermore, whilst Wu et al. reported that, due to their higher viscosity and density, nanofluids resulted in a mitigation of the secondary flow, Mukesh Kumar et al. [9] reported contradictory results. The latter results were attributed to the random motion of the nanoparticles which did not impede the formation of the secondary flow.

The nanofluid pressure drop as a function of the coil geometry was investigated by Kahani et al. [33], Fakoor-Pakdaman et al. [10], Bahremand et al. [22] and Salem et al. [38] who reported lower pressure drops with a decrease in the curvature ratio. The pressure drop was also independent of the coil pitch. The former was principally attributed to the weaker centrifugal forces, hence minimising the effects of the secondary flow on the system pressure drop. The sole studies which investigated the nanofluid pressure drop as a function of the helical coil orientation were reported by Kannadasan et al. [32] and Ali et al. [39]. Both studies reported that the nanofluids in a vertically orientated coil resulted in marginally lower pressure drop increments (over that of pure water) when compared to horizontally orientated coils, ceteris paribus (Fig. 15.7). However, both studies failed to critically analyse these results.

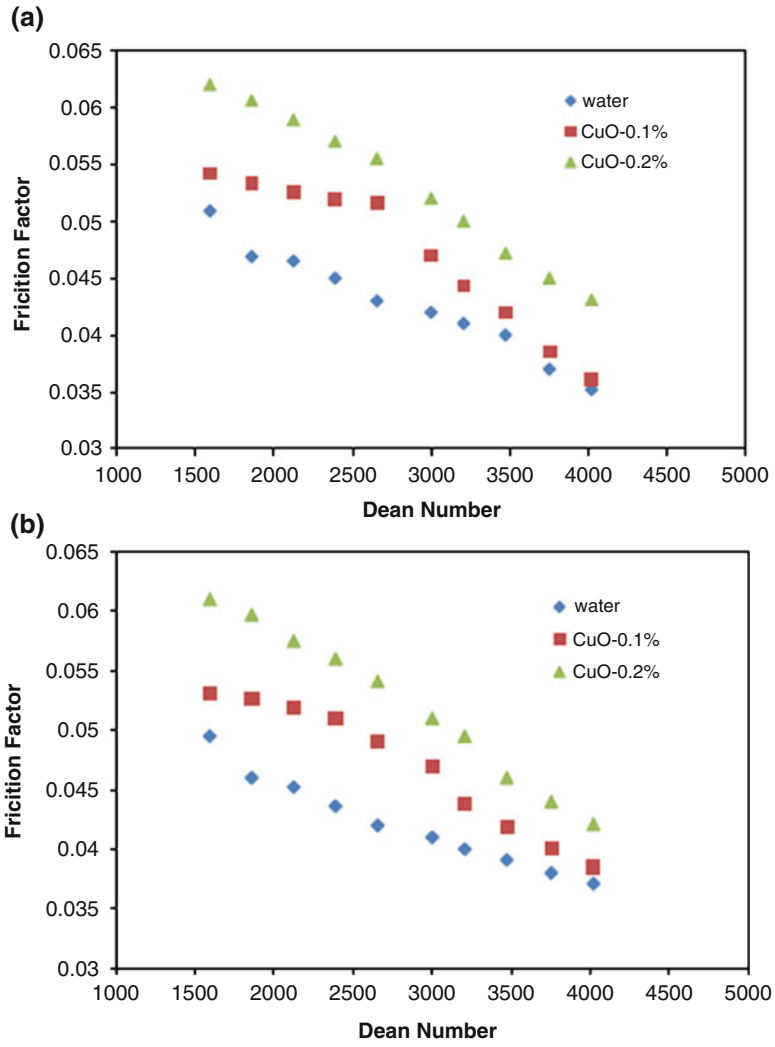

Fig. 15.7 CFD simulation of the CuO nanoparticles in water, friction factor for (**a**) horizontal orientation and (**b**) vertical orientation ([33], Figs. 7 and 8)

15.5 Numerical Work

The earliest numerical study for the heat transfer characteristics with nanofluid flow in helically coiled tubes was reported in 2011 by Sasmito et al. [16]. Quasi all the studies reviewed were developed through the use of commercially available software packages based on the finite volume method, these being the ANSYS CFX and Fluent packages. The majority of the numerical studies on the heat transfer and

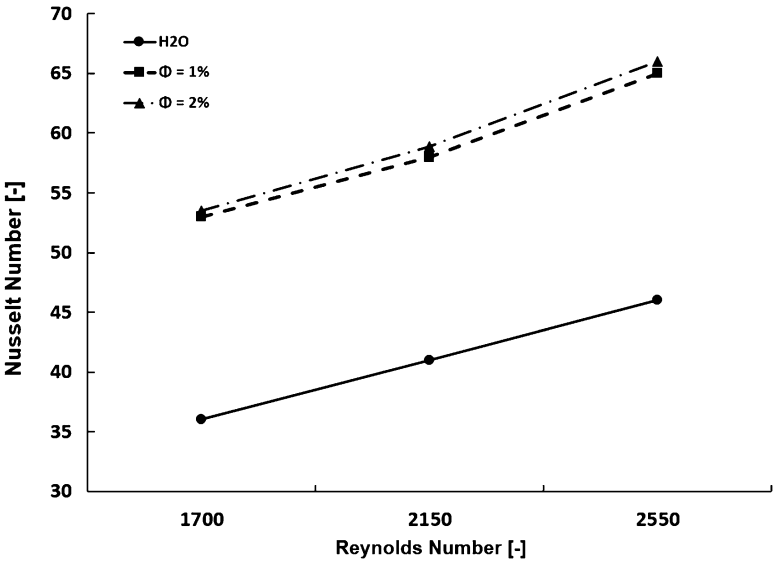

Fig. 15.8 CFD simulation of the enhancement to the Nusselt number with Al_2O_3 nanoparticles to water ([23], Fig. 3a)

flow characteristics of nanofluids in curved tubes assumed that the nanofluid is in single phase [13, 16, 18, 23, 26, 40, 41].This assumption is based on the fact that at a low concentration of nanoparticles ($\varphi < 4\%$), nanofluids behave like a single-phase fluid where no agglomeration or sedimentation occurs.

The numerical studies which investigated the performance of different types of nanofluids in helically coiled tubes were predominantly developed for laminar flow conditions [16, 18, 20, 42]. Khairul et al. [20] concluded that the system frictional pressure drop is a function of the nanoparticle density, and hence, their study reported that CuO-water and SiO_2-water nanofluids yielded the highest and lowest frictional pressure drops, respectively. Moreover, they also concluded that CuO nanoparticles yielded a 7% enhancement in the mean heat transfer coefficient when compared to Al_2O_3 and ZnO nanofluids, ceteris paribus. This contrasts to the findings presented by Narrein and Mohammed [18] who reported that, compared to CuO-water nanofluids, the Al_2O_3-water nanofluids yielded a marginally enhanced Nusselt number.

Jamshidi et al. [23] developed numerical simulations for Al_2O_3-water nanofluids in helically coiled tubes under laminar flow conditions, with nanoparticle volume concentrations in the range of 1–3%. When investigated at the same *Re*, they reported an enhancement of circa 44% in the mean heat transfer coefficient with the dispersion of nanoparticles in water (Fig. 15.8). Moreover, they concluded that nanoparticle volume concentrations in excess of 1% did not yield a significant impact on the heat transfer characteristics. Similar conclusions were also made by Huminic and Huminic [42] through their numerical investigation of the heat

transfer characteristics of CuO and TiO_2 nanofluids in a double tube helically coiled tube heat exchanger. Narrien and Mohammed [18] also reported a reduction in the mean heat transfer coefficient with CuO nanoparticle volumetric concentrations (in water) in excess of 2%. For coiled rectangular tubes, Sasmito et al. [16] reported that for laminar flow, volumetric concentrations in excess of 1% are not recommended for Al_2O_3-water and CuO-water nanofluids. This conclusion was attributed to the significantly lower impact of higher concentration nanoparticles on the mean heat transfer coefficient. The latter conclusion contrasts to the findings reported by Rabienataj Darzi et al. [24], who, for Al_2O_3-water nanofluids ($\varphi = 2$ and 4%) at turbulent flow conditions, reported an increase of 21 and 58% in the mean heat transfer coefficient (over that of water).

Akbaridoust et al. [35] compared their experimental results for CuO-water nanofluids in helically coiled tubes with a range of curvature ratios, to those of a numerical model developed using the FORTRAN programming language. Substantial agreements were reported for the two methods where the mean heat transfer coefficient increased with the Reynolds number, radius of curvature and nanofluid concentration. Mohammed and Narrein [28] investigated the effects of a tube-in-tube heat exchanger design parameters with a CuO-water nanofluid. They concluded that the heat transfer coefficient was enhanced through the reduction of the helix radius and annulus diameter and an increase in the tube diameter. These results are in substantial agreement with experimental investigations reported by Akhavan-Behabadi et al. [34] and Akbaridoust et al. [35].

Some controversy characterises the impact of the nanoparticle concentration on the resultant frictional pressure drop in coiled tubes. Hence, whilst some authors [18, 23, 24] reported an increase in the frictional pressure drop with higher nanoparticle volume concentrations as well as higher nanofluid frictional pressure drops (over that of the base fluid), Sasmito et al. [16] reported that, at a nanoparticle volume concentration of 1%, the calculated frictional pressure drop was lower than that of pure water. Sasmito et al. attributed these results to the fact that at low volume concentrations, the nanoparticles have a minimal effect on the fluid viscosity, whereas the temperature effects on the nanofluid thermo-physical properties are more significant.

Mohammed and Narrein [28] and Aly [26] investigated the nanofluid frictional pressure drop characteristics with the heat exchanger geometry through numerical methods. In agreement with the experimental results reported by Kahani et al. [33] and Fakoor-Pakdaman et al. [10], an increase in the nanofluid frictional pressure drop was reported with a reduction in the coil diameter, whilst the pressure drop decreased with larger tube diameters. These results can be attributed to the reduction in the centrifugal forces with larger helix diameters. The frictional pressure drop was also reported to be independent of the helix pitch. More recently, Bahremand et al. [22] and Rakhsha et al. [21] investigated the heat transfer and frictional pressure drop characteristics with CuO and Ag-water nanofluids in coiled tubes. Both studies reported an increase in the frictional pressure drop and the mean heat transfer coefficient with nanoparticle volume concentrations.

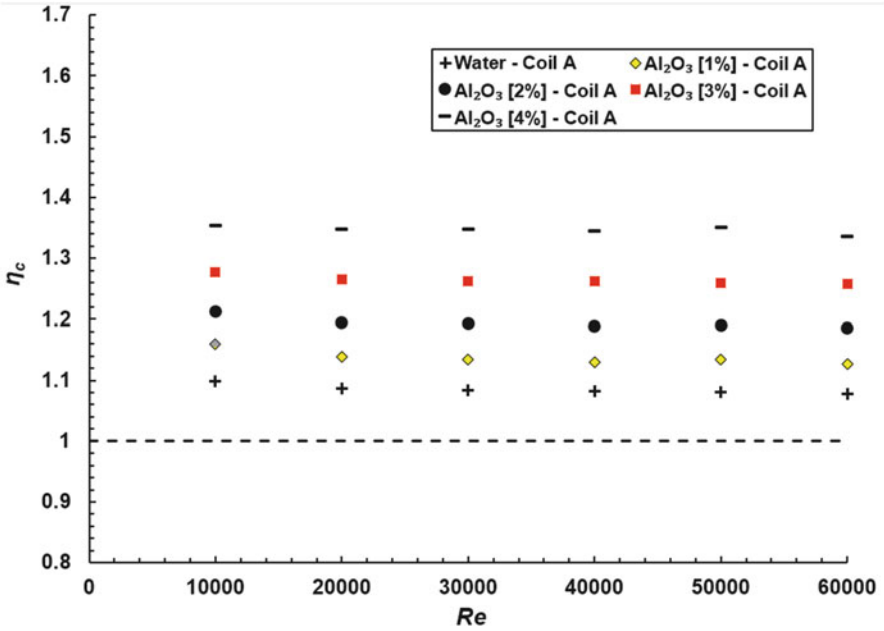

Fig. 15.9 Variation of the performance index with the Reynolds number ([13], Fig. 16)

The nanoparticle diameter effect on the performance characteristics of nanofluids in coiled tubes was investigated by Narrein and Mohammed [18], Bahremand et al. [22] and Tohidi et al. [41]. These studies reported an increase in the heat transfer coefficient with smaller nanoparticle diameters. Moreover, the latter effect was more evident at higher nanoparticle volume concentrations. This is due to the enhanced particle loading, hence affording a larger surface area for heat transfer. In their investigation of the diameter effect on laminar nanofluid flow through curved tubes, Akbarinia and Laur [43] reported that the increase in the nanoparticle diameter does not result in a measurable effect on the flow pattern. However, more recently, Bahremand et al. [22] reported that the diminishing heat transfer performance with larger nanoparticle diameters is partly due to the fact that with larger nanoparticles, their displacement by buoyancy and centrifugal forces decreases. This results in a diminished secondary flow.

More recently, Fsadni et al. [13] presented the sole numerical study on turbulent Al_2O_3-water nanofluid flow in helically coiled tubes with a non-circular, oval-shaped cross-section. Their study reported that the use of nanofluids yielded an overall positive impact on the system efficiency (Fig. 15.9) and, hence, the benefits gained with enhanced mean heat transfer coefficients outweigh the effects of higher frictional pressure drops. Such results are similar to those reported by Aly [26] for circular tubes. This suggests that the use of compact oval-shaped tube sections does not diminish the overall system performance.

15.6 Scope for Further Research

Due to the recent development of nanofluids as a means for the enhancement of the fluid heat transfer characteristics, there is ample scope for further research in this field of study. Evidently, there is a paucity of studies on the use of nanofluids in helically coiled tube heat exchangers at three-phase flow conditions. The latter could be the result of dissolved gases or flow boiling. Such studies are notoriously complex and should be undertaken by research groups with significant experience in the research of multiphase flow. In fact, related studies in nanofluid pool boiling have also presented some conflict over whether nanoparticles can enhance or degrade boiling heat transfer [44]. Tu et al. [45] and Wen and Ding [46] reported an enhancement of up to 60% with nanofluid pool boiling using Al_2O_3 and γ-Al_2O_3, respectively, whilst Das et al. [47] and Jackson and Bryan [48] reported a deterioration in the range of 10–40% with Al_2O_3 and Au nanoparticles, respectively.

Further studies are also required to confirm the optimal concentration of the various types of nanofluids as well as the most appropriate nanofluid for different system parameters. As a case in point, for laminar flow conditions at similar volumetric concentrations, Sasmito et al. [16] reported a marginally enhanced performance with Al_2O_3 nanoparticles, whilst Khairul et al. [20] reported that the optimal results were achieved with CuO nanoparticles. The significant heat transfer coefficient enhancement of 330% reported by Rabienataj Darzi et al. [24] through the use of corrugated tubes in combination with Al_2O_3-water nanofluids should also be investigated further through experimental methods. This enhancement is significantly different to that reported by the empirical and numerical studies reviewed in the current report and hence should suggest a significant potential for further research. Further empirical investigations are also required for the use of graphene nanofluids in coiled tubes. In fact, to date, there are no such studies available in the pertinent literature.

The majority of the pertinent studies available in the open literature have focused their investigations on the resultant heat transfer characteristics. This is evidenced by the paucity of correlations presented for the calculation of the frictional pressure drop when compared to those available for the heat transfer coefficient [6]. Further investigations should be developed to address the conflicting results for the impact of the nanoparticle concentration on the frictional pressure drop as outlined in Sect. 4.2. Moreover, the most recent numerical study on nanofluid flow in helically coiled tubes [22] has concluded that the established and widely used single-phase homogenous model approach is less accurate when compared to the Eulerian-Lagrangian two-phase model. Such conclusions should be further investigated, with a wider range of system parameters.

Studies should also be developed for the purpose of investigating the frictional pressure drop as a sole function of the type of nanoparticles. Such studies are deemed necessary in view of the conclusions made by Hashemi and Akhavan-Behabadi [29] who reported that due to their typical spherical shape, copper oxide nanoparticles could yield lower frictional pressure drops. The open literature

presents a single study on the two-phase frictional pressure drop as a function of the coil orientation [32], where horizontal coils were reported to yield marginally higher frictional pressure drops. However, the authors failed to provide a detailed appraisal for the latter results. Furthermore, this study was developed with copper oxide nanoparticles in water, and hence, further studies are required to investigate the impact of the coil orientation with widely used nanoparticles and base fluids, such as aluminium oxide and oil, respectively. Moreover, the pertinent literature failed to comprehensively investigate the distribution of the secondary phase (nanoparticles) in helically coiled tubes. Therefore, whilst Wu et al. [31] reported that nanofluid flow in coiled tubes did not yield a significant phase separation, no other relevant studies investigated this pertinent flow characteristic. Such avenues for future fundamental research will complement and facilitate the research and development of high-efficiency heat exchangers for numerous technological applications as well as open new opportunities for industry-led heat exchanger tube design, whereby the distribution of the secondary phase could be manipulated for optimised system efficiencies.

15.7 Conclusions

This chapter has provided an overview of the relatively recent investigations in the application of nanofluids in helically coiled tube heat exchangers. The latter are utilised in numerous technological applications, and hence, these studies could potentially yield a significant impact as an energy-efficient initiative. The following bullet points summarise the pertinent findings of the present study:

- The applications of nanofluids in helically coiled tube heat exchangers are in conflict on whether nanoparticles can improve or degrade the heat transfer coefficient. Whilst the majority of authors reported a significant increase in the measured heat transfer coefficient with nanofluids over single-phase water, a contemporary study by a leading research group at the University of Lund has reported a negligible enhancement to the heat transfer performance. This is attributed to the mitigation of the secondary flow due to the higher density and viscosity of the nanofluids. A number of authors have also reported significantly different results with the concentration of nanofluids. In fact, some authors reported a degradation of performance with volumetric concentrations in excess of 1%, whilst other authors reported a significant enhancement to the heat transfer performance.
- The majority of experimental and numerical investigations on nanofluids flowing in helically coiled tubes have reported a significant increment (up to 3.5 times) in the frictional two-phase pressure drop over that of pure water in straight tubes. Such conclusions were mainly attributed to the higher relative mixtures and densities as well as the secondary flow formed in curved tubes. Due to the dominance of the viscosity effects at low fluid velocities, the impact of the

nanoparticle concentration on the two-phase frictional pressure drop is stronger at higher Reynolds numbers. The frictional pressure drop was also reported to be a function of the curvature ratio and the coil orientation with marginally larger pressure drops for horizontal coils.

- Due to their relatively recent development, nanofluids present numerous opportunities for further research.

As previously discussed, the intention of this chapter is not to be all-encompassing, but more to provide an insight into the recent findings in the dynamic and evolving field of nanotechnology.

Acknowledgements The authors of the current investigation would like to thank the University of Central Lancashire, UK, for facilitating the completion of this study as well as the various authors who have been contacted during the course of this study.

Notation List

C_p	Specific heat (J/kgK)
d	Tube diameter (m)
di	Molecule or particle diameter (m)
D	Helix diameter (m)
De	Dean number (−)
h	Convective heat transfer coefficient (W/m^{2}K)
H	Pitch (m)
k	Thermal conductivity (W/mK)
M	Molecular weight (mol/g)
N	Avogadro constant (−)
ΔP	Frictional pressure drop (Pa)
Re	Reynolds number (−)
T	Temperature (K)
T_o	Reference temperature (K)

Greek Symbols

β	Modelling function (−)
δ	Curvature ratio (d_h/D_c) (−)
η	Performance index (−)
κ	Boltzmann constant (J/K)
μ	Dynamic viscosity (Pa s)
ρ	Density (kg/m$^{3)}$
φ	Volume concentration (−)

Subscripts

bf	Base fluid
c	Coil
crit	Critical
eff	Effective
f	Frictional
h	Hydraulic diameter
nf	Nanofluid
np	Nanoparticle
s	Straight tube
tb	Tube

References

1. Goering DJ, Humphrey JAC, Greif R (1997) The dual influence of curvature and buoyancy in fully developed tube flows. Int J Heat Mass Transf 40:2187–2199
2. Austen DS, Soliman HM (1988) Laminar flow and heat transfer in helically coiled tubes with substantial pitch. Exp Thermal Fluid Sci 1:183–194
3. Yildiz C, Bicer Y, Pehlivan D (1996) Influence of fluid rotation on the heat transfer and pressure drop in double-pipe heat exchangers. Appl Energy 54(1):49–56
4. Naphon P (2007) Thermal performance and pressure drop of the helical-coil heat exchangers with and without helically crimped fins. Int Commun Heat Mass Transfer 34:321–330
5. Yildiz C, Bicer Y, Pehlivan D (1997) Heat transfer and pressure drop in a heat exchanger with a helical pipe containing inside springs. Energy Conserv Manage 38(6):619–624
6. Fsadni AM, Whitty JPM (2016a) A review on the two-phase pressure drop characteristics in helically coiled tubes. Appl Therm Eng 103:616–638
7. Singh V, Gupta M (2016) Heat transfer augmentation in a tube using nanofluids under constant heat flux boundary condition: a review. Energ Conver Manage 123:290–307
8. Sarafraz MM, Hormozi F (2014) Experimental study on the thermal performance and efficiency of a copper made thermosyphon heat pipe charged with alumina-glycol based nanofluids. Powder Technol 266:378–387
9. Mukesh Kumar PC, Kumar J, Suresh S (2013) Experimental investigation on convective heat transfer and friction factor in a helically coiled tube with Al_2O_3-water nanofluid. J Mech Sci Technol 27(1):239–245
10. Fakoor-Pakdaman M, Akhavan-Behabadi MA, Razi P (2012) An experimental investigation on thermo-physical properties and overall performance of MWCNT/heat transfer oil nanofluid flow inside vertical helically coiled tubes. Int J Therm Sci 40:103–111
11. Fsadni AM, Whitty JPM (2016b) A review on the two-phase heat transfer characteristics in helically coiled tube heat exchangers. Int J Heat Mass Transf 95:551–565
12. Serrano E, Rus G, Martinez JG (2009) Nanotechnology for sustainable energy. Renew Sustain Energy Rev 15:1646–1668
13. Fsadni AM, Whitty JPM, Stables MA, Adeniyi AA (2017) Numerical study on turbulent heat transfer and pressure drop characteristics of a helically coiled hybrid rectangular-circular tube heat exchanger with Al_2O_3-water nanofluids. Appl Therm Eng 114:466–483
14. Saidur R, Leong KY, Mohammad HA (2011) A review on applications and challenges of nanofluids. Renew Sustain Energy Rev 15:1646–1668
15. Xuan Y, Roetzel W (2000) Conceptions for heat transfer correlation of nanofluids. Int J Heat Mass Transf 43:3701–3707
16. Sasmito PA, Kurnia JC, Mujumdar AS (2011) Numerical evaluation of laminar heat transfer enhancement in nanofluid flow in coiled square tubes. Nanoscale Res Lett 6:376
17. Vajjha RS, Das DK, Namburu PK (2010) Numerical study of fluid dynamic and heat transfer performance of Al_2O_3 and CuO nanofluids in the flat tubes of a radiator. Int J Heat Fluid Flow 31(4):613–621
18. Narrein K, Mohammed HA (2013) Influence of nanofluids and rotation on helically coiled tube heat exchanger performance. Techmochimica Acta 564:13–23
19. Dawood HK, Mohammed HA, Munisamy KM (2014) Heat transfer augmentation using nanofluids in an elliptic annulus with constant heat flux boundary condition. Case Stud Thermal Eng 4:32–41
20. Khairul MA, Saidur R, Hossain A, Alim MA, Mahbubul IM (2014) Heat transfer performance of different nanofluids flows in a helically coiled heat exchanger. Adv Mater Res 832:160–165
21. Rakhsha M, Akbaridoust F, Abbassi A, Majid SA (2015) Experimental and numerical investigations of turbulent forced convection flow of nanofluid in helical coiled tubes at constant surface temperature. Powder Technol 283:178–189

22. Bahremand H, Abbassi A, Saffar-Avval M (2015) Experimental and numerical investigation of turbulent nanofluid flow in helically coiled tubes under constant wall heat flux using Eulerian-Lagrangian approach. Powder Technol 269:93–100
23. Jamshidi N, Farhadi M, Sedighi K, Domeiry G (2012) Optimisation of design parameters for nanofluids flowing inside helical coils. Int Commun Heat Mass Transfer 39:311–317
24. Rabienataj Darzi AA, Farhadi M, Sedighi K, Aallahyari S, Delavar A (2013) Turbulent heat transfer of Al_2O_3 – water nanofluid inside helically corrugated tubes: Numerical Study. Int Commun Heat Mass Transfer 41:68–75
25. Akagawa K, Tadashi S, Minoru U (1971) Study on a gas-liquid two-phase flow in helically coiled tubes. Bull JSME 14(72):564–571
26. Aly W (2014) Numerical study on turbulent heat transfer and pressure drop of nanofluid in coiled tube-in-tube heat exchangers. Energy Conver Manage 79:304–316
27. Ito H (1959) Friction factors for turbulent flow in curved pipes, ASME. J Basic Eng 81:123–134
28. Mohammed HA, Narrein K (2012) Thermal and hydraulic characteristics of nanofluid flow in a helically coiled tube heat exchanger. Int Commun Heat Mass Transfer 39:1375–1383
29. Hashemi SM, Akhavan-Behabadi MA (2012) An empirical study on heat transfer and pressure drop characteristics of CuO-base oil nanofluid flow in a horizontal helically coiled tube under constant heat flux. Int Commun Heat Mass Transfer 39:144–151
30. Fsadni AM, Whitty JPM, Stables MA (2016c) A brief review on pressure drop reduction studies for flow in helically coiled tubes. Appl Therm Eng 109:334–343
31. Wu Z, Wang L, Sunden B (2013) Pressure drop and convective heat transfer of water and nanofluids in a double-pipe helical heat exchanger. Appl Therm Eng 60:266–274
32. Kannadasan N, Ramanathan K, Suresh S (2012) Comparison of heat transfer and pressure drop in horizontal and vertical helically coiled heat exchanger with Cu-water based nanofluids. Exp Thermal Fluid Sci 42:64–70
33. Kahani M, Heris SZ, Mousavi SM (2013) Comparative study between metal oxide nanopowders on thermal characteristics of nanofluid flow through helical coils. Powder Technol 246:82–92
34. Akhavan-Behabadi MA, Fakoor Pakdaman M, Ghazvini M (2012) Experimental investigation on the convective heat transfer of nanofluid flow inside vertical helically coiled tubes under uniform wall temperature condition. Int Commun Heat Mass Transfer 39:556–564
35. Akbaridoust F, Raksha M, Abbassi A, Saffar-Avval M (2013) Experimental and numerical investigation of nanofluid heat transfer in helically coiled tubes at constant wall temperature using dispersion model. Int J Heat Mass Transf 58:480–491
36. Suresh S, Chandrasekar M, Chandra Sekhar S (2011) Experimental studies on heat transfer and friction factor characteristics of CuO-water nanofluid under turbulent flow in a helically dimpled tube. Exp Thermal Fluid Sci 35:542–549
37. Seban RA, Mclaughlin EF (1963) Heat transfer in tube coils with laminar and turbulent flow. Int J Heat Mass Transf 6:387–395
38. Salem MR, Ali RK, Sakr RY, Elshazly KM (2015) Effect of γ-Al_2O_3-water nanofluid on heat transfer and pressure drop characteristics of shell and coil heat exchanger with different coil curvatures. J Thermal Sci Eng Appl 7(041002):1–9
39. Ali AA, Kumaragurubaran B, Suresh S, Babu KL (2015) Heat transfer enhancement in vertical helical coiled heat exchanger by using nanofluid TiO_2-water. Int Res J Eng Technol 2 (9):2480–2484
40. Elsayed A, Al-dadah R, Mahmoud S, Rezk A (2014) Numerical investigation of turbulent flow heat transfer and pressure drop of Al_2O_3/water nanofluid in helically coiled tubes. Int J Low Carbon Technol 0:1–8
41. Tohidi A, Ghaffari H, Nasibi H, Mujumdar AS (2015) Heat transfer enhancement by combination of chaotic advection and nanofluids flow in helically coiled tube. Appl Therm Eng 86:91–105

42. Huminic G, Huminic A (2011) Heat transfer characteristics in double tube helical heat exchangers using nanofluids. Renew Sustain Energy Rev 54:4280–4287
43. Akbarinia A, Laur R (2009) Investigating the diameter of solid particles effects on a laminar nanofluid flow in a curved tube using a two-phase approach. Int J Heat Fluid Flow 30:706–714
44. Taylor RA, Phelan PE (2009) Pool boiling of nanofluids: comprehensive review of existing data and limited new data. Int J Heat Mass Transf 52:5339–5347
45. Tu JP, Dinh N, Theofanous T (2004) An experimental study of nanofluid boiling heat transfer. In: Proceedings of the 6th international symposium on heat transfer, Beijing, China.
46. Wen D, Ding Y (2005) Experimental investigation into the pool boiling heat transfer of aqueous based gamma alumina nanofluids. J Nanopart Res 7(2):265–274
47. Das SK, Putra N, Thiesen P, Roetzel W (2003) Temperature dependence of thermal conductivity enhancement for nanofluids. ASME Trans J Heat Transfer 125:567–574
48. Jackson J, Bryan J (2007) Investigation into the pool boiling characteristics of gold nanofluids. Master's Thesis, University of Missouri, Columbia.

Chapter 16
3D Printing of Pharmaceuticals

Muzna Sadia, Mohamed Albed Alhnan, Waqar Ahmed, and Mark J. Jackson

16.1 Introduction

3D printing is an additive manufacturing process which constructs an object in a layer-by-layer manner using a digital design. Successive layers are made on the top of each other so as to make an object. In a digital design file, a new design can be created using a 3D modelling programme, or a copy of already-existing design can be generated as a 3D model by scanning the object with the help of a scanner or by scanning the data of clinical imaging (i.e., tomography or magnetic resonance imaging (MRI)). To create a design, 3D modelling software slices out the entire object in a horizontal direction to hundreds of layers depending on the size of the object. The file is then uploaded for printing in which the printer reads out all the slices in a 2D fashion and fuses the layers together to make a 3D object [1]. The resolution of printing decides the visibility of the layer; the higher the resolution, the lesser the layer visible with the naked eye.

In pharmaceutical manufacturing, this technique is useful because a distinct geometry of the final product and releasing patterns are achievable which is challenging by mass production. A multi-active polypill can be printed according to the individual patient's need [2] which can solve thousands of problems in personalised treatments. It cannot only increase patient compliance but can reduce the cost on NHS as well [3].

M. Sadia (✉) • M.A. Alhnan
School of Pharmacy and Biomedical Sciences, University of Central Lancashire, Preston, UK
e-mail: MSadia@uclan.ac.uk

W. Ahmed
School of Mathematics and Physics, University of Lincoln, Lincoln, UK

M.J. Jackson
School of Interdisciplinary Studies, Kansas State University, Manhattan, KS, USA

M.J. Jackson, W. Ahmed (eds.), *Micro and Nanomanufacturing Volume II*,
DOI 10.1007/978-3-319-67132-1_16

Fig. 16.1 Photo of Carl Deckard and Joe Beaman (Austin American Newspaper, 1987)

3D printing techniques are also being used widely in biomanufacturing, e.g., tissue engineering, manufacturing of implants, medical devices, etc. [4]. In the areas other than medicine, it is used to build the parts of, for example, fighter jets, architectural models, houses, metal products and automotive [5].

3D printing technique was first developed in the mid-1980s by Charles Hull, when he commercialised and patented the first stereolithography (SL) apparatus. They were the first to introduced STL file format for CAD software which is still being used [6]. In another research group, Carl Deckard and Joseph Beaman patented a new technique using powder instead of liquid the same year as selective laser sintering (SLS) (Fig. 16.1). The term '3D printer' was first used by the professors at MIT who designed an inkjet 3D printer where a layer of ink was deposited on a powder bed to bind the powder together. The powder bed was hence lowered to make another layer over the first one, ultimately making a whole object in this manner [7]. Another type of 3D printing technique, fused deposition modelling (FDM), was patented by Scott Crump in 1989. Scott Crump was a co-founder of Stratasys Ltd. In this type, a semi-solid layer is deposited on a build plate successively to make a final object [7].

16.2 Types of 3D Printing

There are several types of 3D printing techniques out of which powder bed 3D printing, extrusion-based 3D printing and FDM-based 3D printing are explored more for pharmaceutical manufacturing processes than any other technique. Here is a brief overview of the principle, advantages and limitations of these techniques.

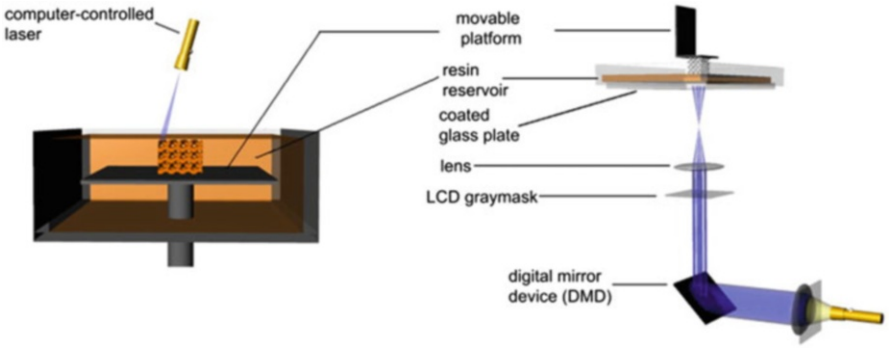

Fig. 16.2 An illustration of two types of stereolithography 3D printer. *Left*, a *bottom-up* system with scanning laser. *Right*, *top-down* setup with a digital light projector (Melchels, F.P.W., J. Feijen, and D.W. Grijpma, A review on stereolithography and its applications in biomedical engineering. Biomaterials, 2010. 31(24): p. 6121–6130.)

16.2.1 Stereolithography

In this technique a solid object is formed from a liquid that is selectively cured by the beams of ultraviolet radiations.

A moveable beam of ultraviolet light strikes on the surface of the photopolymerisable liquid and turns it into a solid layer in a predesigned manner (Fig. 16.2). This solid object or layer is then lowered down, away from the surface according to the desired thickness of the layer. This area is then covered with the liquid again which is cured in the same manner, hence making a final object in several steps [8]. There are two types of stereolithography, bottom up and top down. In the second technique, the support/platform is pulled up after sintering each layer, and hence, the final object is formed. This technique is advantageous as a small amount of resin is required to build an object [1].

This technique is superior to all other techniques producing micron- and submicron-sized objects, which in turn can produce high-resolution object.

The downside of this technique for pharmaceutical manufacturing is a post-printing curing is mandatory and a limited number of resins are available in case of pharmaceuticals. Moreover, the equipment itself is expensive.

16.2.2 Selective Laser Sintering

In this technique, an energy source as a beam of laser sinters the powder where it strikes. The laser is aimed at selective areas onto a powder bed so as to make the shape of the object (Fig. 16.3). This technique produces the object in the same layer-by-layer fashion.

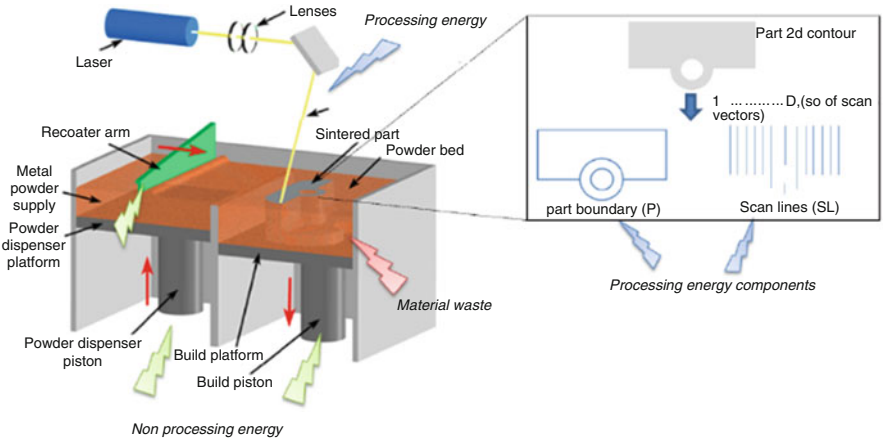

Fig. 16.3 Selective laser sintering process (Verma, A. and R. Rai. Energy efficient modelling and optimisation of additive manufacturing processes. In Solid Freeform Fabrication Symposium, Austin, TX. 2013 [9].)

A powder distributor, first, spreads the powder onto a target area or bed. Then a laser beam strikes onto the powder layer on specific areas within the boundaries. The laser is controlled by aiming it the area to be sintered. In modulating mechanism the laser beam turns on and off so as to cure the powder only when the laser is in distinct boundaries. A moving roller spreads a thin layer of powder on the powder bed. The laser beam then fuses this layer deep enough to join the lower layer of the object, hence making successive layers and eventually an object [6].

The advantages of this technique include the porosity of the build and a highly reproducible and controllable internal geometry. [6].

However, there are some limitations to use this technique in pharmaceuticals, i.e.: post-printing curing is required; a high-energy beam can degrade the starting material; and a limited scan speed is accepted only, which cannot build the objects outside that range [10].

16.2.3 Powder Bed Inkjet 3D Printing

First FDA-approved 3D printing unit for pharmaceuticals called Aprecia introduced their first orodispersible tablet used for the treatment of epilepsy. Inkjet 3D printing technology can manufacture a product with high porosity which was an advantage for the production of fast disintegrating tablets [11].

Powder bed inkjet 3D printers work in a 2D manner to create a 3D object. A piston plate contains the powder to be bound together. The piston lowers down, and a thin layer of powder is spread on it with the help of a roller. A binder solution is sprinkled over a selective region of the powder bed to print object based on the

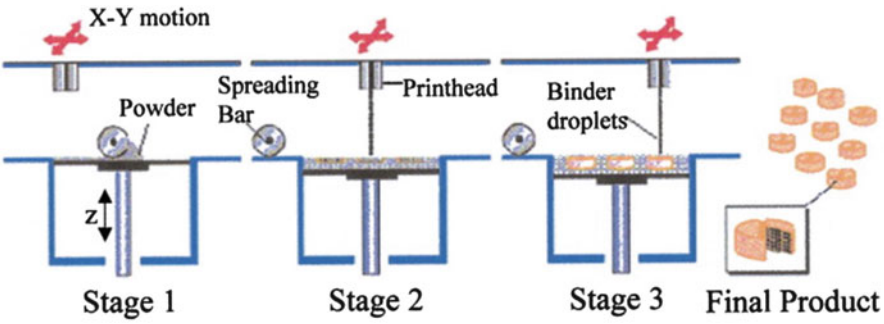

Fig. 16.4 Powder bed inkjet 3D printer (Katstra, W.E., et al., Oral dosage forms fabricated by three dimensional printing. J Control Release, 2000. 66(1): p. 1–9.)

CAD design. The powder particles are bound together with the binder ink and make a 2D object. The piston is lowered again at a predefined distance, and another layer of powder is spread on the piston. For the next layer, the roller is activated to slide the powder on the piston as a thin layer. This process is repeated as many times as required to make an object (Fig. 16.4). The size of the layer in this type of 3D printing is 200 μm. When the object is completed, the powder bed is elevated leaving the wet product on its top. The remaining powder is brushed away [12].

The benefits of this technique are the following: a wide variety of materials are available for printing, the manufacturing does not involve heat and the final product can have more porous structure as compared to conventional manufacturing [13].

The downsides of this technique are the following: a drying time of up to 9 h is required for the final product, and the friability of the tablets is more as compared to compressed tablets. Moreover, a large amout of powder is wasted in this process. For powder bed 3D printing, specialised powder facility is required. Since the printing involves the binding of powder layers already spread at the top, hollow objects cannot be printed using this technique.

16.2.4 Extrusion-Based 3D Printing

In the start of twentieth century, this method for 3D printing was widely used for making tissue scaffolds. In this method a semi-solid paste is extruded out to make a desired shape from a syringe. It can be a continuous flow at room temperature [14].

This technique is different from fused deposition modelling, as the process is carried out at room temperature. The inks/pastes used do not need melting as they are already in a semi-solid state. The semi-solid pastes are first prepared and checked for their rheological properties. To make the pastes with acceptable viscosity, different solvents are used. They should be smooth and homogeneous in order to avoid blockage.

Once the desired paste is formed, it is filled in a cartridge immediately to prevent the solvent loss. They are then extruded out onto a glass slide or building platform

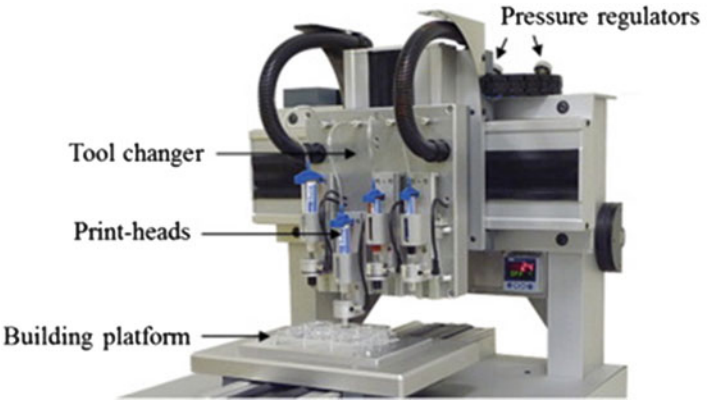

Fig. 16.5 Extrusion-based 3D printer (Khaled, S.A., et al., 3D printing of five-in-one dose combination polypill with defined immediate and sustained release profiles. J Control Release, 2015. 217: p. 308–314.)

to make an object. The syringe tools used for the extrusion have the diameter from 0.4 to 0.8 mm (Fig. 16.5). In terms of tablets, the syringes extrude out the paste in a layer-by-layer manner to make a final object. For core and shell structure, however, a topless shell is first made onto the platform and filled with the core later on. The shell in the end is then covered with the top to make the final object [15].

The extrusion takes place at room temperature which makes it suitable for heat-labile products. A high drug loading (up to 90%) can be achieved using this technology. A complex multidrug dosage form can be manufactured, each having a distinct release profile. Moreover, incompatible substances can be separated in the same drug delivery device (DDD).

The tablet hardness is less than the products already available in the market and so is the friability. A satisfactory hardness can be achieved by increasing the binder ratio in the pastes; hence, the percentage weight loss can be prevented. However, this in turn will alter the drug release. A lack of accurate deposition control makes it difficult to precisely print a tablet shape. Unlike FDM, the layer size is dependent on the size of the tip used. The total printing time is longer, i.e., 25 min (depending on formulation), and the drying time is 24 h [2], which makes this technology unsuitable to be used in dispensing units, e.g., pharmacies.

16.2.5 Fused Deposition Modelling 3D Printing

FDM-based 3D printing is the most commonly used 3D printing because of the cheaper printers and the availability of wide variety of thermoplastic filaments. In this type of 3D printing, a molten filament or ink is deposited onto a build plate in a predefined manner from the software to make a final object of desired/set geometry and shape in a layer-by-layer manner.

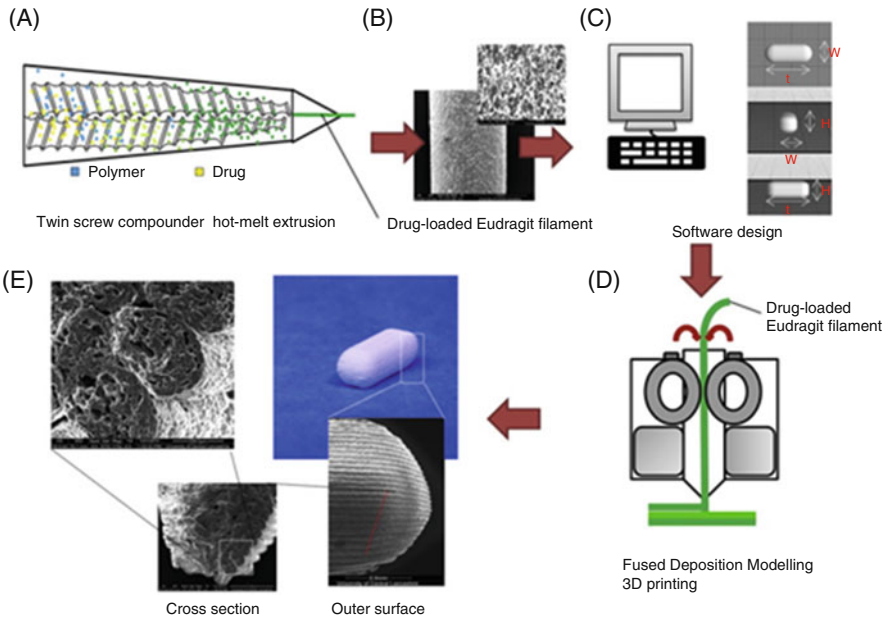

Fig. 16.6 Schematic diagram showing different stages of FDM-based 3D printing (**A**) processing of physical mixture and extrusion of drug loaded filament, (**B**) SEM of drug loaded filament, (**C**) design of capsule shaped tablet in computer software, (**D**) feeding of theophylline loaded filament in 3D printers nozzle and fabrication of a tablet, (**E**) 3D printed tablet with a resolution of 200 micrometre shown in SEM image. (Pietrzak, K., A. Isreb, and M.A. Alhnan, A flexible-dose dispenser for immediate and extended release 3D printed tablets. Eur J Pharm Biopharm, 2015. 96: p. 380–387.)

The diameter of the filament used as an ink is usually 1.75 mm (depends on the type of 3D printer as well). A thermoplastic filament is first loaded into the printer's nozzle which is initially rolled up on a spool outside. The filament is loaded for building up an object in two wheels, which pull the filament inside by an inward flow. The wheels stop rotating when the printer is not building any object. The nozzles travel in an *X* and *Y* direction to make a predefined size of the object, while a *Z*-axis movement is exhibited by the platform to lower down the first layer in order to deposit another layer on the top of it (Fig. 16.6). The resolution of the printing can be set through the software. The layer thickness achieved can be as low as 50 μm that makes an object in diffused layers [7].

There is a heating system around the nozzle which heats the nozzle to a prespecified temperature. The temperature should be high enough to melt the thermoplastic filament in order to extrude it out through a narrow passage or nozzle tip usually 0.4 mm in diameter. As the molten filament comes out of the nozzle, the change in temperature solidifies it. Hence, the first layer is dried and solidified until the second layer is extruded on its top. The speed of the printing can be changed according to the requirement [16]. For example, if the filament takes more time to

solidify, the speed can be decreased so that the first layer is dried enough to get the layers on its top and the object can be prevented from destroying.

FDM 3D printers are low-cost printing units as compared to other 3D printing techniques. An accurate control on layer thickness, size and weight of the product makes it highly reproducible and is suitable to be used in a pharmaceutical setting for personalised therapy. Post-printing curing is not needed as the product is already dry and ready to use [17].

Among multilayered multi-active dosage forms, the layers with different APIs are well separated from each other. The waste of the starting material is minimal. The size of the unit makes it easy to be kept in a dispensing area. Moreover, no solvents are required to make the ink or filament. The product has low friability with higher mechanical resistance. High drug dose uniformity can be achieved from the product [16].

This technique, however, has some drawbacks, e.g., due to high processing temperature, the heat-labile drugs cannot be used. A limited number of pharmaceutical grade polymers are available [18].

16.3 Pharmaceutical Applications of 3D Printing

16.3.1 Stereolithography

This is the first example in which stereolithography technique was used to prepare an oral dosage form (Fig. 16.7). Wang et al. [19] prepared a photoreactive solution first, in different ratios (i.e., 9:1, 6.5:3.5 and 3.5:6.5) of PEGDA and PEG 300 to a volume of 20 mL. Diphenyl (2,4,6-trimethylbenzoyl) phosphine oxide (DPPO) was added as a photoinitiator to a concentration of 1% (w/v). APIs used in this example

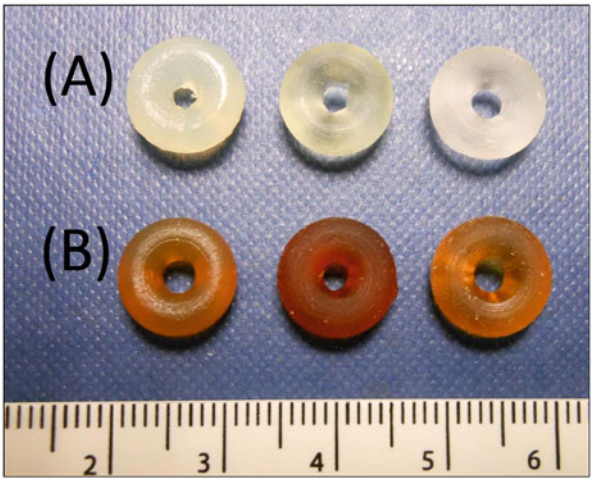

Fig. 16.7 3D printed tablets containing (**a**) paracetamol and (**b**) 4-ASA. From *left* to *right*: 35% PEGDA/65% PEG300, 65% PEGDA/35% PEG300 and 90% PEGDA/10% PEG300 (Wang, J., et al., Stereolithographic (SLA) 3D printing of oral modified-release dosage forms. Int J Pharm, 2016. 503(1–2): p. 207–212.)

were paracetamol or 4-ASA in a concentration of 5.9% (w/w) which was added in the end after the photoinitiator was completely mixed. Different concentrations of PEGDA and PEG300 altered the release of the drugs, e.g., the higher was the PEGDA, the lower was the drug release, while increased concentration of PEG 300 promoted the release of the drug.

16.3.2 Inkjet 3D Printing

Wang et al. [20] fabricated core and shell structure to demonstrate a near-zero-order DDDs (Fig. 16.8). The powder bed was composed of Kollidon SR (a mixture of polyvinyl acetate (PVAc) 80%, polyvinylpyrrolidone K30 (PVP K30), sodium lauryl sulphate and silica) and HPMC 2910. Two types of inks were used for core region, an aqueous solution of 50% PEH and 7.5% of active, 0.1% Tween 20 and 5% PVP K17. An ethanolic binder without a drug was used to form release-controlling matrix containing 15% TEC (triethyl citrate). The solvent of the binder region was 25:75 of water and ethanol. They printed three different formulations with different drug release profiles, by controlling the polymer ratios in the powder region. The release of the drug took place by diffusion mechanism.

Katstra et al. [12] used powder bed 3D printing technique to make solid dosage forms (Fig. 16.9). For the powder layer, cellulose powder and spray-dried lactose were used (for separate formulations). Different binders were used with different drug-releasing properties, i.e., 20%w/w Eudragit E100 and ethanol, 20% w/w

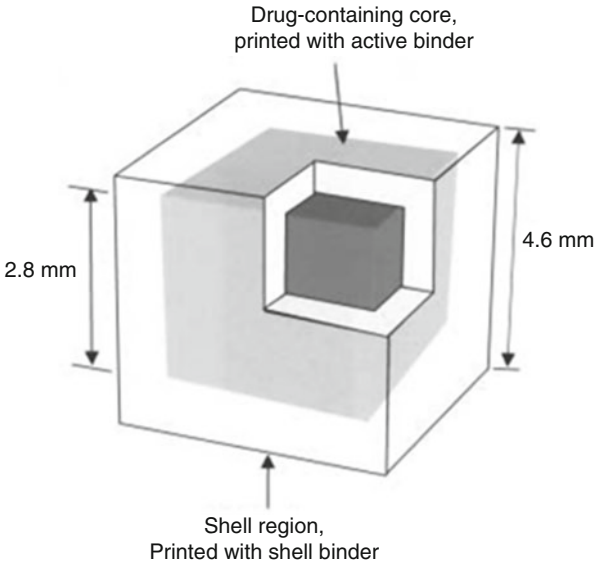

Fig. 16.8 Cubic core-shell cubic structure printed with powder-based inkjet 3D printer (Wang, C.-C., et al., Development of near zero-order release dosage forms using three-dimensional printing (3-DP™) technology. Drug development and industrial pharmacy, 2006. 32(3): p. 367–376.)

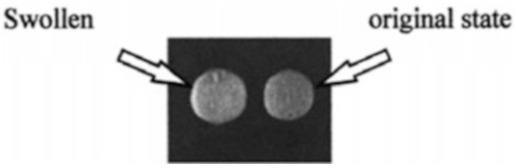

Fig. 16.9 Eudragit RLPO tablets before and after dissolution (Katstra, W.E., et al., Oral dosage forms fabricated by three dimensional printing. J Control Release, 2000. 66(1): p. 1–9.)

Fig. 16.10 3D printed breakaway tablets. *Left*: original tablet as printed. *Centre*: after 30 min in simulated gastric fluid. *Right*: split into two subunits after 45 min (Rowe, C.W., et al., Multimechanism oral dosage forms fabricated by three dimensional printing. J Control Release, 2000. 66 (1): p. 11–17.)

RLPO and acetone solution and 22% PVP with 0.1% Tween 20 in deionised water. The thickness layer was 200 μm.

It was successfully verified by this research that the release rate of the drug can be controlled by altering the quantity of the polymer in each tablet using inkjet 3D printers.

Row et al. [13] printed four different types of tablets using powder bed 3D printing. Immediate extended-release tablets were made using microcrystalline cellulose for powder bed. Eudragit E100 20% w/w and ethanol were printed for one section, while RLPO and acetone (16% w/w) were printed for extended-release section. The API used in this formulation was 30% w/w chlorpheniramine maleate in ethanol. The layer thickness was 200 μm.

For breakaway tablets, Avicel PH301, Pharmatose DCL11 spray-dried lactose and Eudragit L100, 30, 30 and 40%, respectively, were used for the powder bed. The tablets were first printed with placebo layer with Eudragit RLPO 15% in acetone which was followed by diclofenac 30% w/w with 2.5% (w/w) Kollidon in methanol. The tablets were ended up with placebo layer. Layer thickness was 250 μm. The quick dissolve section was 300 μm layer of 22% w/w Kollidon K-25 in water (Fig. 16.10).

In case of enteric dual-pulse release, the powder bed was the same as for breakaway tablets, but the binder was 5% w/w Eudragit L100 in ethanol (200 μm layer thickness). They printed six placebo layers with the binder only. Then an

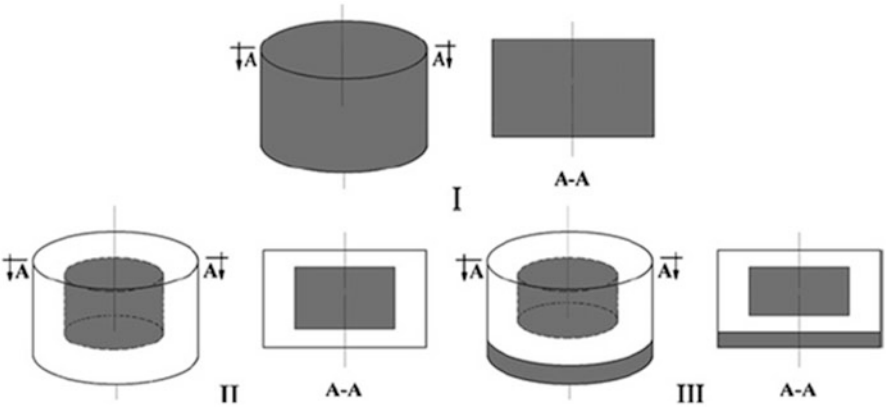

Fig. 16.11 An illustration of LVFX implant design (Huang, W., et al., Levofloxacin implants with predefined microstructure fabricated by three-dimensional printing technique. Int J Pharm, 2007. 339(1–2): p. 33–38.)

active layer containing binder and diclofenac solution was printed followed by six placebo layers; in the end an active layer before two further placebo layers was printed.

Dual pulsatory devices were printed in order to release the drug in the stomach at low pH and in the intestine at high pH. The powder used for the bed was the same as before. However, Eudragit E100 and Eudragit L100 polymers were used in drug compartments. Eudragit E100 was printed with a solution of 13.5% w/w in acetone. The layer thickness was 200 μm. For these DDDs two E100 placebo layers were printed in the beginning which was followed by three drug-containing layers and then two additional placebo layers for the first part of the tablet. The second half was printed with six placebo layers of L100 at the top and the end, sandwiching six active layers inside.

All the formulations were dried overnight in a nitrogen glove box and 48 h in a vacuum.

Huang et al. [21] studied the printing of implants containing levofloxacin. They used L-PLA as a powder bed and 20:80 of ethanol and acetone as a binder ink. They printed different designs and observed that the implants made by conventional method were less porous and uniform than the 3D printed ones (Fig. 16.11). 3D printed implants showed better drug-releasing bi-model profiles than the implants, made by conventional compression methods.

Yu et al. [22] printed DDDs containing two barrier layers at the top and bottom while a drug acetaminophen (APAP) containing segment in between (Fig. 16.12). The drug-containing section was composed of APAP 60% w/w, while the rest of the powder mixture was HPMC, EC, PVP k30 and colloidal silicone dioxide (20%, 10%, 9.5% and 0.5%w/w, respectively). The printed drug delivery devices showed a linear relationship with different diameters, heights, EC concentrations and

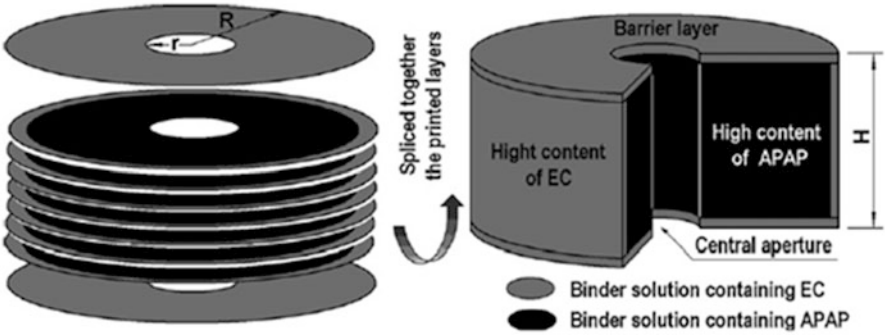

Fig. 16.12 Novel drug delivery devices (Yu, D.G., et al., Novel drug delivery devices for providing linear release profiles fabricated by 3DP. Int J Pharm, 2009. 370(1–2): p. 160–166.)

internal diameter aperture. Moreover, the drug release profiles can be organised by changing the thickness of the passes of binder solutions containing EC.

Yu et al. [23] printed fast disintegrating devices with compact top and bottom section and unbound middle section (Fig. 16.13). The middle region was bound to form the outer region to give the acceptable hardness to the drug delivery devices. They used paracetamol, lactose, PVP K30, mannitol and colloidal silicone dioxide in the ratio of 40:20:9.5:30:0.5, respectively. They used the binder solution with alizarin yellow to 0.5% w/v, PVP K30 5.0%w/v and 75% ethanol in water. The dissolution study showed that these DDDs were disintegrated to release 98.5% of the drug in just 2 min. However, the friability of the tablets was unsatisfactory.

Wu et al. [24], in a study, used PCL powder for the top and bottom layer of the DDD, while the middle part was built with PEO (polyethylene oxide) which was bound by 20% (polycaprolactone) PCL LPS/chloroform solution (Fig. 16.14). They used alizarin yellow and methylene blue.

16.3.3 Extrusion-Based 3D Printing

Khaled et al. [15] prepared bilayer tablets (Fig. 16.15) using immediate-release and sustained-release gels of HPMC 2910 and HPMC 2280, respectively. The gels were prepared by mixing 1 g of HPMC in 30 mL of hot water stirred, and then 70 g of ice was added. The gel was mixed thoroughly by stirring for half an hour in order to make the polymer soluble. The mixture was stored for 24 h to get a gel of acceptable consistency. They used sodium starch glycolate and microcrystalline cellulose as excipients. A powder mixture for IR layer was prepared using guaifenesin and required excipient by mixing for 30 min and HPMC 2910, blended with the powder mixture to make a paste. For SR layer polyacrylic acid was mixed with HPMC 2280 at different percentages. The pastes were filled in separate syringes.

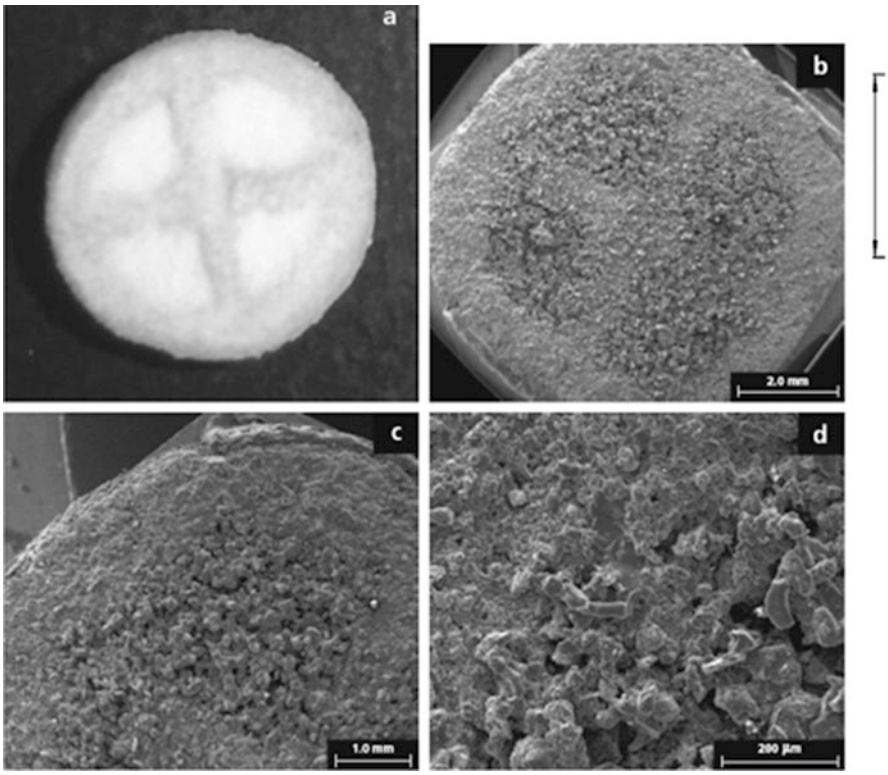

Fig. 16.13 (**a**) Cross section of fast disintegrating drug delivery device and (**b–d**) SEM images at different magnifications (Yu, D.G., et al., Novel oral fast-disintegrating drug delivery devices with predefined inner structure fabricated by Three-Dimensional Printing. J Pharm Pharmacol, 2009. 61 (3): p. 323–329.)

Fig. 16.14 A model drug delivery device (Wu, B.M., et al., Solid free-form fabrication of drug delivery devices. Journal of Controlled Release, 1996. 40(1–2): p. 77–87.)

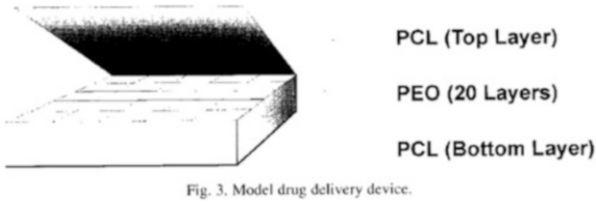

Fig. 3. Model drug delivery device.

Khaled et al., [25] in another study, printed tablets with compartments having different actives with distinct releasing patterns (Fig. 16.16). The HPMC gel was prepared with the same method. The only exception was the addition of ethanol in a ratio of 25:75 in the end and mixed thoroughly. CE, D-mannitol and PEG 6000 were mixed together in a ratio of 55:32:13, respectively. 2.7 g of the powder was mixed with 2.5 mL of the binder solution (acetone and DMSO 3:1 v/v) to make the shell (Fig. 16.17).

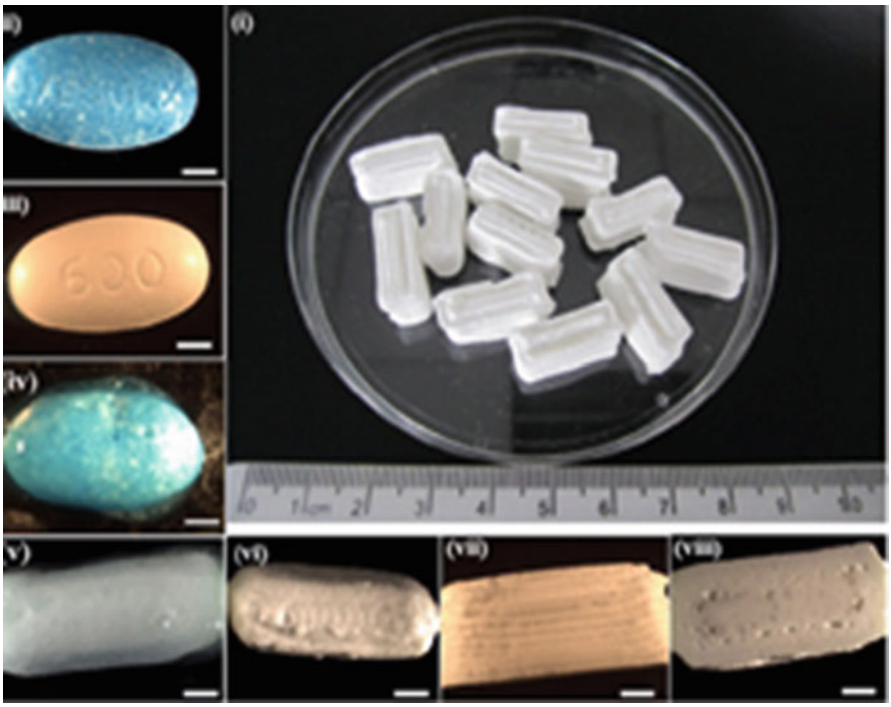

Fig. 16.15 3D printed guaifenesin bilayer tablets (Khaled, S.A., et al., Desktop 3D printing of controlled release pharmaceutical bilayer tablets. Int J Pharm, 2014. 461(1–2): p. 105–111.)

Captopril powder was mixed with required excipients. Hydro-alcoholic gel was then mixed to make a homogeneous mixture. Nifedipine and glipizide were mixed with PEG 6000, with HPMC K100 M and lactose.

Khaled et al. [2] continued the study and successfully printed a polypill containing five active ingredients having distinct releasing patterns and individualised dose combinations (Fig. 16.18). All the actives were separated from each other physically so that there were no incompatibility issues. The polypill had three sustained-release compartments containing pravastatin, atenolol and ramipril. These actives were separately shelled by hydrophobic cellulose acetate shell. They had immediate-release aspirin and hydrochlorothiazide on the top.

16.3.4 Fused Deposition Modelling 3D Printing

Goyanese et al. [26] printed tablets with multilayers containing two actives and DuoCaplet (caplet in caplet) (Fig. 16.19). They customised commercially available PVA filament as an ink for 3D printing. The filament was first cut into pieces, grinded, sieved and then mixed with the drugs either paracetamol or caffeine in

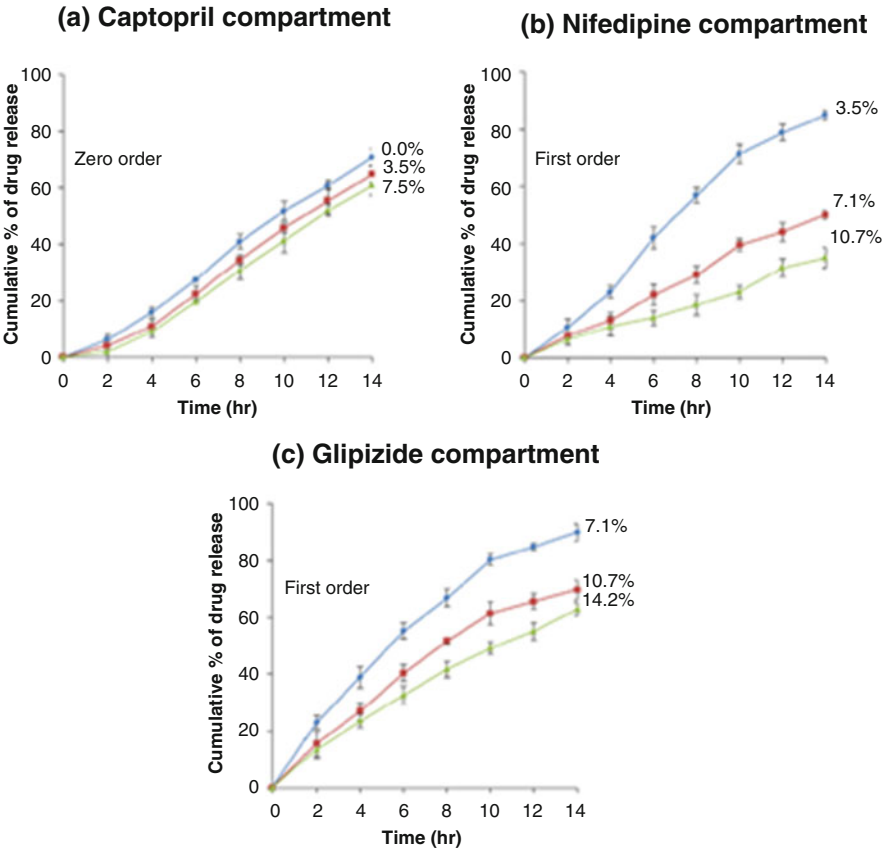

Fig. 16.16 The release of the drug from a polypill having three drug-loaded compartments (Khaled, S.A., et al., 3D printing of tablets containing multiple drugs with defined release profiles. International Journal of Pharmaceutics, 2015. 494(2): p. 643–650.)

pestle and mortar. The filament was then extruded at 180 °C in Noztek Pro. hot melt extruder. The prepared filaments were then used to print tablets at 200 °C.

Goyanes et al. [27] prepared the filament by the method described earlier while the drug used was budesonide. The tablets were printed at 190 °C which were later on coated with Eudragit L100 into a mixture of isopropanol (Fig. 16.20). Talc (50% of the polymer weight) and TEC (10% polymer weight) were then added further to the dispersion prepared for coating.

Goyanese et al. [28] used commercially available PVA filament and fluorescein as a model drug in order to exhibit the proof of principle (Fig. 16.21). The drug loading was different in this method as the drug was incorporated in the filament by placing in the ethanolic solution of fluorescein (2%w/v) with magnetic stirring for 24 h.

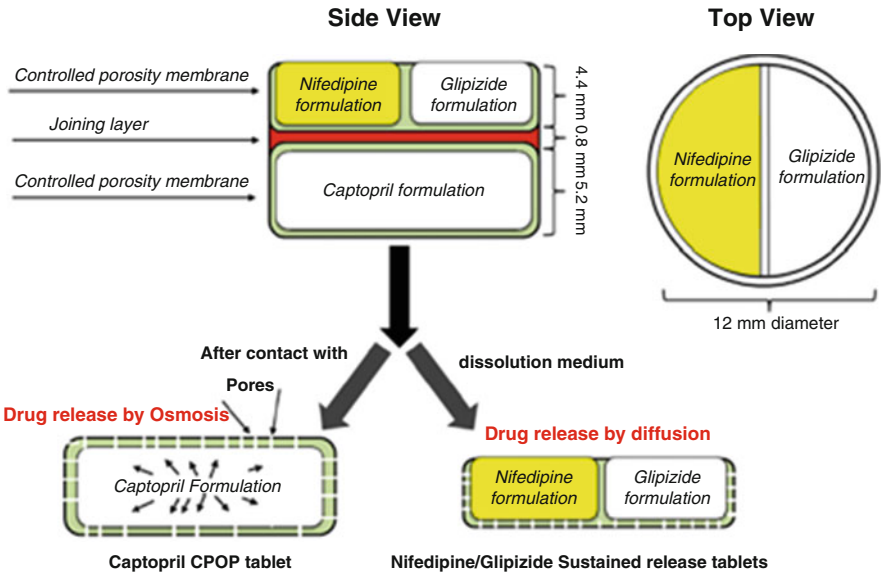

Fig. 16.17 A schematic illustration of captopril osmotic pump and nifedipine and glipizide sustained-release tablets (Khaled, S.A., et al., 3D printing of tablets containing multiple drugs with defined release profiles. International Journal of Pharmaceutics, 2015. 494(2): p. 643–650.)

Goyanese et al. [29] used 4-ASA and 5-ASA drug which was incorporated in commercially available PVA filament. For drug solution, 500 mg of the drug was added in 50 mL of ethanol. Five-metre-long filament was soaked in the solution for 24 h under magnetic stirring and then stored under vacuum desiccator. This study proved that 4-ASA showed degradation at 210 °C while printing, irrespective of the time in the extruder under heat. This suggests that heat-liable drugs will show degradation at higher temperature in FDM 3D printing technique (Fig. 16.22).

In another study, Goyanese et al. [30] printed tablets with different shapes using FDM 3D printer (at 180 °C), to analyse the effect on drug release profile (Fig. 16.23). The formulation of these tablets otherwise is challenging by mass production. A PVA-based filament was used with 4% paracetamol as a model drug. This study demonstrated that the drug release does not depend on surface area itself but on surface area to volume ratio.

In this study, Skowyra et al. [16] used commercially available PVA filament. The drug loading was achieved by incubating PVA filament in a saturated solution of methanol and prednisolone for 24 h. The filament was then dried at 40 °C (Fig. 16.24). The tablets using preprepared filaments were printed at 230 °C. This research successfully proved that tablets with flexible doses can be printed with FDM 3D printer (Fig. 16.25).

In this study, Melocchi et al. [18] printed capsular devices using commercially available PVA filament and in-house produced filament. The filament was extruded using hot melt extruder (HAAKE MiniLab II) with hydroxypropyl cellulose (HPC).

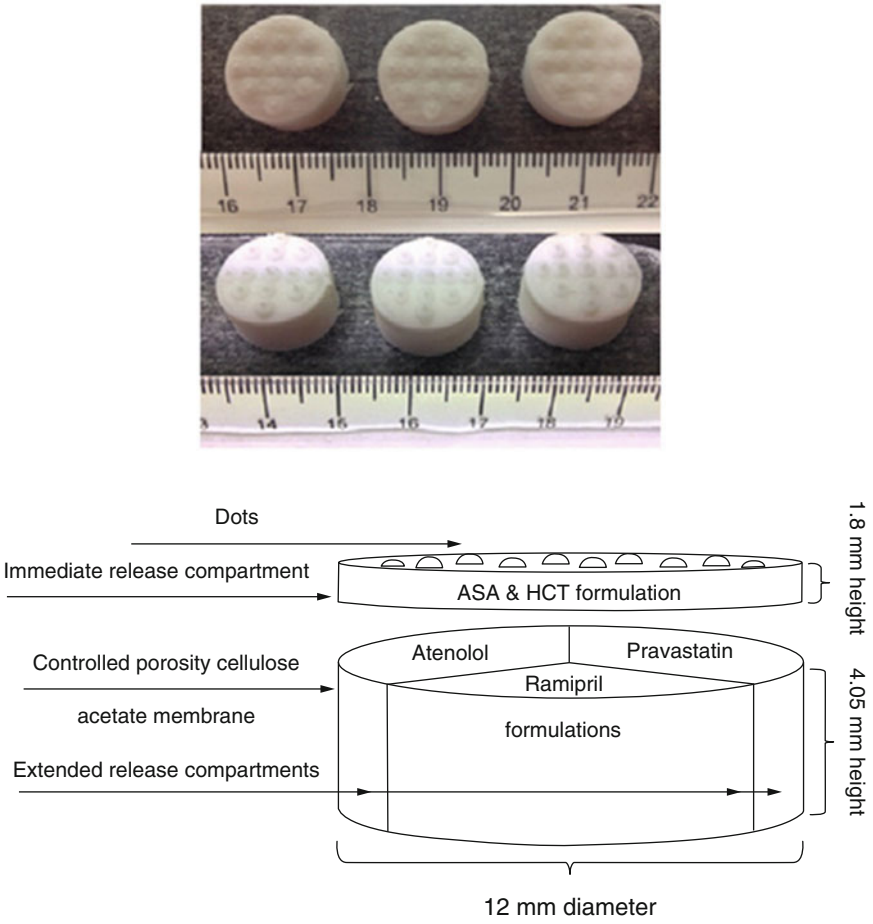

Fig. 16.18 A polypill containing five actives: immediate-release hydrochlorothiazide and aspirin and sustained-release atenolol, pravastatin and ramipril compartments (Khaled, S.A., et al., 3D printing of five-in-one dose combination polypill with defined immediate and sustained release profiles. Journal of Controlled Release, 2015. 217: p. 308–314.)

This study demonstrated a successful printing of capsular devices comparable to commercially available ChronoCap system (Fig.16.26).

In this study, Pietrzak et al. [17] used a methacrylic and cellulose-based polymers for the first time to make filaments using HME. They printed tablets of theophylline with different polymers, i.e., EudragIt L100, Eudragit S100 and HPC SSL in different sizes. They observed a linear relationship between the volumes of the tablet in the software design to the mass of the printed tablets (Fig. 16.27).

Water et al. [31] showed successful printing of personalised discs for inhibition of bacteria and biofilm formation (Fig. 16.28). PLA filament was used for extruding

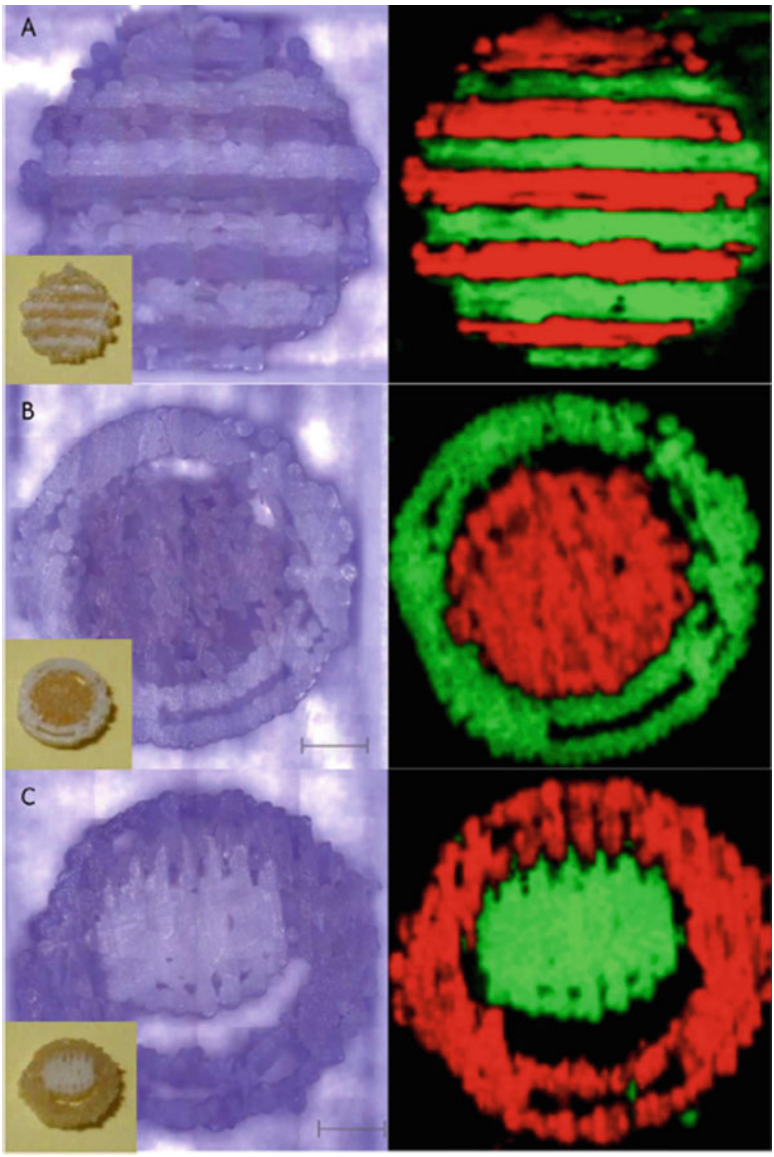

Fig. 16.19 2D Raman mapping images of cross section of the caplets showing distinct layers of different drugs without any mixing. (**a**) Multilayer device of 8.2% paracetamol-PVA and 9.5% caffeine-PVA. (**b**) DuoCaplet of 9.5% caffeine-PVA (outer) and 8.2% paracetamol-PVA (core). (**c**) DuoCaplet of 8.2% paracetamol-PVA (outer) and 9.5% caffeine-PVA (core). Caffeine is green, while paracetamol is red (Goyanes, A., et al., 3D Printing of Medicines: Engineering Novel Oral Devices with Unique Design and Drug Release Characteristics. Mol Pharm, 2015. 12(11): p. 4077–4084.)

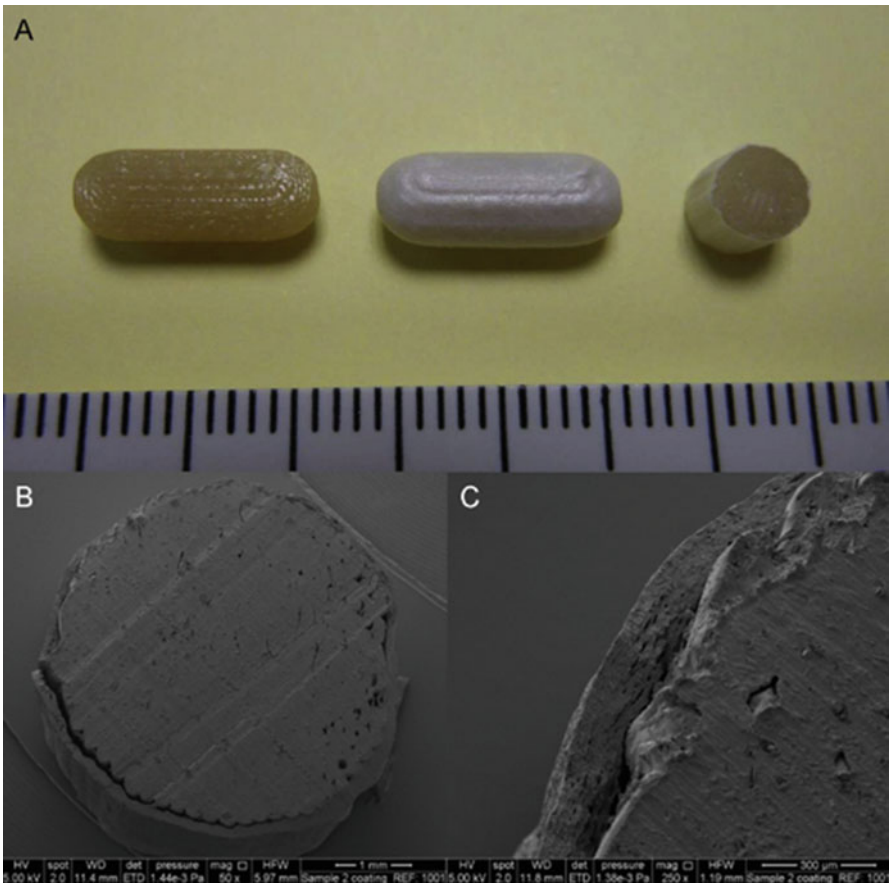

Fig. 16.20 3D printed caplets (**a**) from *left* to *right* before coating and after coating; (**b, c**) internal SEM images of coated caplets (Goyanes, A., et al., Fabrication of controlled-release budesonide tablets via desktop (FDM) 3D printing. Int J Pharm, 2015. 496(2): p. 414–420.)

Fig. 16.21 Images of 3D printed tablets with different infill percentages (Goyanes, A., et al., Fused-filament 3D printing (3DP) for fabrication of tablets. Int J Pharm, 2014. 476(1–2): p. 88–92.)

Fig. 16.22 3D printed fabricated 5-ASA and 4-ASA tablets with different infill percentages (Goyanes, A., et al., 3D printing of modified-release aminosalicylate (4-ASA and 5-ASA) tablets. Eur J Pharm Biopharm, 2015. 89: p. 157–162.)

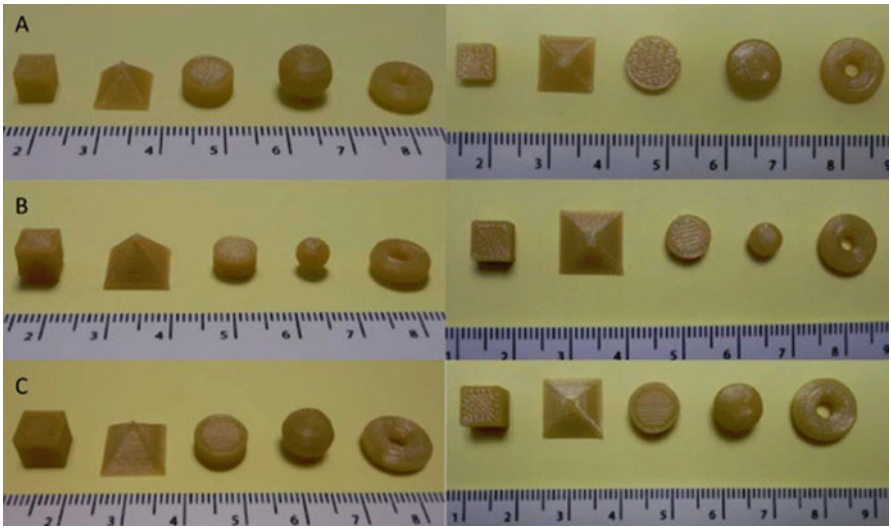

Fig. 16.23 3D printed tablets with different geometries at constant (**a**) surface area, (**b**) surface area/volume ratio and (**c**) mass (scale bar in cm) (Goyanes, A., et al., Effect of geometry on drug release from 3D printed tablets. Int J Pharm, 2015. 494(2): p. 657–663.)

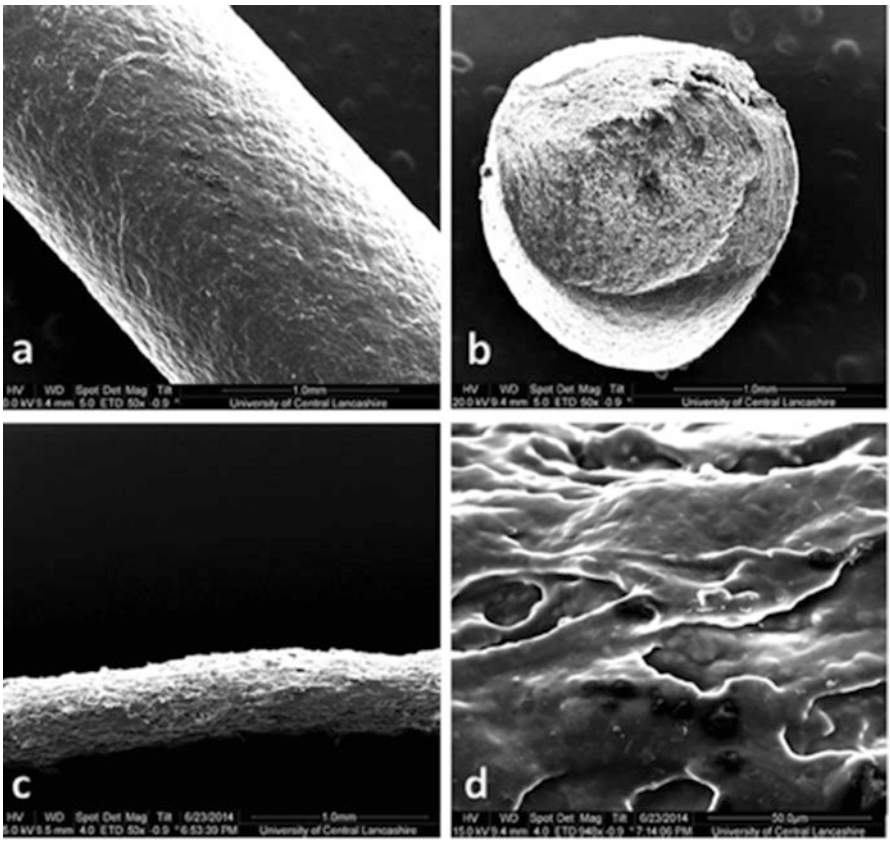

Fig. 16.24 SEM images of PVA filaments: (**a**) surface view, (**b**) cross section, (**c**) 1000 μm magnification, (**d**) 50 μm magnification (Skowyra, J., K. Pietrzak, and M.A. Alhnan, Fabrication of extended-release patient-tailored prednisolone tablets via fused deposition modelling (FDM) 3D printing. European Journal of Pharmaceutical Sciences, 2015. 68: p. 11–17.)

the feedstock material (filament) with the drugs, nitrofurantoin (NF) and hydroxyapatite (HA). The maximum loadings of the drugs were 30% NF and 5% HA. A maximum inhibition with higher drug loading was observed, i.e., with 30% NF and with or without HA 5% but no inhibition at all with lower drug loading from 3D printed devices.

Weisman et al. [32] studied the extrusion of bioactive filament with methotrexate (MTX) and gentamicin sulphate (GS) using PLA pellets. The pellets (20 g) were first coated with 20 microlitre silicon oil. They were recoated with the drug to 1% or 2 0.5 wt% and then extruded at different temperatures. Different beads and

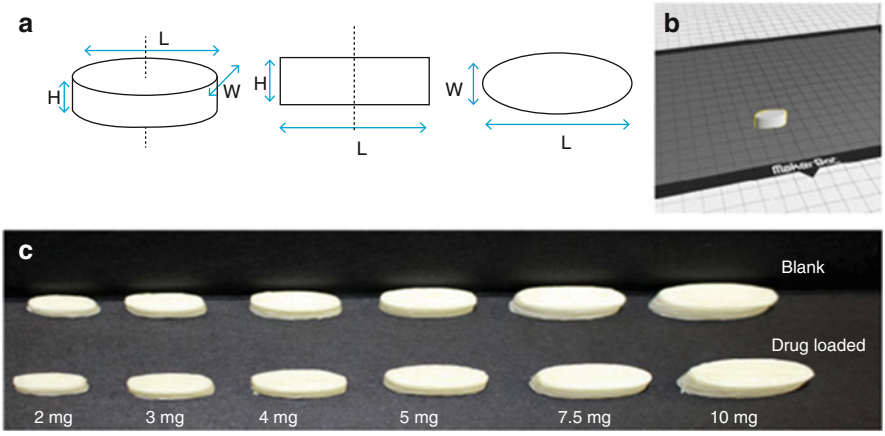

Fig. 16.25 (**a**) 3D design of tablet, (**b**) rendered image of tablet, (**c**) blank (*top*) and prednisolone-loaded PVA-based tablets (*bottom*) (Skowyra, J., K. Pietrzak, and M.A. Alhnan, Fabrication of extended-release patient-tailored prednisolone tablets via fused deposition modelling (FDM) 3D printing. European Journal of Pharmaceutical Sciences, 2015. 68: p. 11–17.)

catheters were successfully printed containing gentamicin and methotrexate (Fig. 16.29). All of these products showed significant effect even at lower doses (1–20.5%).

Sun and Soh [33] developed a method to fabricate customisable tablets with desired release profiles. They fabricated tablets consisting of three compartments and two surface-eroding polymers, one with the drug inside and an impermeable polymer around the tablet (Fig. 16.30). The drug-containing polymer was designed with special geometry so as to release the drug in a desired amount. The impermeable polymer contained an opening at one end. The one-dimensional release of the drug through the opening followed the shape of the drug-containing polymer. The polymer eroded through the opening only.

Alhijjaj et al. [34] used felodipine as a model drug, to fabricate the polymer blends of PEG, PEO and Tween 80, with either Eudragit EPO or soluplus (Fig. 16.31). The temperature used for 3D printing was 150 °C. The purpose of this study was to investigate and adjust the drug release profile of discs fabricated with FDM 3D printing.

Okwuosa et al. [35] printed immediate-release tablets at a low temperature (110 °C). Theophylline and dipyridamole were used as model drugs in a ratio of 10% (Fig. 16.32). They extruded their own filament using HME with PVP (a polymer), TEC (plasticiser), talc (filler) and drug.

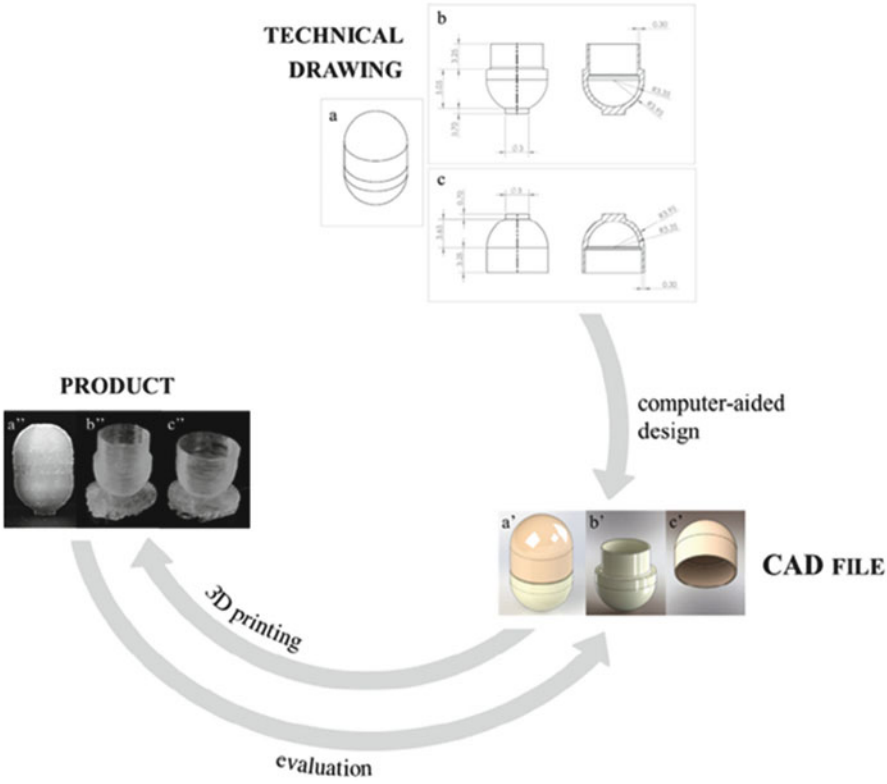

Fig. 16.26 3D printed capsular devices (3D printing by fused deposition modelling (Melocchi, A., et al., 3D printing by fused deposition modelling (FDM) of a swellable/erodible capsular device for oral pulsatile release of drugs. Journal of Drug Delivery Science and Technology, 2015. 30, Part B: p. 360–367.)

Okwuosa et al. [36] fabricated gastric-resistant tablets (as single-step products) using dual FDM 3D printer. The tablets were fabricated as a core and shell structure (Fig. 16.33). This group used theophylline, budesonide and diclofenac sodium as model drugs contained in a PVP matrix (core). The gastric-resistant shell was composed of a methacrylic co-polymer Eudragit L100–55. The shell and core were printed at 185 and 110 °C, respectively.

Sadia et al. [37] tried different pharmaceutical excipients, i.e., tricalcium phosphate, talc, lactose (spray-dried and directly compressible) and cellulose. In this study 5-ASA, captopril, theophylline and prednisolone were used as model drugs in a polymeric matrix of Eudragit EPO. These immediate-release tablets were fabricated at 135 °C (Fig. 16.34).

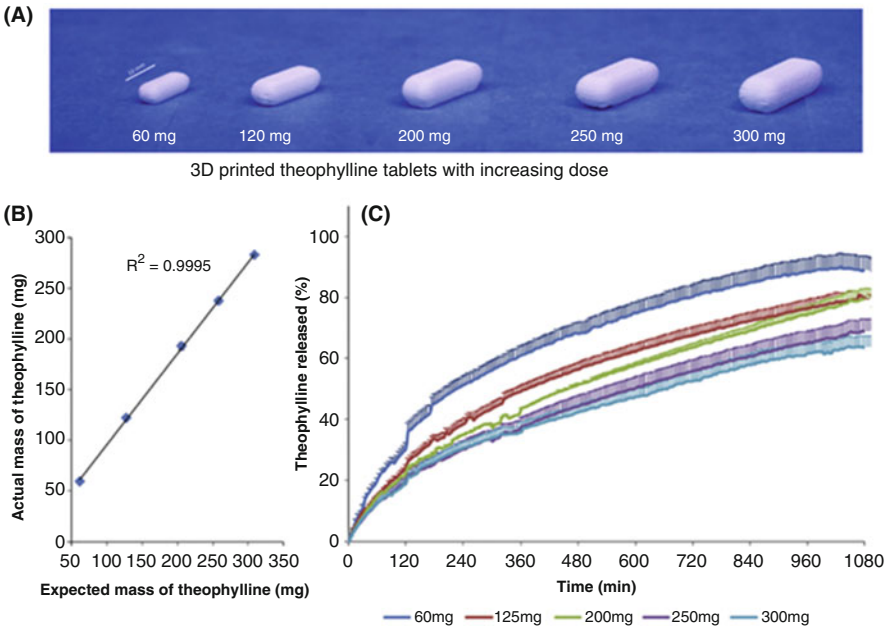

Fig. 16.27 (**a**) 3D printed theophylline tablets with different masses, (**b**) a linear relationship between actual and expected mass of 3D printed tablets, (**c**) drug release from 3D printed tablets of different sizes (Pietrzak, K., A. Isreb, and M.A. Alhnan, A flexible-dose dispenser for immediate and extended release 3D printed tablets. Eur J Pharm Biopharm, 2015. 96: p. 380–387.)

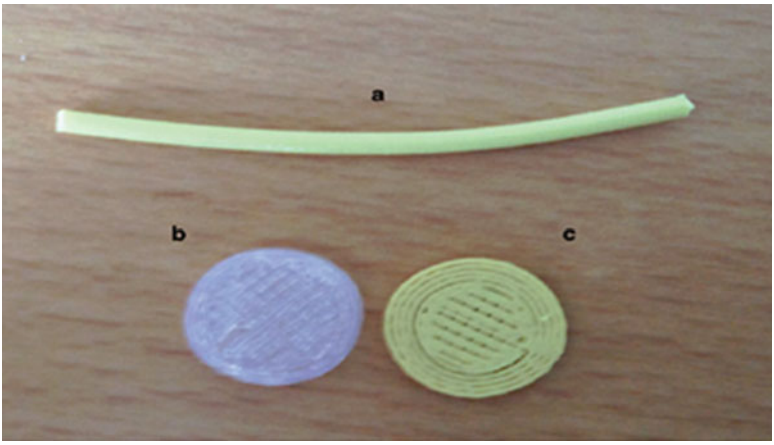

Fig. 16.28 (**a**) Extruded filaments with 20% nitrofurantoin and 3D printed discs of (**b**) PLA; (**c**) disc containing 20% nitrofurantoin (Water, J.J., et al., Three-dimensional printing of drug-eluting implants: preparation of an antimicrobial polylactide feedstock material. J Pharm Sci, 2015. 104 (3): p. 1099–107.)

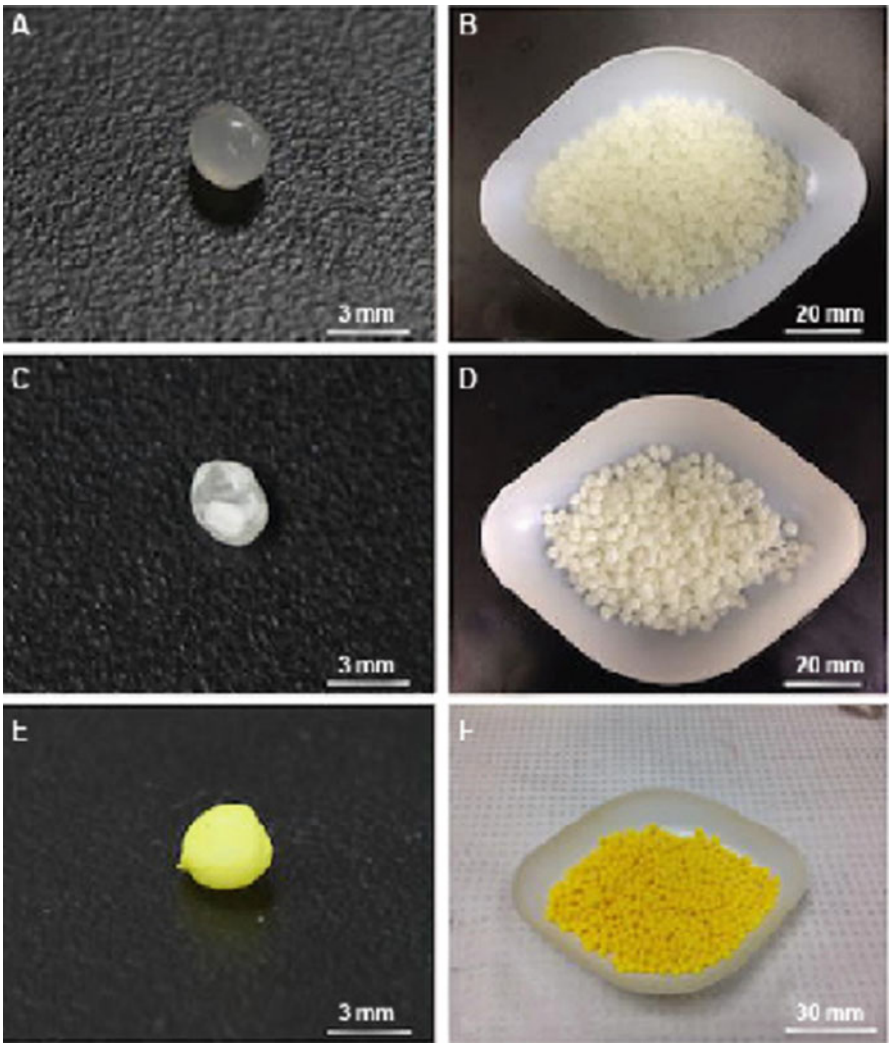

Fig. 16.29 PLA pellets. (**a, b**) Control, (**c, d**) 2.5 wt% gentamicin-coated pellets, (**e, f**) 2.5% methotrexate-coated pellets (Weisman, J.A., et al., Antibiotic and chemotherapeutic enhanced three-dimensional printer filaments and constructs for biomedical applications. International Journal of Nanomedicine, 2015. 10: p. 357–370.)

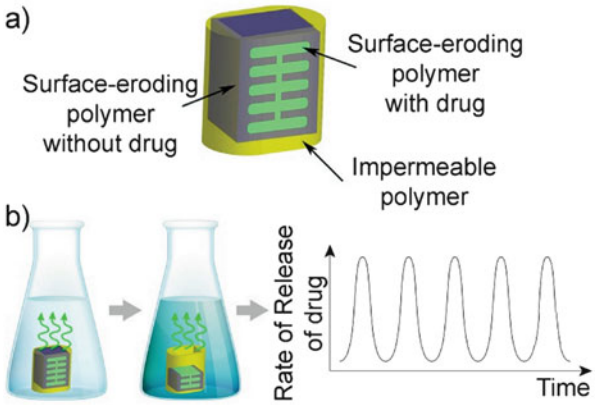

Fig. 16.30 Schematic diagram showing the strategy to deliver the drug as desired (**a**) The design of a tablet for the delivery of drug in a controlled fashion, i.e. the impermeable polymer acts as a protective coating except the top, (**b**) the drug release is one dimensional when immersed in the aqueous solution, the drug release is according to the shape of surface eroding polymer containing the drug. (Sun, Y. and S. Soh, Printing Tablets with Fully Customisable Release Profiles for Personalised Medicine. Adv Mater, 2015. 27(47): p. 7847–7853.)

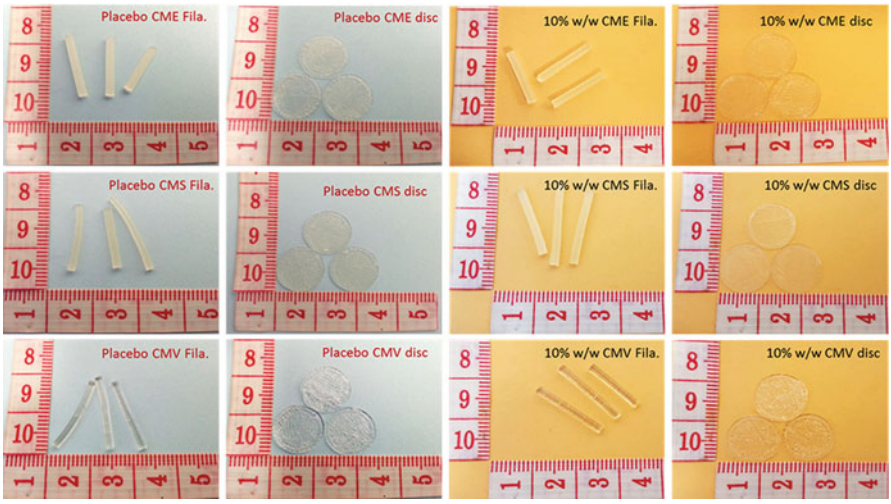

Fig. 16.31 Images showing placebo, drug-loaded HME filaments and 3D printed discs (Alhijjaj, M., P. Belton, and S. Qi, An investigation into the use of polymer blends to improve the printability of and regulate drug release from pharmaceutical solid dispersions prepared via fused deposition modelling (FDM) 3D printing. European Journal of Pharmaceutics and Biopharmaceutics, 2016. 108: p. 111–125.)

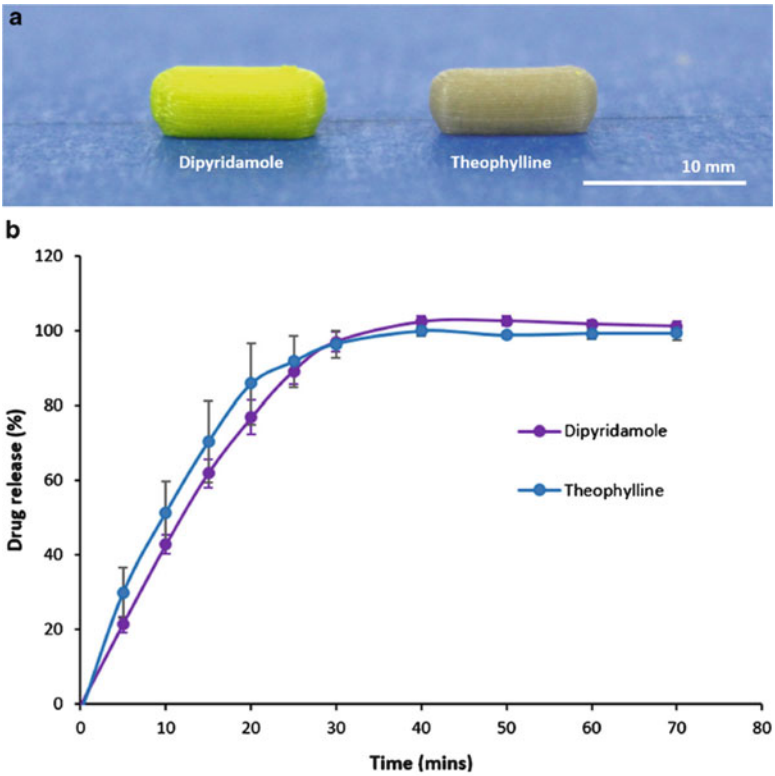

Fig. 16.32 (**a**) 3D printed tablets fabricated with API (**b**) drug release profile of theophylline and dipyridamole from PVP matrix (Okwuosa, T.C., et al., A Lower Temperature FDM 3D Printing for the Manufacture of Patient-Specific Immediate Release Tablets. Pharm Res, 2016. 33(11): p. 2704–2712.)

Zhang et al. [38] fabricated controlled-release tablets with their own extruded filaments. Acetaminophen (APAP) was used as a model drug. For the polymeric matrix, they used HPC LF, HPC EF, HPMC E5, EC N14, Soluplus and Eudragit L100. They prepared three types of formulations: (1) one polymer only with 30% drug loading, (2) binary combination of polymer and (3) an addition of a super disintegrant to the second formulation. In this study, three types of tablets were

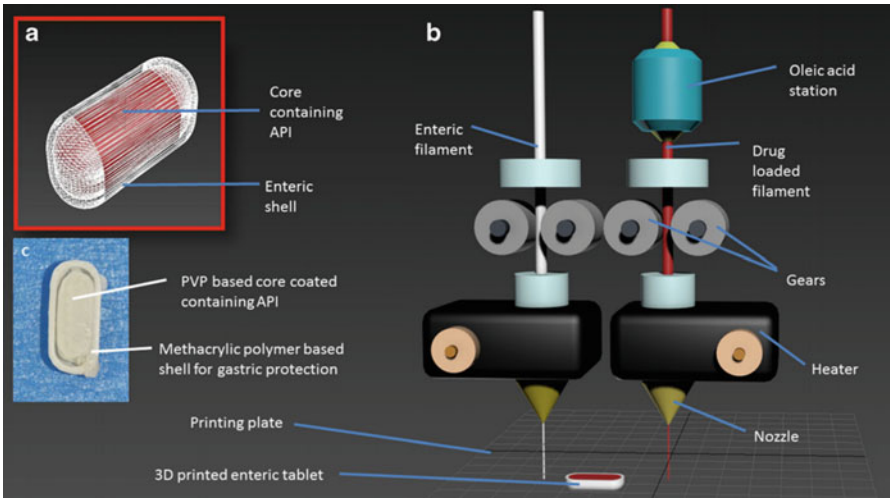

Fig. 16.33 Fabrication of core and shell tablets using dual FDM 3D printer, (**a**) STL file designed via CAD software for core-shell structure, (**b**) dual FDM 3D printer with a lubricating station to facilitate printing, (**c**) a 30% printed shell and core tablet (Okwuosa, T.C., et al., Fabricating a Shell-Core Delayed Release Tablet Using Dual FDM 3D Printing for Patient-Centred Therapy. Pharmaceutical Research, 20,116. 34(2): p. 427–437.)

formulated, i.e., directly compressed physical mixture tablets, directly compressed extrudate tablets and 3D printed tablets at 200 °C (Fig. 16.35). The dissolution profile confirmed that the drug release rate was EXT > PMT > 3DP.

Goyanes et al. [39] fabricated modified-release dosage forms using different grades of pharmaceutical excipient hypromellose acetate succinate (HPMCAS): LG, MG and HG. The formulation was named as printlets (Fig. 16.36). It was determined from the formulations that delayed-release dosage form can be fabricated without the need of any coating. Paracetamol was used as an API in a loading ratio of 5% and 50% w/w. Methylparaben was used as a plasticiser in a ratio of 15%, while a lubricant magnesium stearate was used in a ratio of 5%. The rest of the mixture was a polymer in a proportion of 75 and 40% for 5 and 50% of paracetamol, respectively. The printing was carried out at a temperature of 180–190 °C.

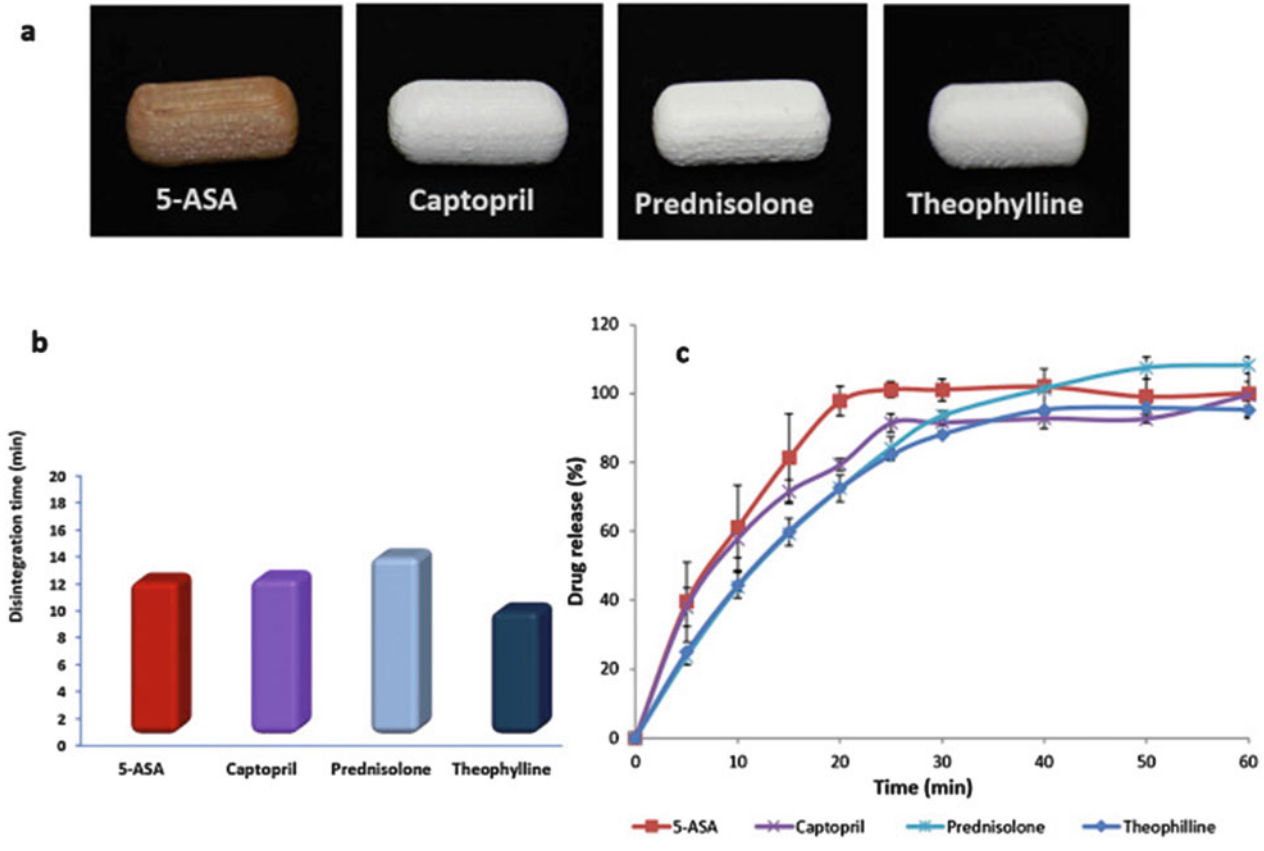

Fig. 16.34 (**a**) 3D printed tablets containing model drugs, (**b**) disintegration time of tablets, (**c**) drug release profile of immediate-release tablets (Sadia, M., et al., Adaptation of pharmaceutical excipients to FDM 3D printing for the fabrication of patient-tailored immediate release tablets. Int J Pharm, 2016. 513(1–2): p. 659–668.)

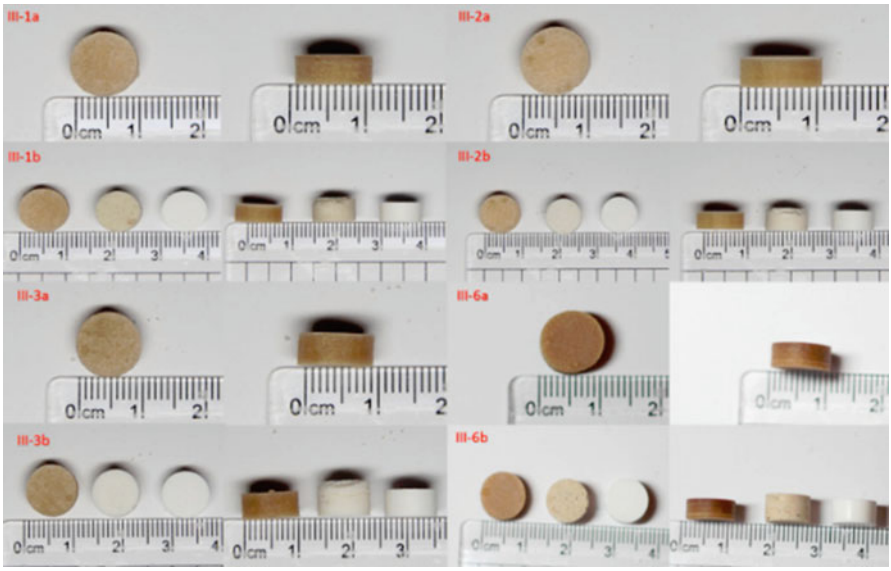

Fig. 16.35 (**a**) 3D printed tablets; (**b**) 3D printed tablets (*left*), extrudate tablets (*centre*), physical mixture tablets (*right*). (Zhang, J., et al., Coupling 3D printing with hot-melt extrusion to produce controlled-release tablets. Int J Pharm, 2017. 519(1–2): p. 186–197.)

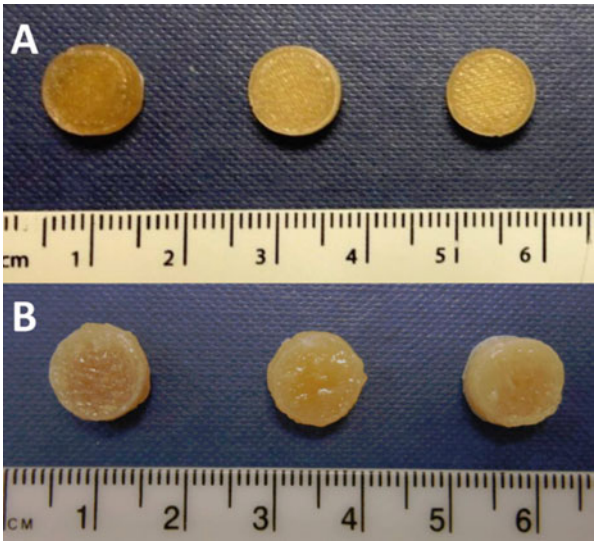

Fig. 16.36 Printlets having (**a**) 5% paracetamol and (**b**) 50% paracetamol. From *left*: HPMAC LG, MG and HG (Goyanes, A., et al., Development of modified release 3D printed tablets (printlets) with pharmaceutical excipients using additive manufacturing. International Journal of Pharmaceutics, 2017. 527 (1–2): p. 21–30.)

16.4 Conclusions

High interest and researches to explore the benefits of 3D printing of pharmaceuticals make it suitable for the future of manufacturing. It can fabricate the products with distinct releasing profiles and different geometries which is challenging otherwise. For the personalisation of the dosage form, it can be kept closer to the patient, e.g., hospital pharmacies and community pharmacies. The accuracy of dose makes it more reliable especially for the drugs having narrow therapeutic indices. Moreover, the multi-active polypill with distinct release profiles decreases the number of tablets taken per day and in return increases adherence.

References

1. Melchels FPW, Feijen J, Grijpma DW (2010) A review on stereolithography and its applications in biomedical engineering. Biomaterials 31(24):6121–6130
2. Khaled SA et al (2015) 3D printing of five-in-one dose combination polypill with defined immediate and sustained release profiles. J Control Release 217:308–314
3. Garber AJ et al (2003) Efficacy of glyburide/metformin tablets compared with initial monotherapy in type 2 diabetes. J Clin Endocrinol Metab 88(8):3598–3604
4. Murphy SV, Atala A (2014) 3D bioprinting of tissues and organs. Nat Biotechnol 32 (8):773–785
5. CSC Leading Edge Forum (2012) 3D printing and the future of manufacturing. FALL. 36.
6. Deckard CR (1989) Method and apparatus for producing parts by selective sintering. Google Patents.
7. Crump SS (1992) Apparatus and method for creating three-dimensional objects. Google Patents.
8. Hull CW et al. (1994) Method and apparatus for production of high resolution three-dimensional objects by stereolithography. Google Patents.
9. Verma A, Rai R (2013) Energy efficient modeling and optimization of additive manufacturing processes. In solid freeform fabrication symposium, Austin, TX.
10. Leong KF et al (2001) Fabrication of porous polymeric matrix drug delivery devices using the selective laser sintering technique. Proc Inst Mech Eng H 215(2):191–201
11. Jacob J (2014) et al. Rapid disperse dosage form containing levetiracetam. Google Patents.
12. Katstra WE et al (2000) Oral dosage forms fabricated by three dimensional printing. J Control Release 66(1):1–9
13. Rowe CW et al (2000) Multimechanism oral dosage forms fabricated by three dimensional printing. J Control Release 66(1):11–17
14. Chia HN, Wu BM (2015) Recent advances in 3D printing of biomaterials. J Biol Eng 9:4
15. Khaled SA et al (2014) Desktop 3D printing of controlled release pharmaceutical bilayer tablets. Int J Pharm 461(1–2):105–111
16. Skowyra J, Pietrzak K, Alhnan MA (2015) Fabrication of extended-release patient-tailored prednisolone tablets via fused deposition modelling (FDM) 3D printing. Eur J Pharm Sci 68:11–17
17. Pietrzak K, Isreb A, Alhnan MA (2015) A flexible-dose dispenser for immediate and extended release 3D printed tablets. Eur J Pharm Biopharm 96:380–387
18. Melocchi A et al (2015) 3D printing by fused deposition modeling (FDM) of a swellable/erodible capsular device for oral pulsatile release of drugs. J Drug Deliv Sci Technol 30(Part B):360–367

19. Wang J et al (2016) Stereolithographic (SLA) 3D printing of oral modified-release dosage forms. Int J Pharm 503(1–2):207–212
20. Wang C-C et al (2006) Development of near zero-order release dosage forms using three-dimensional printing (3-DP™) technology. Drug Dev Ind Pharm 32(3):367–376
21. Huang W et al (2007) Levofloxacin implants with predefined microstructure fabricated by three-dimensional printing technique. Int J Pharm 339(1–2):33–38
22. Yu DG et al (2009) Novel drug delivery devices for providing linear release profiles fabricated by 3DP. Int J Pharm 370(1–2):160–166
23. Yu DG et al (2009) Novel oral fast-disintegrating drug delivery devices with predefined inner structure fabricated by three-dimensional printing. J Pharm Pharmacol 61(3):323–329
24. Wu BM et al (1996) Solid free-form fabrication of drug delivery devices. J Control Release 40 (1–2):77–87
25. Khaled SA et al (2015) 3D printing of tablets containing multiple drugs with defined release profiles. Int J Pharm 494(2):643–650
26. Goyanes A et al (2015) 3D printing of medicines: engineering novel oral devices with unique design and drug release characteristics. Mol Pharm 12(11):4077–4084
27. Goyanes A et al (2015) Fabrication of controlled-release budesonide tablets via desktop (FDM) 3D printing. Int J Pharm 496(2):414–420
28. Goyanes A et al (2014) Fused-filament 3D printing (3DP) for fabrication of tablets. Int J Pharm 476(1–2):88–92
29. Goyanes A et al (2015) 3D printing of modified-release aminosalicylate (4-ASA and 5-ASA) tablets. Eur J Pharm Biopharm 89:157–162
30. Goyanes A et al (2015) Effect of geometry on drug release from 3D printed tablets. Int J Pharm 494(2):657–663
31. Water JJ et al (2015) Three-dimensional printing of drug-eluting implants: preparation of an antimicrobial polylactide feedstock material. J Pharm Sci 104(3):1099–1107
32. Weisman JA et al (2015) Antibiotic and chemotherapeutic enhanced three-dimensional printer filaments and constructs for biomedical applications. Int J Nanomedicine 10:357–370
33. Sun Y, Soh S (2015) Printing tablets with fully customizable release profiles for personalized medicine. Adv Mater 27(47):7847–7853
34. Alhijjaj M, Belton P, Qi S (2016) An investigation into the use of polymer blends to improve the printability of and regulate drug release from pharmaceutical solid dispersions prepared via fused deposition modeling (FDM) 3D printing. Eur J Pharm Biopharm 108:111–125
35. Okwuosa TC et al (2016) A lower temperature FDM 3D printing for the manufacture of patient-specific immediate release tablets. Pharm Res 33(11):2704–2712
36. Okwuosa TC et al (2017) Fabricating a shell-core delayed release tablet using dual FDM 3D printing for patient-Centred therapy. Pharm Res 34(2):427–437
37. Sadia M et al (2016) Adaptation of pharmaceutical excipients to FDM 3D printing for the fabrication of patient-tailored immediate release tablets. Int J Pharm 513(1–2):659–668
38. Zhang J et al (2017) Coupling 3D printing with hot-melt extrusion to produce controlled-release tablets. Int J Pharm 519(1–2):186–197
39. Goyanes A et al (2017) Development of modified release 3D printed tablets (printlets) with pharmaceutical excipients using additive manufacturing. Int J Pharm 527(1–2):21–30

Chapter 17
Manufacturing, Numerical and Analytical Model Limitations in Developing Fractal Microchannel Heat Sinks for Cooling MEMS, Microelectronics and Aerospace Components

T.E. Kode, A.A. Ogwu, A. Walker, M. Mirzaeian, and H. Wu

17.1 Introduction

As a background to this book chapter, the thermal hydraulic properties of fluids in microchannels have been reviewed. Figure 17.1 (Qu and Mudawar) [1] is an electronic component on top of a microchannel heat sink.

In Fig. 17.1, a number of straight microchannels can be seen within the microchannel heat sink. Each of these microchannels divides the bottom surface areas equally. Fluid is allowed to pass through each of the microchannels to remove the heat generated from the electronic component.

Since the microchannels are equidistant from each other, a given microchannel can be observed and analysed as shown. As such, critical dimensions of the given microchannel are given as a, b, c, A, B and C which are channel top wall (a), channel sidewall (b), channel bottom wall (c), heat sink top wall (A), heat sink sidewall (B) and heat sink bottom wall (C), respectively. It is worthy of note that these dimensions represent all the critical surface areas for both the microchannel and the heat sink.

This is because these dimensions define the ratio of microchannel volume to the outer solid volume of the microchannel heat sink. This is important since the cooling fluid fills the channel volume.

T.E. Kode • A.A. Ogwu (✉) • M. Mirzaeian
School of Engineering and Computing, University of the West of Scotland,
Paisley PA1 2BE, UK
e-mail: Abraham.ogwu@uws.ac.uk

A. Walker
School of Mathematics and Statistics, University of the West of Scotland,
Paisley PA1 2BE, UK

H. Wu
School of Engineering and Computing, University of Hertfordshire, Hartfield AL10 9AB, UK

M.J. Jackson, W. Ahmed (eds.), *Micro and Nanomanufacturing Volume II*,
DOI 10.1007/978-3-319-67132-1_17

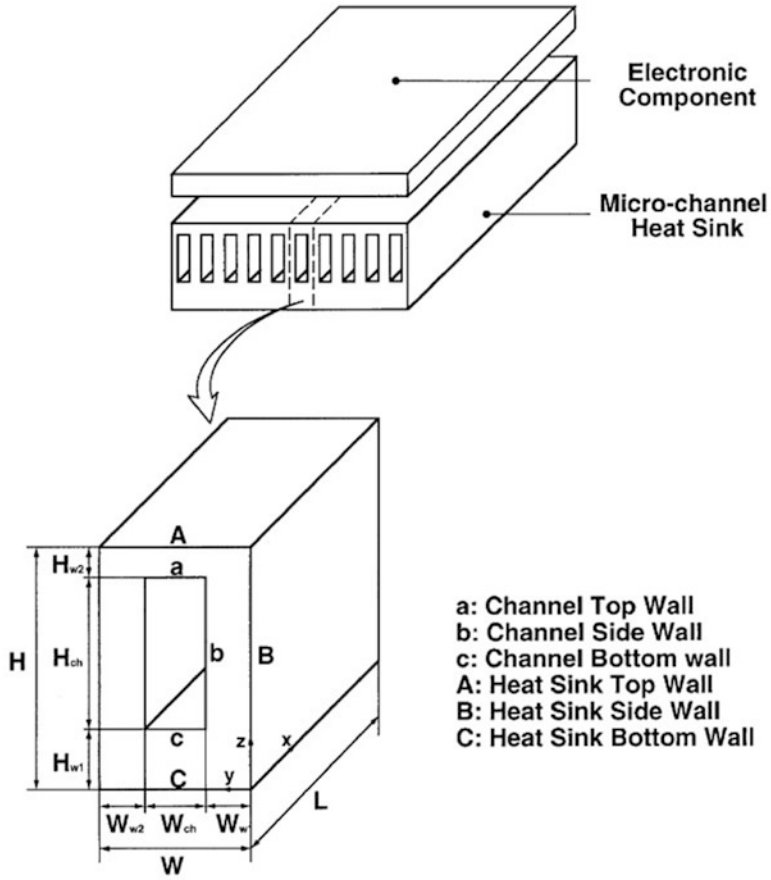

Fig. 17.1 A microchannel heat sink used to cool an electronic component (Qu and Mudawar [1])

17.2 Applications of Microchannels

Applications of microchannels are found in the following cooling systems. In these applications, the objective is to have a cap on a defined maximum temperature on the substrate being cooled. It is also desirable to have uniform temperature distribution for optimal operation of the components on the substrate.

17.2.1 Microchannel Absorber

Figure 17.2 (Kim et al.) [2] is a description of microchannel absorber in miniature electronics cooling system. The main components of the absorption heat pump system include the evaporator, condenser, absorber, desorber, liquid pump and

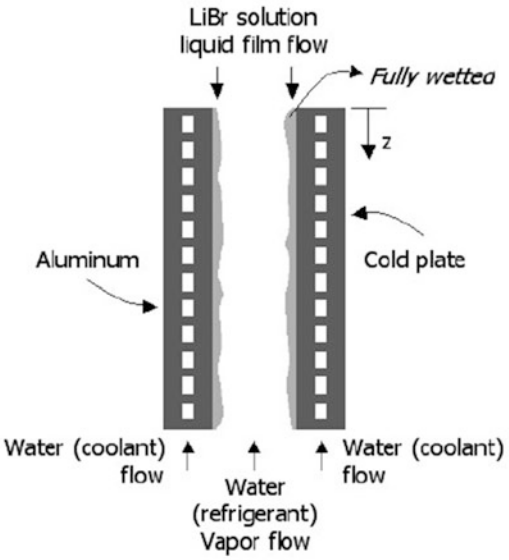

Fig. 17.2 Liquid-cooled microchannel absorber (Kim et al. [2])

expansion devices. In this absorption/desorption process, water/LiBr is used in a condensation/evaporation cycle. As shown in Fig. 17.2, water vapour[1] is absorbed by the strong LiBr solution.

The coolant water allowed to flow through the microchannels is used to take away heat from the vapour. In the process, condensation occurs, and the vapour is absorbed into the LiBr solution. The same process occurs in Fig. 17.3 except that air is the coolant used to take heat away through fin arrays.

17.2.2 Microchannel Tube Banks

Figure 17.4a is the housing for the absorber. The housing has sight ports so that solution flow mechanisms can be visualized. In Fig. 17.4b are microchannel tube arrays, which are also in the housing. These array of tubes have a number of tubes per row and allow for both series and parallel flows. Figure 17.4c is a drip tray that has some tubes attached to it in each of its holes. These allow for solution droplets on the coolant tubes (Nagavarapu et al.) [3].

[1]This occurs when the water/LiBr solution goes through the evaporator.

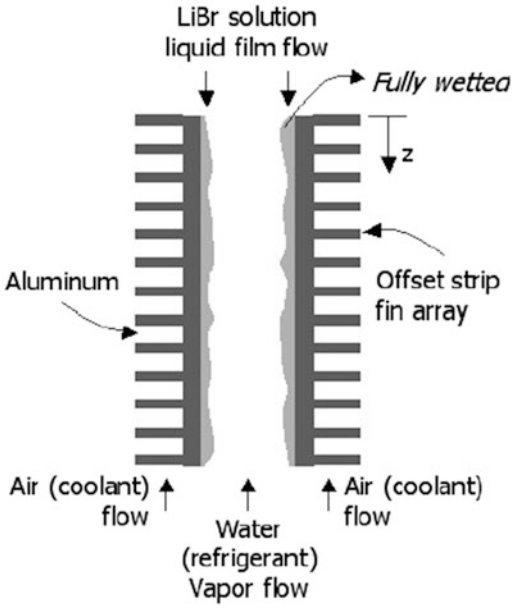

Fig. 17.3 Air-cooled microchannel absorber (Kim et al. [2])

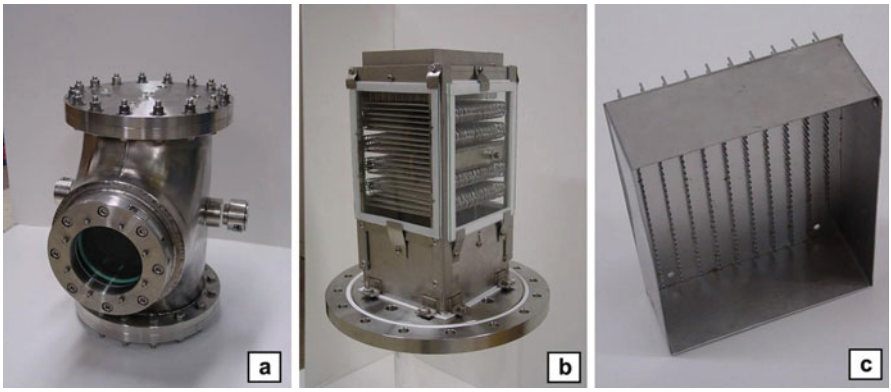

Fig. 17.4 Microchannel tube banks fuel cells (Nagavarapu et al. [3])

17.2.3 Microchannel Tube Banks

Figure 17.5a shows the constructional features of a planar solid oxide fuel cell (Manglik and Magar) [4]. An electrolyte is placed between the cathode (oxygen) and anode (hydrogen). Air is allowed to pass through the interconnectors. As it flows through, oxidation occurs resulting in production of hydrogen and oxygen ions. Figure 17.5b is a description of the movement of ions in the production of water and unused gases. In Fig. 17.5a, rectangular interconnector ducts are used.

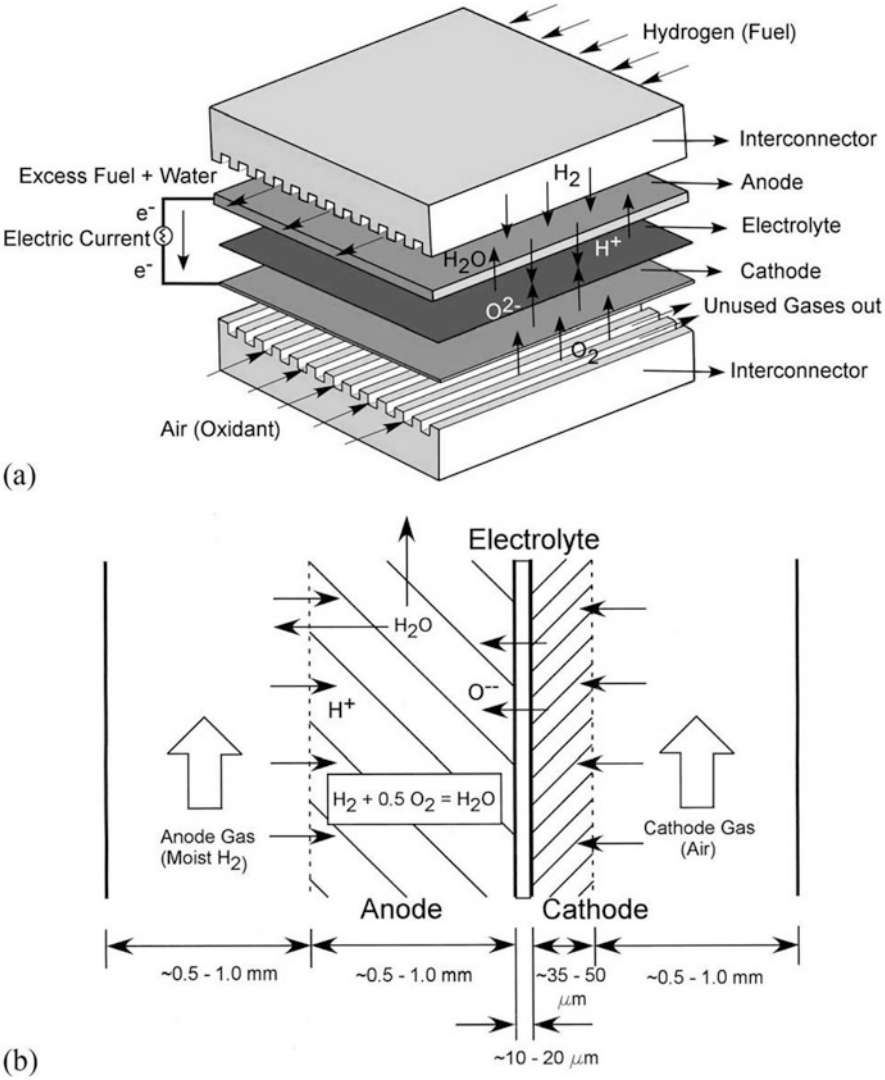

Fig. 17.5 Schematic representation of a typical planar solid oxide fuel cell: (**a**) single cell stack or module and (**b**) stack dimensional configuration and volatile species/oxidant transport (Manglik and Magar [4])

Because of mass transport across the interconnectors and electrodes, electrochemical effects are coupled with the convective heat transfer. Manglik and Magar [4] further considered the effect of different cross-sectional interconnector ducts on the coupled heat and mass transfer equations.

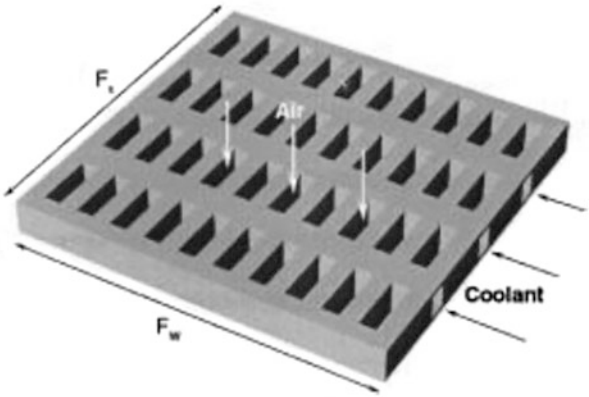

Fig. 17.6 Microchannel heat exchanger radiator engine cooling system (Fell et al. [5])

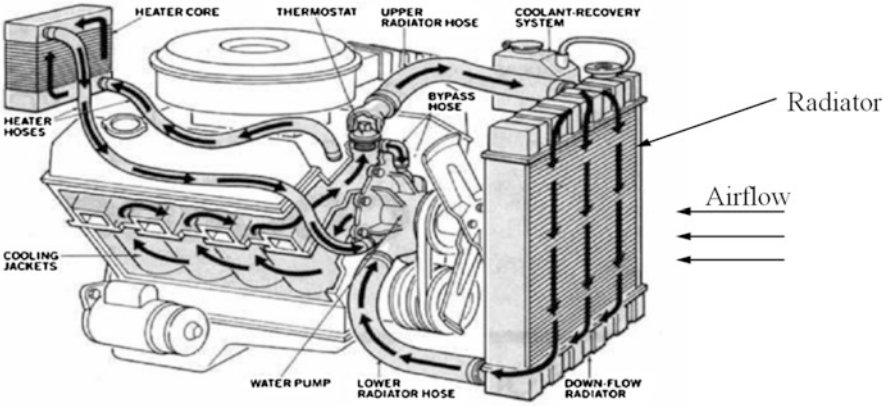

Fig. 17.7 Radiator engine cooling system (Fell et al. [5])

17.2.4 Heat Exchanger

Figure 17.6 (Fell et al.) [5] shows the mechanism behind a radiator heat exchanger application. This is an improved design for radiators. Here, transverse slots are made to allow air through the heat exchanger. This further improves the cooling process as it aids the heat removal process by the liquid coolant.

In Fig. 17.7 [5], the coolant is passed from the engine to the microchannels through pumps. The arrows indicate the paths the coolant follows in the engine cooling system below. The coolant takes the heat away as it passes through the microchannels in the radiator. The radiator can be seen as a component of the engine cooling system. The heat is transferred from the coolant to air around the radiator.

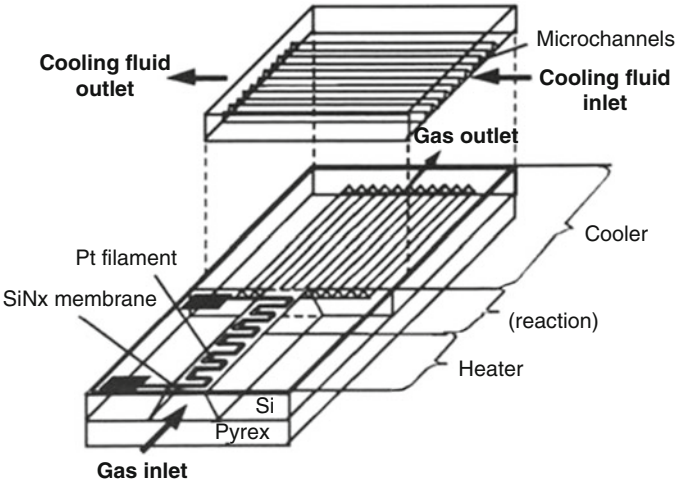

Fig. 17.8 Microchannel reactors (Alepee et al. [6])

17.2.5 Microreactors

In this microchannel reactor, rapid heating and cooling are desired. In the heater section, Pf filaments are used to heat the SiNx membrane. A gas is allowed to flow through the heating duct. Cooling fluid is also allowed to flow through the microchannels as shown. This implies that there is heat transfer from the hot gas to the coolant fluid. As such, this is a heat exchanger configuration. The fluids used could be either gas/gas or gas/liquid. In Fig. 17.8, the direction of fluids is at right angles to each other. The coolant fluid flows into microchannels etched by HF into one of the Pyrex covers, while those for the hot gas are machined by deep plasma etching of the silicon layer (Alepee et al.) [6].

17.3 Why Microchannels?

Recent advancements in microelectronics and biotechnologies have precipitated further research in micro-coolers, micro-biochips, micro-reactors and micro-fuel cells. This has created the need to adapt microchannels for the use in these microfluidic systems (Teng et al.) [7]. Microchannels have very small widths within the range $200\,\mu m \geq D_c > 10\,\mu m$ 200 (Teng et al.) [7]. In Fig. 17.9, microchannels are embedded in a rectangular volume. Figure 17.9 can be derived from Fig. 17.1.

The source of heat can be applied to any surface area besides the front view.

Microchannels are efficient for heat transfer because they have high surface area to volume ratio.

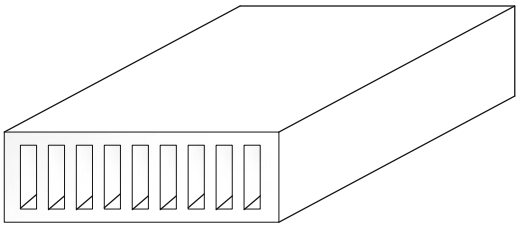

Fig. 17.9 Conventional straight microchannel

It can also be argued that microchannels have high heat transfer coefficient since they have high surface area to volume ratio. This has a cumulative effect considering a number of microchannels used to cool a given substrate (heat-generating device) surface area. This further enhances uniform temperature distribution on the substrate since the heat transfer in the individual microchannels is maximized.

However, even with this number of advantages, there is the issue of high pressure drop. Moreover, the problem of hot spots on the surface of the substrate is also a concern in cooling systems.

17.3.1 Impact Factors

The thermal performances of fluids in microchannel are dependent on certain specifications such as aspect ratio $\frac{w}{l}$ and length to hydraulic diameter ratio,

where w is the width of microchannel and l is the length.

The aspect ratio $\frac{w}{l}$ is less than one.

These specifications define individual microchannel designs. For example, Zhang et al. [8] demonstrated that for a fractal microchannel with 90° bifurcations, an optimized aspect ratio of 0.333 compared to aspect ratios 1 and 0.5 yielded a reduced pressure drop and better heat transfer performance as the Reynolds number increased.

In Fig. 17.10, Escher et al. [9] obtained the parallel network with straight microchannels. The slanting top channel was improvised to obtain uniform pressure drop across the straight microchannels. Escher et al. [9] compared the thermal performances of the branching straight microchannel and the fractal microchannel. This was done considering equal substrate surface areas for both channels.

A performance index was obtained to determine the heat removal rate given input heat flux. This was used as a basis for comparisons of the thermal performances of both microchannels.

From both examples above, it can be inferred that to get an optimal thermal performance, the pressure drop and maximum temperature on the substrate must be minimized.

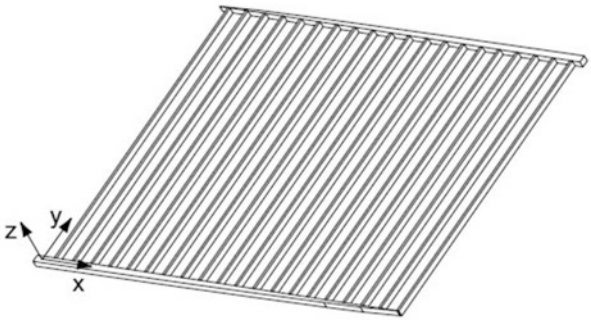

Fig. 17.10 Parallel channel network with straight microchannels (Escher et al. [9])

17.4 Microchannel Designs in the Literature

It can be observed that the geometry of the microchannels is very important in the determination of its thermal performance. For example, two microchannel designs can have equal convective surface areas and different thermal performances. This is because of varying flow paths for the individual designs. This further determines the fluid temperature distribution given the surface area of the substrate. As such, the difference in thermal performance is the result of varying velocity and temperature profiles.

It therefore becomes important to note the inlet and outlet thermal conditions of the fluid. This further involves a careful consideration of a number of parameters such as the friction factor, length to hydraulic diameter ratio and aspect ratio which are essential in the determination of the thermal performance of microchannels.

The friction factor and length to hydraulic diameter ratio are hydraulic parameters of the fluid. The aspect ratio, which is the ratio of the width to the length, is a value independent of the cross-sectional shape of the microchannel.

It therefore follows that the cross-sectional shape is also a variable in the modelling of thermal performance of the microchannel. As such, authors have further compared thermal performances of microchannel designs based on cross-sectional area.

Furthermore, the length of the microchannels has been modified by introducing channels with re-entrant cavities of varying shapes, zig-zag channels and wavy channels. The thermal performances of all these channels have been investigated experimentally, numerically and analytically given different phase/working fluid conditions. This is summarized in the Table 17.1.

17.5 Towards New Designs

It is observed that some of the microchannel designs considered in the literature are optimum considering models intended to minimize pressure drop, while others are optimum with minimized thermal resistance models.

Table 17.1 Critical review of thermo-hydraulic properties of fluids in microchannels

Type of microchannel/material	Phase/ working fluid	Experimental/numerical (steady/transient)/ analytical	References
Fractal/silicon	Single/DI water	Numerical/steady	Zhang et al. (2015) [8]
Y shaped	Single	Analytical	Salimpour and Menbari (2015) [10]
Fan-shaped re-entrant cavities/ silicon	Single/ water	Numerical/steady	Xia et al. (2015) [11]
Rectangular	Two	Experimental	Keepaiboon and Wongwises (2015) [12]
Micro heat exchanger with chevron and straight flow paths	Two	Experimental	Liu and Yang (2014) [13]
Hexagonal, circular and rhombus	Single/ water	Numerical/steady	Alfaryjat et al. (2014) [14]
Y channel/silicon	Single/DI water	Analytical/numerical (steady)/experimental	Yu et al. (2012) [15]
Circular, rectangular, triangular, trapezoidal grooves	Single/air	Numerical/steady	Ramadhan et al. (2012) [16]
Y shaped	Single	Analytical/numerical (steady)	Ghaedamini et al. (2012) [17]
Triangular duct with serpentine path	Single/ water	Numerical/steady	Mohammed et al. (2011) [18]
Triangular duct with serpentine path	Single/ water	Numerical/steady	Chai et al. (2011) [19]
Rectangular	Single/air	Numerical/unsteady	Wang et al. (2011) [20]
Triangular duct with serpentine path	Single/ water	Numerical/steady	Gupta et al. (2008) [21]

A desirable microchannel is such that has optimum performance given minimized pressure drop and thermal resistance models.

It is clear from the foregoing that the geometry is a key factor in determining the thermal performance of microchannels. As such, researchers have examined and compared the thermal performances of various microchannel designs considering the relevant parameters.

This has led to useful insights into optimized microchannel designs. However, there is still need for novel designs in various microchannel applications. As such, we consider two microchannel designs.

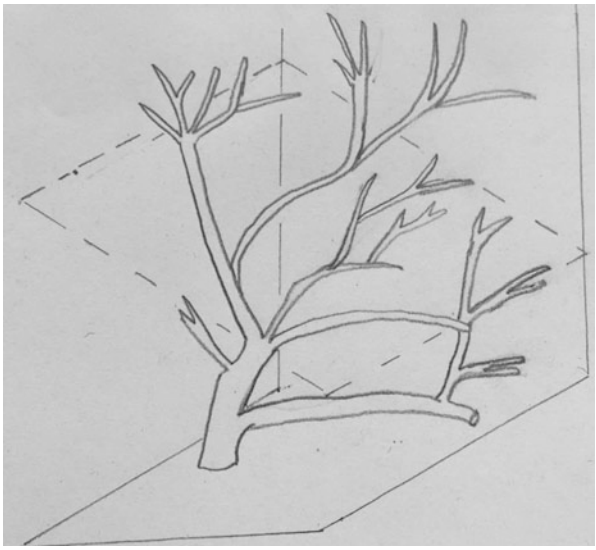

Fig. 17.11 Elliptic fractal microchannel (Kamiya and Takahashi [22])

17.5.1 Elliptic Fractal Microchannels

Figure 17.11 is an elliptic fractal channel 3D structure (Kamiya and Takahashi) [22]. As the name implies, the cross-sectional area of this channel is an ellipse. The mean velocity and the Reynolds friction factor $f\mathrm{Re}_{\sqrt{A}}$ can be derived analytically for fully developed flow as shown by Bahrami et al. [23]. This is done considering the aspect ratio, cross-sectional area A and perimeter.

The aspect ratio, cross-sectional area and perimeter of the elliptic channel can be varied to observe the effects on the thermal and hydraulic parameters for each branching length of the elliptic fractal channel cooling system.

17.5.2 Microchannel with Transverse Ribs in Longitudinal Direction

Chai et al. [24] considered a rectangular channel with transverse ribs to enhance convective mixing. In this work, the rectangular channel was further redesigned for optimization to reduce the pressure drop along the channels to minimum while increasing the heat transfer coefficient.

The optimized microchannel with ribs in the transverse microchambers is shown in Fig. 17.12. The dimensions w, l, d and s are the width, the length of the rectangular rib, the distance from the parallel microchannels to the rib row and the space between two adjoining transverse microchambers, respectively.

These dimensions can be varied to obtain an optimal thermal performance.

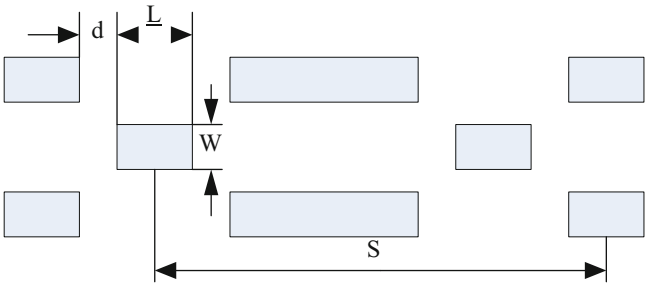

Fig. 17.12 Optimized microchannel with transverse microchambers (Chai et al. [24])

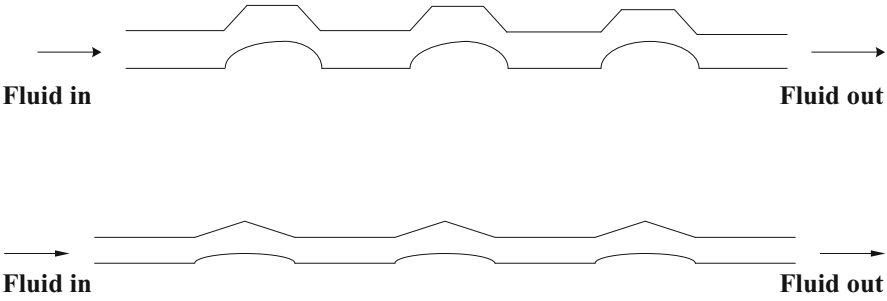

Fig. 17.13 Modified designs

17.5.3 Modified Designs

Having considered the optimization ideas, some modified designs are considered in Fig. 17.13. In Fig. 17.13, the interventions along the straight channel are chosen to achieve optimum thermal performance. The microchannels are like a hybrid of zig-zag and wavy microchannels. As such, one could assume that the thermal properties of both microchannels mentioned are optimized for thermal performance.

The numerical simulation of the heat and mass transfer in these channels in Fig. 17.13 would further give insights into potential modifications that would yield enhanced thermal performance.

17.6 Fractal Microchannels for MEMS, Microelectronics and Aerospace Components

Of all the channels considered, fractal microchannels are unique in the sense that they have a self-repetitive nature. This expands across both the length and breadth of a given surface like a tree. As a result, it is believed that fractal microchannels

have optimum performance that is independent of a given surface area. In essence, the thermal performance of fractal channels is consistent over a range of surface areas, starting from the smallest possible surface area to a projected one. As such, it can be argued that fractal microchannels are suitable for cooling microsurface area substrates.

The use of fractal microchannel heat sinks for cooling microelectronics and aerospace components is quite attractive. This is because of customer demand for microelectronics having more computing power (Alharbi et al.) [25]. However, the continued miniaturization of these components has led to more complex electronic circuitry, increased heat flux and power density on the surface area of the component.

In essence, improved heat exchanger systems are required in industries such as aviation, solar, food and chemical to remove the increased heat flux due to high customer demand. In order to address heat transfer issues in these industries, research on the thermo-hydraulic properties of fluids in microchannel heat exchangers has increased significantly. This research has centred on obtaining satisfactory levels of convective mixing as the fluid passes through the microchannels and still obtaining minimal pressure drop. In essence, the ultimate requirement is to obtain maximum heat transfer coefficient and minimum pressure drop.

The necessary conditions to attain optimum thermo-hydraulic performance as stated above are specified, given:

$$h = \frac{q}{\Delta t} \tag{17.1}$$

where h is the heat transfer coefficient[2] and q is the heat removal rate. The first condition is that the solid-fluid temperature difference $\Delta t \rightarrow 0$. The other condition is that $0 < \tilde{\mathrm{p}} < \mathrm{b}$ where b is the maximum allowable pressure drop.

This is essential to prevent hot spots which arise from the fluid temperature increasing along the channel length (Zhang et al.) [8] while maintaining minimum pressure drop. As such, temperature uniformity on the substrate (microelectronic device) cooled by the heat sink is essential. This is to ensure safe operation of the microelectronic device. However, other scaling factors such as axial conduction in the fluid and channel walls also negatively affect the desired uniform heat transfer.

Normally, the electrical engineer determines the maximum junction temperature at which a microelectronic device must operate. This specification will then be given to the thermal engineer to work with and design a suitable cooling system. However, it is important for the thermal engineer to have fore knowledge of electronic circuits in order to work effectively with the electrical engineer in determining the maximum operating temperature for the microelectronic device.

[2]The heat transfer coefficient is further explained in Eq. 17.2.

In this book chapter, we shall focus on the analytical and numerical modelling of the thermal performance of fractal microchannel heat sinks. This is because of its inherent ability to help achieve uniform temperature distribution on a substrate. In this regard, we shall report on the analytical and numerical model limitations of fractal microchannel heat sinks in obtaining optimum uniform temperature distributions.

In section 1, we consider the analytical model limitations of fractal microchannels. In section 2, we consider the numerical model limitations.

17.7 Section 1

17.7.1 Cooling Mechanisms in Heat Sinks

In this section, we shall start by a review of two different simple cooling systems in microelectronic applications. This is done to give the reader some background knowledge useful in analytical modelling of heat and mass transfer problems.

17.7.1.1 Newton's Convective Cooling

In this cooling system in Fig. 17.14, a moving fluid is used to take heat away from the system. The heat dissipation rate is given by

$$q = h(T_s - T_\infty) \tag{17.2}$$

where q is the surface heat flux, h is the heat transfer coefficient, T_s is the surface temperature of the electronic device and T_∞ is the fluid temperature at a point far from the surface (Jiji) [26].

Equation (17.2) is the Newton's law of convective cooling for internal flows.[3] From Eq. (17.2), it can be seen that the thermal engineer must be able to determine precisely the rate of cooling of the system. This is necessary in the determination of the safe maximum operating junction temperature for the microelectronic device.[4]

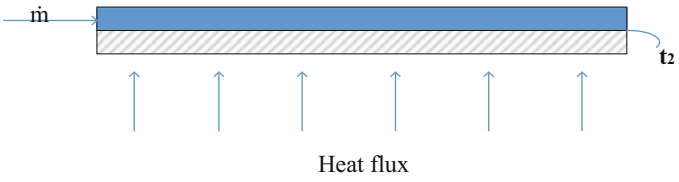

Fig. 17.14 Convective cooling

[3]External flow is not considered here because of the purpose of our illustration.

[4]Maximum junction temperature is not indicated in the simple equation.

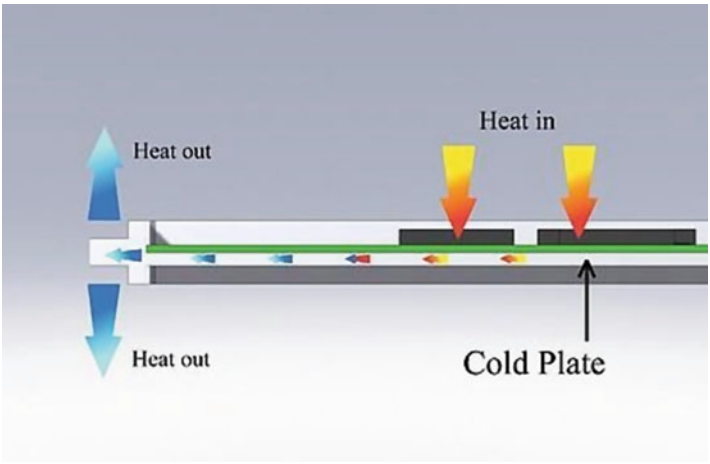

Fig. 17.15 Conduction path from heat source to sidewall (http://www.thermacore.com/news/novel-conduction-cooling-techniques.aspx)

The rate of cooling can easily be related to the mass flow rate of the coolant. However, there are other contributory factors affecting the heat dissipation rate of the system.

For the purpose of illustration, consider the schematic microchannel below. Heat is applied as shown, and we desire to put a cap on the maximum temperature t_2 at the surface of the substrate (microelectronic device). This can be done by minimizing the fluid surface thermal resistance.[5]

17.7.1.2 Conduction Cooling

In certain microelectronic applications, we do not require fluid to take the heat away. This is because of the space needed for convection ducts (Bejan) [28]. In this case, we require high thermal conductivity materials to conduct heat away from the device.

Consider the diagram in Fig. 17.15, heat is applied and flows out in the direction of the arrow as shown in Fig. 17.15.

In this case, the temperature distribution at the base of the cold plate is given by

$$\frac{\partial^2 T}{\partial x^2} = A\left(\frac{\partial T}{\partial y} + \frac{\partial T}{\partial z}\right) \tag{17.3}$$

[5]Intuitively it can be seen that the thermal resistance is a function of the width of the substrate (Vermeersch and De Mey) [27].

where y and z are dimensions of the cold plate (the cold plate is adjoined to a fin or conduction path) and x is the dimension of the heat flow path. T is the temperature; interfacial thermal resistance A is a function of the ratios of the thermal conductivities, thermal diffusivities, aspect ratios of the fin and the cold plate and heat flux.

The first term in Eq. (17.3) gives a description of variation of heat flux from the point the heat is applied to the point it is taken away. The temperature distribution on the cold plate is given by the second and third terms in Eq. (17.3).

Considerations

Here, we consider other factors necessary for an overview of the thermal conditions of the cooling system in Fig. 17.14. It should be noted from the two immediate preceding subsections that some terms in the Navier-Stokes energy equation in Eq. (17.4) are left out:[6]

$$\rho c_p \frac{\partial T}{\partial t} + \rho c_p u.\nabla T = \nabla.(k\nabla T) + Q \tag{17.4}$$

The second term in the equation above has not yet been considered. This is a product containing the fluid velocity and temperature profiles. These quantities can only be determined if the heat transfer coefficient and thermal conductivity are known. The relevant equation in this regard is given below:

$$Nu = \frac{h}{k}L \tag{17.5}$$

where Nu is the Nusselt number, h is the heat transfer coefficient, k is the thermal conductivity of the fluid and L is the characteristic length of the microchannel.

Furthermore, the thermal resistance of the convective cooling system has not been considered with respect to the finite heat capacity of the fluid. Similarly, in the conduction cooling system in Fig. 17.15, the thermal resistance has not been considered.

In convective cooling, there is heat transfer from the heated surface t_2 to the fluid in the microchannel as shown in Fig. 17.14. During this process, there is thermal resistance between the fluid-surface interface. This resistance is given by Nnanna [29]:

$$R_{th1} = \frac{T_{\max} - T_{in}}{q} \tag{17.6}$$

[6]This is because simple models were considered. For example, in Eq. (17.2), the heat dissipation rate can be determined if the dependent variables are known. In addition, conduction and convective cooling were considered separately.

T_{in} is the fluid inlet temperature, $T_{\max}$ is the maximum surface temperature, and q is the heat flux.

In the case of conduction cooling in Fig. 17.15, the thermal resistance is at the interface where the cold plate joins the heat flow path.

The thermal resistance is given by

$$R_{th2} = f(A) \tag{17.7}$$

The thermal resistance in Eq. (17.7) is a function of A. Note that the parameter A has been defined earlier.

From Eq. (17.2), it can be seen that the fluid-surface temperature distributions are reliable parameters in the determination of the heat transfer coefficient. In Eq. (17.4), it can be observed that the velocity profiles[7] are important heat transfer parameters in the determination of the maximum fluid-surface temperature difference.

From Eq. (17.3), it can be seen that the temperature distributions on the heat flow path and cold plate are important thermal properties of the system. These parameters are dependent on the interfacial thermal resistance A. The parameter A can be further precisely determined from experiments. This would help determine the rate of cooling.

In convection cooling, the heat transfer coefficient must be accurately determined considering the fluid-surface thermal resistance. The fluid-surface thermal resistance can be determined if the heat transfer coefficient is known. This can be determined given the inlet fluid temperature and surface temperature distributions. Hence, the max surface temperature $T_{\max} < t_2$ can be determined.

17.7.2 Analytical Modelling of Fractal Microchannel Heat Sinks

Here, analytical modelling of fractal microchannel heat sinks in the literature is reviewed. We start by a description of the fractal microchannel.

17.7.2.1 What Are Fractals?

Fractals are self-repetition structures. It is easy to observe the similarity in these structures as one would consider similar triangles. With similar triangles, corresponding angles are equal. The dimensions of the corresponding sides are in proportion. In essence, the triangles retain the same shape. A fractal structure is a combination of similar components.

[7]The average velocity is determined by the mass flow rate.

17.7.2.2 What Are Fractal Microchannels?

Fractal microchannels are such that branch off like trees from one level to the next. An initial length l_0 first branches off into two and keeps branching to fill a given surface area. The lengths and widths of the microchannels succeeding subsequent branches are determined by fixed length and width ratios. This is further explained in the following equation (Chen and Cheng) [30].

Fractal microchannels have angles of bifurcation from 0° to 90°.[8] They are particularly useful in cooling microsurface area substrates. This is because the branching channels have higher heat transfer coefficient than the parent microchannel (Chen and Cheng) [30].[9] As such, this advantage can be utilized at the first branching level given a minimal surface area.

From an initial length, the ratio of succeeding lengths is given as

$$\gamma = \frac{l_{k+1}}{l_k} \tag{17.8}$$

where $\gamma \approx 10^{-3} m$ and k is the branching level.

Then the length at the kth branch is given as

$$l_k = l_0 \gamma^k \tag{17.9}$$

In addition

$$N = \gamma^{-D} \tag{17.10}$$

where D is the fractal dimension.

Hence,

$$\gamma = N^{-\frac{1}{D}} \tag{17.11}$$

For a fractal network to satisfy the relation above, the ratio of hydraulic diameters d_k and d_{k+1} before and after bifurcation is given as

$$d_k^{\Delta} = N d_{k+1}^{\Delta} \tag{17.12}$$

$$N = \left(\frac{d_{k+1}}{d_k}\right)^{-\Delta} \tag{17.13}$$

[8] This means the angular distance between two branches branching out from a parent microchannel is between 0° and 90°.

[9] This is due to the thinning of the thermal boundary layer resulting from a reduced hydraulic diameter. The thinning guarantees higher rate of diffusion of heat.

Δ is the fractal dimension of the hydraulic diameter distribution. The hydraulic diameter ratio is given as:

$$\beta = \frac{d_{k+1}}{d_k} = N^{-\frac{1}{\Delta}} \tag{17.14}$$

$$d_k = d_0 \beta^k \tag{17.15}$$

where d_0 is the inlet hydraulic diameter.

Assuming laminar thermally developed thermo-hydraulic flow, Eq. (17.16) is obtained.[10] This is because the Nusselt number is constant along the length for such flow:

$$\frac{h_{k+1}}{h_k} = \frac{d_k}{d_{k+1}} \tag{17.16}$$

$h_{k,\ hk+1}$ are the heat transfer coefficients before and after the bifurcation at the *kth* level. Substituting Eq. (17.14) into 1.16, Eq. (17.17) is obtained:

$$\frac{h_{k+1}}{h_k} = \frac{1}{\beta} \tag{17.17}$$

$$h_k = h_0 \beta^{-k} \tag{17.18}$$

It can be seen that the heat transfer coefficient multiplies by a certain factor from the zeroth to the *kth* branch. The aim of this book chapter is to examine the limitations of fractal microchannels in cooling applications despite this advantage.

17.7.3 Analytical Model Limitations of Fractal Channels

In order to understand the rationale behind analytical modelling techniques of fractal microchannels and to understand its limitations, it is important to understand the theory behind the development of the fractal microchannels.

This theory known as the constructal theory,[11] (Bejan) [28] was formulated to obtain minimized pressure drop and minimized thermal resistance. In essence, Bejan [28] considered optimization of pressured distributions distinctly from optimization of temperature distributions. In both cases, a fractal-like structure was

[10]Given laminar thermally developed flow, the fluid temperature profile is constant along the length of the microchannel. Hence, the heat transfer coefficient is constant. Equation (17.16) is valid given symmetric flow.

[11]This theory seeks to explain why the structure and dimensions obtained by Chen and Cheng [30] are optimum for heat and mass transfer.

obtained. In order to address the analytical model limitations, we shall only consider in detail the optimization procedure to minimize the thermal resistance.

The optimization procedure for the minimization of the pressure drop distributions is not considered since Bejan [28] has shown satisfactorily that pressure drop minimization can be considered by minimization of flow path lengths.

If one will achieve minimization of the thermal resistance, it implies that the coolant must follow certain optimized paths on the surface area. One way to go about this problem is to start by optimizing elemental volumes of the heat-generating surface. This is done till the entire volume is optimized. This process is known as the constructal theory (Bejan) [28]. It is the theory behind constructal microchannel designs.

The constructal microchannel is desirable in a number of cooling applications. This is because of its ability to minimize pressure loss, minimize the maximum temperature on the substrate and obtain uniform temperature distributions (Pence) [31]. Despite these promising potentials, the constructal channel is limited because the formulation of its design is based solely on geometric constraints.

For example, while it is generally agreed that thinning the thermal boundary layer will enhance the heat transfer coefficient, the enhancement factor of $\frac{h_{k+1}}{h_k} = \frac{d_k}{d_{k+1}}$ in Eq. (17.16) for the fractal microchannel is only based on the ratios of the diameters before and after a bifurcation. Other factors such as variable heat flux along the fluid-surface interface and variable thermal conductivity have not been considered.

In order to address these limitations, the constructal theory behind the development of the constructal channel shall be re-examined.

17.7.3.1 The Constructal Theory

The constructal theory is the principle behind the geometry of the fractal microchannel for microelectronic devices. We take a new approach in the explanation of the constructal theory. However, the idea behind the constructal theory remains the same. As the name implies, the constructal theory illustrates a systematic build-up to the development of the constructal channel.

An example to illustrate the application of this theory would suffice. Our example is suited for fractal microchannels with T and L joints. Assuming a matchbox (cuboid) on an xy plane with its height in the z-axis direction, a schematic picture of the matchbox (cuboid) when opened from its edges in the z direction can be obtained. Starting from the xy origin, we can determine successive points at which to cut through the matchbox given a simple linear equation such as $4x + 3y + 2z = c$. Let c be a constant volume. The justification for this is that the constructal theory is an optimization procedure for microchannels in a given volume.

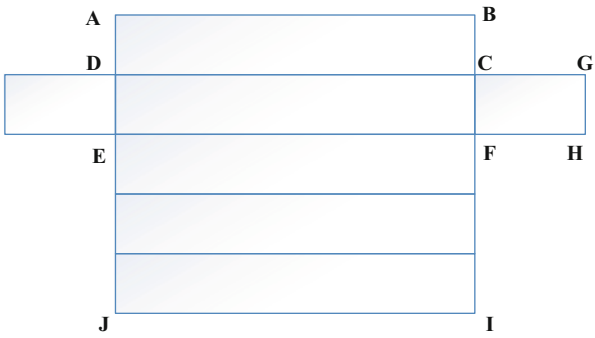

Fig. 17.16 Schematic diagram of opened matchbox

The resulting schematic diagram is shown in Fig. 17.16. This equation is valid as an example, if the total matchbox surface area can be divided into squares of repetitive units. In the same vein, the constructal theory allows for derivation of an optimized volume starting from elemental areas or volumes.[12]

In Fig. 17.16, the number of individual areas of the matchbox cuboid is 7.

So far, we have been able to demonstrate that we can obtain a given number of elemental areas or volumes from a specified volume. Similarly, we can obtain an optimized volume starting from an elemental volume (constructal theory). For convenience, we let the elemental volumes be represented by elemental areas.

In Fig. 17.17, the seven individual volumes of the schematic matchbox are already optimized. This is because it was obtained from cutting through the edges of the 3D matchbox. As such, we do not need to explain the optimization procedure to obtain the surface areas of the volumes.

17.7.3.2 Optimized Thermal Paths

The constructal theory has potential designs for minimization of the maximum thermal resistance. This is done by determining the correct number of optimized volumes. These optimized volumes are then arranged in a certain order to allow the optimized thermal paths through them. Interestingly, our example meets all the above criteria. We only need to include the optimized path lengths in the optimized volumes.

If we decide to remove the rectangular area ABCD[13] in Fig. 17.16 and draw four thin thermal conductivity stripes to divide equally the areas along its length as shown in Fig. 17.17a, we have the structure in Fig. 17.17b.

[12]The optimization starts with elemental volumes. We refer to elemental areas for the purpose of illustration. As such, in a sense, 'areas' and 'volumes' can be used interchangeably.

[13]We decided to adjust the shape and volume of our starting template. The high thermal conductivity path length KL in Fig. 17.17 would best serve volume element ABCD than EFJI in Fig. 17.16.

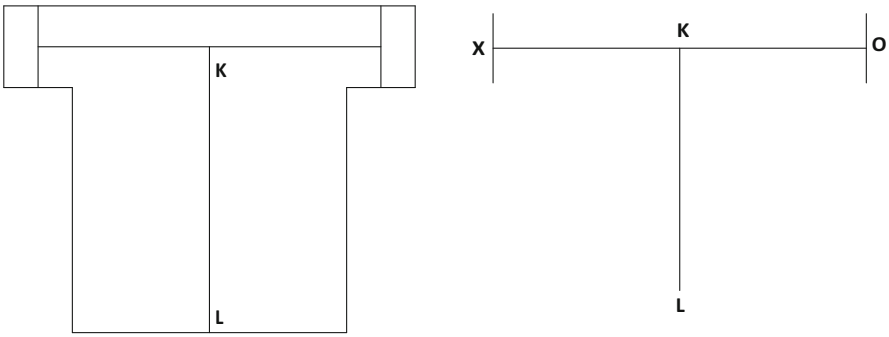

Fig. 17.17 (**a**) Fractal microchannel within a volume space. (**b**) Resulting fractal microchannel

In Fig. 17.17b, three individual *T* microchannels are formed. This shows that there are three constructs. This implies that there were six stages of optimization since each of the construct has two branches.

In the optimization procedure for the constructal theory (Bejan) [28], an optimized elemental volume/construct and a corresponding optimized path length are obtained.

Thereafter, other optimized elemental volumes and corresponding path lengths are obtained in succession until the entire volume space is optimized. Again, after six stages of optimization, a similar channel as shown in Fig. 17.17b will be obtained.

It is worthy of note that from first to the third construct, the shape and size of the starting volume template change. The shape is determined by aggregations of all the *T*-junctions formed. It is assumed here that the thermal performance of the optimized *T* volume shapes does not interact with each other.[14]

This and other limitations in the analytical modelling of the fractal microchannel concerning optimal thermal performance will be discussed in more detail in the next section.

17.7.3.3 Justification of the Limitations of Analytical Modelling of Fractal Microchannel Heat Sinks

Recall the matchbox illustration. One can imagine that during the stages of optimization, the volume of the matchbox increases. For example, two similar *T* channels form the fractal channel in Fig. 17.17b at 90 ° with another *T* channel.

Next, we consider other fractal microchannels having bifurcation angles less than 90 °. We can anticipate that these fractal microchannels also increase in volume during the optimization stages. We consider such a fractal microchannel

[14] Assumption by [28]. This is a limitation in the analytical modelling of fractal microchannels.

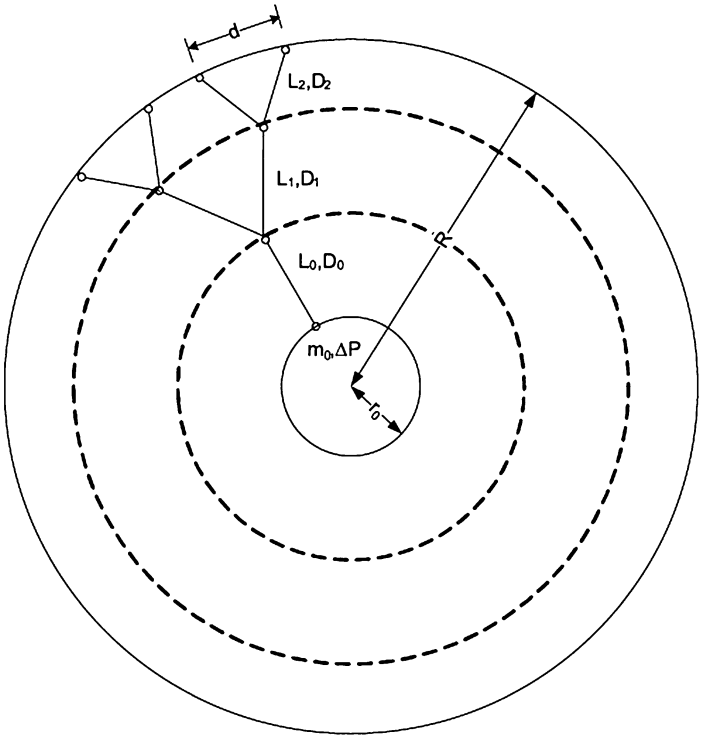

Fig. 17.18 The tree-shaped construct covering the area of a convoluted disc-shaped body (Salimpour and Menbari [10])

as shown below (Salimpour and Menbari) [10]. In this regard, we investigate the procedure in the analytical derivation of the maximum thermal resistance (Salimpour and Menbari) [10].

To investigate the derivations by Salimpour and Menbari [10], we arrange concentric circles to form optimized volumes as shown in Fig. 17.19.

In Fig. 17.19, the innermost shaded volume is hollow. Here, the width of the unshaded volume layer is depicted by line L_1D_1. L_2D_2 depicts the width of the outermost volume layer.

Furthermore, we assume that the amount of heat in Fig. 17.19 can be reduced by the factor of the number of concentric circles of volumes of heat taken either by conduction or both conduction and convection.[15] Given this background, we examine the equations made by Salimpour and Menbari [10].

In Fig. 17.18, the inlet coolant fluid temperature is $T_{0.}$ The highest temperature T_m was observed at the two peripheral corners of convoluted disc. The overall maximum temperature difference is $T_m - T_0$, and the overall thermal resistance is

[15]This is inherent in the assumption made by Bejan [28].

$(T_m - T_0)/q$, where q is the total heat current generated in the convoluted disc ($q'' = q/\pi(R^2 - r^2)$). The thermal resistance is obtained by assuming that the sector is slender enough such that conductive heat transfer occurs through the solid material in the direction perpendicular to the duct. Therefore, by using the first law of thermodynamic for radial duct, they arrived at

$$T_f - T_0 = \frac{q''\pi\left(R^2 - r^2\right)}{n\dot{m}_0 c_p} \tag{17.19}$$

Convection heat transfer equation at the end of duct wall is

$$T_w - T_f = \frac{q''\pi RD}{npNuK_f} \tag{17.20}$$

Invoking Fourier law for the last ring of disc, they obtained

$$T_m - T_w = \frac{\pi^2 R^2 q'}{2n^2 kt} \tag{17.21}$$

where R, r, D, n, $\dot{m}_0$, c_p, Nu, k_f, k and t are external radius, internal radius, diameter of duct, numbers of radial ducts located in convoluted disc, mass flow rate entering each port of internal perimeter, specific heat at constant pressure, Nusselt number, thermal conductivity of fluid, thermal conductivity of disc and the thickness of disc, respectively. In addition, T_f and T_w are the fluid bulk temperature and the duct wall temperature at the duct outlet.

In Eq. (17.20), the heat current that arrives at the wall end of the duct is $(q''\pi R)/n$ which is equal to $hp(T_w - T_f)$, where h is the heat transfer coefficient, obtained from $Nu = hD/k_f$. The value p is the wetted perimeter of the duct cross section. $(T_m - T_w)$ is the temperature distribution on the last ring of disc. The outer part of disc is located along the perimeter of length $d/2$. The heat flux of conduction along the perimeter of this length that arrives at T_m is $kt[4(T_m - T_w)/d]$.

From the Eqs. (17.19), (17.20) and (17.21), they arrived at the thermal resistance:

$$\tilde{T}_m = \frac{1}{M} + \frac{RDkt}{nNuk_f p\left(R^2 - r^2\right)} + \frac{\pi R^2}{2n^2\left(R^2 - r^2\right)} \tag{17.22}$$

where $M = mc_p/kt$ is the nondimensional mass flow rate.

In order to investigate the fractal microchannel in Fig. 17.18, we first note that the second term in Eq. (17.22) is negligible compared to the third term, as observed by Salimpour and Menbari [10]. This shows that heat taken as the fluid goes through the microchannel is significant.

In Eq. (17.20), it is assumed that the temperature difference $T_w - T_f$ reduces by a factor n which is the number of ducts given the local Nusselt number Nu determined

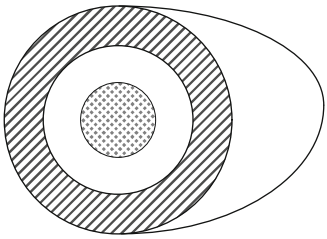

Fig. 17.19 Pear-shaped optimized volume

by the individual duct diameters.[16] However, it can be seen that the average Nusselt number *Nu* was used by Salimpour and Menbari [10] in Eq. (17.20).

Using the local Nusselt number would have provided more accurate temperature distribution. This means taken account of thermal spreading along concentric circles of the disc (Vermeersch and De Mey) [27]. The local Nusselt number was not used because the factor *n* (number of ducts) would have been unjustifiable. Hence, the assumption in Fig. 17.19 is inaccurate. This implies that the concept of optimized volumes for fractal microchannels is inaccurate.

This is the limitation in the determination of the maximum nondimensional thermal resistance as obtained by Salimpour and Menbari [10]. The nondimensional thermal resistance can only be minimized if the geometry itself is optimized. This is the main limitation with analytical modelling of fractal microchannels. In this section, we have demonstrated the analytical limitations of fractal microchannels.

In the next section, we shall examine the numerical model limitations of fractal microchannels. For numerical modelling, the limitations result from the numerical models used in modelling the thermo-hydraulic properties of the flow.

17.8 Section 2

17.8.1 Numerical Models

Computational fluid dynamics (CFD) use numerical methods to solve and analyse heat and mass transfer processes in fluids (Toombes and Chanson) [32]. This is usually done assuming effects such as three-dimensional, multi-fluid, compressible and thermodynamics (Toombes and Chanson) [32]. CFD analyses these problems considering such effects in a given geometry. This is done by having grid points created by meshing on a solution surface (Abbott and Basco) [33]. The solution surface is a connection of all major grid points (Abbott and Basco) [33]. This problem is solved in the solution surface considering finite elements of it.

[16]Note that the factor *n* in Eq. (17.20) is analogous to the number of concentric circles of volumes of heat in Fig. 17.19.

Since numerical models adopt approximate models of thermo-hydraulic properties of flow, it has a number of limitations. However, in this section, we shall limit the discussion of such limitations to fractal microchannels.

17.8.2 Numerical Modelling of Microchannels

Recall that we considered some simple convective and conductive cooling systems in the previous section. If we take, for example, the convective cooling system in Fig. 17.14, it is easy to see that if the heat flux per unit area, mass flow rate, fluid heat capacity is known, we can determine the fluid-surface temperature difference. This is possible if we assume that the thermal resistance is negligible. Assuming we had a number of such microchannels within a heat sink, we now have to consider factors such as temperature distribution, inlet fluid velocity and the relative inlet and outlet positions of the fluid. This is because such factors would affect the thermal performance of microchannel heat sinks.

In order to do this, the microchannel heat sink has to be considered within a geometric space in the Cartesian axis. This implies that numerical modelling allows for more in-depth analysis and examination of fluid thermal properties on minute areas within the geometry of interest.

It therefore follows that the dimensions of the microchannel heat sink assume importance and become a useful variable in heat transfer analysis.

Given this background, we consider such impact factors as aspect ratio and hydraulic diameter of microchannels. This is important in order to understand the limitations of numerical modelling of fractal microchannels.

17.8.2.1 Aspect Ratio

In order to proceed in this discussion, it is useful to review some impact factors. Recall that one of the advantages of microchannels is high surface area to volume ratio. Having this in mind, one can imagine a microchannel in an enclosed volume. Let the microchannel be a rectangle with volume V embedded in a rectangular substrate of a reasonable larger volume $V + \delta$. It becomes clear that the surface area to volume ratio can be modified by allowing the ratio of width to length $\frac{w}{l}$ of the microchannel to vary between the limits 0 and 1.

If we consider more than one microchannel cooling the substrate, then the relative dimensions of the axes of the plane in which the microchannels are embedded assume importance. This has been demonstrated by Foli et al. [34] in the optimal aspect ratio for a constant volume of microchannels. It is quite easy to see that since the microchannels are uniformly spaced, the aspect ratio of the plane determines the aspect ratio of individual microchannels.

However, the spacing between fractal microchannels in the given plane is irrelevant because of their tree structure.

Hence, the analysis of the 'individual' microchannels is less simplified. A numerical analysis between parallel and fractal microchannels can be done given the same aspect ratio and equal surface areas of the plane.

17.8.2.2 Length to Hydraulic Diameter Ratio

Determination of the hydraulic diameter is important as it varies with cross-sectional shapes for different microchannels. The concept of the hydraulic diameter is from the assumption of a fully developed flow (Sharp et al.) [35]. This assumption can be made considering a unidirectional flow. Since the hydraulic diameter is obtained from a control volume, it can be considered as a parameter characteristic of the length of the microchannel. As such, the length to hydraulic diameter ratio is important in the determination of the thermo-hydraulic properties of the fluid in the microchannel.

Below is the step-by-step derivation of the hydraulic diameter (Sharp et al.) [35]:

$$-\frac{dp}{dx}A = \overline{\tau}_w P \tag{17.23}$$

where p is the pressure. P and A are the perimeter and area of the control volume, respectively.

Equation (17.23) shows that the pressure differential in the control volume is determined by the change in shear stress along the perimeter:

where

$$\overline{\tau}_w = \frac{1}{P}\int_p \tau_w dl \tag{17.24}$$

is the wall average stress around the control volume, and the local sheer stress is given by

$$\tau_w = \mu \frac{\partial u}{\partial n}|_{n=0} \tag{17.25}$$

Hence, the derivation of the hydraulic diameter is shown below:

$$D_h = \frac{4A}{P} \tag{17.26}$$

It can be seen that the hydraulic diameter is obtained considering the average stress in a control volume. It therefore follows that the length to hydraulic diameter ratio can only be determined given straight smooth channels and a fully developed

flow. In the case of fractal microchannels, the length to hydraulic diameter is not constant across its length because of the effects of bifurcation.

Such hydraulic effects (bifurcations) can be captured by numerical modelling of minute surfaces of the micro-fractal channels.

17.8.3 Limitations of Numerical Modelling of Fractal Microchannel Heat Sinks

In this section, we examine the numerical model limitations due to applied boundary conditions. We start by considering Fig. 17.20 (Liu and Garimella) [36] in which microchannels are uniformly spaced in a microchannel heat sink given uniform heat flux. As such, we can perform thermal analysis for the heat sink by considering one microchannel.

However, for a fractal microchannel heat sink with the same surface area as Fig. 17.20, thermal analysis of the heat sink cannot be made considering one individual optimized microchannel. This is because individual microchannels of the fractal microchannel heat sink form a tree structure.

The relevant mass, momentum and energy equations that characterize the heat and mass transfer characteristics of the microchannels in Fig. 17.20 are as follows:

$$\nabla.\left(\rho\bar{V}\right) = 0 \tag{17.27}$$

$$\vec{V}.\nabla\left(\rho\vec{V}\right) = -\nabla P + \nabla.\left(\mu\nabla\vec{V}\right) \tag{17.28}$$

$$\vec{V}.\nabla\left(\rho c_p T\right) = \nabla.\left(k_f \nabla T\right) \text{ for the fluid} \tag{17.29}$$

$$\nabla.\left(k_s \nabla T_s\right) = 0 \text{ for the fin} \tag{17.30}$$

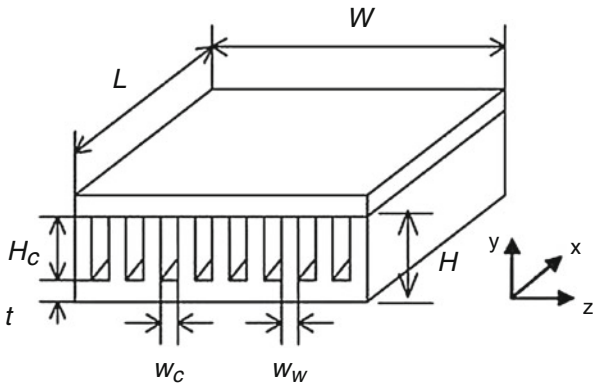

Fig. 17.20 Microchannel heat sink (Liu and Garimella [36])

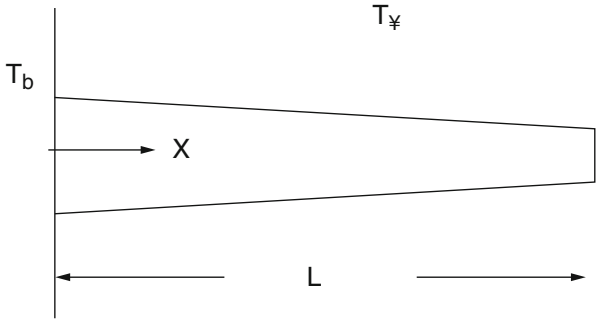

Fig. 17.21 Schematic of a fin (Sen [37])

In Eqs. (17.27), 1.28, 1.29 and 1.30, $\rho, \vec{V}, P, \mu, c_p, k, T$ denotes density, velocity, pressure, viscosity, specific heat capacity, thermal conductivity and temperature. The subscripts s and f are for the fin and fluid, respectively.

Next, we consider one of the microchannels as a fin as shown in Fig. 17.21 (Sen) [37]:

Hence, the fin effectiveness and fin efficiency are defined, respectively.

Fin effectiveness ε_f: This is enhancement factor of the heat transfer rate due to the fin (Sen) [37].

Fin efficiency η_f: This is the enhancement factor of the fin heat transfer rate due to the temperature difference between the temperature at the tip of the fin and the base (Sen) [37].

Longitudinal heat flux along the fin is given as

$$q_x'' = o\left(k_s \frac{T_b - T_\infty}{L}\right) \tag{17.31}$$

Transverse heat flux across the fin is given as

$$q_t'' = o(h(T_b - T_\infty)) \tag{17.32}$$

It can be seen from the above equations that the temperature at the tip of a long fin can be projected as T_∞.[17]

As such, the computational domain for a fin is considered in Fig. 17.22 (Liu and Garimella) [36]. Given the heat flux applied, Liu and Garimella [36] considered the boundary equations below:

$$-k_s \frac{\partial T}{\partial y}\Big|_{y=0} = q'' \tag{17.33}$$

[17]Thus T_∞ serves as a suitable reference point for the temperature at the tip of a long tip.

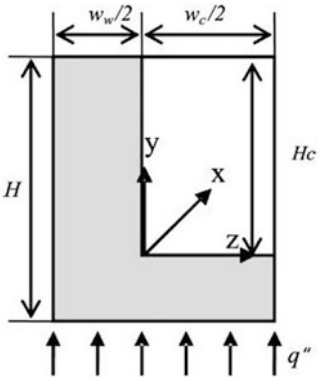

Fig. 17.22 Computational domain (Liu and Garimella [36])

$$-k_s \frac{dT}{dy}\bigg|_{y=0} = \frac{w_c + w_w}{w_w} q'' \tag{17.34}$$

Liu and Garimella [36] noted that when the boundary condition in Eq. (17.33) is applied, it is assumed that the heat taken up by the fin is uniform across its length.[18] In Eq. (17.34), it is assumed that all the heat applied goes up the base of the fin. Liu and Garimella [36] used these two boundary conditions in numerical analysis and observed heat fluxes 55.5 and 333 W/cm^2 into the fluid and fin, respectively. This corresponds to associated errors of 50 and 24 percent, respectively, when compared with the actual computed heat fluxes. As a result, they developed an alternative boundary condition as shown below:

$$q = h\left(\frac{w_c}{2}L\right)\left(T_b - \bar{T}_f\right) + h(H_c L)\eta_f\left(T_b - \bar{T}_f\right) \tag{17.35}$$

Equation (17.35) is a measure of the heat removal rate in the microchannel heat sink system. It can be seen that the heat flux is a function of both w_c and H_c, where η_f is the efficiency of the fin.

Equation (17.35) can be justified considering Fig. 17.23.

In Fig. 17.22, $w_w/2$ is negligible. This assumption is valid if the temperature at the tip of the fin is projected as T_∞. Hence, Fig. 17.23 is considered. This implies that the dimensions H_c, L and W_c / 2 determine the temperature difference $\left(T_b - \bar{T}_f\right)$.

Hence, the boundary condition in Eq. (17.36) was obtained:

$$-k_s \frac{dT}{dy}\bigg|_{y=0} = \frac{2\eta_f \alpha}{2\eta_f \alpha + 1} \frac{w_c + w_w}{w_w} q'' \tag{17.36}$$

[18]This is inherent in Bejan's model.

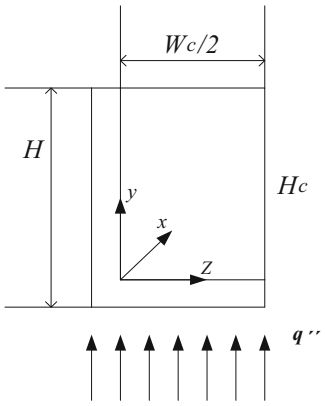

Fig. 17.23 Computational domain

where k_s, η_f, α, q'' are the thermal conductivity of the solid, viscosity of the fluid, aspect ratio of microchannel and heat flux.

Based on the boundary condition in Eq. (17.36), Liu and Garimella [36] and other researchers derived a number of resistance models to explain convective heat transfer in the microchannels. In one of the models, axial conduction was considered. This is shown in Eq. (17.37):

$$k_s \frac{w_w}{2}\left(\frac{\partial^2}{\partial x^2}+\frac{\partial^2}{\partial y^2}\right)\bar{T} - h\left(\bar{T}-\bar{T}_f\right) = 0 \tag{17.37}$$

where

$$\bar{T} = \int_{-\frac{w_w}{2}}^{0} T dz \Big/ \left(\frac{w_w}{2}\right) \tag{17.38}$$

h is the heat transfer coefficient and $\bar{T}_f$ is the fluid temperature.

If the axial conduction term $\dfrac{\partial^2 \bar{T}}{\partial x^2}$ is neglected, the equation reduces to

$$\frac{\partial^2 T}{\partial y^2} = \frac{2h}{k_s w_w}\left(T - T_f(x,y)\right) \tag{17.39}$$

In essence, the axial conduction along the fin can be carefully considered by accurate determination of the fin temperature T. Since axial conduction is an important phenomenon in heat transfer, we review some literature on its effects.

Axial Conduction[19]

Maranzana et al. [39] noted that the coupling between wall and fluid temperatures could not be neglected for low hydraulic diameters because the heat transfer coefficient reaches very high values. Hetsroni et al. [40] used a critical axial conduction value $Mcr \sim 0.01$. This is because wall fluid flux departs from an initial uniform heat flux at the bottom of the substrate which is at a finite distance from the channel walls (Moharana and Khandekar) [41].

Cole and Cetin [42] also investigated the effect of the coupling between wall and fluid by considering axial conduction effects considering wall thickness to channel height ratio given constant wall to fluid conductivity of 2.5. The effects of axial conduction were observed as evidenced in warming of the upstream fluid at low Pe (Peclet number) values. A similar trend was observed when wall to fluid thickness was kept constant and the wall to fluid conductivity ratio varied.

Moharana and Khandekar [41] investigated the effect of aspect ratio of rectangular microchannels on axial back conduction. It was observed that at an optimum aspect ratio of 2.0, a minimum Nusselt number occurs regardless of the thermal conductivity ratio of solid to fluid. It was also observed that decreasing the aspect ratio beyond this minimum value or increasing the channel height for specific channel width results in effective thermal resistance. Moharana and Khandekar [41] also stated that for very low substrate-fluid conductivity ratio $Ksf \approx 12.2$, the actual heat flux experienced at the solid interface length is approximately constant across the channel length. As such, they compared optimum aspect ratio and consequent maximum average Nusselt number along the channel for relative K_{sf} values.

Furthermore, Perry et al. [43] investigated the effect of velocity on temperature distribution with axial conduction effects in a rectangular channel. The velocity profile was into k distinct layers. Then using the Fourier transform of temperature using a finite length, the temperature distribution was obtained. Cole and Cetin [42] argued that the hypothesis that the axial conduction effects would die down with an assumption/consideration solely based on a given finite length would lead to distortion of the temperature distribution. Moreover, D'Aleo and Prasser [44] noted that the semi-finite wall model in analysing transient heat problem would lead to significant errors if there are low-frequency fluctuations and the wall thickness is minute or the thermal conductivity is high.

Using the Green's approach, Cole and Cetin [42] used point heat sources in the formulation of their desired temperature distribution. This is based on the assumption that given a known heating distribution function over a region, the temperature distributions can be determined in the region and another adjacent to it. This can be determined given B_0, which is the contribution to the temperature caused by the heat supplied from the external wall, P_0:

[19]This section was taken from Kode et al. [38].

$$T_1(x, y_1) = \frac{1}{k_1}\int q_{01}(x')G_1 \left(x - x', y_1, y_1' = 0\right)dx' \tag{17.40}$$

$$T_0(x, y_0) = \frac{1}{k_0}\int q_{01}\left(x^1\right)G_0 \left(x - x', y_{0,} y_0' = w\right)dx' + B_0(y_0) \tag{17.41}$$

where

$$B_0(y_0) = \frac{1}{k_0}\int p_0\left(x', y_0'\right)G_0 \left(x - x', y_0, y_0' = 0\right)dx' \tag{17.42}$$

where G_1 and G_0 are Green's parameters on interfaces 1 and 0, respectively, and K_1 and K_0 are the thermal conductivities on interfaces 1 and 0, respectively. T_1 and T_0 are the temperatures on interfaces 1 and 0, respectively.

Lin and Kandlikar [45] also attempted to study axial conduction effects but assumed uniform heat transfer coefficient in their two-dimensional model. Maranzana et al. [39] noted that the error because of the assumption of a uniform heat transfer coefficient is low given a two-dimensional analysis of the axial conduction problem. Lin and Kandlikar [45] also assumed a net flow of heat conduction in the direction of the flow in their model.

Rahimi and Mehryar [46] investigated the effects of axial conduction in a circular cross-sectional microchannel considering a two-dimensional analysis. In this work, they noted the effects of axial conduction at both the entrance and exit of the microchannel. As such, they obtained the entrance local Nusslet number, the ending region Nusselt number and the ending length. The ending length was considered as opposed to the entrance length as they noted that the ending length was much longer than the entrance length. At any rate the effects in the end region were a result of the upstream axial effect in the fluid.

It is interesting to note that the Nusselt number in the entrance region was lowered though there was high heat flux in the wall as a result of axial conduction. The local heat transfer coefficient is given as

$$h_x = \frac{q'w_i}{\pi D_i(T_{w_i} - T_b)} \tag{17.43}$$

where q' is the heat transfer per unit length, w_i is the internal wall, D_i is the internal duct diameter, T_{wi} is the temperature of internal wall and T_b is the temperature of bulk fluid. It was noted that there was no noticeable increase in the temperature of the bulk fluid T_b even though the temperature of the inner wall of the channel increased significantly. As a result, the Nusselt number lowered in this region. The Nusslet number in the end region was also lowered as it deviated from the value in

the middle portion of the channel, which had a Nusselt number of 4.364. Following these results, the ending length was obtained as

$$Le^* = \frac{Le}{\mathrm{RePr}D_i} \tag{17.44}$$

where Re, Pr, and Di are the Reynolds number, Prandtl number and inner diameter.

This was the starting point to get a correlation for the axial conduction number:

$$M = \left(\frac{k_s}{k_f}\right)\left(\frac{D_0 - {D_i}^2}{D_i L}\right)\frac{1}{\mathrm{RePr}} \tag{17.45}$$

where k_s, k_f and L are the thermal conductivity of the solid, thermal conductivity of the fluid and the length.

This was later modified because the relation of M and Le^* did not give a monotonous curve. The modified Eq. (17.46)

$$M' = M\frac{L}{D_i\mathrm{RePr}} = \left(\frac{k_s}{k_f}\right)\left(\frac{{D_0}^2 - {D_i}^2}{{D_i}^2}\right)\frac{1}{\mathrm{Re}^2\mathrm{Pr}^2} \tag{17.46}$$

was then used to get a correlation with the ending length Le^* which was derived after a number of tests and experiments.

Tiselj et al. [47] investigated the effect of axial conduction in triangular microchannels. It was observed that axial conduction was very high in the entrance region of the channel. They noted that the heat flux reduced drastically to zero at some point close to the entrance of the channel. In the next region, the axial conduction is in a direction opposite to that of the flow of the fluid; after this region is a singular point where heat flux is transferred from the microchannel to the fluid.

In summary, it is observed from the above literature that entrance effects, and length to hydraulic diameter ratio have considerable effects on axial conduction. Furthermore, the assumption in Eq. (17.39) is accurate for rectangular microchannels with an optimum aspect ratio (Moharana and Khandekar) [41].

From Eq. (17.33), it follows that if the axial conduction term is neglected, the terms $\left(\frac{w_c}{2}L\right)$ and $(H_c L)$ are determining factors in the temperature distribution $T(x, y)$. From this equation, it is clear that the convective area is important in the determination of the heat gained by the fluid. As such, following Liu and Garimella [36], we consider the convective surface area of fractal microchannels, in order to examine appropriate boundary conditions for fractal microchannels. In the case of fractal microchannels, the convective surface area is given by

$$S = 2\pi d_0 L_0 \frac{1-(N\beta\gamma)^{m+1}}{1-N\beta\gamma} \tag{17.47}$$

when $m = 1$

$$S = 2\pi d_0 L_0 (1 + N\beta\gamma) \tag{17.48}$$

Here we note that the convective area for fractal microchannels is dependent on β and γ. It is clear from the equation that we can have different values of β and γ with the same value for the convective area. Furthermore, fractal microchannels are associated with variability of heat transfer coefficient as such; we consider the uniform temperature boundary condition in heat transfer analysis. Hence, we consider uniform temperature boundary conditions to analyse the variation of surface heat flux.

17.8.3.1 Uniform Temperature Boundary Conditions in Numerical Modelling of Fractal Microchannel Heat Sinks

The following relations are relevant when uniform temperature boundary conditions are used (Jiji) [26]. The variable heat flux for an infinitesimal strip along the length of the channel is given by

$$dq_s = h(x)[T_s - T_m(x)]Pdx \tag{17.49}$$

$$q_s''(x) = h(x)[T_s - T_m(x)] \tag{17.50}$$

Hence, we shall consider some applications of the uniform temperature boundary conditions in literature.

Yu et al. [15] conducted a combined numerical and experimental study of the fractal microchannel heat sink and compared results with the conventional straight channel heat sink for Reynolds number between 150 and 1200. Their calculation of average heat transfer coefficient was given by

$$h = \frac{Q}{A_h \Delta T_{m,loc}} \tag{17.51}$$

where

$$\Delta T_{m,loc} = \frac{\Delta T_{\max} - \Delta T_{\min}}{\ln\left(\frac{\Delta T_{\max}}{\Delta T_{\min}}\right)} \tag{17.52}$$

Their results show that that the heat transfer in the fractal microchannel was enhanced but at the cost of higher pressure drop. Zhang et al. [48] investigated the thermal and hydraulic performance of fractal microchannels with both one and two

branching levels, respectively. They noted that both the friction factor and the hydraulic diameter increase with a decrease in the aspect ratio as shown in *Part A* (Zhang et al.) [48]. It follows that a larger aspect ratio results in a higher total pressure drop at a rapidly increasing rate. However, the heat transfer increases as the aspect ratio decreases. This is due to a larger contact area (Tiselj et al.) [47].

Zhang et al. [8] also investigated thermal and flow behaviour of bifurcations and bend in fractal-like microchannel networks considering secondary and recirculation flows. Velocity and vorticity distributions in both T joints and L bends were investigated considering factors such as the pressure variations, Reynolds numbers, aspect ratios and the fluid characteristics in both the diffluent and confluent flows.

For T joints, it was observed that varying pressure distributions exist in both the diffluent and confluent flows with the potential for achieving minimal temperature difference between the constant wall temperature and the mean bulk temperature in a bid to achieve uniform temperature distribution. However, it was noted that when fluid flows through the L bend, both the pressure and temperature increase.

Zhang et al. [48] concluded in the former study that the aspect ratio of 0.333 was the best as vorticity increased with increase in Reynolds number which resulted in lower pressure drop and better heat transfer when compared to aspect ratios 1 and 0.5. In their previous study, the effect of aspect ratio and branching levels of fractal microchannels was found to have substantial hydrodynamic and thermal performance of the fluid.

Zhang et al. [48] used the subsectional integral method to determine the heat transfer characteristics of the fractal microchannel. They obtained correlations for straight rectangular cross sections for fractal microchannels by determination of relevant lengths at points of bifurcations and bends. As such, the thermal characteristics of component lengths were integrated over the entire channel length. This is shown in the equations below:

$$\bar{f} = \frac{1}{x^+}\int_0^{x^+} f_x d_x^+ = \frac{1}{x^+}\left[\int_0^{x_1^+} f_1 d_x^+ + \int_{x_1^+}^{x_2^+} f_2 d_x^+ + \ldots + \int_{x_{n-1}^+}^{x_n^+} f_x d_x^+\right] \tag{17.53}$$

$$N\bar{u} = \frac{1}{x^*}\int_0^{x^*} Nu_x dx^* = \frac{1}{x^*}\left[\int_0^{x_1^*} Nu_1 d_x^* + \int_{x_1^*}^{x_2^*} Nu_2 d_x^* + \ldots + \int_{x_{n-1}^*}^{x_n^*} Nu_x d_x^*\right] \tag{17.54}$$

where $x+$ and x^* represent the characteristic lengths of the friction factor and the Nusselt number, the subscript n represents the number of the level and f_x and Nu_x are the local friction factor and the local Nusselt number of each branch in the developing region.

From the above, we note approximate ways in the determination of fluid temperature distribution. Yu et al. [15] tried to obtain the temperature distribution directly by using the log mean difference considering fluid inlet and outlet temperatures. Zhang et al. minimizes the errors by using integration limits within the

characteristic lengths of the friction factor and Nusselt number within the developing region.

It is worthy of note that the sub-integral method is an improved way to obtain the thermal performance of fractal microchannels. This is because it takes into account the local heat transfer coefficient for each branch in the fractal microchannel. However, we note that under uniform temperature boundary conditions, the mean fluid temperature varies within an infinitesimal length dx. As such, the limits considered in the sub-integral method are far longer than dx.

17.8.3.2 Practical Considerations

There are other limitations associated with the use of fractal microchannel heat sinks that are not directly related to numerical or analytical model limitations.

Escher et al. [9] compared the thermal performance of fractal microchannels with straight microchannels having a slanting manifold. It was concluded that the thermal performance of the straight microchannels outperformed the fractal microchannels. This finding was based on a performance index that quantified the heat dissipation rate of both channels given pressure drop constraints. In Escher et al. [9] analysis, the convective heat transfer areas of both fractal and straight microchannels were not identical. They postulated that this was not a useful basis to make comparisons.

However, in Chen and Cheng [30] comparisons of thermal performances in fractal microchannels and straight microchannels, a different result was obtained. In their analysis, the convective heat transfer areas of both channels were identical. Their findings show that the thermal performance of the fractal channels outperformed that of parallel channels.

Pence and Enfield [49] compared the thermal performances of both fractal microchannels and straight microchannels. They made this comparisons using different area ratios and using both square and rectangular cross sections. It was found that lower wall surface temperatures in the fractal-like heat sink can be achieved for convective area ratios AR values greater than 0.5. This result is valid when square cross sections are considered in fractal and parallel microchannels.

Pence and Enfield [49] also found that when the heights of the channels were varied, the fractal microchannels had the steepest positive response given a determined benefit to cost ratio. This indicates that the aspect ratio of the fractal microchannels is quite responsive to its thermal performance.

It has been demonstrated from the foregoing that a comparative analysis of the convective heat transfer area is useful in thermal performance analysis. This is because one can determine the variations in the performance index with respect to parameters like aspect ratios and length ratios. However, it is also important to take note of Pence and Enfield [9] observation for practical applications.

This is because the surface area of the substrate to be cooled has to be considered when implementing designs. In this regard, it is not practicable to evaluate the

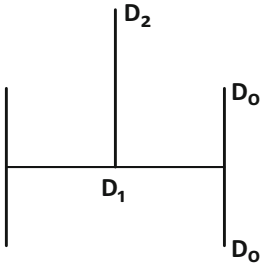

Fig. 17.24 Fractal channel unit (Bejan [28])

thermal performance by considering convective surface area ratios. This is because both parallel channels and fractal microchannels are optimized differently.

One limitation in this regard is that fractal microchannels are ideally suited to cool circular substrates.[20] Fractal microchannels can be optimized considering parameters like the circumference of the substrate, width and length ratios. In the case of rectangular substrates, this is not the case.

Furthermore, parallel channels are simply aligned on the substrate to fill the convective area. The distance between one channel and the next could be taken as twice the width of an individual channel (Alharbi et al.) [25]. On the other hand, fractal microchannels are optimized by considering the branching factor.

Let us consider Figs. 17.24 and 17.25.

The channels in Figs. 17.24 and 17.25 are being used to cool substrates of equal surface areas. For convenience, we disregard the manifold and heat collection areas. We also disregard the fact that fractal microchannels have variable widths and lengths. In Fig. 17.24, it is seen that the thermal conductivity path D_2 branches into D_1. Thermal conductivity path D_1 branches into four D_0 thermal conductivity paths.

In Fig. 17.24, we let two assemblies represent a unit worthy of comparison with the parallel channels. This is because this is the basic unit of the fractal microchannel heat sink that was considered earlier which suitably optimizes the entire surface area. If we consider a fluid flowing in this unit, we can consider D_2 to be the point where the entire heated fluid is collected.

By inspection, it seems the total convective surface area of the parallel microchannel is more than that of the fractal microchannel. This is because Fig. 17.25 has five channels A1, A2, A3, A4 and A5 of equal areas, the sum of which is greater than the aggregate area of all the four microchannels in the fractal channel unit. Note that this conclusion is contrary to Chen and Cheng [30] where the fractal microchannel was considered to have greater heat transfer areas than parallel microchannels.[21]

At any rate, for the fractal microchannel to be considered a suitable replacement for the parallel microchannels, it must be able to dissipate more heat from the system given pressure drop constraints.

[20]This has been demonstrated in derivation of Fig. 17.19.

[21]Chen and Cheng [30] did not consider the area of the substrate being cooled.

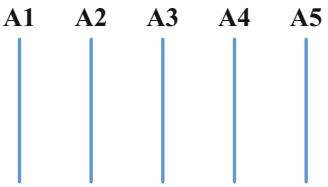

Fig. 17.25 Straight parallel channels

From Figs. 17.24 and 17.25, theoretical estimates for thermal performance can be made before manufacturing the microchannels. However, it is important to note that such specifications will deviate from initial values after manufacturing. We discuss such in the succeeding section.

17.8.4 Manufacturing Constraint of Fractal Microchannel Heat Sinks (An Example)

Given manufacturing constraints, Carter et al. [50] developed straight, fractal microchannels with bifurcation angles 90 °, 60 ° and 20^0. Using the equation $A = \frac{2}{3}Nwd$, where $\frac{2}{3}wd$ is the area of a parabola and N is the maximum number of channels, they obtained microchannel properties and dimensions for the microchannels integrated in silicon carbide (SiC). This is shown in the Table 17.2 [50].

From Table 17.2, we obtain Table 17.3.

It can be seen from Table 17.2 that the column *ratio of cross-sectional area of the tree/straight* for single crystal SiC is 1.230. This value is distinctively different from the other values in the column. This is because it is greater than 1.

It is expected that the ratio would be less than 1. This is because the column *ratio max # tree/straight* is 0.5. It is also important to note that all values in the column ratio *of cross-sectional area of the tree to straight* should be ideally less than 0.5 if the tree channel would be considered a suitable alternative to straight channels. This would mean that the tree channel would have a higher convective heat transfer area than the straight channel.

Furthermore, we note that the material property of the substrate significantly impacts on the manufacturing constraint. This is because all values for polycrystal SiC in the column *ratio of cross-sectional area of the tree/straight* were less than 0.5 except the value for single crystal SiC.

In conclusion it can be inferred that both the material property of the substrate and the manufacturing constraint would influence the thermal performance of the fractal channel.

Table 17.2 Nominal geometric dimensions for tree and straight microchannels (Carter et al.) [50]

Type	Diverg angle (°)	Max # chnls	Min nom. chan. width (μm)	Mat'l	Meas. chan. width (μm)	Meas. chan. depth (μm)	Cross-sect chan. area (mm^2)
Straight	NA	16	62.5	Poly	56	224	0.135
Tree	60	8	125	Poly	145	228	0.177
Tree	20	8	125	Poly	148	272	0.214
Straight	NA	8	125	Poly	146	301	0.214
Tree	90	8	125	Poly	166	287	0.254
Straight	NA	16	125	Single	145	180	0.278
Tree	20	8	125	Single	193	332	0.342
Straight	NA	16	125	Poly	143	565	0.860

Table 17.3 Deductions

	Type		Ratio max #: tree/straight	Mat'l	Ratio cross-sect chan. Area (mm^2) tree/straight
	Tree	Straight			
Diverg angle (°)	20	NA	0.5	Poly	0.249
Diverg angle (°)	60	NA	0.5	Poly	0.206
Diverg angle (°)	90	NA	0.5	Poly	0.295
Diverg angle (°)	20	NA	0.5	Single	1.230

17.8.5 Cooling in Electronic and Microelectronic Components

As stated earlier, a number of considerations are important in thermal designs for electronic components. Designs must be developed with the outlet temperature and maximum junction temperature in mind. In electronic circuits, heat dissipation requirements of each device, optimal fluid flow paths and arrangement of devices must be considered for optimum designs. The pressure drop and flow rate requirements for the cooling liquid are also important (Kandlikar) [51].

Kandlikar [51] note that devices with relatively high operating temperatures should be located towards the fluid exit point. As such the spacing between these devices and the specific locations of the devices must be considered.

As stated earlier, it is advisable that the thermal engineer works hand in hand with the electrical engineer to achieve optimal designs. Having decided on an optimum design of the cold plate, optimum temperature distributions can be obtained for the electronic device geometry. Then, the maximum allowable temperature can be determined.

in a typical electronic circuit for analysis (Blinov et al.) [52]:

$$\Delta T_{(jc)T} = P_{IGBT}.R_{(thjc)T} \tag{17.55}$$

$$\Delta T_{(jc)D} = P_{FWD}.R_{(thjc)D} \tag{17.56}$$

$\Delta T\ (jc)_T$ is the transistor temperature difference junction-to-case; $\Delta T\ (jc)_D$ is the diode temperature difference junction-to-case; P_{IGBT} is the total transistor losses; P_{FWD} is the total diode losses; $R(thjc)_T$ is the transistor thermal resistance junction-to-case; $R(thjc)_D$ is the diode thermal resistance junction-to-case. The required heat sink thermal resistance is then approximated by

$$R_{thsa} = \frac{T_J - T_A}{P_{tot}} - R_{thjc} - R_{thcs} \tag{17.57}$$

R_{thcs} is the thermal resistance of the thermal interface material (TIM), P_{tot} is the total heat load, T_J is the desired junction temperature of the semiconductor, and T_A is the ambient temperature.

For convective cooling, R_{thsa} in Eq. (17.54) should be determined considering Eqs. (17.3) and (17.7). For conduction cooling, Eq. (17.8) is considered.

One area where the thermal and electrical engineer can work together is in the determination of the dimensions and designs of the cold plate. This is to ensure that certain targets like maximum allowable temperature are met.

The thermal engineer must also put into consideration all the thermal resistances and conductivities in the determination of maximum junction temperature. This is particularly important when fractal microchannels are used for cooling. This is because fractal microchannel designs are optimized based on minimization of the thermal resistance by allowing the heat flux to follow specified paths.

17.8.5.1 Fractal Microchannels to Cool MEMS Components

Husain and Kim [53] and other researchers have investigated thermal performances in a number of geometries. This is because the various geometries of microchannel heat sinks are a reliable factor in the determination of the thermal performances in various applications.

Fractal microchannels can have application in the cooling of MEMS bimorph cantilever beams. This is because of the nature of the thermal response of the beam array connected to the electronic device simulator. The longer (300 μm) MBCBs were positioned at the centre of the EDS to begin cooling the hottest areas of the EDS or resistor first while the shorter, stiffer beams (200 μm) were positioned closest to the probe pads. It is observed that the EDS is coolest at the probe ends and hottest in the middle (Coutu Jr. et al.) [54].

The initial variable lengths of the MEMS bimorph cantilever can be determined given the desired temperature operating range by the application of the constructal theory on the surface of the electronic device simulator (EDS). This is done considering some factors such as the number of beams attached to the EDS, aspect

ratio of the EDS, spacing between the beams, individual beam lengths, thermal contact resistance and material to obtain the beam deflection. This would further facilitate uniform temperature distribution on the surface of the EDS since the accuracy of the thermal response of the beams is enhanced.

17.8.5.2 Fractal Microchannels to Cool Aerospace Components

The importance of reliability testing of aerospace components which are subjected to extreme temperatures has been investigated by a number of authors (Bazu and Shea) [55, 56]. The focus on the reliability has been due to a number of concerns such as thermal shocks, mechanical shocks and other phenomena. It is widely agreed upon in the literature that such factors have adverse effects on the operational performances of aerospace components. This could even lead to a total failure of the components.

Given the title of this chapter, we shall focus only on the effects of thermal shocks. In this regard, we investigate how fractal microchannels can be used to mitigate the effects of thermal shocks.

Recall that fractal microchannels are assumed to be ideal for obtaining uniform temperature distribution on the surface substrate. This also implies a reasonable reduction of the possible maximum temperature on the substrate. This potential has been demonstrated in the previous section considering the ratio of the thermal conductivities of the conduction path and the substrate given the surface area constraint.

To further create fractal microchannel designs to minimize the operating range of temperatures of aerospace components, the thermal diffusivity of the material (s) that constitute the fractal microchannels must be considered at the initial stages of the designs. In this way the surface area for cooling is further optimized.

This would make the aerospace components less subject to thermal cycles. In essence, the operating range of temperatures of the components would be reduced.

17.9 Conclusions

In this book chapter, the analytical and numerical model limitations of fractal microchannels have been considered. The analytical limitations have been demonstrated by considering the limitations in the optimization procedure in analytic models. The numerical limitations have been discussed considering approximation techniques in numerical modelling. In addition, it was observed that the material property of the substrate has significant effect on the manufacturing constraint. Both factors impact on the thermal performance of fractal microchannels. Furthermore, the practical limitations of fractal microchannels for use in electronic and microelectronic devices have been considered. This is due to aspect ratio and substrate surface area constraints. In this regard, electrical and material properties

of the devices and components have also been considered. Suggestions on optimum use of fractal microchannels for MEMS bimorph cantilever beams have been provided. Lastly, consideration of the thermal diffusivity of the material(s) that constitute the fractal microchannel would enhance optimization of the surface area for cooling. This would help minimize the effects of thermal shocks in aerospace components.

Acknowledgements Permissions will be requested from CRC Press (Taylor and Francis) to use some of the referenced materials in this book chapter.

References

1. Qu W, Mudawar I (2002) Analysis of three-dimensional heat transfer in microchannel heat sinks. Int J Heat Mass Transfer 45:3973–3985
2. Kim YJ, Joshi YK, Fedorov AG (2008) Performance analysis of air-cooled microchannel absorber in absorption based miniature electronics cooling system. J Mech Sci Technol 22 (2):338–349
3. Nagavarapu AK, Garimella S (2013) Falling-film absorption around microchannel tube banks. J Heat Transfer 135(12):1–10
4. Manglik RM, Magar YN (2016) Heat and mass transfer in planar anode-supported solid oxide fuel cells: effects of interconnect fuel / oxidant channel flow cross section. J Thermal Sci Eng Appl 7:1–10
5. Fell B et al. (2007) High efficiency radiator design for advanced coolant. pp 1–50.
6. Alépée C et al. (2000) Fast heating and cooling for high temperature chemical microreactors. 3rd international conference on microreaction technology, pp 514–525.
7. Teng J et al. (2012) Fluid dynamics in microchannels. Intechopen, pp 403–436.
8. Zhang C et al (2015) Investigations of thermal and flow behavior of bifurcations and bends in fractal-like microchannel networks: secondary flow and recirculation flow. Int J Heat Mass Transfer 85:723–731
9. Escher W, Michel B, Poulikakos D (2009) Efficiency of optimized bifurcating tree-like and parallel microchannel networks in the cooling of electronics. Int J Heat Mass Transfer 52 (5-6):1421–1430. https://doi.org/10.1016/j.ijheatmasstransfer.2008.07.048
10. Salimpour MR, Menbari A (2015) Analytical optimization of constructal channels used for cooling a ring shaped body based on minimum flow and thermal resistances. Energy 81:645–651
11. Xia G, Chai L, Zhou M, Wang H (2015) Effects of structural parameters on fluid flow and heat transfer in a microchannel with aligned fan-shaped reentrant cavities. Int J Therm Sci 50:411–419
12. Keepaiboon C, Wongwises S (2015) Two-phase flow patterns and heat transfer characteristics of R134a refrigerant during flow boiling in a single rectangular microchannel. Exp Therm Fluid Sci 66:36–45
13. Liu WC, Yang CY (2014) Two-phase flow visualization and heat transfer performance of convective boiling in micro heat exchangers. Exp Therm Fluid Sci 57:358–364. https://doi.org/10.1016/j.expthermflusci.2014.06.002
14. Alfaryjat AA et al (2014) Influence of geometrical parameters of hexagonal, circular, and rhombus microchannel heat sinks on the thermohydraulic characteristics. Int Commun Heat Mass Transfer 52:121–131

15. Yu X et al (2012) International journal of heat and mass transfer a study on the hydraulic and thermal characteristics in fractal tree-like microchannels by numerical and experimental methods. Int J Heat Mass Transfer 55(25-26):7499–7507
16. Ramadhan AA, Al Anii YT, Shareef AJ (2012) Groove geometry effects on turbulent heat transfer and fluid flow. Heat Mass Transfer 49:185–195
17. Ghaedamini H, Salimpour MR, Campo A (2012) Constructal design of reverting microchannels for convective cooling of a circular disc. Int J Therm Sci 50(6):1051–1061. https://doi.org/10.1016/j.ijthermalsci.2011.01.014
18. Mohammed HA, Gunnasegaran P, Shuaib NH (2011) Influence of channel shape on the thermal and hydraulic performance of microchannel heat sink. Int Commun Heat Mass Transfer 38(4):474–480
19. Chai L et al (2011) Numerical simulation of fluid flow and heat transfer in a microchannel heat sink with offset fan-shaped re-entrant cavities in sidewall. Int Commun Heat Mass Transfer 38 (5):577–584
20. Wang YH, Yang YT (2011) Three-dimensional transient cooling simulations of a portable electronic device using PCM (phase change materials) in multi-fin heat sink. Energy 36 (8):5214–5224. https://doi.org/10.1016/j.energy.2011.06.023
21. Gupta R, Geyer PE, Fletcher DF, Haynes BS (2008) Thermo-hydraulic performance of a periodic trapezoidal channel with a triangular cross-section. Int J Heat Mass Transfer 5:2925–2929
22. Kamiya A, Takahashi T (2007) Quantitative assessments of morphological and functional properties of biological trees based on their fractal nature. J Appl Physiol 102(6):2315–2325
23. Bahrami M, Yovanovich MM, Culham JR (2006) Pressure drop of fully-developed, laminar flow in microchannels of arbitrary cross-section. J Fluids Eng 128:1036–1044
24. Chai L et al (2013) Optimum thermal design of interrupted microchannel heat sink with rectangular ribs in the transverse microchambers. Appl Therm Eng 51(1-2):880–889. https://doi.org/10.1016/j.applthermaleng.2012.10.037
25. Alharbi AY, Pence DV, Cullion RN (2004) Thermal characteristics of microscale fractal-like branching channels. J Heat Transfer 126(5):744–752
26. Jiji LM (2009) Heat convection, 2nd edn. Springer, Berlin, Heidelberg
27. Vermeersch B, De Mey G (2008) Dependency of thermal spreading resistance on convective heat transfer coefficient. Microelectron Reliab 48:734–738
28. Bejan A (1997) Constructal-theory network of conducting paths for cooling a heat generating volume. Int J Heat Mass Transfer 40(4):799–816
29. Agwu Nnanna AG (2010) Thermo-hydraulic behavior of microchannel heat exchanger system. Exp Heat Transfer 23(2):157–173. https://doi.org/10.1080/08916150903402823
30. Chen Y, Cheng P (2002) Heat Transfer and pressure drop in fractal tree-like microchannel nets. Int J Heat Mass Transfer 45:2643–2648
31. Pence D (2010. Available at:) The simplicity of fractal-like flow networks for effective heat and mass transport. Exp Thermal Fluid Sci 34(4):474–486. https://doi.org/10.1016/j.expthermflusci.2009.02.004
32. Toombes L, Chanson H (2011) Numerical limitations of hydraulic models. 10th hydraulics conference (July), pp 2322–2329.
33. Abbott MB, Basco DR (1989) Computational fluid dynamics: an introduction for engineers. Wiley, New York
34. Foli K, Okabe T, Olhofer M, Jin Y, Sendhoff B (2006) Optimization of micro heat exchanger: CFD, analytical approach and multi-objective evolutionary algorithms. Int J Heat Mass Transfer 49(5-6):1090–1099. https://doi.org/10.1016/j.ijheatmasstransfer.2005.08.032
35. Sharp KV, Adrian RJ, Santiago JG, Molho JI (2002) Liquid flows in microchannels. In: The MEMS handbook. CRC Press, Boca Raton, FL, pp 1–48. https://doi.org/10.1201/9781420036572.ch10
36. Liu D, Garimella SV (2011) Analysis and optimization of the thermal performance of microchannel heat sinks. Int J Numer Methods Heat Fluid Flow 15(1):7–26

37. Sen M (2008) Analytical heat transfer. Department of Aerospace and Mechanical Engineering, University of Notre Dame, Notre Dame, IN
38. Kode TE, Wu H, Ogwu AA (2015) Critical review of the thermo-hydraulic properties of fluids in micro channels. Proceedings of the international sustainable energy and environmental protection (SEEP) conference, pp 1–12.
39. Maranzana G, Perry I, Maillet D (2004) Mini- and micro-channels: influence of axial conduction in the walls. Int J Heat Mass Transfer 47:3993–4004
40. Hetsroni G, Mosyak A, Pogrebnyak E, Yarin LP (2005) Heat transfer in micro-channels: comparison of experiments with theory and numerical results. Int J Heat Mass Transfer 48:5580–5601
41. Moharana MK, Khandekar S (2013) Effect of aspect ratio of rectangular microchannels on the axial back conduction in its solid substrate. Int J Microscale Nanoscale Therm 4(3-4):1–8
42. Cole KD, Çetin B (2011) The effect of axial conduction on heat transfer in a liquid microchannel flow. Int J Heat Mass Transfer 54:2542–2549
43. Perry I, Jannot Y, Maillet D, Fiers B (2009) Effect of velocity distribution on external wall temperature field for a flat microchannel. Exp Heat Transfer 23:27–43
44. D'Aleo FP, Prasser HM (2013) Transient heat flux deduction for a slab of finite thickness using surface temperature measurements. Int J Heat Mass Transfer 60:616–623
45. Lin TY, Kandlikar SG (2012) A theoretical model for axial heat conduction effects during single-phase flow in microchannels. J Heat Transfer 134:020901–020906
46. Rahimi M, Mehryar R (2012) Numerical study of axial heat conduction effects on the local Nusselt number at the entrance and ending regions of a circular microchannel. Int J Therm Sci 59:87–94
47. Tiselj I, Hetsroni G, Mavko B, Mosyak A, Pogrebnyak E, Segal Z (2004) Effect of axial conduction on the heat transfer in micro-channels. Int J Heat Mass Transfer 47:2551–2565
48. Zhang CP et al (2013) Numerical and experimental studies on laminar hydrodynamic and thermal characteristics in fractal-like microchannel networks. Part B: investigations on the performances of pressure drop and heat transfer. Int J Heat Mass Transfer 66:939–947. https://doi.org/10.1016/j.ijheatmasstransfer.2013.07.021
49. Pence D, Enfield K (2004) Inherent benefits in microscale fractal-like devices for enhanced transport phenomena. In: Design and nature II: comparing design in nature with science and engineering. WIT Press, Boston, Southampton, UK pp 317–327
50. Carter JA, Forster LA, Stitt MD (2009) Fabrication and performance of tree-branch microchannels in silicon carbide for direct cooling of high-power electronics applications. Annual IEEE semiconductor thermal measurement and management symposium, pp 128–133.
51. Kandlikar SG, Hayner CN (2009) Liquid cooled cold plates for industrial high-power electronic devices—thermal design and manufacturing considerations. Heat Transfer Eng 30 (12):918–930
52. Blinov A, Vinnikov D, Lehtla T (2011) Cooling methods for high-power electronic systems. Sci J Riga Tech Univ 29(1):1–8
53. Husain A, Kim KY (2008) Shape optimization of micro-channel heat sink for microelectronic cooling. IEEE Trans Compon Packag Technol 31(2):322–330
54. Coutu RA Jr, LaFleur RS, Walton JPK, Starman LA (2016) Thermal management using MEMS bimorph cantilever beams. Exp Mech Exp Mech 56(7):1293–1303. https://doi.org/10.1007/s11340-016-0170-1
55. Bazu M et al (2007) Quantitative accelerated life testing of MEMS accelerometers. Sensors 7:2846–2859
56. Shea H (2006) Reliability of MEMS for space applications. 6111:1–10.

Chapter 18
Microvascular Coaptation Methods: Device Manufacture and Computational Simulation

R.A.J. Wain, J.P.M. Whitty, and W. Ahmed

18.1 Introduction

The practice of joining blood vessels has been ongoing since the late nineteenth century, although it was initially restricted to animal studies and experimental techniques. At this time, fine silk thread and curved needles had been introduced [1], which was a significant advancement on previous suture materials such as leather, tendon, and catgut [2], although these were used for wound closure rather than vascular repair. It was not until the mid-twentieth century, circa World War II, that vascular anastomoses were performed whilst repairing or reconstructing traumatic injuries [3]. The natural progression from repairing vascular injuries was to perform these procedures in smaller and smaller vessels. Of course, this necessitated use of an operating microscope and development and manufacture of finer suture materials, needles, and more delicate instruments.

This chapter aims to provide details of the common microvascular anastomotic devices and their manufacture.

R.A.J. Wain (✉)
Institute of Translational Medicine and School of Mathematics, University of Birmingham, Birmingham, UK

School of Medicine, University of Central Lancashire, Preston, UK
e-mail: richwain@doctors.org.uk

J.P.M. Whitty
School of Medicine, University of Central Lancashire, Preston, UK

W. Ahmed
School of Mathematics and Physics, University of Lincoln, Lincoln, UK

M.J. Jackson, W. Ahmed (eds.), *Micro and Nanomanufacturing Volume II*,
DOI 10.1007/978-3-319-67132-1_18

18.2 Coaptation Methods

Numerous methods exist for performing/aiding the process of microvascular anastomosis; however, these are principally divided into two groups: suture and non-suture techniques. Details of the full range of these techniques have been published elsewhere in the literature [4–6]. This section focuses on the most frequently employed methods and provides an overview of the development and manufacturing process of each.

18.2.1 Microvascular Suture

Currently, the majority of microvascular suturing is performed using fine, non-absorbable, monofilament material attached to a curved, atraumatic needle. The microsuture material itself is comprised of a polymer, often polypropylene or nylon, and is produced into a fine, uniform thread via a series of steps. This process varies slightly from manufacturer to manufacturer, but is essentially the same. Firstly, the desired polymer is synthesized from a series of monomers and combined as necessary to create the desired final product. In the case of Ethilon,[1] the monofilament is composed of the long-chain aliphatic polymers Nylon 6 and Nylon 6,6, and in the case of Prolene,[2] the monofilament comprises an isotactic crystalline stereoisomer of polypropylene, a synthetic linear polyolefin.

Following polymer synthesis, the melted material undergoes a process known as pelletization. Here, the hardened polymer is cut into small pellets to facilitate transport within the production plant. The polymer pellets are then pushed through an auger under pressure to a die through which the polymer can be extruded and stretched into a thread. The stretching and rolling of the thread occurs at varying speeds to allow the tensile strength of the material to be adjusted to the specific requirements needed. Resultant strands of suture are finally coated with a lubricant, such as silicone, to permit smooth glide through soft tissue. The lengths of suture material are then ready to be attached to the needle itself.

18.2.2 Microvascular Needle

The needle is usually made of a stainless steel alloy and starts as a long length of wire. This wire is then heated and stretched to set the required diameter of the needle, in the case of microneedles approximately 0.03 mm. Wires are then cut into

[1] Produced by Ethicon Inc., Johnson & Johnson, Somerville, NJ, USA

[2] Produced by Ethicon Inc., Johnson & Johnson, Somerville, NJ, USA

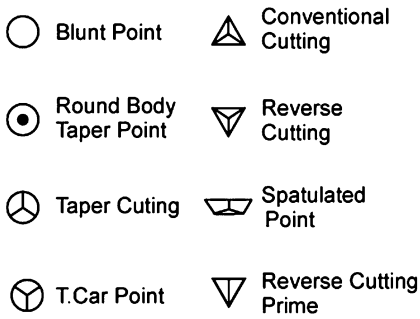

Fig. 18.1 Needle cross sections [7]

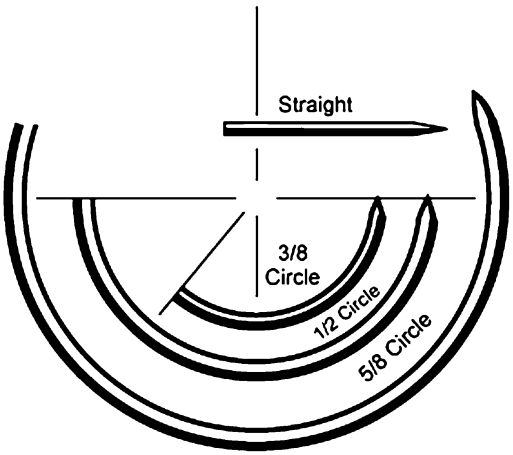

Fig. 18.2 Needle shapes [7]

short lengths needed for each needle, approximately 3–4 mm, and are subsequently processed to create the sharp tip.

The needle's cross section can be engineered to minimize trauma in very delicate procedures or indeed have a cutting edge to permit transition through tougher tissues (Fig. 18.1). This is done by coining, a process of stamping the metal into its desired shape. The tips of the needles are then finely ground to ensure they are sharp, and all pass through a high-speed vision system, which detects any anomalies in the contour of the needles. Each needle is subsequently curved into a particular profile that can range from 3/8 to 5/8 of a circle to allow for variation in technique depending on access, although most needles for microvascular anastomoses are typically round-bodied with a tapered tip and are 3/8 of a circle (or 135°) (Fig. 18.2).

At this stage some manufacturers heat-treat their needles to improve the mechanical properties before the needle's surface undergoes electropolishing. The electropolishing process involves immersion into a temperature-controlled bath containing an electrolyte such as sulphuric or phosphoric acid, followed by passage of an electrical current through the solution. Unwanted debris on the

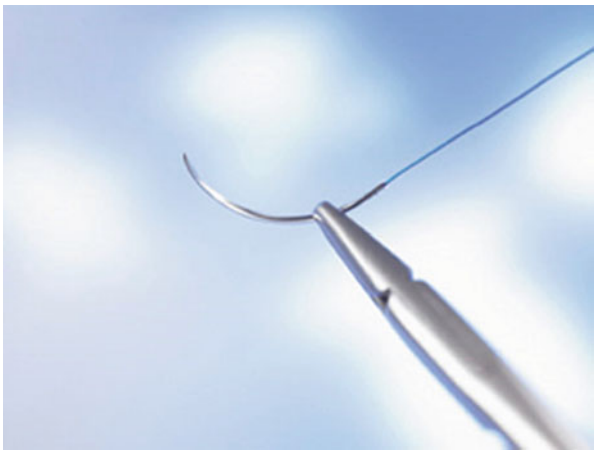

Fig. 18.3 Suture crimped into place in the end of an atraumatic needle [8]

surface of the needle is removed via this process to reveal a needle with a uniform finish. Needles are then coated in a lubricant, again often silicone, and are all penetration tested.

Unlike traditional needles, where the thread is attached using an 'eye' in the end of the needle, atraumatic needles have an axial hole within the needle into which the thread is placed and secured (Fig. 18.3). This minimizes local trauma to any soft tissues. In the case of microneedles, the hole cannot be created using a drill, as the diameter is too fine (approximately 0.03 mm), for this reason a laser is used instead, which has proven to be a fast and accurate technique.

Finally, the polymer thread and needle are connected by crimping the fine thread inside the hole produced by the laser. All sutures are then subjected to a 'pull test' where a predetermined traction is placed onto the newly crimped join to ensure a successful coupling. The suture and thread are lastly inserted into their packaging and sent for sterilization, usually using ionizing radiation, before being distributed for use in theatre.

18.2.3 Microvascular Coupler

The commercially available microvascular anastomotic coupling (MAC) system produced by Synovis[3] was developed in 1986 by Ostrup [9, 10] (Fig. 18.4), after studying an earlier device produced by Nakayama [11]. However, the concept of joining vessels using a ring-pin device was described nearly a hundred years before this by Payr, who fashioned his ring-pin coupler from magnesium [12].

The principle of the ring-pin device is that the cut vessel ends are passed through the high-density polyethylene rings and everted backwards over the sharp stainless

[3]Synovis Micro Companies Alliance Inc., 439 Industrial Lane, Birmingham, AL 35211, USA

Fig. 18.4 Microvascular anastomotic coupling (MAC) system—Synovis [13]

steel pins. The two rings are then pressed together, where the pins interlock, to permit a well-sealed anastomosis with no foreign material present in the lumen. The MAC system is capable of coapting vessels ranging from 0.8 to 4.3 mm diameter with a wall thickness no greater than 0.5 mm [14]. As can be seen in Fig. 18.4, the coupler rings are held in either side of a winged delivery instrument by parallel tracks, designed to keep the rings aligned and steady during surgery. Once the vessels are in place, the wings are pressed together by twisting a handle at the opposite end of the delivery instrument.

This device has several other advantages in that the anastomosis can be performed much more quickly than a traditional hand-sutured repair, and it also has the potential to accommodate a degree of size mismatch. Thrombosis rates in venous coupled anastomoses are also less than standard sutured anastomoses [15]. A recent advance in the MAC system is the addition of an integrated 20 MHz ultrasonic Doppler probe [16], the so-called flow coupler (Fig. 18.5). This allows continuous postoperative monitoring of the flow within an anastomosis. It is commonly applied to the vein, as interruption of arterial inflow will also lead to loss of venous return and hence loss of signal. Its main advantage is perceived to be a more timely detection of anastomotic failure thereby leading to rapid intervention to rectify the problem.

Whilst Synovis did not divulge specific details of the coupler's manufacturing process, it is clear the coupler itself is an assembly of a moulded high-density polypropylene ring and individually produced stainless steel pins. The pins are likely to be manufactured in a similar way to the suture needles, i.e., lengths of stainless steel wire will be cut to the appropriate size and coined to the desired profile, in this case a round body. The pins would then be electropolished before being inserted into the ring in alternate holes to permit interlocking of the opposing ring-pin device (Fig. 18.6). The ring-pin assemblies are then placed into the delivery system shown in Fig. 18.4, which is then packaged and sterilized ready for distribution. The winged delivery system is disposable, but is attached to a re-usable twisting handle that is sterilized between operative cases.

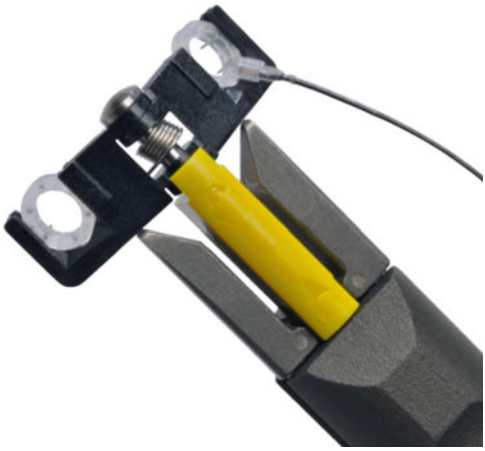

Fig. 18.5 Synovis flow coupler [17]

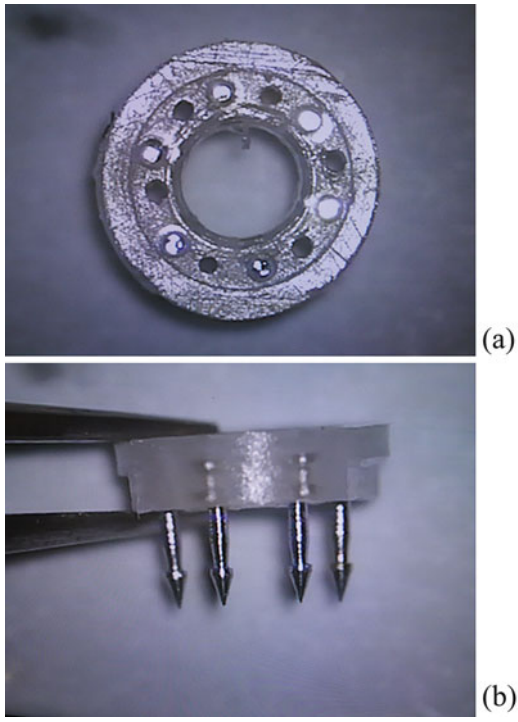

Fig. 18.6 Micrographs of coupling device (**a**) plan and (**b**) side elevation [18]

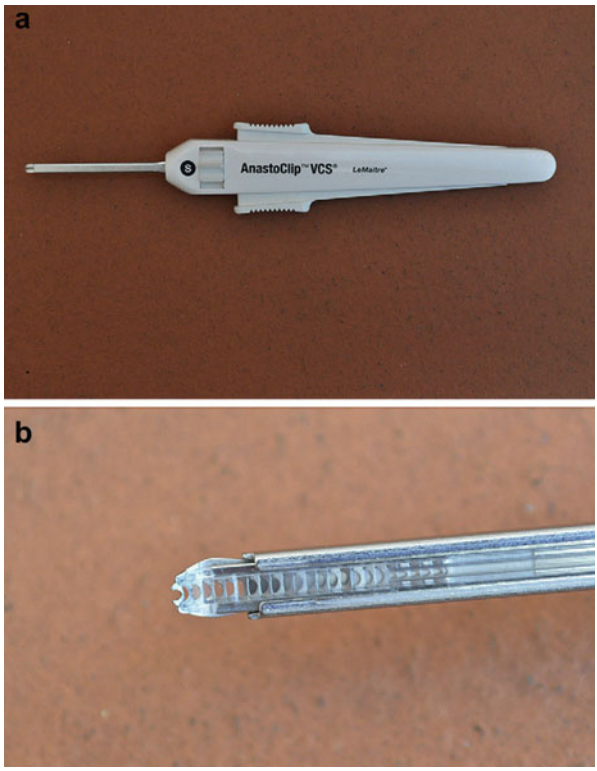

Fig. 18.7 VCS AnastoClip device [22]

18.2.4 Anastomotic Clips

Bikfalvi is credited with publishing the first clipped vascular anastomosis in 1953 [19], after which there have been several evolutions. Two principal anastomotic clip systems are commercially available for performing microanastomosis, although neither is as widely accepted as the aforementioned coupler.

The first is a non-penetrating clip known as the vessel closure system (VCS)[4] (Fig. 18.7), which involves placing sequential clips across the anastomotic site held in position temporarily by microsutures. This has been reliably used in some centres with excellent results [20–22] (Fig. 18.8).

The microclips are manufactured from medical grade titanium in two sizes 0.9 and 1.4 mm. Each is available as part of a self-reloading applicator which holds 25 clips. During clip placement the vessel walls are everted using a specific pair of forceps called Sliding Everting Forceps,[5] and these permit differential movement of each of the vessel walls allowing perfect alignment prior to clip application [23].

[4] Autosuture, United States Surgical Corporation, Norwalk, CT, USA

[5] SEF® Warm Co., Mechelen, Belgium

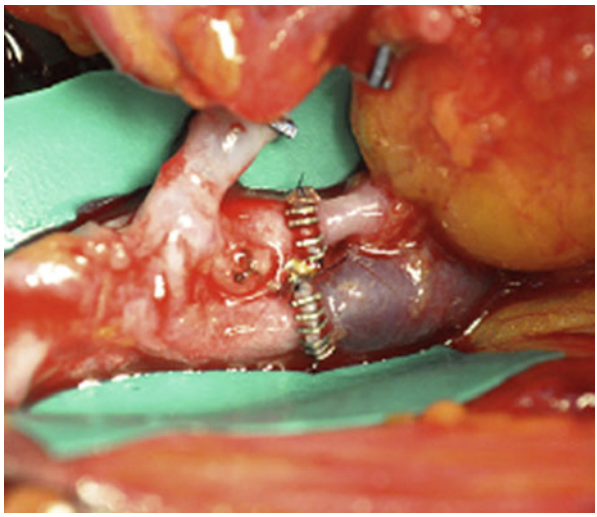

Fig. 18.8 VCS AnastoClips in for arterial and venous microanastomoses [22]

In contrast to the VCS, the second microclip device described here, known as the U-Clip,[6] comprises penetrating clips that pass through the vessel wall. Whilst this device negates the need for sutures, the clips remain present within the lumen, unlike those of the VCS. The U-Clips are less prevalent in routine clinical practice but have some studies endorsing their use [24–26].

The U-Clip itself is composed of an alloy of nickel and titanium known as nitinol. It is manufactured in a spiral-like configuration and possesses the characteristic of superelasticity. This allows the alloy clip to be flexible whilst maintaining a constant stress. The clip is applied via a delivery system comprising of a suture needle (available in equivalent sizes to standard microsurgical needles) attached to a flexible suture-like member (Fig. 18.9). A release mechanism is situated at the opposite end of the device, which is triggered after the clip has been placed in the desired position within the microanastomosis. Once the clip is deployed, it returns to its original configuration as a coil, which acts in the same way as a knotted suture (Fig. 18.10). Due to its superelasticity, the clip exerts a preset and consistent tension thereby eliminating the variance seen in hand-tied sutured anastomoses.

18.3 Computational Simulation of Microvascular Coaptation

This section describes use of computational fluid dynamics (CFD) for simulating flow through microvascular anastomoses. In particular we focus on vessels coapted using standard interrupted sutures and those anastomosed with the commercially available ring-pin coupling device.

[6]Medtronic, Inc.; Minneapolis, MN, USA

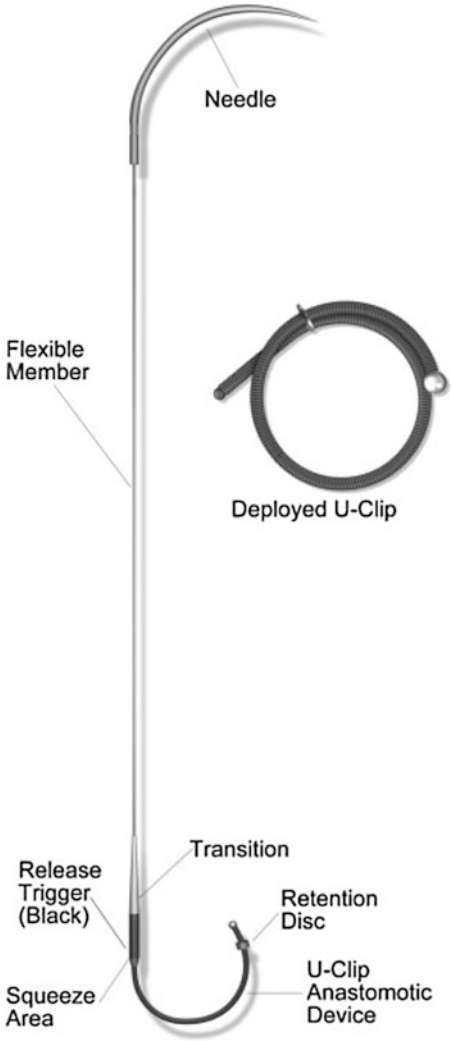

Fig. 18.9 U-Clip delivery system assembly [26]

Fig. 18.10 U-Clip after release from delivery system [27]

18.3.1 Background of CFD for Blood Flow

CFD is a method employed to predict flow fields in a particular circumstance by solving a series of mathematical equations. It enables information to be gained about particular flow patterns that would be impossible to create experimentally. Experiments investigating physiological flows, particularly related to haemodynamics, were pioneered by Perktold and his research group in the latter twentieth century [28–31]. As developments progressed with medical imaging, the potential for integrating the two techniques became apparent, producing realistic vascular geometries [32–34]. Comprehensive reviews of image-based CFD for vascular applications have been compiled by both Steinman [35] and Taylor [36]. A further consideration for CFD within blood vessels is the influence of surgical intervention, in this case an anastomosis. It is inevitable that joining two vessel ends by any means will produce a change in shape of the vessel lumen and as such will affect intravascular flow. A range of studies have been performed to investigate flow in differing vascular anastomoses [37]; however, there is little published work investigating microvascular flows.

18.3.2 CFD for Simulating Flow in Microvascular Anastomoses

Few studies have explored the haemodynamics of microvascular anastomoses, although there is steady progress being made in this area. Initial studies used finite element models (FEM) for comparison of end-to-end and end-to-side anastomoses [38, 39], with the specifics of end-to-end anastomosis with size discrepancy being investigated by another group [40]. Whilst the aforementioned studies have employed computational simulation techniques to research anastomotic flow patterns, neither has explored the specific method of coaptation, namely, sutures or a device, and whether this influences flow.

18.3.3 Simulation in Coapted Vessels Using Sutures and Couplers

It is the absence of data surrounding microanastomotic flow, with regard to the method of coaptation, which led our group to investigate this further. The first study was intended to compare haemodynamics in idealized anastomoses performed using sutures and the ring-pin coupling device [41]. This demonstrated a significantly less thrombogenic flow profile in the coupled anastomosis (Fig. 18.11a, b).

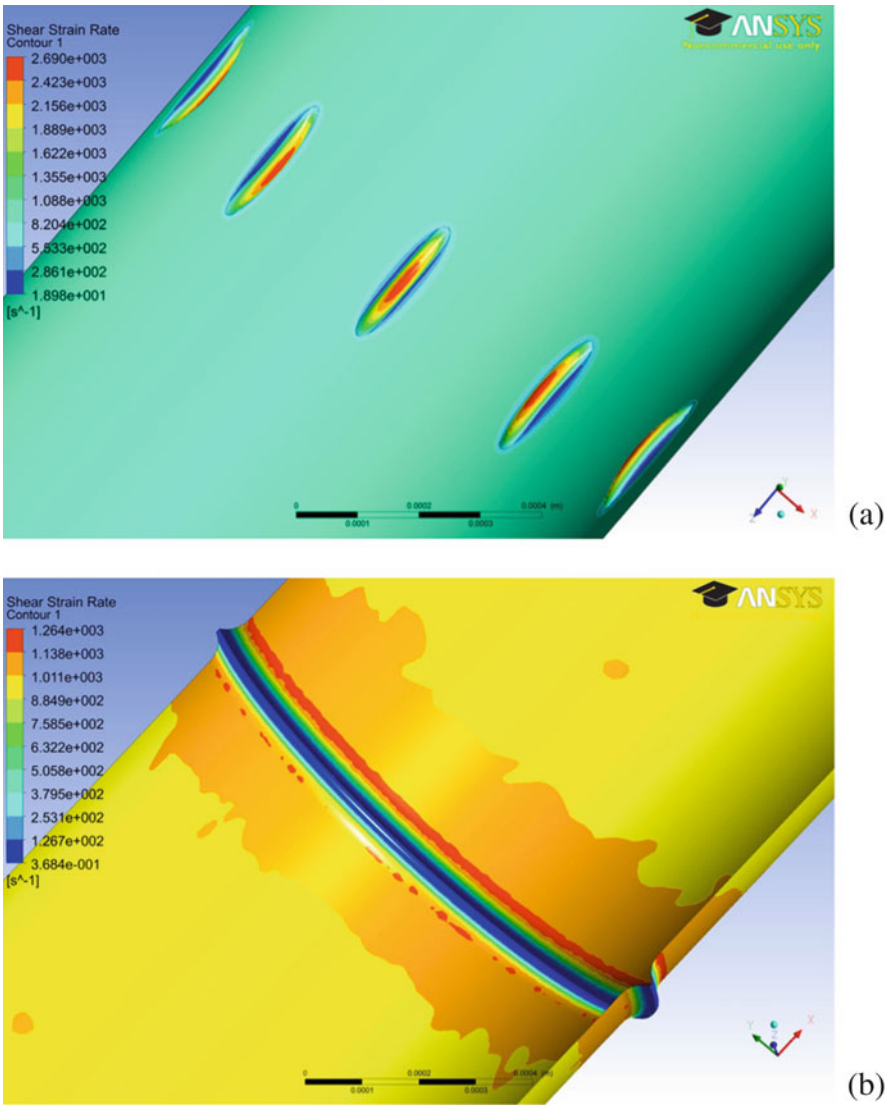

Fig. 18.11 SSR profile of (**a**) sutured anastomosis and (**b**) coupled anastomosis [41]

More recently, we developed our sutured anastomosis simulation to more accurately reflect the variation seen in suture position [42], concluding that severe angles and close suture spacing increase the local shear strain rates and with it the potential for platelet activation and blood clot formation (Fig. 18.12a, b).

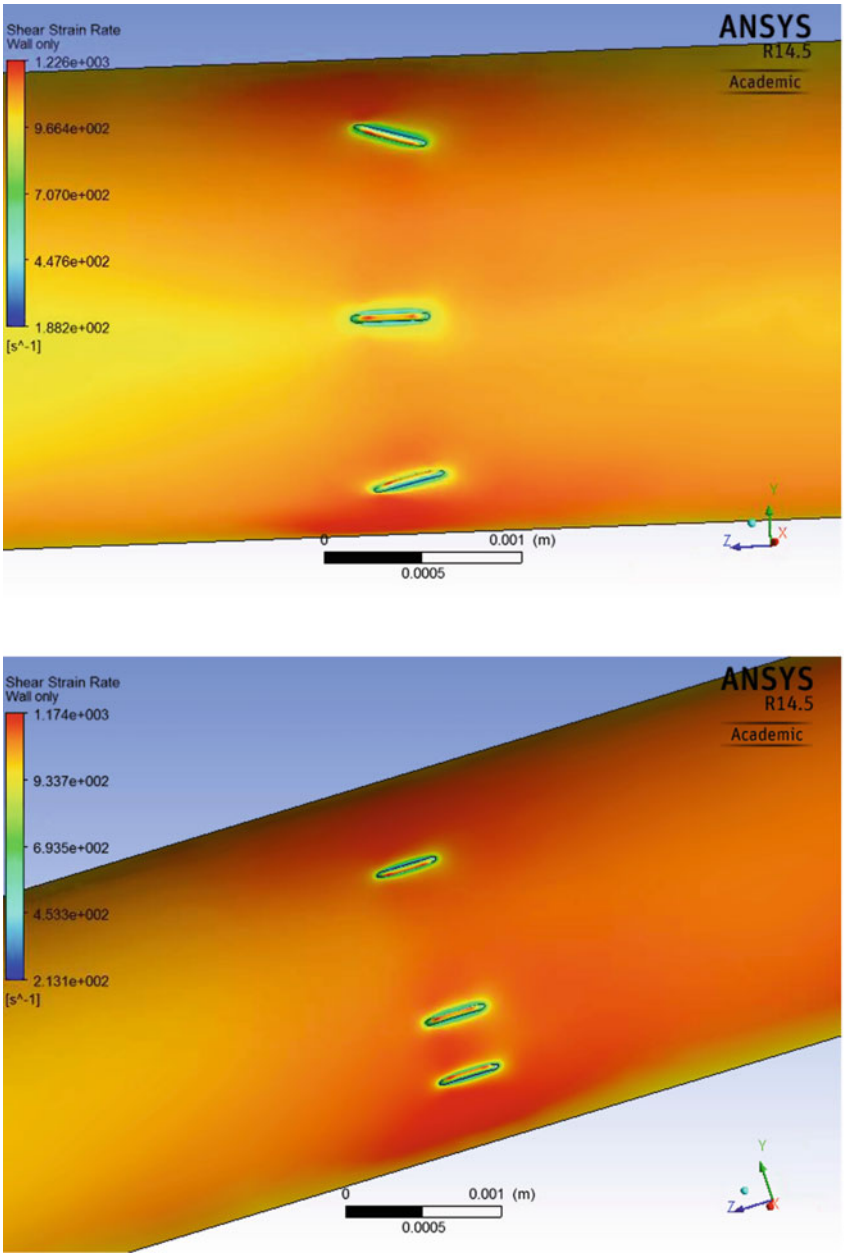

Fig. 18.12 SSR profile in sutured anastomoses investigating effect of suture angle (**a**) and suture spacing (**b**) [42]

18.3.4 Future Directions

Whilst our work in this field is novel and may serve to reinforce good practice or perhaps even influence change, we recognize that it remains largely idealized. In an attempt to make our simulations more physiologically representative, further consideration will be given to factors such as the influence of pulsatile flow, the material properties of the suture and/or coupling device and their fluid-structure interaction, and the influence of vessel wall compliance.

Acknowledgements The authors would like to thank the following companies for specifically providing information pertaining to the manufacture of their products: (1) Surgical Specialties Corporation, 50 Braintree Hill Office Park, Suite 101, Braintree, MA 02184, USA, (2) Ethicon Inc., Johnson & Johnson, Somerville, NJ, USA.

References

1. Jassinowsky A (1889) Die Arteriennhat: Eine experimentelle Studie. Inaug Diss Dorpat. 1–103.
2. Mackenzie D (1973) The history of sutures. Med Hist 17(2):158–168
3. Rickard RF, Hudson DA (2014) A history of vascular and microvascular surgery. Ann Plast Surg 73(4):465–472
4. Zeebregts CJ, Heijmen RH, van den Dungen JJ, van Schilfgaarde R (2003) Non-suture methods of vascular anastomosis. Br J Surg 90(3):261–271
5. Pratt GF, Rozen WM, Westwood A, Hancock A, Chubb D, Ashton MW et al (2012) Technology-assisted and sutureless microvascular anastomoses: evidence for current techniques. Microsurgery 32(1):68–76
6. Wain RAJ, Hammond D, McPhillips M, Whitty JPM, Ahmed W (2016) Microvascular anastomoses: suture and non-suture methods. In: Ahmed W, Jackson MJ (eds) Surgical tools and medical devices. Springer, Cham, Germany, pp 545–562
7. Suture Needles | Surgical Needle Manufacturer | Dolphin Sutures [Internet] (2016) Available from: http://www.dolphinsutures.com/suture-needles
8. Suture-image 1_small.jpg [Internet] (2016) Available from: https://www.aesculapusa.com/assets/base/image/aic/products/woundclosure/sutures/Suture-image 1_small.jpg
9. Ostrup LT (1976) Anastomosis of small veins with suture or Nakayama's apparatus. A comparative study. Scand J Plast Reconstr Surg 10(1):9–17
10. Ostrup LT, Berggren A (1986) The UNILINK instrument system for fast and safe microvascular anastomosis. Ann Plast Surg 17(6):521–525
11. Nakayama K et al (1962) A simple new method for small vessel anastomoses (free autograft of the sigmoid included). Surgery 52:918–931
12. Payr E (1900) Beitra¨ge zur Technik der Blutgefa¨ss- und Nervennaht nebst Mittheilungen u¨ber die Verwendung eines resorbirbaren Metalles in der Chirurgie. Arch Klin Chir (62):67Y93
13. Fernández Díaz J, Naval Gías L, Sastre Pérez J, Rodríguez Campo F, Muñoz-Guerra M (2012) Sutura mecánica microvascular en cirugía reconstructiva de cabeza y cuello. Rev Esp Cir Oral Maxilofac 34(4):145–150
14. Synovis Micro | Products | GEM Microvascular Anastomotic COUPLER [Internet] (2016) Available from: http://www.synovismicro.com/lsds/sm/products/gem_microvascular_anastomotic_coupler.page?

15. Jandali S, Wu LC, Vega SJ, Kovach SJ, Serletti JM (2010) 1000 consecutive venous anastomoses using the microvascular anastomotic coupler in breast reconstruction. Plast Reconstr Surg 125(3):792–798
16. Synovis Micro | Products | GEM Flow COUPLER Device and System [Internet] (2016) Available from: http://www.synovismicro.com/lsds/sm/products/gem_flow_coupler_device_and_system.page?
17. flowcoupler.jpg [Internet] (2016) Available from: http://www.lmtsurgical.com/wp-content/uploads/flowcoupler.jpg
18. Wain RAJ (2013) Computational modelling of blood flow through sutured and coupled microvascular anastomoses [Internet] [Master of Science, by Research]. University of Central Lancashire. Available from: http://www.uclan.ac.uk/research/index.php
19. Bikfalvi A, Dubecz S (1953) Observations in animal experiments with mechanised vessel suture. J Int Chir 13(5):481–496
20. Zeebregts C, Acosta R, Bölander L, van Schilfgaarde R, Jakobsson O (2002) Clinical experience with non-penetrating vascular clips in free-flap reconstructions. Br J Plast Surg 55 (2):105–110
21. Zeebregts CJ, Kirsch WM, van den Dungen JJ, Zhu YH, van Schilfgaarde R (2004) Five years' world experience with nonpenetrating clips for vascular anastomoses. Am J Surg 187 (6):751–760
22. Reddy C, Pennington D, Stern H (2012) Microvascular anastomosis using the vascular closure device in free flap reconstructive surgery: a 13-year experience. J Plast Reconstr Aesthet Surg 65(2):195–200
23. De Lorenzi F, van der Hulst RRWJ, Boeckx WD (2002) VCS auto suture stapled microvascular anastomoses in lower leg free flaps. Plast Reconstr Surg 109(6):2023–2030
24. Taylor J, Katz R, Singh N (2006) Use of the U-clip for microvascular anastomosis. Microsurgery 26(8):550–551
25. Baynosa RC, Stutman R, Mahabir RC, Zamboni WA, Khiabani KT (2008) Use of a novel penetrating, sutureless anastomotic device in arterial microvascular anastomoses. J Reconstr Microsurg 24(1):39–42
26. Maher JL, Roehl KR, Mahabir RC (2012) A prospective evaluation of U-clips for arterial microvascular anastomoses. J Reconstr Microsurg 28(8):543–548
27. Raja SG, Dreyfus GD (2004) Off-pump coronary artery bypass surgery: to do or not to do? Current best available evidence. J Cardiothorac Vasc Anesth 18(4):486–505
28. Perktold K, Florian H, Hilbert D (1987) Analysis of pulsatile blood flow: a carotid siphon model. J Biomed Eng 9(1):46–53
29. Perktold K, Peter R (1990) Numerical 3D-stimulation of pulsatile wall shear stress in an arterial T-bifurcation model. J Biomed Eng 12(1):2–12
30. Perktold K, Nerem RM, Peter RO (1991) A numerical calculation of flow in a curved tube model of the left main coronary artery. J Biomech 24(3–4):175–189
31. Perktold K, Resch M, Peter RO (1991) Three-dimensional numerical analysis of pulsatile flow and wall shear stress in the carotid artery bifurcation. J Biomech 24(6):409–420
32. Steinman DA (2002) Image-based computational fluid dynamics modeling in realistic arterial geometries. Ann Biomed Eng 30(4):483–497
33. Leuprecht A, Perktold K, Kozerke S, Boesiger P (2002) Combined CFD and MRI study of blood flow in a human ascending aorta model. Biorheology 39(3–4):425–429
34. Antiga L, Piccinelli M, Botti L, Ene-Iordache B, Remuzzi A, Steinman DA (2008) An image-based modeling framework for patient-specific computational hemodynamics. Med Biol Eng Comput 46(11):1097–1112
35. Steinman DA, Taylor CA (2005) Flow imaging and computing: large artery hemodynamics. Ann Biomed Eng 33(12):1704–1709
36. Taylor CA, Steinman DA (2010) Image-based modeling of blood flow and vessel wall dynamics: applications, methods and future directions: 6th international bio-fluid mechanics

symposium and workshop, March 28-30, 2008 Pasadena, California. Ann Biomed Eng 38 (3):1188–1203
37. Migliavacca F, Dubini G (2005) Computational modeling of vascular anastomoses. Biomech Model Mechanobiol 3(4):235–250
38. Al-Sukhun J, Lindqvist C, Ashammakhi N, Penttilä H (2007) Microvascular stress analysis. Part I: Simulation of microvascular anastomoses using finite element analysis. Br J Oral Maxillofac Surg 45(2):130–137
39. Al-Sukhun J, Penttilä H, Ashammakhi N (2011) Microvascular stress analysis: Part II. Effects of vascular wall compliance on blood flow at the graft/recipient vessel junction. J Craniofac Surg 22(3):883–887
40. Rickard RF, Meyer C, Hudson DA (2009) Computational modeling of microarterial anastomoses with size discrepancy (small-to-large). J Surg Res 153(1):1–11
41. Wain RAJ, Whitty JPM, Dalal MD, Holmes MC, Ahmed W (2014) Blood flow through sutured and coupled microvascular anastomoses: a comparative computational study. J Plast Reconstr Aesthetic Surg 67(7):951–959
42. Wain RAJ, Hammond D, McPhillips M, Whitty JPM, Ahmed W (2016) Microarterial anastomoses: a parameterised computational study examining the effect of suture position on intravascular blood flow. Microvasc Res 105:141–148

Index

M.J. Jackson, W. Ahmed (eds.), *Micro and Nanomanufacturing Volume II*,
DOI 10.1007/978-3-319-67132-1